Sheffield Hallam University

A Sheffield Hallam University thesis

A study into the formation of patina on copper-containing antifouling marine coatings

Matthew Paul Kitchen

A thesis submitted in partial fulfilment of the requirements of

Sheffield Hallam University

for the degree of Doctor of Philosophy

November 2021

I hereby declare that:

1. I have not been enrolled for another award of the University, or other academic or professional organisation, whilst undertaking my research degree.

2. None of the material contained in the thesis has been used in any other submission for an academic award.

3. I am aware of and understand the University's policy on plagiarism and certify that this thesis is my own work. The use of all published or other sources of material consulted have been properly and fully acknowledged.

4. The work undertaken towards the thesis has been conducted in accordance with the SHU Principles of Integrity in Research and the SHU Research Ethics Policy.

5. The word count of the thesis is 75,761.

Name	*Matthew Paul Kitchen*
Date	*November 2021*
Award	*PhD*
Faculty	*College of Business, Technology and Engineering*
Director(s) of Studies	*Dr Oliver Lewis*

Abstract

Antifouling (fouling control) coatings are used to protect underwater marine structures from the colonisation by organisms which can increase a structure's mass and reduce the efficiency of vessels. Antifouling coatings, which are used to prevent their attachment, contain biocidal pigments, such as cuprite (Cu_2O) readily releasing Cu^{2+} ions into the environment, which are toxic to fouling organisms at concentrations of 10 $\mu g.cm^{-2}.day^{-1}$. However, these coatings may form a blue-green patina surface layer, leading to unnecessary maintenance operations due to the perceived reduction in protection and aesthetics, costing both time and money. Therefore, accelerated testing methodologies are required to reproduce naturally formed patina, allowing the patination characteristics of different coating formulations to be observed, with the aim of reducing patina formation.

While patination of copper in the marine environment has been extensively researched, there is less information on the patination of antifouling coatings. The analysis of patinated paint flakes removed from in-service vessels found that clinoatacamite ($Cu_2Cl(OH)_3$) was the most commonly detected copper patina.

DC electrochemical tests were then carried out to determine the most appropriate environments that would result in an acceleration in antifouling coating patination. Clinoatacamite developed in chloride containing electrolytes, with the 10% sodium chloride electrolyte having the highest corrosion rate, while a further increase in corrosion rate was observed in elevated temperatures up to 55°C. Analysis of the Pourbaix diagrams for the different sodium chloride concentrations and temperatures also found that the stability domain for $Cu_2Cl(OH)_3$ occurred between pH 6 and 8.5 with a neutral pH being selected for testing of the coatings.

The blue-green clinoatacamite patina found on in-service vessels was reproduced when testing under immersion, evaporation, and salt spray laboratory conditions. The quickest patination rate and highest levels of clinoatacamite were observed in the neutral 10% sodium chloride electrolyte under immersion conditions. This was associated with the increase in clinoatacamite density due to the reduction in patina particle size and an overall increase in the thickness of an adherent patina layer. This testing procedure allows for the rapid qualification of different antifouling coating formulas and their resistance to patina formation, and therefore reduce the need for the reapplication of coatings prior to their expected end of service life.

Acknowledgements

I would firstly like to express my deepest gratitude to my director of studies Dr Oliver Lewis, who not only found an interesting topic to study and an industrial partner to help support the program, also suggested that I pursue a PhD. His guidance, support and unending patience were invaluable. To Dr Hywel Jones for helping to develop my understand the different aspects of the PhD.

I would like to thank International Paints (AkzoNobel) and Dr Alistair Finnie without which access to real world samples would not be possible, while his passion and understanding of the project was infectious.

I would like to thank the technical and administrative staff in MERI without whom nothing could be done.

I would show my appreciation to Dr Nicholas Farmilo for allowing me the time and space to complete this PhD whilst offering his unending enthusiastic support, guidance, and wisdom over the years. I hope I can live up to his expectations.

Table of Contents

[ix]

List of Figures

[xiii]

[xvi]

[xvii]

	mapped area after being exposed to the neutral 10% electrolyte at 45°C under different immersion times.	
216	– BSE micrographs of the cross-section through the modified BQA 644 coating including an elemental composite image, chlorine and copper maps and the semi-quantitative EDX analysis of the mapped area after being exposed to the neutral 30% electrolyte at 45°C under different immersion times.	478
217	– BSE micrographs and semi-quantitative EDX analysis of the surface of the BQA 644 coating exposed to the neutral electrolytes containing different sodium chloride concentrations at 45°C under evaporating conditions after the electrolyte had fully evaporated up to 672 hours.	479
218	– BSE micrographs and semi-quantitative EDX analysis of the surface of the BQA 644 coating exposed to the neutral electrolytes containing different sodium chloride concentrations at 45°C under evaporating conditions after the electrolyte had fully evaporated up to 408 hours.	480
219	– BSE micrographs and semi-quantitative EDX analysis of the surface of the BQA 644 coating exposed to the neutral salt spray environment after different immersion times.	481
220	– BSE micrographs and semi-quantitative EDX analysis of the surface of the modified BQA 644 coating exposed to the neutral salt spray environment after different immersion times.	482
221	– EDX spectra of the surface of the BQA 644 and modified BQA 644 coatings following the salt spray testing after different exposure times.	483

List of Tables

[xx]

Chapter 1: Introduction

Biofouling is the process in which marine organisms attach themselves to hard underwater surfaces and is of particular concern when they become attached to manmade structures, such as offshore foundations for wind farms and oil platforms. Extra design considerations of these structures are required to accommodate the increased load caused by the fouling community, raising their cost. The colonisation of underwater and splash zone metallic structures may also allow for microbial induced corrosion to occur, leading to localised pitting corrosion, weakening the structure, and therefore reducing its service life. Furthermore, fouling may reduce the cathodic corrosion protection of metallic structures should the sacrificial anodes become fouled, which can increase their corrosion rate.

Shipping is a major industry where fouling is detrimental to the efficiency of marine vessels, as it can increase the hydrodynamic drag, reducing the maximum speed and increase the fuel consumption and costs. Therefore, antifouling or fouling control coatings have been developed to prevent marine organisms from settling by making the local environment toxic, killing the organism before it has chance to become established. There are a wide range of biocidal pigments that may be included in antifouling coatings offering preferential toxicity to different organisms. However, the most widely used biocidal pigment in antifouling coatings is cuprite (Cu_2O) as it is highly effective at protecting underwater surfaces against fouling. When cuprite is oxidised in water, cupric ions (Cu^{2+}) are released, which is toxic when consumed by marine organisms in sufficiently high concentrations.

One concern when using cuprite, or any other toxic pigment, as an antifoulant is the ecological impact on the marine biosphere. Copper is an essential element for life, however when the concentration of copper in the organism becomes too high it becomes toxic. For the species that are likely to attach to ships' hulls this can occur at relatively low concentrations of cupric ions. When these species die, they are likely to be consumed by other organisms, which can lead to the bioaccumulation of copper in the food chain. However, the amount of copper that is released into the environment from natural sources is thought to be approximately 100 times greater than that released from copper containing antifouling paints (Pidgeon, 1993). Swain et al., (1982) observed that the natural copper concentration in the open ocean was at 0.3 $\mu g. L^{-1}$ increasing to 3.0 $\mu g. L^{-1}$ in coastal waters and 24 $\mu g. L^{-1}$ in industrial wastewater. Therefore, the release of cupric ions from antifouling coatings is thought to have a minimal impact to the marine biosphere.

Cuprite has a reddish colour and is therefore generally used in paints with a similar red or brown colour. However, when the cupric ions react with the chloride ions in the environment, they form an insoluble copper chloride compound. These compounds tend to have a blue-green appearance which can precipitate onto the painted surface. The formation of the copper chloride compound could have a two-fold effect of reducing the aesthetics of the coating and reducing the cuprite release rate (Lindner, 1988). This can lead the owners to take their ship to dry dock to have the copper chloride product removed or the hull coated, costing both time and money. The reaction mechanism allowing the copper chloride product to deposit onto ships' hulls is poorly understood therefore further study is required to identify what the copper chloride product is and ways to accelerate its formation for testing.

[2]

1.1 Aims and Objectives

The aims of the project are to develop an understanding of the patination process and to develop accelerated patination test methods to determine an antifouling coatings' resistance to patination, to improve the coating against patination to inform and improved future coating formulations.

The objectives are:

- To review the literature on patination of copper in marine environments and identify the variables which can accelerate patination.

- To identify in-service patina compounds using various compositional analysis techniques including XRD, SEM and EDX.

- To patinate antifouling pigments and coatings to reproduce in-service patina compounds, qualifying the conditions required for patination to occur.

- To develop an accelerated experimental package to predict the effectiveness of a coating against patination prior to commercialisation.

Chapter 2: Literature Review

2.1   What Is Fouling?

Marine biofouling is a natural phenomenon where marine organisms such as microbial slimes, macroalgae and barnacles naturally adhere to, colonise, and grow on hard unprotected underwater surfaces (Woods Hole Oceanographic Institute, 1952a). This process can be undesirable, especially on man-made structures, with the colonisation process starting within hours following the immersion of a clean surface. It is estimated that there are more than 40,000 species of fouling organisms which can be categorised as bacteria, flora, or fauna (Almeida et al., 2007; Salta et al., 2009; Woods Hole Oceanographic Institute, 1952a).

Fouling organisms naturally live in shallow coastal waters (Marine Corrosion Sub-Committee, 1944), taking advantage of the heat, light and abundance of nutrients when compared to the deep ocean (Salta et al., 2009). Therefore, the colonisation of ships hulls commonly occurs when they are within these waters.

The most frequently recorded fouling organism on a non-toxic surface is the attached or sessile type (Woods Hole Oceanographic Institute, 1952a). The major hull biofouling organisms have been identified as barnacles, algae, bryozoans, cnidarians, ascidians, and annelids (Salta et al., 2009) which settle in their larvae or spore form, taking nutrients from their local environment. As they grow, they secrete a powerful adhesive over a larger area, securing themselves to the substrate (Anderson et al., 2003; Callow & Callow, 2002), making their detachment increasingly difficult through external means, such as from ocean currents. Of the fouling groups identified, barnacles tend to be the most frequently recorded species (Floerl et al., 2010; Salta et al., 2009; Woods

Hole Oceanographic Institute, 1952a), becoming established after a four-week period. Motile species, such as zoospores may also be present in the fouling community however, as they are able to detach from the hard surfaces and move to more suitable areas where nutrients are more plentiful (Callow & Callow, 2006), and are therefore less likely to become detected.

2.1.1   Colonisation Of Hard Underwater Surfaces By Marine Organisms

It is traditionally believed fouling occurs in four stages, following a successional establishment of the community. The four stages include: the formation of the conditioning film, the attachment and growth of bacteria, the development of unicellular and finally multicellular organisms (Figure 1). These stages will be considered in more detail in the following sections.

Substrate	Conditioning film	Primary Colonisers	Secondary Colonisers	Tertiary Colonisers
	Organic material	Micro fouling organism		Macro fouling organisms
		Bacteria	Unicellular eukaryotes	Multi Cellular organisms
Initial	0 – 1 hour	1 – 24 hours	1 – 7 days	1 – 3 weeks
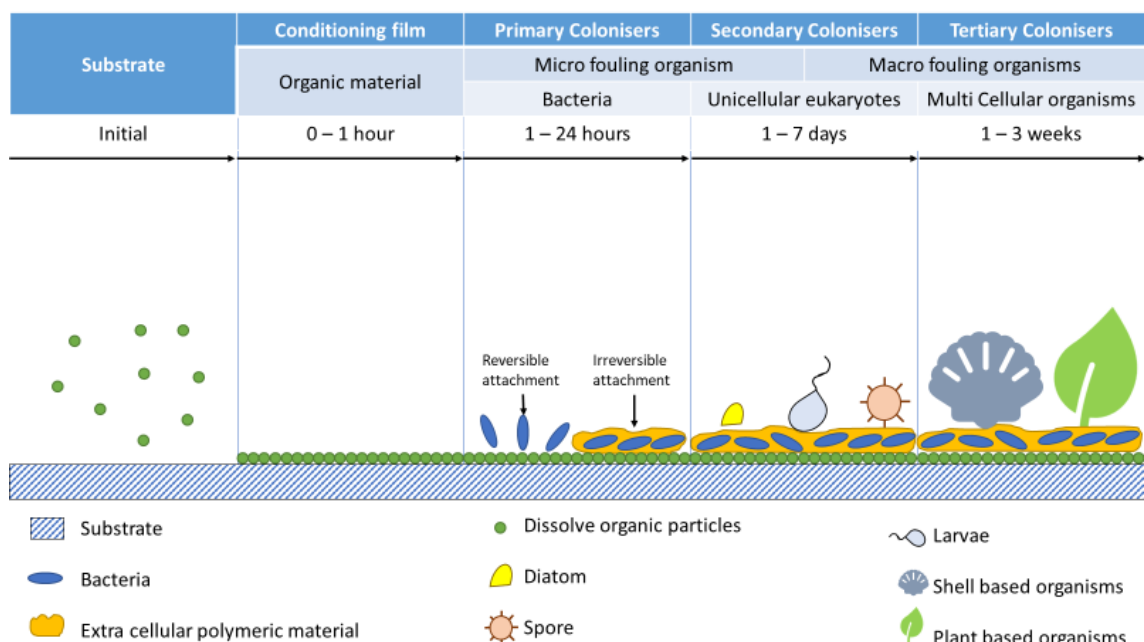
Figure 1 – Colonisation of hard underwater surface by marine organisms, adapted from Abarzua & Jakubowski, (1995), Alberto J Martín-Rodríguez et al. (2015) and Chambers et al. (2006)

2.1.1.1 *The formation of the conditioning film*

The first stage of the colonisation process occurs soon after the exposure of the substrate to the marine environment, where Baier (1972) found high concentrations of protein after 10 minutes. While its concentration varied with time where Little, Brenda & Zsolnay (1985) determined that the substrate was covered with organic molecules with an area density of 8 $ng.mm^{-2}$ after 15 minutes, rising to 10 $ng.mm^{-2}$ after 1 hour. Similar to what was observed in Taylor et al. (1997), Baier (1980), Baier (1981) and Marszalek et al. (1979).

This is where a complex mixture of organic and inorganic molecules, are adsorbed through physiochemical interactions between the substrate and surface-active solutes (Little, Brenda & Zsolnay, 1985; Maki et al., 1990; Taylor et al., 1997), forming the "conditioning film". The composition and structure of the conditioning film can vary depending on the substrate material (Little, Brenda & Zsolnay, 1985; Maki et al., 1990; Taylor et al., 1997), molecules available in the local environment (Hwang et al., 2012; Bakker et al., 2003; Jain & Bhosle, 2009), the geographical location (Catao et al., 2021), the length of time immersed (Maki et al., 1990), and the time of year (Garg et al., 2009; Jain & Bhosle, 2009). However, it tends to be dominated by the presence of degraded organic material including; nucleic acid, aromatic acid, humic material, lipids, polysaccharide (Taylor et al., 1997), uronic acid, proteins and aldose with carbohydrates being the most abundant (Garg et al., 2009; Jain & Bhosle, 2009).

Furthermore, the conditioning film may modify the surface properties of the substrate making it more favourable to the bacterial colonisation. For example, Taylor et al. (1997) determined that the least compatible surfaces for colonisation were those with

an intermediate critical surface tension of 20-30 $mN.m^{-1}$ which was associated with the poor bio-adhesiveness of these surfaces (Baier et al., 1968; Gucinski & Baier, 1983). While Thome et al. (2012) determined that hydrophobic surfaces became more hydrophilic and hydrophilic surfaces became more hydrophobic over time. This may alter the critical surface tension sufficiently to make the surface more compatible to the absorption of organic molecules which can promote the attachment and growth of bacteria (Jain & Bhosle, 2009).

The presence of the conditioning film is not a prerequisite for the attachment of biofouling organisms (Callow & Callow, 2006), however it may alter the surface of the substrate sufficiently to provide preferential sites for the fouling organisms to attach (Jain & Bhosle, 2009; Cao et al., 2011; Colwell, 1983).

2.1.1.2 *Primary Colonisers - Bacterial Settlement*

Following the formation of the conditioning film primary colonisers such as bacteria attach to the substrate, occurring between 1 and 24 hours after the exposure of the substrate to the environment (Fletcher & Loeb, 1979; Wahl, 1989). There are two phases to bacterial colonisation an instantaneous reversible phase (adsorption) and a time dependant irreversible phase (adhesion) (Marshall et al., 1971). The first phase is controlled by physical forces such as Brownian motion (Yebra et al., 2004), electrostatic interaction (Fletcher & Loeb, 1979), gravity (Walt et al., 1985) and Van-der-Waals forces (Cheng et al., 2019). The second phase is the irreversible attachment of the bacteria to the substrate and its subsequent growth (Hinsa et al., 2003).

Bacteria must penetrate a well structure layer of H_2O molecules, 40-100 μm thick, by means of micro-turbulence, bacterial motility, or diffusion to settle on the substrate

(Wahl, 1989). As the bacteria approaches the substrate physical forces interact with the bacteria, of which gravity may be of most importance, which acts in synergy with other forces enhancing bacterial adhesion (Walt et al., 1985). However external factors such as kinetic forces from the flow speed, Van-der-Waals attractive and electrostatic repulsive forces may influence gravity's effectiveness.

Most bacteria and conditioning films are negatively charged resulting in two competing forces acting on the bacteria as it approaches the substrate. The Van-der-Waals force, which attracts bacteria within a few hundred nanometres to the substrate, and a repulsive electrostatic force, immobilising it within 3-20 nm of the substrate (Fletcher et al., 1984). Polysaccharide fibrils are then produced to overcome the electrostatic repulsion anchoring and pulling the bacteria towards the substrate (Marshall et al., 1971), resulting in the irreversible settlement phase. This polymeric binding material modifies the substrate, reducing the rate of attachment once a monolayer of bacteria has formed (Fletcher & Loeb, 1979).

The fouling community is constantly evolving due to external factors such as predation, competition, and physical disturbance, resulting in variations in the types of bacteria present on the substrate material (Chunyan et al., 2012). However, there is generally a sequential colonisation of bacteria, where rod shaped pioneers arrive first followed by coccoid, stalked, and filamentous forms of bacteria (Wahl, 1989).

2.1.1.3 *Secondary colonisers – Unicellular Micro-organisms*

Secondary colonising species such as yeasts, fungi, protozoa, diatoms, and macroalgae spores (Caron & Sieburth, 1981; Cuba & Blake, 1983; de Carvalho, Carla 2018; Marshall et al., 1971; O'Neill & Wilcox, 1971) may settle on the substrate following the

formation of the conditioning film and bacterial growth within hours to days of immersion, where diatoms tending to dominate the surface (Caron & Sieburth, 1981). However, O'Neill & Wilcox, (1971) observed no association between the bacterial development and the diatom settlement and Maki et al. (1990) found that bacteria had no effect on larva attachment when compared to clean surfaces. Furthermore, diatoms may attach directly to clean surfaces in the absence of bacteria after a few hours' exposure (Cooksey & Wigglesworth-Cooksey, 1995). Diatoms may passively foul submerged surfaces after 8 hours immersion (O'Neill & Wilcox, 1971) requiring external forces such as gravity, water currents, turbulence as well as electrostatic and Van-der-Waals forces for it to become attached (Cao et al., 2011).

2.1.1.4 *Tertiary colonisers – Multicellular Macro-organisms*

Tertiary colonisation of multi-cellular macro-organisms such as macroalgae spores, barnacle larvae, bryozoans, molluscs, polychaete, tunicates, and coelenterates (Abarzua & Jakubowski, 1995) are considered to be the final phase in marine biofouling. As macroalgae spores develop into a macrofouling organism once matured they can belong both micro and macrofouling communities (Von Oertzen et al., 1989). These tertiary colonisers attach to the microfouling film (Abarzua & Jakubowski, 1995) creating a 3-dimensional fouling community, especially as they begin to grow. These species can form within several days to weeks following immersion and are most damaging as they reduce the sailing efficiency (Wahl, 1989).

Although some larvae from biofouling species have been able to colonise a substrate prior to the formation of a conditioning film (Hung et al., 2005; Lau et al., 2003; Maki

et al., 1990) it is generally agreed that it is the conditioning film formation is the first stage in the fouling processes (Chambers et al., 2006; Costerton, 1999).

2.2 Biofouling On Marine Vessels

The significance of marine biofouling in the marine industry has been understood for millennia with one of the first recordings of fouling written by Greek essayist Plutarch (46-119 C.E.). Plutarch (2018) wrote *"… when weeds, ooze and filth stick upon its sides the stroke of the ship is more obtuse and weak…"* indicating the difficulty of rowing a boat covered with fouling organisms. A small increase in the surface roughness of a marine vessels hull, due to fouling, can significantly increase the frictional drag forces, which increases the fuel consumption and carbon emissions, decreasing its range and top speed.

2.2.1 Forces Acting On Marine Vessels

As marine vessels sail through the ocean forces act upon the vessels hull which need to be overcome to allow it to move. The major resistance mainly comes from below the waterline in the form of the hydrodynamic drag which can be split into two interdependent forces "Frictional" or "Viscous" resistance and "Residual" or "Wave-making" resistance.

The viscosity of the medium the vessel is travelling through causes the frictional resistance component to form as the speed it travels around the hull varies due to the formation of eddy waves, observed at each change in section, and turbulence, absorbing energy from the movement of the vessel. The size, shape, length, surface roughness and speed of the vessel affects the magnitude of the frictional component. At low to medium speeds (up to 20 knots) this component accounts for 70-90% of the

total drag, dropping to 40% at higher speeds (between 25 and 35 knots) (Lackenby, 1962; Lindholdt et al., 2015). For design purposes, the British Admiralty traditionally allowed for an increase in frictional resistance of 0.25% per day out of dock in temperate waters and 0.5% per day in tropical waters (Marine Corrosion Sub-Committee, 1944).

The residual resistance accounts for the remaining drag and is cause by the movement of the vessel through the water, pushing it out of the way, causing the pressure differences around the hull. To maintain equilibrium, a wave is formed ahead of the vessel proportional to the driving force, resulting in hydrodynamic drag. This drag component dominates at higher speeds. (Tupper, 2013; Woods Hole Oceanographic Institute, 1952c)

Air resistance is the final component of the total drag however it only tends to be a small proportion accounting for approximately <2% for slow vessels and <10% for faster vessels (Wang et al., 2018).

2.2.2 The Effect of Surface Roughness on Marine Vessels

Significant research has been undertaken to reduce the frictional forces acting on the marine vessel as it has the greatest influence on the hydrodynamic drag and is controlled by the design of the vessel and its surface roughness. Therefore, without a complete retrofitting of the hull the only way to reduce the frictional forces is to control its surface roughness. This is done by applying various coatings to protect it from corrosion and marine biofouling (Lindholdt et al., 2015).

Various factors can affect the surface roughness of the vessels' hull from mechanical treatments such as steel sheet rolling and sand blasting processes, to damage of the

coatings allowing corrosion and biofouling to occur (Oliveira et al., 2018; Schultz, 2004; Schultz, 2007). The lowest frictional resistances are achieved when a hydrodynamically smooth coating surface is applied, requiring a maximum peak to maximum valley height (Rt) of <20 μm. However, a surface roughness of 150 μm is typically measured out of dry dock (Johansson, 1985; Lackenby, 1962; Oliveira et al., 2018; Schultz, 2007). Therefore, the lowest theoretical frictional forces may not be achieved without careful surface preparation and coating application.
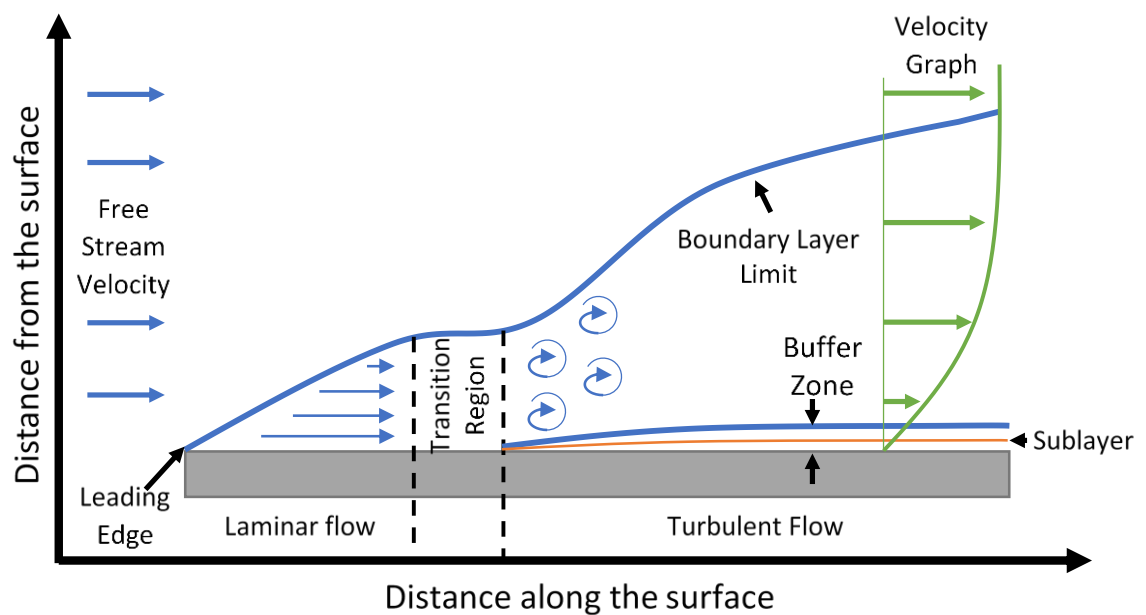
Figure 2 – Schematic showing the regions within the boundary layer. Adapted from Ab Rahman et al. (2016)

The boundary layer forms in the area closest to the surface when there is a relative movement between the hull and the medium it is travelling through. The viscosity of the medium impedes its flow around the hull resulting in the formation of the boundary layer. Within this region a velocity gradient is generated where next to the hull no flow is recorded and at some distance away a freestream velocity is observed (Figure 2). The thickness of the boundary layer may increase along the length of the vessel, with its size dependant on its speed and length, also affecting the magnitude of the hydrodynamic drag. (Schultz & Swain, 2000; Schultz, 2007)

[12]

The boundary layer is generally considered to consist of three regions an inner viscous and outer layer and an overlapping transition log-law region (Ligrani, 1989). The inner viscous layer consists of 10-20% of the boundary layer and can be further divided into two with a thin "linear sublayer", next to the hull where the velocity gradient is linear, and the "buffer layer", where the flow becomes turbulent (Schultz & Swain, 2000). This inner layer is affected by the frictional velocity, kinematic viscosity, and the roughness height (Schultz, 2007). The inner viscous layer may be affected by the surface roughness of the marine vessels hull. When the surface roughness is small a hydrodynamically smooth regime forms, where changes to the fluid flow caused by the roughness height is dampened by its viscosity (Schultz 2007). With increasing roughness, the fluid flow becomes disrupted as the protrusions emanate above the linear sublayer causing an increase in frictional drag and changes to the boundary layer thickness (Oliveira et al., 2018; Schultz & Swain, 2000; Schultz, 2007).

The outer layer consists of the remaining 80-90% of the boundary layer where the flow is turbulent (Schultz & Swain, 2000) and is generally thought to be independent of the surface roughness (Schultz, 2007).

2.2.3   Biofouling Of Marine Vessels Hulls

As the hull of a marine vessel becomes fouled an increase in the weight and fuel consumption along with a reduction in maximum speed is experienced as there is an increase in surface roughness and shear stresses along the hull. This in turn increases the frictional component of the total hydrodynamic drag. (Chambers et al., 2006)

Of the four stages of fouling previously discussed Townsin & Anderson (2009) split them into three categories namely slime (the conditioning, bacterial and microfouling layers), weed and shell (macrofouling layer).

2.2.3.1 *Slime*

Various studies have been conducted both on the laboratory scale or model sized samples (Benson et al., 1938; Lewkowicz & Das, 1986; Loeb et al., 1984; Picologlou et al., 1980; Schultz, 2007; Watanabe et al., 1969) and full-size vessels (Denny, 1951; Lewthwaite et al., 1985; Schultz et al., 2011) to determine the effect that slime has on the frictional resistance. All the studies found that once the slime film had formed an increase in frictional resistance of between 5 and 20% was either observed or predicted on marine vessels. The magnitude of the increase in frictional resistance was influenced by the thickness of the slime film. For example, when the paint colour beneath the slime film was visible with a light slime covering an increase in frication resistance of 5-10% was observed (Denny, 1951; Schultz, 2007). The formation of a heavy slime layer, where the underlying paint colour was not visible, an increase in frictional resistance of up to a 20% can be found (Lewthwaite et al., 1985; Picologlou et al., 1980; Schultz et al., 2011). Furthermore, the presence of the slime film has a greater effect on the frictional resistance than a coating with a similar roughness (Picologlou et al., 1980), which can be difficult to model due to its varying thickness and morphology along the hull (Lewthwaite et al., 1985).

The slime layer cannot be removed through hydrodynamic forces even at 30 knots (Yebra et al., 2004), yet it may be easily removed through mechanical means, suggesting that its formation may be within the inner boundary layer of the buffer

[14]

layer protecting it from the higher hydrodynamic shear forces experienced at higher speeds.

2.2.3.2 *Shell based biofouling*

An increase in surface roughness is attributed to the settlement and growth of macro-organism on marine vessels hull increasing the frictional resistance. Of the three categories (i.e., slime, shell and weed), shell or calcareous organisms, such as barnacles, are the easiest to model as their characteristics such as height diameter and distribution can be easily measured and experimented with (Townsin, 2003). However, with advances in antifouling/fouling control technology the development of calcareous fouling on marine vessels hulls is less common than it used to be.

Kempf (1937) predicted that the maximum drag would occur when 75% of the hull was covered with barnacles, reducing by a third when only 5% of the surface was covered. This was further supported by Lindholdt et al. (2015); Monty et al. (2016); Schultz (2004); Schultz (2007) and Schultz et al. (2011) where a significant increase in frictional resistance, power requirements and reduction in speed was recorded when the wetted surface was lightly fouled by barnacles. As the surface became more heavily fouled the rate of increase in frictional resistance slowed, where taller barnacles resulted in a greater surface roughness and therefore higher frictional resistances.

2.2.3.3 *Plant based biofouling*

The effect of filamentous algae on frictional resistance is more difficult to model where Schultz & Swain (2000) and Schultz (2000) found an increase of between 110-125% and 33-187%, respectively, when compared to the smooth condition. The large increase in frictional resistance may result from the filaments growing beyond the

boundary layer projecting into the freestream increasing the turbulence and hydrodynamic drag. Furthermore, the variations in frictional resistance can be attributed to the inhomogeneity of the settlement and development of the algae resulting in filaments of varying lengths and densities being present.

2.2.4   Cost Of Biofouling Of Marine Vessels

2.2.4.1 *Direct Costs*

Shipping is one of the most efficient modes of transporting goods around the world contributing approximately 3.3% of the global emissions of carbon dioxide and other greenhouse gases and airborne emissions such as sulphur and nitrous oxides and particulate matter (International Maritime Organization, 2009). It is estimated that 50-70% of the cost associated with shipping comes from fuel (Rehmatulla & Smith, 2015). However, as the hull becomes fouled the associated increase in frictional resistances and weight, reducing the maximum speed and movability, therefore increase the fuel consumption up to 40% (Milne, 1990).

There are various factors which may indicate when cleaning is required for example NSTM (2006) recommends that the hull is inspected regularly recording the amount of fouling at various position of the hull, producing a fouling rating (FR) (summarised in Table 1). When the rating of FR-40 with a 20%> coverage for ablative and FR-50 with a 10%> coverage for a foul release coating is observed then cleaning should be scheduled.

Table 1 – Summarised fouling ratings (FR) in order of increasing severity (NSTM, 2006)

Description of condition	NTSM Fouling Rating (FR)
Hydrodynamically smooth surface	0
Typical as applied AF coating	0
Deteriorated coating or light slime	10-20
Heavy slime	30
Small calcareous fouling or weed	40-60
Medium calcareous fouling	70-80
Heavy calcareous fouling	90-100

A reduction in performance may also indicate when cleaning is required such as when there is a 1 knot reduction in speed at a given shaft rotation, a 5% increase in fuel consumption or a 5% increase in shaft revolutions to maintain a particular speed. (NSTM, 2006)

An estimated annual increase in fuel consumption of 1.4% was observed when comparing a hydrodynamically smooth surface to the as applied coating with a typical surface roughness (Rt) of 150 μm. Once fouled with a heavy slime layer (FR-30) or small calcareous fouling organisms (FR-60) an estimated increase in annual fuel consumption of 10.3% and 20.4%, respectively, relative to a hydrodynamically smooth surface was calculated. (NSTM, 2006)

The removal of the biofouling from the hull can improve the fuel consumption of the vessels. However, this may require time in the dry dock which costs time and revenue through lost time at sea. Therefore, a balance between the cost of reduced speed and increased fuel consumption, with the costs associated with maintaining the hull, such as conditioning, cleaning and repainting, needs to be achieved (Oliveira et al., 2018).

Three types of cleaning operations are available with a full cleaning operation removing all the fouling from below the waterline, an interim clean removing fouling from the propellers, shafts, struts, and rudders to a partial clean removing fouling from

specific areas of the hull (NSTM, 2006). The intermediate and partial cleaning regimes may extend the amount of time the vessel can be in the ocean before needing dry docking. The estimated cost of the cleaning varies depending on the size of the vessel and the type of cleaning required. For a full clean a cost of $10.61-$ 13.85/m^2 and an interim clean of $6.07-$8.71/m^2, figures taken from Schultz et al. (2011) for the cleaning of an Arleigh Burke Destroyer with a wetted surface area of 3001 m^2 and adjusted for inflation. Furthermore, depending on the type of cleaning this may be done underwater or in drydock.

The removal of the fouling from the hull increases its fuel efficiency, where Adland et al. (2018) observed that an intermediate underwater clean can reduce the fuel consumption by 9% whereas a full dry dock cleaning can reduce the fuel consumption by 17%. Similar results were also observed by Bohlander (1991) where the change in power consumption between a fouled and cleaned hull was 8-18%.

2.2.4.2 *Indirect costs*

Along with the associated direct costs of increasing fouling from increased fuel consumption and the cleaning of the hull to remove fouling several indirect costs may also be observed such as from; increased wear and tear on the engines; the accidental removal of antifouling/anticorrosion coatings from the hull and subsequent repair; the unintended translocation of fouling invasive species from various places on the planet damaging local ecosystems; the transportation and storage of fuel at ports and refilling of vessels due to reduction in fuel efficiencies; with a reduction in speed and manoeuvrability, the amount of time at sea may increase increasing staff costs from wages and sustenance; etc.

2.3   Prevention Of Biofouling On Marine Vessels

2.3.1   History Of Antifouling Coatings

The importance of making an efficient sailing vessel has been known about for millennia with the hulls, up to the 18th/19th century, being constructed from wood. Archaeological evidence found that bitumen was used on reeds boats (circa 5000 B.C.) making them watertight and better able to travel in water (Connan et al., 2005). Early examples of antifouling/fouling control technology may date back to the ancient Phoenicians and Carthaginians (circa 1000 B.C.) who were reputed to have circumnavigated Africa, exploring the west coast of Europe, and travelling to Britain for tin. It was said that these civilisations used pitch and possibly copper to protect ships' bottoms. Further development in antifouling may be observed in 500 B.C where arsenic and sulphur were said to have been mixed with oil before being applied to the hull (Woods Hole Oceanographic Institute, 1952a).

One of the most frequently used materials used to protect ships bottoms was lead used by the ancient Greeks (3rd Century B.C.), the Romans (3rd Century B.C. – 1st Century A.D.), English (15th-18th Century A.D.), Spanish (16th Century A.D.) and French (17th Century A.D.) (Woods Hole Oceanographic Institute, 1952a). While its ability to control fouling was poor, it did offer protection against ship worm. However, lead sheeting suffered from galvanic corrosion due to contact with copper or iron nails used to secure it to the hull, eventually stopping it from being used.

Further methods of protecting the hull were trialled with pitch, tar, resin, tallow, animal hide, hair and seal tar all being used. However, it was not until the 17th Century A.D. that the first recording of antifouling technology where William Beale 1625 applied for a patent for a mixture of cement, powdered iron, and a copper compound

(Woods Hole Oceanographic Institute, 1952b). While several other patents were also granted, it was not until 1758 when the first recorded use of copper sheathing of the H.M.S Alarm wooden hull and its antifouling ability was observed. Eventually copper sheathing became widespread throughout the 18th and 19th Centuries. (Woods Hole Oceanographic Institute, 1952a)

The introduction of iron hulls in the 1830's resulted in a renewed interest of antifouling technologies as the copper sheathing traditionally used on wooden vessels could no longer be used as it accelerated the corrosion of the hull, due to the galvanic effect between copper and iron. Several antifouling paints were also being developed which contained toxic pigments such as copper oxide, arsenic and mercury oxide and were mixed with organic binders. (Woods Hole Oceanographic Institute, 1952a)

In 1847 the first successful antifouling paint was developed by William John Hay, where copper compound powder pigments were mixed in a non-conductive varnish isolating the copper from the iron hull, thus preventing galvanic corrosion. Several other copper compounds containing paints were also developed using rosin, tar, naphtha, or benzene to suspend a copper compound. By the end of the 19th Century multi-layered paints were being used where an anticorrosive layer was applied before adding the antifouling layer. (Woods Hole Oceanographic Institute, 1952a)

Following the Second World War and the introduction of synthetic petroleum-based resins and binders antifouling/fouling control technology was able to continue to develop with four main types being available today, namely controlled depletion, self-polishing, hybrid, and more recently fouling release coatings.

2.3.2 Current Antifouling Coatings

Traditional antifouling paints used either a seawater insoluble synthetic (vinyl, acrylic, or chlorinated rubber) (Michelis & Gougoulidis, 2015), or soluble natural (rosin) (Lejars et al., 2012) polymer matrices to suspend the biocidal pigment.

The insoluble matrix relies on the solubility of the biocidal pigment to allow it to leach out of the paint through interconnecting pores resulting in a leach layer (Yebra et al., 2004). These paints have good mechanical properties however after a certain time the leach layer is thickened to such an extent that the leach rate falls to a rate too low to prevent fouling (Ferry & Ketchum, 1946).

To prevent the reduction in protection soluble matrix polymer coatings were developed using rosin. A high dissolution rate was observed with these coatings as the carboxyl groups within the rosin reacts with the sodium and potassium in seawater causing it to dissolve (Peres et al., 2014). While this coating maintains a good leach rate, they are brittle leading to cracking and are readily oxidised with a large leach layer (Michelis & Gougoulidis, 2015). Furthermore, the efficiency of the coatings is reduced under static conditions due to the formation of calcium and magnesium soap films which are difficult to remove (Yebra et al., 2004).

The following section examines the different antifouling coatings in more detail.

2.3.2.1 *Controlled Depletion Polymer Coatings*

A balance between the mechanical strength of the insoluble coatings and the high leach rate of the soluble coatings was found with the development of the controlled depletion polymer (CDP) coatings. This is where the rosin binder is reinforced with an insoluble polymer allowing a high strength coating with a controllable leach rate to be

developed (Almeida et al., 2007). The biocidal pigment is incorporated into the slightly soluble coating which once hydrated allows the pigment to diffuse out leaving a porous matrix behind (Lejars et al., 2012), as illustrated in Figure 3. CDP coatings tend to be heavily loaded with biocidal pigments to ensure the longevity of the coatings ability to prevent/control fouling (Almeida et al., 2007).
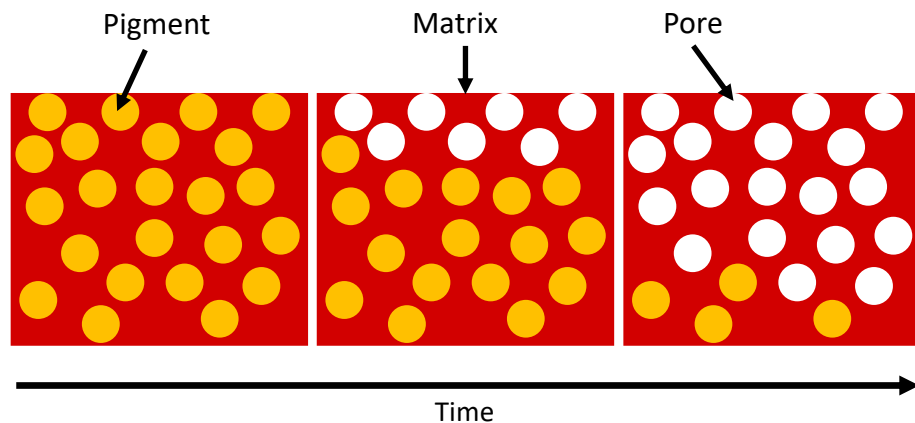
Figure 3 – Cross-section schematic showing the effect of exposure time on the CDP antifouling coating.

CDP coatings tend to be less effective than other coatings, tending to be used where fouling is less prevalent (Michelis & Gougoulidis, 2015). The dissolution of the pigment results in the formation of a thickening porous leach layer, which as it grows reduces the release rate and therefore the coatings' protectiveness, making the thickness of the leach layer life limiting (Bressy et al., 2009; Ferry & Ketchum, 1946; Michelis & Gougoulidis, 2015). Furthermore, an annual increase in surface roughness was measured by Yeginbayeva & Atlar (2018) due to the formation of the porous network.

Marine vessels that use a CDP coating tend to require dry-docking every three years to either remove or seal the leach layer prior to recoating the vessel, otherwise the new coating may become detached (Almeida et al., 2007; Lejars et al., 2012; Michelis & Gougoulidis, 2015; Yebra et al., 2004).

2.3.2.2 Self-Polishing Co-polymer

SPC coatings were developed to provide a constant leach rate of the biocidal pigment over the lifetime of the coating, which was achieved through the hydrolysis with seawater. The dissociated Na^+ and Cl^- ions are inserted between O and pendant atoms of the SPC molecule, splitting the functional group from the polymer backbone (Kwon et al., 2020). The decomposition of the SPC molecule maintains high concentrations of the biocidal pigment near the coating surface (Figure 4). Kiil et al., (2001) determined that the polishing rate was unaffected by speed, with similar rates observed at 20 and 30 knots, suggesting that the rate of hydrolysis was the controlling factor influencing the polishing rate of the coatings. The gradual polishing allows for a stable and controllable leach layer to form with a reduction in surface roughness, when compared to the as applied coating (Howell & Behrends, 2006).
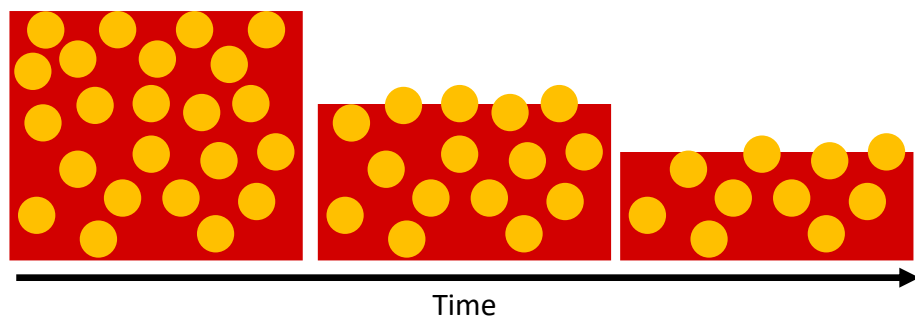
Time

Figure 4 – Cross-section schematic showing the effect of exposure time on the SPC antifouling coating.

The biocidal pigments are mixed into acrylic or methacrylic copolymers matrices, which easily hydrolyse when in contact with seawater (Lejars et al., 2012). The initial leach rate of the biocide is lower than that observed with the CDP coatings, with a porous matrix forming, through with seawater can diffuse, following pigment dissolution (Bressy et al., 2009). The SPC matrix tends to be hydrophobic preventing the seawater from penetrating more than a few microns from the surface. However, seawater can diffuse deeper into the coating with increased pigment dissolution,

reacting with the hydrolytically unstable carboxyl groups, making the porous coating brittle (Lejars et al., 2012), which when combined with increased hydrodynamic drag causes the coating to fracture and erode away (Bressy et al., 2009; Michelis & Gougoulidis, 2015). The leach layer thickness tends to be stable at approximately 10-20 µm over the life of the coating, with a polishing rate of 5-20 µm a year, allowing an extended dry-docking interval of up to five years (Almeida et al., 2007; Kiil et al., 2001). An increase in surface roughness of 4.8% was measured after five years, whereas the CDP coating had an increase of 10% over 3 years (Lejars et al., 2012).

2.3.2.3 *Hybrid coatings*

The advantageous properties of the CDP coating, such as the surface tolerance and attractive volume solid, and the self-polishing rate, controllable biocide release and reduction in leach layer thickness of the SPC coatings, are combined to produce a hybrid coating (Michelis & Gougoulidis, 2015). Pigments are release from the coating matrix through a combination of hydration and hydrolysis forming a leach layer (Lejars et al., 2012). The leach layer becomes brittle and is polished away through wave action, maintaining a constant layer. These coatings tend to last for between 3-5 years (Taylan, 2010), with the surface roughness increasing by 10% after 5 years (Lejars et al., 2012).
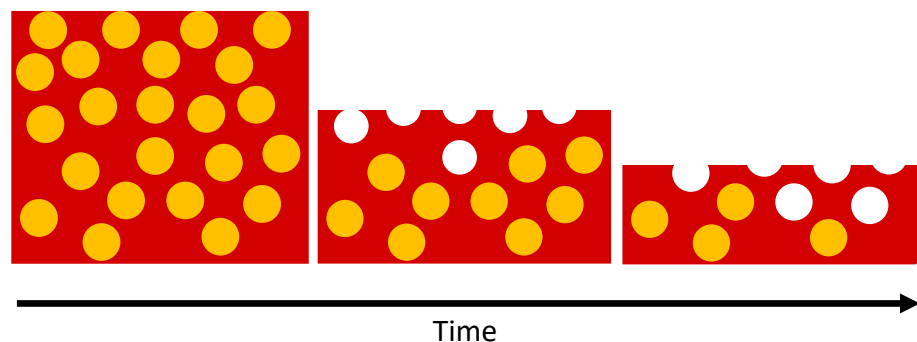
Figure 5 – Cross-section schematic showing the effect of exposure time on the hybrid antifouling coating.

[24]

2.3.2.4 Fouling Release

Fouling release (FR) coatings have been developed as an alternative to biocide containing antifouling coatings where the low surface energy (hydrophobic), low friction and surface roughness preventing the attachment, or reducing the adhesion strength, of fouling organisms (Candries et al., 2001; Chambers et al., 2006; Yebra et al., 2004). The low surface roughness of these coatings reduces the hydrodynamic drag and therefore fuel consumption of these vessels (Anderson et al., 2003; Candries et al., 2001). The minimum relative adhesive strength has been observed at 22-24 mN/m (Webster & Chisholm, 2010), with polymers such silicone, fluoropolymer, hybrid, and hydrogel silicone providing a fouling release region of between 20 and 30 mN/m (Dafforn et al., 2011; Townsin, R. L. & Anderson, 2009).
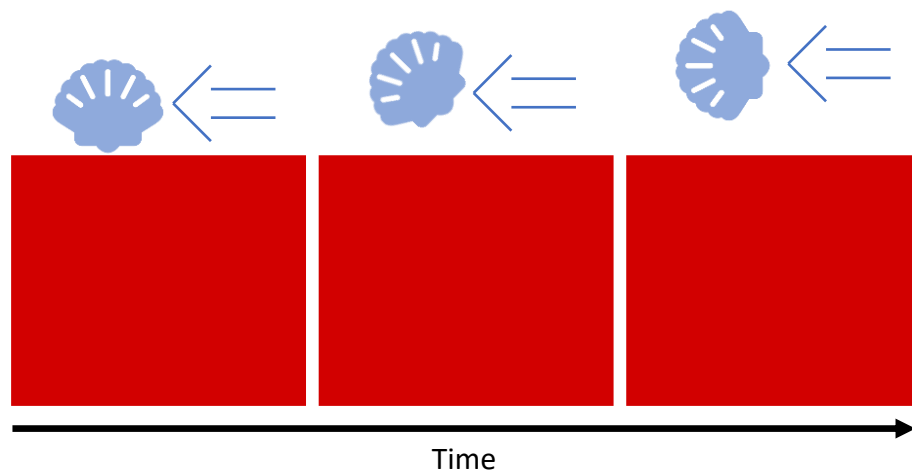
Figure 6 – Cross-section schematic showing the effect of hydrodynamic drag on the settlement of marine fouling organisms on fouling release coatings. The blue arrows represent the hydrodynamic drag force acting on the fouling organism.

The "non-stick" nature of these coatings may result in the fouling organisms becoming detached from the vessel under their own weight (Berglin et al., 2003), or as the vessel is sailing caused by the shear stresses acting it (Anderson et al., 2003; Chambers et al., 2006; Dafforn et al., 2011). Generally, the vessel needs to be traveling at speeds greater than 8 knots to ensure that the hydrodynamic forces are sufficiently high to

[25]

remove the fouling. However, FR coatings are still susceptible to the formation of the slime layer which can be difficult to remove, even at 30 knots (Candries et al., 2001; Chambers et al., 2006; Lejars et al., 2012). These coatings typically have a life cycle of 5-10 years, with the surface roughness increasing by 1.4% after five years (Lejars et al., 2012).

The low surface energy of these coatings also means that they have a poor adhesive strength to the substrate and therefore requires a tie-coat to support the FR topcoat (Lejars et al., 2012). Furthermore, these coating have poor mechanical properties which means that they can be easily damaged (Yebra et al., 2004).

2.3.3 Biocides In Antifouling Coatings

Several biocides have been developed for the use in antifouling coatings with Tributyltin (TBT) being the most effective compound, which gained popularity since the 1960s and 70s (Almeida et al., 2007; Yebra et al., 2004). However, this caused detrimental ecological side effects to non-target marine life, where the deformation of oyster shells at 2-20 ng/L (Alzieu et al., 1986; Alzieu, Claude, 1998) and the development of male sexual characteristics on female gastropods (imposex) at <2 ng/L (Bryan et al., 1986; Gibbs & Bryan, 1987) were observed. These environmental concerns led to the strict regulation and eventual ban in the application of TBT coatings from the 1st January 2003 and the total phase out of TBT coatings from 1st January 2008 (Walmsley, 2006).

Today the most popular biocide in use in antifouling coatings has returned to the traditional copper compounds as they are broadly toxic to most fouling organisms. Copper is present mostly in the form of cuprite (Cu_2O) pigments (Comber et al., 2002;

Lindgren et al., 2018). As such they are the focus of this study. However, some species are tolerant to high levels of copper (Hall, 1980), therefore booster biocides such as copper pyrithione, zinc oxide, zinc pyrithione and zinc ethylenebis-(dithiocarbamate) (Zineb) (Lejars et al., 2012) are added to antifouling coatings to improve their efficiency.

2.3.3.1 *Copper based biocide*

Copper is an essential element for life as it required for growth, metabolism, and enzyme activities (Cid et al., 1995; Zhao, L. et al., 2014). Low levels naturally exist in the marine environment where generally <1 ppb and up to 10 ppb are typically detected in seawater (Georgopoulos et al., 2001). However there needs to be a careful balance of copper, if the concentration is too high it can accumulate, readily binding to the essential amino acids (Harris & Gitlin, 1996) and damage cell wall membranes (Lim et al., 2006), becoming lethal as it restricts organisms' growth and metabolism. However low levels of copper may also slow the development of organisms (Grosell, 2011).

Although copper is not considered to be hazardous to human health, it is the most toxic metal to marine organisms (Swain et al., 1982), with the exceptions of silver, which may be expensive to use as a biocide, and mercury and TBT which have been banned due to their damaging effects on the marine environment and non-target species. Copper on the other hand has a low tendency towards bioaccumulation and only requires a small amount to be released to control fouling.

The toxicity of copper has been widely studied and is dependent on its ability to be adsorbed or transferred from food or water to somewhere that can experience the toxic effects (Woody & O'Neal, 2012). The cuprite pigment readily releases the toxic

[27]

cupric ion (Cu^{2+}) when in contact with seawater which can be easily absorbed by most organisms.

It is generally accepted that the minimum average cuprite leach rate of $10 \, \mu g.cm^{-2}.day^{-1}$ is required to prevent fouling in seawater (Ferry & Ketchum, 1946; Ketchum et al., 1945). While Lindgren et al. (2018) observed that a release rate of $4.68 \, \mu g.cm^{-2}.day^{-1}$ was enough the prevent fouling. However, this was conducted in a low fouling risk environment meaning less copper may have been required. Therefore, the release rate of the antifouling coatings may be tailored depending on the environment it is exposed to.

2.3.4   Failure Of Antifouling Coatings

The failure of copper containing antifouling/fouling control coatings occurs when there is a build-up of fouling species on the painted surface. This happens when the biocide release rate drops below a critical level to maintain a toxic environment for the biofouling species. There are several factors that may allow this to occur, depending on the type of coating used;

- The removal of the antifouling coating due to mechanical damage for example from fender and berth impacts, the movement of the anchor along the hull, collisions with debris in the oceans and abrasion along the seafloor. This exposes unprotected areas of the hull where fouling organisms can attach. (Anon, 2007; Santhakumaran, 1988)

- The biocide is released from the paint matrix resulting in the formation of a leach layer. The thicker this leach layer becomes, the further the biocidal pigment needs to travel, and therefore the lower the leach rate becomes until

[28]

it reaches a critical level where fouling can occur. (Bressy et al., 2009; Ferry & Ketchum, 1946)

- The reaction of the copper pigment with the environment to form an insoluble copper chloride complex, or patina. This patina is porous and allows the leach rate to be maintained as was observed in Lindgren et al. (2018) where the release rate of copper on a newly applied coating copper was $100\ \mu g.cm^{-2}.day^{-1}$ dropping to $10-20\ \mu g.cm^{-2}.day^{-1}$ once the patina layer had formed. While the patina remains porous, the antifouling ability of the paint is retained, however should the density and thickness of the patina increase then the release rate of the biocidal pigment is reduced leading to possible failure of the coating. The formation of the patina layer is of interest to this study.

- The formation of the slime layer on the coating may also inhibit the release of the biocide to the environment (Schatzberg, 1996). When using a cuprite biocide these released cupric ions could become trapped next to the surface allowing it to form the patina layer, reducing the effectiveness of the antifouling coating (Lindner, 1988) and therefore allow fouling species to settle.

- Furthermore, Ramesh et al. (2014) determined that the shape of the vessel would affect the polishing rate of the SPC antifouling coatings due to variations in the shear stress along the hull, leading to the premature failure in certain areas. Where the coating would polish quicker in high shear stress regions than other areas reducing the effective lifetime of the coating. While in low shear stress regions, the release of the biocide may be insufficient to prevent fouling of the hull.

[29]

2.4 Copper

Copper is believed to be the first metal to be utilised by man dating back to 8700 B.C. used in jewellery, tools, and weapons (Copper Development Association Inc., 2018; Davis & Committee, A.S.M.I.H., 2001). Today copper is used in a wide range of industries such as in electronics and heat exchangers due to its high electrical and thermal conductivities, as well as water pipes and architecture due to its relatively high corrosion resistance and pleasing aesthetics (Copper Development Association Inc., 2013; Davis & Committee, A.S.M.I.H., 2001). The mechanical properties of copper also allow it to be easily manufactured into various shapes, while its high ductility allows it to be easily drawn and extruded into wires and pipes.

Pure copper is rarely found in nature, with approximately 90% coming from copper sulphide family of ores due to their relatively high copper content and ease of extraction, with oxides taking up the remaining 10% (Davis & Committee, A.S.M.I.H., 2001; Hosford, 2005). These ores are processed either through smelting or hydrometallurgical processes where copper is leached from the ore when exposed to dilute sulphuric acid and electrolytically refined, producing 99.95% pure copper (Davis & Committee, A.S.M.I.H., 2001). However, once the pure copper has been processed it readily patinates, reacting with oxygen in the environment to form a passive oxide layer.

2.4.1 Copper Patination

Patination is a general term related to the formation of a thin film on the surface of a material, its thickness and type depend on its age and the environment it is exposed to. The term patina was first coined in 1748 to describe the green film that was found on excavated copper roman dishes known as 'patens' (Graedel et al., 1987; Harper,

2015). Today patina is mostly used to describe the degradation of copper and copper-based alloys when exposed to environmental contaminates, resulting in the formation of thin inorganic compounds on metal surfaces. The patina colour may be affected by its thickness, coverage, and composition (FitzGerald et al., 2006).

The patination process occurs due to the higher energy state of un-reacted metals, such as pure copper, when exposed to the environment. The pure copper is thermodynamically unstable readily reacting with certain trace species in the environment, such as oxygen, chlorine, and sulphur, from pure, marine, and polluted environments, respectively, to form metallic compounds with a lower energy state.

Data compiled from various authors since the early 1900's suggests that there was a reduction in the time to form a green patina layer from 10-20 years to 5-10 years (Graedel et al., 1987). It is thought that the increase in industrialisation, released atmospheric pollutants, such as sulphides into the atmosphere was to blame for the higher patination rate. However, with the introduction new legislation putting tighter controls on pollution it is expected that the patination rate is to decrease (FitzGerald et al., 2006).

The typical corrosion rates for four archetypal atmospheres have been reported by (Fuente et al., 2008) and are as follows:

- Rural Atmosphere: $0.2 - 0.6 \, \mu m. \, year^{-1}$
- Marine Atmosphere: $0.7 - 1.5 \, \mu m. \, year^{-1}$
- Urban Atmosphere: $0.9 - 2.2 \, \mu m. \, year^{-1}$
- Industrial Atmosphere: $1.5 - 2.5 \, \mu m. \, year^{-1}$

2.4.2 Stages Of Patination

The patination process occurs in several stages from the initial oxidation and growth of the oxide on the pure copper substrate to the complexation of the oxide due to a reaction with trace reactive species within the environment.

2.4.2.1 *Passivation Of The Copper Substrate*

The corrosion and passivation of copper in an aerated, oxygen rich, medium has been thoroughly studied which consists of two competing processes, the formation and breakdown of the passive layer.

The first process is the formation of the passive layer, which has been studied by various authors where four different passivation mechanisms were identified: 1) an air formed passive film due to a reaction between pure copper and the atmosphere; 2) the reaction of with trace impurities in the environment resulting in a salt layer; 3) through the chemisorption of a anhydrous solvent; 4) by reaction with oxygen resulting in the formation of a oxide or oxyhydroxide. (Evans, 1971; Hoar, 1967; Kruger, Jerome, 2003)

Highest corrosion rates are measured when un-oxidised copper is exposed to the environment. An oxide layer can form acting as a barrier to the environment, slowing ion transport to and from the substrate, reducing the corrosion rate (EL-Mahdy, 2005).

It is generally accepted that the formation of a thin film of cuprite (Cu_2O) is the primary oxidation product when copper is exposed to an oxygen rich environment (FitzGerald et al., 2006; Fuente et al., 2008; Graedel et al., 1987; Rice et al., 1981) forming at the metal-electrolyte interface. In clean ambient air a 1.6 nm cuprite layer is instantaneously formed on pure copper, followed by a parabolic growth of the oxide

until it reaches 5 nm where further growth is slowed (Fuente et al., 2008; Rice et al., 1981), increasing to 23 nm after 6 months (Masudome & Abe, 2011). The formation and growth of this passive oxide film changes the colour of the copper from a salmon pink to a more recognisable reddish brown copper colour. As this film grows and ages the patina oxide becomes brown and eventually blackens (Masudome & Abe, 2011). The speed at which this patina forms may be influenced by the surface roughness where a rough surface with an increased surface area would allow for fast thickening kinetics of oxide islands that form on the copper substrate (Zhou & Yang, 2004).

The initiation stages of the anodic copper dissolution occurs at areas of weakness in the lattice structure, such as at the grain boundaries or defects in the copper, resulting in the production of cuprous or cupric ions (Liao et al., 2011) following reactions in Equation 1 and Equation 2.

$$Cu \rightarrow Cu^+ + e^-$$ *Equation 1*

$$Cu \rightarrow Cu^{2+} + 2e^-$$ *Equation 2*

The reduction of oxygen occurs at the cathodic sites following Equations 3 or 4.

$$O_2 + 4H^+ + 4e^- \rightarrow 2H_2O$$ *Equation 3*

$$O_2 + 2H_2O + 4e^- \rightarrow 4OH^-$$ *Equation 4*

Cuprite has been shown to precipitate on copper surfaces when the cupric ion concentration reaches approximately $7 \times 10^{-5}\ Mole/Litre$ (Bianchi & Longhi, 1973), while a current density of $50\ \mu A/cm^2$ can also promote its precipitation (Faita et al., 1975) once OH^- ions have been adsorbed (Equation 5) (Chialvo et al., 1984).

$$2Cu^+ + OH^- \rightarrow Cu_2O + H^+$$ *Equation 5*

When exposed to aqueous solution various factors such as pH, temperature and active species can affect the formation and breakdown of the passive film formed on copper.

[33]

2.4.2.2   *Influence Of Solution pH*

While the presence of H^+ had not been found to have a direct role in the reduction of copper, the pH of the electrolyte has been observed to influence its corrosion in several ways. Reiber (1989) identified three main factors that are influenced by the pH of the electrolyte. The first factor was that the pH may alter the oxygen reduction of the half-cell reaction where in acidic electrolytes the potential of the oxygen half-cell was driven in the anodic direction increasing its corrosivity.

The second factor was due to changes in the speciation of copper as the pH was altered. Pourbaix (1966) demonstrated that the pH of the solution can have a profound effect on the passivation of copper for example in acidic solutions the dissolution of the copper electrode is favoured whereas in alkaline solutions passivation was favoured.

When un-oxidised copper was exposed to a weakly acidic or alkaline chloride free solutions it passivates by reacting with water or OH^- ions in solution forming Cu_2O. Three types of reaction may occur to form the cuprite layer:

1) Precipitation reaction between the cupric and hydroxide ions, Equation 5 (Faita et al., 1975)

2) Direct reaction between the copper and the hydroxide ions, Equation 6 (Faita et al., 1975), or water, Equation 7 (Metikoš-Huković et al., 2000),

$$2Cu^+ + 2OH^- + 2e^- \rightarrow Cu_2O + H_2O \qquad \text{\textit{Equation 6}}$$

$$2Cu + H_2O \rightarrow Cu_2O + 2H^+ + 2e^- \qquad \text{\textit{Equation 7}}$$
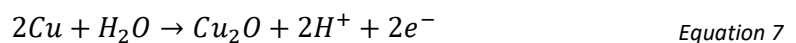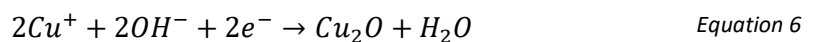
3) Disproportioning reaction between the copper metal cupric ions and water, Equation 8 (Xiong et al., 2011).

[34]

$$Cu + Cu^{2+} + H_2O \rightarrow Cu_2O + 2H^+ \qquad \text{\textit{Equation 8}}$$
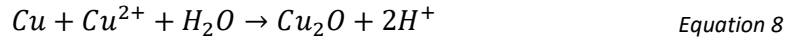
A duplex layer passive film has been observed by various authors to form on copper surfaces consisting of an inner Cu_2O layer which is oxidised further to form an outer layer of $CuO/Cu(OH)$ (Babić et al., 2001; Kear et al., 2004; Kunze et al., 2001; Kunze et al., 2004; Maurice et al., 1999; Metikoš-Huković et al., 2000; Wan et al., 2012; Yamashita et al., 1980), slowing the anodic dissolution through:

$$Cu_2O + 2OH^- \rightarrow 2CuO + H_2O + 2e^- \qquad \text{\textit{Equation 9}}$$

Or

$$Cu_2O + 2OH^- + H_2O \rightarrow 2Cu(OH)_2 + 2e^- \qquad \text{\textit{Equation 10}}$$
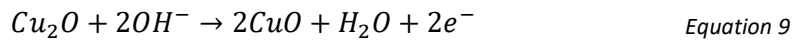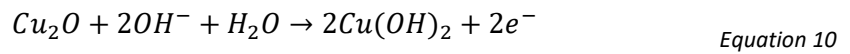
The anodic oxidation of Cu^+ ions previously discussed may also contribute to the formation of the outer layer (Babić et al., 2001) via the following Equation 11:

$$Cu^+(aq) + (2-x)H_2O \rightarrow CuO_x(OH)_{2-2x} + 2H^+ + 2e^- \qquad \text{\textit{Equation 11}}$$
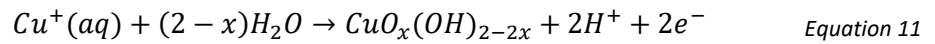
The third factor was the stability of the passivating film as will be discussed in further sections.

2.4.2.2.1 Acidic Solutions

In acidic solutions lower than pH 5 the Cu_2O layer is highly soluble (Chapter 5.2) (Pourbaix, 1966; Brusic et al., 1991), reducing the thickness of the oxide layer, with it still being detectable above pH 4 (Di Quarto et al., 1985). However, below pH 4 the oxide film becomes highly porous and unstable allowing the free dissolution of cupric ions from the copper surface into solution (Feng et al., 1997), where the dissolution of the copper metal was controlled by diffusion of the cupric ions through the electrolyte.

Various authors observed that when chloride was present within the acidic medium, Cu_2O is no longer the main phase as the cupric ions combine with chloride to passivate the copper surface with a $CuCl$ layer through Equations 12 and 13, at chloride concentrations less than 1 M (Lee & Nobe, 1986):

$$Cu + Cl^- \rightarrow CuCl + e^- \qquad\qquad \textit{Equation 12}$$

$$CuCl + Cl^- \rightarrow CuCl_2^- \qquad\qquad \textit{Equation 13}$$

With increasing chloride concentrations further cuprous chloride complexes such as $CuCl_3^{2-}$ and $CuCl_4^{3-}$ are favoured (Lee & Nobe, 1986).

Modestov et al. (1995) observed that while the Cu_2O is highly soluble in acidic solutions, a poorly protective layer of Cu_2O was found beneath the $CuCl$ layer. It was therefore concluded that the $CuCl$ forms first on the copper electrode in acidic solutions followed by the formation of the Cu_2O. Whereas Bacarella & Griess (1973) did not find evidence of the protective layer.

As the pH of the solution goes above pH 5 the oxide film becomes more compact changing the rate determining step from being controlled by the diffusion of ions into solution at <pH 4 to being controlled by the diffusion of ions through the Cu_2O layer (Feng et al., 1997). This can allow the Cu_2O layer to form upon oxidation due to the following Equation 14:

$$Cu_2O + 2H^+ + 2Cl^- \rightarrow 2CuCl + H_2O \qquad \textit{Equation 14}$$
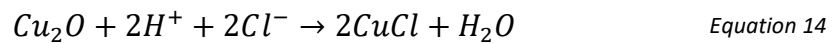
2.4.2.2.2 Neutral Solutions

In neutral (pH 6-8) chloride free solution dissolved oxygen can reduce on the copper surface depending on the number of catalytic sites available and the potential of the electrode. The reduction in oxygen results in the generation of OH^- ions (Equation 4), increasing the local pH of the electrolyte to more alkaline values (King et al., 1995).

The adsorption of the OH^- ions on to the surface of the electrode initiates the passivation of the copper (Kunze et al., 2001; Maurice et al., 1999; Maurice et al., 2000), favouring the formation of Cu_2O (Chan et al., 1999), protecting the copper from

corrosion. The thickness of the passive film increases with time, as evidenced by an increase in polarisation resistance (Feng et al., 1996) and through physical observations such as cross-sectional SEM analysis (Clarelli et al., 2014). Furthermore, Antonijevic et al. (2009) observed that with increasing electrolyte pH the OCP of the electrode became more electronegative with approximately 100 mV difference between pH 8 and 12.3 in borax buffers. However, the OCP was more variable when 0.05M NaCl was present, with pH 8 being more electronegative than pH 12, indicating a lack of linear relationship between pH and OCP when aggressive ions are present.

The formation of the oxide layer on copper has been discussed by many authors with two main mechanisms being observed. The first mechanism indicates the formation of the oxide film is due to the dissolution of cupric ions and the precipitation of the Cu_2O and CuO layer on to the copper surface (Aljinović et al., 2000; Chialvo et al., 1986; El-Tantawy et al., 1981; Metikoš-Huković et al., 2000; Vrsalović et al., 2018; Yamashita et al., 1980). This mechanism is governed by the diffusion and mass transport of copper ions through the surface layer of corrosion products.

The second mechanism is due to the nucleation and growth of the Cu_2O and CuO phase. North & Pryor (1970) observed the growth of the Cu_2O, in chloride solutions, to form epitaxially which implies that it is a direct anodic corrosion product where the crystallographic orientations are aligned to the substrate, discussed later, rather that the precipitation from solution where a random orientation may be expected. Becerra et al. (1988) observed the nucleation and growth of the CuO to follow a 2D growth mechanism under charge transfer control. A direct growth mechanism for the Cu_2O and $CuO/Cu(OH)$ system has been proposed in neutral and weakly alkaline solutions

(Lohrengel et al., 1987; Speckmann et al., 1985; Strehblow & Titze, 1980). While Chialvo et al. (1984) concluded the mechanism for growth of the passive oxide film to depend largely on the oxidation conditions.

When chloride ions are present a $CuCl$ film forms which can continue to growth due to the porous nature of the film, providing little protection against the environment, allowing chloride ions to reach, and cupric ion to be released from, the surface.

2.4.2.2.3 Alkaline Solutions

The high concentration of OH^- ions in chloride free alkaline solutions improves the passivity of copper (Liao et al., 2011) as the OH^- ions ready adsorbs onto the copper surface forming Cu_2O (Babić et al., 2001).

$$Cu + OH^- \rightarrow Cu(OH)_{ads} + e^- \qquad \text{Equation 15}$$

$$2Cu(OH)_{ads} \rightarrow Cu_2O + H_2O \qquad \text{Equation 16}$$
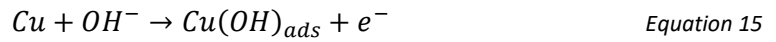
The initial formation of the oxide layer in a pH 9 sodium chloride solution was determined to follow a linear growth law (Chen et al., 1998). As the film grows the growth transitions to a parabolic rate as the diffusion of ions through the oxide layer becomes the rate determining step. Kruger (1959) determined that the Cu_2O film grows with parabolic kinetics on the primary crystal plane with CuO precipitating from solution on top of the Cu_2O layer slowing its growth. This results in the formation of a self-limiting, stable, duplex passive layer (Chen et al., 1998).

Strehblow & Titze (1980) measured the total thickness of the duplex layer, using X-ray photon and ion scattering spectroscopy, to be approximately 7 nm where the inner Cu_2O layer was approximately 1.2 nm, the CuO was up to 2 nm and the $Cu(OH)_2$ layer was up to 4 nm. The total thickness of the oxide varied depending on the

alkalinity and the length of time exposed to the solution where the greater the alkalinity and exposure times results in thicker the oxides.

The breakdown of water on the copper surface may result in the generation of protons due to the breakdown of water shown by reaction Equation 17.

$$Cu^0 + H_2O \rightarrow CuOH_{ad}^- + H^+$$
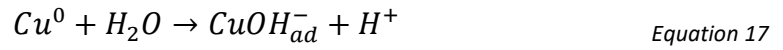
This results in the local increase in acidity of the solution at or around the electrode surface. The level of acidity continues to increase as the amount of adsorbed $CuOH_{ads}^-$ ions increases until a single uniform layer had formed (Bech-Nielsen et al., 2002). This process weakens the binding lattice on the copper surface which may peel off and expose a fresh copper surface, resulting in a continuous reaction, increasing the level of acidity over the exposure period. This can result in an initial ennobling of the OCP as a passive film is formed (Antonijevic et al., 2009), hindering the anodic reaction. As the level of acidity increases the OCP can shift to more active potentials, shown in Annibaldi et al. (2012), as the passive film dissolves and exposes the copper substrate to the electrolyte.

In buffered alkaline chloride containing solutions de Chialvo et al. (1985) found that there was a competition between the formation of the Cu_2O and the nucleation and growth of the $CuCl$ layer. However, it has also been observed in that the Cu_2O and $CuCl$ layer may form simultaneously in a borate buffered solution (Milić et al., 2008). The formation of the Cu_2O or $CuCl$ layer largely depends on the concentration of chloride and pH of the solution.

2.4.2.3 *Temperature*

At elevated temperatures the corrosion rate of copper is exacerbated (Boulay & Edwards, 2001; Kristiansen, 1977; Ochoa et al., 2015; Wan et al., 2012). Generally, as the temperature is increased by 10°C the reaction rate approximately doubles based on the Arrhenius equation. With an increase in temperature, the charge transfer and surface layer resistance are reduced, while the double and surface layer capacitance, and the elemental diffusion reaction rates increase (Vrsalović et al., 2016), leading to an acceleration of the copper dissolution. This increase in activity on the copper surface causes the E_{Corr} potential to shift towards more electronegative values (Al-Abdallah et al., 2009; Ochoa et al., 2015). However, this increase in activity does not necessarily increase the corrosion rate of copper.

The corrosion rate of copper has been shown to follow a non-linear increase with temperature where Samie et al. (2007) determined that the mass loss between 15°C and 25°C did not vary significantly. However higher corrosion rates were measured by Ijsseling et al. (1982) when exposing copper-nickel alloy exposed to seawater between 10°C and 30°C when compared to 40°C and 50°C, which was thought to be due to the rapid formation of compact corrosion products at higher temperatures, such as that observed in Kong et al. (2017) at 60°C. Furthermore, Kristiansen (1977) found that the maximum corrosion rate was measured at 50°C reducing at higher temperatures. This suggests that a relatively low temperatures of up to 25°C the difference in the corrosion rate would be negligible, with an increase being expected up to 50°C while at higher temperatures a reduction in the corrosion rate may occur due to lower concentrations of dissolved oxygen.

The temperature of the environment also affects the breakdown potential (E_B) where Figueroa et al. (1986) found that between 0 and 15°C E_B decreased but increases between 25 and 50°C. The authors concluded that this was caused by the competing effects caused by the rise in temperature namely the increase in the reaction rate involved in the passivation of copper and the increase in the protectiveness of the passive layer. This may lead to the increase in general corrosion observed at higher temperatures (Thomas & Tiller, 1972).

2.4.2.4 Active Species

Chlorine has been determined to be one of the most powerful halogen oxidising agents, readily stripping electrons from and reacting with materials and is readily available in the marine environment. Its presence in solution tends to dominate the reaction over oxygen (Atlas et al., 1982; Reiber, 1989). However, the amount of free oxygen in solution is an important aspect to consider, as this species takes place in the cathodic reaction (Equation 4). The amount of dissolved oxygen in solution with respect to temperature has been observed by various authors and is summarised in Geng & Duan (2010). It was observed that as the temperature was increased the amount of dissolved oxygen decreases, following an exponential decay, with the curve tending to level off around 60°C. The reduction in dissolved oxygen also decreases the cathodic reaction rates, which in turn influences the corrosion rate (Dortwegt & Maughan, 2001).

2.4.2.5 Crystallographic Orientation

The crystallographic orientation has been shown to influence the corrosion and patination characteristics of copper, where it has been shown that the structure of the passive film mirrors that of the substrate where the Cu_2O (1 1 1) and Cu_2O (0 0 1)

films are formed on Cu (1 1 1) and Cu (0 0 1), respectively (Kunze et al., 2001; Kunze et al., 2004; Maurice et al., 2000; Zhou & Yang, 2004). However, when examining the outer layer of the duplex oxide formed on copper in 0.1 M NaOH (Kunze et al., 2004) observed that CuO (0 0 1) formed on both Cu (1 1 1) and Cu (0 0 1) substrates.

The thickness of the passive film was also influenced by the crystallographic orientation where the Cu_2O (1 1 1) passive film was thicker with a greater crystallinity, lower conductivity, and defect density than that formed with the (0 0 1) and (1 1 0) orientations (Gao et al., 2009; Kunze et al., 2004; Martinez-Lombardia et al., 2014; Ogata et al., 2016). Zhou & Yang (2004) also observed different thickening rates with oxide islands forming quickest in the Cu (1 1 0), however Cu (1 1 1) was not measured. While (Ogata et al., 2016) observed that Cu_2O (1 1 0) had a higher defect density than the (0 0 1) and (1 1 1) orientations.

The corrosion resistance of copper was shown to be strongly dependant on the crystallographic orientation in pure water and that containing NaCl where Ogata et al. (2016) observed that the lowest corrosion rate was recorded on the Cu (1 1 1) surface and the highest on the Cu (1 1 0) surface in pure water. Kunze et al. (2004) also found the Cu (1 1 1) surface had the fewest corrosion products in $0.1\ M\ NaOH$ suggesting it had a low corrosion rate. It was shown in Ogata et al. (2016) that the chloride concentration influences the corrosion rate of the of the different crystallographic planes, where adding $0.01\ mM$ to a pure water system accelerated the corrosion rate of the Cu (0 0 1) and Cu (1 1 1) planes. However increasing the concentration to $0.1\ mM$ only influenced the corrosion rate of the Cu (1 1 1) surface, while the Cu (1 1 0) remained unaffected. A similar increase in the activity of the Cu (1 1 1)

surface was noted in $5\ mM\ NaCl$ and $10\ mM\ HCl$ (Martinez-Lombardia et al., 2014). Finally, a galvanic effect may be observed where the dissolution of the $Cu\ (1\ 1\ 1)$ surface was found to accelerate when adjacent to $Cu\ (0\ 0\ 1)$ (Ogata et al., 2016).

2.4.3   Breakdown Of Passive Layers

The formation of the duplex Cu_2O, $CuO/Cu(OH)_2$ passive layer increases the corrosion protection as it provides a physical barrier against the environment. However, competing with the passivation process is the breakdown (general dissolution) of the passive layers.

The first steps degrading this passive film is through the adsorption of halide anions (Kong, D. et al., 2018), such as chloride ions, which are most damaging for many materials (Cui et al., 2019). Milošev et al., (2006) observed that at concentrations above $0.02M$, significantly lower than seawater of $0.5M$, promoted pitting corrosion of passive metals. This indicates that at chloride concentrations above a critical value the protectiveness of the passive film is reduced. On a copper substrate the presence of chloride results in the production of $CuCl^-$, $CuCl_2^-$ and $CuCl_3^-$ ions, depending on the concentration (Lee & Nobe, 1986), where more complex ions are formed at higher chloride concentrations (Zhao, H. et al., 2013). These ions diffuse through the passive layer making it susceptible to localised pitting corrosion.

When copper is initially exposed to chloride containing electrolytes, an incubation period is generally observed prior to the activation or breakdown of copper passivity (Janik-Czachor & Janik-Czachor, 1981; Pistorius et al., 1994; Pistorius & Burstein, 1992; Starosvetsky et al., 2006; Szklarska-Smialowska & Janik-Czachor, 1967; Thomas et al., 1972; Tromans & Silva, 1997). This is due to the competition between the adsorption

of OH^-, promoting passivation and film growth, and Cl^- ions, promoting dissolution (King, 2002). This results in a competition between the formation of the Cu_2O and the nucleation and growth of the $CuCl$ layer prior to its breakdown (Modestov et al., 1995). However, OH^- ions tend to adsorb at a faster rate (King, 2002) as it has a lower adsorption energy, when compared to Cl^- ions (Taylor et al., 2018). This may explain why copper patinas formed in a chloride media have an inner layer is mostly Cu_2O and an outer layer of copper chloride complexes.

To describe the breakdown mechanism three general categories are discussed by most authors (Böhni, 1987; Macdonald & Lei, 2016; Soltis, 2015) including 1) ion migration and penetration of the passive film 2) adsorption or displacement of ions which leads to 3) thinning, breakdown, and repair of the passive film.

The ion migration and penetration mechanism involves the transfer of halide anions through oxygen vacancies present in the oxide lattice. The most aggressive halide anions are chloride ions due to their relatively small diameter which allows them to migrate through the vacancies in the lattice reaching the metal surface (Hoar et al., 1965). Once through the oxide layer, dissolution of the metal surface may occur, transferring metal ions through the porous oxide layer.

The adsorption and displacement mechanism initiates with the adsorption of aggressive anions on the oxide surface, which may displace the oxygen in the lattice and enhance the transfer of soluble metal cations from the oxide into the electrolyte. The incorporation of aggressive anions such as chloride contaminates the passive film leading to higher ionic conductivities making the process autocatalytic (Hoar et al., 1965; Soltis, 2015). This may lead to the continued thinning of the passive layer until it

is no longer present allowing active dissolution of the substrate metal to occur (Böhni, 1987; Heusler & Fischer, 1976a; Heusler & Fischer, 1976b).

The mechanical breakdown of the passive film has been proposed to be either the main step or an additional process in combination with other mechanisms where discontinuities in the oxide film giving the metal substrate access to the environment (Galvele, 1976; Sato, Norio, 1982; Videm & Institutt, 1974). As the oxide film grows structural changes occur resulting in compressive and tensile stresses to develop (Li, 2016). Provided the compressive stresses outweigh the tensile stresses the oxide film should remain intact. However, Evans, (1960); Galvele, (1976) and Videm & Institutt, (1974) found evidence that oxide films with high internal stresses were prone to cracking.

The internal stresses within the oxide continue to grow until it reaches a critical thickness beyond which it fractures exposing the substrate to the environment (Sato, 1971). In the presence of aggressive anions such as chloride the thickness of the oxide is reduced. Hoar (1967) theorised that the adsorption of similarly charge aggressive anions into the oxide reducing its surface tension as they push each other and by extension the oxide film apart, forming cracks which expose the metal substrate to the environment. Furthermore, Xu (1993) determined that the adsorption of chloride into the oxide film relaxes the compressive stresses in the passive film allowing the tensile stresses to dominate resulting in cracking and the localised breakdown of the passive film.

2.4.3.1 *Localised breakdown of the passive film*

Corrosion pits may nucleate where the passive film on metals is locally destroyed, occurring around defects in the substrate material such as around dislocations, grain boundaries or non-metallic inclusions (Böhni, 1987; Eklund, 1974; Hoar et al., 1965; Liao et al., 2011; Pistorius & Burstein, 1992; Streicher, 1956), forming anodic and cathodic sites. These pits may re-passivate, resulting in meta-stable pitting, or propagate, leading to stable pit growth. For a meta-stable pit to become stable a 2-dimensional salt film, such as $CuCl$, forms over activated sites, providing a diffusion barrier, preventing re-passivation (Starosvetsky et al., 2006). Other factors that may enable stable pit growth would be due to high chloride concentrations or low pH values preventing re-passivation. In chloride containing electrolytes once initiated pit growth becomes self-sustaining (Hoar et al., 1965). It has also been suggested that early meta-stable pits may provide sites where pitting corrosion can propagate (Strehblow, 2016).

The level of pitting on copper varies depending on the concentration of aggressive ions in the electrolyte, exposure time, thickness of the electrolyte layer, temperature of the electrolyte and the crystallographic orientation of the copper electrode.

The amount of pitting observed on the copper surface is time dependant where the protection of the passive film is reduced, in chloride containing electrolytes, with increasing immersion times (Bech-Nielsen et al., 2002; Milić & Antonijević, 2009; Thomas, J. et al., 1972). This allows for copper ions to be dissolved and diffused into solution where they react with chloride ions forming copper chloride compounds (Gu et al., 1996; Millet et al., 1995).

Furthermore, the concentration of pits can be related to the thickness of the electrolyte above it. For example, Liao et al. (2011) found pitting corrosion in the bulk 3.5% NaCl solution, however under thin electrolyte conditions (100-400 μm) no pitting was found. Alkalinity electrolytes contain higher the concentrations of OH^- ions which can passivate the copper surface forming Cu_2O (Raship et al., 2016). At a stable pH the concentration of OH^- and H^+ ions would be relatively consistent. However, under thin electrolyte conditions higher quantities of diffused oxygen maybe present, which can be electrochemically reduced, following Equation 4, increasing the concentration of OH^-ions (Venkatraman et al., 2011) at the copper surface. This increase in OH^- at the electrode surface under thin electrolyte conditions suggests that sites affected by the chloride ions could quickly re-passivate when compared to the bulk electrolyte. Furthermore, an inverse relationship between the corrosion product quantity and the thickness of the electrolyte layer was observed (Liao et al., 2011).

2.4.4 Complexation Of The Patina

When cuprite is exposed to active species such as chloride, sulphide, or hydroxide the thermodynamic stability of the cuprite patina is reduced allowing it breakdown to form cupric ions. These ions can readily react with the active species in the environment forming different and often more complex copper compounds.

In the marine environment chloride ions are most prevalent and can enhance the corrosion rate of copper by breaking down the passive film, forming an insoluble copper hydroxy chloride, such as atacamite $(Cu_2Cl(OH)_3)$ and clinoatacamite $(Cu_2Cl(OH)_3)$. These complex compounds are less protective than cuprite, due to their porous structure and are poorly soluble in water resulting in a continuous

increase in patina corrosion product thickness (Strandberg, 1998). Due to the precipitation of the copper compounds over the substrate a consistent corrosion rate is achieved, proportional to the concentration of chloride ions in the electrolyte (EL-Mahdy, 2005), peaking at a sodium chloride concentration of $10\ \mu g.cm^{-2}$ in pure air (Strandberg & Johansson, 1998). The corrosion rate is also inversely proportional to its thickness (Farro et al., 2009; Graedel, 1987), where thick patina layers limits ion diffusion to and from the substrate. Strandberg & Johansson, (1998) also observed that cuprite rapidly formed tenorite (CuO) when it was exposed to a highly oxidising environment containing sodium chloride.

2.4.5 Patina Morphology

Copper patinas forms highly porous, defect rich layers with a poor cohesion and adhesion to the substrate (Farro et al., 2009; Franey & Davis, 1987). These patinas also have a low compactness, showing signs of fragility, creating conditions which are favourable to ions diffusion to and from the surface (Franey & Davis, 1987; Fuente et al., 2008; Nunez et al., 2005). The size of the pores may limit the diffusion of some ions into and out of the patina. However, it is thought that the chloride ions, with a thermodynamic radius of 1.72 Å can diffuse through the bulk patina more readily than sulphate ions, with a thermodynamic radius of 2.58Å (Jenkins & Thakur, 1979), and react with the cuprite.

It has been widely reported that copper patinas form two distinct layers; the inner layer next to the copper substrate is a continuous layer of cuprite; the outer layers of the complexation of the cuprite layer forming copper compounds such as brochantite ($Cu_4SO_2(OH)_6$), posnjakite ($Cu_4SO_4(OH)_6 \cdot H_2O$) and atacamite ($Cu_2Cl(OH)_3$)

(Franey & Davis, 1987; Fuente et al., 2008; Graedel et al., 1987; Holm & Matterson, 1982; Nassau et al., 1987). However, in a study by Opila (1987) cross-sectional analysis through a 100-year-old patina exposed to the atmosphere found the layers were less distinct. With carbon and sulphur species found at the outermost layer while cuprite made up the bulk of the patina, atacamite and other chloride containing species were also found distributed throughout the thickness of the patina. Opila (1987) also observed that there were different zones in copper patinas formed in the marine environment where the inner and outermost zones were rich in chlorine, with nantokite ($CuCl$) and atacamite respectively were detected, whereas chlorine was not dominant between these zones. The formation of nantokite is considered to be a precursor for the formation of atacamite (Zhang et al., 2014).

The porous, defect rich, nature of the patina allows for the formation of multiple corrosion cells resulting in the continued growth of the patina, in addition to creating spatial heterogeneous chemical distribution throughout the patina, resulting in variations in the measured intensity of copper complexes (Farro et al., 2009).

As the patina continues to grow, the rate of transport of cupric ions from, and reactive species to, the substrate slows limiting the growth of the patina layer following a parabolic growth law. FitzGerald et al. (2006) reported that the copper patina growth rate reduced from 2 µm to 0.2 µm per year over a 15-year period, which was due to the thickening patina, providing more protection against the ingress of moisture and other species from the environment. Furthermore, on samples between 15 and 152 years old the cuprite layer was found to be consistent at 6 µm, it was suggested that the friable nature of the patina, allowing thicker layers to be easily washed away,

combined with the complexation of the cuprite patina, resulted in the consistent thickness.

The composition and morphology of the formed patina is dependent on the environment it is exposed to and is therefore affected by the geographical location, climatic conditions, and pollutants in the environment. The most common pollutants that can affect the formation of patinas are sulphate and chlorides, although others such as NO_2, O_3 and H_2S also play a role (Fuente et al., 2008). In addition, atmospheric contamination by particles such as silicon, carbon, aluminium, phosphorous, iron etc. can become trapped with the patina layers but do not form copper compounds. These particles can block the pores aiding in the reduction of the rate of patination (Veleva & Farro, 2012).

2.4.6 Factors Affecting The Patina Formation

The corrosion of copper is electrochemical in nature where the anodic dissolution of the copper surface is observed, forming cuprous (Cu^+) or cupric ions (Cu^{2+}), which are soluble in water (Antonijevic et al., 2009; Fuente et al., 2008; Strandberg & Johansson, 1998). The cathodic component of the reaction occurs due to oxygen diffusion through the electrolyte, which is then reduced at the copper surface, reacting with the released cuprous ions forming oxides and hydroxides mainly resulting in the formation and parabolic growth of the passive cuprite film as discussed previously. With the patina complexation, it is possible to deduce the likely environmental conditions it was exposed to, where the presence of copper sulphates may have resulted from exposure to polluted environment, while copper chloride would indicate a chloride rich environment, typically found in marine or coastal environments.

[50]

2.4.6.1 *Copper oxide*

As discussed previously cuprite formation is generally the first sign of patination regardless of the exposure conditions, forming a porous network of large octahedral crystals allowing for the oxidation of the substrate to continue (Nunez et al., 2005). In alkaline media containing chloride ions, films of cuprous oxide are favoured over basic copper chloride (Antonijevic et al., 2009; Beverskog & Puigdomenech, 1998; Kear et al., 2004).

The oxidation rate of copper is controlled by the diffusion of ions through the cuprite layer releasing the cuprous ions, which in the presence of water further oxidise to cupric ions following two partial electrochemical reactions shown in Equations 4 and 11 (FitzGerald et al., 2006; Fuente et al., 2008).

2.4.6.2 *Copper Chloride*

In the marine environment chloride ions are prevalent, which can breakdown the passive layer, enhancing the anodic dissolution of the copper, decomposing the cuprite layer to tenorite (CuO) and allow for the formation of soluble nantokite ($CuCl$). The oxidation of the nantokite produces further copper chloride complexes which precipitate on top of the cuprite layer, releasing H^+, while raising the pH at the cathodic sites. (Strandberg & Johansson, 1998)

Several different copper chloride compounds that have been identified (Table 2), from nantokite to a hydrated copper chloride, many of which have a similar chemical formula but are differentiated due to the atomic crystal structure. For example, there are three cupric hydroxychlorides with a chemical formula of $Cu_2Cl(OH)_3$ namely botallackite, atacamite and clinoatacamite which have a crystal structure of

[51]

monoclinic, orthorhombic, (Sharkey & Lewin, 1971) and monoclinic (Jambor et al., 1996), respectively.

Table 2 – Table of copper oxides and copper chlorides showing their crystal structure, chemical formula and Gibbs free energy (Frost, 2003; Graedel et al., 1987; Hutchison & Scully, 2018; Lewis et al., 2009; Scott, 2000; Stull & Prophet, 1971).

Substance	Crystal system	Formula	$\Delta G^0{}_{298}(kJ/mol)$
Cuprite	Cubic	Cu_2O	-140.9
Tenorite	Monoclinic	CuO	-128.8
Nantokite	Cubic	$CuCl$	-119.7
β Copper (I) chloride	Hexagonal	$CuCl$	
Tolbachite	Monoclinic	$CuCl_2$	-161.6
Eriochalcite	Orthorhombic	$CuCl_2.H_2O$	-655.9
Melanothallite	Orthorhombic	$Cu_2.OCl_2$	-381
Atacamite	Orthorhombic	$Cu_2.Cl(OH)_3$	-1339.2
Paratacamite	Rhombohedral	$Cu_2.Cl(OH)_3$	-1338
Botallackite	Monoclinic	$Cu_2.Cl(OH)_3$	-1322.6
Clinoatacamite	Monoclinic	$Cu_2.Cl(OH)_3$	-1341.8
Copper (II) chloride	Monoclinic	$CuCl(OH)$	*
Beta Copper (II)	Orthorhombic	$CuCl(OH)$	*
Calumetite	Orthorhombic	$Cu(OH.Cl)_2.2H_2O$	*
Anthonyite	Monoclinic	$Cu(OH.Cl)_2.3H_2O$	*
Copper (II) Chloride	Orthorhombic	$Cu_7.O_4(OH)_{10}.H_2O$	*

*Data unavailable in the literature

Atacamite and clinoatacamite are commonly found in chloride rich environments (Oswald & Feitknecht, 1964; Strandberg, 1998), and are thus of interest to this study, however, no agreement has been reached relating to the factors which allow for one phase to form instead of another. While there was a difference between the thermodynamic stability of these two phases it has been generally agreed that there are specific conditions and kinetic factors, such as salt concentration and temperature, affecting the nucleation and growth of these crystals (Pollard et al., 1989; Sharkey & Lewin, 1971; Strandberg & Johansson, 1998). The formation of the different copper chloride phases results in a volume expansion creating internal stresses within the corrosion product allowing them to be easily removed (Zhang et al., 2014). It is thought that the formation and diffusion of $CuCl_2{}^-$ controls the kinetics of the anodic

dissolution (Deslouis et al., 1988; Starosvetsky et al., 2006; Tromans & Silva, 1997) and therefore directs the nucleation and growth of atacamite or inhibits the nucleation and growth of clinoatacamite (Sharkey & Lewin, 1971).

Paratacamite and anatacamite are two further polymorphs that have been discussed in the literature. However, paratacamite was stabilised by the incorporation of Zn^{2+} or Ni^{2+} for Cu^{2+} in one of the four distorted octahedral sites (Grice et al., 1996; Jambor et al., 1996) and is therefore isomorphic compared to the other phases. While anatacamite was officially discredited in 2015 (Hålenius et al., 2015).

In marine environments airborne hygroscopic chloride rich particles deposit onto the surface drawing moisture from the air to form high chloride concentration electrolytes, promoting high corrosion rates (Veleva et al., 1996). In addition, Chico et al. (2005) found that the quantity of the corrosion products was proportional to the chloride concentration. Overtime the corrosion rate decreases as the cuprite dominated patina layers is converted to clinoatacamite (EL-Mahdy, 2005; Veleva et al., 1996).

2.4.6.3 *Atacamite*

Atacamite has the orthorhombic crystal structure (Figure 7) and is soluble in weak acid (Graedel, 1987). Atacamite is abundant in patinas formed near marine environments due to the influence of sea-salt aerosols, tending to be present after long exposure periods (Fuente et al., 2008).

The polymorphs of atacamite follow the Ostwald step rule, which states that if a chemical reaction can result in several products, then the first product to form is the least thermodynamically stable and the last to form is the most thermodynamically stable (Van Santen, 1984). In the corrosion of copper, the first phases to form are cuprite, tenorite or nantokite which reacts and changes phase into botallackite followed by atacamite and finishing with clinoatacamite (Table 2) (Frost, 2003).

The initial conditions required for the formation of atacamite are the presence of Cu^{2+} from copper surface and Cl^- from the marine environment. These ions react together to form a basic copper chloride $CuCl_2$. Sharkey & Lewin, (1971) showed significant amounts of $CuCl^+$ were created when sodium chloride was added to solutions containing low concentrations of $CuCl_2$ allowing atacamite to form. Graedel (1987) also found that stable atacamite formation occurred at chloride ion concentrations greater than 10^4 ppm in a pH range of 3.5 - 5.5. However, its solubility in weak acids suggests that it formed when isolated from the aqueous layer. Opila, (1987) observed that chlorides were distributed throughout the patina however in older patinas these tend to be located next to the substrate, as the chlorides can diffuse through the porous network. Therefore, in thicker, older patinas atacamite is preferred as it was

protected from the environment by the growth of a new patina layer, as well as the

abundance of the diffused chloride ions.
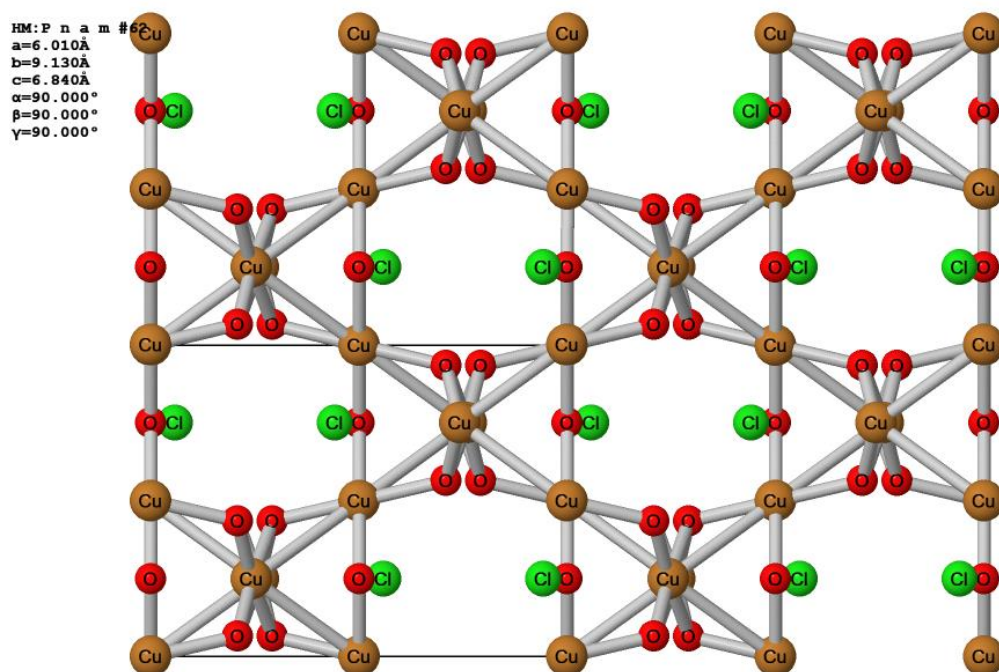
Figure 7 – Crystal structure of atacamite in a 2x2x2 cell viewed from the "x" direction. Produced using the Jmol software (Jmol, 2021) using the data from (Parise & Hyde, 1986)

Should a solution contain high concentrations of $CuCl^+$ further additions of sodium

chloride can result in the reduction of atacamite due to form other copper chloride

complexes such as $CuCl_2^0$, $CuCl_3^-$ and $CuCl_4^{2-}$. Furthermore, should the

concentration of the copper chloride complexes reach concentrations of between 3

and 20% of the total copper (II) content the effect of $CuCl^+$ is reduced and

paratacamite (clinoatacamite) can be formed. (Sharkey & Lewin, 1971)

Botallackite is the least thermodynamically stable $Cu_2Cl(OH)_3$ phases which develops as crusts of minute platy interlaced crystals (Figure 8). It is rarely observed in nature as it rapidly recrystallises to atacamite or clinoatacamite (Anthony et al., 2003; Jambor et al., 1996; Pollard et al., 1989).

HM:P 1 21/m 1 #11
a=5.717Å
b=6.126Å
c=5.636Å
α=90.000°
β=93.070°
γ=90.000°
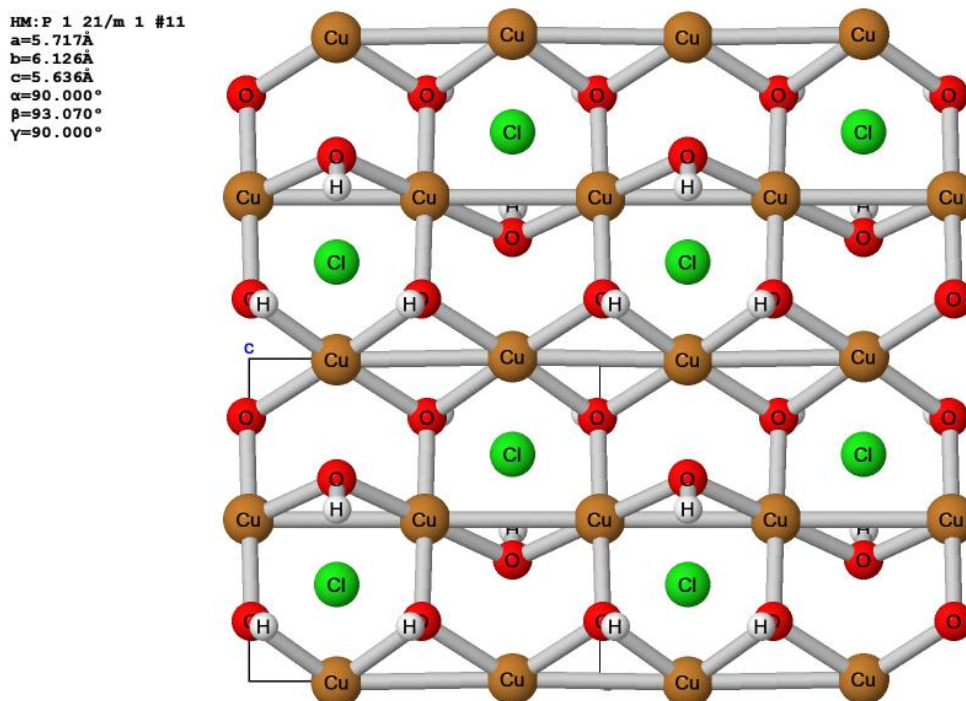
Figure 8 – Crystal structure of botallackite in a 2x2x2 cell viewed from the "x" direction. Produced using the Jmol software (Jmol, 2021) using the data from (Hawthorne, 1985).

Pollard et al. (1989) determined that the formation of botallackite may occur when the concentration of Cu^{2+} and Cl^- ions are low enough prevent the direct nucleation and crystallisation of atacamite or clinoatacamite. Furthermore, it was also demonstrated that leaving botallackite in solution or increasing the chloride concentrations to greater than $0.2\ mol.dm^{-3}$, would cause rapid recrystallisation to the other phases. Therefore, it should be dried to prevent this from happening. While Yoder et al. (2011) observed that once synthesised botallackite remained stable for a year in a closed vial, and over a week in air, solutions of water, $0.2M\ NaCl$ and $0.1M\ CuCl_2$.

2.4.6.5 *Paratacamite*

Paratacamite is one of the copper compounds that is regularly discussed when the environment contains chloride ions and was first characterised by (Smith, 1906) where it was determined to have a rhombohedral or pseudo-rhombohedral crystal structure (Figure 9). Paratacamite appears as a secondary phase growing in a layered structure on cuprite with a Gibbs free energy of $-1338\ kJ.mol^{-1}$ (Scott, 2000), slightly lower than atacamite at $-1339.2\ kJ.mol^{-1}$ suggesting that they could form under similar conditions.

HM:R -3 #148
a=13.654Å
b=13.654Å
c=14.041Å
α=90.000°
β=90.000°
γ=120.000°
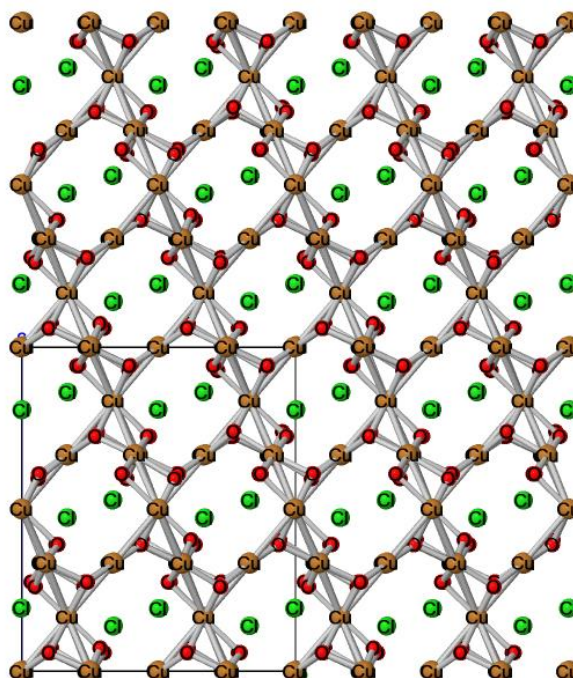
Figure 9 – Crystal structure of paratacamite in a 2x2x2 cell viewed in the "x" direction. Produced using the Jmol software (Jmol, 2021) using the data from (Fleet, 1975).

While paratacamite had been linked to atacamite, Raman spectroscopic analysis of the compound by Frost et al. (2002) determined that it was an isomorphic compound with a different structure, and therefore a separate mineral to the atacamite polymorphs. In 1996 the clinoatacamite polymorph was identified and it was discussed by Grice et al. (1996) and Jambor et al. (1996) that many of the previous studies may have

incorrectly identified the clinoatacamite as paratacamite such as in Pollard et al. (1989), Sharkey & Lewin, (1971) and Walter-Levy & Goreaud (1969). Furthermore, Lopesino et al. (2018) observed that this misidentification was commonly observed in the literature, even in studies post 1996, due to subtle differences between the XRD patterns (Chu et al., 2011) and therefore many of the studies identifying paratacamite should be attributed to clinoatacamite instead.

Fleet, (1975) and Jambor et al. (1996) found that paratacamite had Jahn-Teller distortion in three of the four Cu^{2+} sites while the fourth site is angle distorted, leading to a rhombohedral crystal structure and a space group of $R\bar{3}$. Fleet (1975) determined that the stabilisation of this phase occurred by the partial substitution of non-Jahn-Teller distorting cations (M^{2+}), such as Zn^{2+} and Ni^{2+}, into ⅓ to ½ of the angle distorted sites, leading to the chemical formula of $Cu_3(Cu, M^{2+})(OH)_6Cl_2$. Jambor et al. (1996) observed that 2-3% and up to a maximum of 14.8% zinc was required to be incorporated into the crystal structure to form paratacamite. While Braithwaite et al. (2004) showed that a transition from clinoatacamite and paratacamite occurred when the crystal structure contained 5-17.5% zinc, with up to 2.7% zinc being detected in clinoatacamite. This suggests that relatively high concentration of the non-Jahn-Teller distorting cations are required to form paratacamite.

2.4.6.6 *Clinoatacamite*

Clinoatacamite is a recently discovered atacamite polymorph which has a monoclinic crystal structure (Figure 10) (Grice et al., 1996; Jambor et al., 1996). Its formation was shown to be preferred in electrolytes that do not contain non-teller distorting cations where less than ⅓ of the angle distorted sites are occupied in the crystal lattice (Braithwaite et al., 2004).
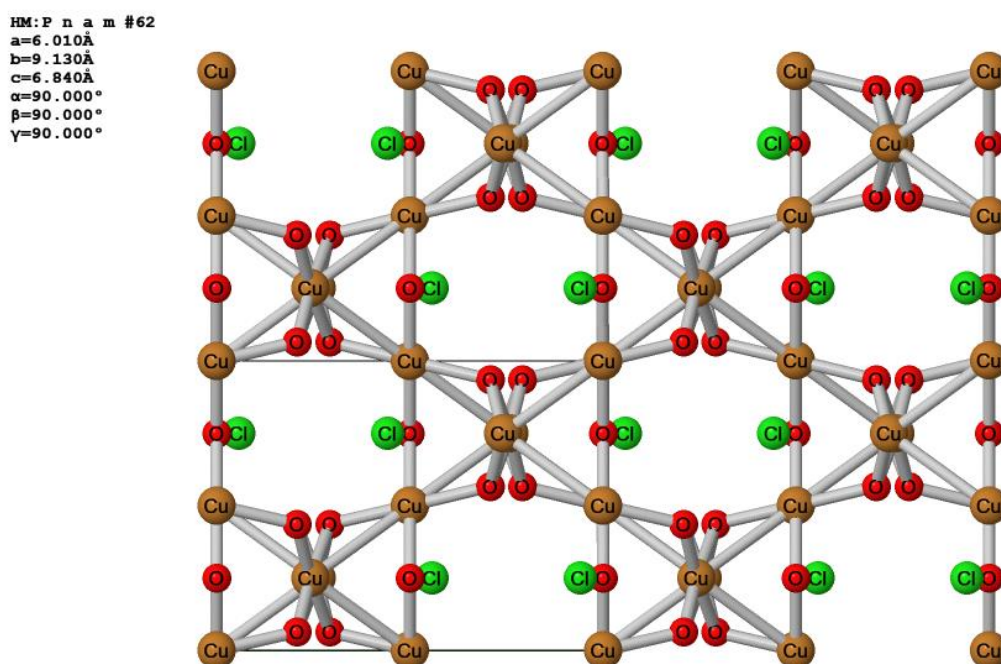
Figure 10 – Crystal structure of clinoatacamite in a 2x2x2 viewed from the "x" direction. Produced using the Jmol software (Jmol, 2021) using the data from (Grice et al., 1996).

Strandberg & Johansson (1998) determined that, while atacamite was not always detected in laboratory experiments, clinoatacamite was always found, pointing to the higher thermodynamic stability of this phase. Clinoatacamite has also been shown to form in neutral chloride containing electrolytes/environments due to the hydrolysis of Cu^{2+} ions by the following Equation 18 (EL-Mahdy, 2005).

$$2Cu^{2+} + Cl^- + 3H_2O = Cu_2Cl(OH)_3 + 3H^+ \qquad \text{\textit{Equation 18}}$$
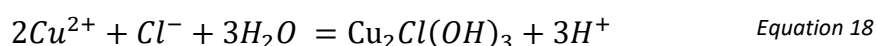
Sharkey & Lewin (1971) determined that clinoatacamite (incorrectly identified as paratacamite) formed in solutions containing low concentrations of $CuCl_2$. As this was

increased, a transition between clinoatacamite and atacamite was measured up to a concentration of $CuCl_2$ at 0.1F ($\sim 13.4\ g.L^{-1}$) where only atacamite was formed. This result was supported by Walter-Levy & Goreaud (1969) who found that pure clinoatacamite ("paratacamite") formed if the $CuCl_2$ concentration was 0.04F ($\sim 5.4\ g.L^{-1}$), while atacamite dominated the patina corrosion product if the concentration of $CuCl_2$ was between 0.17 and 0.22F ($\sim 22.9 - 29.8\ g.L^{-1}$). Furthermore Pollard et al. (1989) observed that atacamite converts to clinoatacamite ("paratacamite") if the sodium chloride concentration was less than $0.4\ mol.dm^{-3}$ ($\sim 23.4\ g.L^{-1}$).

Oswald & Feitknecht (1964) suggested that synthesising atacamite resulted in a dense layer which was stable at room temperature, however Pollard et al. (1989) determined that clinoatacamite ("paratacamite") was thermodynamically stable up to 40°C. This shows the close relationship between atacamite and clinoatacamite formation where slight changes in the variables can result in the formation of either phase.

2.4.7 Grain Size

Franey & Davis (1987) measured a direct correlation between the grain size and the surface defect density to the thickness of the patina, where the higher the defect density the thicker the patina, due to faster cuprous ion transportation. Nairn et al., (2003) also observed that the nucleation of an epitaxial cuprous oxide film occurred at the grain boundaries. The film grew laterally across the surface, orientating the cuprous oxide grains to that of the existing copper as it reacted with oxygen in the environment. While patina was shown to penetrate surface grain boundaries in older copper samples (FitzGerald et al., 2006).

[60]

2.5 Seawater Variables

2.5.1 Properties

Variations in seawater properties can occur on the local and global scales and are dependent on several factors such as the ecosystem, season, geographical location, local environmental pollutants, and ocean currents (Shifler, 2005). It is generally accepted that the salinity of seawater at 25°C is 35 $g.kg^{-1}$, with Table 3 showing the typical major seawater constituents as reported by (Lyman & Abel, 1958).

Table 3 – Major constituents of seawater (Lyman & Abel, 1958).

	Constituent		$g.kg^{-1}$ of water	Parts per thousand
Cation	Sodium	Na^+	0.4590	10.556
	Magnesium	Mg^{2+}	0.1046	1.272
	Calcium	Ca^{2+}	0.0200	0.400
	Potassium	K^+	0.0097	0.380
	Strontium	Sr^{2+}	0.0003	0.013
	Sum		0.5936	12.621
Anion	Chloride	Cl^-	0.5353	18.980
	Sulphate	SO_4^{2-}	0.0551	2.649
	Bicarbonate	HCO_3^-	0.0023	0.140
	Bromide	Br^-	0.0008	0.065
	Fluoride	F^-	0.0001	0.001
	Sum		0.5936	21.835
	Boric Acid	H_3BO_3		0.026
	Total			34.482

However, salinity variations may occur when exposed to high temperatures, resulting in evaporation, or fresh water, such as from the melting of polar ice caps or river estuaries, increasing or decreasing the salinity, respectively. This variation in global annual surface salinity (Figure 11, top) can range of between $31 - 37\ g.kg^{-1}$.

2.5.2 Factors Governing the Corrosivity of Seawater

There are several factors which affect the corrosivity of seawater including temperature, oxygen content, salinity, pH, and flow rate. It has been found that the corrosion rates are higher in shallow waters where the temperatures and bioactivity are higher (Sawant et al., 1993).

2.5.2.1 *Temperature*

It is generally accepted that with an increase in temperature the corrosion rate of copper also increases. This may be due to the modification of the properties of the cuprite layer at elevated temperatures allowing faster diffusion of species through this layer, enhancing the corrosion rate (EL-Mahdy, 2005). An increase in activity was also recorded by Abdallah et al. (2009) as the electrolyte temperature increases. Furthermore, Kong et al. (2017) also observed an increase in electrode activity with the E_{corr} becoming more electronegative (active), while an increase in current density was also measured suggesting an increase in corrosion rate as the temperature was increase to 80°C. However, it was also shown that the corrosion resistance increased with temperature, peaking at 60°C before declining with temperature, which may be due to the formation of compact a corrosion product. While Chico et al. (2005) found that small variations in the corrosion rate were recorded between 5 and 30°C. Global variations in surface seawater temperature (Figure 11, middle), could allow for differences in the corrosion rate to be measured.

With the global shipping tending to occur in medium to high salinity and temperature waters (Figure 11) it may therefore be assumed that the patination rate of the antifouling coatings would be similar all things being equal.

Annual salinity at the surface (one-degree grid)

Annual temperature [°C] at the surface (one-degree grid)
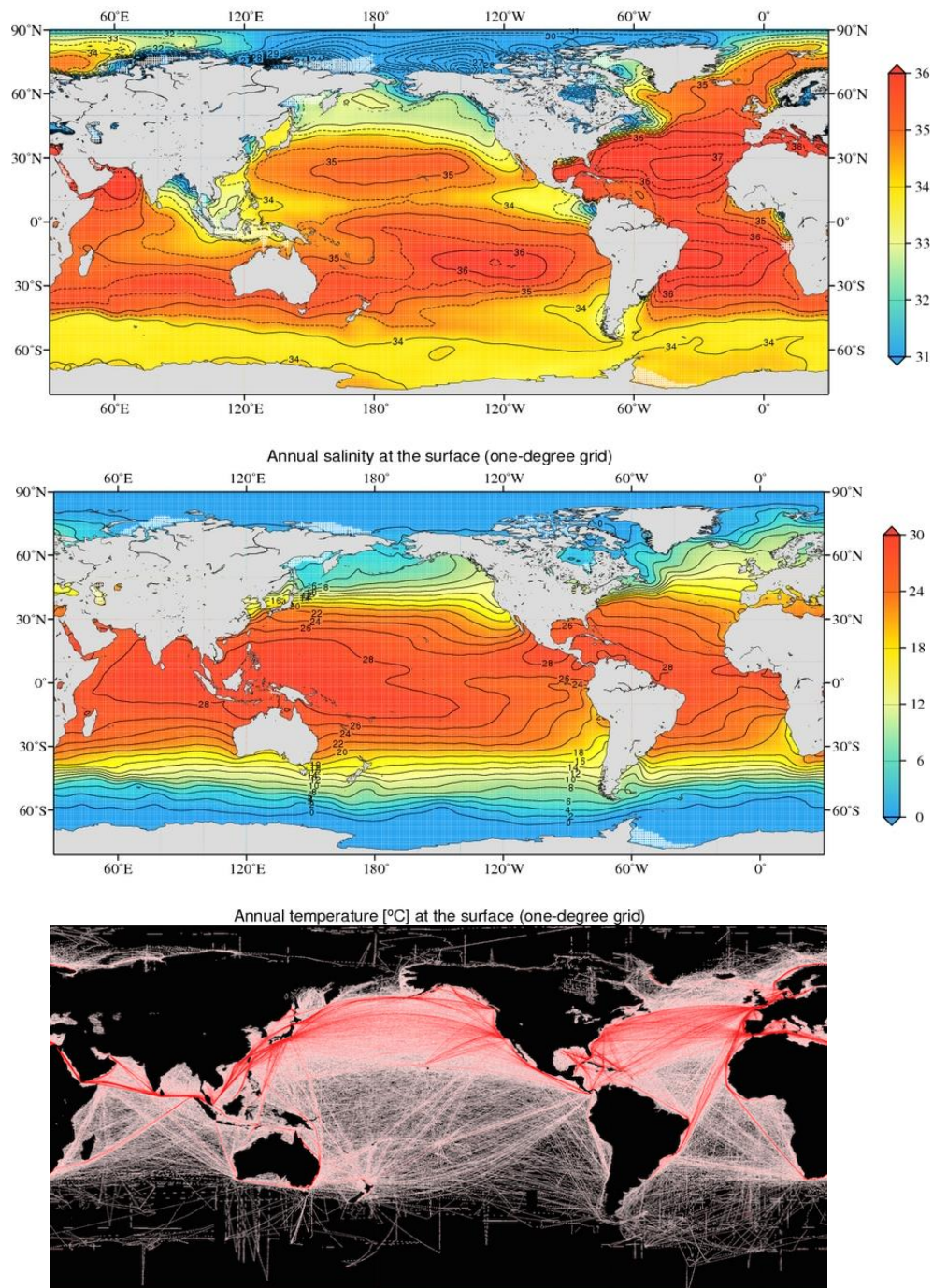
Figure 11 – Top image – World Ocean Atlas annual surface salinity between 2005 -2012 with a 0.5% contour interval (Zweng et al., 2013). Middle image – World Ocean Atlas annual surface temperature between 2005 and 2012, with a 2°C contour interval (Locarnini et al., 2013). Bottom image – Global marine traffic (gCaptain, 2014).

2.5.2.2 *Oxygen content*

The dissolved oxygen content may be the one of the most important factors when considering the corrosivity of seawater (Farro et al., 2009). The highest corrosion rates have been recorded in areas with a relatively high availability of dissolved oxygen (Nunez et al., 2005), which may up to 12 ppm (Shifler, 2005). Bioactivity can also affect

the oxygen concentrations where in shallow coastal waters higher temperatures and large amounts of nutrients are available compared to the open ocean, promoting photosynthesis by marine plants, while the decomposition of organic matter can decrease the oxygen content (Farro et al., 2009; Nunez et al., 2005). Furthermore, the oxygen concentration tends to decrease with increasing temperature or salinity. However, these factors also influence the corrosion rate and therefore the effect may be negligible.

2.5.2.3 *pH*

Copper corrodes in the presence of hydrogen ions (Equation 19). The lowering of the electrolyte pH results in the presence of increasing concentrations of hydrogen ions which can therefore enhance the corrosion rate of copper. (EL-Mahdy, 2005)

$$2Cu + 4H^+ + O_2 = 2Cu^{2+} + 2H_2O$$
<div align="right">*Equation 19*</div>
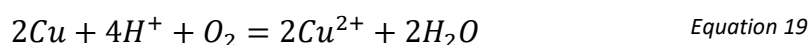
The pH of the electrolyte has been shown to affect its electrochemical properties where the pH becomes more alkaline the OCP of the copper electrode is more negative, lowing the current density and increasing the activity of the copper (Antonijevic et al., 2009). Furthermore, the copper patinas tend to be weakly soluble in electrolytes with a low pH. Seawater in the open ocean has a surface pH of 8.1 however with increasing CO_2 emissions a reduction of approximately 0.1 pH units has been measured since preindustrial values (IPCC, 2019). However the high pollution levels associated with harbour and coastal waters result in lower pH values such as that observed in Kokuhennadige et al. (2013) of 7.83 and Zaqoot et al. (2009) of 7.75. This suggests that copper would corrode at an accelerated rate in polluted seawater when compared to the open ocean.

2.5.2.4 *Flow rate*

The flow rate of seawater has been found to increase the corrosion rate by removing the protective film, promoting the diffusion of corrosive species to the metal surface or through the erosion of the metal surface. However, the flow rate may have a beneficial effect on the corrosion rate by increasing the passivation rate, remove corrosive ions or transporting protective ions to the metal surface and therefore reducing the corrosion rate. (Shifler, 2005)

2.5.3 Marine Environmental Zones

FitzGerald et al. (2006) found that the outdoor corrosion of copper was approximately two orders of magnitude greater than indoor corrosion, suggesting that the protective nature of the cuprite layer is degraded in the presence of an electrolyte. Within the marine environment this can be further increased due to the presence of chloride ions.

When structures, such as ships hulls, are exposed to the marine environment several zones can be identified, including: 1) Atmospheric; 2) Splash/spray; 3) Tidal; and 4) Full immersion (see Figure 12), a further zone 5) Mud/sediment has also been identified. Antifouling coatings are generally applied to surfaces where fouling organisms have the greatest chance to become attached, such as those areas that are under constant immersion (zone 4). However variations in the tidal height, analogous to the light and deep loading condition of marine vessels, mean that these coatings may also be placed in zone 3. The splash/spray and atmospheric zones only anticorrosive paints are applied however these environments may provide favourable conditions allowing accelerated patination of the antifouling coatings to occur as the different zones are known to influence the corrosion rate of metals (Melchers & Jeffrey, 2012; Powell & Michels, N/D). Therefore zones 1-4 are of most interest to this study.
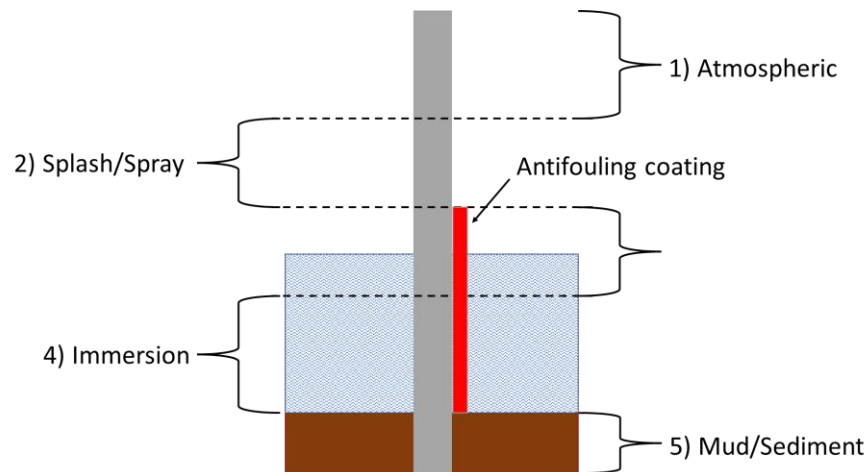
Figure 12 – Visual depiction of the marine environmental zones. Adapted from (Veleva & Farro, 2012)

Veleva & Farro (2009) observed that the highest corrosion rate of 0.071 mm/year occurred within the mean tidal zone, where the poorly adhered patina could be easily removed, exposing the substrate to high oxygen concentration seawater as well as being exposed to a constant source of wetness. The lowest corrosion rate was observed in the atmospheric zone of 0.016 mm/year, while the splash/spray and full immersion zones were less aggressive than the tidal zone with a corrosion rate of 0.025 and 0.032 mm/year, respectively.

2.5.3.1 *1) Atmospheric Zone*

In the marine environment sea salt aerosols form in the atmospheric zone due to the breaking of waves, wind blowing across the surface of the water and the movement of marine vessels through the water. This creates a fine mist of chloride rich water droplets which can deposit onto exposed surfaces which can concentrate through evaporation allowing corrosion to occur.

The time of wetness affects the amount of corrosion that occurs (Shifler, 2005), which is affected by the orientation of the surface, adding an extra layer of complexity when determining the corrosivity in this environment (EL-Mahdy, 2005). For example, samples positioned in horizontally will experience a higher corrosion rate than those

orientated vertically as moisture can collect on the surface increasing the time-of-wetness. This can also dissolve atmospheric contaminates, such as chlorine in the marine environment, which can concentrate during evaporation, accelerating corrosion. Erosion corrosion may also occur, however to a lesser extent, as the concentrated electrolyte drains away. The cyclic wet and drying may be equivalent to the corrosion characteristics like that of the splash/spray zone (Schumacher, 1979).

In addition to the airborne sea salt particles, samples are also exposed to greater amounts of free oxygen than the other zones which can lead to the formation of high levels of cuprite, as well as the possible formation of copper sulphate phases resulting from atmospheric pollution (Veleva & Farro, 2012). Anticorrosive coatings are generally applied in this region to protect the substrate from the high levels of chloride rich water droplets, with the risk of fouling being insignificant in this zone.

2.5.3.2 *2) Splash/spray zone*

The splash/spray zone is thought to be the most aggressive as this area is wetted with splashes of highly aerated seawater, creating a differential aeration cell aiding the corrosion process (Veleva et al., 1996). The water may also contain bubbles that can dislodge protective films that may have formed. Cuprite and atacamite tend be present in this zone (Schumacher, 1979). Generally anticorrosion coatings are applied in this region as it is more difficult for the marine biofouling species to settle and is therefore less detrimental than the risk of corrosion.

2.5.3.3 *3) Tidal Zone*

Changes in the tide or loading of marine vessels can vary the water level allowing for similar characteristics to that of the splash spray/zone to occur where a differential

aeration cell is formed. However, unlike the splash/spray zone this area is cyclically wetted resulting in longer periods of corrosion to occur (Schumacher, 1979). In addition, poorly adhered patina can be easily removed through wave action in this zone exposing fresh copper. This can allow corrosion to continue unimpeded resulting in the most aggressive conditions being found at the average tidal line (Nunez et al., 2005; Veleva et al., 1996; Veleva & Farro, 2012). When considering the tidal zone in relation to antifouling coatings it may be represented by the loading condition of the marine vessel. For example, if a cargo vessel is fully loaded with containers then it would sit deeper in the water, equivalent to high tide, however instead of it being at this level approximately every 12 hours, as might be expected for a stationary object such as that shown in Figure 12, it would remain at this point for days or weeks between ports. Therefore, antifouling coatings are applied at the waterline between the low and deep loading conditions of the marine vessel.

2.5.3.4 *4) Full Immersion*

Areas in the full immersion zone are exposed to similar conditions to that of the tidal zones however they constantly exposed to seawater saturated with oxygen. Veleva & Farro (2012) found that copper patinas formed in the tidal zone were like that formed in the full immersion zone with atacamite being the sole majority phase. A parabolic corrosion rate was measured in this zone where the corrosion rate decreases with time due to the formation of an increasingly protective patina. The diffusion of oxygen through the patina to the substrate is a limiting factor controlling the rate of corrosion which was measured by Farro et al. (2009) to be 2.88 $g.m^{-2}.yr^{-1}$.

Chapter 3: Methodology

The following section describes the various experimental and analytical techniques that were used to determine; the natural patina compounds that were found on the surface of in-service paint flakes, the corrosion properties of copper and the copper patina products that were produced within the different test environments, as well as describing the various laboratory experiments that were used to accelerate the patination of cuprite pigments, pure copper coupons and antifouling coatings.

3.1   In-Service Paint Flakes.

During routine inspections, samples of antifouling coating paint flakes were obtained from the hull of 14 merchant vessels. These samples were removed from below the waterline areas, that were deemed to have formed green-blue discolouration upon visual assessment. Table 4 shows the source of the paint flakes, the specific coating and the antifouling pigments as identified from their Safety Data Sheet (SDS). The paint flakes came from a range of coating types including examples of the three main classes of biocidal antifouling coatings namely Controlled Depletion Polymer (CDP), Self-Polishing (SPH) "hybrid" coatings, and Self-Polishing Copolymer (SPC) coatings. These coatings rely on different mechanisms to control the release of biocide, either principally using water-soluble non-polymeric binder components (CDPs), the use of seawater-reactive binder polymers (SPCs), or a combination of both (SPHs) (Finnie & Williams, 2010). Where information on the type of coating was not available, analysis of the coating allowed for the identification of pigments that were present.

Only limited information was available regarding each ship's trading route and operational parameters, but it was assumed that the range of samples collectively

represented typical in-service exposure conditions. Photographs of the paint flakes were captured prior to further detailed analysis.

These samples were analysed using the methods outlined in Chapter 3.4.6 specifically X-ray Diffraction (XRD) to determine the phase composition of the patina. Cross-sections of the paint flakes were placed between a spring clip to hold it vertical, placed into 30 mm circular moulds and encapsulated in a Buehler EpoxiCure™ 2 two-part epoxy. Once cured the samples were polished to a 1 μm finish using standard metallographic practices. Both the top surface and cross-sections were analysed in the Scanning Electron Microscopy (SEM), using the Backscattered Electron and Energy Dispersive X-ray (EDX) detectors to observe the thickness and elemental composition of the patina and depletion/leach layers.

Table 4 – Summary of the paint flake samples detailing the source, paint type, colour, and antifouling pigments present.

Paint Flake	Source	Paint type	Original Colour	Antifouling pigments (%)				
				Cuprite	Zinc Oxide	Copper Pyrithione	Zinc Pyrithione	Zineb
1	MSC Marianna	Intersmooth 460 (SPC)	Dark Red	25-50	x	x	2.5-10	x
2	YK Sovereign		Dark Red					x
3	Leonis		Dark Red					x
4	MSC Tasmania		Dark Red					x
5	Campion Pride		Dark brown					x
6	BR Cormorant		Red					x
7	British Integrity		Red					x
8	Sonagol	Interspeed 7460 (SPC)	Red	25-45	x	<4.5	x	x
9	Old patinated panel		Red					x
10	Orpheus Orchid	Interswift 655 (SPH)	Brown	25-50	10-25	1-2.5	1-2.5	x
11	Sitamarie		Dark Red					x
12	Hartlepool Marina (wood)	Interspeed 6400 (CDP)	Red	25-50	10-25	x	x	<10
13	Overseas Mindoro	Not provided	Red	✓	-	-	-	x
14	Large paint flake		Red	✓	-	-	-	-

3.1.1   Pigments

Samples of the typical pigments used in the antifouling coatings including cuprite (Pigment Number (PN): KT2047 and KT2031), zinc oxide (PN: PW1528), copper pyrithione (PN: KT2000), zineb (PN: KT2013), zinc pyrithione (PN: KT3012), haematite (PN: ER0016), silicon dioxide (PN: FA0110) and titanium dioxide (PN: PT0247) were provided by AkzoNobel. These pigments were analysed using the method outlined in Chapter 3.4.6.1 with the results being shown in Appendix 2 providing a database to compare the pigments against the patina that had formed on the antifouling coatings.

3.2   Pourbaix Diagrams

Pourbaix first derived the potential-pH diagrams from the Nernst equation using the thermodynamic data associated with the electrode-electrolyte system to show the most probable equilibrium domains where certain ions and compounds are thermodynamically stable. It was assumed that there was a limiting concentration of metal ions that can be thermodynamically dissolved, which was arbitrarily set at $1 \times 10^{-6} M$ (Pourbaix, 1966), equivalent to $0.06 \, mg/L$ of copper. Below this value the metal would be thought to be immune to corrosion while above it the metal could freely corrode. Using the results from the analysis of the in-service paint flakes and the Pourbaix diagrams specific environments can be targeted to ensure similar patina compounds could be produced at accelerated rates.

The Pourbaix diagrams also show the stability of water at atmospheric pressure indicated by two sloping dashed lines, between these lines water is stable (Pourbaix, 1966). At potentials above the upper line, the oxygen equilibrium line, oxygen evolution will occur. At potentials below the lower line, the hydrogen equilibrium line, hydrogen is evolved.

HSC Chemistry® version 6.0 (Roine, 2006) software package was used to produce the Pourbaix diagrams for the Copper—Cl—H$_2$O system. To create the diagrams the concentration of copper ions was set at $1 \times 10^{-6}\ M$ while the chloride concentrations included $0\ M$ (0% NaCl) $0.171\ M$ (1% NaCl), $0.599\ M$ (3.5% NaCl), $1.71\ M$ (10% NaCl) and $5.14\ M$ (30% NaCl). With Table 5 showing the species that were selected and the thermodynamic data at the different temperatures, taken from the database compiled by (Roine, 2006).

Table 5 – Species considered when constructing the Pourbaix Diagrams for the Cu-Cl-H$_2$O system. Data taken from the HSC Chemistry® version 6.0 software (Roine, 2006).

Species \ Temperature	Gibbs Free Energy ΔG (kcal/M)				Species \ Temperature	Gibbs Free Energy ΔG (kcal/M)			
	25°C	35°C	45°C	55°C		25°C	35°C	45°C	55°C
Cu	0	0	0	0	CuO_2^{2-}	-41.22	-40.095	-38.948	-37.781
$Cu(FCC)$	0.003	0.003	0.003	0.003	$CuOH^+$	-30.21	-29.825	-29.443	-29.063
$CuCl$	-28.686	-28.55	-28.415	-28.281	$Cu(OH)_4^{2-}$	-156.97	-155.002	-152.998	-150.958
$CuCl_2$	-41.522	-41.168	-40.816	-40.464	Cu_2OH^{3+}	-16.424	-15.95	-15.496	-15.06
$Cu_2Cl(OH)_3$	-160.042	-158.815	-157.587	-156.361	$Cu_2(OH)_2^{2+}$	-67.825	-67.166	-66.516	-65.875
CuO	-30.611	-30.389	-30.167	-29.946	$Cu_3(OH)_4^{2+}$	-151.42	-149.779	-148.142	-146.509
Cu_2O	-35.336	-35.153	-34.971	-34.788	$Cu(OH)O^-$	-60.096	-59.21	-58.311	-57.399
Cu^{2+}	15.545	15.546	15.547	15.548	Cl^-	-31.372	-31.079	-30.774	-30.459
Cu^+	11.946	11.77	11.591	11.408	Cl_3^-	65.864	66.5	67.158	67.84
$CuCl^+$	-16.352	-16.101	-15.856	-15.619	ClO^-	-8.668	-8.094	-7.508	-6.912
$CuCl_2^-$	-58.026	-57.53	-57.038	-56.549	ClO_2^-	4.108	4.784	5.471	6.167
$CuCl_3^-$	-75.324	-74.275	-73.24	-72.218					
$CuCl_4^{2-}$	-103.557	-101.923	-100.304	-98.697					

3.3   DC Electrochemical Techniques

A series of DC electrochemical techniques were used to analyse the different variables that may contribute to the acceleration of copper corrosion and therefore accelerate the production of copper patinas. The DC techniques included open circuit potential measurements, potentiodynamic polarisation with Tafel analysis and potentiostatic polarisation.

3.3.1   Experiment Setup

The DC electrochemical test methods use a similar setup consisting of a three-electrode electrochemical cell with a macro copper working in the different environmental variables described in the following section.

3.3.1.1 *Macro Electrodes*

The working electrodes were created by taking 10 mm long sections from a 11.3 mm diameter 99.9% pure copper rod and partially drilling a 3 mm diameter hole into the sectioned surface. An insulated copper electrical wire was inserted into the hole with a lead-free solder to create an electrical connection. The electrode was mounted in a two-part epoxy resin leaving a circle of copper, 11.3 mm diameter, exposed following standard metallographic practices to produce a clean surface with a 1200 grit finish. The sample was washed to remove grinding debris under running water, degreased and dried using acetone and a hot air drier.

3.3.1.2 *Three Electrode Cell*

A standard three-electrode cell arrangement was used for the electrochemical tests using the copper working electrode, a saturated potassium chloride and silver/silver chloride (Ag/AgCl) double junction reference electrode and a platinum auxiliary

electrode with a 1 cm^2 surface area. The electrochemical measurements were performed using the Uniscan multichannel potentiostat G560RM.

3.3.1.3 *Test Environments*

Antifouling coatings may be used in a range of environments from open ocean where the average annual sea temperature can range from between 0°C and 30°C (Locarnini et al., 2013) with an average pH 8.1 (IPCC, 2019) and a salinity of 3.5% (Lyman & Abel, 1958), to polluted harbours where the pH is acidified (Kokuhennadige et al., 2013 and Zaqoot et al., 2009), to areas of low salinity such as freshwater tributaries or where freshwater reaches the sea. Therefore a range of variables, summarised in Table 6, were selected which could satisfy the different environments while also accelerating the patination of antifouling paints.

Table 6 – Electrolyte conditions used for the DC electrochemical experiments

Condition	Variable				
Sodium Chloride Concentration (%)	0	1	3.5	10	30
Temperature (°C)	25	35		45	55
pH	4		7		10
Volume (mL)	150				
Environment	Stagnant i.e. no agitation with fresh solution used for each sample				

The ability to maintain temperatures below 20°C under laboratory conditions, for any length of time, was limited and while temperatures above 25°C are unlikely to be experienced in the natural environment, the higher temperatures are expected to acceleration in the patination of antifouling coatings was expected to occur at elevated temperatures. The temperature of the electrolyte was maintained to ± 1°C using a temperature-controlled water bath, with a thermometer being used to ensure the correct temperature was maintained.

The pH values of 4, 7 and 10 selected are not typically found in the seawater environment, however they were selected to provide environments in which different patina compounds may form. The pH of the electrolytes was monitored using a Hanna Edge pH meter and was modified using 1% hydrochloric acid (S.G. 1.0048) or 1% sodium hydroxide solutions to the required pH.

While 3.5% NaCl is typically used as an equivalent electrolyte to seawater, it is thought that the higher sodium chloride concentrations of 10% and 30% would accelerate the patination of the coatings while the 0% and 1% would represent the freshwater/ low saline conditions that the antifouling paints may be exposed to. An analytical grade sodium chloride, with 0.145% total impurities, 0.008% bromide, 0.1 ppm copper and trace levels (<1 ppm) organics, was weighed to ensure the correct electrolyte concentration using a 2 decimal place digital balance. This was dissolved in a volumetric flask with deionised water, with a resistivity of 15.1 MΩ, to make 1L of electrolyte.

3.3.2 Open Circuit Potential

The Open Circuit Potential (OCP) or corrosion potential (E_{corr}) measures the electrical potential of an anode (copper working electrode), with respect to a reference electrode (Ag/AgCl) when exposed to the electrolyte. The OCP is achieved when both the anodic and cathodic reactions are acting freely, in equilibrium, on the anode surface, where there is zero-net current ($i_0 = i_a = i_c$) (Thompson & Payer, 1998). The potential of the working electrode can be measured over extended periods to observe how the potential varies with time.

The magnitude of the potential relates to the activity of the anode in the electrolyte with a more negative potential having a greater activity where they release electrons more readily (Shreir et al., 1994), which may suggest that the anode is reacting with the electrolyte at a greater rate. This technique can therefore be used to indicate the solutions which are likely to accelerate the corrosion of metals. Further electrochemical techniques, such as potentiodynamic polarisation, are required to determine how the different variables affect the anodic and cathodic reactions on the working electrode.

3.3.2.1 *OCP Experimental Procedure*

Using the experiment setup outlined in Chapter 3.3.1, the OCP of the copper electrode exposed to the different electrolytes, pH values and temperatures was recorded over a 24-hour period at a frequency of 1 measurement every 10 seconds.

3.3.2.2 *Copper Immersion*

Further analysis of the electrode surface was required to understand how the different variables affected its patination under short exposure times which could be used to relate what the OCP data was showing to what was happening on the surface. Due to the size of the working electrode, flat sheets of copper where sectioned into coupons approximately 10 mm x 10 mm x 0.1 mm using a guillotine. Prior to testing, the copper coupons were dipped into a gently agitated 10% hydrochloric acid (S.G. 1.0474) bath, at room temperature, for 5 minutes to remove the naturally formed surface oxide. The coupons were then immersed in 1 litre deionised water and rinsed under a constant stream of deionised water to remove the acid wash before being dried using industrial methylate spirit (I.M.S.), paper towel and hot air. An example of one of the prepared test coupons is shown in Figure 13.
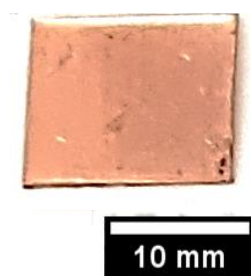
Figure 13 – Example image showing the surface of the copper coupon following the oxide stripping procedure.

The coupons were then placed into beakers with one side facing skyward where the ions in the electrolyte could freely interact with the surface, whereas the groundward side was sat on the bottom of the beaker reducing ion availability. The beakers were filled with 80 ml of the electrolytes under the and conditions outlined in Chapter 3.3.1.3 i.e. temperature of 25, 35, 45 and 55°C, pH of 4, 7 and 10 and sodium chloride concentrations of 0%, 1%, 3.5%, 10% and 30% and covered to reduce evaporation. A water bath was used to maintain the temperature of the electrolyte over the 24-hour period.

After the 24-hour immersion the samples were removed from their solution, rinsed in deionised water to remove traces of sodium chloride and dried using industrial methylated spirits and hot dry air. The samples were stored in a vacuum desiccator, to prevent further patination, prior to analysing the exposed skyward side of the coupon using SEM, EDX and XRD.

3.3.3   Potentiodynamic Polarisation

Potentiodynamic polarisation techniques are widely used to assess metals and environments. Analysis of the polarisation curve (Figure 14) allows for: the estimation of the activation and passivation potentials and current densities, the corrosion rate, corrosion potential (E_{corr}) and the sensitivity of the metal to localised (pitting)

corrosion when it is exposed to an electrolyte with respect to a range variables, such as temperature, pH and chloride concentration.
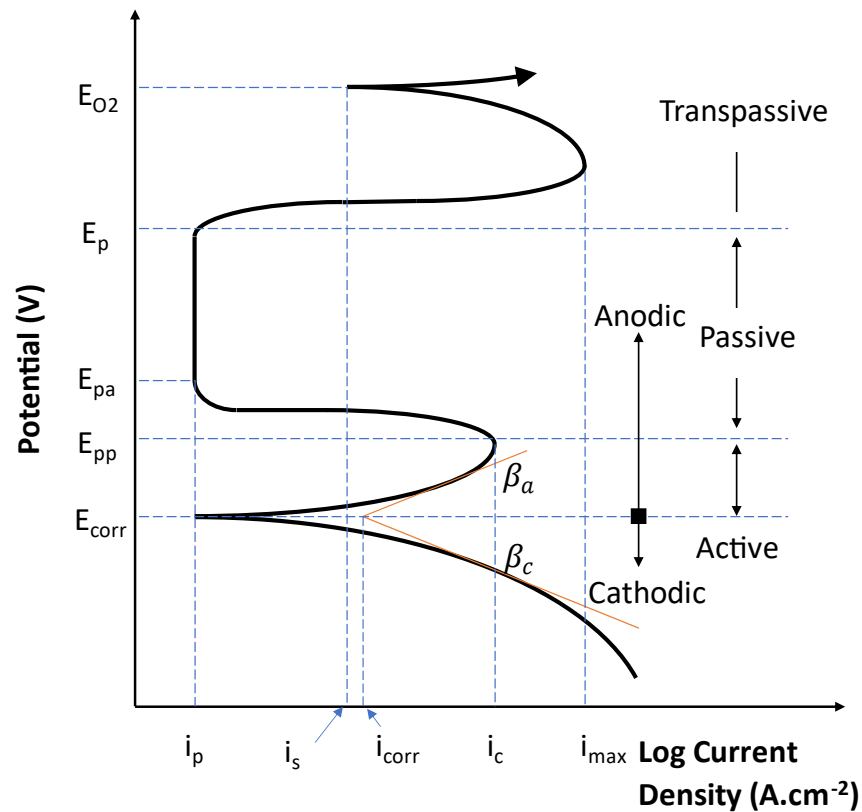
i_p = Passive Current Density E_{pa} = Passive Potential
i_{corr} = Corrosion Current Density E_{corr} = Corrosion Potential
i_s = Secondary Current Density E_{o_2} = Oxygen Evolution
i_c = Critical Current Density E_{pp} = Primary Passive Potential
i_{max} = Maximum Current Density E_p = Pitting Potential

Figure 14 – Hypothetical potentiodynamic polarisation curve with three possible regions that could be observed. Adapted from (Perez & Springerlink, 2004)

Potentiodynamic polarisation requires a standard three electrode cell to be used (see Chapter 3.3.1.2). The curve, such as that shown schematically in Figure 14, is produced by applying a potential between the working and auxiliary electrodes and recording the current response. The applied potential results in either the preferential anodic or cathodic reactions on the surface of the working electrode to occur. As the potential is scanned at a certain rate (Chapter 3.3.3.1) from an electronegative potential, with respect to the OCP, to more electropositive values, both cathodic and anodic

information about the system can be recorded. When the potential reaches the desired value, the test is terminated. In this work the potential was scanned from -200 mV vs OCP to 600 mV vs Ag/AgCl. To reduce any inaccuracies to the measurements caused by the solution resistance the distance between the working and reference electrodes was kept to less than 10 mm.

3.3.3.1 *Sweep Rate*

The sweep rate, i.e. the rate at which the potential is changed over time, can affect the behaviour of materials. In general, for a given potential, the faster the sweep rate the higher the resulting current (Thompson & Payer, 1998). This in turn can mask important kinetic data about the system. Therefore, the sweep rate was optimised to observe the pseudo steady state conditions (Chapter 6.1.1.1). In this work a copper electrode was potentiodynamically polarised in a neutral pH, naturally aerated 3.5% NaCl electrolyte at 25°C using six sweep rates of 0.025, 0.25, 0.5, 1, 2, and 25 mVs^{-1}. After comparing the polarisation curves a scan rate of $1\ mV.s^{-1}$ was determined to produce an accurate curve and was therefore selected for further polarisation testing.

3.3.4 Tafel Extrapolation

Further analysis of the cathodic and anodic domains present in the potentiodynamic polarisation curves allows for the corrosion current density to be determined and therefore an estimated corrosion rate can be calculated. While the estimated corrosion rate is not always the same as that found from mass loss measurements its relative speed has meant that it has become a widely used technique (Frankel, 2016).

The Tafel region of the polarisation curve is considered to be a linear portion of the polarisation curve at between ± 50 mV and ± 250 mV of the E_{corr} that extends at least

one decade of the logarithmic current density scale (Princeton Applied Research, N/D). This linear region is then extrapolated until both the anodic and cathodic portions intersect at around the E_{corr}, at this point the rate of the cathodic reaction is equal to the anodic reaction (Thompson & Payer, 1998), resulting in the identification of the corrosion current density (Figure 14 and shown in more detail in Figure 15).
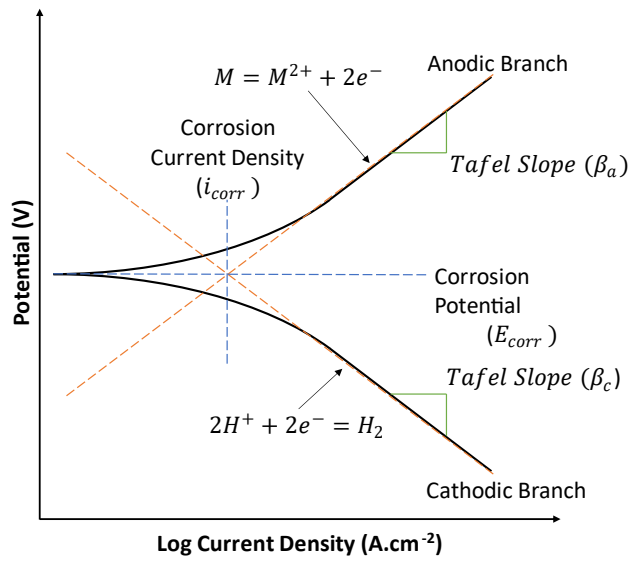
The anodic slope is given by:

Equation 20

$$\beta_a = 2.303 \frac{RT}{\alpha nF}$$

The cathodic slope is given by:

Equation 21

$$\beta_c = 2.303 \frac{RT}{(1 - \alpha)nF}$$

Where:

$F = Faraday\ constant\ (C.mol^{-1})$,
$n = number\ of\ electrons$,
$R = Gas\ constant$,
$T = Absolute\ temperature\ (K)$
and
$\alpha = Charge\ transfer\ coefficient$
$(J.mole^{-1}.K^{-1})$

Figure 15 – Tafel extrapolation of the potentiodynamic polarisation curve. Adapted from (Kakaei et al., 2019)

Once the i_{corr} value was determined, the polarisation resistance (R_p), i.e. the ability of a material to resist corrosion, can be calculated from the Stern-Geary equation (Equation 22), and assuming uniform corrosion, the corrosion rate (Equation 23) and mass loss (Equation 24) can be estimated.

$$i_{corr} = \frac{\beta_a.\beta_c}{2.3\ (R_p)(\beta_a + \beta_c)}$$

Equation 22

$$Corrosion\ Rate\ (mm.yr^{-1}) = \frac{3.27 \times 10^{-3}\ i_{corr}\ EW}{\rho}$$

Equation 23

$$Mass\ Loss\ (g.m^{-2}.d^{-1}) = 8.954 \times 10^{-3}.i_{corr}.EW$$

Equation 24

Where ρ = density ($g.cm^{-3}$) and EW is the equivalent weight.

[80]

3.3.4.1 *Tafel Analysis*

The data collected from the potentiodynamic polarisation curves was plotted in OriginPro® 2020 and analysed to determine the linear portion of the curves within ± 50 – 250 mV of the OCP on the anodic and cathodic branches. Once these sections of the curve were identified a linear fitting function was applied with the lines being extend until they crossed. At this crossing point the E_{corr} and i_{corr} values were recorded and used to calculate the corrosion rate.

3.3.5 Potentiostatic Polarisation

Potentiostatic polarisation is a technique where a constant potential is applied to an electrode for a certain length of time to drive an electron transfer reaction, resulting a current response (Lin et al., 2019). This technique can be used to observe the cathodic and anodic behaviours of materials. For example, if a cathodic potential, more negative than E_{Corr}, is applied to the electrode it is protected from corrosion as the surface is supplied with excess electrons which can break down water. This process may be used to clean corrosion products (ASTM G1, 2017) as hydrogen bubbles are created at the substrate which can lift the weakly adhered corrosion product from the electrode. However, if the electrode has an anodic potential, more positive than the E_{Corr}, is applied the electrode surface becomes activated and corrosion can occur. This can used to inform on factors such as stress corrosion susceptibility and crevice corrosion (Shreir et al., 1994a; Shreir et al., 1994b). In this study potentiostatic polarisation was used to accelerate patination rate and control the type of patina that was formed.

3.3.5.1 *Potentiostatic Polarisation Of Copper Anodes*

A range of potentials that were selected that were likely to produce the desired patina found after assessing the patinated in-service paint flakes and Pourbaix diagrams. The mass of the anode was recorded before potentiostatic polarisation at 100, 200, 300, 500, 700 and 1000 mV vs Ag/AgCl in a 200 ml, neutral pH, 3.5% NaCl electrolyte, at 25°C for 30 minutes. The patina formed on the electrode surface was analysed using SEM and XRD techniques, which was then removed using tissue paper to record the mass loss of the electrode. The patina that had developed in the electrolyte was filtered, rinsed with deionised water to remove traces of salt water, and dried for further analysis.

To observe the effect of time on the patina product produced the electrode was polarised at 500 mV vs Ag/AgCl for 30 minutes in a neutral 3.5% NaCl electrolyte, at 25°C for 30 minutes before being left for 24 hours and was processed for XRD analysis, as described in Chapter 3.4.6.

The effect of the volume on the patina products was also investigated by polarising at 500 mV vs Ag/AgCl for 30 minutes in a neutral pH 3.5% electrolyte in volumes of 50 ml, 200 ml, 400 ml, and 500 ml. The patina was processed as described previously for XRD analysis as described in Chapter 3.4.6.

The final variable considered was the sodium chloride concentration and therefore the two potentials were selected 130 and 260 mV vs Ag/AgCl, which were selected based on the potentiodynamic polarisation curves where the current density shifted into a pseudo passive region where patina could form. The electrode was polarised in neutral pH 1%, 3.5%, 10% and 30% NaCl electrolytes at 25°C for 5 hours. The patina was

processed for XRD analysis as discussed in Chapter 3.4.6, with the mass loss of the electrode also being recorded.

3.3.5.2 *Potentiostatic Polarisation of Antifouling Coatings*

Potentiostatic polarisation of antifouling coatings was performed to replicate the accelerated patination results collected from similar testing on copper electrodes.

An Intersmooth® 7465Si antifouling coating, containing zinc oxide and copper pyrithione in addition to the main biocidal agent of cuprite, was applied to a mild steel substrate with a wet film thickness of 200 µm using a draw down blade. The use of a mild steel substrate provided a simple check to determine if any coating defects were present as iron oxide corrosion products would form. Should a copper substrate be used and defects in the coating be present then the corrosion products would match the expected patina products to that found on the antifouling coatings, masking the effectiveness of this technique.

A control immersion test cell and a potentiostatic polarisation cell (Figure 16) were used to observe whether the acceleration in patination can be achieved in similar fashion to the copper electrode. Each cell was created by attaching an acrylic tube, with an internal diameter of 25 mm, to the coated surface using a 50/50 mix of gum rosin and beeswax to create a watertight seal. Each experiment was performed in duplicate with 20 ml of freshly mixed 3.5% NaCl electrolyte modified to pH 7 at ambient (approximately 22°C ±1°C) temperature.

A three-electrode cell was then created by inserting an Ag/AgCl reference and platinum electrode into the tube and making the mild steel substrate the working electrode. From this, the OCP of the immersion cell could be recorded. Furthermore,

using the results from the potentiodynamic and potentiostatic polarisation of a copper anode the potential of the antifouling coating was set to 260 mV vs Ag/AgCl and held over a 48-hour period.
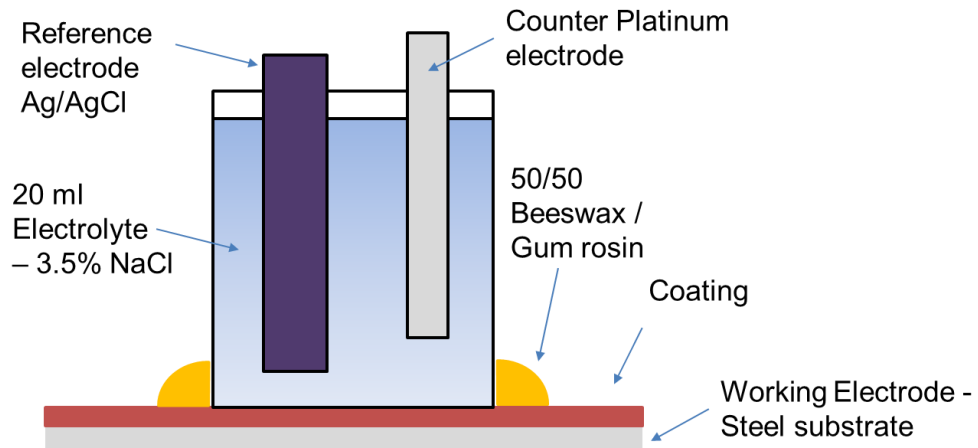
Figure 16 – Potentiostatic antifouling coating corrosion test cell

3.4   Laboratory Exposure Testing

Following the electrochemical testing the number of variables were reduced to focus on those likely to a) accelerate the patination, b) produce a similar patina to what was observed in-service and c) the variables that antifouling coatings maybe to be exposed to. The laboratory testing focused on creating test cells that contained different samples for patination including 99.9% pure copper coupons and cuprite pigment as controls and antifouling coatings.

3.4.1   Test Conditions

Many of the laboratory exposure tests relied on leaving samples in the electrolytes for a long period of time (a maximum of 672 hours or 4 weeks) under stagnant conditions. Therefore, the control of the chloride concentration, temperature and pH of the electrolytes was important. Each test cell contained 80 mL of electrolyte at the start of each experiment and Parafilm was used to cover the test cells to reduce evaporation when required. The mass of the test cells was recorded daily for the first 168 hours

then every 72 hours thereafter with the cells being regularly topped up to the correct mass with fresh deionised water, ensuring the chloride concentration remain consistent, where appropriate.

3.4.1.1 *Chloride concentration*

The electrolytes were the same as those used for the electrochemical testing i.e., 0%, 1%, 3.5%, 10% and 30%, made using analytical grade sodium chloride.

3.4.1.2 *Temperature*

Two temperatures were selected for the laboratory exposure testing at 25°C and 45°C ± 2.5°C with a relative humidity (RH) of 50 and 60 respectively. The testing took place in a water bath and oven where the temperature was maintained to ±1°C and ±3°C, respectively, of the target throughout the experiment.

3.4.1.3 *pH*

A neutral (7) pH was used for the testing as the Pourbaix diagrams indicated that this would produce the patina found in literature and on the in-service paint flakes. The pH of the electrolytes monitored daily for the first 168 hours and then every 72 hours thereafter to observe changes in pH and, where necessary the pH was modified, using a 1% (vol/vol) hydrochloric acid or 1% (wt/vol) sodium hydroxide solution.

3.4.2   Samples

3.4.2.1 *Antifouling coatings*

Initial testing focused on one type of antifouling coating "BQA 644" trade name Interspeed 6400® which contains a range of pigments, identified in Table 7. This coating is a hybrid providing the advantages of the controlled depletion polymer (CPD) and self-polishing systems allowing them to be analysed in one coating. The coating brochure states that it has an in-service life of up to 36 months (International, 2017).

Upon request the BQA 644 coating formulation was modified ensuring that all pigments except cuprite were omitted to observe the effect of cuprite loading and whether the additional pigments in the BQA 644 affect the patination rate.

Table 7 – Antifouling paints provided

Antifouling coatings (type)	Pigments
Interspeed® 6400 (CDP/SPS) BQA 644	Cuprite (Cu_2O) Zinc Oxide (ZnO) Copper Pyrithione ($C_{10}H_8CuN_2O_2S_2$) Zineb ($C_4H_6N_2S_4Zn$)
Interspeed® 6400 (CDP/SPS) Modified BQA 644	Cuprite (Cu_2O)
Intersmooth® 7465Si (SPC)	Cuprite (Cu_2O) Zinc Oxide (ZnO)

The antifouling coatings were applied to multiple flat 100 mm x 150 mm x 3 mm polypropylene panels using a "Sheen Adjustable Micrometre Film Applicator" draw down blade applying a wet film thickness of approximately 200 µm.

Following the testing the samples were sectioned using the Struers Accutom precision cutter, without coolant to preserve the patina that had formed, allowing the surface and cross-section through the coating to analysed. The cross-sectioned samples were stacked together such that the coating of one sample was facing the polypropylene bottom of another, allowing them to be distinguished. The very bottom sample was after 672 hours while the top sample was after 0 hours. The stacked cross-section was then mounted in the two-part epoxy and ground to a 1 µm finish using standard metallographic practices.

3.4.2.2 *Other samples*

To observe whether encapsulating the cuprite pigment in a polymer matrix affects the patination rate, a control sample of the same cuprite pigment (approximately 0.4 g)

used in the coatings was tested in a similar manner to that of the antifouling coatings. A further control sample of pure copper coupons (approximately 10 mm x 10 mm x 0.1 mm) was also tested to elucidate whether the cuprite pigment patinates at a faster rate than copper.

3.4.3 Test Procedures

Four laboratory test methods were considered to provide an accelerated simulation of the different conditions experienced by antifouling coatings when applied to an ocean-going vessel, namely full immersion, waterline, and splash/spray zones (Chapter 2.5.3, Figure 9), with the testing carried out described in the following sections.

3.4.3.1 *Immersion Testing*

The immersion cells were created by attaching a 45 mm internal diameter acrylic tube to 50 mm x 50 mm coated squares panels using molten beeswax and gum rosin (50/50 mix by weight). The immersion cell was used to simulate the conditions on antifouling coatings when they are beneath the waterline. To observe the effect of time on patina formation one of the test cells was removed every 168 hours for further analysis with the electrolyte being filtered to capture any loose patina, using Whatman Grade 1 Qualitative Filter Papers, with a particle retention of 11 μm (GE Healthcare Life Sciences, 2018), the coating surface was also rinsed with deionised water to remove traces of sodium chloride.

3.4.3.2 *Evaporation Cell*

The evaporation cell was used to observe the effect of a constantly increasing chloride concentration has on the patination rate of the samples listed in Chapter 3.4.2 and was performed in triplicate. This may be observed during the evaporation of a water droplet, however due to the electrolyte volume this occurred over an extended time.

The cell was left to evaporate at 22 ± 1°C and 45 ± 1°C for a maximum of 672 hours resulting in the formation of crystalline sodium chloride crystals intermixed with copper patina. This crystalline deposit was dissolved in deionised water at 22°C and filtered using Whatman Grade 1 Qualitative Filter Papers, to separate the insoluble patina product from the sodium chloride for further analysis. The filtered particulate was rinsed again with deionised water to remove traces of sodium chloride and dried in an oven at 50°C for 20 minutes.

3.4.3.3 *Salt Spray Corrosion Testing*

A neutral salt spray corrosion test was performed according to ASTM B117 using an Ascott CC450-iP salt spray cabinet to simulate the splash/spray conditions that occur on antifouling paints that are above the waterline and therefore determine whether it could be used to accelerate the patination of antifouling coatings. The BQA 644 and Modified BQA 644 antifouling coatings were applied to 21 25 mm x 50 mm polymer panels to assess whether the cuprite pigment loading and/or other pigments in the coating effects the patination rate. The samples were placed on a plastic racking and spaced out to ensure no cross contamination or pooling of the salt solution was possible (Figure 17).
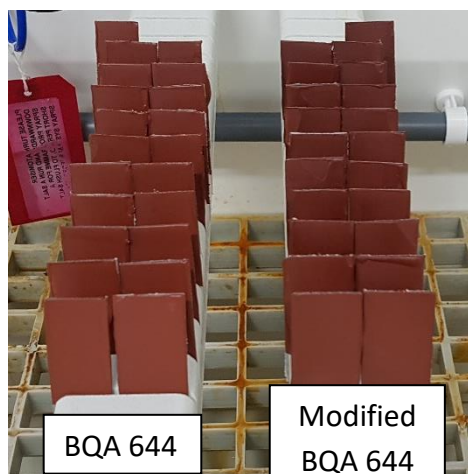
Figure 17 – Example sample positioning. Image captured prior to salt spray corrosion testing.

The salt spray solution was prepared by dissolving sodium chloride, with 0.145% total impurities, 0.008% Bromide, 0.1 ppm copper and trace levels (<1 ppm) organics, into high purity deionised water, with a conductivity <20 µS/cm at 25°C, in sufficiency quantities to create a 5% (wt/V) solution. While the pH of the solution was monitored using a Hanna Edge pH meter and adjusted using dilute hydrochloric acid and sodium hydroxide, as required, to 6.95.

The salt spray cabinet was operated continuously for 336 hours with a 10-minute break after 24, 48, 72, 168 and 336 hours to remove three samples of each coating, which were dipped in 500 ml deionised water to remove excess salt solution and left to dry. These samples were then analysed using SEM and XRD techniques.

3.4.4   Scanning Electron Microscopy

The Scanning Electron Microscope (SEM) is a powerful technique which is used in a vast number of fields from forensic investigations and medical science to materials research and has gained wider recognition since its commercialisation by the Cambridge Instrument Company in 1965 (Egerton, 2005).

Light microscopes are limited due to the wavelength of visible light of between 400 and 700 nm and the size of the numerical aperture, resulting in a low depth of field and magnification (0.08 μm at 1200x respectively) with a spatial resolution of 200 nm and therefore flat, smooth samples are preferred in light microscopes (Smallman & Ngan, 2014). However, SEMs use a finely focused beam of electrons to scan across the surface of the specimen which have a shorter wavelength than visible light allowing higher magnification (up to 1,000,000x), spatial resolution (1-10 nm) and depth of field images when compared to light microscopes (Egerton, 2005). Figure 18 shows the main components of the SEM.

SEM operate under high vacuum, removing any particles or molecules from the chamber which may prevent the electron beam from reaching the specimen surface, which must therefore be vacuum compatible. The electrons are generated at the top of the column using tungsten or LaB_6 sources either by heating a filament (thermionic emission) or through producing a large potential gradient across a fine tip tungsten wire (Field Emission Gun) (Williams & Carter, 1996).
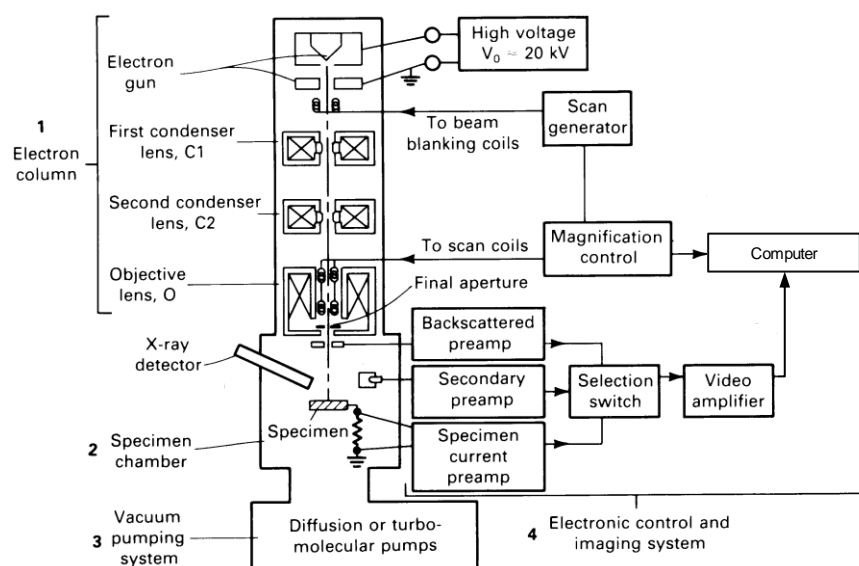
Figure 18 – Basic components of the SEM, adapted from (Verhoeven, 1986)

A high potential difference between the electron source and the anode (up to 30 kV) is used to accelerate the electrons through a series of apertures, electromagnetic and objective lenses to focus the diverging electron beam until it enters the vacuum chamber where the specimen is located. The electron beam is then scanned in a "raster" pattern to build-up an image of the surface of the specimen line by line with slower the scan rates providing improved image quality.

When the electrons reach the specimen, a surface charge may build up which can result in a reduction in image quality, image drift as well as several other phenomena. Therefore, a conductive path must be present to allow the electrons to flow to ground. Non-conductive samples may be coated with a conductive layer, several nanometres thick, such as carbon or gold. The SEM may also be used in a low vacuum mode where a vapour is pumped into the chamber removing the charge from the sample allowing it to be analysed.

The electron beam can penetrate the surface of materials, resulting in the formation of an interaction volume from which secondary electrons (SE), backscattered electrons (BSE) and characteristic X-rays and other signals are generated (Figure 19).

Secondary electrons are generated near to the specimen surface, within approximately the first 2 nm, resulting in the production of a topographic image. These secondary electrons are generally low energy (<100 eV) and occur due to the inelastic collision between the electron beam and the weakly bound outer-shell electrons causing them to be ejected from their atom (Egerton, 2005). Once the ejected electrons reach the vacuum chamber, they are attracted to a secondary electron detector (Everhart-

Thornley detector or ETD) via a positively charged mesh at approximately 200 V (Smallman & Ngan, 2014).
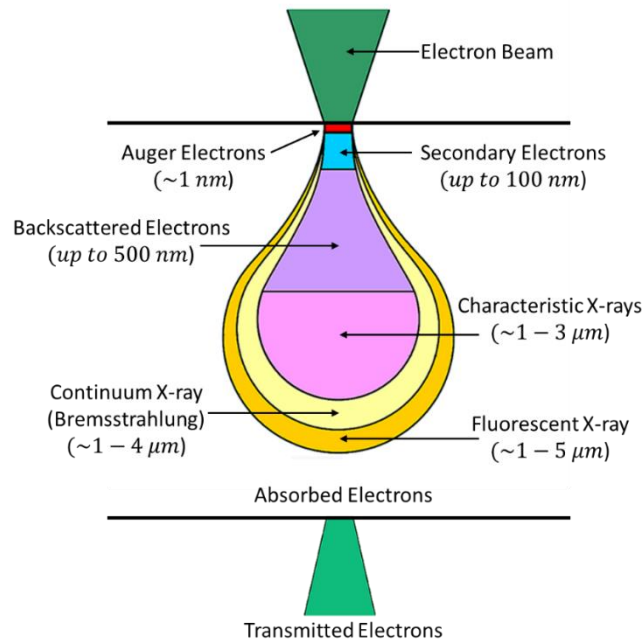
Figure 19 – A visual representation of the generation depth, spatial resolution and the information released from the surface due to electron beam interaction. Adapted from (JEOL, 2019)

Backscattered electrons are high energy electrons which are produced some tens to hundreds of nanometres below the surface of the specimen and are a result of the electron beam being elastically scattered at an angle of greater than 90 degrees, with the detector typically being mounted below the objective lens above the specimen. The number of BSEs produced is proportional to the atomic number of the material being analysed, resulting in formation of an atomic number contrast image, where changes in contrast are due to variations in elemental composition. For example, a low atomic number element would have present as a dark region and a high number would present as a light region in the image. (Egerton, 2005)

In this work, the samples requiring SEM examination were analysed, depending on their availability, in the FEI Nova Nano 200 and Quanta 3D SEM's which were both

equipped with the same field emission gun with SE and BSE detectors for imaging. Using the propriety software the thickness of coating and patina layer and the diameter of patina particles were measured. An energy dispersive X-ray (EDX) detector was also used to determine the elemental composition of the materials being analysed. The non-conductive antifouling coating and mounted samples were attached to an aluminium stub using an adhesive carbon tab. A line of silver-containing paint was applied from the top to the bottom of the mounted samples prior to being coated with approximately 20 nm layer of carbon to render the samples conductive, using the EMITECH K950X carbon coater (EMITECH, 2008). Gold was not used to coat the samples as when performing EDX analysis the Au peaks may overlap that of other elements such as sulphur which may need to be identified.

3.4.5   Energy Dispersive X-ray Analysis

The high energy electrons from the incident beam can impart enough energy to the electron around the nucleus of the atoms, in the surface of the specimen being analysed, to cause it to be ejected (Figure 20). This vacancy results in the atom gaining a charge. For the atom to return to the ground state an electron from a higher energy outer shell moves to fill the vacancy left in the inner shell, releasing a monoenergetic photon of X-ray energy, characteristic of the atom it is released from. The X-ray energy released is associated with the shell where the vacancy is located and the shell where the electron is moving from to fill the vacancy. For example, an electron from the L shell fills the vacancy in the K shell releasing a K_α X-ray, whereas a K_β X-ray is produced by an M shell electron filling a K shell vacancy.
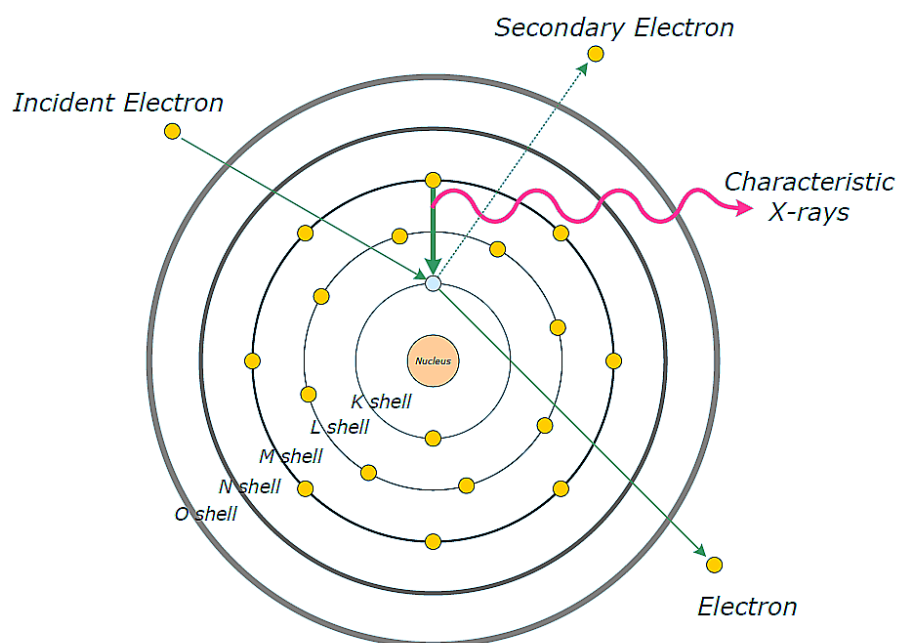
Figure 20 – Schematic showing the characteristic X-ray generation because of higher energy electrons filling vacancies caused by the ejection of lower energy electrons. (JEOL, 2019)

Using an Energy Dispersive X-ray (EDX) detector the X-ray energies and intensities can be measured allowing the elements present to be semi-quantitatively identified. However, low atomic number elements are difficult to detect, unless they are in high concentrations, as they are typically absorbed by the detector window, which is typically made from beryllium or carbon. Detection of carbon (C) and oxygen (O) are possible if they are in high concentrations however boron (B) and nitrogen (N) are more difficult. A further complication is that carbon can be deposited by the electron beam which can cause higher levels of carbon than were original present, giving inaccurate results. Furthermore, misidentification of the elements present may occur due to the overlapping of characteristic X-ray energies released from different elements i.e., the K_α from one element may overlap with the L peak from another, such as sodium (Na) with a K_α of 1.041 and zinc with a L_β of 1.012. Therefore, it is important to understand the material being analysed and the environment to which it has been exposed to ensure the correct elements are identified in the analysis.

[94]

3.4.6 X-ray Diffraction

While EDX analysis can provide elemental information about the surface of specimens it cannot show how the atoms are arranged. For example, the EDX spectra may show that copper, oxygen, and chlorine are present on a copper-rich substrate at a certain concentration, which may indicate that a copper chloride compound was present. However, there are many different copper chloride compounds, discussed previously (Chapter 2.4.6.2 Table 2), and therefore further analysis is required to determine the compounds present. X-ray diffraction is one such method that can provide this information.

X-ray diffraction is an analytical technique used to study crystalline (single crystal or polycrystalline) materials, which provides a range of information allowing for the determination of the phases present, as well as other parameters such as the crystal orientation, grain size, crystallinity, lattice strain and crystal defects.

A crystalline material is one whose atomic structure is assembled in regular and repeating 3-dimensional patterns with each atomic plane being separated by a uniform distance (d), the size of which varies depending on the material being analysed. The atomic structure is arranged into one of 14 possible Bravais lattices (Figure 21) and are described by the three lattice vectors a, b and c and the angles of each vector α, β and γ (Cullity, 2014).
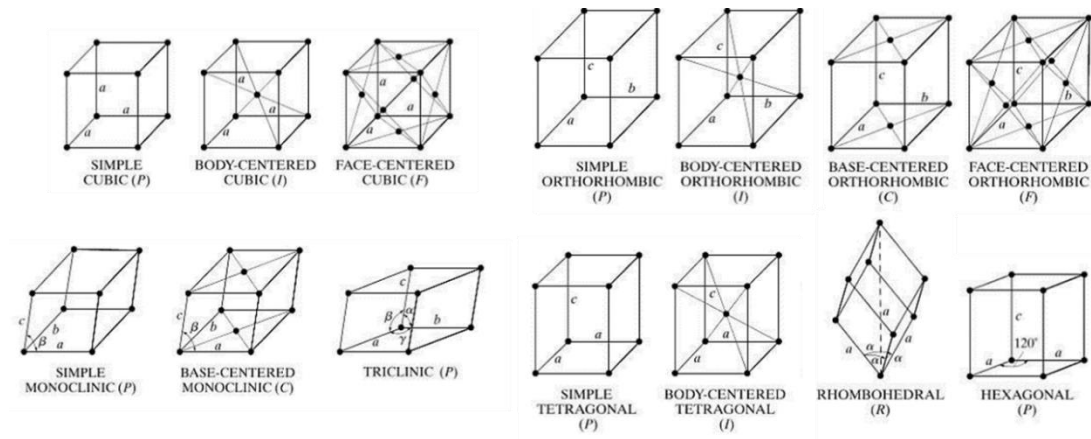
Figure 21 – Graphical representation of the Bravais lattices taken from (Cullity, 2014)

The distance between the atomic planes is measured to determine what crystalline phases are present in a material. The short wavelength of a beam of monochromatic X-ray photons allows them to penetrate the gaps between the atomic planes. When the X-rays collide with an atom in its path they scatter and diffract. If multiple of these waves are an integer of the wavelength this can result in the production of constructive interference peaks and are formed at specific angles (Figure 22).
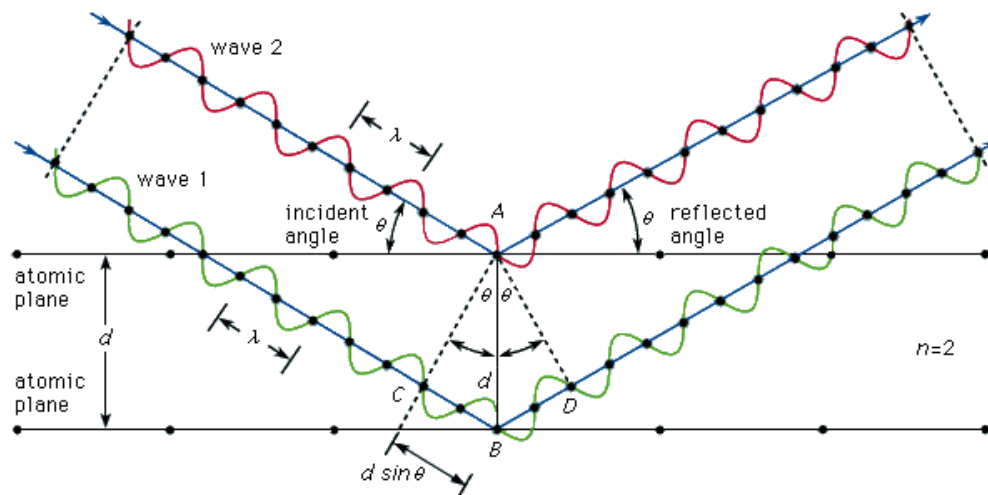
Figure 22 – Bragg diffraction, retrieved from (The Editors of Encyclopaedia Britannica, 2016)

By rotating the detector and/or the source around the sample and using Bragg's law (Equation 25) the d-spacing of different crystalline materials can be calculated and the phases identified.

$$n\lambda = 2d \sin \theta$$ *Equation 25*

[96]

Where n is an integer, λ is the wavelength of the incident X-ray beam, d is the spacing between the atomic planes and θ is the angle between the incident X-ray beam and the scattering planes.

Analysis of the copper patina compounds that had formed through the potentiostatic polarisation, immersion, and evaporation cells experiments were analysed using the Philip X'pert diffractometer with Copper Kα radiation ($\lambda = 1.5418 \text{ Å}$), operated at 40 kV and 40 mA, using the PIXcel 1D detector and scanning from 10° to 70°. The X-ray optics was set using the following parameters: nickel beta filter, 0.04 rad soller slits, mask of 10 mm, divergent and antiscatter slits of 0.125° and 0.25° respectively.

The analysis of the XRD pattern was performed using HighScore Plus software with the Powder Diffraction File (PDF) 2 database of phases. While the PDF 2 database has an exhaustive list of compounds available, some of the pigments used in the antifouling coatings were unavailable and were therefore characterised using the method outlined in Chapter 3.4.6.1 to enable their peaks to be differentiated from other compounds. For the XRD analysis three main types were performed powder diffraction, glancing angle and gonio diffraction.

3.4.6.1 *Powder Diffraction*

Powder diffraction was used to characterise the pigments used in antifouling coatings and the loose formed patina that had been produced through the experimental program. When large quantities of power were available it was mounted and compressed into a 16 mm diameter sample holder, for smaller quantities a backgroundless silicon wafer was used, which does not introduce a silicon peak to the XRD trace.

Each grain of the powder would contain many crystal lattices, which due to the mounting process, would be randomly orientated within the sample holder. The sample holder is rotated at 4 revs/min to ensure that enough of the grains are correctly orientated to allow the constructive diffraction peaks from each possible plane.

3.4.6.2 *Glancing angle*

Glancing angle XRD was used to characterise the patina formed on copper coupons (10 mm x 10 mm x 0.1 mm) while reducing the signal from the substrate. When using this technique, the incident beam was set to 5° and the beam knife was used to reduce the background scattering at low angles.

Glancing angle or grazing incidence XRD is a technique where the X-ray beam is positioned and held at a small angle relative to the specimen being analysed. The detector is then scanned through the required angular range to produce the XRD pattern. This technique limits the penetration depth of the X-ray beam while elongating the area of analysis, making it suitable for the study of thin surface films and in this case allowing more of the patina produced at the surface to be analysed.

3.4.6.3 *Surface analysis*

For the characterisation of paint flakes, the laboratory produced patinated antifouling coatings and copper coupon surfaces the XRD was performed using the multipurpose sample stage, which after aligning and levelling the samples were scanned using the theta/theta configuration. This is where the sample remains stationary, and the X-ray source and detector rotate around the sample.

3.4.6.4 *Depth of X-ray penetration*

The estimated depth X-rays penetrate into a material can be calculated using the mass absorption calculator (MAC) available in the HighScore Plus software. This uses the mass absorption coefficient (μ/ρ), taken from international tables (The International Union of Crystallography, 2004). In many cases the material being analysed contains many different elements or compounds therefore the (μ/ρ) for the whole system is needed. This can be calculated using Equation 26 where (W) is the atomic weight percentage.

$$(\mu/\rho)_{Compound} = W_1 \times (\mu/\rho)_1 + W_2 \times (\mu/\rho)_2 \ldots + W_n \times (\mu/\rho)_n \qquad \text{\textit{Equation 26}}$$

Using the mass adsorption coefficient, the theoretical density of the compound (ρ) which is a combination of the specific gravity of the material as well as an estimated packing density, the path length (L) can be calculated using Equation 27. Where (I_L) is the intensity of X-rays returning from the sample and (I_0) is the initial intensity.

$$I_L = I_0 \times exp^{-(\mu/\rho)\rho L} \qquad \text{\textit{Equation 27}}$$

The penetration depth (T), in microns, can then be calculated using Equation 28

$$T = 0.5\,L \times \sin(\vartheta) \qquad \text{\textit{Equation 28}}$$

X-rays can penetrate deeper than the calculated penetration depth but only 0.09% of the information recorded in the diffraction pattern comes from this depth with the largest contribution coming from ½ the penetration depth (Figure 23).
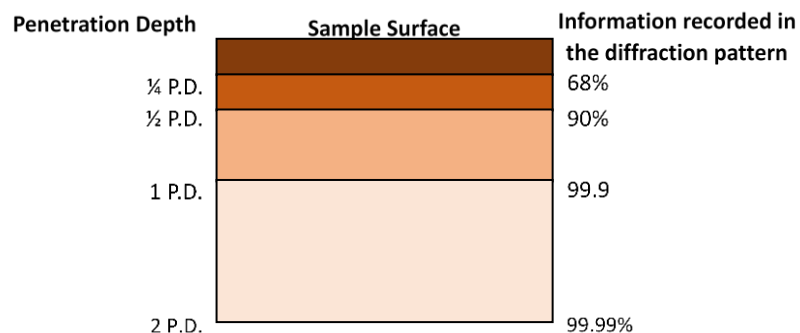
Figure 23 – Schematic showing the amount of information collected in the diffraction pattern in relation to the penetration depth (PANalytical, 2006).

[99]

Chapter 4: Analysis Of Naturally Patinated Antifouling Coatings

4.1. Introduction

Antifouling coatings are applied to manmade underwater structures where the formation of biofouling communities would be detrimental to their operation. One of the most common uses of these coatings is on the hulls of marine vessels. The hull can be split into three sections: the freeboard, underwater and boot top (Figure 24).
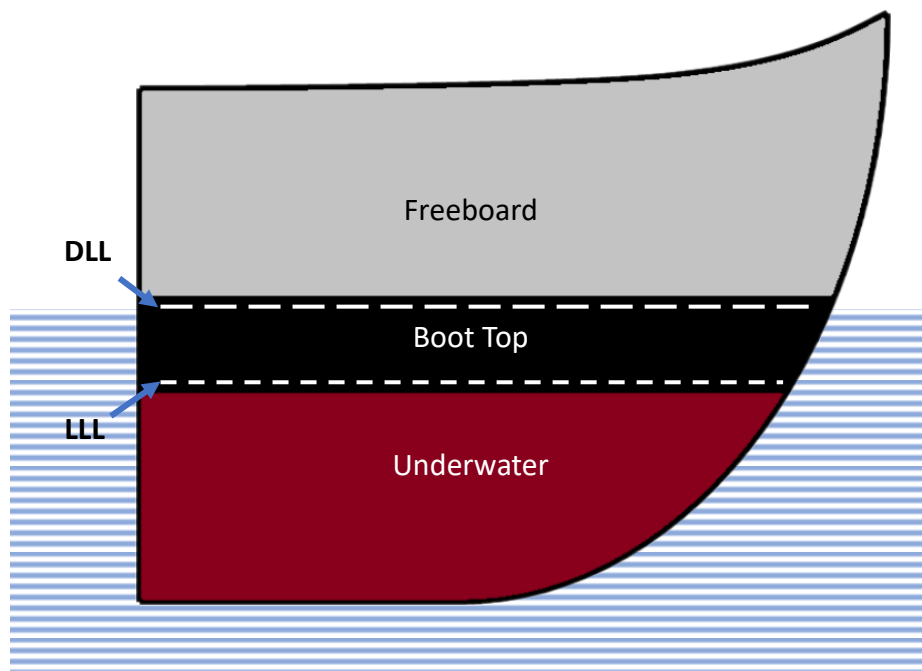
Figure 24 – Depiction of a ship's hull showing the position of the freeboard, boot top and underwater sections along with the deep load line (DLL) and light load line (LLL). Adapted from (Leggat, 2018).

The freeboard section is above the waterline, exposed mostly to the atmosphere and as such does not require antifouling coatings. Below the waterline, the hull is constantly exposed to seawater and therefore antifouling coatings are required. The boot top is located between the freeboard and underwater sections of the hull. This area is within the two loading extremes, the light-load line (LLL), located above the underwater section, where the vessel is transporting the minimum load, and the deep-load line (DLL) tending to be below the freeboard section where the vessel is carrying the maximum load. The position of the load lines depends on several factors including

[100]

the season, geographical location, and type of water the vessel is passing through (Barrass & Derrett, 2012). The Merchant Shipping (Load Line) Regulations 1998 (Merchant Shipping, 1998) require the lines to be "painted in white or yellow if the background is dark", which can mean in many instances that the boot top is painted black also allowing for a clear separation between the underwater and freeboard sections. The position of the waterline can vary depending on the laden condition of the vessel allowing fouling organism to become attached. Therefore antifouling coatings are required within the boot top region.

Although biocide-free antifouling coatings have been available for several years, biocidal antifouling coatings, sometimes called 'fouling control' coatings, are still in very widespread commercial use, such as those discussed in Muthukrishnan et al., (2014) and Lagerström et al., (2018). Many of these products continue to use biocidal copper compound pigments, often in combination with other biocides to provide protection against a broad spectrum of fouling species. The most commonly used biocidal copper compound is cuprite (Cu_2O), usually in combination with certain organic or metalorganic biocides (Yebra et al., 2004).

As part of the International Convention of the Safety of Life at Sea (SOLAS) treaty, which established the safety measures in the construction, equipment, and operation of merchant vessels, it is required that they undergo a survey of the hull in dry dock at least twice within a five-year period, with an intermediate inspection within 36 months (Anish, 2020). During these inspection periods the coatings are reported to have become discoloured with a green-blue layer forming (Goulding, 2016; International, N/D; Marine Superstore, N/D), suggesting that the copper-based pigments had reacted

[101]

with the environment to form a new copper chloride compound and precipitated onto the surface. While copper patinas are porous, allowing the release of cupric ions and maintaining the antifouling ability of the coatings, an increase in density and/or thickness of the patina may reduce the release rate by blocking access to the Cu_2O pigment (Lindner, 1988). Furthermore, the patina reduces the aesthetics which in turn may result in the perception that the coating had failed, thereby causing ship owners to replace the coating ahead of schedule. The time in dry dock costs the owner of the ship money, not only to have the ship in dock but also in lost revenue. To maintain the efficiency, most antifouling coatings are designed to last between 3-5 years, depending on their formulation (CDP, SPH or SPC), allowing the coatings to be maintained, repaired, or replaced during the schedule maintenance.

This section will present the analysis of paint flakes sourced from the underwater sections of the hull to determine the type of patina that had formed. The results from this analysis are critical as without understanding what copper patinas are formed naturally, on paint flakes exposed to the marine environment, it would not be possible to determine the variables required to reproduce the patina under controlled laboratory conditions.

4.2. Results and discussion

4.2.1. XRD analysis

The exact amount of time the paint flakes were exposed to the sea water environment is unknown however it could be assumed that based on the SOLAS treaty that they were exposed for a minimum of 2 years and a maximum of 5 years. However, anecdotally, copper-based antifouling coatings have been said to patina much quicker (Finnie, 2015). The colour of the received paint flakes for analysis were found to have changed from their original red or brown appearance to the typical green or green-blue colouration associated with the formation of a patina compound, due to the reaction of the cuprite pigment with the marine the environment. The paint flakes also show the typical layering of the coatings (Figure 25) indicating that while the antifouling coatings can maintain the efficiency of the vessel, by preventing the colonisation of biofouling species, additional measures are required to protect the hull from the environment.
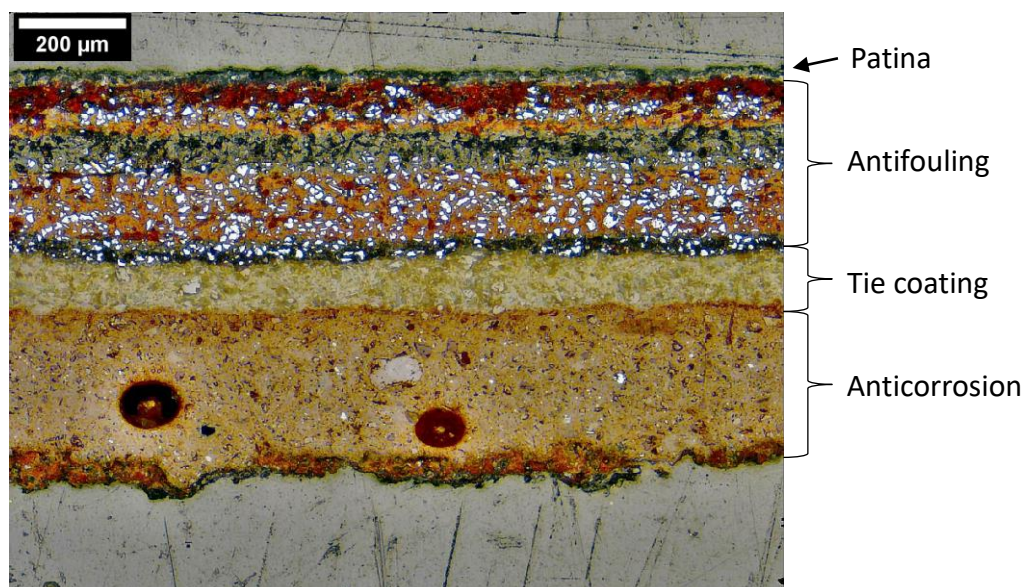
Figure 25 – Example image captured using an optical microscope of Paint Flake 1 which had been mounted in a two-part epoxy and ground to a 1 μm finish showing the coating system used to protect ships hulls including an anticorrosion applied to the hull, a tie coating and evidence of multiple antifouling coatings, which had been applied on top of each other, probably following a reduction in performance.

[103]

A typical example paint flake XRD analysis is shown in Figure 26, comparing the pattern produced from glancing angle, where the incident X-ray beam is fixed at a low angle (5°) with the detector being scanned through the angular range, and gonio XRD techniques, where both the incident beam and detector are scanned through the angular range. Further XRD patterns of the paint flakes are shown in Appendix 1.
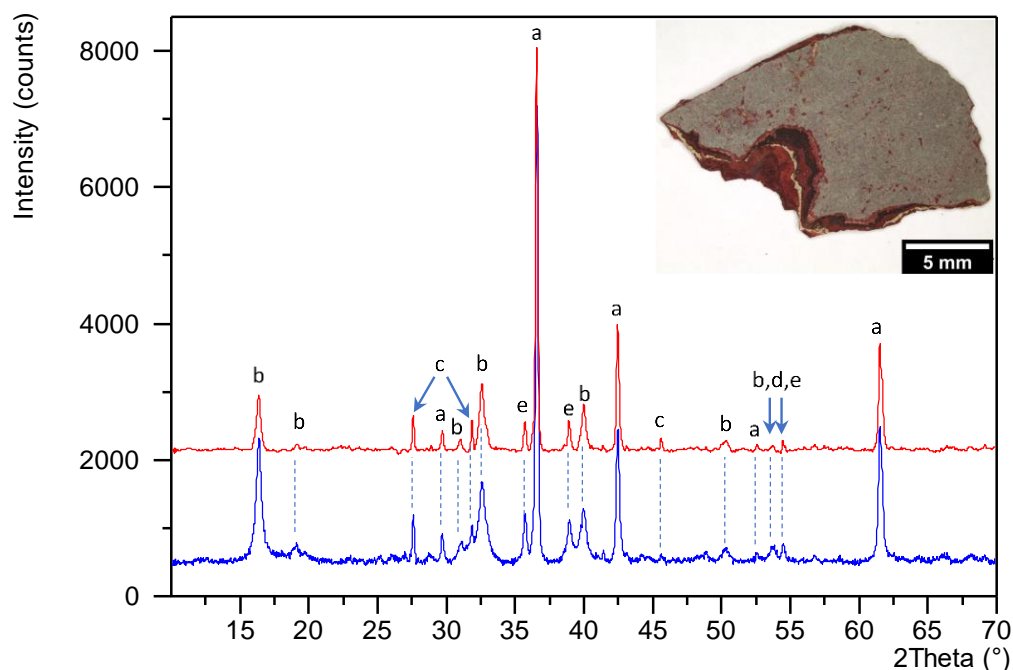
Figure 26 – Example XRD analysis of the Paint Flake 1, shown above, removed from MSC Marianna. The blue and red lines represent the glancing angle and gonio XRD techniques, respectively. The peaks were identified as a = cuprite, b = clinoatacamite, c = Sodium chloride, d = silicon dioxide and e = tenorite.

Using the MAC described in (Chapter 3.4.6.4) the X-ray penetration depth was calculated for the cuprite containing found control coating. This was done by assuming a packing factor, based on the concentration of cuprite in the coatings, of between 0.25 and 0.5 (International Paint Ltd, 2008), a density of 6.15 g.cm^{-3}, and an incident angle of 35° the gonio technique. It was determined that the X-rays can penetrate between 90 – 180 μm. The typical recommended dry film thickness of antifouling coatings is 125 μm (International Paint Ltd, 2010; International Paint Ltd, 2016) while multiple coatings can be applied throughout the history of the vessel, without the

removal of previous layers (Figure 25). Therefore, only the crystalline pigments within the antifouling coating should be analysed and not the tie or anticorrosion layers. However, when using a 5° glancing angle the penetration depth is reduced to approximately 13.8 – 27.5 µm, allowing more signal from the surface-formed patina to be detected. A typical patina thickness on copper in the marine environment has been shown to be approximately 7.6 µm after 2 years (Zhang et al., 2014a), the minimum time elapsed between the inspection of antifouling coatings, and up to 14 µm after 16 years (Fuente et al., 2008). Assuming similar thicknesses form on antifouling coatings containing cuprite pigments, this suggesting that 11.5 – 42.3% of the X-ray volume is associated with the patina when using the gonio method increasing to 75.2 – 100% when using the glancing angle technique, where 68% of the diffraction pattern is collected from ¼ the penetration depth (PANalytical, 2006).

Both techniques resulted in peaks being detected at similar angles, confirming that the same compounds were detected. However, when using a glancing angle of 5°, the signal intensity from the crystalline pigments in the paints were suppressed (i.e., cuprite [a], silicon dioxide [d] and tenorite [e]) while the signal from compounds presents on the surface (such as clinoatacamite [b] and sodium chloride [c]) was increased by between 1 and 15 times that of the gonio measurement, aiding with their identification. Furthermore, broader peaks were observed with some of the peaks being masked when comparing the glancing angle and gonio XRD patterns. This phenomenon is typically observed with glancing angle measurements due to limitations with the X-ray optics.

In some circumstances the glancing angle technique was able to detect low intensity peaks that may have been masked by the background radiation in the gonio measurements. Therefore, the results from both techniques were used to identify the phases present and these are summarised in Table 8 (pigments in the coating) and Table 9 (compounds formed on the surface of the coating).

While the PDF-2 database contained a vast selection of phases it does not have every possible compound and in some instances different data for the same compound. Therefore, powder XRD of the individual pigments used in the antifouling coatings was performed to differentiate between peaks associated with the compounds present in the coating and those formed during service. The XRD patterns from the pigment analysis are shown in Appendix 2.

XRD analysis of the patina formed on the paint flakes determined that a copper chloride-based patina was detected on each paint flake. Clinoatacamite ($Cu_2Cl(OH)_3$) was the most commonly detected patina as summarised in Table 9, which also happened to be the most thermodynamically stable of the copper hydroxychloride compounds, with the largest Gibbs free energy (Frost, 2003). Lindner (1988) also used XRD to quantify the compound that had formed on blueish-green layer formed on antifouling coatings in the ocean environment where atacamite/paratacamite (*clinoatacamite) and cuprite were reported.

Copper (I) chloride ($CuCl$) was the second most commonly detected copper chlorine-based compound, and was the only phase detected on Paint Flakes 3 and 5. The self-polishing nature of these paint flakes and the formation of weakly adhered patina compounds may have resulted in the loss of the more complex patina due to water

action against the hull, allowing the complexation, precipitation, and deposition process to restart. Copper (I) chloride has been shown to be a precursor to the more complex patina compounds (Sharkey & Lewin, 1971; Zhang et al., 2014a) leading to the formation of atacamite which, following the Oswald step rule, goes on to form clinoatacamite. This may account for the combination of copper (I) chloride and clinoatacamite being detected on Paint Flake 6 and the presence of atacamite and clinoatacamite on Paint Flake 10. While atacamite was the only patina compound detected on Paint Flake 12.

The XRD characterisation also revealed the presence of sulphur-based copper patina products including the most thermodynamically stable compound of brochantite ($Cu_4SO_4(OH)_6$), with precursor compounds of djurleite ($Cu_{1.97}S$), copper sulphate hydrate ($CuSO_4(H_2O)_5$) and anilite (Cu_7S_4) also being found on Paint Flakes 2, 4, 6 and 8, respectively, along with the copper chloride patina clinoatacamite and copper (I) chloride. The presence of both chlorine and sulphur-based copper patina products suggests that these paint flakes were exposed to polluted seawater for a period of time, where SO_4^{2-} can react either with the copper ions released from the antifouling coatings, such as that shown in Equation 29, or with the copper chloride phases to form the sulphur-based compounds (Equation 30).

$$4Cu^{2+} + SO_4^{2-} + 6OH^- = Cu_4(OH)_6SO_4 \qquad \textit{Equation 29}$$

$$2Cu_2Cl(OH)_3 + SO_4^{2-} = Cu_4(OH)_6SO_4 + 2Cl^- \qquad \textit{Equation 30}$$
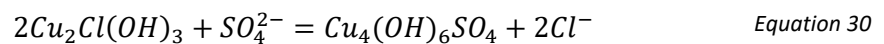
While SO_4^{2-} is a typical component of seawater, with a concentration of 2.7 g/l (Lyman & Abel, 1958), the levels have been shown to be elevated around coastal regions where Nessim et al. (2015) detected on average 3.068 g/l which mostly associated with inorganic sources (Melchers, 2015). Elevated sulphate levels are also commonly

[107]

detected in port or harbours (Schleich, 2004) and in the most severely polluted regions the levels of sulphate can be up to 5 g/l (5000 ppm) or higher (Wiener et al., 2010). Fitzgerald P. et al. (1998) determined that brochantite $(Cu_4SO_4(OH)_6)$ required high concentrations of SO_4^{2-}, of between 300 and 750 ppm, to form. Therefore, the presence of brochantite on Paint Flake 2 indicates that it was exposed to highly polluted seawater with Paint Flakes 4, 6 and 8 also being exposed to polluted waters for a long enough period for the sulphur-based patina to form. Furthermore, once brochantite forms it is likely to persist as it was insoluble in water (Graedel et al., 1987) while it also had a higher Gibbs free energy of $-2194.4\ kJ.mol^{-1}$ (Zittlau et al., 2013) and was therefore less likely to transform to clinoatacamite with a Gibbs free energy of $-1341.8\ kJ.mol^{-1}$ (Frost, 2003).

Table 8 – Summary XRD analysis detailing the pigments that were identified in the paint flakes taken from in-service vessels using both the gonio and glancing angle measurements. The compounds that were present are indicated by the PDF database identification number taken from the HighScore Plus software. Phases marked as "unavailable" were not present in the PDF database however they were identified using the XRD analysis from the pigments used in the paint.

Paint Flake	Coating Type	Antifouling Pigments					Filler pigments		
		Cuprite (Cu_2O)	Zinc Oxide (ZnO)	Tenorite (CuO)	Copper Pyrithione ($C_{10}H_{10}CuN_2O_2S_2$)	Zinc Pyrithione ($C_{10}H_8N_2O_2S_2Zn$)	Haematite (Fe_2O_3)	Silicon dioxide (SiO_2)	Titanium Dioxide (TiO_2)
1	Intersmooth 460 (SPC)	01-075-1531	-	00-005-0661	-	-	-	01-081-0068	-
2		01-075-1531	-	00-005-0661	-	-	01-072-0469	-	00-034-0180
3		01-075-1531	-	00-005-0661	Unavailable	-	-	01-083-2467	-
4		01-075-1531	-	00-005-0661	-	Unavailable	-	01-083-1827	-
5		01-075-1531	-	01-072-0629	-	-	-	-	-
6		01-075-1531	-	-	-	-	-	-	-
7		01-075-1531	-	00-005-0661	-	-	01-085-0599	-	01-071-0650
8	Interspeed 7460 (SPC)	01-075-1531	-	01-072-0629	Unavailable	-	-	01-081-0068	-
9		01-075-1531	01-075-0576	01-072-0629	Unavailable	-	-	01-083-1830	01-087-0710
10	Interswift 655 (SPH)	01-075-1531	01-079-0206	-	Unavailable	Unavailable	01-085-0987	01-079-1906	01-086-0147
11		01-075-1531	01-075-0576	-	-	-	00-024-0072	01-085-0798	-
12	Interspeed 6400 (CDP)	01-075-1532	01-079-0206	-	-	-	-	-	01-073-224
13	Not provided	01-075-1531	-	00-005-0661	-	-	-	01-083-1413	-
14		01-075-1533	-	-	-	-	01-086-0550	-	01-072-1148

Table 9 – Summary XRD analysis showing compounds that were detected on the surface of the patinated paint flakes using both the gonio and glancing angle measurements. The compounds that were present are indicated by the PDF database identification number taken from the HighScore Plus software.

| Paint Flake | Coating Type | Reaction Products | | | | | | | Other |
| | | Copper (I) Chloride ($CuCl$) | Atacamite ($Cu_2Cl(OH)_3$) | Clinoatacamite ($Cu_2Cl(OH)_3$) | Copper Sulphide | | Copper Sulphate Hydrate ($CuSO_4(H_2O)_5$) | Brochantite ($Cu_4SO_4(OH)_6$) | Sodium Chloride ($NaCl$) |
					Djurleite ($Cu_{1.97}S$)	Anilite (Cu_7S_4)			
1	Intersmooth 460 (SPC)	-	-	01-086-1391	-	-	-	-	01-072-1668
2		-	-	01-086-1391	-	-	-	01-085-1316	01-072-1668
3		01-073-1496	-	-	-	-	-	-	01-072-1668
4		-	-	01-086-1391	01-015-0157	-	-	-	01-072-1668
5		01-082-2116	-	-	-	-	-	-	01-072-1668
6		01-082-2116	-	01-086-1391	-	01-072-0617	-	-	-
7		-	-	01-086-1391	-	-	-	-	01-072-1668
8	Interspeed 7460 (SPC)	-	-	01-086-1391	-	-	01-075-2079	-	-
9		-	-	01-086-1391	-	-	-	-	01-072-1668
10	Interswift 655 (SPH)	-	01-071-2027	01-086-1391	-	-	-	-	01-072-1668
11		-	-	01-086-1391	-	-	-	-	01-072-1668
12	Interspeed 6400 (CDP)	-	01-071-2027	-	-	-	-	-	01-072-1668
13	Not provided	-	-	01-086-1391	-	-	-	-	01-072-1668
14		-	-	01-086-1391	-	-	-	-	01-072-1668

[110]

4.2.2. SEM Analysis Of The In-Service Paint Flake

Based on the visual inspection of the samples three paint flakes were selected for surface and cross-sectional SEM analysis Paint flakes 1 (SPC) and 10 (SPH), and the rich blue-green area found on Paint Flake 12 (CDP) (Figure 27). These paint flakes selected due to their composition and patina concentration, with both the top surface and cross-sections being analysed in the SEM

| **Paint Flake 1** | **Paint Flake 10** | **Paint Flake 12** |

Figure 27 – Photographs of the paint flakes used for SEM analysis

SEM analysis of the surface of Paint Flake 1 (Figure 28a) found that it had a non-uniform surface with no evidence of regular shaped cuprite pigments present, such as those shown in cross-section (Figure 28b), suggesting that they had leached out of the surface layer. However EDX analysis of the surface confirmed that relatively high copper concentrations were present, which combined with the colour of the paint flake (Figure 27) and high levels of chlorine detected (Figure 28c), suggests that the paint had patinated to form a copper chloride compound. However when examining the high magnification BSE micrograph of the cross-section through the coating an obvious patina film was not found on the top of the coating such as that found on Paint Flake 10 (Figures 32b and 33a). Therefore the patina may have precipitated within the porous network left behind by the dissolution of the cuprite pigment.

Spectrum	Element (wt%)								
	O	Mg	Al	Si	Cl	Ca	Ti	Fe	Cu
1	25.7	3.0	1.5	1.8	16.1	5.2	3.9	1.0	41.9
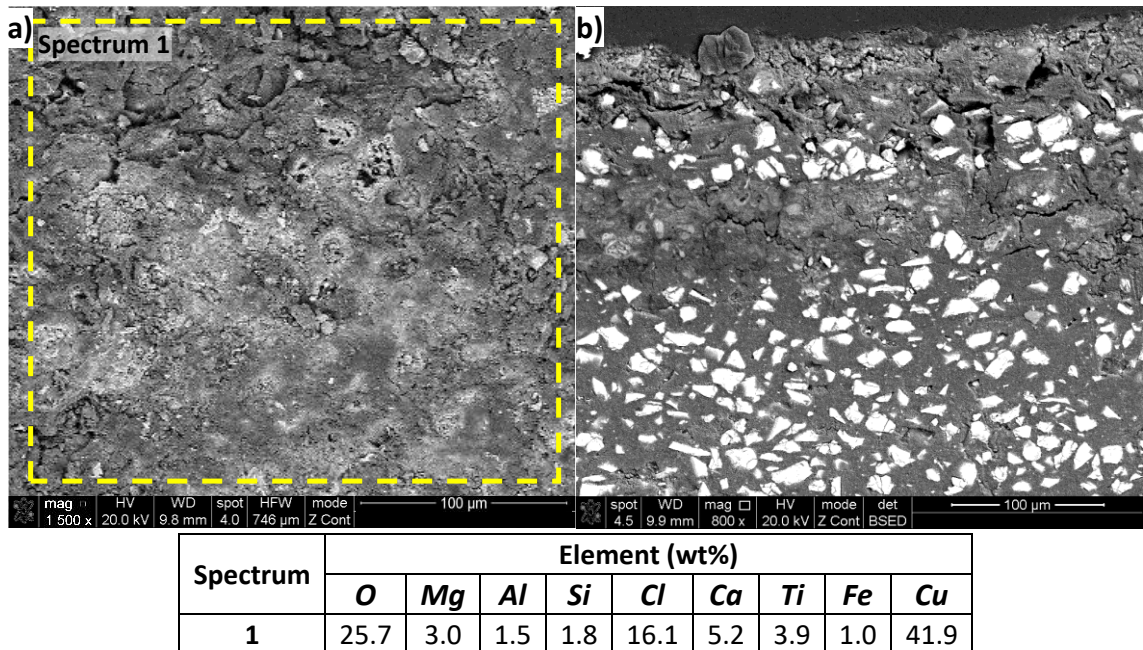
Figure 28 – SEM analysis of Paint Flake 1 a) BSE micrograph of the paint flake surface with the dashed yellow box indicating the position of the semi-quantitative EDX analysis shown in c). b) BSE cross-sectional micrograph at the coating surface showing the leach layers.

A low magnification cross-section through Paint Flake 1 is shown in Figure 29 where six distinct layers were found. Using elemental mapping, shown in Figure 30 and Figure 31, to determine the relative concentration of the elements in the different layers it was possible to surmise the function of each layer in the overall coating system.

Layer 1, the innermost layer, consisted of a coating that contained carbon from the polymeric matrix and pigments including iron, titanium, silicon, magnesium, and sulphur. It was 262.5 ± 14.4 μm thick and was likely to have been a primer coating which could act as a protective layer to prevent the seawater from reaching the steel hull.

Layer 2 consisted of high levels of chlorine along with magnesium and silicon (probably magnesium silicate) which was 83.3 ± 6.7 μm thick and would be used as a tie coat to promote adhesion of the antifouling coating (Layer 3) to the primer.
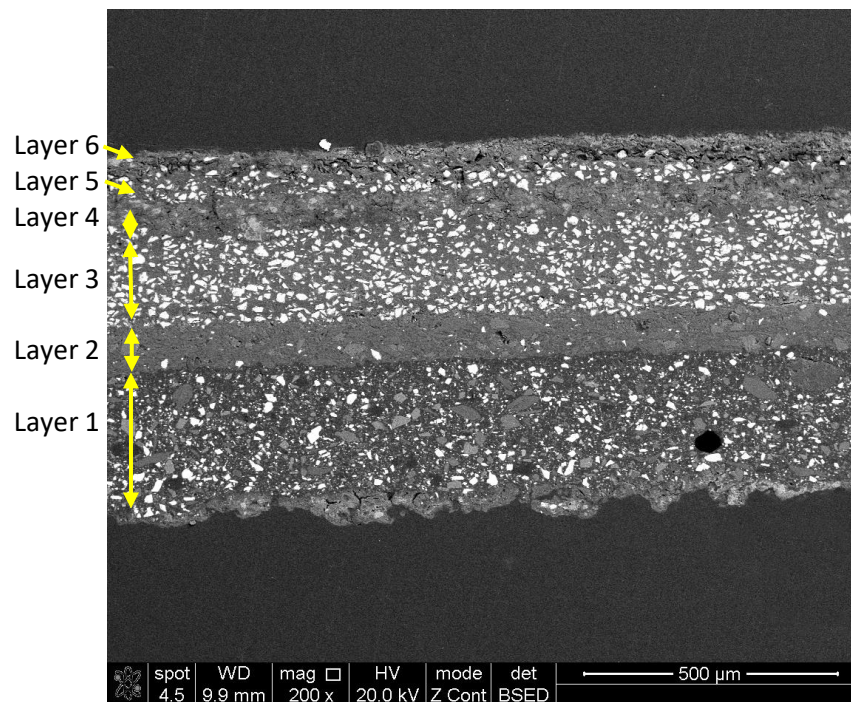
Figure 29 – BSE micrograph of a cross-section through the whole of Paint Flake 1 with arrows indicating the location of the antifouling coatings and areas of copper depletion
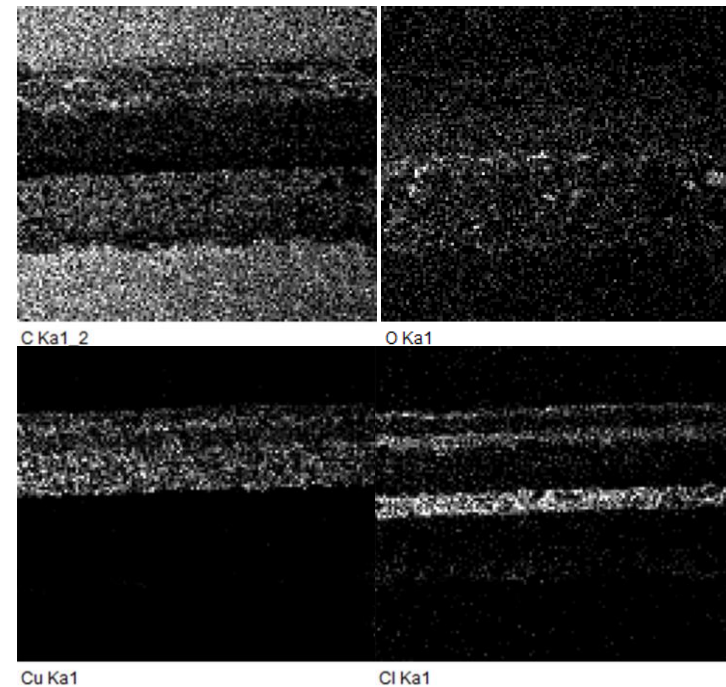
Figure 30 – EDX elemental maps of Paint Flake 1 shown in Figure 29. Maps indicate the presence of carbon, copper, chlorine, and oxygen showing the high amount of chlorine at the surface of the paint.
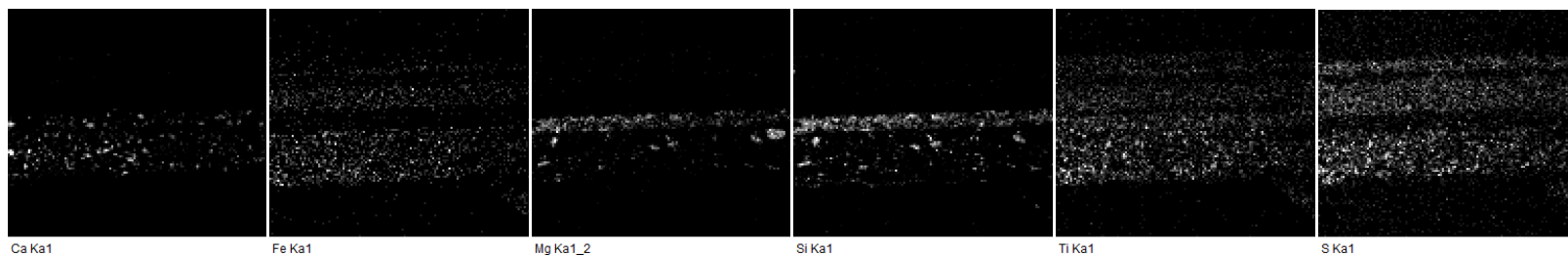
Figure 31 – Further EDX elemental maps showing other elements present in Paint Flake 1 including, from left to right; calcium, iron, magnesium, silicon, titanium, and sulphur

[113]

Layers 3 to 6 indicated that two antifouling coatings have been applied to the vessels hull. The first antifouling coating applied to the tie coating (Layer 3) was approximately 180.3 7.9 µm thick, which was rich in cuprite pigments along with sulphur, titanium, and iron, with a 55.9 ± 8.3 µm leach layer on top (Layer 4) i.e. an area where the cuprite pigments had been released from the coating leaving a porous matrix with a low copper concentration. High chlorine levels and low concentrations of copper were associated with this layer. While the thickness of the leach and cuprite rich layers suggests that this coating was a CDP. A second antifouling coating was applied directly on top of the first coating showing a similar pattern with Layer 5 being rich in copper, while Layer 6, the outermost layer, had elevated levels of chlorine. However, the total thickness of the coating, leach and remaining copper layers, of 92.3 ± 4.3 µm, 55.2 ± 5.1 µm and 42.9 ± 7.2 µm, respectively, were much smaller than the first coating. This suggests a different coating type such as a SPC or hybrid coating was used, allowing the pigment depleted matrix, and any patina that may have formed previously, to be removed through wave action. While copper patina was found to precipitate on the surface of the coating on Paint Flake 7, the high levels of chlorine and low concentration of copper associated with Layer 6 may indicate that the patina had developed within this layer.

SEM analysis of the surface of Paint Flake 10 found that the surface had a granular appearance, as observed optically (Figure 27), with smooth islands, approximately 70 µm wide, dispersed across the surface (Figure 32a) associated with large patina compounds on the paint. Surface EDX analysis (Figure 32c), where X-rays are generated from a depth of approximately 2 µm (Titus et al., 2019), detected elements

associated with the pigments in the coating substrate namely copper, zinc, magnesium, calcium, titanium, and oxygen, with chlorine also being found. While chlorine has the potential to react with the zinc and magnesium pigments in the paint it forms highly soluble compounds, whereas insoluble compounds form when copper reacts with chlorine which precipitates on to the surface. Therefore, over time the surface is covered with a copper chloride (clinoatacamite) compound.

The semi-quantitative EDX analysis of the two areas (Figure 32a, spectrum 1 and 2) determined that higher concentrations of copper and chlorine and lower levels of magnesium and titanium were detected on the islands, suggesting that they were either thicker or denser than the granular regions. This may also suggest that they were the first regions for patina to precipitate, as the thickness of the patina layer continues to increase with time following a parabolic growth law (Farro et al., 2009). The granular appearance of most of the surface suggest that the patina compound precipitates out as individual particles which grow but do not necessarily join with other particles as the exposure time was increased. This can result in the porous nature of copper patinas.

Further higher magnification cross-sectional analysis of Paint Flake 10 (Figures 32b and 33a) found a layer approximately 850 – 900 nm thick had patina layer deposited on top of the coated surface, which, was confirmed to be rich in copper (Figure 33b) and chlorine (Figure 33c). The mapping indicates that there was a higher concentration of chlorine when compared to the copper map within this layer, which was determined to be clinoatacamite via XRD analysis.

A discontinuous patina layer was found (Figures 32b and 33a), with individual particles and defects evident within the layer, like those observed in Fuente et al. (2008) and Zhang et al. (2014b), confirmed the porous nature of copper patina, allowing the marine environment to reach the coating surface. The paint was designed to undergo hydrolysis with seawater causing the outer layers to become brittle and be easily polished away through hydrodynamic drag on the hull. This prevents the formation of thick leach and patina layers (Figure 33a), such as that found when compared to Zhang et al. (2014a).

Spectrum	Element (wt%)							
	O	Mg	Si	Cl	Ca	Ti	Cu	Zn
1	36.0	1.9	0.6	13.4	0.6	5.6	36.9	5.0
2	36.1	1.9	0.7	11.3	0.7	8.4	35.6	5.3
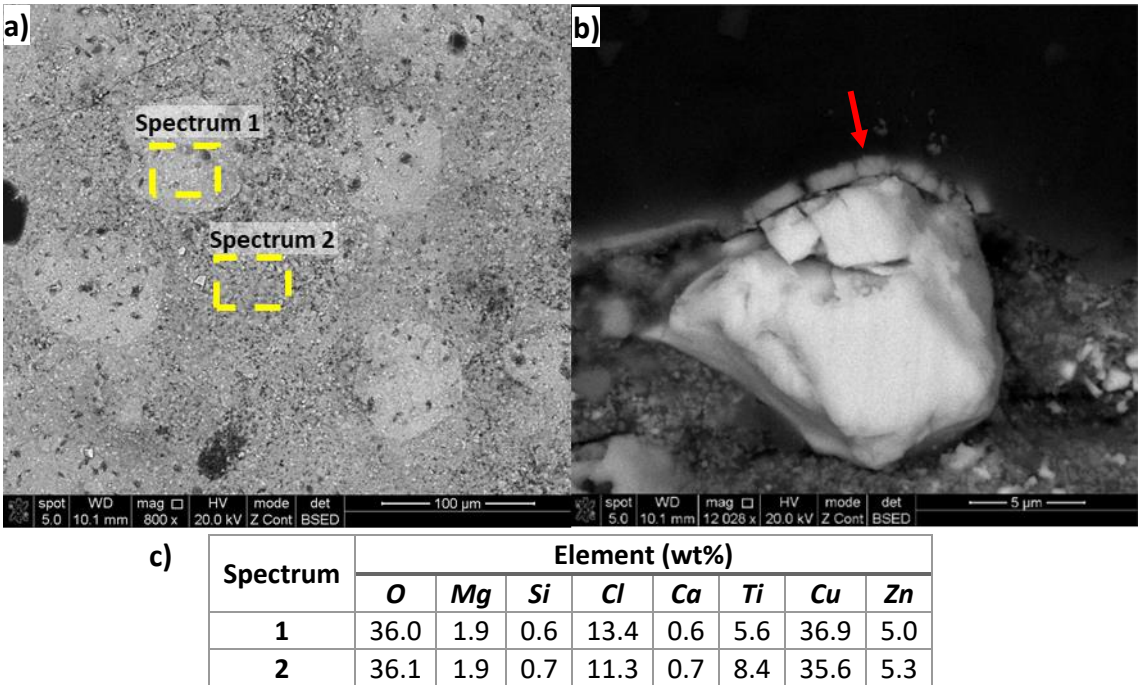
Figure 32 – SEM analysis of Paint Flake 10. a) low magnification BSE micrograph of the paint flake surface with the dashed yellow boxes indicating the position of the semi-quantitative EDX analysis shown in c). b) High magnification BSE cross-section micrographs showing the formation of patina on a cuprite pigment highlighted by the red arrow.
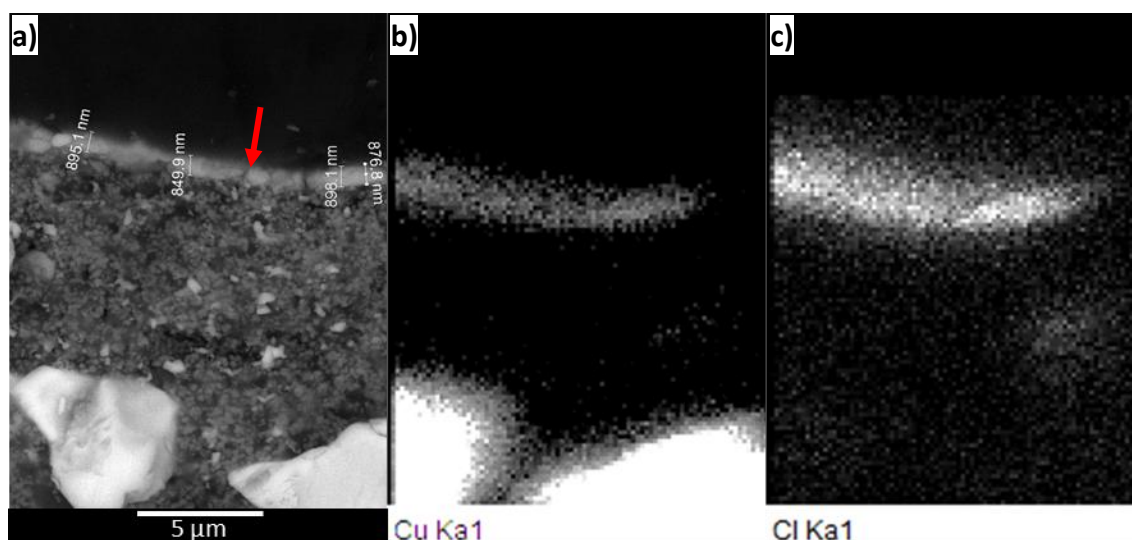
Figure 33 – SEM analysis of Paint Flake 10. High magnification BSE cross-section micrographs showing the formation of patina on the coating surface (a), highlighted by the red arrows, and elemental maps showing the concentration of copper (b) and chlorine (c).

SEM analysis of surface Paint Flake 12 found that it had a granular appearance (Figure 34a), like Paint Flake 10, with high levels of copper and chlorine also being detected (Figure 34b). However, surface cracks were observed, which may have been caused by stresses applied to the outer surface as the paint flakes were removed. Further evidence of cracking was found in cross-section (Figure 34c, highlighted by the blue arrow), which penetrated approximately 48 μm from the surface.

Paint Flake 12 is CDP coating which allows for the formation of a leach layer where pigments are dissolved from the coating matrix leaving a porous network for seawater to penetrate and react with the copper ions. Evidence of the leach layer can be seen in Figure 34c where a uniform lighter contrast region 15.1 ± 1.7 μm from the surface was observed. No copper containing pigments were detected with only traces of copper (Figure 34d) along and high concentrations of chlorine (Figure 34e) found during elemental mapping. Furthermore, no exterior patina layers were observed in cross-section despite the blue-green colouration observed optically (Figure 27), however atacamite was detected via XRD analysis, suggesting that chloride had entered the

porous network and reacted with the copper ions forming patina within rather than on top of the coating as in Paint Flake 10. The formation of a uniform leach layer also suggests that a constant dissolution of the pigments occurred across the coating.

Element	Spectrum 1 (wt%)
O	38.4
Mg	0.6
Si	0.4
S	0.4
Cl	11.1
Ca	0.5
Ti	0.8
Fe	3.2
Cu	34.1
Zn	10.5
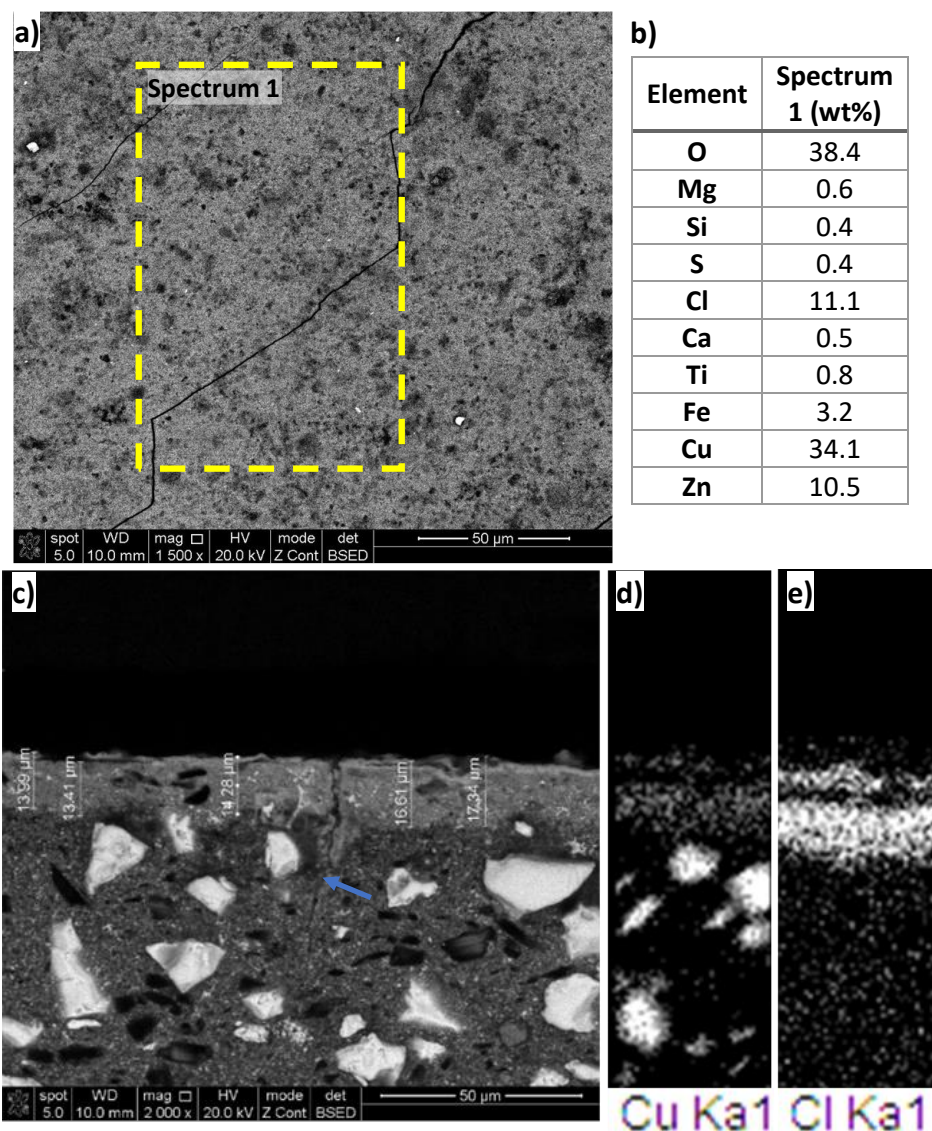
Figure 34 – SEM analysis of Paint Flake 12 showing a) BSE micrograph of the paint flake surface with the dashed yellow box indicating the position of the semi-quantitative EDX analysis shown in b), c) high magnification cross-sectional BSE micrograph with a blue arrow highlighting a crack in the coating, with elemental maps d) and e) showing the concentrations of copper and chlorine, respectively.

4.3. Conclusions

XRD analysis determined that a copper chloride patina had formed on all paint flakes, with clinoatacamite being the most commonly detected compound, followed by copper (I) chloride and atacamite. In addition to the copper chloride patina, some of the paint flakes also contained sulphur-based patina compounds of djurleite, anilite, copper sulphate hydrate and brochantite indicating that they were exposed to polluted seawater. Table 10 below summarises the results of the SEM analysis of the three coatings

Table 10 – Summery table of results from the paint flake analysis

Paint Flake / Paint Type	Visual Description	SEM analysis		Cross section	Patina compound
		Surface			
		Description	Semi-quantitative EDX (wt%)	Description	
1 **SPC**	Dull blue-green colour patina with a continuous coverage	Non-uniform surface with no cuprite pigments visible	Cu (41.9), Cl (16.1), O (25.7)	Multi-layer paint flake including an anticorrosion, tie coat and two antifouling coatings with the outer layer having a uniform leach layer ~55 μm thick rich in chlorine with copper also being detected suggesting the patina had formed within the porous network left by the dissolution of the cuprite pigment.	Clinoatacamite
10 **SPH**	Light blue-green patina with an intermittent coverage	Smooth islands ~70 μm wide surrounded by a granular structure	Cu (36.0), Zn (5.0), Cl (13.4), O (36.0)	850-900 nm thick discontinuous patina layer rich in copper and chlorine found on top of the coating	Clinoatacamite
12 **CDP**	Rich blue-green patina with a continuous coverage	Granular structure with no visible cuprite pigments	Cu (34.1), Zn (10.5), Cl (11.1), O (38.4)	Similar to Paint Flake 1 with a uniform leach layer thickness ~15 μm devoid of cuprite pigments however rich in copper and chlorine.	Atacamite

[120]

Chapter 5: Thermodynamic Analysis Of Copper Patination Under Equilibrium Conditions

5.1   Introduction

The copper patina compounds that had formed on copper containing antifouling coatings removed from the hull of in-service vessels were characterised using SEM and XRD analytical techniques. This allowed the possible reactants present in the environment to be surmised (i.e., chloride and sulphide) from that required to form the specific patina compounds. However, only a limited amount of information can be gleamed from this with regards to the thermodynamic processes occurring, as well as the favourable conditions which may contribute to accelerating patina formation. Using the information gathered from the paint flakes and the HSC software several Potential-pH, or "Pourbaix" diagrams were produced.

Furthermore, under equilibrium conditions, metals can freely interact with the environment allowing the natural corrosion potential or open circuit potential (OCP) to be measured. This OCP may be compared to the Pourbaix diagrams which could then inform on what compounds are thermodynamically favoured. While antifouling coatings contain cuprite as the main copper based biocidal agent, a solid fully dense cuprite electrode was unable to be produced from the pigment which would allow electrochemical measurements to take place. Therefore, a 99.9% pure copper electrode was substituted for cuprite to enable OCP measurements under controlled equilibrium conditions. These materials are closely related sharing a similar standard cell potential where the cupric ions reduced to copper at 0.340 V vs Standard

Hydrogen Electrode (SHE) (Equation 31) and copper oxidises to cuprite at 0.360 V vs

SHE (Equation 32) (Haynes, 2012).

$$Cu^{2+} + 2e^- \rightarrow Cu = 0.340\ V\ vs\ SHE \qquad \text{Equation 31}$$

$$2Cu + 2OH^- \rightarrow Cu_2O + H_2O + 2e^- = 0.360\ V\ vs\ SHE \qquad \text{Equation 32}$$
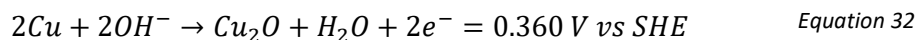
5.2   Pourbaix Diagram Construction

Pourbaix or potential-pH diagrams were first established to summarise the thermodynamic data relating the electrochemical and corrosion behaviour of metals in water and as such are widely used in aqueous chemistry, such as corrosion studies. These diagrams provide a visual representation of the pH and potential ranges that are necessary for the metal to be immune from corrosion, for a passive layer or where the metal can freely corrode. (Pourbaix, 1966)

Copper Pourbaix diagrams in various aqueous media have been reported previously in the literature however they were generally limited to 25°C with chloride concentrations of between $10^{-3}\ M$ and $1.5\ M$ (Bianchi & Longhi, 1973; King, Fraser et al., 2012; Van Mulylder et al., 1962), while Beverskog & Puigdomenech (1998) reported diagrams up to 100°C.

A series of Pourbaix diagrams for the Cu-Cl-H₂O system were produced using specialist software to examine the thermodynamic behaviour of copper and how different chloride concentrations and temperature variables affects the different stability domains, of the species considered in Chapter 3.2 (like those considered by others Beverskog & Puigdomenech, 1998; King, Fraser et al., 2012). Temperatures of 25°C, 35°C, 45°C and 55°C and chloride concentrations of 0% ($0\ M$), 1% ($0.171\ M$), 3.5% ($0.599\ M$), 10% ($1.71\ M$) and 30% ($5.14\ M$), were selected for analysis.

5.2.1 Cu-Cl-H₂O Pourbaix Diagram Analysis

Figures 35-39 show the Pourbaix diagrams for the different sodium chloride concentrations and temperatures where immune, passive, and corrosive regions were identified. The immune region occurred when the potential of the copper and the pH of the electrolyte was such that copper would remain unaffected by corrosion. The passive region was observed in alkaline electrolytes where the Cu_2O, CuO and $Cu_2Cl(OH)_3$ domains were observed which may form protective films on the copper electrode. Corrosion regions were also observed under acidic conditions with the formation $CuCl_2^-$ in chloride containing electrolytes (Figures 36-39), $CuCl^+$ at concentrations above 3.5% (Figures 37-39), Cu^{2+} in all electrolytes and Cu^+ in the 0% chloride electrolyte above 35°C (Figure 35). While under alkaline conditions $Cu(OH)_4^{2-}$ domains were unaffected by the chloride concentration with an increase in temperature shifting the vertical equilibrium line to less alkaline values.

Analysis of the Pourbaix diagrams found that the stability domains varied with temperature and chloride concentration. In general, with increasing temperatures, the vertical pH lines, where two phases were in dynamic equilibrium, moved to lower pH values. While the horizontal equilibrium lines, indicating the irreversible electrochemical reactions requiring an overpotential to form, became more electronegative (active). This suggests that elevated temperatures increased the activity of the different domains, allowing the different species to form at lower potential and pH values.

In each system, the size of the $CuCl_2^-$ domain increased with chloride ion concentration as the lower horizontal equilibrium potential became more

electronegative. For example, at 25°C the equilibrium potential moved from -280 mV at 1% to -440 mV at 30%, reducing the immunity area of copper. A similar pattern was observed with increasing temperature however this was to a lesser extent with the lower equilibrium potentials shifting to more electronegative potentials by approximately 40 mV for every 10°C increase in temperature. This is consistent with the Le Chetalier principle where the position of equilibrium moves to counteract the change in the environment, such as an increase in temperature. Furthermore, the upper equilibrium potential became more positive with increasing temperature (by approximately 20 mV over the whole temperature range) and chloride concentrations (from approximately 200 mV in the 1% to 300 mV in the 30% electrolytes at 25°C), while the vertical pH equilibrium line of the Cu_2O domain was also observed to shift to more alkaline values. This indicates that thermodynamic stability of $CuCl_2^-$ formation is improved with increasing chloride concentration and temperature.

The chloride concentration had the greatest influence in acidic solution where at greater than 3.5% NaCl an additional stability domain of $CuCl^+$ was formed in acidic conditions pushing the Cu^{2+} domain to potentials higher than the oxygen equilibrium line. However, in alkaline environments the size of the CuO domain decreased to some extent with increasing chloride concentration, and was less dependent on temperature, as observed by Beverskog & Puigdomenech (1998).

In the chloride containing systems the presence of a $Cu_2Cl(OH)_3$ domain was observed at positive potentials between pH 6 and 8.5, mostly sacrificing the stability domain of CuO, while at 1% and 3.5% NaCl the Cu^{2+} and $CuCl^+$ domains, respectively, were also affected. The position of this domain was found to vary with

increasing chloride concentrations where the lower pH equilibrium line moved to more neutral values, while the upper pH equilibrium line became more alkaline, at a greater rate, increasing the size and therefore stability of this domain. The temperature had a major influence on the $Cu_2Cl(OH)_3$ domain reducing in size with increasing temperature as the CuO stability increased. This effect was most keenly observed at 1% where the $Cu_2Cl(OH)_3$ domain was no longer visible at temperatures above 45°C (Figure 36).

Angel et al. (2021) Bianchi & Longhi (1973) observed that the $Cu_2Cl(OH)_3$ phase is expected to form on copper when exposed to seawater environments, with this species also being detected on in-service antifouling coatings shown in Chapter 4.2.1, therefore this domain will be targeted when testing the cuprite containing antifouling coatings under laboratory conditions.
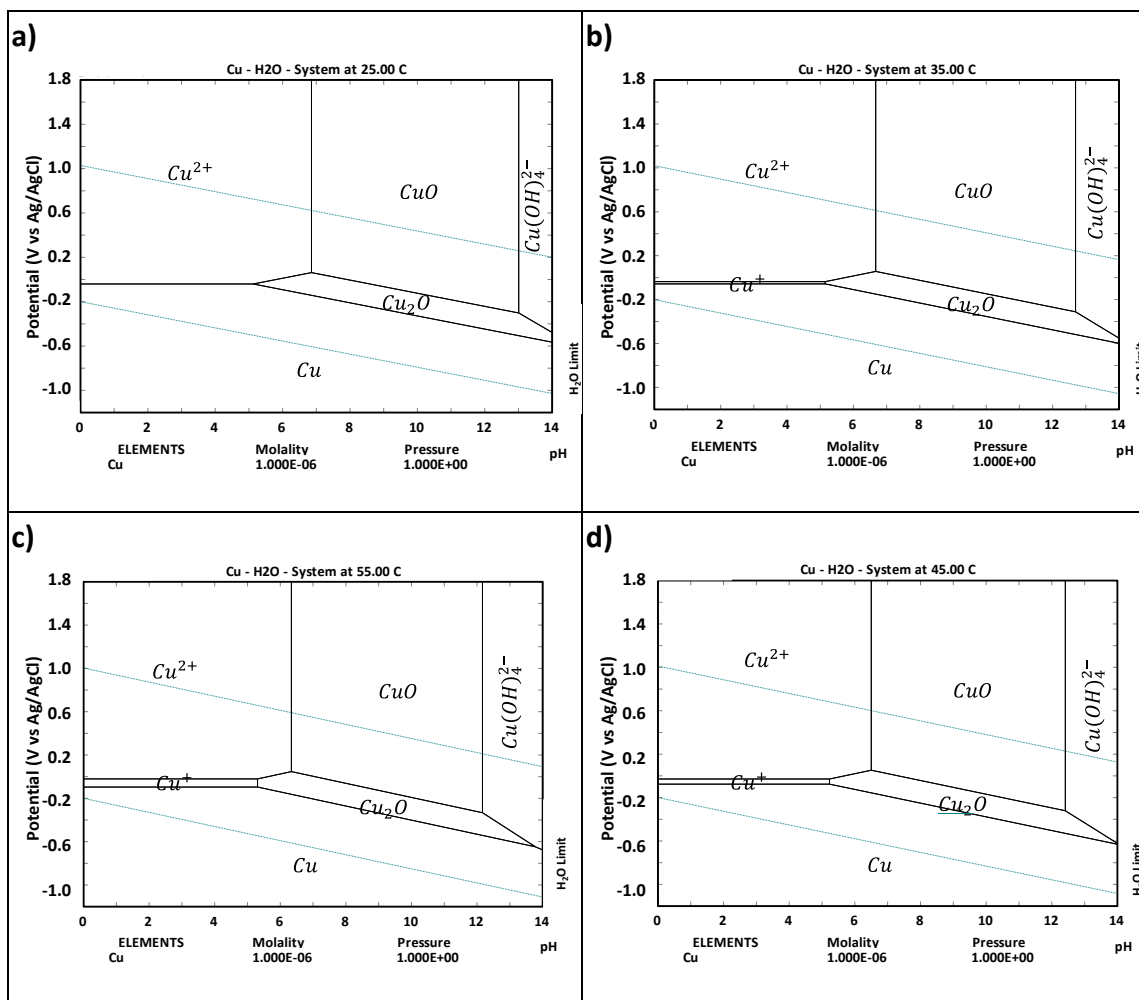
Figure 35 – Pourbaix diagrams for the Cu-H2O system at a) 25°C, b) 35°C, c) 45°C and d) 55°C with a total chloride concentration of $0\ M$ and a dissolved copper concentration of $1 \times 10^{-6}M$, using the thermodynamic data shown in Table 5.

[126]
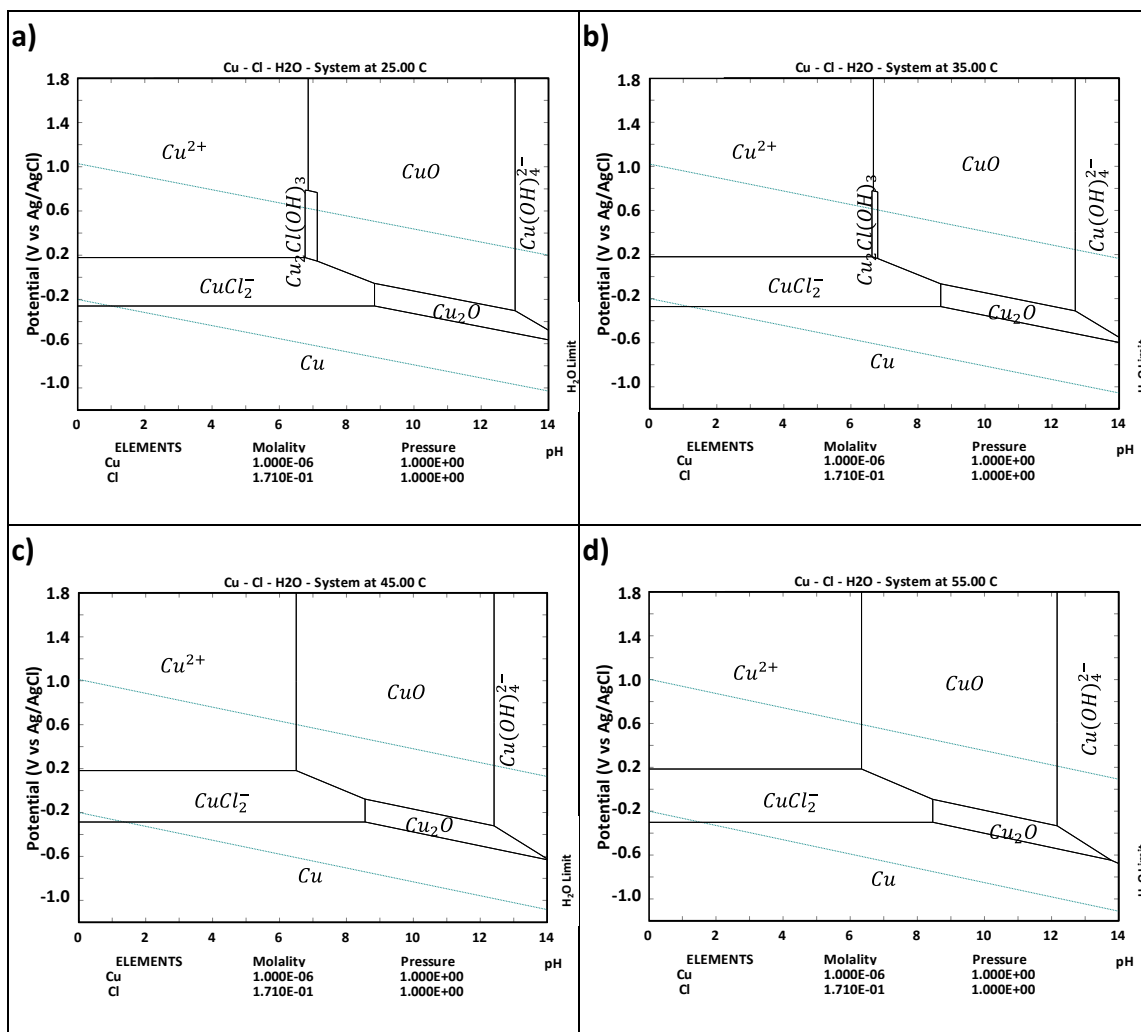
Figure 36 – Pourbaix diagrams for the Cu-Cl-H$_2$O system at a) 25 °C, b) 35 °C, c) 45 °C and d) 55 °C with a total chloride concentration of 0.171 M (1% NaCl) and dissolved copper concentration of 1×10^{-6} M, using the thermodynamic data shown in Table 5.
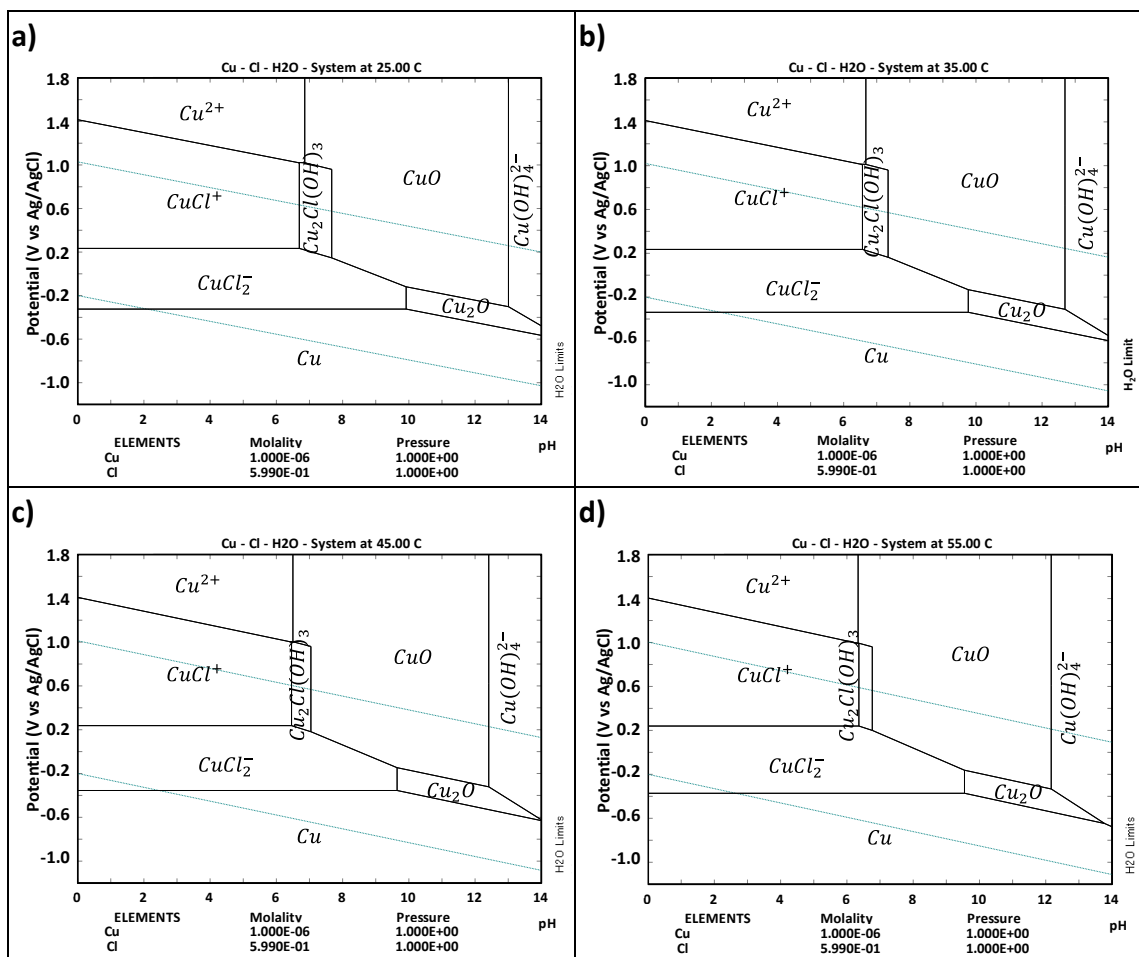
Figure 37 – Pourbaix diagrams for the Cu-Cl-H₂O system at a) 25℃, b) 35℃, c) 45℃ and d) 55℃ with a total chloride concentration of 0.599 M (3.5% NaCl) and dissolved copper concentration of $1 \times 10^{-6} M$, using the thermodynamic data shown in Table 5.
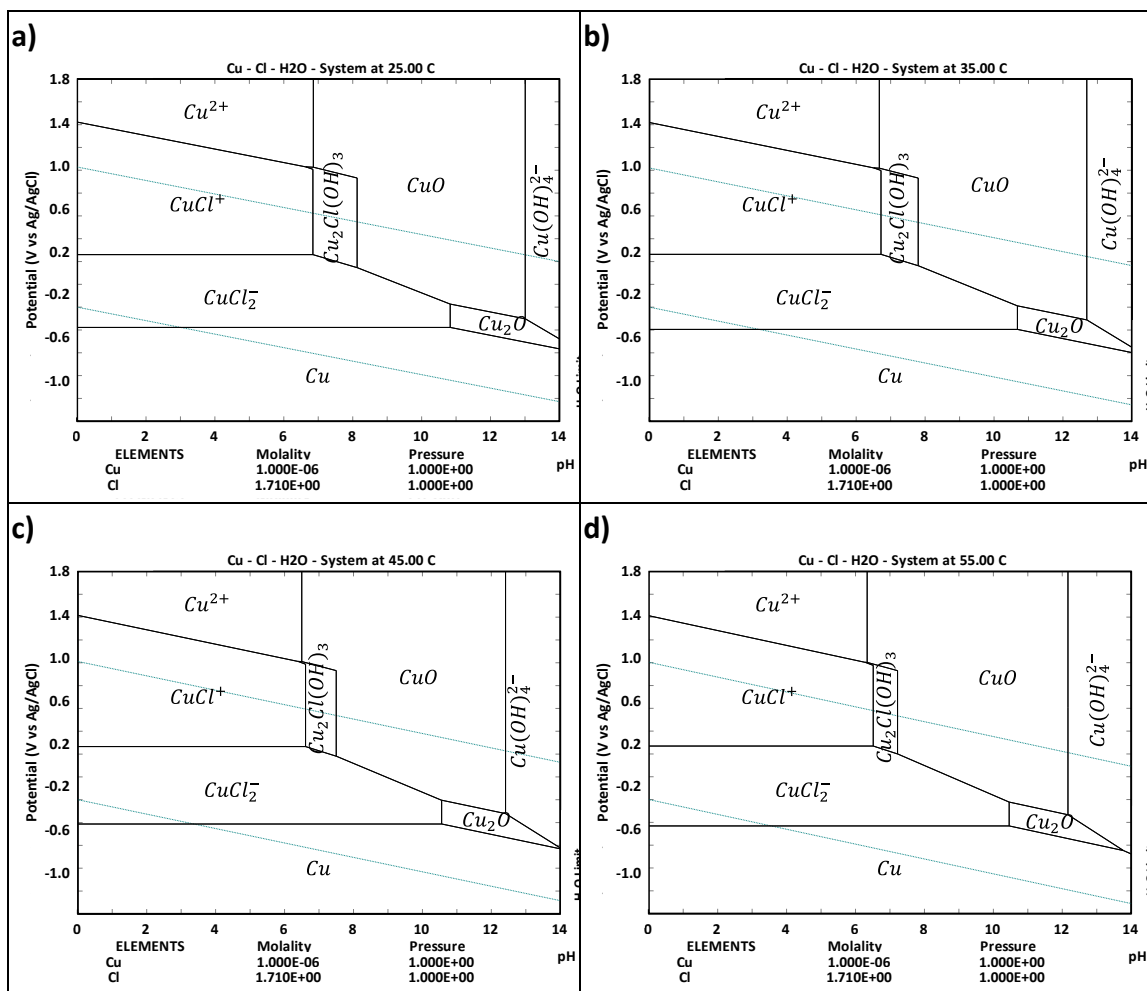
Figure 38 – Pourbaix diagrams for the Cu-Cl-H₂O system at a) 25 °C, b) 35 °C, c) 45 °C and d) 55 °C with a total chloride concentration of $1.71\ M$ (10% NaCl) and dissolved copper concentration of $1 \times 10^{-6} M$, using the thermodynamic data shown in Table 5.
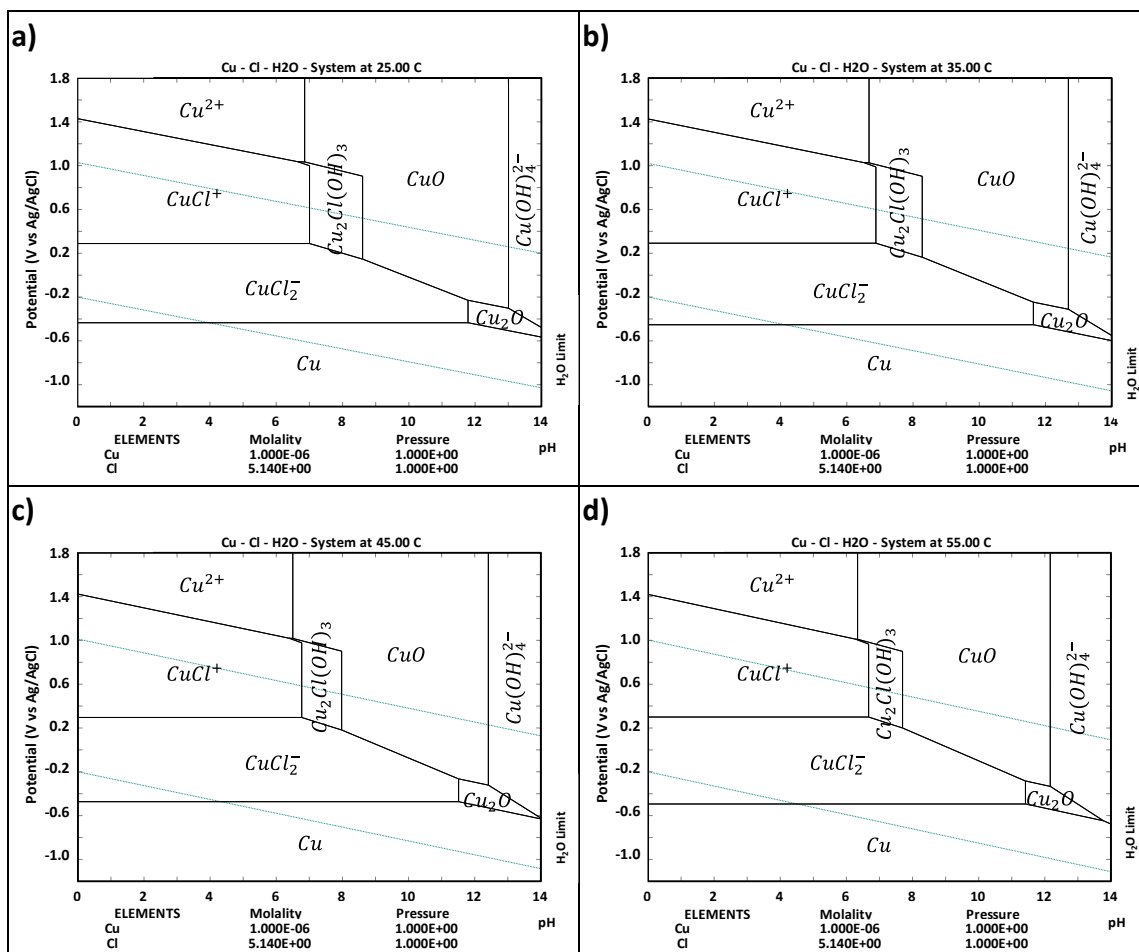
Figure 39 – Pourbaix diagrams for the Cu-Cl-H₂O system at 25℃, 35℃, 45℃ and 55℃ with a total chloride concentration of $5.14\,M$ (30% NaCl) and dissolved copper concentration of $1 \times 10^{-6}M$, using the thermodynamic data shown in Table 5.

5.2.2 Open Circuit Potential Analysis

Analysis of the OCP curves for the different temperatures, sodium chloride concentrations and pH values under equilibrium conditions showed that the potential stabilised during the exposure time, where they became more electropositive (noble) within the first few hours of exposure to 0% NaCl (i.e., deionised water), while in the chloride containing electrolytes, the OCP rapidly became more electronegative (active) with exposure time, stabilising within approximately 1800 seconds. The following sections will discuss the results in more detail.

5.2.2.1 The Effect Of Sodium Chloride Concentration On The OCP

Figure 40 shows an example of how the NaCl concentration within the electrolyte affected the OCP as recorded over 24 hours. The open circuit potential in the 0% electrolytes became more positive than the initial potential over the exposure period, which was also at more positive potentials than the chloride containing electrolytes. This was probably due to the lack of aggressive ions and the formation of a multi-layer protective passive film where the slow reaction rate between the dissolved oxygen (O_2) and hydroxide (OH^-) ions resulting in the increased OCP stabilisation time.

When the copper electrode was exposed to the chloride-rich environment it rapidly forms a poorly protective passive layer allowing for the transportation of aggressive species (i.e., Cl^- ions) to, and soluble species ($CuCl_2^-$ ions) from, the electrode surface. This leads to a diffusion limiting reaction and therefore a stabilisation of the potential to occur. Under open circuit conditions a mixed $CuCl$ and Cu_2O layers may also form on to the surface of the electrode allowing it to passivate under short exposure periods (Ferreira et al., 2004; Zhou et al., 1997). However over long exposure periods this

[131]

chloride rich patina tends to form a porous structure providing a poor protection to the electrode (Faita et al., 1975), which may lead to a slight activation of the potential over time.
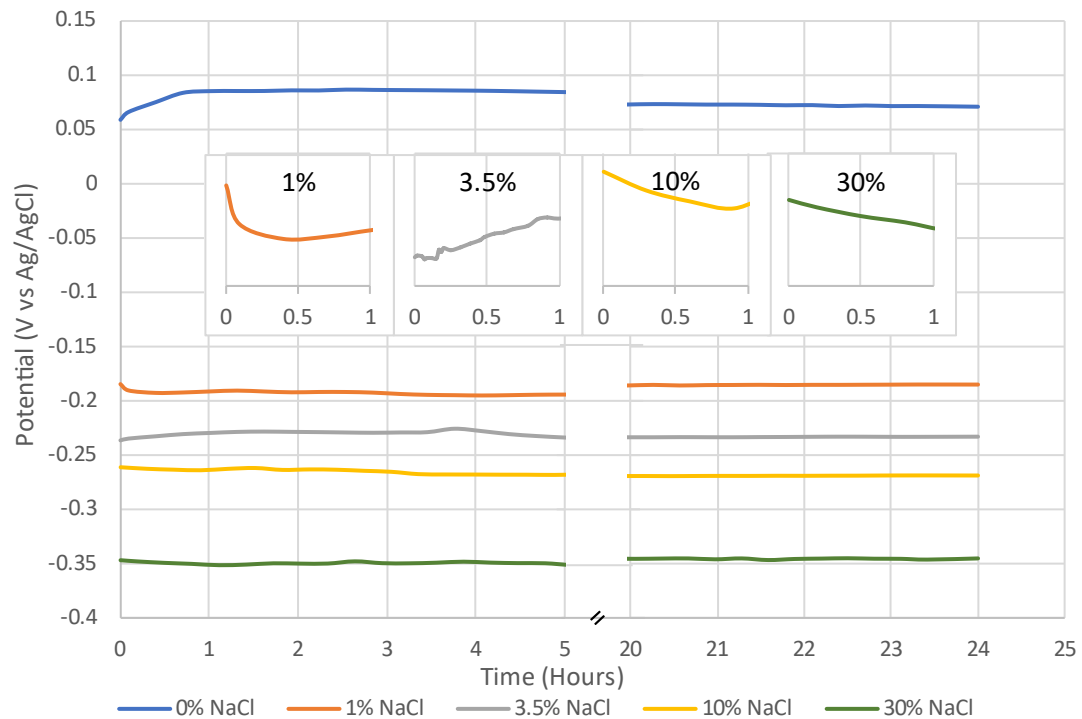
Figure 40 – Example OCP measurements of copper at 35°C in a pH 7 electrolyte showing the effect of sodium chloride concentration over a 24-hour period, with the cut-outs showing the magnified view of the OCP in the chloride containing electrolytes after 1 hour.

An activation of the potential was observed within the first 600-3600 seconds following the exposure to the chloride containing electrolytes (Figure 40) where the OCP, on average, became 21.0 ± 17.0 mV more electronegative than the initial potential. The initial reduction in potential suggests that the stability of the naturally air formed oxide, which Keil et al. (2007) determined to be approximately 3 nm thick, was significantly reduced in the presence of chloride ions resulting in the activation of the surface of the electrode. This may be associated with the degradation and incorporation of chloride ions into the oxide layer, leaving the more active copper substrate exposed to the corrosive medium, and therefore stabilising the OCP at more

[132]

electronegative potentials (Vrsalović et al., 2016). Vrsalović et al. (2018) also observed a rapid stabilisation of copper within 10 minutes in a $0.5M$ NaCl electrolyte while Badawy & Al-Kharafi (1999) observed a general steady-state OCP occurring within the first 15 minutes in acidic, neutral, and alkaline buffered electrolytes

The chloride ions can inhibit the cathodic reaction on the copper surface which results in the electrode becoming more electronegative (Mayanna & Setty, 1974). An increase in chloride concentration reduces the number of cathodic sites on the electrode that can be inhibited, increasing the activity of the anodic regions, shifting the potential to more electronegative values. Analysis of the OCP curves found that the potential stabilised after extended exposure periods generally at more electronegative potentials than what was recorded following the initial exposure to the test environment.

5.2.2.2 The Effect Of Temperature On The OCP

Example open circuit potential curves are provided in Figure 41 showing the variation in OCP with respect to time in a 3.5% NaCl electrolyte at pH 7 over a 24-hour period (further OCP curves are available in the Appendix 3a). An overview of the pH, temperature, and sodium chloride concentrations is shown in Figure 43.

The OCP of the copper electrode in the electrolytes containing sodium chloride became more electronegative with increasing temperature from 25°C to 55°C of between 35 and 55 mV, with the following trend of $25°C \rightarrow 35°C \rightarrow 45°C \rightarrow 55°C$ from most to least noble. Indicating that the activity of the electrode increases with temperature. Similar results were found in Ochoa et al. (2015) where the E_{Corr}

increase by between 30 and 55 mV as the temperature was increased from $25°$ to $55°C$ in $0.01, 0.1$ and 1 mol/L NaCl electrolytes.

The OCP recorded in the 0% electrolyte were found to have a greater variability compared to that recorded in the chloride rich environment (Appendix 3, Figure 149). At temperatures up to 45°C (Appendix 3, Figures 150 and 151) the electrodes became generally more electronegative with increasing temperature by approximately 15 and 35 mV in the pH 4 and 10 electrolytes, respectively. However, at 55°C the electrodes became more electropositive, compared to the 45°C, by approximately 47 and 33 mV, respectively (Appendix 3, Figure 152).

At pH 4 and 7 fewer potential spikes were observed with increasing temperature where the OCP curve produced at 55°C achieved a steady value with little variation in the potential over the exposure period. However, at pH 10 the opposite was true where the potential recorded at 55°C tended to be more variable than that at 25°C especially in the 0, 1 and 10% NaCl electrolytes. This may be due to the formation of a weakly protective CuO film, which forms in alkaline electrolytes, on the surface which had an increased solubility with increasing temperature. The unstable OCP suggest that the electrodes were actively forming and breaking down a protect passive film resulting potential transients from more noble potentials to more active potentials, respectively. Whereas the stable OCP curves indicate that the electrodes are being uniformly affected by the electrolyte.
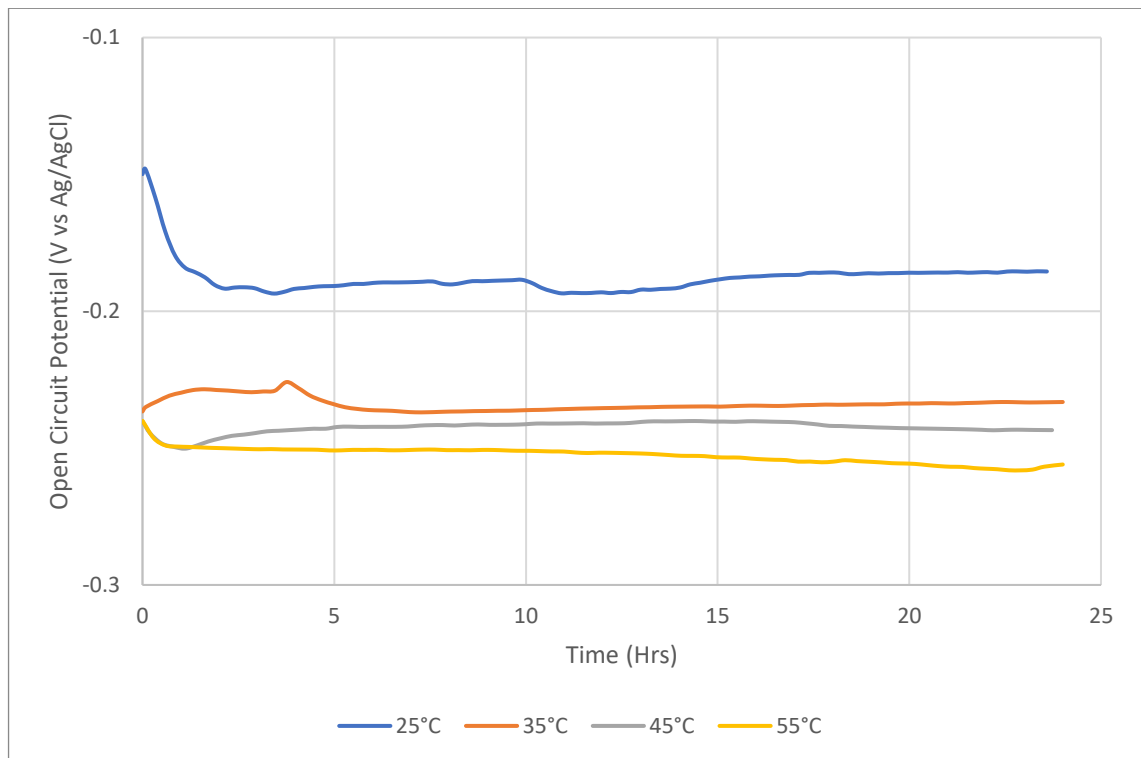
Figure 41 – Example copper OCP measurements showing the effect of temperature in a 3.5% NaCl electrolyte at pH 7. Further OCP measurements of the different electrolytes are shown in Appendix 3a.

Benson & Krause Jr., (1984) determined that the oxygen solubility in water was reduced with increasing temperature, reducing from $14.62 \, mg/L$ at 0°C to $6.41 \, mg/L$ at 40°C in a 0% saline solution and was calculated to be $5.2 \, mg/L$ at 55°C using Natural Resources Research Institute, (2015). The salinity also affected the oxygen solubility reducing to $11.85 \, mg/L$ in a 30% saline solution at 0°C (U.S. Geological Survey, 2018). The oxygen concentration was also important in the patination process of copper where King et al. (1995) showed that as the oxygen concentration was reduced from $6.40 \, mg/L$ to $0.02 \, mg/L$ the E_{Corr} values became more electronegative. They explained that this was due to the cathodic reaction becoming increasingly mass transfer limited rather than kinetically limited, however due to the slow oxygen reduction of copper, joint kinetic and mass transfer control of the cathodic reaction was able to be maintained even in deaerated solutions. Imai et al., (2009) also observed that there was a slight reduction in the etch rate of a copper

[135]

wafer by approximately $0.01\ mm/min$ when the oxygen concentration was reduced from $5\ mg/L$ to $0.6\ mg/L$. Furthermore, King (2002) determined that tenorite tended to form in greater thicknesses than cuprite at high oxygen concentrations. This suggests that while the oxygen concentration was reduced with temperature the relatively high concentrations of oxygen at 55°C and the slow oxygen reduction of copper suggests that it would have a negligible effect.

5.2.2.3   The Effect Of pH On The OCP

Figure 42 shows that there is no linear relationship between the pH of the different electrolyte and the OCP of the electrode. Antonijevic et al. (2009) observed a similar trend however the OCP was found to become more electronegative with increasing alkalinity in low chloride electrolytes. However, some general trends were found where the potentials recorded at pH 4 tended to be more electronegative than at other pH values, while the OCPs recorded at pH 7 had an intermediate potential between that of the pH 4 and 10 electrolyte. Similar results were observed in Faita et al. (1975) where the OCP was ennobled as the alkalinity was increased especially when the pH was above 8.3. Yan & Sun (2017) also observed that the OCP was more electronegative in acidic (pH 4.8) electrolytes when compared to alkaline (pH 8.3). However, in highly alkaline electrolytes with pH values exceeding 12 the OCP of the electrode was found to become more electronegative than in mildly acidic environments (Feng et al., 1997; Yan & Sun, 2017). This was attributed to be due to the formation of a poorly protective CuO film which had an increasing solubility in higher alkalinity electrolytes and therefore experienced a greater corrosion tendency than the mildly acidic and alkaline environments.

When comparing the OCP with respect to the pH of the electrolyte it was found that the 0% NaCl had the largest potential range of between 27 and 112 mV vs Ag/AgCl. This further highlights the variability of the OCP in solutions that do not contain NaCl as the electrode is mostly affected by the concentration of dissolved oxygen and hydroxyl ions present in the electrolyte. With an increase in NaCl concentration the number of aggressive chloride ions is increased. While this shifts the OCP to more electronegative values it also results in a reduction in the variation of the OCP with pH where the maximum difference was recorded at 5-49 mV in the 1% and 7 – 47 mV vs Ag/AgCl in the 3.5% NaCl electrolytes. In the 10% electrolyte the potential range narrowed further to between 7 – 35 mV vs Ag/AgCl and at 30% the potential range was between 9 – 40 mV vs Ag/AgCl. This decrease in potential difference with respect to pH when the NaCl concentration is increased indicates that the pH has a smaller effect on the OCP than NaCl.
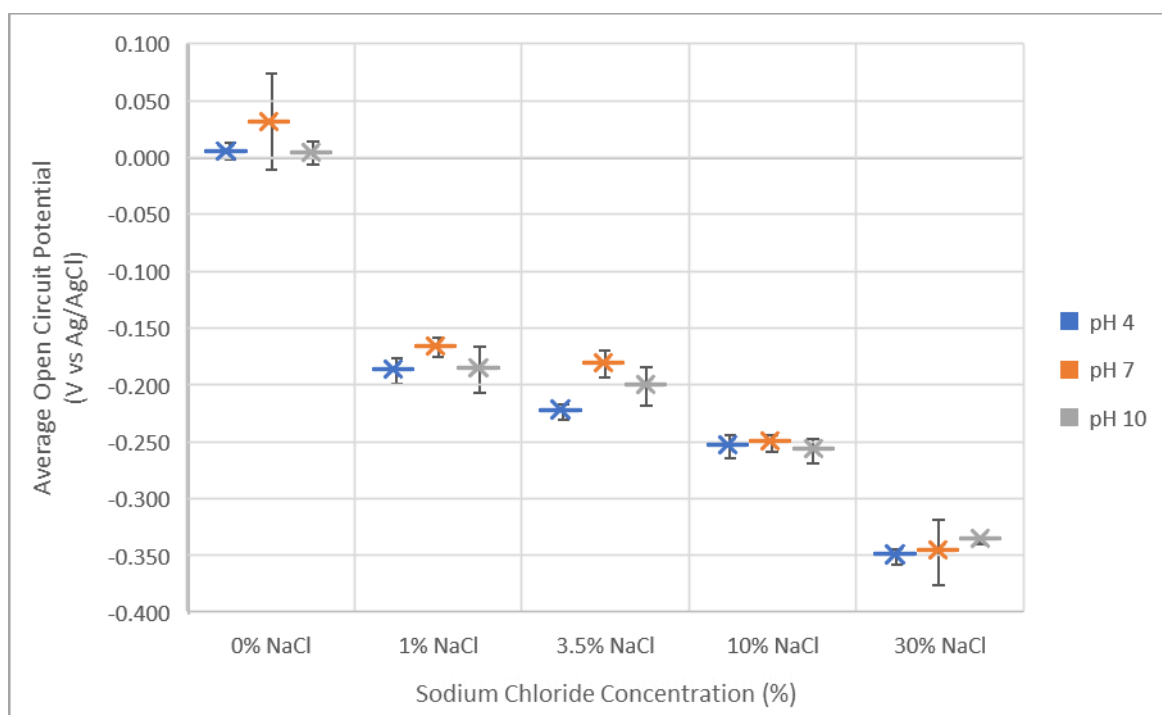
Figure 42 – Example chart showing the effect of pH has on the open circuit potential at 25°C in the different sodium chloride concentration electrolytes over 24 hours (additional charts at 35°C, 45°C and 55°C are shown in the Appendix 3b).

[137]

5.3   The Relationship Between The Cu-Cl-H$_2$O Pourbaix Diagrams And The OCP Of Copper Under Equilibrium Conditions

Figure *43* shows how the average OCP values recorded over 24 hours on the copper electrode was modified when the environmental variables, such as sodium chloride concentration, pH, and temperature, are altered. From the chart is can be seen that the OCP values recorded in the 0% NaCl electrolytes were more variable when compared to the electrolytes containing NaCl. In general, the copper electrode in the pH 4 and 10 electrolyte followed a similar trend where an increase in temperature resulted in an increase in electronegativity up to 45°C at 55°C the potentials were found to be ennobled, while the pH 7 electrolyte remained at the most electropositive values with no obvious trend with changing temperature.

Each of the solutions containing sodium chloride followed similar trends, where increasing temperature resulted in a near linear shift of the OCP towards more electronegative values of between 25 mV vs Ag/AgCl and 70 mV vs Ag/AgCl. With increasing chloride concentrations, the OCP also shifted towards more electronegative values with the largest step between 0% and 1% NaCl of between 140 and 250 mV vs Ag/AgCl and progressively smaller steps as the chloride concentration was increased of between 15 and 96 mV vs Ag/AgCl at 3.5% NaCl, and 25 and 70 mV vs Ag/AgCl at 10% NaCl. Similar tends were also observed when analysing the Pourbaix diagrams. This may be due to the limited number of cathodic sites on the copper electrode becoming saturated by chloride ions reducing their effect of increasing the activity of the electrode. Altering the pH of the electrolytes seems to have the smallest effect on the activity of the electrode, with the difference in the potentials ranging between 5 and 50 mV vs Ag/AgCl for the chloride containing electrolytes.

[138]

From the Pourbaix diagram analysis the potential range for the different species was shown to change with increasing temperature, however the thermodynamically stable species between 25°C and 55°C remained consistent when compared to the measured OCP. Therefore, it was determined that using the immunity and upper equilibrium potentials taken from the respective Pourbaix diagrams at 25°C for the highlighted species would allow the relationship between the OCP and Pourbaix (Figure 43) to be analysed.

Figure 43 suggests that under equilibrium conditions when copper is exposed to 0% sodium chloride (deionised water) electrolytes at pH 4 is actively dissolves with the formation of Cu^{2+} ions in solution, at all temperatures. In neutral electrolytes copper spontaneously oxidises forming Cu_2O at 25°C, CuO at 35°C and 55°C, and a mixture of Cu_2O and CuO at 45°C, whereas at pH 10, copper should also spontaneously oxidise forming CuO.

At each temperature when relatively low concentrations of chloride were present (1% and 3.5%) copper would be expected to actively dissolve resulting in $CuCl_2^-$ species forming at pH 4 and pH 7, while at pH 10 Cu_2O is expected. At higher chloride concentrations (10% and 30%) the copper would actively dissolve resulting in the formation of $CuCl_2^-$ in all electrolytes and temperatures.
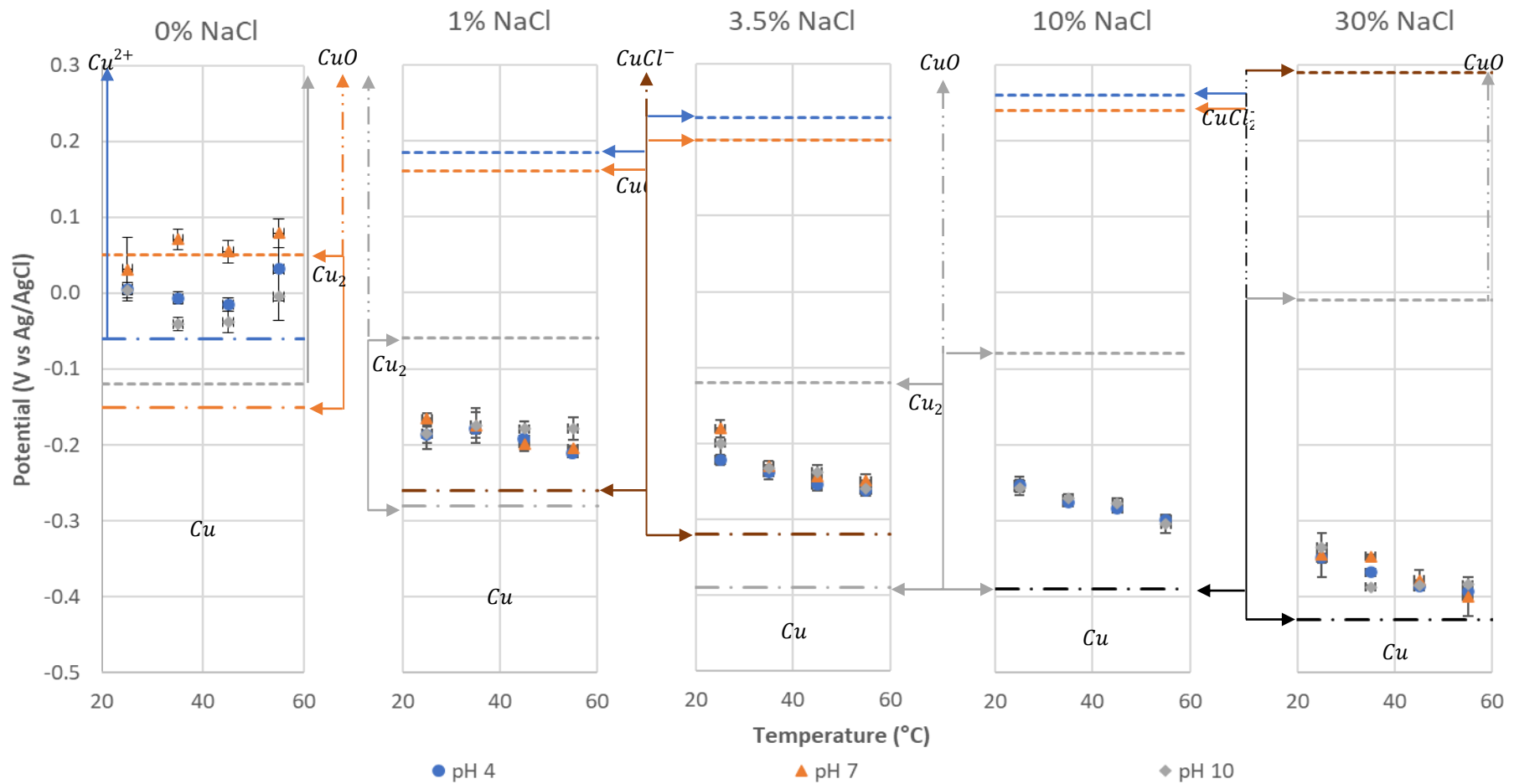
Figure 43 – Charts comparing the averaged OCP data over the 24-hour period for the different sodium chloride concentrations, pH values and temperatures with the potential ranges for the Cu, Cu^{2+}, Cu_2O, CuO and $CuCl_2^-$ domains taken from the respective Pourbaix diagrams at 25°C. The immunity equilibrium potential for the different pH values is represented by —·(pH 4), —·(pH 7), —·(pH 10), —·(pH 4 and 7) and —·(pH 4, 7 and 10), while the upper equilibrium potential is represented by ----(pH 4), ----(pH 7), ----(pH 10) and ----(pH 4 and 7) for the different species.

[140]

5.4   Surface Analysis

While Pourbaix diagrams can be used to describe all the reversable and irreversible reactions that are thermodynamically possible, for a particular system, it does not provide information on the kinetic parameters leading to species formation, such as the reaction rates. Therefore, analysis of the copper coupons after 24 hours immersion under the different environmental conditions (Chapter 3.3.1.3, Table 6) was required.

5.4.1   Visual Examination

When oxides are stripped from the copper surface it has salmon pink colouration (Fitzgerald P. et al., 1998) as can be seen in Figure 44. An oxide layer then forms when exposed to oxygenated environments which thickens over time, changing its colour. The two main oxides that develop on the copper are cuprite (Cu_2O) and tenorite (CuO), which tend to have a red-brown and dark brown-black colouration, respectively (Fitzgerald P. et al., 1998).
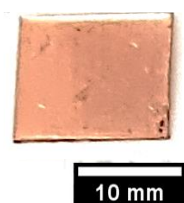
Figure 44 – Example image showing the surface of the copper coupon following the oxide stripping procedure.

Figure 45 shows the surface of the copper coupons following the 24-hour immersion test.   Samples have been arranged to allow for a direct comparison between the different sodium chloride concentrations, pH values and temperatures and therefore observe how these variables affect the patination of copper.

From this it is possible to see that there is an interdependency of these three variables where the coupons only developed a red-brown cuprite colouration at 25°C in the 0% NaCl electrolytes at pH 4 and 10. Indeed, when analysing the Pourbaix diagram the

[141]

spontaneous formation of cuprite is expected at pH 10 with Cu^{2+} present at pH 4, which may go on to react with water molecules to form the cuprite compound. Yet, the colour of the coupons at pH 7 remained unchanged suggesting that no visible patina layer had formed within the 24-hour immersion period. Similar observations were made on those exposed to the chloride containing electrolytes where $CuCl_2^-$ is expected to form at pH 4 and 7.

Increasing the temperature of the electrolytes to between 35°C and 55°C resulted in the coupons changing colour, suggesting a patina layer had formed. This may be caused by an increase in reaction rate, as observed in the Arrhenius Law, where generally for a 10°C increase in temperature the reaction rate doubles. Therefore, as the temperature was increased from 25°C more copper ions could be released from the coupon surface. These ions could then react with oxygen and chlorine in the electrolyte more quickly, forming copper oxide compounds, such as cuprite, at an accelerated rate, resulting in the increased patina formation observed on the coupon.

In general, the colour of the coupons in the high sodium chloride concentration electrolytes of 10% and 30% remained consistent with the oxide stripped sample regardless of temperature or pH, suggesting that no patina had formed. These high chloride solutions are known to actively dissolve the copper (King et al., 2012), resulting in the production of $CuCl_2^-$ ions as indicated in the Pourbaix diagrams. This may prevent the development of patina on the coupon surface under relatively short time scales. Under longer time scales it may be expected that the increased concentrations of $CuCl_2^-$ maybe high enough or had been exposed for long enough to form more complex copper chloride compounds.

[142]
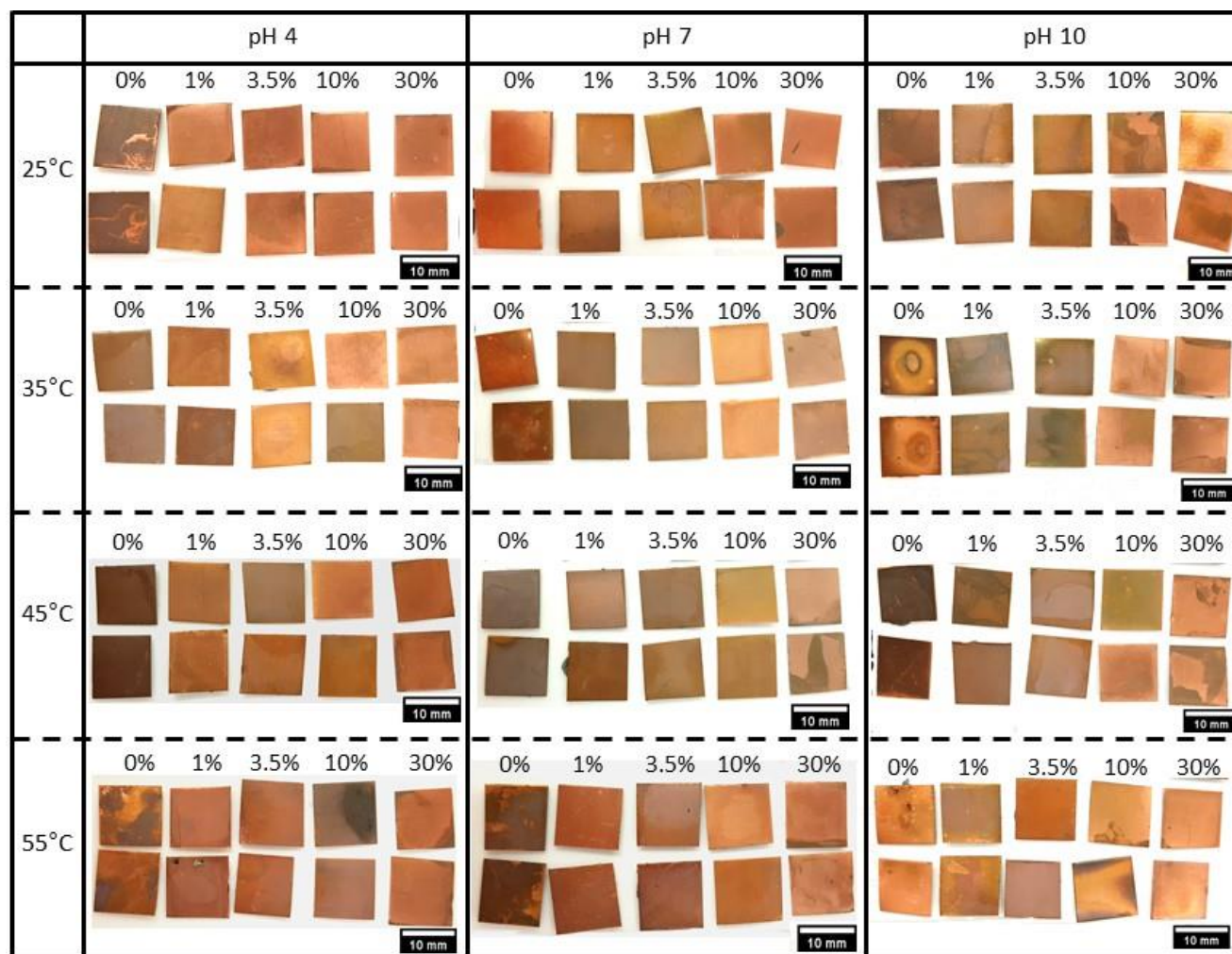
Figure 45 – Photographs showing the surface of copper coupons that have been exposed to the various solution chloride concentrations, temperatures, and pH for 24 hours.

[143]

5.4.2   SEM Analysis Of Coupon Surfaces

From the optical examination, when immersed in the different electrolytes at 25°C only the coupons exposed to 0% at pH 4 and 10 showed a variation in the colour of the coupons suggesting that only these samples had patinated. With increasing temperature more of the coupons had changed colour with the largest change being observed at 45°C, suggesting an increase in patination rate, with the coupons appearing to have a similar or reduced level of patination at 55°C. Therefore, as this study is focused on the acceleration of patination it was determined that only the coupons exposed at 45°C were analysed in the SEM. This was done using the Nova Nano SEM using the BSE detector combined with the EDX detector to provide a semi-quantitative analysis of the elements present.

The initial surface morphology of the copper coupons in the as-received and following the oxide stripped conditions are shown in Figure 46 with the surface after immersion in the different electrolytes shown in Figures 48 to 57.

5.4.2.1   As-Received Surface

Examination of the copper coupons in the as-received condition (Figure 46a and b) found the general surface features associated with the manufacture of the copper sheets i.e. parallel grooves. Copper is a relatively soft and malleable material which is ductile due to its face centred cubic crystal structure (Davis & Committee, A. S. M. I. H., 2001). When manufacturing copper sheets, copper ingots are typically heated to between 700 and 900°C (Chernysheva et al., 1976; Solve & Anders, 1956) to improve their malleability and ductility and therefore reducing the amount of energy needed to compress the ingots. Once heated, the ingot is forced through a series of rollers to

[144]

reduce its thickness in the later stages of the sheet production the copper is cold rolled to the desired thickness (Davis & Committee, A. S. M. I. H., 2001), resulting in plastic deformation. The parallel grooves are impressions left in the surface of the copper sheet as it goes through the final cold rolling stage.

Analysis of the coupons following the oxide stripping procedure found a series of <500 nm diameter pits distributed across the surface which tended to be present in areas of highest plastic deformation, following the parallel grooves (Figure 46c and d). Plastic deformation introduces a series of dislocations within the lattice structure as well as surface breaking defects, such as slip steps, resulting in localised high energy areas which can act as anodic sites with respect to the bulk material making these areas prone to pitting (Li & Li, 2005; Wu & Singh, 2019).

Li & Li (2005) and Yin & Li (2005) that with increasing plastic deformation the OCP of a copper in dilute nitric acid and sodium chloride solutions, shifted towards more electronegative values. However, Robin et al. (2012) observed the opposite effect with increasing deformation the OCP became ennobled in a sulphuric acid solution. It was noted that Li & Li (2005) and Yin & Li, (2005) lightly etched their copper electrodes prior to testing to remove the surface deformation caused by the polishing process and therefore only the plastic deformation caused by the reduction in thickness following the rolling process was measured. Robin et al. (2012) however introduced plastic deformation through the sample preparation by grinding the copper to a 600-grit finish and there was no mention of etching to remove the surface plastic deformation prior to testing. Therefore, the conflicting observations may be caused by the different surface conditions of copper. Robin et al. (2012) and Yin & Li (2005) also

reported a reduction in the corrosion resistance with increasing plastic deformation due to the increase in dislocation density, increasing the activation energy, promoting pitting corrosion and galvanic corrosion at the grain boundaries.

To confirm that the stripping procedure removed the oxide layer, a semi-quantitative EDX analysis before and after stripping was performed where the oxygen concentration was found to reduce from 0.8 to 0.1 ± 0.1 wt% (Figure 47).
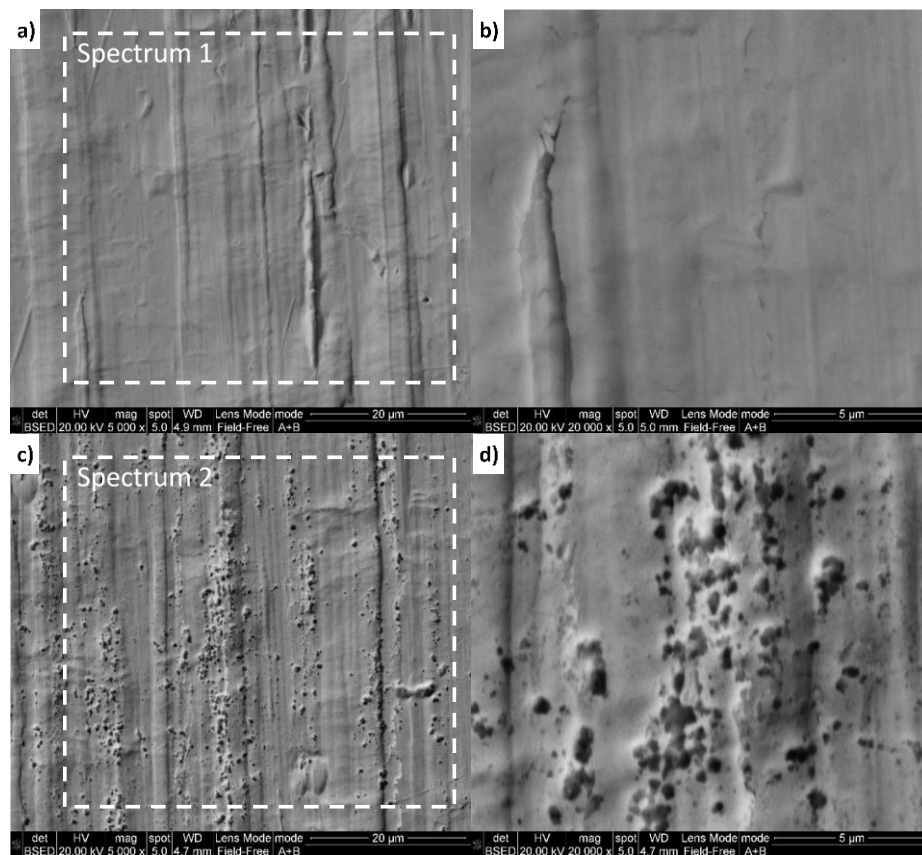
Figure 46 – Example BSE micrographs showing a) a low and b) and high magnification image of the coupon surface in the as-received condition and c) a low and d) high magnification image of the coupon surface following the oxide stripping procedure prior to testing. The dashed white boxes indicate the locations of the EDX analysis.
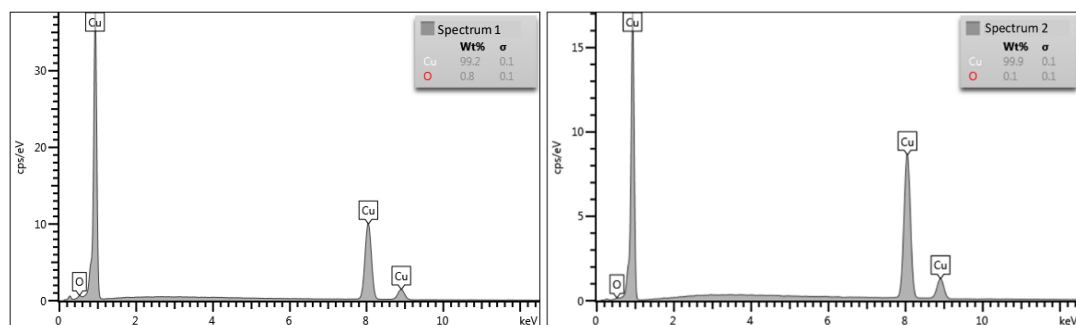
Figure 47 – EDX spectra and semi-quantitative analysis of the areas highlighted in Figure 46

The morphologies of the copper coupons following the 24 hours immersion in a 0% NaCl electrolyte at pH 4, 7 and 10 are shown in Figure 48. From these micrographs it was possible to see that two unique crystalline structures had formed on the oxide stripped surface.

At pH 4 and 7 the crystals had a cubic polyhedron structure typical of what might be expected for a cuprite (Cu_2O) patina (Hua et al., 2011; Zhang et al., 2009), which had diameters of approximately 427.5 ± 167.7 and 468.8 ± 160.0 nm, respectively (see Chapter 5.4.3.1 for more detail particle size analysis). However, at pH 10, the crystals had an acicular monoclinic structure approximately 776.7 ± 168.5 nm long, typically associated with a tenorite (CuO) patina. This confirms the difference in the visual inspection of the copper coupons shown in Figure 45. Similar observations were made in Feng et al. (1997) yet their testing was conducted at 30°C with no patina being found in the pH 10 electrolyte, while monoclinic crystals developed at higher alkalinity levels (pH 13). This may suggest that with increasing temperature the rate at which monoclinic crystals form in basic solutions increases. Furthermore, Zhang et al. (2018) observed tenorite crystals forming on the copper substrate in alkaline electrolytes after 72 hours at 40°C.

At pH 4 and 10 the general surface morphology of the copper coupon was visible with patina following the grooves from the rolling process, however, at pH 7 this morphology was less evident. The solubility of copper oxide increases in acidic solutions (Palmer, 2011), which may result in a lower density (Feng et al., 1997) and/or

thinner (Brusic et al., 1991) patina film forming than that observed at pH 7, which would also be less protective. With increasing pH, the density and/or thickness of crystal formation increases, where cuprite was the most stable copper oxide species that forms in neutral (pH 6 – 8) electrolytes (Badawy & Al-Kharafi, 1999; Zhang et al., 2018).

In the pH 7 electrolyte small dendrites of monoclinic crystals formed on top of the cubic crystals (Figure 48d). Semi-quantitative EDX analysis of the two crystals found that the cubic structure had a composition of 91.4 wt% (Cu) and 8.6 wt% (O) (Figure 49, spectrum 3) similar to the molecular weight cuprite of 88.8 wt% (Cu) and 11.2 wt% (O) (Webmineral, 2012a). While the dendrites had an elemental composition of 79.8 wt% (Cu) and 20.2 wt% (O) (Figure 49, spectrum 4) similar to the molecular weight of tenorite of 79.9 wt% (Cu) and 20.1 wt% (O) (Webmineral, 2012b). The OCP of copper in the 0% electrolyte at 45°C was found to be at the equilibrium potential between the cuprite and tenorite domains allowing both compounds to be present, with cuprite initially dominating the surface (Figure 43). If the coupons were left in the electrolyte for ≥336 hours (Chapter 7.1.1.1) it would be expected that the surface would be covered with the monoclinic crystals resulting in the dual oxide layer observed by other authors. Generally copper patinas have been reported to form a duplex oxide with the primary cuprite layer forming on the copper substrate, which then reacts with the environment allowing the formation of a tenorite layer as discussed earlier, or other copper compounds. The rate of which increases in the presence of water (Liu et al., 2006a; North & Pryor, 1970).

Analysis of the coupon in the pH 10 electrolyte determined that no polyhedron cubic cuprite crystals were found, with the acicular monoclinic crystals, which due to size and of the crystals and thickness of the layer, tended to follow the surface morphology of copper coupon. Liu et al. (2006a) observed that the selective synthesis of CuO can occur through the oxidation of copper in hot (60°C) alkaline solutions, also shown in Wang et al. (2003) and Liu et al. (2006b) and at 40°C Wen et al., (2005). This is where the copper coupon releases copper ions into solution react with the OH^- ions to form $[Cu(OH)_4]^{2-}$ (Equation 33). These copper complex ions are then transformed to CuO in hot alkaline solutions (Equation 34). The OCP of copper in this electrolyte also suggests that CuO should form (Figure 43).

$$Cu^{2+} + 4OH^- \rightarrow [Cu(OH)_4]^{2-}$$

Equation 33

$$[Cu(OH)_4]^{2-} \rightarrow CuO + H_2O + 2OH^-$$

Equation 34
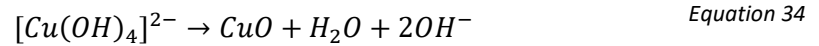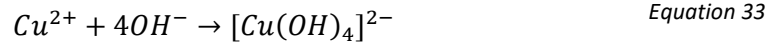
Liu et al. (2006a) also suggested that at temperatures lower than 30°C the formation of $Cu(OH)_2$ rather than CuO would dominate, which was also observed in Wen et al. (2005).
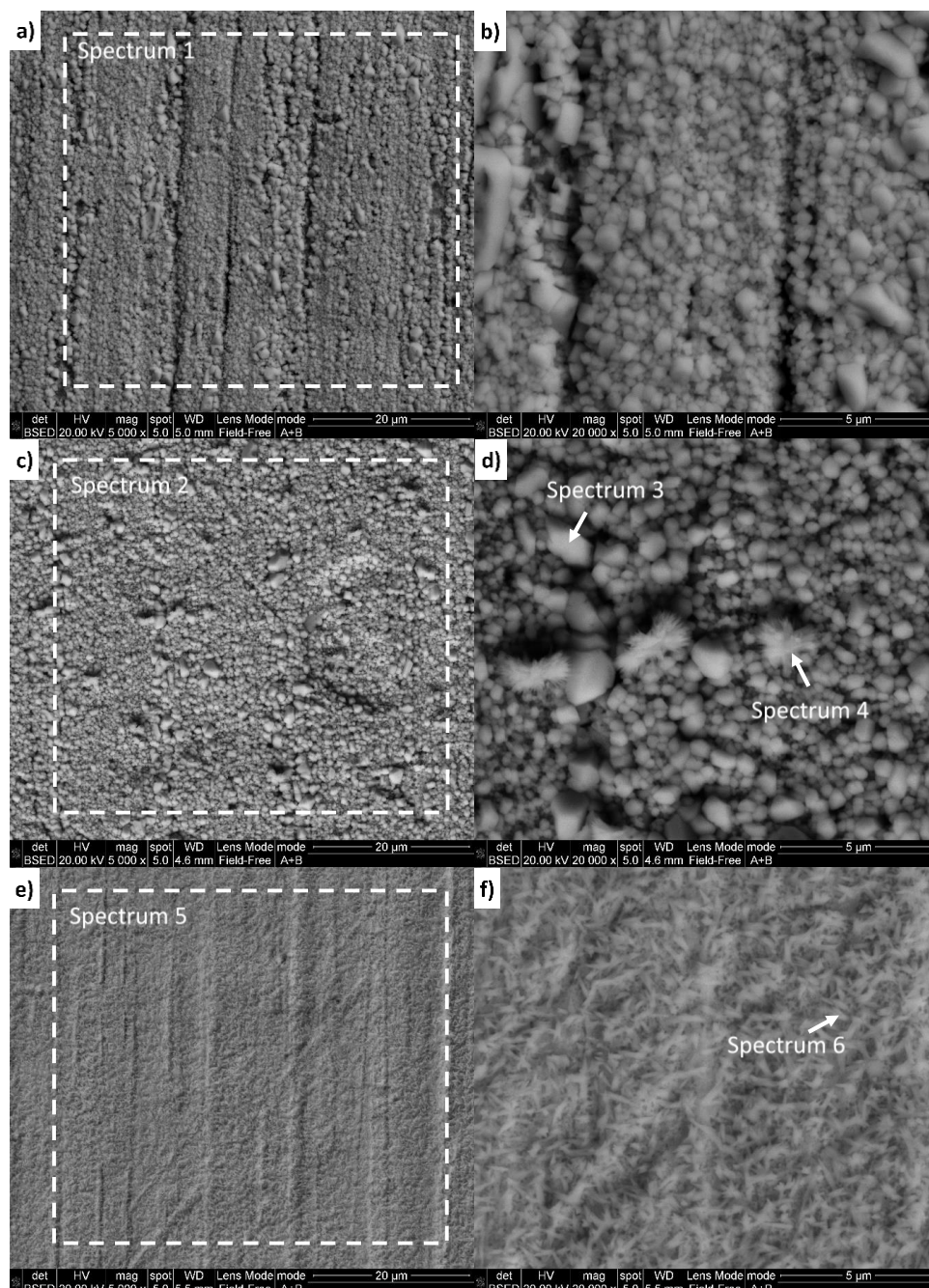
Figure 48 – Example low and high magnification BSE micrographs of the copper coupon surfaces after they had been exposed to the pH 4 (a and b), 7 (c and d) and 10 (e and f) 0% NaCl electrolytes at 45 ℃ after 24 hours, respectively. The white dashed boxes indicate the locations for EDX analysis.

Spectrum	Cu (wt%)	O (wt%)
1	93.6	6.4
2	93.4	6.6
3	91.4	8.6
4	79.8	20.2
5	93.9	6.1
6	84.2	15.8
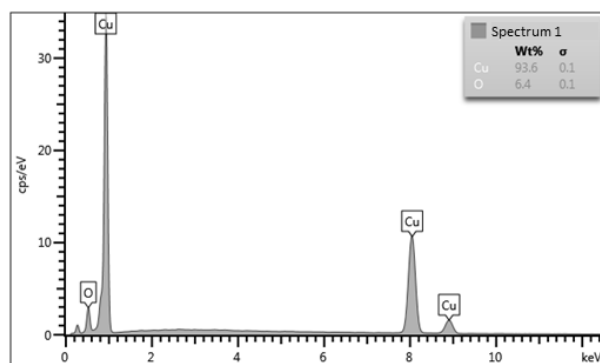
Figure 49 – Example EDX spectrum and semi-quantitative EDX analysis of the areas highlighted in Figure 48.

[150]

Figures 50 and 52 show the general patina morphology found on the copper coupons when they were exposed to the 1% and 3.5% electrolytes, respectively, at the different pH values. From these images it is possible to see that the structure of the patina had changed from that formed in the 0% electrolytes, which may have caused the colour of the coupons to become visibly lighter as the NaCl concentration was increased (Figure 45).

In the 1% electrolytes, an inhomogeneous dispersion of cubic crystals was observed on the surface of the coupons immersed in the pH 4 (Figure 50a-b) and 7 (Figure 50c-d) electrolytes, with the substrate being visible in some areas. This increase in porosity compared to the 0% electrolyte suggests that the patina would be less protective. As the pH of the electrolyte was changed to more neutral values a reduction in porosity was observed along with an increase in the average size and number of crystals being found. Similar observations were made by Liao et al. (2011) where the main corrosion product after 2 hours in a 3.5% NaCl electrolyte was cuprite. When comparing the Pourbaix diagram and the OCP of the copper in these electrolytes the active dissolution of copper substrate is expected with the formation of $CuCl_2^-$ ions. Evidence of the substrate dissolution was observed in Figure 50 c) and d) with the evidence of crystallographic etch pits, discussed in detail in Chapter 0.

At pH 10 (Figure 50e-f), the patina morphology had evolved from the acicular monoclinic structure found in the 0% electrolyte to having a cubic structure with a mixture of large crystals (~1150 nm) with smaller crystals (~430 nm) filling the pores

such that the substrate was no longer visible. The OCP and Pourbaix diagram analysis suggests that at this pH the spontaneous formation of cuprite would be expected. Similar observations were made in Chan et al. (1999), in which cuprite was found to form in thicker layers in alkaline electrolytes when compared to neutral and acidic electrolytes, hindering the migration of chloride ions through the oxide. Furthermore Feng et al. (1997) observed that the patina formed under alkaline conditions was more protective with the corrosion rate of the substrate increasing as pH decreased from pH 10 to pH 3. The patina found on the copper coupons when exposed to the 3.5% electrolyte (Figure 52) had a similar cubic morphology to that of the 1% electrolytes with, however, a reduction in porosity at pH 4 and 7.

Semi-quantitative EDX analysis (Figures 51 and 53) of the patina layers formed in the 1% and 3.5% NaCl electrolytes found that as the pH was increased from 4 to 10 the oxygen concentration also increased, indicating an increase in density or thickness of the patina layer. This confirmed the SEM observations made on the surface of the coupons.

The oxygen concentration for the 1% and 3.5% NaCl electrolytes were similar at comparable pH values, indicating that while the chloride ions can promote the patination of copper it has a smaller effect as the pH becomes more alkaline (Antonijevic et al., 2009; Arjmand & Adriaens, 2012). Furthermore, Milić & Antonijević (2009) showed that the chloride ion concentration does not affect the formation of oxidation products except for concentrations of $0.001 \ M.dm^{-3}$ in sodium tetraborate. Faita et al. (1975) also observed that the OCP became less electronegative in

increasingly alkaline solutions, indicating an improvement in protective ability of the passive film.

Finally, no chlorine was detected on the bulk surface of the copper coupons exposed to any of the electrolytes. It is known that in chloride rich solutions cuprite is favoured as the initial patina product in the initial stages, especially in alkaline electrolytes (Antonijevic et al., 2009). However, after a relatively long incubation period copper chloride phases can form following fast passivation, pre-activation, and breakdown stages (Starosvetsky et al., 2006), which from the current analysis would suggest that this is greater than 24-hours.
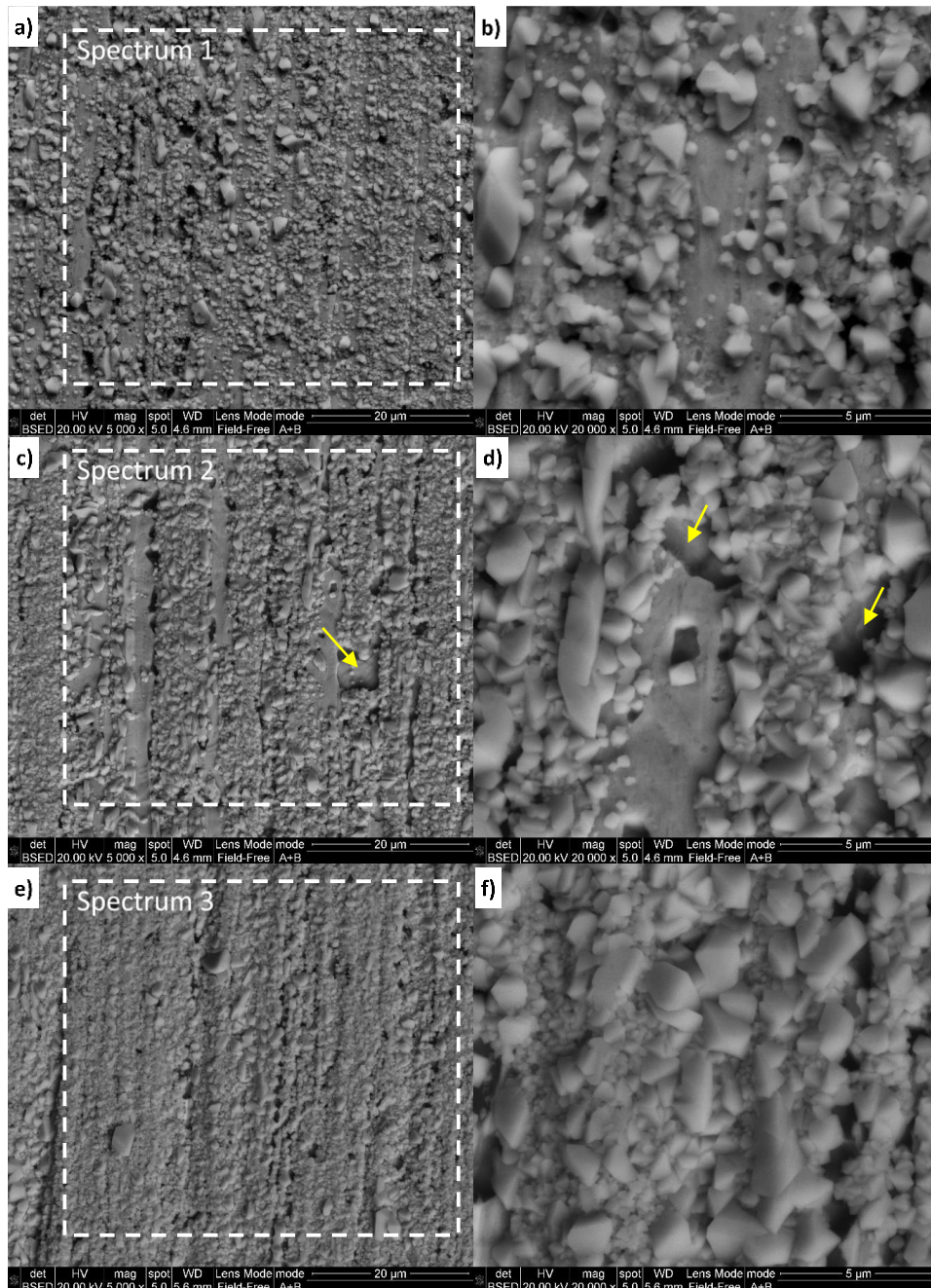
Figure 50 – Example low and high magnification BSE micrographs of the copper coupon surfaces after they had been exposed for 24 hours to the pH 4 (a and b), 7 (c and d) and 10 (e and f) 1% NaCl electrolytes at 45℃, respectively. The white dashed boxes indicate the locations for EDX analysis. The yellow arrows indicate the location of crystallographic etch pits.
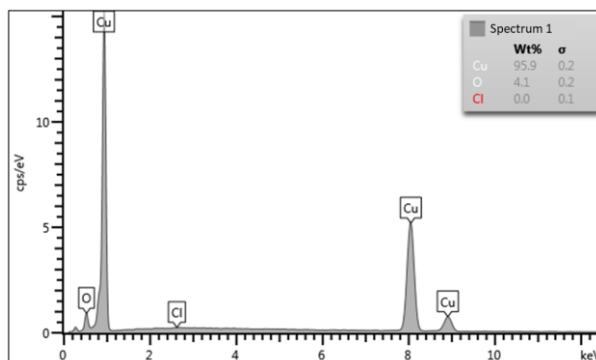
	Cu (wt%)	O (wt%)	Cl (wt%)
Spectrum 1	95.9	4.1	0.0
Spectrum 2	94.40	5.5	0.1
Spectrum 3	92.1	7.8	0.1

Figure 51 – Example EDX spectrum and semi-quantitative EDX analysis of the areas highlighted in Figure 50

[154]
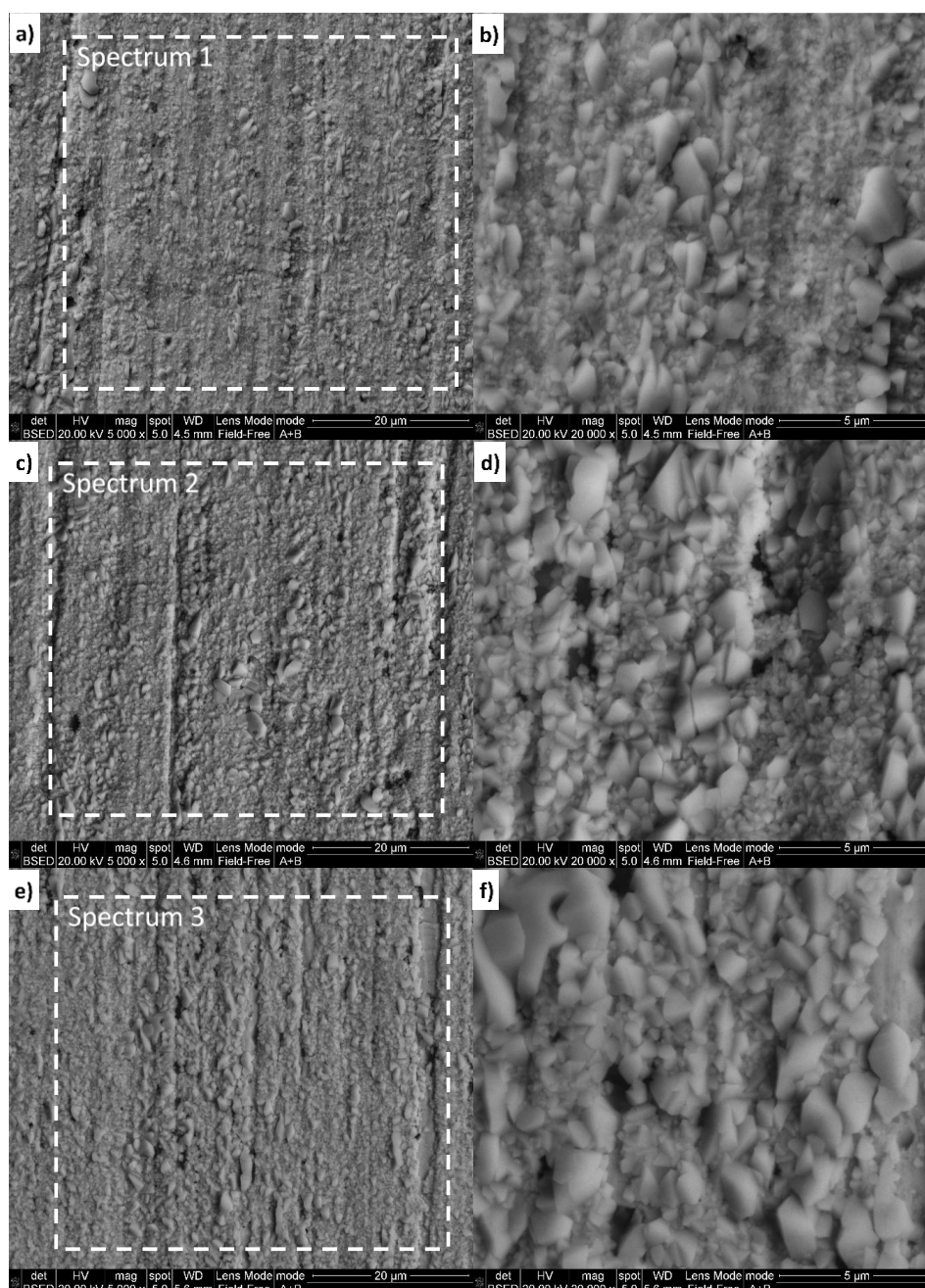
Figure 52 – Example low and high magnification BSE micrographs of the copper coupon surfaces after they had been exposed to the pH 4 (a and b), 7 (c and d) and 10 (e and f) 3.5% NaCl electrolytes at 45 ℃ after 24 hours, respectively. The white dashed boxes indicate the locations for EDX analysis.

Spectrum	Element (wt%)		
	Cu	O	Cl
1	95.5	4.4	0.1
2	94	5.8	0.2
3	92.7	7.2	0.1
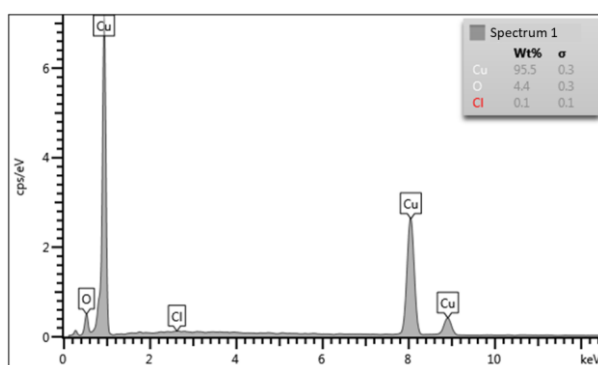
Figure 53 – Example EDX spectrum and semi-quantitative EDX analysis of the areas highlighted in Figure 52

[155]

The crystalline structure found in the other electrolytes was not visible on the coupons exposed to the 10 and 30% electrolytes at 45°C for 24 hours (Figures 54 and 56). This indicates that a copper oxide patina layer had not formed, which would change the colour of the coupon to that observed in the 0-3.5% NaCl electrolytes (Figure 45). The stability of patina was shown to decrease with increasing chloride concentrations, reducing the passivity of the copper (Millet et al., 1995) where the patina film dissolves as fast as it forms (Hoar et al., 1965). This allows the coupon to maintain the unoxidised copper colour. Furthermore, the surfaces appear to have undergone general dissolution with the growth and coalescence of micro-pits at each pH value. This general dissolution mechanism would be expected when compared to the results gathered from the Pourbaix diagrams where $CuCl_2^-$ is thermodynamically stable at the measured OCP in the electrolytes. The pits tended to be wide and shallow with a smooth texture at the bottom suggesting that the surface of the coupon had been etched around the copper grains, otherwise known as crystallographic etch pits.

Crystallographic etch pits occur on metal surface undergoing uneven active dissolution (Galvele, 1978; Örnek, 2019) which was dependent on the environmental conditions the metal is exposed to, and the crystallographic orientation of the grains in its microstructure. Mayanna & Setty (1974) measured that the corrosion potentials relative to the crystallographic orientation, which had the following trend of $(111) \rightarrow (100) \rightarrow (110)$ from most to least noble in chloride ion concentrations of $< 7.5 \times 10^{-3}\ M$. In a chloride ion concentration of $10^{-2}\ M$ the order changed to $(110) \rightarrow (100) \rightarrow (111)$. Whereas in ethylenediamine the (100) orientation was

most stable followed by (110) and (111) (Jenkins, 1960). In further work by Martinez-Lombardia et al. (2014) the highest dissolution rate was observed on the (111) orientated grain especially when they appear together with smaller (001) grains. While copper with the (111) orientation in water had the most noble potential (Kruger, 1959), which was thought to be due to this orientation having the highest work function, releasing electrons more easily.

Copper is a polycrystalline material which has a mixture of grains with a random crystallographic orientation within the microstructure (Suwas & Gurao, 2014). As discussed, the various crystallographic orientations have different dissolution characteristics which can result in the formation of an inconsistent corrosion propagation into the metal. Once the corrosion front has travelled through the fast-dissolving grains and reached the grain boundary of a different crystallographic orientation it may continue parallel to it, resulting in the formation of an intergranular morphology (Laferrere et al., 2013; Zhang, X. et al., 2017).

When examining the surface of the copper coupons it was found that as the pH was increased to more alkaline values, with the surface tending to favour passivation, the effect of the chloride ions on corrosion was reduced, especially in the 10% NaCl electrolyte, with the severity of the pitting being greatest at pH 4. Similar observations were made by Antonijevic et al. (2009) and Modestov et al. (1995). However, it should also be noted that the presence of chloride ions can be detrimental to the formation of a passive film at acidic pH values. This implies that to enable an increase in the patination rate of copper containing antifouling coating that the electrolyte should have a neutral to acidic pH.

At pH 4 the pits appear to be deeper and wider when compared to the surface exposed to the pH 7 and 10 electrolytes, with the surface between the pits being predominantly unaffected by corrosion. Sieradzke & Kim (1992) observed that the depth and degree of coalescence of the crystallographic etch pits are indicative of the overall corrosion rate of the surface. Furthermore, the local reduction in the pH and enrichment of chloride ions at the corrosion front, due to the rapid hydrolysis of copper, is likely to provide favourable conditions for dissolution to occur especially in acidic electrolytes (Zhang et al., 2017). However, the surface of the copper coupon at pH 7 in the 30% NaCl electrolyte was found to be covered with a mixture of sub-micron pits with fewer larger pits, suggesting the coupon surface was being more aggressively dissolved when compared to the other electrolytes.

The semi-quantitative EDX analysis of the coupons exposed to the pH 4 electrolytes determined that the copper coupon oxygen concentration increased to similar levels to that found on the as-received coupon. When combined with the surface morphology this suggests that the copper surface is undergoing dissolution rather than oxidation reactions (Figure 54a, Spectrum 1). Unlike at acidic pH values where the oxide layer is weakly soluble, in neutral and alkaline electrolytes the oxide layer was able to grow resulting in an oxygen concentration of between 3 and 5 wt%. In some localised areas on the coupons exposed to the 10% NaCl pH 7 (highlighted in Figure 54 Spectrum 3) and the 30% NaCl at pH 7 and 10 (highlighted in Figure 56 Spectrum 3 and 5, respectively) electrolytes there are areas that were rich in copper, oxygen and chlorine, suggesting a copper chloride compound may have formed.
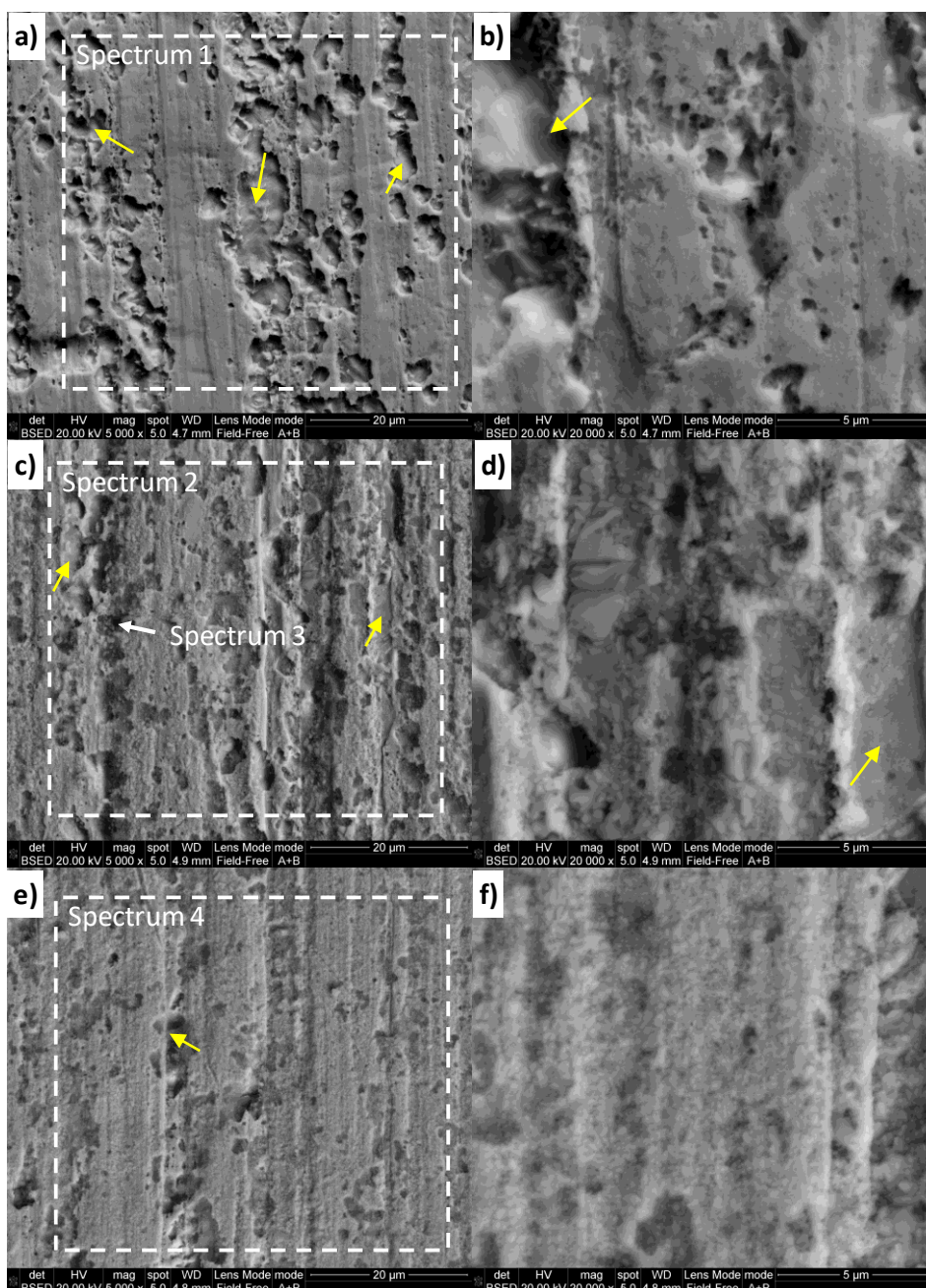
Figure 54 – Example low and high magnification BSE micrographs of the copper coupon surfaces after they had been exposed to the pH 4 (a and b), 7 (c and d) and 10 (e and f) 10% NaCl electrolytes at 45 ℃ after 24 hours, respectively. The white dashed boxes indicate the locations for EDX analysis. The yellow arrow indicates example positions of the crystallographic etch pits.

Spectrum	Element (wt%)		
	Cu	O	Cl
1	99.3	0.6	0.1
2	96.7	3.1	0.2
3	83.7	12.2	4.1
4	96.0	3.7	0.2
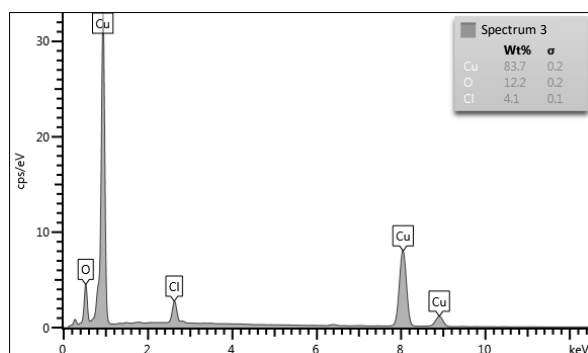
Figure 55 – Example EDX spectrum and semi-quantitative EDX analysis of the areas highlighted in Figure 54

[159]
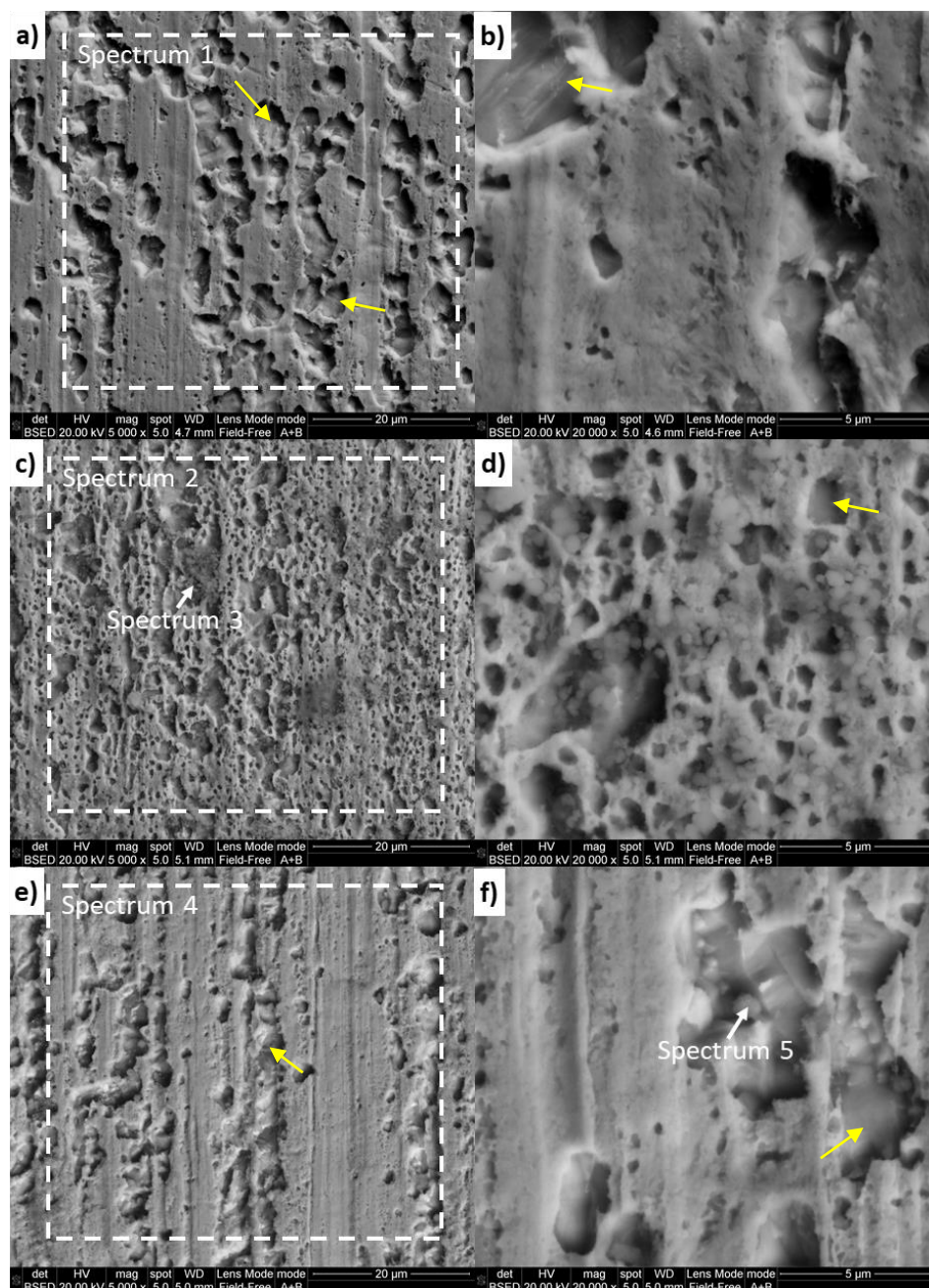
Figure 56 – Example low and high magnification BSE micrographs of the copper coupon surfaces after they had been exposed to the pH 4 (a and b), 7 (c and d) and 10 (e and f) 30% NaCl electrolytes at 45 ℃ after 24 hours, respectively. The white dashed boxes indicate the locations for EDX analysis. The yellow arrows indicate example positions of crystallographic etch pits.

Spectrum	Element (wt%)		
	Cu	**O**	**Cl**
1	99.0	0.9	0.1
2	94.7	4.6	0.7
3	88.0	9.2	2.8
4	96.6	3.0	0.4
5	87.6	8.4	4.1
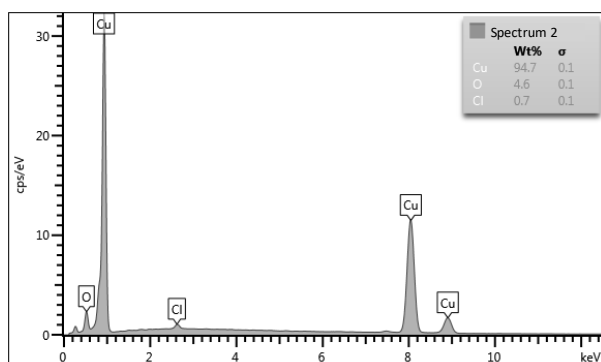
Figure 57 – Example EDX spectrum and semi-quantitative EDX analysis of the areas highlighted in Figure 54

[160]

5.4.2.5   Other Features

Further analysis of the surface of the copper coupons found 'islands' which were rich in copper, chlorine and oxygen in the pH 4 3.5% and 30% NaCl (Figures 59 to 61) and pH 7 10% NaCl (Figure 58) electrolytes. The presence of these elements suggests the formation of a copper chloride compound such as Nantokite ($CuCl$). These islands tend to nucleate at weak points in the oxide film (Modestov et al., 1995) where the cupric ions form more easily, reacting with the chloride ions in the electrolyte allowing the precipitation of $CuCl$ to occur at these sites (Starosvetsky et al., 2006).

The copper substrate beneath and extending a short distance away from the islands appears smooth and unaffected by the formation of patina or general dissolution, suggesting that the islands had become cathodic. Further examination of the surface indicates that the islands experience sacrificial cathodic protection where the anodic region encircling the island corrodes preferentially, resulting in a 'halo' of deeper and/or wider pits. As the anodic sites corrode, they provide excess electrons to the cathodic region protecting it from corrosion, similar to the sacrificial anodic protection used to protect ships hulls from corrosion (Anish, 2020). The galvanic throwing power of the anodic region is limited as they may have similar electrochemical properties (Presuel-Moreno et al., 2008), resulting in relatively small areas being protected.

Examination of the islands at high magnification (Figure 60) found that they contained equiaxed cubic crystals with a diameter of approximately 561.3 ± 130.1 nm. These crystals were rich in copper, oxygen and chlorine as indicated by the EDX maps shown in Figures 59 and 61, and the semi-quantitative EDX analysis shown in Figures 58 and 60. These crystals are typical of what might be expected from nantokite ($CuCl$) which

has a cubic crystal structure (Graedel et al., 1987) and is also thought to be an intermediate copper chloride phase which forms prior to more complex copper chloride compounds (Cooper & Bartlett, 1958; Josefowicz et al., 1993), especially in high chloride ion concentration solutions (El Warraky et al., 2004). The formation of this chloride phase occurs as the chloride ions are adsorbed on to the surface and react with the copper (Cooper & Bartlett, 1958) which leads to a mass transfer limited reaction.
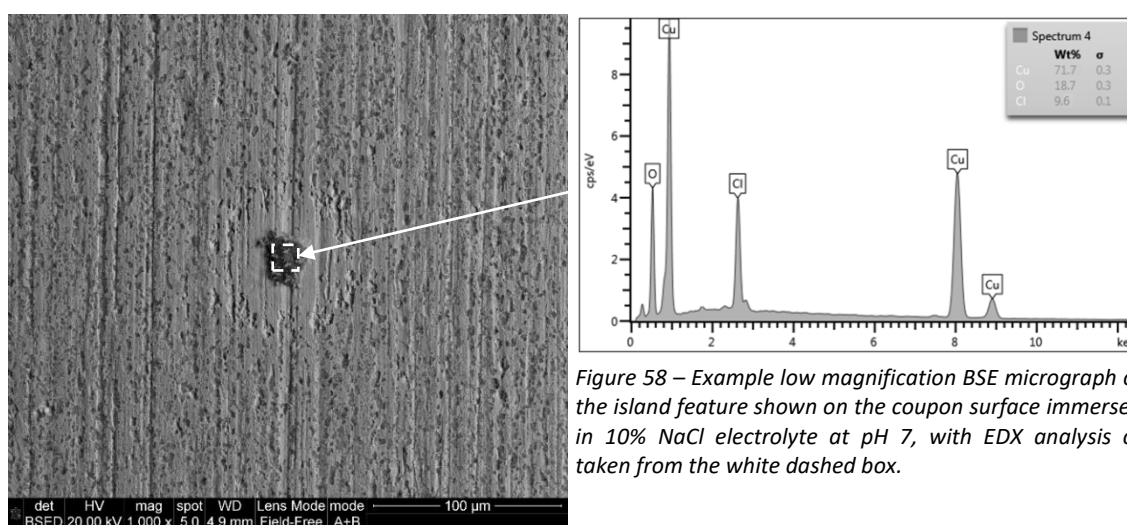
Figure 58 – Example low magnification BSE micrograph of the island feature shown on the coupon surface immersed in 10% NaCl electrolyte at pH 7, with EDX analysis of taken from the white dashed box.
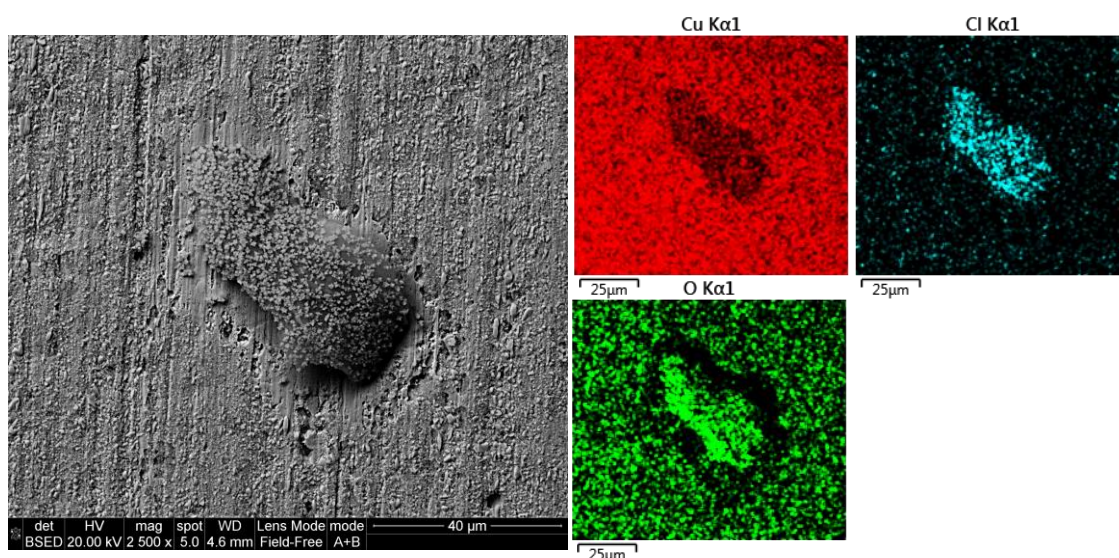
Figure 59 – BSE micrograph and EDX mapping of the island feature found on the surface of the copper coupon immersed in the pH 4 3.5% NaCl electrolyte at 45°C for 24 hours.

[162]

Spectrum	Element (wt%)		
	Cu	O	Cl
1	60.9	28.6	10.5
2	64.0	27.0	9.0
3	92.5	3.5	4.0
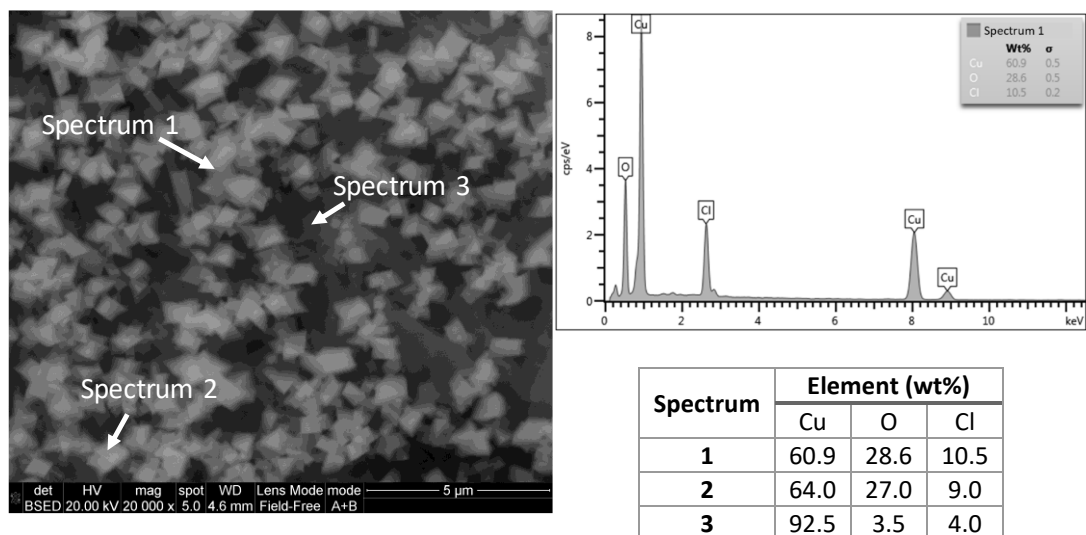
Figure 60 – High magnification BSE micrograph of the island feature shown in Figure 59 with an example EDX spectra and semi-quantitative analysis of the areas indicated by the white arrows.
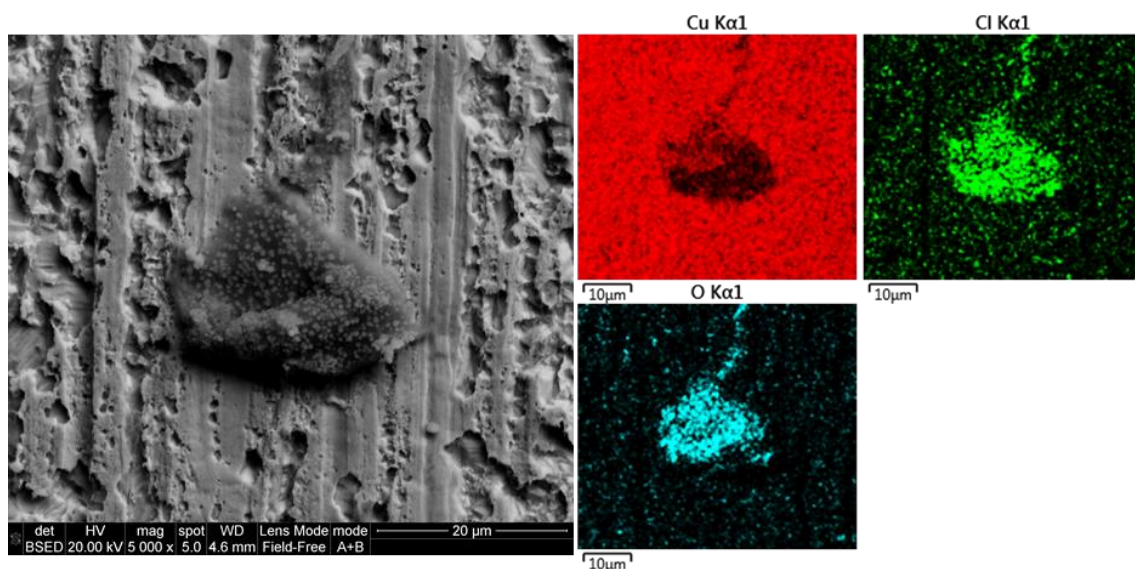
Figure 61 – BSE micrograph and EDX mapping of the island feature found on the surface of the copper coupon immersed in the pH 4 30% NaCl electrolyte at 45°C for 24 hours.

5.4.3 Patina Analysis

5.4.3.1 Patina Particle Size Analysis

The high magnification BSE micrographs were used to measure the size of the cubic crystals that had formed on the coupon surface following the 24-hour exposure to the different electrolytes, with the average size being plotted and shown in Figure 62. It was found that with increasing alkalinity and sodium chloride concentrations resulted in an increase in the diameter of the crystals. Feng et al. (1997) also observed that the nucleation and growth of cuprite crystals was favoured in alkaline environments, which was proportional to the supersaturation of soluble copper species near the copper surface. Furthermore, the solubility of the patina crystals is increased in acidic environments (Graedel et al., 1987) which may also lead to smaller crystals being observed in acidic compared to alkaline environments.

	0%	1%	3.5%	10%	30%
pH 4	427.5	657.4	810.7	0	0
pH 7	468.8	912.3	1100.7	0	0
pH 10	776.7	1168.3	1283.0	0	0
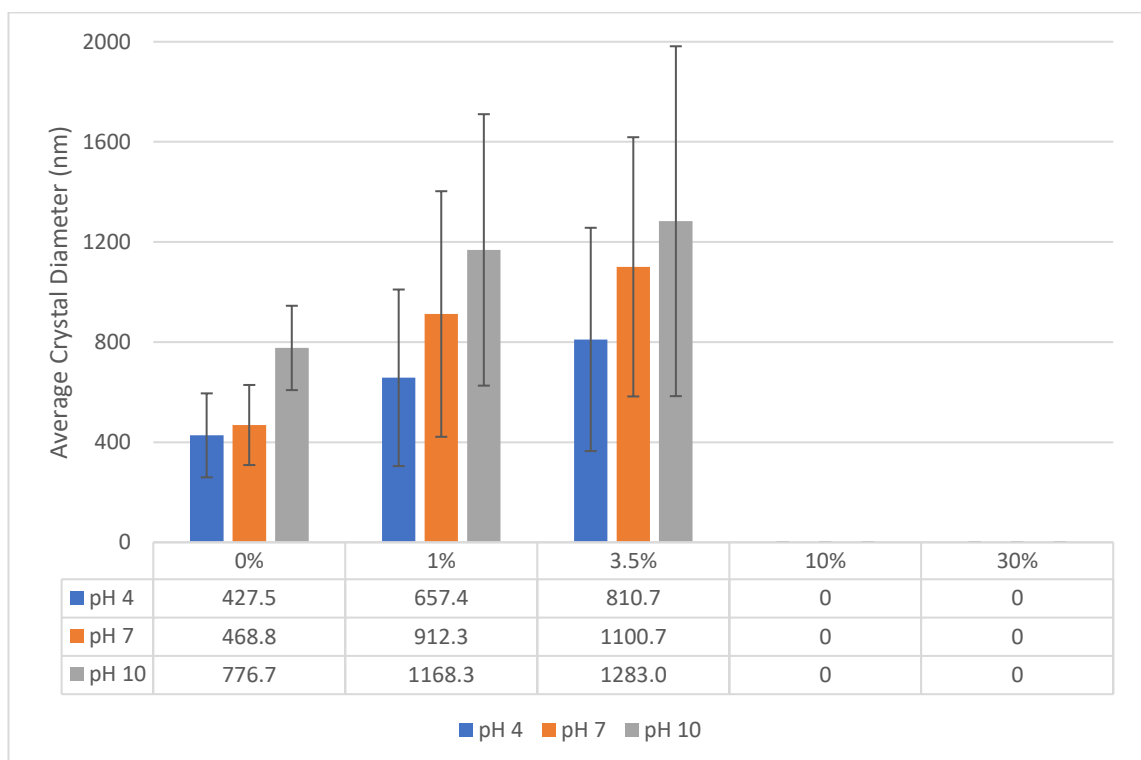
Figure 62 – The average diameter of the crystal observed on the surface of the copper coupon after immersion in the different electrolytes at 45°C for 24 hours. Error bars are the standard deviation of 150 crystals measured on the coupon surface.

[164]

Another factor which may increase the availability of copper ions in solution is related to the chloride concentration where the OCP became more electronegative, increasing the electrode activity at higher chloride concentrations. This releases more soluble copper species into the electrolyte, which surrounded the copper surface. These ions can then nucleate, react, and be incorporated into copper patina producing larger crystals. The increase in patina crystals was only observed in the electrolytes up to 3.5% NaCl at 10% and 30% no measurable patina crystals were found as the surface underwent general dissolution. However, it is possible that the $CuCl_2^-$ ions released into the electrolyte could precipitate out as other copper complexes in solution. Further analysis of Figure 62 found a relatively high standard deviation which increased with chloride concentration indicating the heterogeneous nature of the crystal sizes after short exposure times where patina nucleation and growth increased with chloride concentrations up to 3.5%.

5.4.3.2 Glancing Angle XRD Of The Patina Formed On The Copper Coupons

Glancing angle XRD, optimised at 5°, was used to ensure that the signal from the thin patina layer, formed on the coupon, was high enough to be analysed above the background radiation and limit the signal from the copper coupon. An example of the collected XRD data is shown in Figure 63.
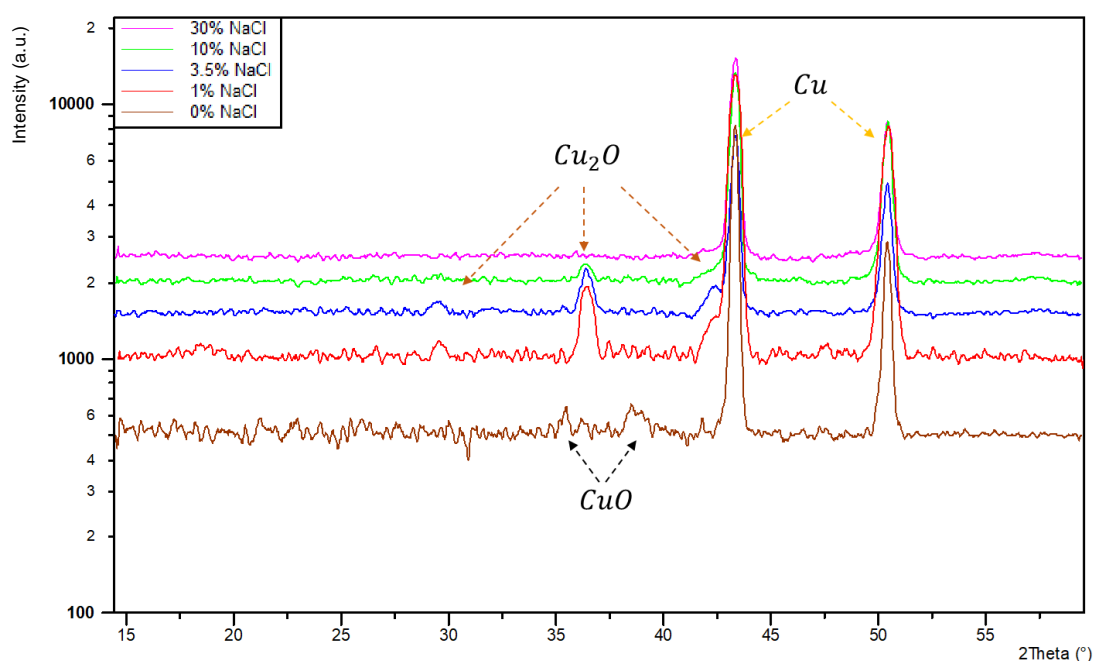
Figure 63 – Example glancing angle XRD traces comparing the phases present on the copper coupons surface after exposure for 24 hours at 45°C in the various sodium chloride concentration electrolytes modified to pH 10. The traces are post processing, offset by 500 counts, and stacked on top of each other for comparison of the phases present.

Figure 64 shows the semi-quantitative analysis of the concentration of copper patina detected on the surface of the coupons that have been exposed in the various electrolytes and temperatures selected for the testing. The XRD analysis confirmed what was postulated following the visual assessment and SEM analysis, where the main patina phase that had formed on the discoloured copper coupons was cuprite. While the OCP and Pourbaix diagram analysis suggests that $CuCl_2^-$ species should be present they can form cuprite following Equations 13 and 35. Antonijevic et al., (2009) also detected cuprite during the initial immersion of copper in sodium chloride.

[166]

$$2CuCl + H_2O = Cu_2O + 2H^+ + 2Cl^-$$ <div style="text-align: right">*Equation 35*</div>
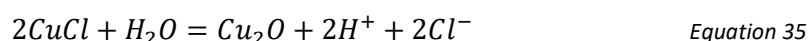
Tenorite was also determined to be the main phase on the coupons exposed to the 0% electrolyte at pH 10 at 35°C and 45°C (Figures 63 and 64, pH 10). This confirmed the OCP measurements of the electrode at 35°C and 45°C which were within the tenorite equilibrium domain, while the SEM and EDX of the coupon at 45°C analyses found particles consistent with tenorite. However, the OCP and Pourbaix diagram also suggests that tenorite should form at 55°C yet it was not detected via XRD. It has been shown that the solubility of tenorite increases with temperature in alkaline environments (Navarro et al., 2014) which may result in the layer being less stable, leaving the coupon with an unoxidised appearance.

While islands rich in copper and chlorine were observed on surface of the coupons exposed in the 10% and 30% NaCl electrolytes following the SEM analysis (Figures 58 – 61), they were not detected in the XRD analysis. It is probable that this was due to the relatively small size and fine distribution of these features producing a low peak intensity, which was lost in the background radiation.

The patina formation at each pH value followed similar trends; when the temperature of the electrolyte was increased from 25 to 55°C the percentage of copper patina detected also increased, tending to reach a maximum at 55°C. The pH also affected the amount of cuprite that was detected which had the following trend pH 4 < pH 7 < pH 10. Cuprite has been shown to be slightly soluble in acidic environments which may lead to the lower concentrations being observed at pH 4 when compared to the alkaline environments, where the presence of high concentrations of OH^- ions can promote cuprite formation.

A similar trend was noted when analysing the XRD data of the copper coupon at the different temperatures where, as the chloride concentration was increased from 0% to 30%, the amount of patina that was detected tended to decrease. This was shown in the 30% electrolyte where no patina was detected at any temperature or pH value while cuprite was only detected in the pH 4 and 10 electrolytes containing 10% NaCl, at elevated temperatures. As the chloride concentration was increased El Warraky et al. (2004) observed a competition between the hydrolysis of the $CuCl$ phase to produce a compact and less soluble Cu_2O (Equation 35) and its dissolution through the formation of $CuCl_2^-$ (Equation 13). This suggests that the dissolution of the Cu_2O layer exceeds the rate of formation under short (24-hours) immersion periods at high chloride concentrations.

Despite high chloride concentrations and acidic conditions tending to result in low concentrations of cuprite, the highest levels were detected in the 3.5% NaCl and pH 4 electrolyte at 55°C. At this temperature, under these conditions, high concentrations of copper ions would be available at the coupon surface allowing cuprite crystals to nucleate and grow at a faster rate than they dissolve.
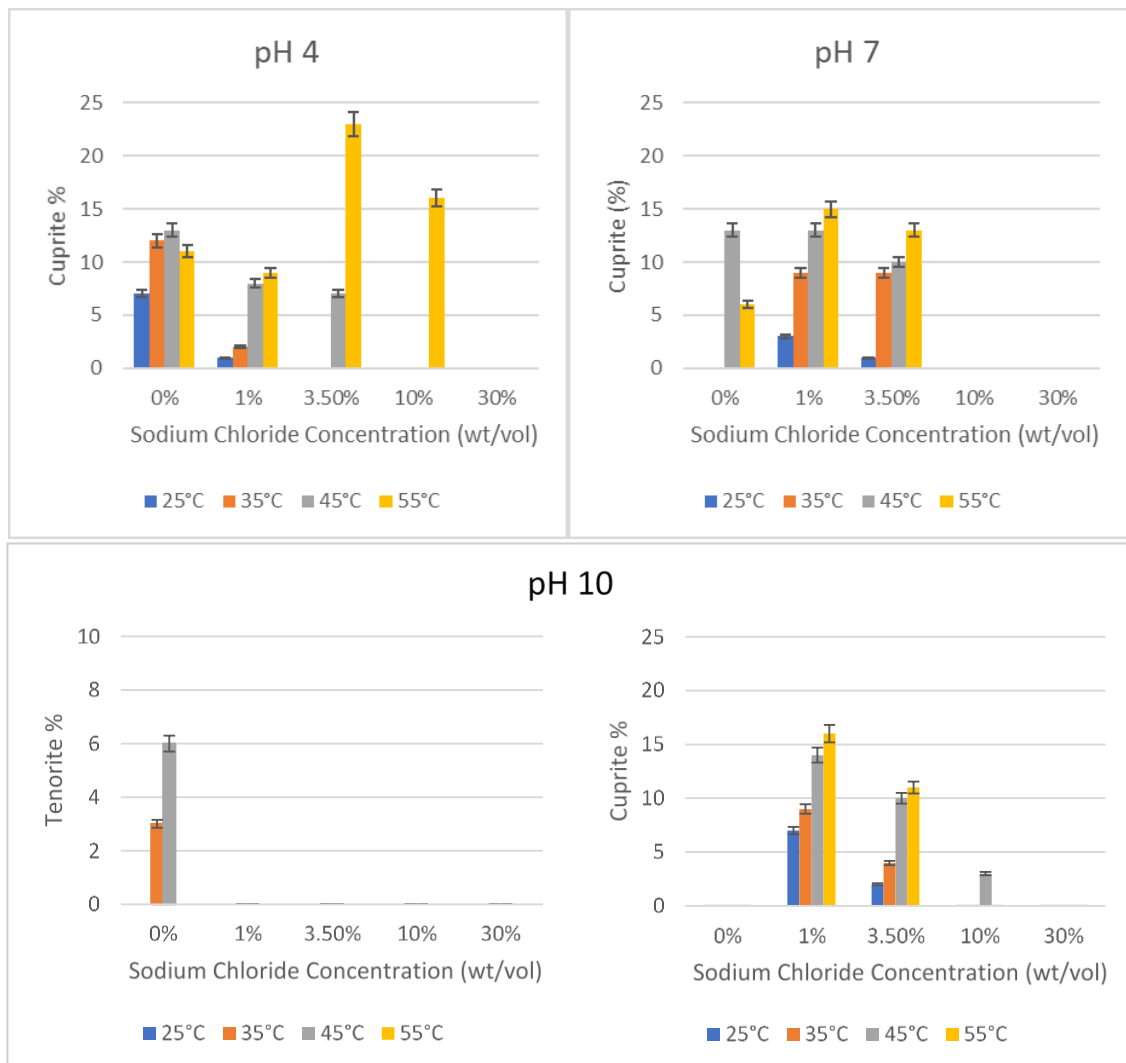
Figure 64 – Charts showing the semi-quantitative analysis XRD analysis of the phases present on the copper coupons after 24 hours exposure in the various electrolytes, with a 95% confidence interval.

5.4.3.3 Patina Thickness

Using the HighScore Plus software Mass Absorption Calculator (MAC) the depth of X-ray penetration can be estimated. With a 5° incident beam it was estimated that the maximum X-ray penetration depth was up to 4.271 μm in copper, 6.883 μm in cuprite and 7.003 μm in tenorite, assuming a packing factor of 1 i.e., a fully dense material.

Using the semi-quantitative XRD analysis of the phases present and a packing factor of 1 a combined mass absorption coefficient and density can be used to estimate the maximum X-ray penetration, which was found to be larger than that of pure copper. Therefore, it was assumed that anything larger than the penetration in copper was a contribution from the patina layer (Figure 65). However, this technique does not consider the porosity of the patina layer where a thick, porous layer may have the same adsorption characteristics as a thin dense layer and therefore errors can arise. For example, a packing factor of 1 with a 7% cuprite layer gives a penetration depth of 4.395 μm and a cuprite thickness of 0.124 μm, reducing the packing factor of cuprite to 0.75 produces a combined packing factor of 0.983, resulting in a penetration of 4.531 μm and an estimated cuprite layer thickness of 0.260 μm. Furthermore, this technique can only take an average measurement of the thickness across the surface being analysed and does not consider thickness variations such as those observed in the SEM where the substrate could be seen and therefore the patina was not present. The growth of the crystals also was likely to result in varied thickness where it can be assumed that the larger crystals visible on the surface would be thicker than the smaller crystals.
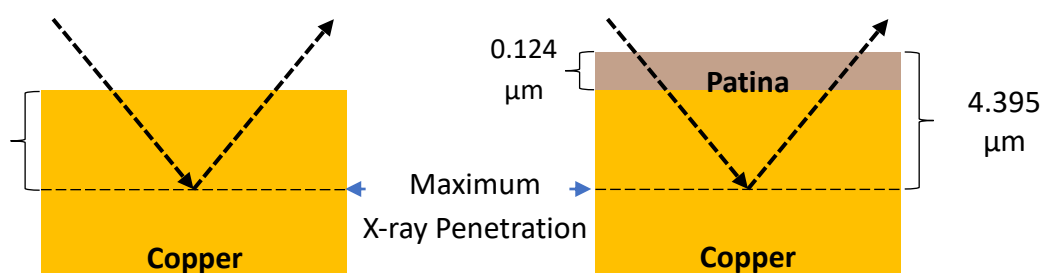
Figure 65 – Schematic of the showing the theoretical X-ray penetration as calculated using MAC in pure copper (left) and the calculated X-ray penetration in copper with a 7% patina layer, determined from the semi-quantitative XRD analysis (right).

The thickness of the patina followed similar trends to those observed in the semi-quantitative EDX analysis where the increase in temperature and increasing alkalinity of the electrolytes generally resulted in formation of a "thicker" patina (Figure 66). However, Feng et al. (1997) observed an opposite trend after 24 hours in simulated tap water where, after measuring the patina more accurately using weight loss and coulometry cathodic reduction methods, the thickest and most porous patina was found at pH 4 while the thinnest and most dense patina formed at pH 10.

When comparing the calculated thickness of the patina layers at equivalent temperatures in the different electrolytes it was found that there was a general trend towards a reduction in thickness with increased chloride concentrations. This is contrary to the measurement of the crystal size which were shown to generally increase with chloride concentrations. The averaging of the thickness measurement using this method and the relatively few crystal diameters measured using the SEM may have led to this mismatch in the analysis. Further analysis of the patina film would be required to verify its thickness using other quantifiable methods such as Focus Ion Beam Scanning Electron Microscopy where a physical measurement of the film can be made following milling operations.

[171]

The maximum patina thickness in the 0% electrolyte at each pH value was found at 45°C where the cuprite formed in the pH 4 and 7 electrolytes had an equivalent thickness of 231 nm, which is in the same order of magnitude to that reported by Feng et al. (1997) of 350-450 nm at pH 4 and approximately 250 nm at pH 7. Tenorite was detected in the pH 10 electrolyte and while it was present in relatively low concentrations when compared to the cuprite in the other solutions the maximum thickness was calculated to be higher at 316 nm, owning to the lower density of tenorite when compared to cuprite.

Temperature was also shown to influence the thickness of the patina that had developed where in the 1% and 3.5% the thinnest patina was detected at 25°C. As the temperature was increased the thickness also continued to increase reaching a maximum at 55°C, irrespective of pH (Figure 66). This suggests that elevated temperatures should be used to form a thick patina at an accelerated rate.
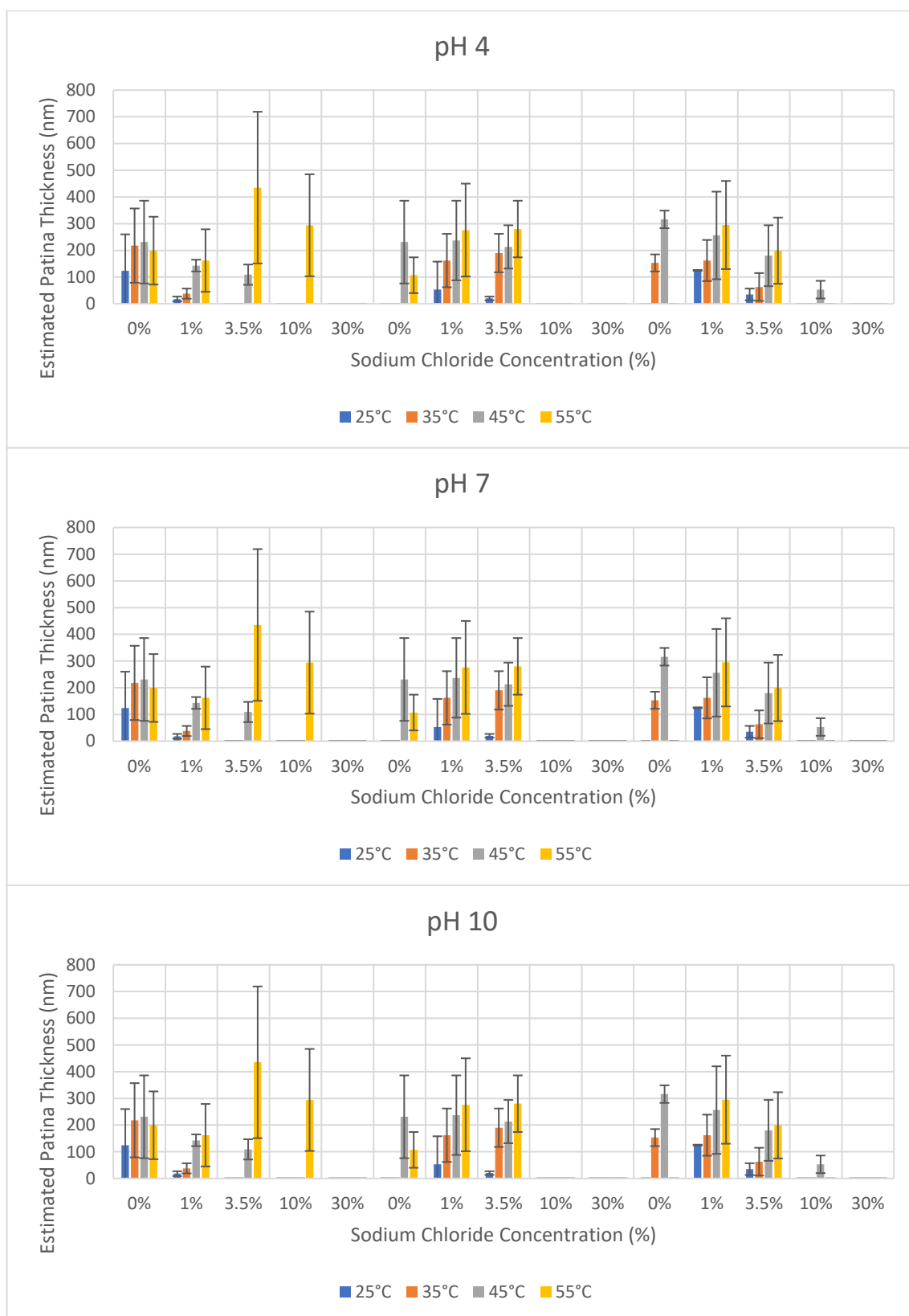
Figure 66 – Estimated patina thickness calculated from the semi-quantitative XRD analysis after the 24 hours exposure in the various electrolytes, with error bars based on the thickness calculated with a cuprite/tenorite packing factor of 0.75.

5.5   Summary

5.5.1   Pourbaix Diagram Analysis

Cu-Cl-H$_2$O Pourbaix diagrams were produced to examine the effect of temperature and chloride concentrations had on the species that were thermodynamically stable under equilibrium conditions. Initial observations found that the immunity equilibrium potential became more electronegative as both were increased, with the chloride levels having the largest influence. The $Cu(OH)_4^{2-}$ domain, present in each diagram, was found to be independent of chloride with the vertical equilibrium pH line only shifting to more alkaline values as the temperature was increased. Furthermore, the Cu_2O domain in each system remained relatively unaffected by the temperature with the vertical pH equilibrium lines shifting to more alkaline values with increasing chloride concentrations.

When chloride was in the system additional stability domains of $CuCl_2^-$ and $Cu_2Cl(OH)_3$, and $CuCl^+$ at concentrations above 1% and 3.5%, respectively, were present. The size, and therefore the stability, of the $CuCl_2^-$ and $Cu_2Cl(OH)_3$ domains increased with chloride concentration. When raising the temperature, the size of the $CuCl_2^-$ domain also increased, however the $Cu_2Cl(OH)_3$ domain reduced in size, while the $CuCl^+$ remained unaffected by both variables.

5.5.2   OCP Analysis

The OCP of copper in the different electrolytes and environmental conditions was generally found to stabilise within the first 1800 seconds following the initial exposure. For the electrolytes containing NaCl the potentials stabilised at more electronegative values than the first readings, suggesting the removal of a natural air-formed oxide

[174]

film. With an increase in electrolyte temperature the OCP curves were found to have fewer potential transients suggesting a reduction in the formation and breakdown of a protective passive film, with the surface of the electrode being more uniformly affected. Whereas in the solutions containing 0% NaCl the potentials tended to stabilise after longer immersion periods of between 1-5 hours at more electropositive values that that recorded following the initial immersion. This may indicate the slow formation of a protective oxide film on the electrode surface.

5.5.3 Relationship Between Pourbaix And OCP

Using the Pourbaix diagrams it was possible to estimate the species that were thermodynamically stable at the OCP of the copper electrodes in the different environments, i.e., $0 - 30\%$ NaCl, pH 4, 7 and 10 and $25 - 55°C$. In the 0% electrolytes Cu^{2+} (at pH 4 $25 - 55°C$), Cu_2O (pH 7 at 25°C) and CuO (pH 7 at $35 - 55$ and pH 10 $25 - 55°C$) species are expected to form at the recorded OCP. In the chloride containing electrolytes similar trends were also observed with $CuCl_2^-$ species expected to form at the OCP of copper exposed to the 1% and 3.5% at pH 4 and 7 and $25 - 55°C$, and 10 and 30% at each variable. In the 1% and 3.5% electrolytes at pH 10 Cu_2O is expected at the OCP.

5.5.4 Surface Analysis

Visual inspection of the copper coupons found that their colour changed from the pink of the oxide stripped sample to a darker brown colour. The brown colouration was found to increase and darken with increasing temperature and chloride concentration up to 3.5%, suggesting that these variables accelerate the patination rate of copper. In the 10% and 30% electrolytes the coupons remained relatively unaffected by

[175]

patination which may be due to the general dissolution of the coupon surface preventing patina deposition and formation of $CuCl_2^-$.

SEM, EDX and XRD analysis of the coupons exposed to the 45°C 0% electrolyte at pH 4 and 7 found that cubic cuprite crystals had formed with a diameter of approximately 427.5 nm and 468.8 nm, respectively, and a ~231 nm thick layer. The accuracy of the method used to determine the thickness of the patina layer was limited as it assumed that the patina was fully dense and that it is uniformly distributed across the surface of the coupon and therefore taking an average measurement. The XRD measurement does not consider variations in the thickness due to different sized patina crystals or porosity within the patina, resulting in the large error bars shown in Figure 66.

In the pH 10 electrolyte acicular monoclinic tenorite crystals were observed, which were approximately 776.7 nm long forming a ~316 nm thick layer. Cuprite was also detected in the 1% and 3.5% electrolytes at each pH with the size of the cubic crystals and thickness of patina layer increasing with temperature and alkalinity. This indicates that cuprite is the initial patina layer that forms in chloride rich electrolytes, requiring extended immersion periods, beyond 24 hours, to form more complex copper chloride patinas. While increasing the chloride concentration tends to reduce the size of the cuprite crystals and thickness of the layer where, in the 10% and 30% electrolytes, generally no patina was observed with the surface showing the expected general dissolution characteristics, with the formation of crystallographic etch pits.

Chapter 6: Patina Formation Under Accelerated Conditions

6.1   Introduction

The patination of antifouling coatings has been demonstrated in Chapter 4 with the formation of a green/blue copper compounds which was commonly identified as clinoatacamite. This patination tends to occur in natural seawater with a neutral pH and a 3.5% salinity, however, the coating patination rate can be variable with some taking days and other months or years to form. Therefore, an accelerated laboratory test was required to determine the susceptibility of the coatings to form a patina layer. To that end a series of electrochemical tests, including potentiodynamic and potentiostatic polarisation were performed using a 99.9% pure copper electrode as a substitute for the cuprite pigment in the antifouling coatings, to assess the different variables i.e., temperature, pH, and salt concentration. Tafel analysis of the potentiodynamic polarisation curves provides information on the corrosion and therefore patination properties of copper allowing the variables which may accelerate its formation to be identified. While using the Pourbaix diagram in combination with the potentiostatic polarisation the formation of specific patina compounds may be targeted and driven at a faster rate than those formed under equilibrium conditions.

6.1.1 Potentiodynamic Polarisation

6.1.1.1 *Effect Of Scan Rate On The Potentiodynamic Polarisation Curves Of Pure Copper*

In this study the potential scan rate was set at different rates to observe their effect on the polarisation of copper in an 3.5% NaCl electrolyte at 25°C with a pH of 7, allowing the optimum sweep rate to be determined where the important kinetic information can be collected and analysed. This scan rate would then be used to polarise the copper electrode in the different electrolyte variables i.e., pH 4, 7 and 10, 25°C, 35°C, 45°C and 55°C, and 0%, 1%, 3.5%, 10% and 30% NaCl.

A relatively rapid scan rate (i.e., $25\ mV.s^{-1}$) may be used if the anodic activity is expected to be high as this helps to minimise the film formation on the electrode surface and therefore the current density only relates to the electrode. However, a fast scan rate can distort the data as the pseudo steady state conditions are not maintained. By comparison a relatively slow scan rate (i.e., <2 $mV.s^{-1}$) can allow a time for a film to form and may also be used when the electrode is unlikely to be active in the electrolyte. The results from such an experiment are likely to represent the results gained from long term environmental exposure.

Figure 67 shows the potentiodynamic polarisation curves produced at 6 different scan rates where a high scan rate of $25\ mV.s^{-1}$ was initially set and was progressively reduced to $0.025\ mV.s^{-1}$ to observe the difference between the curves.
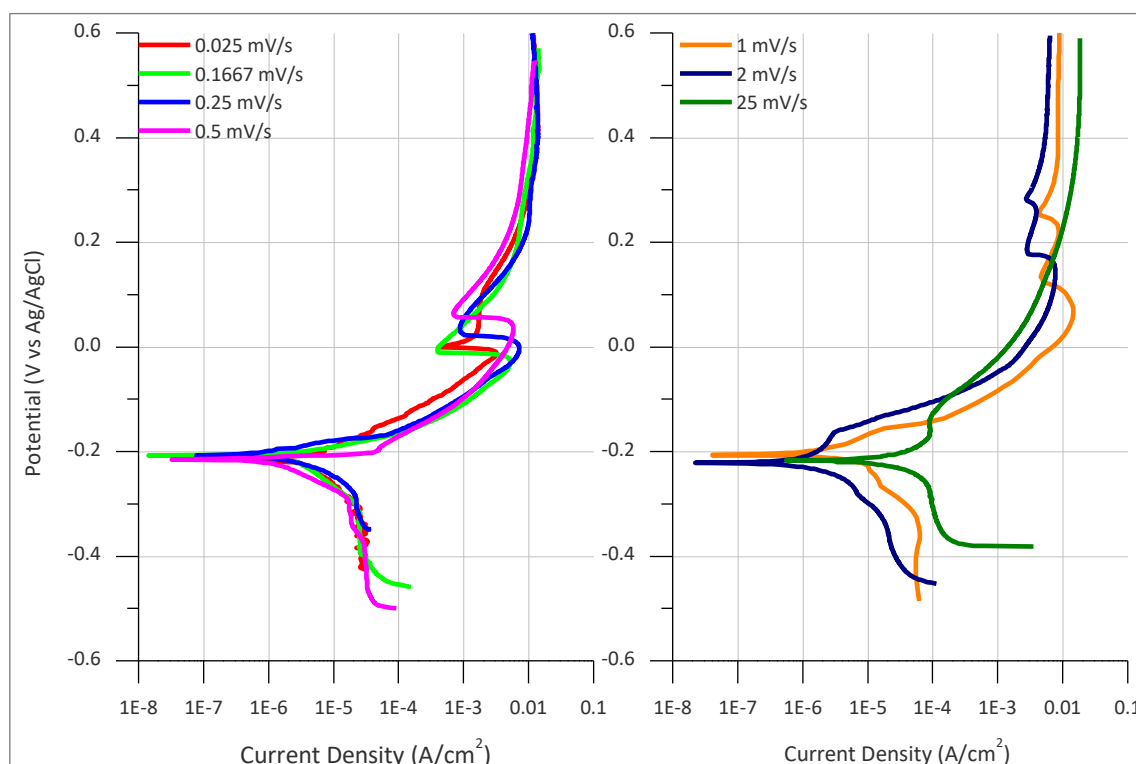
Figure 67 – Influence of the different scan rates on the potentiodynamic polarisation curves on a copper electrode immersed at 25°C in a naturally aerated 3.5% NaCl electrolyte at pH 7.

When comparing the curves produced at the different scan rates it was found that at rapid scan rates of $25\ mV.s^{-1}$ the current density was shifted towards higher values, which may be due to the reduction in the interfacial capacitance between the electrode surface and the electrolyte (Zhang et al., 2009) improving the current to flow and reducing the charging transfer resistance. The high scan rates also results in faster reaction kinetics where the diffusion layer is reduced (Amatore et al., 2003), allowing more ions in the electrolyte to reach the electrode surface at a faster rate. The electrode also did not passivate, resulting in a exponential increase in current density between -100 mV and 500 mV, after which the limiting current density of the potentiostatic system was reached.

Whereas at lower scan rates the current densities were in the same order of magnitude and the curves that were produced were similar. At low scan rates the

passivation of the copper was observed with the formation of secondary reductions in current density, measured in the anodic portion of the curve, indicating the psuedo-passivation of the electrode. At $2\ mV.s^{-1}$ and $1\ mV.s^{-1}$ two distinct peaks within the anodic portion were observed, however at $0.5\ mV.s^{-1}$ and $0.25\ mV.s^{-1}$ a single broad peak was found suggesting that the second peak was masked as the rate of chemical reaction of the surface approaches the rate of change in potential. The curve produced at the lowest scan rate of $0.025\ mV.s^{-1}$ was found to have spikes in the current density within the cathodic portion of the graph, indicating a variable oxygen reduction reaction rate, while in the anodic portion a single sharp reduction in current density was found as the electrode passivated followed by a broad peak and then an increase in current density as the passive film was broken down and the copper ions could be freely oxidised from the electrode surface.

It is generally thought that the slower the scan rate the more information that can be gathered from the curve, where it is recommended in ASTM G59 that a scan rate of $0.1667\ mV.s^{-1}$ is used (ASTM International, 2014). However, this can result in lengthy experiments and may lose information about rapid anodic activity. Therefore, a compromise between the speed of the experiment and the data that can be gleamed was required. It was determine that reducing the scan rate to below $2\ mV.s^{-1}$ resulted in the formation of similar shaped graphs showing the passivation potentials within the anodic portion of the curve. However the curves produced at 2 and $1\ mV.s^{-1}$ allowed additional information within the passivation part of the curve to be gathered. Therefore a scan rate of 1 mV was set for each of the

potentiodynamic polarisation measurements within the various electrolytes and exposure conditions.

6.1.1.2 *Effect of Chloride Concentration on the Potentiodynamic Polarisation Curves of Pure Copper*

Figure 69 shows an example of the typical potentiodynamic polarisation curves of copper in the different concentrations of sodium chloride in a pH 7 electrolyte at 25°C. Regardless of temperature or pH the polarisation curves generated in the different sodium chloride concentration electrolytes followed similar trends.
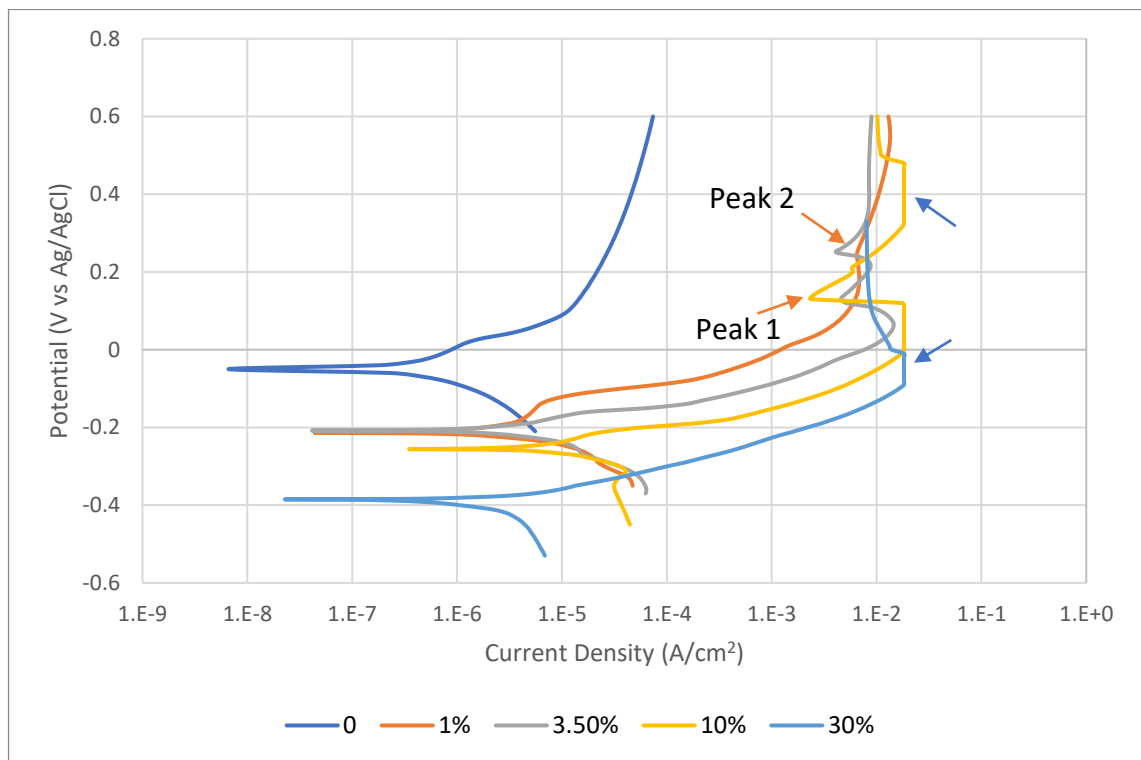
Figure 69 – Example anodic potentiodynamic polarisation curves for copper showing the effect of sodium chloride concentration (% w/v) in a pH 7 electrolyte at 25°C. The blue arrows indicate the maximum current density that could be measured by the potentiostat. The orange arrows highlight peaks in current density within the anodic portion of the curves.

Features on the potentiodynamic polarisation curves were shown to be affected by the increase in sodium chloride concentration. One of these features was the current density of the curves. Both the cathodic and anodic portions of the polarisation curves produced in the 0% electrolytes had the lowest current density, due to weaker copper

[181]

substrate dissolution mechanisms compared to the electrolytes containing sodium chloride. Instead, the curve demonstrated an exponential increase in current with increasing applied potential indicating charge transfer kinetics (Elhousni et al., 2017).

When chloride ions were present in the electrolyte, they are adsorbed uniformly onto the electrode surface causing both the anodic and cathodic portions of the curve to shift towards higher current densities, as passivation was prevented with an increase in metal electro-dissolution (Elsner et al., 1988). When increasing the sodium chloride concentration from 0% to 10%, an increase in the rate of adsorption and consistency of the chloride ion layer on the electrode surface was expected following Elsner et al. (1988), causing the polarisation curves to shift towards higher current densities. Milošev et al. (2006) and Starosvetsky et al. (2006) also observed the increase in current density when the sodium chloride concentration was increased from $0.01\ M$ to $1.0\ M$ and $0.015\ M$ to $1.5\ M$, respectively. However, in the 30% electrolytes the cathodic portion of the current density is reduced below that found in the 10% electrolytes. This can be related to the Levich relationship where the increase in viscosity, caused by the high concentration of sodium chloride, restricts the diffusion of ions to and from the electrode surface, reducing the limiting current density (Cáceres et al., 2007).

With increasing sodium chloride concentrations, the E_{Corr} value, the point where the lowest current density is recorded, was found to shift to more electronegative values suggesting an increase in electrode activity. A relatively large increase in activity was recorded between 0 and 1% of 110-220 mV, with a relatively smaller increase of 8-

55mV between 1% and 3.5% and 48-92 mV and 90-114 mV between 3.5-10% and 10-30%, respectively.

It was discussed in Hoar et al. (1965) and Milić et al. (2008) that the potential of metals becomes more negative as the chloride concentration was increased. A similar trend was observed in Figure 70 where in the electrolytes that contained sodium chloride an approximately linear change in E_{corr} potential was measured with increasing chloride concentration, highlighting the activating effect of the chloride ions.
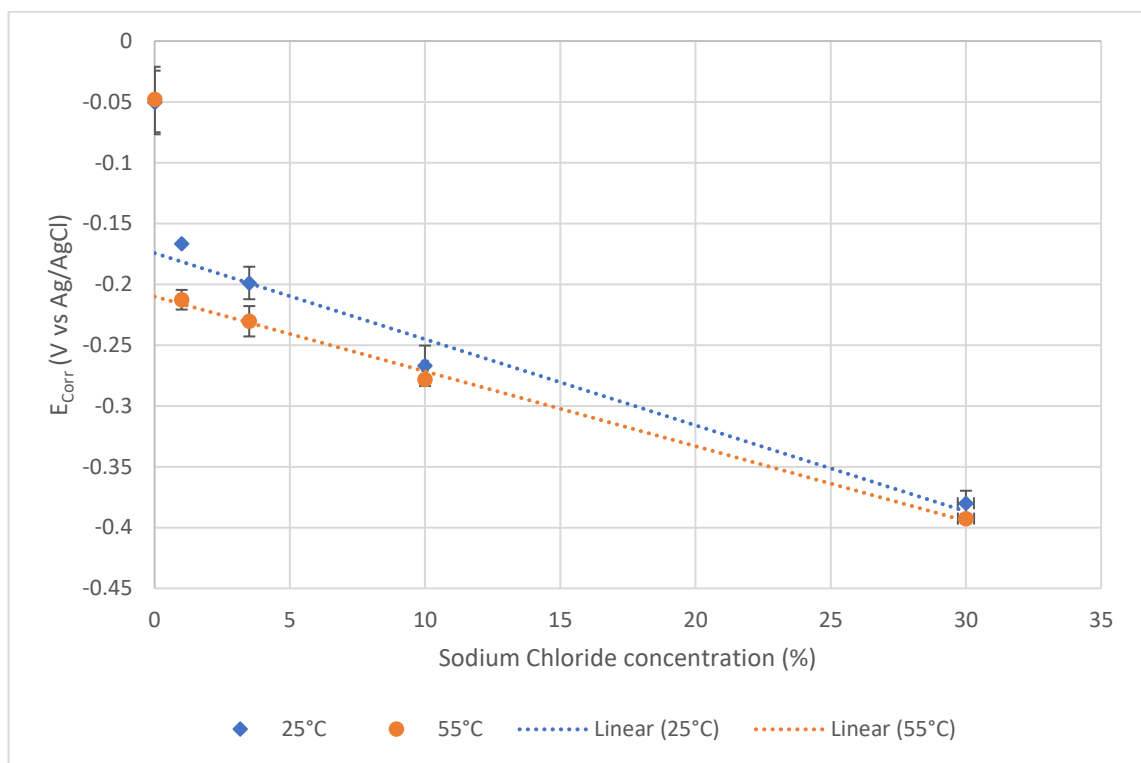
Figure 70 – Chart showing the effect of sodium chloride concentration on the average E_{corr} measurements recorded in a pH 7 electrolyte at 25 °C and 55 °C. The error bars on the y-axis represent the standard deviation of the measured E_{corr} values, while the x-axis error bars represent the experimental error when mixing the solutions which was determined to be <0.5% for each electrolyte.

In the electrolytes containing sodium chloride an active corrosion region is observed where a large increase in current density was found over a relatively small increase in potential. Within this region a small inflection in the curves was observed where the potential increased faster than the current, this was also observed in the 0%. Elhousni

et al. (2017) determined that this inflection was due to the formation of Cu_2O and/or CuO on the electrode surface limiting the diffusion of reactive species.

With increasing polarisation potential, the electrode reaches the critical current density where the primary passivation potential was recorded (Chapter 3.3.3, Figure 14) as seen in the 1% and 3.5% polarisation curves. However the critical current density in the 10% and 30% electrolytes was masked due to limitations of the potentiostatic system resulting in the constant current density of $1.81 \times 10^{-2} \ A.cm^{-2}$, known to be the highest current that could be measured when using this potentiostat, over an 110 and 80 mV potential window, respectively, shown in Figure 69. When moving the potential to more electropositive values past the primary passivation potential the current density decreases as the passive film grows faster than its complexation by chloride ions or mass transport to the bulk solution, eventually resulting in the formation of two secondary anodic peaks, where the $CuCl$ film reached the maximum coverage. These peaks were most visible in the 3.5 and 10% electrolytes labelled in Figure 69, but are also visible in the 1% electrolyte. The first peak (Peak 1) represents the potential at which copper oxidises to Cu^+ and the second peak (Peak 2) is the oxidation of Cu^+ to Cu^{2+} ions which form due to the breakdown of the passive film and the dissolution of the copper substrate (Antonijevic et al., 2009; Arjmand & Adriaens, 2012; Strehblow et al., 2001). The potential range where these peaks and the pseudo-passive region formed were dependant on the chloride concentration where at 1% NaCl the potential range extended over approximately 500 mV, reducing to approximately 260 mV and 170 mV at 3.5% and 10%, respectively. Ochoa et al. (2015) and Vrsalović et al. (2017) also observed a

reduction in the pseudo-passive region of the anodic polarisation curve with increasing chloride concentrations. As the potential was driven to more electropositive values and the polarisation curve leaves the pseudo-passive region a competition between the formation of the $CuCl$ and the production of Cu^+ and Cu^{2+} ions and there complexation to $CuCl_2^-$ was observed, where the diffusion of these ions into the bulk electrolyte becomes rate limiting (Kear et al., 2004).

When testing in the 30% electrolyte no inflections were found in the active corrosion portion of the curve suggesting that the Cu_2O/CuO film was not forming. The electrode passivated resulting in a reduction in current density which remained consistent at $1 \times 10^{-2}\ A.cm^{-2}$ as the potential was driven to more electropositive values. This constant current density may have been caused by the high dissolution rate of the electrode resulting in a film free surface. Similar results have been shown in Braun (1979) when the chloride concentration was greater than $2\ mol.dm^{-3}$.

6.1.1.3 *Effect of pH on the Potentiodynamic Polarisation Curves of Pure Copper*

Initial examination of the polarisation curves, such as the examples shown in Figure 72, found that the electrolyte pH had a minimal effect on their shape. All three curves have the same typical features such as the E_{Corr}, the passivation potential and the secondary anodic peaks within the pseudo-passive region of the curve where Cu^+ and Cu^{2+} ions are produced. However, some subtle differences can be seen in each electrolyte.
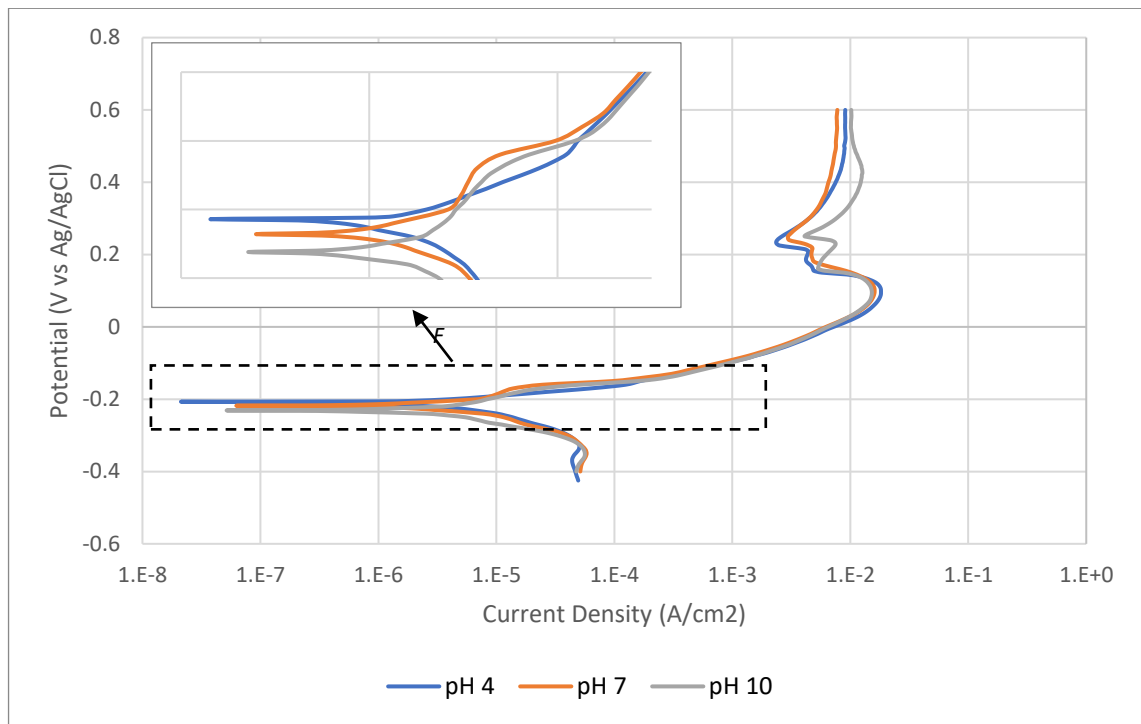
Figure 72 – Example chart showing the effect of pH, modified to ± 0.1 the target value prior to testing, had on the potentiodynamic polarisation curves in a 3.5% sodium chloride electrolyte at 35 ℃.

Firstly, the pH of the electrolyte affects the inflection in the active corrosion region in the anodic portion of the curve. At pH 4 this inflection was not present in any of the electrolytes as there was a consistent increase in current density with potential. This inflection maybe associated with the formation of quasi-protective Cu_2O/CuO layers which are known to be highly soluble and porous in acidic electrolytes (Brusic et al., 1991; Feng et al., 1997; Pourbaix, 1966), suggesting that a stable film was unable to form in this region. Furthermore, the passivation potential at pH 4 tends to be at more electropositive values when compared to pH 7 and 10 in the chloride containing electrolytes suggesting that more energy was required to allow a stable film to form. The higher potential also produces OH^- ions through the breakdown of water molecules at the cathode, which improve the passivity of copper (Liao et al., 2011). These ions are available at higher concentrations in neutral and alkaline electrolytes allowing the inflections to occur at pH 7 and be more prominent at pH 10. This trend

[186]

was observed in all but the 30% electrolytes, probably due to the faster dissolution kinetics in this electrolyte, controlled by the mass transport of $CuCl_2^-$ species away from the electrode surface. Furthermore, the passivation potential tends to be lower in alkaline solutions, showing that copper passivates more readily in alkaline electrolytes. This can be seen in the Pourbaix diagrams (Chapter 5.2.1) where Cu_2O and CuO form preferentially in alkaline electrolytes where these anodic oxides dissolve too fast in acidic electrolytes to provide passivity (Kunze et al., 2004).

The pH of the electrolyte also had a variable effect on the E_{Corr} value, with the sodium chloride concentration becoming the dominating factor at higher concentrations. Figure 73 shows an example of the E_{corr} recorded at 35°C (the charts for 25°C, 45°C and 55°C are available in Appendix 4), where in the 1% and 30% electrolytes the most noble potentials recorded at pH 4, while the active potentials were recorded at pH 10. Whereas the most active potentials in the 3.5% and 10% electrolytes were recorded at pH 4 and 10, respectively. Variations in the E_{Corr} were reduced as the sodium chloride concentration was increased whereas at 0% NaCl variations of 2-73 mV were measured decreasing to 1-12mV at 30%. Suggesting that chloride concertation had a greater influence over the polarisation curves than the pH of the electrolyte, which was also observed in Arjmand & Adriaens (2012).
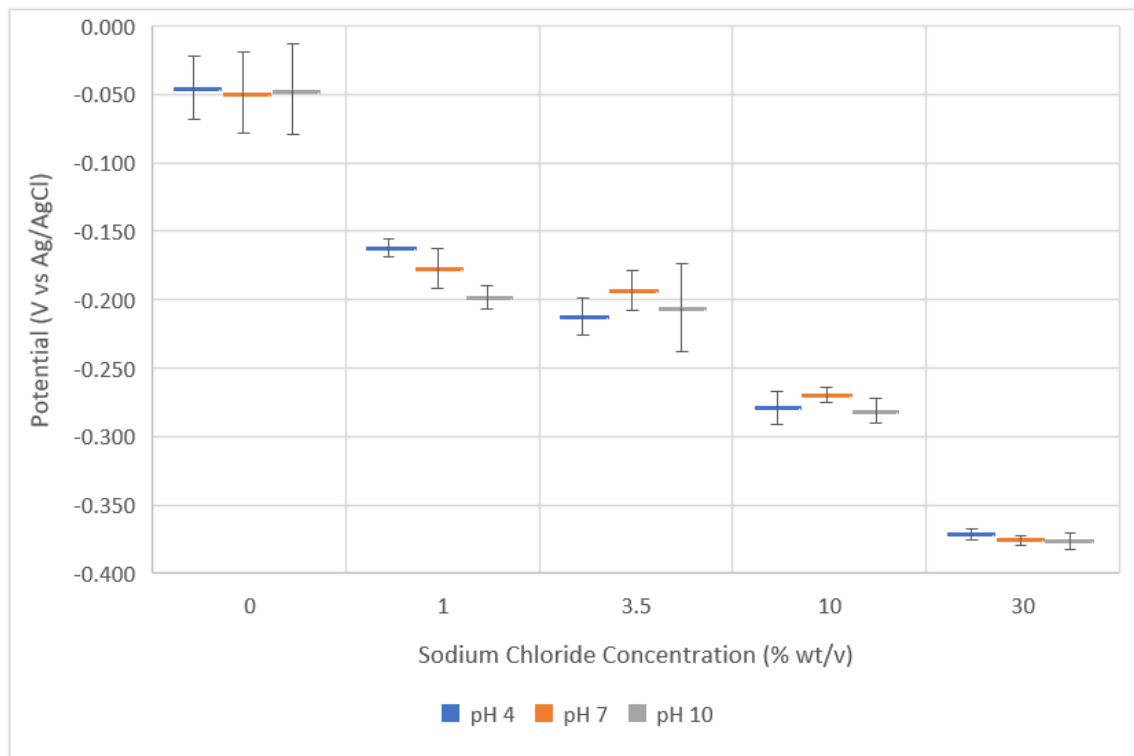
Figure 73 – Example chart showing the effect of pH on the average E_{corr} measurements for the different sodium chloride concentrations in a 35℃ electrolyte. The pH was modified to ± 0.1 the target value. The error bars on the y-axis represent the standard deviation measured between the E_{corr} values recorded in the replicated potentiodynamic polarisation curves

6.1.1.4 *Effect of Temperature on the Potentiodynamic Polarisation Curves of Pure Copper*

Temperature was the final variable considered with an example of the polarisation curves produced in a 3.5% NaCl electrolyte at pH 4 shown in Figure 74. Initial observations found that the inflections in the anodic portion of the curve found in the pH 7 and 10 electrolytes became less prominent as the temperature was increased with the inflections disappearing at 55°C. This suggests that the corrosion of the copper electrode occurs at a faster rate preventing the initial formation of Cu_2O/CuO layers at higher temperatures. Furthermore, a reduction in oxygen concentration by approximately 63% (Natural Resources Research Institute, 2015), was expected between the electrolytes at 25°C and 55°C, which may prevent the initial formation of the oxide layers.

[188]
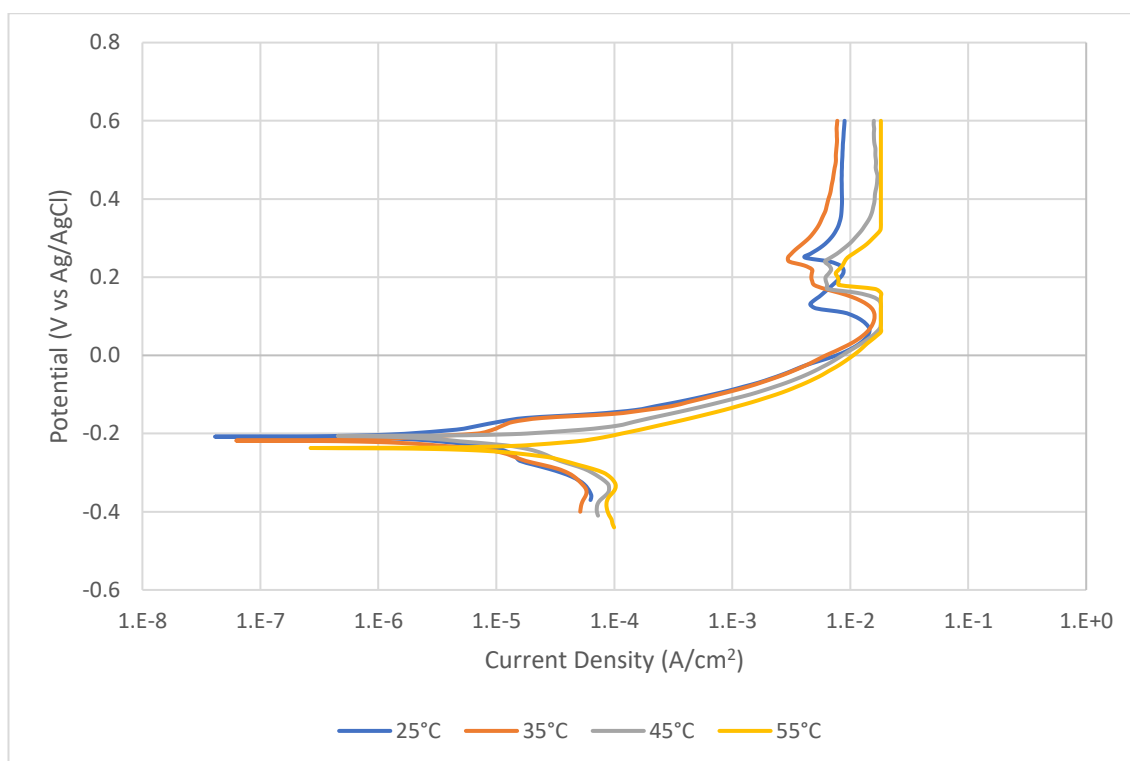
Figure 74 – Example chart showing the effect of temperature which was held at ± 1℃ of the target value, on the potentiodynamic polarisation curve in a 3.5% sodium chloride electrolyte at pH 7.

At elevated temperatures (Figure 74, 55°C) and chloride concentrations the current density reached the maximum that the potentiostatic system could measure, resulting in a constant current being recorded with increasing potential. This prevented an accurate interpretation of the curves, however using the general shape before and after this linear region the missing profile of the curve could be estimated. In the 1 and 3.5% electrolytes the passivation current increased with increasing temperature, along with the passivation potential becoming more electropositive suggesting a reduction in corrosion resistance and increased difficultly at passivating copper at higher temperatures. However, in the 10 and 30% electrolytes the passivation potential became more electronegative with increasing temperature, while the current density achieved similar values. This suggests that while temperature can affect the corrosion properties of copper in dilute solutions the chloride content becomes the dominating factor at higher concentrations.

[189]

With increasing temperatures, the secondary anodic peaks found in the pseudo-passive region in the 1% electrolyte became more defined with two individual peaks becoming visible, especially at 45°C and 55°C. However, in the 3.5% and 10% electrolytes the peaks became less defined with increasing temperature, with a narrowing of the pseudo passive potential range over which these peaks formed being recorded. Ochoa et al. (2015) and Prajatelistia et al. (2019) also experienced a similar phenomenon. Prajatelistia et al. (2019) observed that at lower temperatures (25-40°C) $CuCl$ formation was preferred creating an inhibiting film which can cover the electrode and therefore reduce the corrosion process, reducing the current density. However, at higher temperatures $CuCl_2^-$ forms faster and is transferred quicker allowing the electrode to remain active.

At 55°C in the 10% electrolyte, no specific secondary anodic peaks were observed where, following an initial reduction, the current density reached a steady state, with a constant current density being recorded as the potential was driven to more positive values. This stable current density was owing to the consistent formation and diffusion of $CuCl_2^-$ into the electrolyte. Similar observations were made in the 30% electrolytes at all temperatures and pH values suggesting that the chloride concentration is also a factor in determining whether the formation of $CuCl$ or $CuCl_2^-$ is preferred. When examining the copper coupons after 24 hours immersion in the 30% electrolyte (Chapter 5.4.2.4) where the surface showed evidence of dissolution with no film formation present. This confirmed that the production of $CuCl_2^-$ ions is preferred over film formation at high chloride concentrations, resulting in the shape of the

polarisation curves in the 30% electrolyte under the different pH and temperature variables.

It was generally observed that with increasing temperature the E_{corr} value measured became more electronegative (Figure 75), as has been shown previously Al-Abdallah et al. (2009) and Ochoa et al. (2015). This indicates that there was an increase in electrode activity between 25°C and 55°C where the potential became more electronegative by 6-48 mV, 26-45 mV, 10-37 mV and 13-25 mV at 1%, 3.5%, 10% and 30%, respectively. However, the increase in electrode activity with temperature was not observed in the 0% electrolyte with the potentials being more variable.
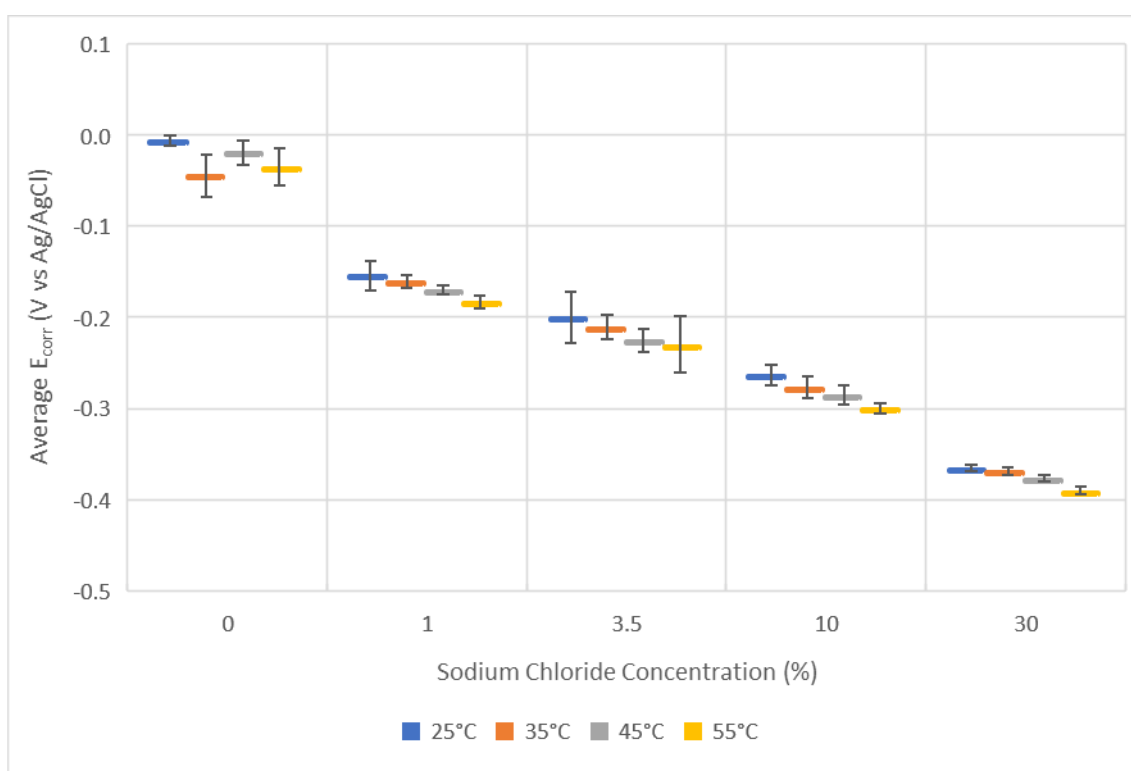
Figure 75 – Example chart showing the effect of temperature on the average of three E_{corr} measurements for the different sodium chloride concentrations in a pH 4 electrolyte. The temperature was held at ± 1℃ of the target value. The error bars on the y-axis represent the standard deviation between E_{corr} values recorded on the replicated potentiodynamic polarisation curves.

[191]

6.2 Tafel Analysis Of The Polarisation Curves

From the polarisation curves collected of copper electrodes in chloride containing electrolytes, shown in Chapter 6.1.1.2, three distinct regions could be identified within the anodic portion of the curves, which have been observed and discussed in various studies (Kear et al., 2004; Khaled, 2011; Prajatelistia et al., 2019; Vrsalović et al., 2017; Wang et al., 2014).

The first region formed around the corrosion potential where apparent Tafelian behaviour could be observed. Within this region the electrode was influenced by the mass transport of cuprous ions away from the electrode surface into the bulk electrolyte and charge transfer kinetics.

The second region occurs at a potential window where the electrode goes through an active to passive transition, where the mass transport is the rate controlling step. This happens as a $CuCl$ film precipitates onto the surface of the electrode at a faster rate when compared to the reaction between $CuCl$ and Cl^- ions to more complex corrosion products, or the mass transport of $CuCl$ into the bulk electrolyte. The current density drops as this film develops until the coverage reaches a critical value, resulting in the formation of the secondary anodic peaks within this region.

The third region was observed as the potential was driven towards more positive values the $CuCl$ film is dissolved releasing $Cu\ (I)$ and $Cu\ (II)$ species which diffuse into the bulk solution from the electrode-electrolyte interface and therefore becomes rate limiting.

As has been discussed by various authors, the anodic dissolution of copper in aerated sodium chloride electrolytes obeys Tafel laws (Al-Mobarak et al., 2010; Al-Mobarak et al., 2011; Khaled, 2011) and therefore further analysis of the polarisation curves within the apparent Tafel region allows for the kinetics of the electrode-electrolyte system to be determined. While it is possible to perform the analysis using only the anodic or cathodic branches of the curves it is preferred that both are used (Mccafferty, 2005). From the Tafel analysis the corrosion potential (E_{Corr}), corrosion current density (i_{Corr}) and the Tafel constants, βa and βc could be extracted. Using this information, the corrosion resistance and corrosion rate was calculated using the equations shown in Chapter 3.3.4.

The Tafel analysis was accomplished by extrapolating the linear portions of the anodic and cathodic branches to their intersection. This linear section of the curves was determined to occur over at least 1 decade on the semi-logarithmic scale current density and was generally recorded within the potential range of between ± 50 mV and ± 150 mV from the OCP.

An example of the Tafel curve extrapolation is shown in Figure 76 (see Appendix 5a for further Tafel plots). The position of the anodic and cathodic extrapolations is reliant on the interpretation and judgement of the interpreter and can be subjective. However, a similar position for the anodic portion of the Tafel extrapolation ($β_a$) was shown in Wang et al. (2014), and after studying all the polarisation curves this was determined to be an appropriate position for the analysis. The extracted and calculated corrosion parameters are summarised in Tables 11 to 15, with the full parameters in Appendix 5b.

[193]
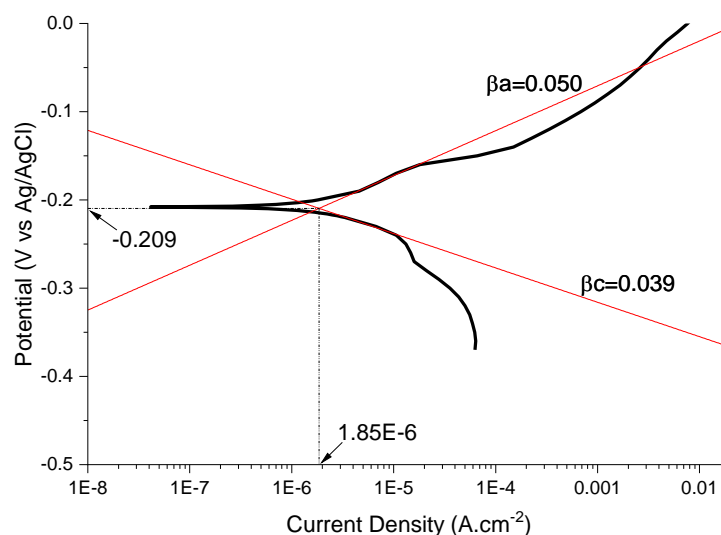
Figure 76 – Example Tafel extrapolation for a copper electrode in a 3.5% NaCl electrolyte at pH 7 and 25℃

A ±7 mV variation was measured when comparing the E_{corr} values taken from the Tafel extrapolation and the potential recorded at the lowest current density, while there was a standard deviation of 10 mV, suggesting that there was a good agreement between the two methods of extracting the equilibrium potential of the electrode. A greater variability was observed between the Tafel E_{Corr} values and OCP measurements (Chapter 5.2.2) with an average difference of ± 15 mV and a standard deviation of 13 mV. Similar variations between the calculated and measured potentials have been observed previously (Diop et al., 2017). The difference in potentials can arise from human error when performing the Tafel extrapolation or surface modification where the thin atmospheric oxide film formed is removed through electropolishing of the surface, which may also reduce the surface roughness, as electrode was polarised through anodic potentials.

The E_{Corr} values collected from the Tafel extrapolation were found to become more electronegative with increasing temperature in the solutions containing sodium chloride. This was observed previously when measuring the potential of the copper

[194]

electrode in an electrolyte using long term OCP (Chapter 5.2.2) and when the potential was recorded at the lowest current density (Chapter 6.1.1).

In the 0% NaCl electrolyte there was no clear trend observed between the temperature and pH with the E_{Corr} values becoming more electronegative (active) between 25°C and 35°C and then electropositive (noble) up to 55°C. It has been shown that in acid electrolytes copper electrode dissolution occurs, suggesting the most electronegative values would be recorded at pH 4, while in alkaline electrolytes film formation is preferred and therefore the lowest E_{Corr} would be recorded at pH 10. However, it was found that the potentials varied between approximately -5 mV and -38 mV at pH 4, and -4 mV and -71 mV at pH 10. Whereas the potentials measured in the pH 7 electrolytes had a greater consistency tending to have more electronegative potential values than the other pH values at each temperature of between -48 and -59 mV. This suggests that the electrode was mostly unaffected by the temperature of the electrolyte with an equilibrium between the electrode dissolution and film forming occurring due to equal concentrations of H^+ and OH^- ions.

Furthermore, the E_{Corr} values followed similar trends to those observed in previous sections where the increase in sodium chloride concentration shifted the potential towards more electronegative values, with the electrodes in 30% NaCl recording the most active potentials and the electrodes in the 0% recording the most noble.

The i_{Corr}, values in each electrolyte, tended to increase with temperature, as was evidenced in the shifting of the potentiodynamic polarisation curve towards higher current densities, shown in Figure 74. A similar trend was also observed by previously authors (Al-Sammarraie & Raheema, 2017; Vrsalović et al., 2016).

[195]

Furthermore, the i_{Corr} values were also found to increase with increasing sodium chloride concentrations up to 10% followed by a reduction in i_{Corr} between the 10% and 30% sodium chloride electrolytes. A similar relationship between i_{Corr} and chloride concentration has been observed previously (Boden, 1971; Starosvetsky et al., 2006). However, most studies focus on copper exposed to a seawater environment, hence the most frequently quoted concentrations of NaCl in an electrolyte in literature are up to 3.5% or 0.599 M (Bech-Nielsen et al., 2002; Boden, 1971; Khaled, 2011; Otmačić & Stupnišek-Lisac, 2003; Vrsalović et al., 2016; Wang et al., 2014), with studies rarely reporting values above 1.5 M or 8.8% (Braun, 1979; Starosvetsky et al., 2006; Zhao et al., 2013). Therefore, comparing the results from the high sodium chloride concentrations to other published studies was difficult.

Similar E_{Corr} and i_{Corr} values were recorded in electrolytes with the same sodium chloride concentration and at the same temperature but at the different pH values, indicating that the pH had a negligible effect on the electrodes. Bacarella & Griess (1973) and Brossard (1983) confirmed that the anodic process was independent of the pH the electrolyte where the dissolution of copper surface was controlled by the transport of $CuCl_2^-$ away from the surface into the bulk electrolyte (Kear et al., 2004) and that the H^+ and OH^- ions do not directly influence this corrosion rate. Furthermore, it was observed that within the apparent Tafel region that the polarisation behaviour of copper was similar in acidic, neutral, and alkaline chloride electrolytes (Antonijevic et al., 2009; Arjmand & Adriaens, 2012; Faita et al., 1975; Reiber, 1989).

Table 11 – Corrosion parameters of copper in a 0% NaCl electrolyte at various pH and temperature values obtained following Tafel extrapolation

pH	Temperature (°C)	E_{Corr} (mV vs Ag/AgCl)		i_{Corr} (µA.cm^{-2})		Corrosion Rate (µm.yr^{-1})		Rp (kΩ.cm^{-2})	
		Avg.	STD	Avg.	STD	Avg.	STD	Avg.	STD
4	25	-4.7	3.4	0.7	0.4	16.9	8.6	17.2	1.5
	35	-24.6	14.7	1.1	0.1	29.4	13.2	8.5	3.4
	45	-16.7	21.8	3.7	1.9	86.3	43.5	9.1	5.6
	55	-40.3	20.4	1.1	1.5	71.4	23.8	11.7	6.7
7	25	-48.1	24.1	0.3	0.1	7.8	1.6	75.5	25.7
	35	-44.9	24.7	0.5	0.2	12.1	5.4	25.2	18.0
	45	-58.9	12.0	0.9	0.3	20.9	6.5	11.2	2.9
	55	-38.5	30.4	1.4	0.5	45.9	10.7	15.6	6.5
10	25	-11.5	10.9	0.7	0.3	16.4	7.9	30.1	7.8
	35	-80.6	49.0	1.2	0.1	28.9	2.8	26.2	12.7
	45	10.6	2.5	1.0	0.2	23.8	4.2	33.5	6.1
	55	-4.5	57.8	0.4	0.1	8.3	2.2	50.1	17.5

Table 12 – Corrosion parameters of copper in a 1% NaCl electrolyte at various pH and temperature values obtained following Tafel extrapolation

pH	Temperature (°C)	E_{Corr} (mV vs Ag/AgCl)		i_{Corr} (µA.cm^{-2})		Corrosion Rate (µm.yr^{-1})		Rp (kΩ.cm^{-2})	
		Avg.	STD	Avg.	STD	Avg.	STD	Avg.	STD
4	25	-164.4	5.1	1.2	0.3	31.5	6.0	7.9	2.2
	35	-167.0	5.9	4.4	1.2	101.7	27.9	3.0	0.5
	45	-170.2	5.2	7.7	0.4	202.4	61.2	1.7	0.3
	55	-182.9	12.8	11.2	5.6	314.4	131.6	1.3	0.4
7	25	-173.5	10.9	1.0	0.2	23.9	1.3	9.6	1.2
	35	-181.1	14.0	4.2	2.0	118.2	61.7	3.9	1.4
	45	-186.9	4.8	8.8	2.3	204.0	53.3	1.9	0.2
	55	-211.2	15.9	12.0	1.2	268.2	34.4	1.4	0.1
10	25	-198.6	16.4	1.2	0.3	28.3	7.4	8.0	1.5
	35	-201.6	13.3	2.3	1.0	52.9	23.2	7.2	3.8
	45	-200.6	7.4	4.4	0.8	142.5	86.4	3.4	1.4
	55	-201.9	7.0	11.8	5.0	273.0	115.3	1.9	0.5

Table 13 – Corrosion parameters of copper in a 3.5% NaCl electrolyte at various pH and temperature values obtained following Tafel extrapolation

pH	Temperature (°C)	E_{Corr} (mV vs Ag/AgCl)		i_{Corr} (μA.cm^{-2})		Corrosion Rate (μm.yr^{-1})		Rp (kΩ.cm^{-2})	
		Avg.	STD	Avg.	STD	Avg.	STD	Avg.	STD
4	25	-211.0	14.8	3.7	1.9	70.0	43.8	3.7	1.5
	35	-206.3	12.4	4.4	2.8	105.5	48.9	2.4	0.8
	45	-224.7	7.9	8.7	1.4	208.4	83.1	1.9	1.1
	55	-243.0	35.3	14.3	3.5	280.1	38.9	0.8	0.2
7	25	-195.3	22.2	1.7	0.3	39.2	86.3	5.9	0.8
	35	-213.3	9.9	3.9	1.6	91.2	37.1	3.7	0.7
	45	-220.8	9.1	10.4	4.6	237.6	92.9	1.2	0.1
	55	-234.8	13.9	13.2	5.2	293.5	101.5	1.0	0.3
10	25	-220.2	11.1	2.4	0.7	55.8	17.1	5.2	0.3
	35	-221.4	23.6	4.5	1.2	108.1	48.5	3.3	1.0
	45	-233.8	18.6	8.2	2.5	189.9	57.2	2.9	0.2
	55	-285.3	14.9	13.9	6.3	323.1	146.4	1.2	0.3

Table 14 – Corrosion parameters of copper in a 10% NaCl electrolyte at various pH and temperature values obtained following Tafel extrapolation

pH	Temperature (°C)	E_{Corr} (mV vs Ag/AgCl)		i_{Corr} (μA.cm^{-2})		Corrosion Rate (μm.yr^{-1})		Rp (kΩ.cm^{-2})	
		Avg.	STD	Avg.	STD	Avg.	STD	Avg.	STD
4	25	-268.6	10.2	5.6	0.2	129.1	4.4	2.2	1.0
	35	-273.4	5.2	6.8	0.8	156.8	18.6	1.1	0.1
	45	-288.2	9.1	13.4	3.2	317.2	93.5	1.6	0.4
	55	-304.3	3.5	15.8	5.7	377.5	141.4	1.5	0.6
7	25	-267.5	14.4	5.5	1.0	127.6	25.5	2.4	1.0
	35	-270.5	6.8	6.1	0.7	141.9	15.1	1.4	0.2
	45	-280.2	9.8	15.8	1.3	361.4	162.2	1.3	0.2
	55	-300.8	7.8	20.0	6.4	408.6	165.6	1.3	0.5
10	25	-275.8	12.6	4.0	0.7	93.3	15.9	2.7	1.4
	35	-284.6	9.7	8.3	0.6	192.5	17.7	0.9	0.3
	45	-287.2	7.5	10.8	4.8	278.7	82.6	1.0	0.2
	55	-292.4	6.2	23.0	2.1	533.3	49.1	1.1	0.1

Table 15 – Corrosion parameters of copper in a 30% NaCl electrolyte at various pH and temperature values obtained following Tafel extrapolation

pH	Temperature (°C)	E_{Corr} (mV vs Ag/AgCl)		i_{Corr} (µA.cm⁻²)		Corrosion Rate (µm.yr⁻¹)		Rp (kΩ.cm⁻²)	
		Avg.	STD	Avg.	STD	Avg.	STD	Avg.	STD
4	25	-371.6	0.1	4.0	0.4	92.1	9.5	3.6	0.4
	35	-378.2	2.1	5.1	0.4	118.3	9.4	3.2	0.8
	45	-379.3	2.0	8.2	0.8	191.5	18.6	2.4	0.3
	55	-393.0	6.9	8.8	1.0	194.5	50.0	3.4	1.7
7	25	-386.1	9.9	3.0	1.0	69.0	24.3	7.0	1.9
	35	-379.1	0.0	5.0	0.6	116.1	13.6	3.4	0.3
	45	-384.7	0.2	6.2	2.6	144.6	60.2	2.7	0.3
	55	-395.5	6.7	6.1	1.0	150.5	75.2	2.3	0.2
10	25	-376.6	2.5	4.2	0.7	97.2	16.7	3.9	0.4
	35	-381.1	12.4	4.4	0.8	105.2	24.6	3.9	0.9
	45	-382.4	5.7	5.0	0.3	112.1	11.9	2.8	0.9
	55	-398.2	4.9	5.2	1.3	119.7	30.2	2.4	0.4

Using the information taken from the Tafel extrapolation the instantaneous corrosion rate was calculated using the equations shown in Chapter 3.3.4, where it was assumed that the electrode corroded uniformly over the exposure period, without forming a protective patina layer. However, it has been shown that corrosion rate decreases with increasing immersion time (Feng et al., 1996; Liao et al., 2011; Nunez et al., 2005) as the cuprite layer undergoes a parabolic growth rate (FitzGerald et al., 2006), slowing the transport of $CuCl_2^-$ from the electrode surface to the electrolyte. Furthermore, copper has been shown to experience pitting corrosion in the presence of chloride ions (de Chialvo, et al., 1985; El Warraky et al., 2004).

Analysis of the instantaneous corrosion rate found, except for the pH 10 0% NaCl, a linear increase in corrosion rate when the temperature was raised between 25°C and 55°C in each electrolyte. A visual representation of how the temperature and sodium chloride concentration affected the corrosion rate is shown in Figure 77 where the 10% sodium chloride electrolytes were shown to have the highest corrosion rate

regardless of temperature or pH, while the lowest corrosion rate was found in the 0% NaCl electrolytes.

A drop in the calculated corrosion rate was found when increasing the sodium chloride concentration from 10% to 30% to be in line with, or less than, that calculated in the 3.5% NaCl electrolytes. This may suggest that when exposing the electrode, surfaces in contacting with 3.5% or 30% electrolytes would experience similar dissolution mechanisms. However, when comparing the surfaces following the 24 hours immersion in the different electrolytes (Chapter 5.4.2) an oxide layer had formed on the coupon in the 3.5% NaCl electrolyte while the surface of the 30% was the most severely attacked, despite the lower apparent corrosion rate to that of copper in the 10% NaCl electrolytes.

The other feature associated with copper in the 30% electrolyte was the formation of the cathodic curve at lower current densities, suggesting the cathodic reduction reactions (with the most common reactions shown in Equations 3 and 36 in acidic electrolytes, and Equation 37 in neutral and alkaline electrolytes (Shreir et al., 1994) as a result of electron transfer are slower than in the other electrolytes.

$$2H^+ + 2e^- \rightarrow H_2$$
<div align="right">*Equation 36*</div>

$$2H_2O + O_2 + 4e^- \rightarrow 4OH^-$$
<div align="right">*Equation 37*</div>

It is possible that this was caused by either the slower diffusion of species to and from the electrode surface due to the increase in viscosity (Banakar, 1991), or a reduction in the number of cathodic sites on the electrode surface, or a combination of the two. The high concentration of Cl^- ions in the electrolyte would form an increased number of anodic sites on the electrode surface and therefore increase the severity of corrosion. However due to the increase in electrolyte viscosity the diffusion of $CuCl_2^-$

[200]

away from the electrode surface into the bulk electrolyte would be reduced making it the rate determine step, resulting in the lower calculated corrosion rate.
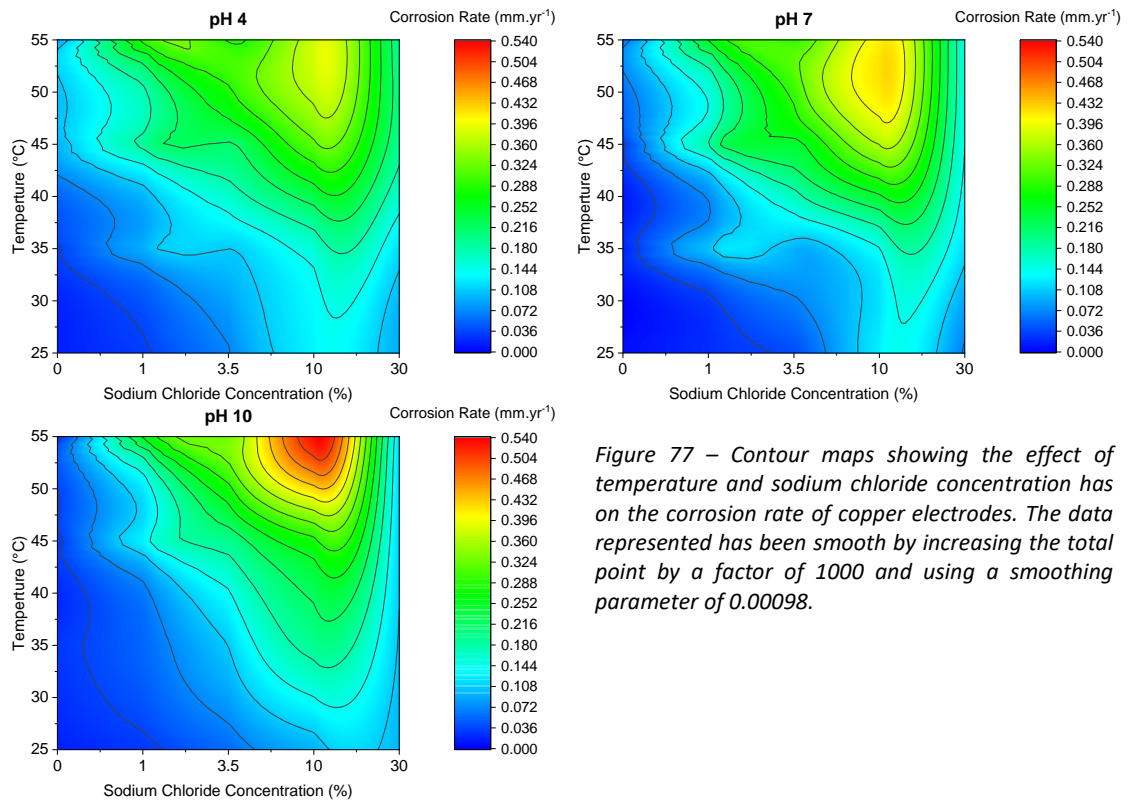
Figure 77 – Contour maps showing the effect of temperature and sodium chloride concentration has on the corrosion rate of copper electrodes. The data represented has been smooth by increasing the total point by a factor of 1000 and using a smoothing parameter of 0.00098.

Further calculations based on the Tafel extrapolation allowed for the corrosion resistance (Rp), the resistance of the electrode to oxidation. Rp is directly related to the corrosion rate and inversely proportional to i_{Corr} (Toshev et al., 2006) and was calculated using Equation 22, the results of which are shown in Tables 11-15 with a visual representation of how the temperature and sodium chloride concentration, at the different pH values, affects the Rp shown in Figure 78.

The highest Rp values were recorded in the 0% electrolyte for each of the temperatures and pH values, with the pH 7 electrolyte at 25°C being the most corrosion resistant. As the sodium chloride concentration was increased the Rp tended to decrease, similar to the observations in Arjmand & Adriaens (2012). With the lowest

Rp values tending to be recorded in the 10% NaCl electrolytes except for pH 4 at 55°C were the 3.5% NaCl had the lowest Rp of each of the test environments. Furthermore, with increasing temperature a reduction in the Rp was recorded in all but the 0% electrolytes at pH 7 where a general increase was recorded. Similar observations were made previously (Al-Sammarraie & Raheema, 2017; Otmačić & Stupnišek-Lisac, 2003).

While the Rp values are for the instantaneous exposure of copper to the electrolytes have been calculated, it has been shown that for extended immersion times Rp increases (Feng et al., 1996) due to the formation of a protective passive layer.
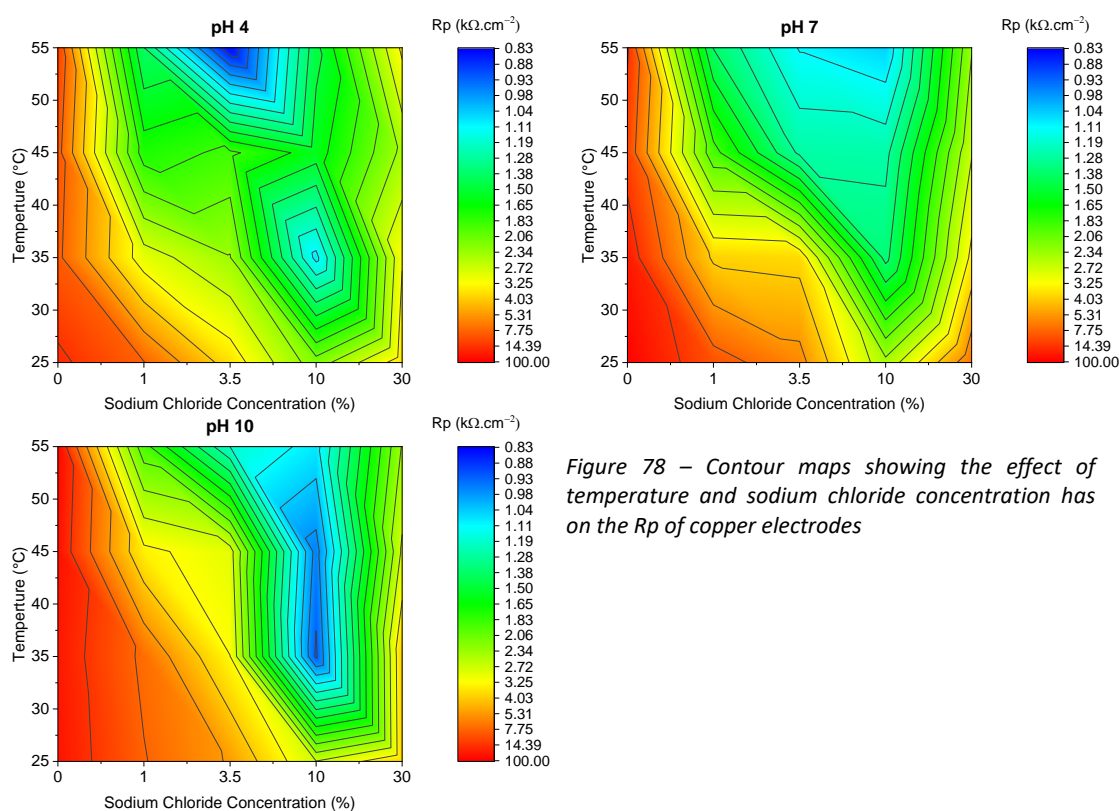
Figure 78 – Contour maps showing the effect of temperature and sodium chloride concentration has on the Rp of copper electrodes

6.2.1   Potentiostatic Acceleration Of Copper Patination

The natural formation of copper patina is generally a slow process which can take several years to develop and is highly dependent on the environmental conditions copper was exposed to including, the composition, presence, and concentration of atmospheric pollutants (Graedel, 1987; Strandberg, 1998a; Strandberg, 1998b), cycles between wet and dry phases (EL-Mahdy, 2005) and the temperature and humidity (Stoch et al., 2001; Strandberg & Johansson, 1998). Several methods already exist and have been discussed in literature for use in architecture and restoration to accelerate the patination of copper. These methods include using one or a combination of heating, immersion, exposure to acidic vapours or the application of acidic pastes, which can take between 2 and 15 days to develop (Bendezu et al., 2007; Hernández et al., 2011; Kim et al., 2014). However, to reproduce and accelerate the patina on antifouling coatings these methods cannot be used as they may result in different compounds to the naturally formed being produced.

The most commonly detected copper patina in chloride rich marine environments, where copper containing antifouling coatings are applied, was clinoatacamite $Cu_2Cl(OH)_3$ of which atacamite and botallackite are polymorphs. The acceleration of copper patination to form $Cu_2Cl(OH)_3$ can be achieved by using the Pourbaix diagram and anodically polarising the electrode at specific potentials where this phase was shown to be thermodynamically stable (Figure 79a), which in a 25°C 3.5% (0.599 M) NaCl electrolyte at was found to be at pH 7 between 200 and 1000 mV vs Ag/AgCl. This electrolyte was selected as it closely matched that of the natural seawater environment antifouling coatings are going to be exposed to and therefore increase the likelihood of similar patina compounds being produced. The

[203]

reaction kinetics was thought to influence the $Cu_2Cl(OH)_3$ polymorphs (Strandberg & Johansson, 1998). Therefore a series of potentials, associated with the $Cu_2Cl(OH)_3$ domain, were selected to accelerate the reaction kinetics (i.e. 100 mV, 200 mV, 300 mV, 500 mV, 700 mV and 1000 mV vs Ag/AgCl), and therefore determine if the applied potential can influence the development of the patina compounds. The potentiostatic polarisation testing can also assess different variables that may influence the patina compounds that are formed such as the amount of time immersed, the volume of the electrolyte and sodium chloride concentration, helping to inform on the subsequent testing of antifouling coatings. Figure 79b shows the anodic portion of the potentiodynamic polarisation curve for copper in a pH 7 3.5% NaCl electrolyte at 25°C which suggests that polarisation at 100 mV would fall within the passivation potential suggesting that a copper oxide may form on the electrode surface. At between 200 and 1000 mV vs Ag/AgCl the potentials fall within the pseudo-passive, film forming region of the polarisation curve.
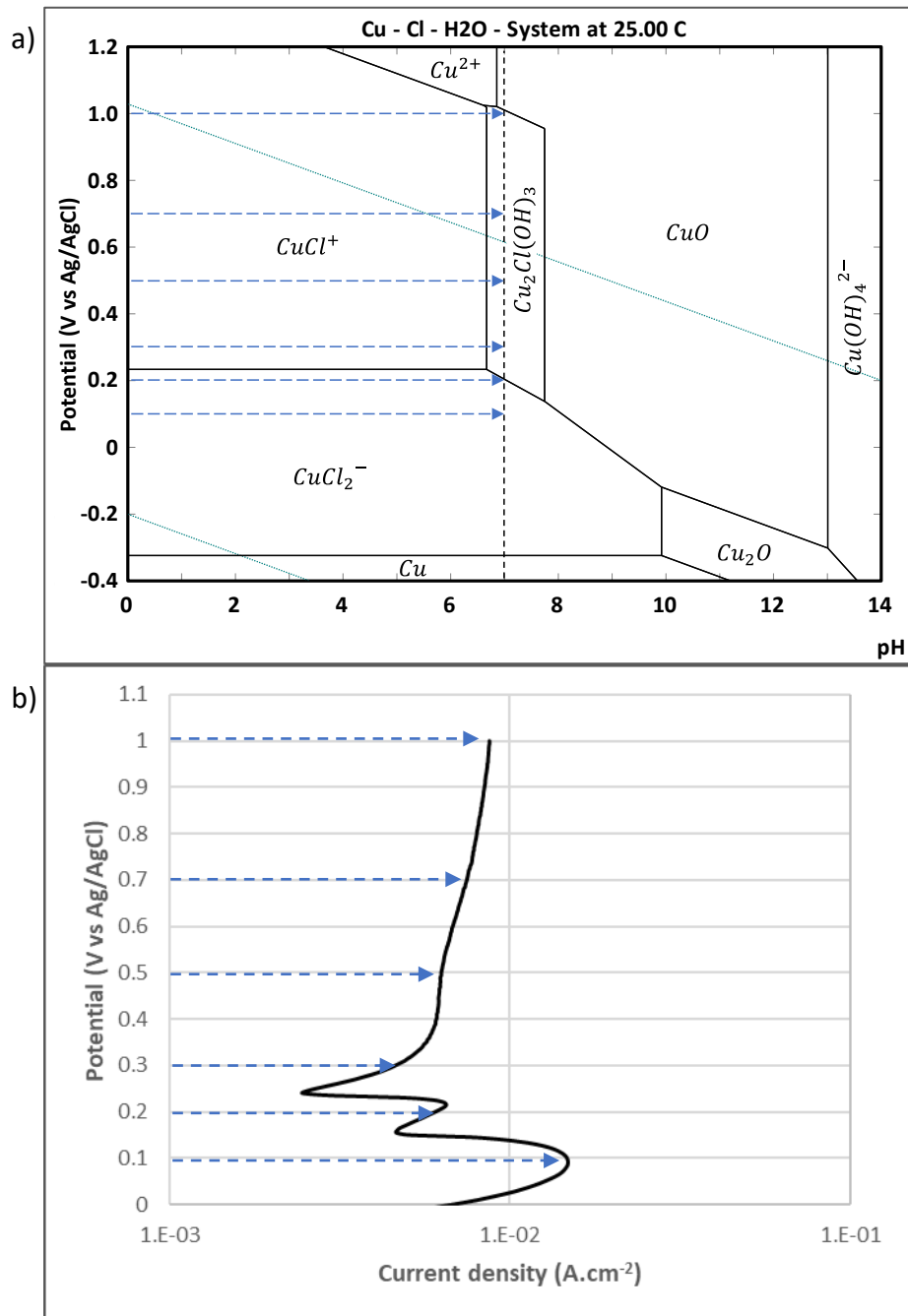
Figure 79 – a) Pourbaix diagram created for the Cu-Cl-H₂O system at 25°C, with a copper concentration of $1 \times 10^{-6} M$ and chloride concentration of $0.599 M$. The dashed vertical line is at neutral pH with the dashed arrows showing the polarisation potentials the copper electrode was polarised at for 30 minutes. b) Typical anodic potentiodynamic polarisation curve of copper pH 7 3.5% NaCl electrolyte at 25°C with dashed blue arrows showing the position of the polarisation potential on the curve.

6.2.1.1 *30-minute Anodic Potentiostatic Polarisation*

The potentiostatic polarisation curves (Figure 80) show that the anodic behaviour of copper was like other passive metals in chloride environments, such as that observed in Judge et al. (2017). The application of the potential resulted in an initial spike

reaching a maximum current density for approximately 30 seconds, associated with the presence atmosphere formed oxide. With increasing polarisation time, the current density decreases, suggesting the formation of a planar barrier film as described in Despić & Parkhutik (1989). The current density eventually reaches a minimum entering an incubation stage where the barrier film can grow incorporating the chloride ions that had arrived at the surface through migration and diffusion (Cabot et al., 1991). At a critical thickness Despić & Parkhutik (1989) determined that micropores nucleate and propagate across the surface, affecting the electric field in the double layer, accelerating the transport of ions into the electrolyte (Judge et al., 2017), which may lead to localised pitting corrosion. This resulted in an increase in current density, which may also be associated with the formation of metal salt crystals on the surface, like those described in Nikolov & Girginov (1983). Eventually the current density tended to stabilise after 30 minutes due to an equilibrium between the breakdown, salt film formation and re-passivation of the electrode surface.
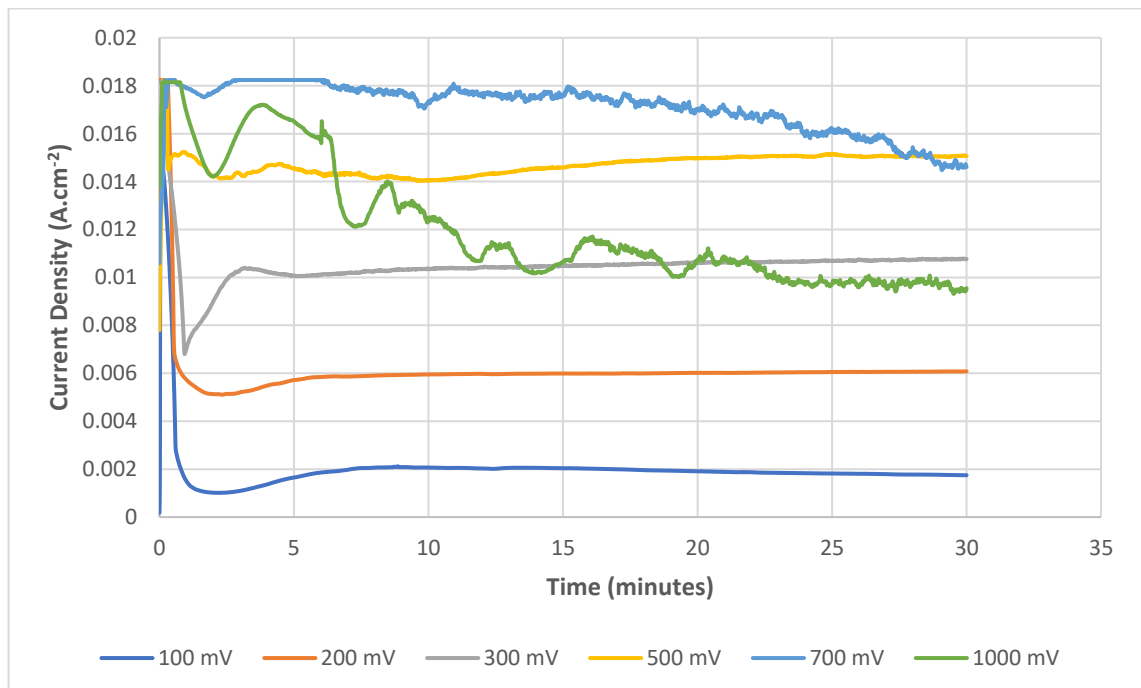
Figure 80 – Potentiostatic polarisation of a copper electrode at potentials of 100 mV, 200 mV, 300 mV, 500 mV, 700 mV and 1000 mV vs Ag/AgCl in a 3.5% NaCl electrolyte at 25 ℃

[206]

Further analysis of the polarisation curves (Figure 80) found an initial peak in current density occurred within the first 20 seconds as any air formed oxide was stripped resulting in the formation of copper ions. An incubation period is then reached, where Starosvetsky et al. (2006) and Prajatelistia et al. (2019) refers to the formation and growth of a two-dimensional copper (I) chloride ($CuCl$) layer, inhibiting the electrode surface, causing the current density to drop to a minimum after 50-160 seconds.

After an incubation period where the $CuCl$ layer developed, the curves produced at 100 mV, 200 mV, 300 mV and 500 mV vs Ag/AgCl followed a similar trend where the current density increased to higher values. This can be attributed to the breakdown of the protective film due to the ingress of chloride ions (Judge et al., 2017). Eventually the current density reached a stable value indicating that a steady state has been achieved between the formation of $CuCl$ on the electrode surface and its breakdown and diffusion into the bulk electrolyte through the production of $CuCl_2^-$, which becomes rate limiting.

However, when observing the potentiostatic polarisation curves produced at 700 mV and 1000 mV vs Ag/AgCl the current density was found to oscillate with a general trend towards lower values over the measurement period. The relatively small current oscillation observed throughout the polarisation at 700 mV vs Ag/AgCl, and as the current stabilised after 22 minutes when polarising at 1000 mV vs Ag/AgCl, may indicate pit formation on the electrode surface which can increase the surface area.

According to the Pourbaix diagram, shown in Figure 79a, the oxygen equilibrium line, the theoretical potential where oxygen evolution occurs at the electrode electrolyte surface, is below 700 mV vs Ag/AgCl and therefore oxygen would form beneath any

surface films present. This can weaken their attachment, exposing an unprotected area to the electrolyte. A large potential difference between the oxygen line and the 1000 mV vs Ag/AgCl was observed when the electrolyte was at pH 7, this could have resulted in the production of a significant amount of oxygen at the electrode surface displacing the protective film, which may account for the several larger reductions in current density as the protective film was removed and rebuilt.

Figure 81 shows the average current density recorded within the final 60 seconds of the potentiostatic polarisation where a stable current for each of the potentials was observed. The current density was shown to increase sharply between 100 mV and 300 mV vs Ag/AgCl indicating the activation of the copper surface, reaching a peak at 500 mV vs Ag/AgCl. At between 700 mV and 1000 mV vs Ag/AgCl the current density decreases, which may be due to the formation of oxygen bubbles on the surface blocking the electrolyte from reaching the surface and reducing the exposed surface area. The relatively high oxygen levels at the electrode surface may also promote the formation of an oxide layer. The charge followed a similar trend with a large increase in current between 100 mV and 300 mV Ag/AgCl, which continued to increase, at a reduced rate, peaking at 700 mV vs Ag/AgCl. While at 1000 mV vs Ag/AgCl a reduction in the charge was measured. Using Faradays law, the charge can be used to calculate the mass loss (Chapter 6.2.1.2).
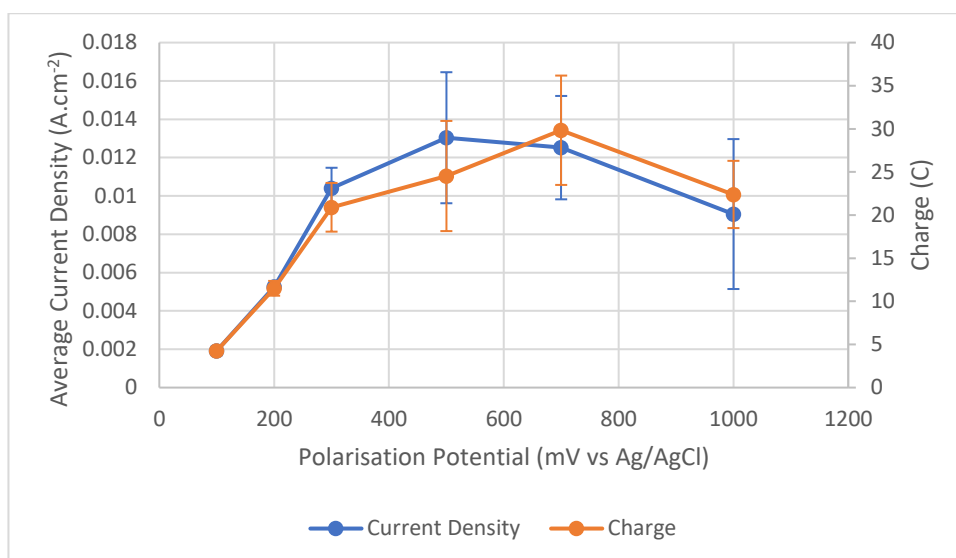
Figure 81 – The average current density taken from the last 60 seconds of the three potentiostatic polarisation curves following potentiostatic polarisation in a 3.5% NaCl electrolyte for 30 minutes at the different potentials. The charge was also measured from the area beneath the current time chart. The error bars are the standard deviation.

Further analysis of the potentiostatic polarisation curves, shown in Figure 82a, found that the incubation period decreased with increasing potential up to 500 mV vs Ag/AgCl, where the $CuCl$ layer forms faster but is only stable for a short amount of time (Yan et al., 2020). Starosvetsky et al. (2006) also observed a similar trend and associated it with a decrease in the competition between the formation of the $CuCl$ layer and its reduction which can lead to higher levels of Cl^- near the electrode surface.

Yan et al. (2020) surmised that at higher potentials the rate of cuprous ion production may be greater than the rate of diffusion to the bulk electrolyte. This can cause a layer of cuprous ions to form under static conditions slowing the diffusion of chloride ions to the electrode surface, which could have caused the general trend towards a reduction in current density (Figure 80), the reduction in current density observed after 500 mV vs Ag/AgCl (Figure 81) and the increase in incubation time (Figure 82).

[209]
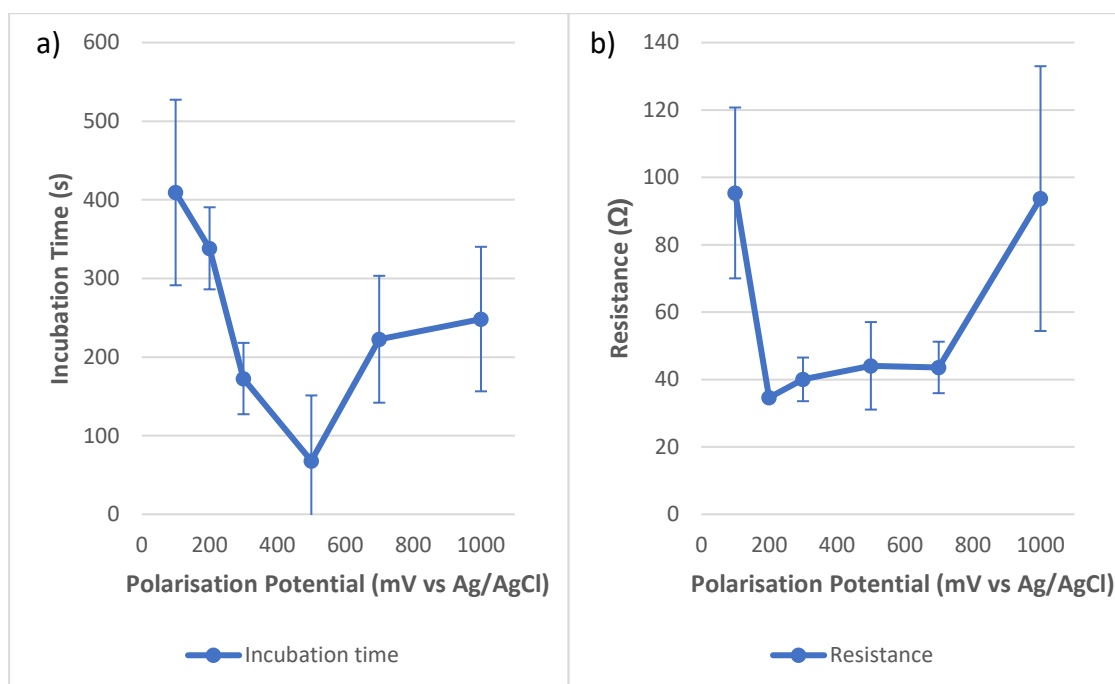
Figure 82 – Charts showing the average a) incubation time and b) resistance of the patina recorded at the lowest current. The error bars are the standard deviation of the three measurements.

As discussed earlier the formation of a protective layer occurs within the first 5 minutes of polarisation where the current is reduced to a minimum within the incubation period. Using this minimum current value and the polarisation potential the total resistance of the electrode-electrolyte interface was calculated, shown in Figure 82b. The interfacial resistances calculated at 100 and 1000 mV vs Ag/AgCl were highest at 95.4 Ω and 93.7 Ω, respectively.

During the initial exposure of copper to the chloride-rich environment, a loosely adhered $CuCl$ layer forms on the electrode surface through Equation 38 during the incubation period.

$$Cu^+ + Cl^- \rightarrow CuCl$$ *Equation 38*

With long incubation periods, the $CuCl$ layer may become thicker and/or denser than that formed at higher potentials with shorter incubation periods. The change in this layer could reduce the flow of ions to and from the electrode surface resulting in the relatively high resistance measurements.

[210]

Furthermore according to the Pourbaix diagram (Figure 79a) $CuCl_2^-$ ions would, theoretically, be produced when polarising at 100 mV, while $CuCl_2^-$ may also be associated with the dissolution of the $CuCl$ film through Equation 13.

As these ions interact with the hydroxyl ions in the electrolyte, they can form Cu_2O at the electrode surface providing a more effective barrier to the electrolyte, through Equation 39.

$$2CuCl_2^- + 2OH^- \rightarrow Cu_2O + H_2O + 4Cl^-$$
<div align="right">*Equation 39*</div>
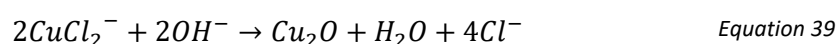
This can in turn increase the number of chloride ions at the electrode surface reacting with the $CuCl_2^-$ ions further increasing the Cu_2O layer and possibly also account for the higher resistance observed.

Between 200 and 700 mV vs Ag/AgCl the Pourbaix diagram indicates that $Cu_2Cl(OH)_3$ should theoretically be the thermodynamically stable compound forming at the electrode surface. This patina is known to be highly porous allowing Cl^- ions to easily pass through the layer and reach the electrode substrate (Nunez et al., 2005), which could cause the observed reduction in resistance to between 34.6 Ω and 44 Ω (Figure 82b).

It was shown in the Pourbaix diagram (Figure 79a) that polarising copper at 1000 mV vs Ag/AgCl bordered the $Cu_2Cl(OH)_3$ and CuO stability domains, producing an equivalent Rp to that observed when polarising at 100 mV vs Ag/AgCl (Figure 82b). This may indicate the preferential formation of CuO or the presence of high concentrations of copper ions at the electrode electrolyte interface slowing diffusion in the system.

[211]

6.2.1.2 *Electrode Mass Loss*

A mass loss was recorded when potentiostatically polarising copper electrodes at different potentials in the neutral 3.5% NaCl electrolyte, which was found to increase between 100 mV and 700 mV vs Ag/AgCl from approximately 1.7 mg to 11.8 mg (Figure 83a). This indicates that with increasing polarisation potential the amount of copper ions in the electrolyte and therefore the amount of patina that can be produced also increases. However, at 1000 mV vs Ag/AgCl a reduction in the mass loss was observed. This potential was above the oxygen formation line shown in the Pourbaix diagram suggesting that oxygen evolution was promoted. This may consume a proportion of the applied electrons reducing the amount available to oxidise the metal surface and therefore result in the reduction in mass loss. The production of oxygen at the electrode surface may also reduce the conductivity of the copper, causing the reduction in current density observed in Figure 80, further reducing the mass loss. This suggests that potentiostatic methods maybe used to accelerate the patination of copper or copper-based products. However, the potential should be limited to less than 700 mV vs Ag/AgCl to maintain efficiency. A similar trend was observed when calculating the theoretical mass loss calculated from the total current passing through the circuit (Figure 81), using Faradays Law (Equation 40) where the mass loss was directly proportional to the charge in coulombs.

$$m = \frac{M(\sum I)t}{zF}$$
<div align="right">*Equation 40*</div>

Where m = mass loss, M = Molecular weight of copper ($63.55\ g.mol^{-1}$), t = time (s), z = number of electrons involved in the oxidation/reduction reaction ($z = 2$), $\sum I$ =Total current and F = Faraday' s constant (96,485).

<div align="center">[212]</div>

Both the actual and theoretical mass losses were in close agreement with each other, especially at low polarisation potentials.

a)
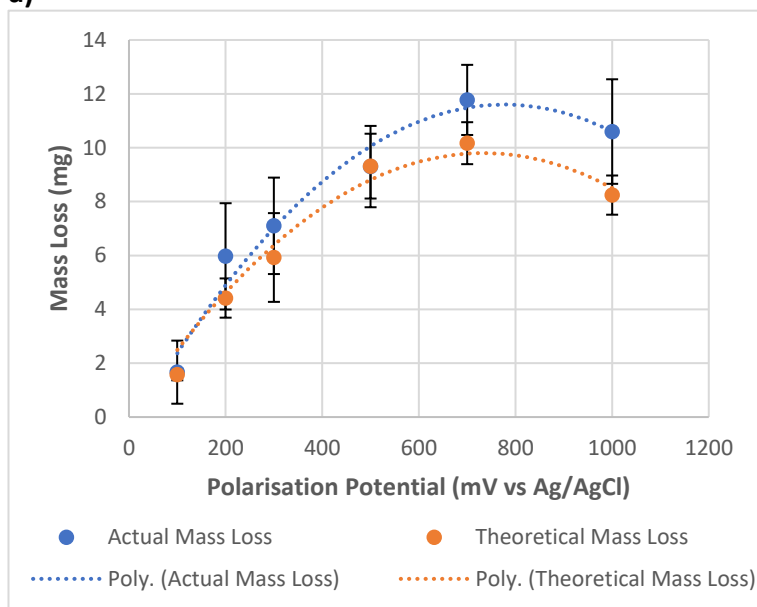
Polarisation Potential (mV vs Ag/AgCl)	Faradaic efficiency (ηF)
100	1.06
200	1.35
300	1.20
500	1.00
700	1.16
1000	1.29

Figure 83 – a) Chart showing the theoretical and actual mass loss for the electrode after 30 minutes anodic polarisation at 100 to 1000 mV vs Ag/AgCl. The error bars are the standard deviation derived from the triplicate samples. b) table showing the Faradic efficiency of the potentiostatic polarisation.

The Faradaic efficiency (ηF) of the potentiostatic polarisation systems were analysed by comparing the ratio of the actual to the theoretical mass loss where the ηF was found to be greater than or equal to 1 (Figure 83b). At values greater than 1 suggests that other factors may be at work which increase the mass loss, such as corrosion processes not related to the applied potential (Despić & Parkhutik, 1989).

Further inaccuracies in determining the Faradaic efficiency may be observed when examining the current trends (Figure 79). At potentials above 100 mV vs Ag/AgCl the current exceeds the maximum current of 20.6 mA able to be recorded by the potentiostatic system within the first five minutes of polarisation. This suggests that the actual charge passing through the electrode was greater than what was measured and therefore the Faradaic efficiencies may be closer to 1.

[213]

6.2.1.3 *Electrode Analysis*

6.2.1.3.1 Surface Morphology

The surface morphology of the electrodes was analysed using both low magnification optical images (Figure 84) and high magnification SEM images (Figure 85) after they were exposed to a neutral pH 3.5% NaCl electrolyte at 25°C and potentiostatically polarised for 30 minutes, at the different anodic potentials.

The colour of the electrode surface was found to change following the polarisation. At 100 and 200 mV vs Ag/AgCl (Figure 84a and b, respectively) the electrodes had the golden orange colour typically associated with copper. At higher polarisation potentials the electrode surface was found to be covered with a weakly adhered surface film, which was missing in some locations exposing the substrate. The colour of this film varied; at 300 and 700 mV vs Ag/AgCl (Figure 84c and e, respectively) the film had a yellow/green colouration while at 500 mV vs Ag/AgCl the film had a greener hue (Figure 84d). At 1000mV vs Ag/AgCl the electrode substrate had a reddish colouration with patches of a blue-green surface film. The differences in the colour may be associated with the compound produced, porosity, thickness, and roughness of the film (Fredj & Burleigh, 2011).
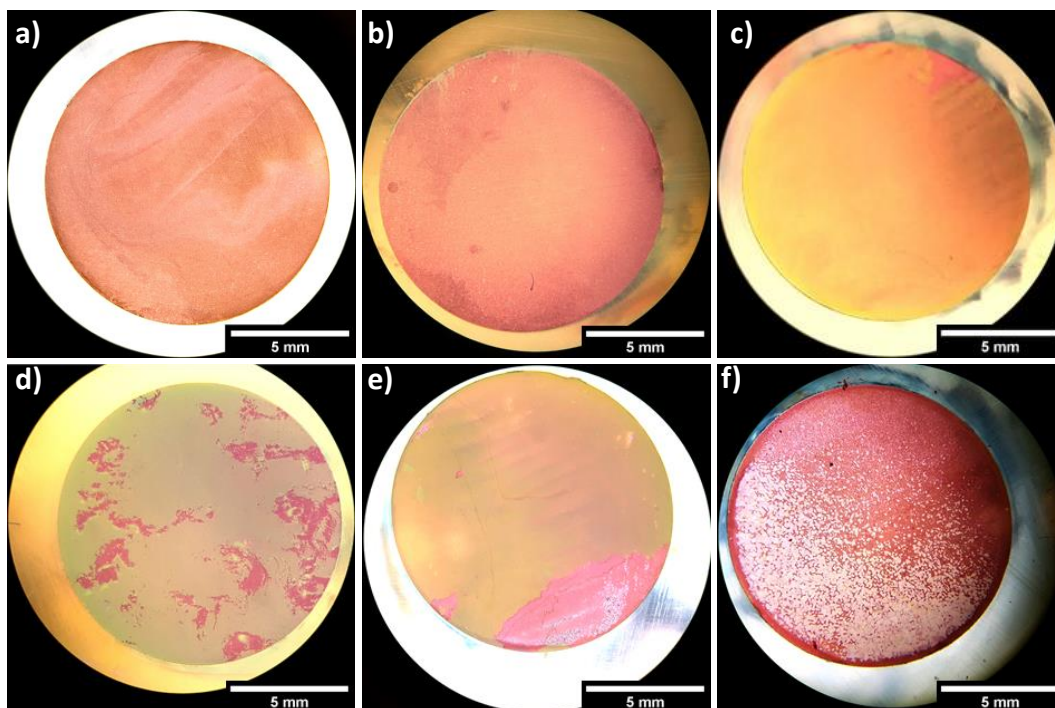
Figure 84 – Images of the surface of the copper electrodes following the 30-minute anodic potentiostatic polarisation at a) 100 mV, b) 200mV, c) 300 mV, d) 500 mV, e) 700 mV and f) 1000 mV vs Ag/AgCl, in the pH 7, 3.5% NaCl electrolyte at 25°C.

High magnification SE imaging of the copper electrode after it had been anodically polarised at 100 mV vs Ag/AgCl found a series of channels etched into the surface (Figure 85a). These channels are typical of the electrochemical dissolution of copper when exposed to a corrosive electrolyte (Liao et al., 2011) and are associated with the high electrochemical activity of the grain boundaries and form thinner protective layers when compared to the grain body (Lapeire et al., 2017). Aggressive anions, such as Cl^-, also tend to concentrate around the grain boundaries (Hoar et al., 1965) which can enhance the etching of the surface. Each sample was taken from the same copper rod and mounted in the same orientation therefore it is assumed that they had an equivalent grain size. When the copper electrode was anodically polarised at 200 mV vs Ag/AgCl the electrochemical activity of the grain boundaries was enhanced increasing the number, depth, and width of the etch channels found after 30 minutes (Figure 85b) increasing the number of copper ions in the electrolyte.

[215]

According to the Pourbaix diagram (Figure 79a), the polarisation of copper at 100 and 200 mV in a neutral pH 3.5% NaCl electrolyte at 25°C produces copper ions which react with the chloride ions to form soluble $CuCl^{2-}$ ions which enter the electrolyte. These ions can then precipitate out of the electrolyte as insoluble copper compounds. EDX analysis of the polarised electrode surfaces found that the oxygen concentration had decreased from 3.9 wt% at 100 mV vs Ag/AgCl to 1.3 wt% at 200 mV vs Ag/AgCl, while only a small concentration of chlorine was detected at 0.4 wt% and 0.2 wt%, respectively. This confirms that the soluble $CuCl^{2-}$ ions did not precipitate from the electrolyte back onto the substrate to form a chloride-rich film. The relatively high concentration of oxygen suggests that only a thin oxide layer was present giving the electrodes the typical copper colourations. As the applied anodic potential was increased the oxide film forming capability of the substrate was reduced resulting in a thinner oxide layer, which therefore reduces the measured oxygen concentration.

The example potentiodynamic polarisation curve shown in Figure 79b suggests a pseudo-passive, film forming region formed when the potential was increase to between 200 and 1000 mV vs Ag/AgCl. However, no film was observed on the electrode surface polarised at 200 mV vs Ag/AgCl with only small patches at 1000 mV vs Ag/AgCl. These potentials, according to the Pourbaix diagram, theoretically border the stability domain region where $Cu_2Cl(OH)_3$ compound forms, however in practice the 200 mV vs Ag/AgCl may favour the formation of $CuCl^{2-}$ ions and therefore a surface film could not be produced. While at 1000 mV vs Ag/AgCl the potential may be high enough to allow oxygen bubbles to form which can release the

[216]

film from the surface, or the dissolution of the surface may be faster than the rate of film formation resulting in areas free from the surface film.
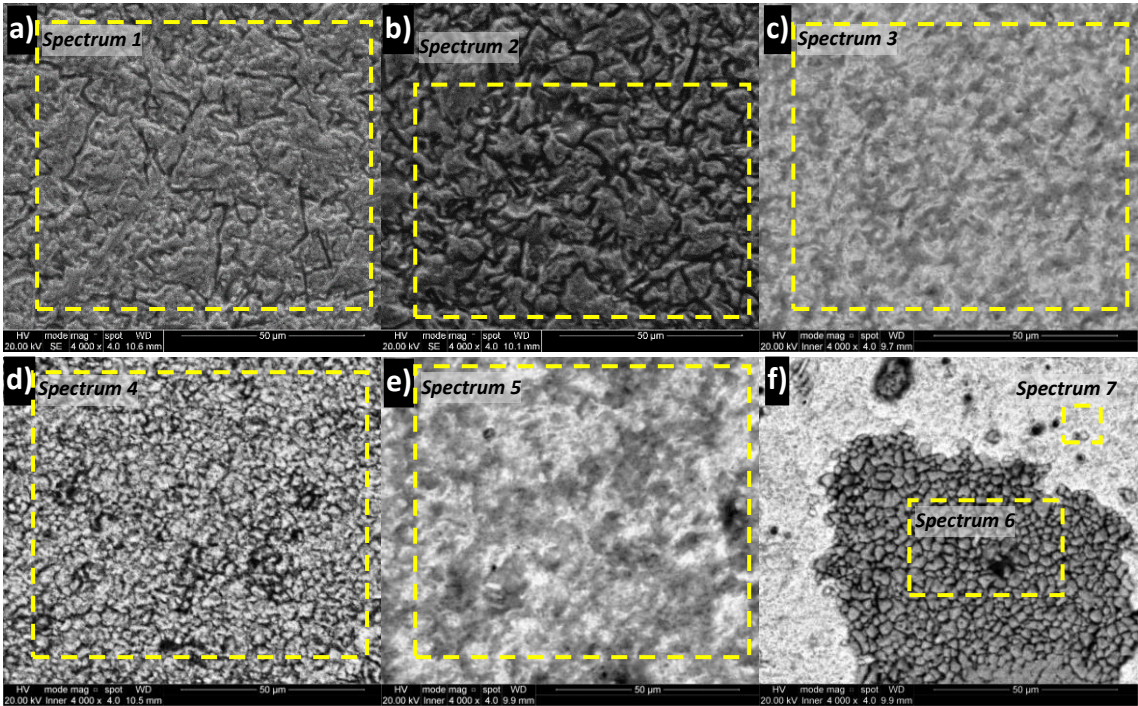
Figure 85 – High magnification SEM imaging of the copper anode surface following 30-minute anodic potentiostatic polarisation at a) 100 mV, b) 200mV, c) 300 mV, d) 500 mV, e) 700 mV and 1000 mV vs Ag/AgCl, in the pH 7, 3.5% NaCl electrolyte at 25°C. The yellow dashed boxes indicate the location of the EDX analysis.

Table 16 – Example EDX spectra and semi-quantitative analysis of the yellow dashed line boxes shown in Figure 85

Spectrum Label	Element (wt%)		
	Cu	O	Cl
Spectrum 1 (100 mV)	95.8	3.9	0.4
Spectrum 2 (200 mV)	98.5	1.3	0.2
Spectrum 3 (300 mV)	89.3	6.6	4.1
Spectrum 4 (500 mV)	70.7	3.8	25.4
Spectrum 5 (700 mV)	84.3	9.8	5.9
Spectrum 6 (1000 mV)	66.0	1.6	32.5
Spectrum 7 (1000 mV)	98.3	1.2	0.6

The copper electrode surface was covered with a chlorine rich film after potentiostatically polarising above 200 mV vs Ag/AgCl. BSE analysis of the surface of the electrodes polarised at 300 and 700 mV vs Ag/AgCl (Figure 85c and e, respectively) found that had a similar morphology with a dark grey contrast film, which lacked structure, surrounded by the lighter contrast potentiostatically etched copper

[217]

substrate. The relative similarities between the surface of the electrode at the two polarisation potentials may suggest why they have a similar colour when examined optically. While the slight difference in chlorine concentration of 4.1 wt% and 5.9 wt%, respectively, may suggest that there was an increase in the coverage of the film at 700 mV vs Ag/AgCl, as indicated in Figure 85e.

The electrode surface polarised at 500 mV vs Ag/AgCl was covered with a film which had a granular morphology. The largest diameter of 50 patina particles were measured manually using the SEM software resulting in an average diameter of 2.70 ± 0.84 μm. EDX analysis of this film also determined that it had a chlorine concentration of 25.4 wt%, which was greater than that formed at 300 and 700 mV vs Ag/AgCl, suggesting that the film was thicker with fewer X-rays being generated from the copper substrate. Furthermore, the difference in the film structure may also influence its colour producing a greener hue compared to than the other samples.

At 1000 mV vs Ag/AgCl a discontinuous film developed with a granular morphology had developed with a larger average grain size of 3.16 ± 1.10 μm and a higher concentration of chlorine of 32.5% than that found at 500 mV vs Ag/AgCl, suggesting that it formed in thicker films. In the areas where the film was not present the oxygen and chlorine concentrations were like that found at 200 mV vs Ag/AgCl, however the surface lacked the potentiostatically etched channels at the grain boundaries, suggesting that whole grains were actively being dissolved.

6.2.1.3.2 XRD analysis of the electrode surface

The potentiostatic polarisation of the copper electrodes at the various potentials resulted in the production of insoluble compounds which formed on the electrode

[218]

surface and found in the electrolyte. Once the 30-minute experiment was concluded the electrodes were immersed in fresh deionised water, to remove traces of sodium chloride, and dried prior to further analysis. The XRD analysis of the electrode surface was done using a multipurpose sample stage.

Figure 86 shows the XRD analysis of the electrode surface where, in addition to the major peaks of copper at 43.35° and 50.4°, small peaks associated with tenorite (CuO) were also present at each polarisation potential. According to the Pourbaix diagram (Figure 79) when polarising copper at 100 mV vs Ag/AgCl tenorite forms when the electrolyte pH was between 8.1 and 13, however at increasing polarisation potentials of between 200 and 1000 mV vs Ag/AgCl tenorite could be formed over a wider pH range of between 7.8 and 13. This suggests that there was a localised increase in alkalinity at the electrode surface allowing tenorite to precipitate onto the surface. At 100 and 200 mV vs Ag/AgCl no additional peaks were observed as the soluble $CuCl_2{}^-$ ions dissolve into the electrolyte, confirming the visual and SEM/EDX analysis of the surface where no visible films or increase in chlorine concentrations were detected.
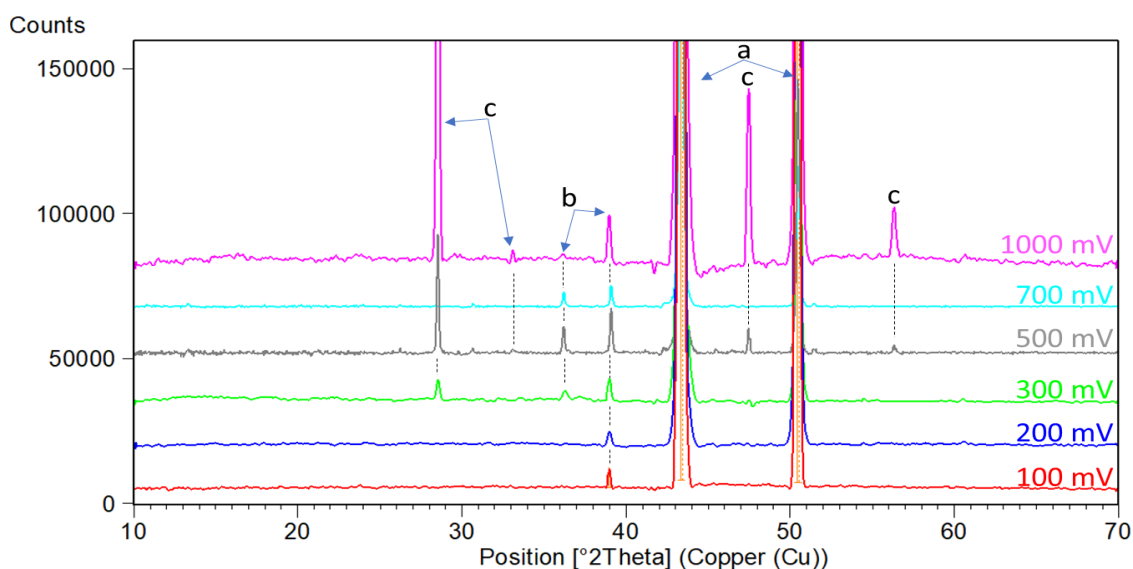
Figure 86 – Comparative XRD analysis of the compounds found on the electrode surface following anodic polarisation at 100, 200, 300, 500, 700 and 1000 mV vs Ag/AgCl for 30 minutes in a neutral 3.5% NaCl electrolyte at 25°C. Peaks labelled a = Cuprite, b = Tenorite and c = Copper (I) chloride.

However, XRD analysis of the chlorine-rich film formed on the electrode surface after potentiostatically polarising at 300, 500 and 1000 mV vs Ag/AgCl found additional peaks associated with copper (I) chloride ($CuCl$). This is known to be a precursor to the clinoatacamite phase and its presence on the electrode surface suggests that while the Pourbaix diagram indicates clinoatacamite should form at these potentials, it does not form directly on the electrode. It was however shown to precipitate out of the electrolyte, forming an insoluble particulate, as shown in the following section (Chapter 6.2.1.4). Therefore, it may be expected that when accelerating the patination of antifouling coatings either potentiostatically, or through other means, basic copper (I) chloride compounds would be expected to be present in the first instance followed by its complexation to clinoatacamite.

After potentiostatic polarisation at 700 mV vs Ag/AgCl a chloride-rich film was found with a similar weight percentage and appearance to that formed at 300 mV vs Ag/AgCl suggesting a similar XRD pattern would be expected. However, no peaks were detected associated with the copper (I) chloride film.

[220]

Figure 87 shows the particulate, captured in the filter paper after it had been rinsed with deionised water to remove traces of sodium chloride and dried. When polarising copper at 100 mV vs Ag/AgCl a golden coloured particulate was observed suggesting the formation of a copper oxide compound. At increasing polarisation potentials, the particulate colour changed forming a dark green compound at 200 mV Ag/AgCl a blue green compound at 500 and 700 mV vs Ag/AgCl and a green compound at 1000 mV vs Ag/AgCl. From the Pourbaix diagram (Figure 79a) it was shown that between 200 and 1000 mV vs Ag/AgCl a $Cu_2Cl(OH)_3$ compound may form. However, the variation in colour suggests that either different copper chloride compounds are forming or the concentration, size and/or shape of the particles are different.
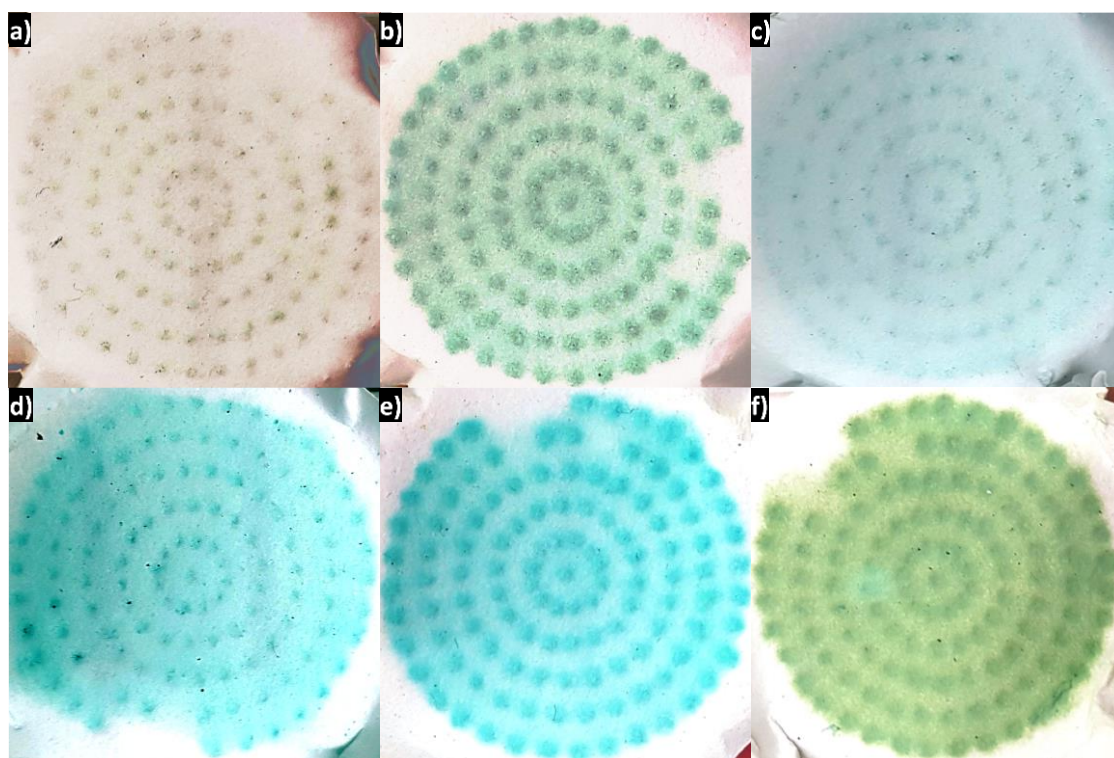
Figure 87 – Images of the filtered particulate collected following the 30-minute anodic potentiostatic polarisation of copper electrodes at a) 100 mV, b) 200 mV, c) 300 mV, d) 500 mV, e) 700 mV and f) 1000 mV vs Ag/AgCl

XRD analysis was performed to determine the compounds that had formed at the different polarisation potentials using the rotating stage set at 4 revs/s scanning over

an angular range of 10° to 60°. Due to the small volume that was produced the particulate was transferred to a backgroundless silicon wafer, for the XRD analysis.

Figure 88 shows an example of the comparison between the XRD traces of the particulate produced at the different polarisation potentials with Figure 89 showing the semi-quantitative analysis provided by the HighScore Plus analysis software.
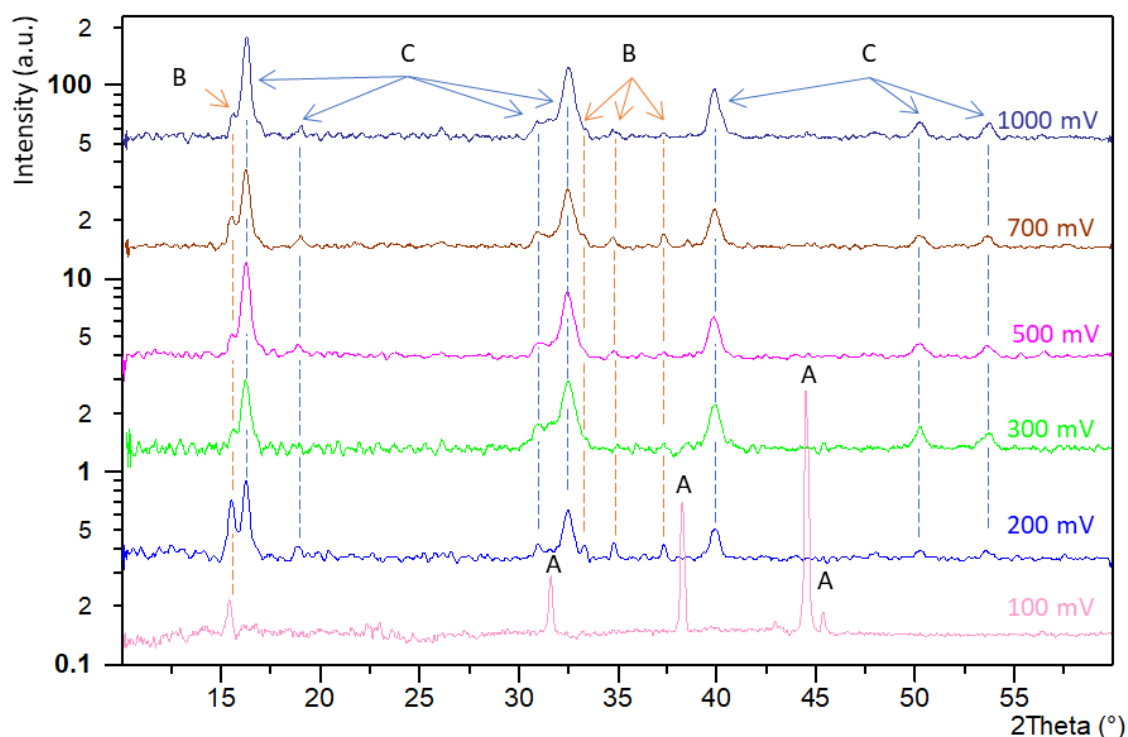
Figure 88 – Comparative XRD analysis of the compounds produced when polarising the copper electrode at different potentials in a pH 7, 3.5% NaCl electrolyte at 25°C. Peaks labelled A = Cuprite, B = Botallackite and C = Clinoatacamite.

Analysis of the filtered particulate determined the presence of cuprite and botallackite at 100 mV vs Ag/AgCl and botallackite and clinoatacamite at 200 to 1000 mV vs Ag/AgCl. Semi-quantitative analysis of the particulate formed at 100 mV vs Ag/AgCl determined that the formation of cuprite was the preferred reaction as it was detected in higher concentrations than the botallackite compound. According to the Pourbaix diagram $CuCl_2^-$ was stable at this potential and therefore the formation of cuprite occurs through the reaction between $CuCl_2^-$ and OH^- shown in Equation 39.

[222]

Of the three $Cu_2Cl(OH)_3$ phases botallackite is known to be first to crystallise with the lowest formation energy of $-1322.6\ kJ.mol^{-1}$. This phase is metastable and rapidly recrystallises to the other stable polymorphs of atacamite and clinoatacamite. The phases can form through two route the oxidation of cuprite to copper chloride, shown in Equation 41.

$$Cu_2O + 2H^+ + 2Cl^- \rightarrow 2CuCl + H_2O \qquad\qquad \textit{Equation 41}$$
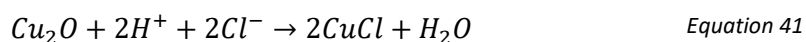
And the hydrolysis of copper chloride to botallackite through Equation 42, which in turn can help drive the conversion of cuprite to copper chloride.

$$4CuCl + O_2 + 2Cl^- \rightarrow 2Cu_2Cl(OH)_3 + 2H^+ + 2Cl^- \qquad \textit{Equation 42}$$
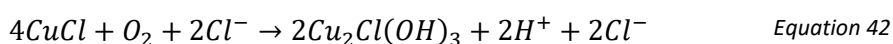
Or through the direct oxidation of $CuCl_2^{\ -}$ in the presence of dissolved oxygen in the electrolyte to botallackite through Equation 43

$$2CuCl_2^{\ -} + O_2 + 2H_2O \rightarrow Cu_2Cl(OH)_3 + 3Cl^- + OH^- \qquad \textit{Equation 43}$$
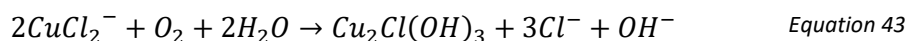
The formation of the two $Cu_2Cl(OH)_3$ phases at 200 to 1000 mV is unsurprising as between these potentials, according to the Pourbaix diagram, $Cu_2Cl(OH)_3$ should be stable, forming as a result of the hydrolysis of the $CuCl$ layer via the Equation 44.

$$4CuCl + O_2 + 4H_2O \rightarrow 2Cu_2Cl(OH)_3 + 2H^+ + 2Cl^- \qquad \textit{Equation 44}$$
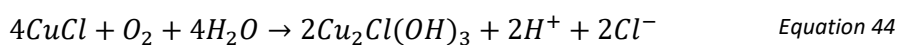
Or through the production of cuprous ions at the electrode surface, such as that seen in Equation 43, and their interaction with the electrolyte resulting Equation 45.
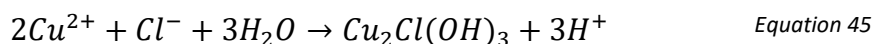
$$2Cu^{2+} + Cl^- + 3H_2O \rightarrow Cu_2Cl(OH)_3 + 3H^+ \qquad \textit{Equation 45}$$

Semi-quantitative analysis of the particulate determined that clinoatacamite was the major $Cu_2Cl(OH)_3$ and botallackite was the minor compound formed at potentials between 200 and 1000 mV vs Ag/AgCl. The analysis showed no clear trend to indicate

[223]

if the applied potentials affected the formation of botallackite with the highest levels being recorded at 200 and 700 mV of 20% and 12% respectively, and lower concentrations of 4-5% at 300, 500 and 1000 mV vs Ag/AgCl. Therefore, the different coloured particulate formed between 200 and 1000 mV vs Ag/AgCl must be associated with the concentration, size and/or shape of the particles as the blue-green patina colouration is caused by the $Cu\,(II)$ ion in the compounds, which acts as the colour forming ion (Leygraf et al., 2019).

In the study by Pollard et al. (1989) it was determined that botallackite was the preferred phase to form at low chloride concentrations, when more chloride was added to the system it recrystallised to atacamite, eventually clinoatacamite at higher concentrations, which became the only phase present after long exposure periods. In the current study, the exposure period was relatively short with only botallackite and clinoatacamite being detected with no evidence of atacamite. Similarly, Strandberg & Johansson (1998) only observed clinoatacamite in their laboratory experiments.

In the current study, the bulk chloride concentration should remain relatively stable during the polarisation of the copper electrode, tending to decrease as it is consumed during the formation of the insoluble $Cu_2Cl(OH)_3$ compound. The applied potential may cause anodic pitting to occur which may increase the chloride concentration at the electrode surface as chloride ions are drawn into the pit to maintain neutrality, allowing the metastable botallackite to recrystallise to clinoatacamite.
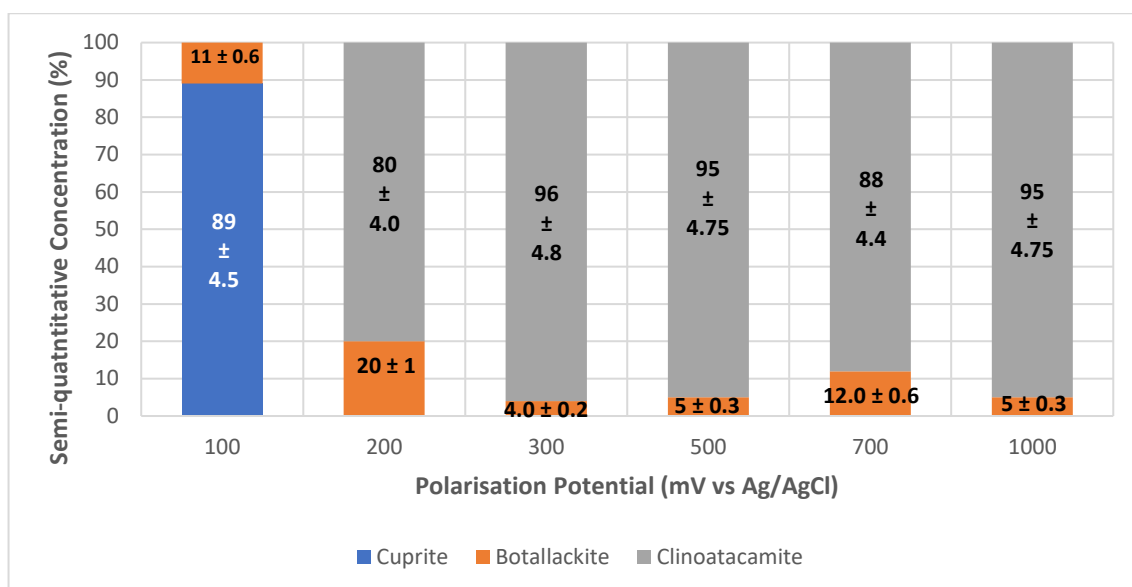
Figure 89 – Semi-quantitative XRD analysis of the compounds produced during the polarisation of the copper electrode in a pH 7, 3.5% NaCl electrolyte at 25 ℃ with a 95% confidence interval.

6.2.2   Effect Of Electrolyte Volume

As mentioned previously Pollard et al. (1989) observed that in electrolytes with high chloride ion concentrations clinoatacamite is the preferred $Cu_2Cl(OH)_3$ phase. In the current study the relative chloride concentration remained constant as a 3.5% NaCl electrolyte was used for each experiment with only the volume of the solution being altered. The copper electrode was polarised at 500 mV vs Ag/AgCl, as it had a Faradaic efficiency of 1, for 30 minutes. The insoluble particulate that had formed was filtered rinsed in deionised water and dried for XRD analysis (examples shown in Appendix 6), with the semi-quantitative analysis shown in Figure 90.
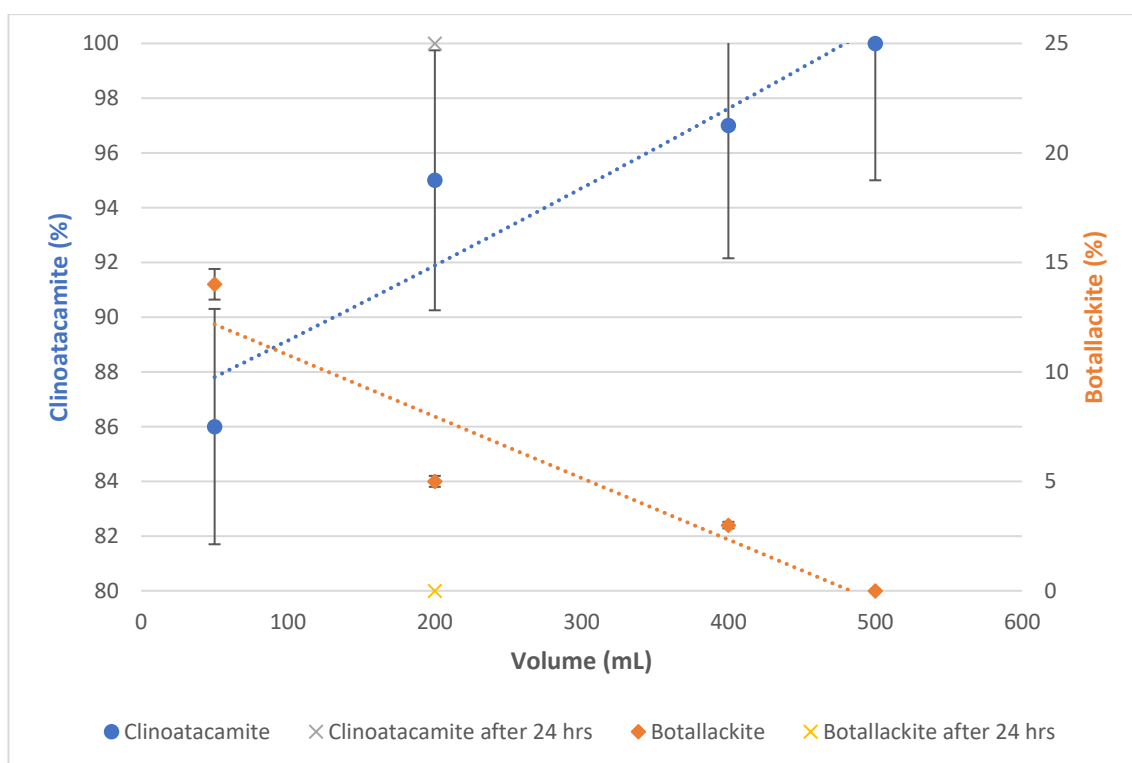
Figure 90 – Chart showing the semi-quantitative XRD analysis of the filtered particulate in various volumes of 3.5% NaCl electrolyte at 25℃ after polarising at 500 mV vs Ag/AgCl for 30 minutes.

An approximately linear reduction in the botallackite concentration was observed, as the electrolyte volume was increased, recrystalising to clinoatacamite. This may suggest that the preferred formation of clinoatacamite may be associated more with the total availability of the chloride ions in the electrolyte compared to copper ions

[226]

and not the relative concentration. For example, the ratio of copper to chloride ions in the 50 mL 3.5% electrolyte assuming a mass loss of 10.2 mg would be approximately 1:10, resulting in 14% botallackite being detected indicating fewer chloride ions were available when compared to the 500 mL where 10.5 g of chlorine was present resulting in a ratio of 1:103 and no botallackite being detected. Furthermore, after leaving the particulate formed in the 200 mL electrolyte for 24 hours, only clinoatacamite was detected, confirming similar observations made in other studies where clinoatacamite was the major $Cu_2Cl(OH)_3$ phase detected after extended exposure periods (Pollard et al., 1989; Strandberg & Johansson, 1998; Veleva et al., 1996).

6.2.3   Effect Of Sodium Chloride Concentration

As was found in Chapter 6.1.3.1 the polarisation of copper at different potentials results in the formation of an insoluble patina compound both on the electrode surface and within the 3.5% electrolyte. To observe what effect the chloride concentration has on the patination of copper two fixed potentials of 130 and 260 mV vs Ag/AgCl were selected and measured in triplicate. These potentials were determined to be within the pseudo-passive/film forming potential window following the analysis of the potentiodynamic polarisation experiments, and lie in the $CuCl_2^-$ and $Cu_2Cl(OH)_3$ stability domains (Figure 91), respectively, at pH 7 for the $Cu - Cl - H_2O$ system at 25°C. Each experiment was performed in 200 mL of electrolyte starting at pH 7, which was held at 25°C using a water bath throughout the 5-hour experiment with a plastic film covering to reduce evaporative losses.
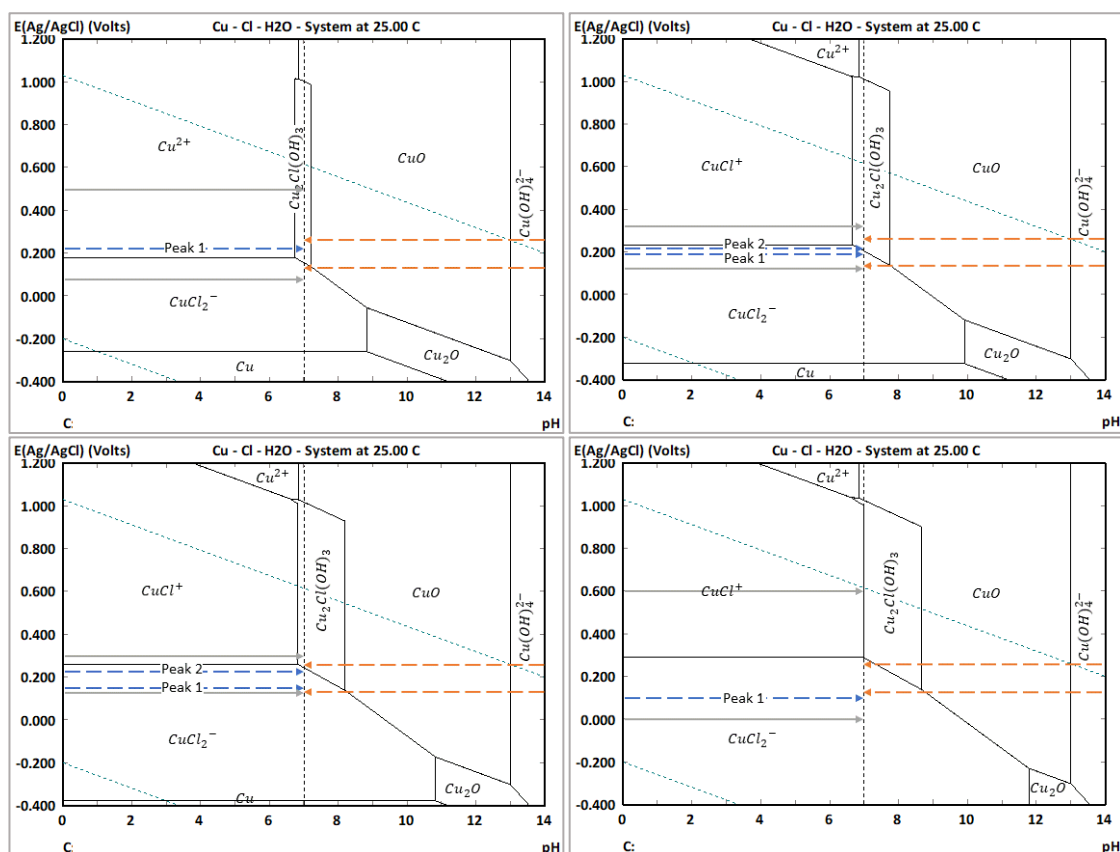
Figure 91 – Pourbaix diagrams produced using the HSC chemistry software for the 1% (top left), 3.5% (top right), 10% (bottom left) and 30% (bottom right) NaCl concentrations showing the potential ranges for the maximum pseudo-passive/film forming potential range (——▸), the average anodic peak potential taken from the potentiodynamic polarisation curves (— —▸) and the potentiostatic polarisation potential (— —▸). The vertical dashed line indicates the neutral potential.

6.2.3.1 Potentiostatic Polarisation Curves

The potentiostatic polarisation curves produced at 130 and 260 mV vs Ag/AgCl followed similar trends regardless of the applied potential (Figure 92 and 93, respectively). The 1%, 3.5% and 10% NaCl electrolytes were found to have an initial spike in current density within the first 60 seconds after which the current density dropped to a minimum, where it remained for a short incubation time, before climbing up as the salt film degraded, eventually reaching a relatively stable current density until the end of the experiment. However, for the 30% NaCl electrolyte and initial increase in current density was measured within the first 20 seconds after which the current remained relatively stable tending to decrease over the 5-hour polarisation period.

[228]
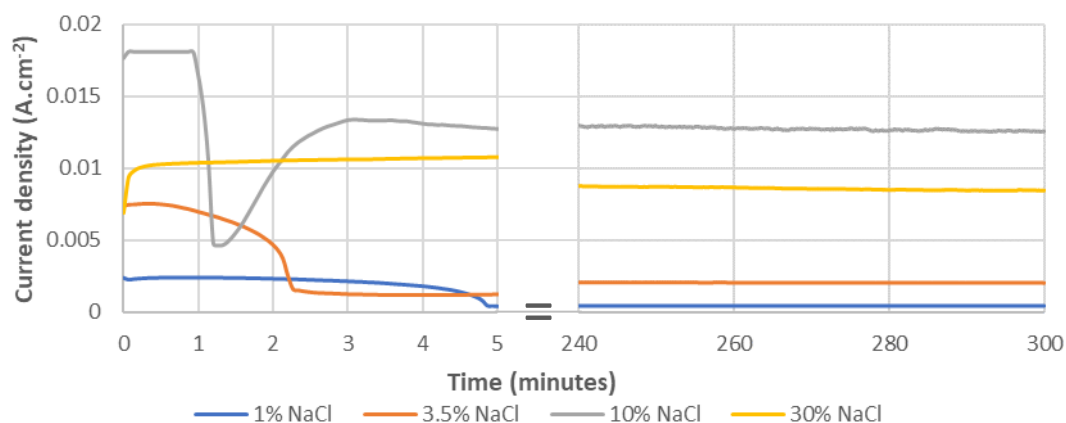
Figure 92 – Potentiostatic polarisation curves showing the effect of NaCl concentration on the current density of a copper electrode polarised at 130 mV vs Ag/AgCl within the first 15 and final 60 minutes
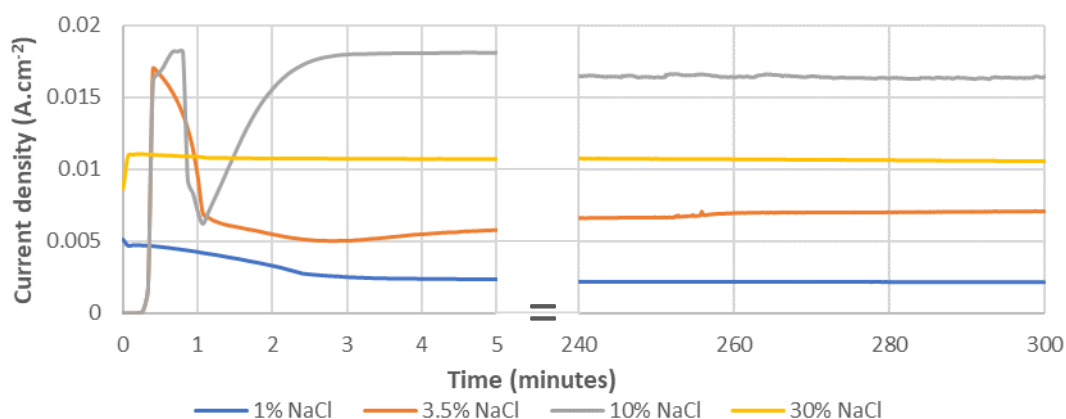
Figure 93 – Potentiostatic polarisation curves showing the effect of NaCl concentration on the current density of a copper electrode polarised at 260 mV vs Ag/AgCl within the first 15 and final 60 minutes

Furthermore, a linear increase in current density and therefore corrosion rate was recorded with increasing sodium chloride concentration up to 10%. While the current density recorded in 30% electrolyte was lower, resulting in a lower corrosion rate and therefore mass loss when compared to 10%, which is thought to be due to the Levich rule as discussed earlier (Chapter 6.1.1.2). Similar trends were also observed following the Tafel analysis (Chapter 6.1.2) where the 10% electrolyte was also found to have the highest current density and therefore the highest corrosion rate.

[229]

6.2.3.2 *Mass Loss*

Potentiostatic polarisation, resulted in the dissolution of the copper electrode where the mass loss was proportional to the applied potential. Figure 94 shows that there was a similar trend where a linear increase in mass loss was recorded with increasing chloride concentrations up to 30% NaCl, while the electrodes polarised at 130 mV vs Ag/AgCl experienced a lower mass loss than that found at 260 mV vs Ag/AgCl. Chico et al. (2005) also observed this phenomenon where the quantity of the corrosion products formed was proportional to the amount of chloride present in the electrolyte.
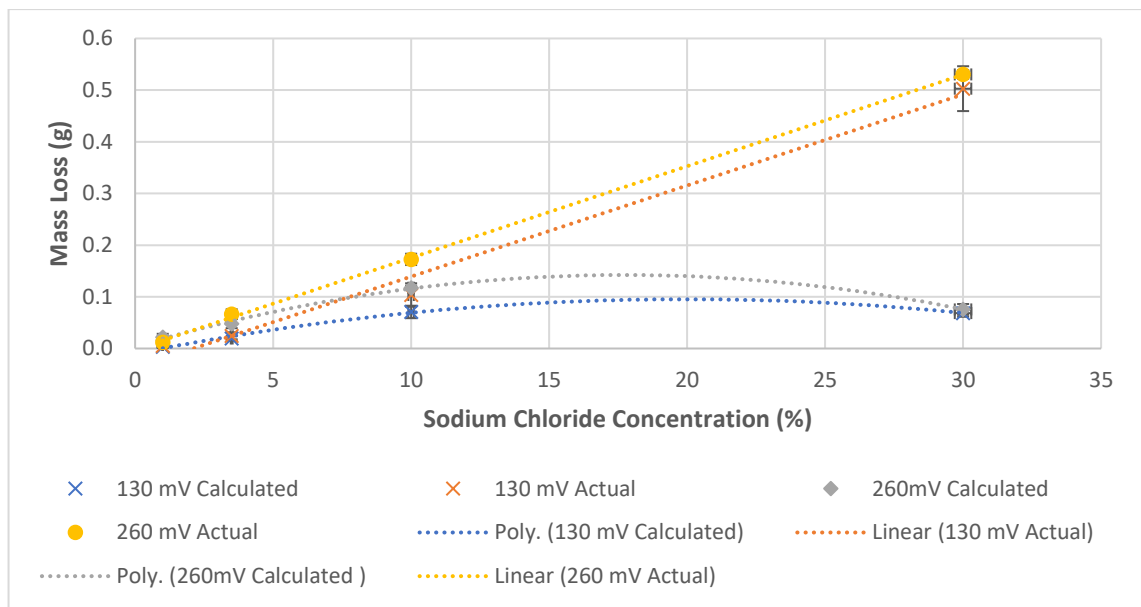
Figure 94 – Comparison of the theoretical and actual mass loss recorded after the 5-hour potentiostatic polarisation at 130 and 260 mV vs Ag/AgCl in the electrolytes with different NaCl concentrations.

However, when using the charge recorded over the polarisation period to determine the theoretical mass loss, and comparing it to the measured mass loss, a difference between the two values was observed. At low chloride concentrations a small difference between the two values was found, as both showed a linear relationship in mass loss with increasing chloride concentrations, up to 10% NaCl, with the actual mass loss being higher at all chloride concentrations. At 30% NaCl a large difference in

the mass loss was found where the actual mass loss followed the linear trend observed at lower chloride concentrations, reaching 0.50 ± 0.04 g and 0.53 ± 0.01 g, respectively. However, the calculated mass loss was approximately 7 times lower at 0.069 g and 0.076 g, respectively. The differences in the calculated and actual mass loss may be associated with the conductivity of the electrolyte as well as other corrosion processes that may be taking place that are not associated with the application of a potential due to the high concentration of chloride ions at the electrode surface.

The conductivity of an electrolyte represents its ability to carry electrical charge, which according to Arrhenius theory, is determined by the ions present in the electrolyte. Therefore, with increasing NaCl concentration more Na^+ and Cl^- ions would be present and therefore the conductivity was increased. Widodo et al. (2018) found a linear relationship between the sodium chloride concentration and conductivity. Therefore, in a highly conductive electrolyte such as that associated with the 10 and 30% NaCl the current required to pass the applied potential was reduced, which can decrease the accuracy of the theoretical mass loss calculations. Furthermore, the formation of the copper salt film formed at between 1 and 10% did not form at 30%, as the electrode surface was saturated with Cl^- ions, allowing a lower current to be passed as the electrode was dissolved.

6.2.3.3 Electrode Surface Analysis

The colour of copper patina has been shown to be dependent on the amount of patina that was present and its chemical composition, where a copper oxide has a red/brown to black colouration as the patina thickens. However, the colour of the patina was less dependent on the environment it was exposed to with Lopesino et al. (2018) and Vrsalović et al. (2018) showing a green-blue patina developed in a chloride rich environment while Fitzgerald et al. (1998) found a similar coloured compound in a sulphide rich environment. Leygraf et al. (2019) attributed the characteristic blue-green colour of the basic copper salts to the presence of the Cu^{2+} ions, which was present in all compounds found in the outer patina layer.
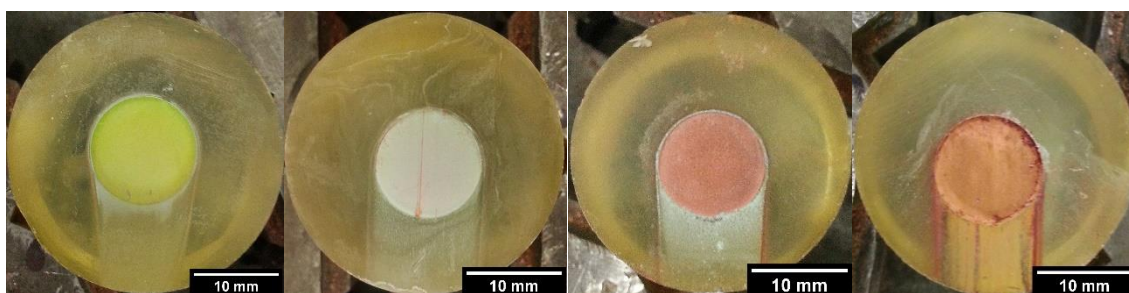
Figure 95 – Photographs of the electrodes, mounted centrally within a two-part epoxy, after polarisation at 260mV vs Ag/AgCl (bottom row) from left to right in 1%, 3.5%, 10% and 30% NaCl electrolytes.

Examination of the surface of the electrodes following the 260 mV vs Ag/AgCl polarisation (Figure 95) found that the colour of the patina changed depending on its chloride concentration. In the 1% electrolyte the patina was olive green, whereas in the 3.5% NaCl was the typical green-blue associated with the $Cu_2Cl(OH)_3$ compound. The substrate was not visible on these electrodes suggesting that the patina was, according to Leygraf et al., (2019), thicker than 12 μm. In the 10% electrolyte this blue-green patina was still present however more of the copper substrate was visible indicating and was therefore thinner when compared to the 3.5% electrolyte. At 30% no green-blue patina was visible on the electrode, which had receded some distance

into the epoxy mount indicating high levels of copper dissolution, which would have prevented the patina from settling on the electrode surface. Analysis of the patina formed in the different electrolytes is shown in Chapter 6.2.3.4.

6.2.3.4 *Filtered Particulate*

The potentiostatic polarisation of copper at both 130 and 260 mV vs Ag/AgCl in the electrolytes containing different concentrations of sodium chloride resulted in the formation of an insoluble particulate (Figures 96 and 97) similar to that observed following the polarisation at different potentials (Chapter 6.2.1.3.1). Following the filtering, rinsing, and drying procedures the colour of the particulate was found to be influenced by the compounds that were present. In the 1% electrolyte, at both potentials, the $Cu_2Cl(OH)_3$ compounds dominated, with clinoatacamite being the major phase present (Figure 98), resulting in the blue-green colouration. Cuprite was found to be produced as the sodium chloride concentration was increased resulting in the formation of the red colouration as the ratio of cuprite to clinoatacamite increased from approximately 1:0.30 and 1:0.08 in the 3.5% electrolyte to 1:4.70 and 1:3.76 when polarising at 130 and 260 mV vs Ag/AgCl, respectively.
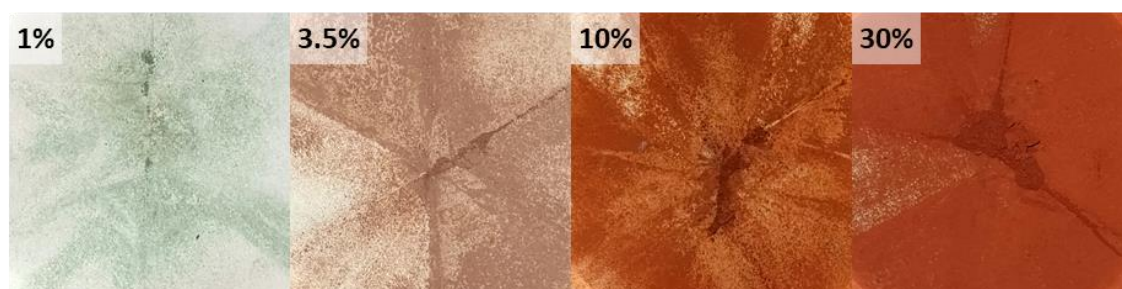
Figure 96 – Filtered particulate following the potentiostatic polarisation of the copper electrode at 130 mV vs Ag/AgCl in the electrolytes containing the different sodium chloride concentrations.

[233]
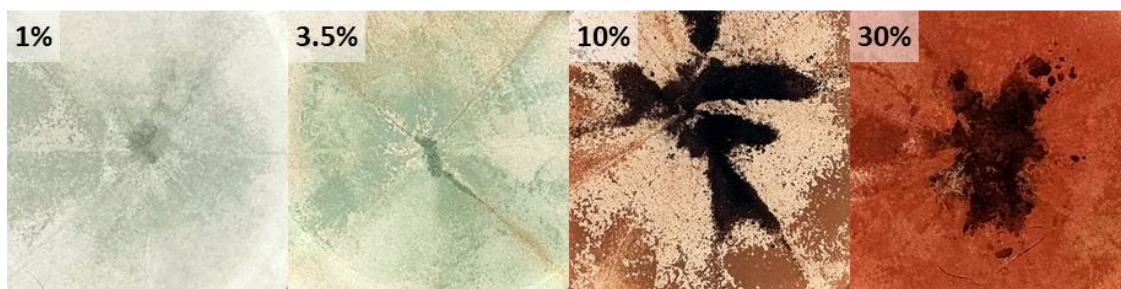
Figure 97 – Filtered particulate following the potentiostatic polarisation of the copper electrode at 260 mV vs Ag/AgCl in the electrolytes containing the different sodium chloride concentrations.

When polarising at 130 mV vs Ag/AgCl the formation of $CuCl_2{}^-$ ions apparently stable according to the Pourbaix diagram. Cu^+ ions from on the electrode surface at this potential, which can react with the Cl^- in the electrolyte to form $CuCl_2{}^-$, through Equations 13 and 38.
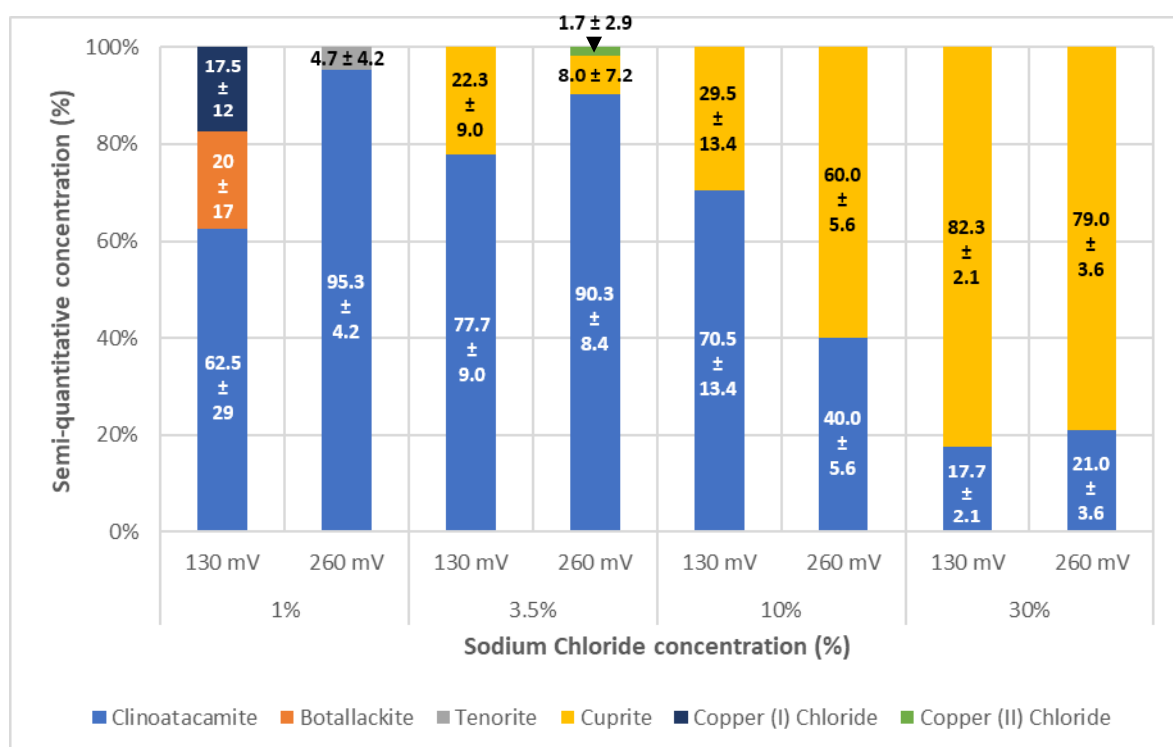
Figure 98 – The average semi-quantitative XRD analysis of the insoluble particulate filtered from the electrolyte following potentiostatic polarisation at 130 and 260 mV vs Ag/AgCl

The $CuCl_2{}^-$ ions can then crystallise to $Cu_2Cl(OH)_3$ through Equation 43. While this explains the formation of the $Cu_2Cl(OH)_3$ compound is does not account for the formation of the different phases where botallackite was only detected in the 1% electrolyte 130 mV vs Ag/AgCl, while clinoatacamite was detected in all electrolytes at

[234]

both potentials. Where the semi-quantitative analysis (Figure 98) of the particulate determined that, while clinoatacamite was the major phase present, high levels of botallackite were also detected. Botallackite is described to be the first $Cu_2Cl(OH)_3$ phase to form which can rapidly recrystallise to more stable copper chloride phases under certain conditions.

Pollard et al. (1989) and Sharkey & Lewin (1971) showed that the concentration of $CuCl_2^-$ ions can influence the phases produced, where concentrations above 0.01 M botallackite was recrystallised to other $Cu_2Cl(OH)_3$ phases. In the 1% electrolyte the mass loss was determined to be relatively small and therefore a low concentration of $CuCl_2^-$ could form compared to the other solutions, allowing botallackite to remain in the 1% electrolyte.

The chloride concentration of the electrolyte was also seen to influence the recrystallisation of botallackite. Pollard et al. (1989) observed that at chloride concentrations greater than $0.2\,M$, botallackite rapidly recrystallises to clinoatacamite. In the 1% electrolyte the chloride concentration was at $0.171\,M$ and therefore a low recrystallisation rate of botallackite to clinoatacamite would be observed allowing both to be detected after the 5-hour polarisation.

Furthermore, copper (I) chloride and botallackite were detected in approximately equal concentrations. The copper (I) chloride phase is the precursor to the formation of $CuCl_2^-$ as seen in Equations 13 and 38. However due to the relatively low concentration of chloride in the electrolyte the recrystallisation to $CuCl_2^-$ was depressed, allowing $CuCl$ to be present in the particulate.

[235]

According to the Pourbaix diagram the precipitation of the $Cu_2Cl(OH)_3$ compound may be expected when polarising at 260 mV vs Ag/AgCl. This direct precipitation results in the faster formation of the $Cu_2Cl(OH)_3$ phase when compared to the 130 mV vs Ag/AgCl therefore allowing more time for the botallackite phase to recrystallise to clinoatacamite. At higher potentials the formation of the Cu^{2+} ion was preferred (Strehblow et al., 2001) resulting from the oxidation of the copper electrode through Equation 2, or the oxidation of Cu^+ ions through Equation 46.

$$Cu^+ = Cu^{2+} + e^- \qquad \text{\textit{Equation 46}}$$

When the concentration of Cu^{2+} ions at the electrode surface was high enough $Cu_2Cl(OH)_3$ can form through Equation 45. Tenorite may also precipitate should the production of $Cu_2Cl(OH)_3$ be slow enough and the electrolyte contain sufficient OH^- ions through Equation 47

$$Cu^{2+} + 2OH^- = CuO + H_2O \qquad \text{\textit{Equation 47}}$$

Recrystallising to $Cu_2Cl(OH)_3$ through Equation 48.

$$2CuO + Cl^- + 2H_2O \rightarrow Cu_2Cl(OH)_3 + H^+ \qquad \text{\textit{Equation 48}}$$

Further analysis found that the electrode mass increased linearly as the chloride concentration was increased, with the polarisation potential also influencing the mass loss. The semi-quantitative XRD analysis confirmed that as the chloride concentration was increased the relative concentration of clinoatacamite reduced while the levels of cuprite increased. Using the mass loss of the electrode and the semi-quantitative XRD analysis of the phases present the mass of the cuprite and clinoatacamite phases could be estimated (Figure 99). It was found that the chloride concentration affected the amount of cuprite and clinoatacamite that had formed in the electrolytes where an increase in sodium chloride concentration resulted in an increase in copper phases.

[236]

Similar concentrations of cuprite were detected after polarising the copper electrode at 130 and 260 mV vs Ag/AgCl in the 1% (0 mg and 0 mg, respectively), 3.5% (5.7 mg and 5.3 mg, respectively) and 30% (414 mg and 419 mg, respectively) electrolytes. However, in the 10% electrolyte the mass of the cuprite phase produced at 130 mV was less cuprite than that formed at 260 mV resulting in the curves shown in Figure 99.
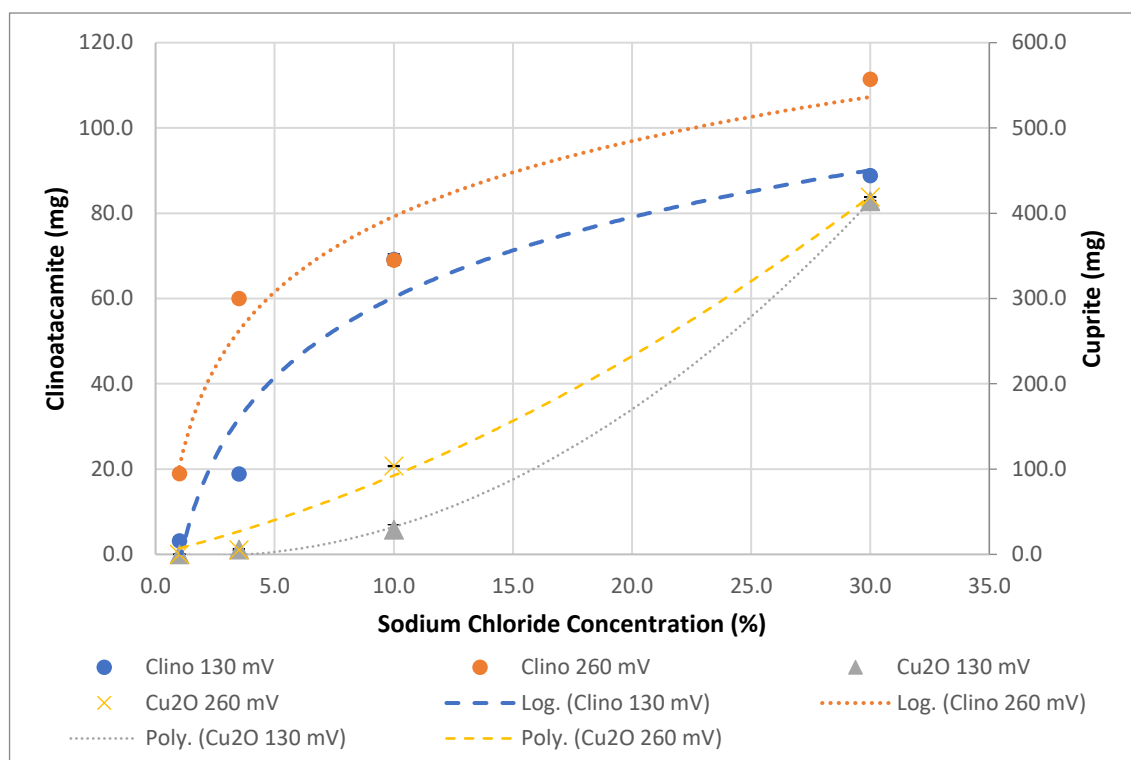
Figure 99 – The estimated mass of the cuprite and clinoatacamite phases based on the total mass loss and the semi-quantitative analysis. The error bars are hidden by the marker.

Analysis of the clinoatacamite phase found that it continued to increase with chloride concentration following a logarithmic trend. This suggests that while an increase in chloride concentration accelerated the production of copper ions, as the dissolution of the copper electrode dominates while the precipitation of clinoatacamite becomes more difficult. This could be due to the consumption of chloride ions from the electrolyte or due to a patina film forming on the electrode surface. This allows the excess copper ions to enter the electrolyte by travelling through the porous patina film at increasing concentrations, depending on the chloride concentration, which were

[237]

converted to cuprite when they reacted with the OH^- ions in the electrolyte through Equation 49.

$$2Cu^{2+} + 2OH^- \rightarrow Cu_2O + H_2O$$ *Equation 49*
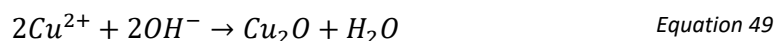
While the Pourbaix diagram shows the thermodynamic stability ranges for different phases it does not show the speed at which the phases form. This can be seen when comparing the particulate formed in the 3.5% electrolytes when polarising at 100-300 mV vs Ag/AgCl for 30 minutes compared to that formed when polarising at 130 and 260 mV vs Ag/AgCl for 5 hours. Botallackite and clinoatacamite compounds were detected after polarising for 30 minutes, while after 5 hours clinoatacamite and cuprite were the dominate phases. This confirms that metastable botallackite readily converts to the more stable clinoatacamite phase over time. The presence of cuprite, in the particulate formed over 5 hours, may suggest that the free chloride ions have been consumed quickly by the formation of copper chloride phases allowing the copper ions release from the electrode surface to precipitate out as cuprite or the speed of Cu^{2+} was greater than the complexation to other copper chloride species.

6.3 Summary

6.3.1 Potentiodynamic Polarisation

The potentiodynamic polarisation experiments scan rate was optimised at 2 mV.s^{-1} producing a clearly defined curve, displaying evidence of secondary reductions in current density in the anodic portion of the curve, in the presence of chloride ions.

Of the three variables investigated, the chloride concentration was found to have the greatest influence over the potentiodynamic polarisation curves where a 1% NaCl concentration shifted of the E_{corr} to more electronegative values. This trend continued with increasing chloride concentrations up to 30%. The presence of chloride (up to 10% NaCl) also moved the anodic and cathodic portions of the curve to higher current densities, indicating increased corrosion rates. This suggests that higher chloride concentrations would result in the acceleration of copper patination.

Pseudo-passive regions were observed in chloride containing electrolytes, up to 10%, with a reduction in current density in the anodic portion of the curve, associated with the production of Cu^+ and Cu^{2+}. However, a reduction in the anodic and cathodic current densities was found in the 30% electrolyte, while a stable current density was recorded when the potential increased above the passivation potential, suggesting that the electrode was in dynamic equilibrium. Under these conditions the formation of a stable patina layer would be unlikely as the surface is constantly being dissolved, resulting in a large concentration of patina compound within the electrolyte.

The pH of the electrolyte had minimal effect on the polarisation curves especially with increasing chloride concentrations. Changes to the shape of the active corrosion region of the anodic portion of the curve were observed when an inflection found in the pH 7

[239]

and 10 electrolytes, associated with the formation of Cu_2O/CuO layers, was not seen in the pH 4 electrolyte which may be due to their solubility at this pH, as indicated by the Pourbaix diagrams.

In the chloride containing electrolytes an increase in the electrode activity was observed with increasing temperature where the E_{Corr} value shifted to more electronegative values while the current density of the cathodic and anodic curves were increased. The increase in temperature also affected the formation of the inflection noted in the active corrosion portion of the anodic curve, while at higher temperatures it was not present. Furthermore, the pseudo-passive region also reduced in size with increasing temperature with a constant current density, similar to the 30% electrolytes, becoming visible in the 10% electrolyte at high temperatures. This indicates that temperature can also play a role in the acceleration of copper patination.

Tafel analysis of the polarisation curves determined that the 10% NaCl electrolyte had consistently the highest corrosion rates and therefore the highest patination rate. Furthermore the pH of the electrolyte also enhance the corrosion with those at pH 10 having the highest rates overall.

6.3.2   Potentiostatic Acceleration Of Copper Patination

The potentiostatic polarisation of copper allowed for several variables to be considered which may influence the speed and type of patina compound that may form under laboratory testing. Using the Pourbaix diagram produced for the $Cu - Cl - H_2O$ system at 25°C in at 3.5% (0.599 M) NaCl a series of potentials were selected to observe the patination of copper at an accelerated rate and to determine whether

the applied potential can affect the compounds that are formed. It was found that the potentiostatic polarisation of copper was able to accelerate patina formation of complex blue-green copper compounds being detected after 30-minute polarisation. Two $Cu_2Cl(OH)_3$ polymorphs were found when polarising copper within its equilibrium potential window, i.e., between 200 and 1000 mV vs Ag/AgCl, where the major phase of clinoatacamite and minor phase of botallackite were detected. The potentiostatic polarisation potential did not significantly influence the semi-quantitative concentration of these phases with 300 mV, 500 mV and 1000 mV vs Ag/AgCl all detecting between 4% and 5% botallackite. While at 200 and 700 mV vs Ag/AgCl botallackite was detected at 20% and 12%, respectively. This indicates that while potentiostatic polarisation can accelerate clinoatacamite formation, the exposure time is also a factor that needs to be considered.

The polarisation potential influenced the mass loss and therefore the amount of patina that was produced. A similar trend was observed when comparing the actual and theoretical mass loss which peaked and then reduced at 700 and 1000 mV vs Ag/AgCl, respectively. This reduction in mass loss may be associated with the production of oxygen at the electrode surface consuming a proportion of the applied electrons while introducing an insulating layer reducing the conductivity of the copper anode. Therefore potentiostatic polarisation should be performed at potentials less than 700 mV vs Ag/AgCl to maintain the efficiency of the process.

The amount of botallackite produced was influenced by the electrolyte volume with relatively high concentrations being detected at 50 mL reducing to 0% at 500 mL suggesting that the botallackite formation was influenced by the ratio of copper to

[241]

chloride ions where 1:<100 allows botallackite to be present in addition to clinoatacamite while 1:>100 produces only clinoatacamite. This may explain why botallackite is rarely observed on copper samples exposed to the marine environment (Pollard et al., 1989) and was not detected on the paint flakes removed from marine vessels (Chapter 4.2.1), where the infinite number of chloride ions available means that it can readily transform to clinoatacamite. Furthermore, the transient nature of botallackite was also displayed where it was shown to recrystallise as clinoatacamite after leaving it in the electrolyte for 24 hours.

The effect of sodium chloride concentration and Cu^+ or Cu^{2+} production was also considered. This was determined by potentiostatic polarising copper electrodes in the different electrolytes, at 25°C and pH 7, at the potentials where the two anodic peaks within the pseudo-passive region are known to release high concentrations of Cu^+ or Cu^{2+}, i.e. 130 and 260 mV vs Ag/AgCl. The shape of the potentiostatic polarisation curves produced a similar shape to those produced previously where the maximum and then minimum current density was recorded within first 5 minutes of polarisation, before climbing to reach a stable current density for the remainder of the experiment.

The magnitude of the current density increased with sodium chloride concentration with the highest current densities, and therefore theoretical mass loss, being recorded in the 10% electrolyte, with a reduction being observed at 30%, thought to be due to the Levich rule. However, a linear increase in the actual mass loss was recorded up to 30%. This divergence in mass loss may be a result of an increase in electrolyte conductivity and/or due to additional corrosion processes taking place at the electrode surface that are not related to the application of the potential.

XRD analysis of the copper compounds produced after the potentiostatic polarisation confirmed that clinoatacamite was produced in increasing amounts at higher chloride concentrations, plateauing after 10%. While polarising at 260 mV vs Ag/AgCl tended to also enhance the clinoatacamite concentration. However pure clinoatacamite was not formed with additional compounds of botallackite, copper (I) chloride and tenorite being found in the 1% electrolyte and cuprite in the 3.5%-30% electrolytes. The amount of cuprite increased with chloride concentration, dominating the filtered particulate at 10% and 30%, suggesting the electrode surface was dissolving faster than the rate of clinoatacamite formation. While the production of Cu^+ or Cu^{2+} expected at approximately 130 mV and 260 mV vs Ag/AgCl, respectively, did not greatly influence the formation of the copper compounds.

The results of the potentiostatic polarisation suggest that short term polarisation at between 200 mV and 700 mV vs Ag/AgCl in a 1% or 3.5% pH 7 electrolyte at 25°C, followed by a 24-hour immersion in the same electrolyte, would produce relatively high concentrations of a pure clinoatacamite compound, such as that found on the paint flakes removed from marine vessels (Chapter 4.2.1) and observed by various authors on copper exposed to the marine environment (Lindner, 1988; Nunez et al., 2005; Strandberg & Johansson, 1998; Veleva et al., 1996; Veleva & Farro, 2012).

Chapter 7: Application Of Experimental Techniques To Accelerate Patina Formation On Antifouling Coatings.

7.1 Long Term Immersion and Evaporation Testing

The analysis of the patina formed on antifouling paint flakes that were removed from in-service vessels (Chapter 4) determined that clinoatacamite was the most common phase to form, which following the Pourbaix analysis, was determined to develop in near neutral sodium chloride electrolytes. The OCP, potentiodynamic polarization and Tafel analysis determined that the corrosion of copper was most active in the 10% NaCl electrolyte regardless of pH or temperature (Chapter 6). However, to confirm that the patination of the antifouling coatings was also influenced by the NaCl concentration and temperature, additional immersion and evaporation testing was required. The following sections will detail the long-term immersion and evaporation testing used to assess the patination rate of cuprite rich antifouling coating BQA 644 containing booster biocides and a modified BQA 644 coating containing only the cuprite biocidal pigment, while copper and cuprite were included as controls.

7.1.1 Visual Examination Of Patina Formation

Photographs of the cuprite powder, BQA 644 coating, BQA 644 cuprite only coating and the copper coupon where taken, through the electrolyte, daily to document the changes in their colour, which can indicate when new compounds had formed. Tables 17-24 show a selection of the photographs from the initial exposure of the samples to the electrolyte and then every 24 hours for the first 96 hours and then weekly after 168 hours up to 672 hours, for the immersion test cells. This was repeated for the evaporation cells for either 672 hours at 25°C or until the electrolyte had fully evaporated, typically 384-408 hours for the samples at 45°C.

[244]

7.1.1.1 *Patination Of Copper Coupons*

Tables 17 and 18 show example images detailing the progression of patination observed on the surface of the copper coupons after being exposed to the different electrolytes under immersion and evaporating conditions at 25°C and 45°C.

The patination of the copper coupons initiated with the formation of a brown layer associated with a copper oxide, typically cuprite (FitzGerald et al., 2006; Fuente et al., 2008; Graedel et al., 1987; Rice et al., 1981). A brown oxide layer formed on the coupons exposed to the 0% electrolyte under both immersion and evaporation conditions. Under immersion conditions at 25°C the coupon developed brown spots after 336 hours, which remained visible, with the brown colouration increasing in intensity until the experiment was terminated. Similar features were observed under evaporating conditions after 336 hours, the whole surface had patinated after 672 hours, suggests an enhancement in the patination characteristics. This may be associated with an increase oxygen as it can diffuse through the electrolyte to the coupon surface more quickly as the electrolyte volume was reduced, accelerating the patination rate (Liao et al. 2011 and Venkatraman et al. 2011).

An increase in temperature to 45°C enhanced the patination of the copper coupon where a brown compound was observed in the immersion cell after 24 hours, covering the surface after 336 hours. Similarly at 45°C, under evaporation conditions a brown patina compound was found to develop after 48 hours with a uniform layer visible after 168 hours increasing in thickness and uniformity after 336 hours where the majority of the substrate can no longer be seen.

Table 17 – Table showing images of the copper coupons coated sample when exposed to 0%, 1%, 3.5%, 10% and 30% NaCl electrolytes at 25°C and 45°C after 0, 24, 48, 72, 96, 168, 336, 504 and 672 hours under immersion conditions. The coupons are approximately 10 x 10 mm.

NaCl	Copper coupon – Immersion – 25°C										Copper coupon – Immersion – 45°C									
%	0	24	48	72	96	168	336	504	672	End	0	24	48	72	96	168	336	504	672	End
0																				
1																				
3.5																				
10																				
30																				

Table 18 – Table showing images of the copper coupons coated sample when exposed to 0%, 1%, 3.5%, 10% and 30% NaCl electrolytes at 25°C and 45°C after 0, 24, 48, 72, 96, 168, 336, 504 and 672 hours under evaporating conditions. The coupons are approximately 10 x 10 mm.

NaCl	Copper coupon – Evaporation – 25°C										Copper coupon – Evaporation – 45°C									
%	0	24	48	72	96	168	336	504	672	End	0	24	48	72	96	168	336	408	End
0																			
1																			
3.5																			
10																			
30																		-	

[246]

When exposing the coupons to the 1% and 3.5% electrolytes they formed a brown patina after 24 hours, typically associated with cuprite, which continued to thicken with time eventually forming the blue-green patina associated with copper chloride compounds, occurring after 96 and 168 hours at 25°C, respectively. However, at 45°C a blue-green patina did not develop on the coupons in the 1% electrolyte, which was visible in the 3.5% electrolyte after 336 hours. Upon conclusion of the testing the samples were rinse in deionised water to remove traces of sodium chloride, this was confirmed following XRD analysis where no sodium chloride peaks were detected in the patterns produced from the different coupons (Appendix 8c, Figures 163 and 164). Further inspection of the coupons found that the blue-green patina layer remained on the coupons exposed at 25°C while at 45°C it was not visible. This suggests that the blue-green patina formed at 25°C was more strongly adhered to the coupon that that formed at 45°C. While similar trends were also observed under evaporating conditions.

In the 10% electrolyte under both immersion and evaporation conditions at 25°C a light brown coloured surface patina formed after 24-hour exposure after 168 hours a blue-green patina had developed on top of the brown patina, which thickened with increasing immersion time. This confirms the duplex nature of patina formation where, in chloride rich environments observed in various studies (Leygraf et al., 2019; Opila, 1987; Watanabe et al., 2007; Zhang et al., 2014), with an inner layer of cuprite with an outer layer of copper chloride. When rinsing the coupons, a small amount of patina was lost from the surface from the sample in the immersion cell, whereas in the evaporation cell approximately 50% of the blue-green patina had been removed.

[247]

At 45°C in the 10% electrolyte the surface underwent mild patination with some brown discolouration of the coupon observed after 24 hours, which remained consistent throughout the experiment. A small amount of blue-green patina had developed on the surface after 336 hours, however most of the patina was found within the test cell away from the coupon. This suggests that the rate of copper ion generation from surface was greater than the patination rate of the coupon. Similar characteristics were observed on the coupon in the evaporation cell at 45°C where no visible patina was found during the experiment. This may be due to the increase in activity at the coupon surface at 45°C as evidenced by the increase in OCP with temperature recorded in Chapter 5.2.2, enhancing the surface dissolution observed in Chapter 5.4.2.4, which prevented the copper chloride precipitate compounds from adhering strongly to the copper substrate.

Furthermore, an increase in activity was recorded in the 30% electrolyte were the OCP was more electronegative than at 10%, while Chapter 5.4.2.4 also displayed the high activity of the copper coupon when exposed to the 30% electrolyte resulting in the formation of crystallographic etch pits and general dissolution of the surface, preventing the surface from patinating. After 336 hours, some blue-green spots were visible in the immersion cell, increasing marginally by the end of the experiment. However, in the evaporation cell no patina was observed until the salt crystals had been rehydrated allowing a brown layer to be observed.

7.1.1.2 *Patination of Cuprite Pigment*

Table 19 shows the progression of patination observed when exposing the cuprite powder to the different sodium chloride electrolytes under immersion conditions at 25°C and 45°C, over the 672-hour period. Following the testing, the powder was filtered from the different electrolytes, rinsed with deionised water to remove traces of sodium chloride and dried, before being compressed into the powder sample mount for XRD analysis.

At 25°C the cuprite pigment exposed to the 0% electrolyte remained unaffected throughout the experiment with some darkening observed after 672 hours. When inspecting the cuprite powder in the sample holder for XRD analysis this had a similar colouration to the starting powder. However, at 45°C darkening of the pigment occurred after 168 hours forming a brown colouration. As the exposure time progressed it became darker having an almost black appearance after 672 hours. The darkening of the pigment suggests that a new compound had formed. As only copper ions, hydrogen and oxygen were present in the cell it is likely to be tenorite, which typically has a black appearance (Webmineral, 2012). When this was mixed with the red of the cuprite it may have resulted in the dark brown appearance observed on the samples compressed into the power sample mount. While further XRD analysis of the powder would confirm the compounds present in the sample (Chapter 7.1.2.2.1).

When sodium chloride was present in the electrolyte, the cuprite powder tended to develop a blue-green colouration as the immersion time progressed. This colouration is known to be caused by the presence of Cu^{2+} ions (Leygraf et al., 2019) and suggests the formation of a copper chloride compound. At increasing sodium chloride

concentrations, the rate of colour change and therefore the speed of cuprite powder patination also increased. Where the cuprite developed a blue-green colouration after 672 hours, 504 hours, 96 hours and between 48 and 72 hours in the 1%, 3.5%, 10% and 30% electrolytes, respectively. When inspecting the rinsed and dried powder following the immersion testing it was found to form a blue compound with increasing intensity at higher chloride concentrations, suggesting that more cuprite powder was converted to a copper chloride compound. However, not all the cuprite powder had patinated, with clusters of the powder remaining unaffected. These clusters may have formed due to the high surface tension of the powder in the electrolyte preventing it from dispersing evenly. Furthermore, the original red colour was visible in the XRD mount samples especially in the 10% and 30% electrolytes.

Similar observations were found at 45°C with clusters of cuprite powder failing to patinate, however the general patination rate of the cuprite powder was increased with the blue-green colouration being visible after 504 hours, 168 hours, 48-72 hours, and 48 hours in the 1%, 3.5%, 10% and 30% electrolytes, respectively. This suggests an increase in the patination rate with increasing temperature and sodium chloride concentrations. However, the powder was found to have a green colouration following the rinsing and drying stage with similar colours being observed in the 1% and 3.5%, and 10 and 30% electrolytes, while at 25°C the patina had an equivalent bluer colouration regardless of the sodium chloride concentration, which became more intense due to the increase in the patina concentration. This suggests that the sodium chloride concentration had a minimal effect on the colour of the patina, with it mainly influencing the amount of cuprite powder that had been converted to a copper

[250]

chloride compound. While the temperature and therefore speed of the reaction was also shown to influence its colour producing a patina dominated by the blue colouration at 25°C.

Furthermore, the blue and green dominating colour of the patina was observed when analysing the patina formed following the potentiostatic polarisation at different potentials (Chapter 6.1.3.4), however the XRD analysis did not detect any significant differences in the compounds that were produced. Therefore, it is likely that although they have different colours, similar compounds were formed at 25°C and 45°C in the different sodium chloride containing electrolytes, with the size, shape or quantity of the compound influencing its colour.

Table 19 – Table showing images of the cuprite samples when exposed to 0%, 1%, 3.5%, 10% and 30% NaCl electrolytes at 25°C and 45°C after 0, 24, 48, 72, 96, 168, 336, 504 and 672 hours under immersion conditions. The height of the images equals 45 mm unless otherwise indicated.

[252]

Table 20 shows the images of the patination of cuprite powder under evaporating conditions where an acceleration in patination was observed when compared to the samples under immersion conditions. As observed under immersion conditions, the cuprite powder in the 0% electrolyte at 25°C remained unaffected maintaining the original red colouration, while at 45°C a dark down patina was found.

A green patina developed in the 1% electrolyte which was intermixed with the cuprite pigment after 336 hours, becoming more prevalent after 504 hours and bluer after 672 hours. This patina colour was not found under immersion conditions. Furthermore, an increase in patination rate was observed in the evaporation cell forming a blue-green patina at earlier times when compared to the immersion conditions of 336 hours, 72 hours, and 24 hours in the 3.5%, 10% and 30% NaCl electrolytes, respectively.

A similar increase in the patination rate was observed at 45°C where a blue-green patina formed after 384 hours, 168-336 hours, 24 hours, and 48 hours in the 1%, 3.5%, 10% and 30% sodium chloride electrolytes, respectively, with the electrolyte evaporated from the cell between 384 and 408 hours. The accelerated patination under evaporating conditions may be associated with the constant increase in sodium chloride concentration and oxygen availability as the electrolyte volume reduced, increasing the likelihood that copper and chloride ions would interact with each other and therefore precipitate a copper chloride patina.

The patina colour was influenced by the NaCl concentrations where at 25°C the cuprite powder developed a similar green colouration in the 1% and 3.5% electrolytes, while at 10% and 30% a green-brown and brown coloured patina had formed respectively. At 45°C green patina had developed increasing in intensity with NaCl concentration.

[253]

Table 20 – Table showing images of the cuprite samples when exposed to 0%, 1%, 3.5%, 10% and 30% NaCl electrolytes at 25°C and 45°C after 0, 24, 48, 72, 96, 168, 336, 504 and 672 hours under evaporating conditions. The height of the images equals 45 mm unless otherwise indicated.

NaCl	Cuprite – Evaporation – 25°C											Cuprite – Evaporation – 45°C										
%	0	0	24	48	72	96	168	336	504	672	XRD mount	0	0	24	48	72	96	168	336	384	408	XRD mount
0																					-	
1																						
3.5																						
10																					-	
30																					-	

[254]

7.1.1.3 *Patination of the BQA 644 Coating*
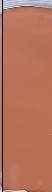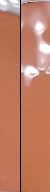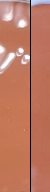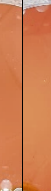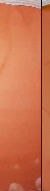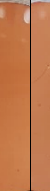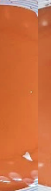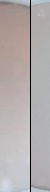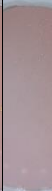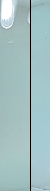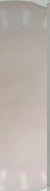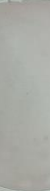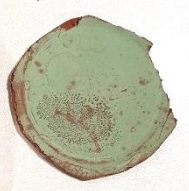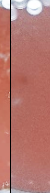
Table 21 shows a selection of images of the BQA 644 coated samples under immersion conditions up to 672 hours, at 25°C and 45°C. The colour of the coating remained unaffected in the 0% electrolyte indicating no patina had formed. While in the 1% electrolyte the coating colour remained consistent, appearing marginally lighter after 672 hours, which may indicate the start of the coating degradation and/or patination.

A blue compound uniformly covered the surface of the coating, at both temperatures, as the sodium chloride concentration was increased. At 25°C, in the 3.5% electrolyte, the rich red coating colour faded after 24 hours, developing a blue colouration after 168 hours, increasing in intensity between 336 and 504 hours. At 45°C the coating also developed a blue tone after 24 hours which continued to develop to 168 hours and remained consistent to the end of the immersion period, suggesting an acceleration in the patination of the coating with increased temperature.

In the 10% electrolyte, at both temperatures, the coating developed a blue-green colouration after 24 hours, which became more intense with exposure time. A qualitative visual assessment after 672 hours suggested that the patina had formed a thicker layer when compared to the other electrolytes. Chapters 6.1.1.2 and 6.1.2 showed that the 10% electrolyte had the highest corrosion rate which may also be associated with the highest patination rate and therefore increased patina thickness.

A loosely adhered patina compound was shown in the 30% electrolytes initially developed after 24 hours at 25°C, while after 672 hours a qualitatively thin blue-green patina layer was visible on dried samples after 672 hours, which was not visible at 45°C. This suggests that there was a reduction in the copper ion release rate from the coating, as the cuprite powder readily patinated under similar conditions.

[255]

Table 21 – Table showing images of the BQA 644 coated sample when exposed to 0%, 1%, 3.5%, 10% and 30% NaCl electrolytes at 25 °C and 45 °C after 0, 24, 48, 72, 96, 168, 336, 504 and 672 hours under immersion conditions. The height of the images equals 45 mm.

NaCl	BQA 644 – Immersion – 25°C											BQA 644 – Immersion – 45°C										
%	0	0	24	48	72	96	168	336	504	672	Final	0	0	24	48	72	96	168	336	504	672	Final
0																						
1																						
3.5																						
10																						
30																						

[256]

A qualitative visual assessment of the BQA 644 under evaporation conditions determined that the coating patinated quickest in the 3.5% electrolyte, at both temperatures, forming a thicker layer than that formed in the other electrolytes as the coating substrate was still visible on these samples (Table 22). The coating surface was uniformly covered with a blue-green patina at 25°C with a green patina forming at 45°C, both patinas remained intact following the cleaning procedure.

Patination of the coatings was also found to initiate more quickly when compared to the immersion testing patina had developed after 168 hours, 48 hours, 24 hours, and 24 hours in the 1%, 3.5%, 10%, and 30% electrolytes, respectively. A further increase in patina initiation rate was observed at 45°C with the blueing of the coating occurring after 72 hours, 24 hours, 24 hours, and 24 hours, respectively.

It was determined that blue-green patina layer found on Paint Flakes 1 and 2, 4 – 10 and 12 – 14 (Appendix 1) were a similar colour when compared to the patina formed on the coatings following the immersion testing in neutral 3.5% and 10% electrolytes, at 45°C. While the richer green colour of Paint Flakes 3 and 11 were a closer match to the 10% electrolyte at 25°C. However, under evaporating conditions the colour of Paint Flakes 1 and 2, 4 – 10 and 12 – 14 matched the patina formed in the 3.5% and 10% electrolytes, while Paint Flakes 3 and 11 match that of the 3.5% electrolyte at 45°C.

This indicates that laboratory testing of cuprite containing antifouling coatings should be conducted in a 10% electrolyte when assessing the likelihood of patination. This also confirms similar trends observed when immersion testing cuprite powder as well as the electrochemical testing (Chapter 6) where the copper patination rate peaks in the 10% electrolyte at elevated temperatures.

[257]

Table 22 – Table showing images of the BQA 644 coated sample when exposed to 0%, 1%, 3.5%, 10% and 30% NaCl electrolytes at 25°C and 45°C after 0, 24, 48, 72, 96, 168, 336, 384, 408 and 504 and 672 hours under evaporating conditions. The height of the images equals 45 mm.

NaCl	BQA 644 – Evaporation – 25°C											BQA 644 – Evaporation – 45°C										
%	0	0	24	48	72	96	168	336	504	672	Final	0	0	24	48	72	96	168	336	384	408	Final
0																					-	
1																					-	
3.5																						
10																					-	
30																					-	

[258]

7.1.1.4 *Patination of the Modified BQA 644 Coating*

A uniform blue-green patina compound layer developed on the modified BQA 644 coating surface when immersed in the different NaCl electrolytes, (Table 23). At 25°C it had a lighter hue when compared to that formed at 45°C. The rate at which the coatings patinated depended on the temperature and NaCl concentration within the cell. Under each exposure condition in the 0% electrolyte, the coating remained unaffected with only some slight discolouration observed once the electrolyte was removed and the cell dried.

A small region patinated on the coating exposed to the 1% electrolyte at 25°C, which initiated after 96 hours. At 45°C the coating was found to patinate more uniformly developing a blue-green layer which thickened with exposure time, masking the red colour of the modified BQA 644 coating. However, at 25°C under evaporating conditions the coating remained unaffected (Table 24). While at 45°C discolouration of the coating was accelerated, initiating after 24 hours, and developing a blue hue after 48 hours, becoming more intense with exposure time finishing at 360 hours.

With increasing chloride concentrations, the time taken for the patina on the coating to initiate was reduced under both testing conditions, while the higher temperatures further enhanced its formation. At 45°C the patination of the samples exposed to the 3.5% and 10% electrolytes initiated after 24 hours, producing a uniform blue patina for the first 168 hours. With increasing exposure time, the colour of the patina changed to a greener shade after 336 hours, which intensified until the end of the exposure. A similar colour change at 25°C under immersion conditions however the final patina colour was brighter than that formed at 45°C.

[259]

Table 23 – Table showing images of the modified BQA 644 coated samples when exposed to 0%, 1%, 3.5%, 10% and 30% NaCl electrolytes at 25°C and 45°C after 0, 24, 48, 72, 96, 168, 336, 504 and 672 hours under immersion conditions. The height of the images equals 45 mm.

NaCl	Modified BQA 644 – Immersion – 25°C											Modified BQA 644 – Immersion – 45°C										
%	0	0	24	48	72	96	168	336	504	672	Final	0	0	24	48	72	96	168	336	504	672	Final
0																						
1																						
3.5																						
10																						
30																						

[260]

Table 24 shows the effect of the evaporating conditions on the patination of the modified BQA 644 coating where a similar greening of the patina layer was observed under at 45°C in the 3.5% and 10% electrolytes. However, this was duller and formed at an accelerated rate when compared to that found in the immersion cells of between 96-168 hours, and 168-336 hours, respectively. At 25°C, the patina initiated similarly after 24 hours however, it took longer for the blue/blue-green patina to develop.

In the 30% electrolyte a loose blue patina product had formed in the immersion and evaporation cells at both temperatures, which upon conclusion of the testing was easily removed during the rinsing of the cell and rehydration of the sodium chloride crystals. However, in all but the immersion cell at 25°C a thin patina layer remained once dried.

The patina formed on the surface of the modified BQA 644 coating in the immersion cell at 25°C following the 672 hours testing it was found to have formed a similar blue-green colour regardless of the sodium chloride concentration. This trend was also observed at 45°C producing a slightly bluer patina than that found at 25°C suggesting its colour was not influence by the sodium chloride concentration. Further similarities were also observed in the evaporation cell where a similar blue-green patina colour developed in the 3.5% and 10% electrolytes at 25°C, while at 45°C a bluer patina was observed with a lighter patina formed in the 1% and 3.5% electrolytes when compared to 10% and 30%.

Both the BQA 644 and the modified BQA 644 coatings were exposed to the equivalent environmental conditions for approximately equal exposure times and volumes, using the same parent electrolyte. However, it was found that the colour of the patina that

had formed was different with the modified BQA 644 coatings tended to be brighter with a richer blue and green colouration. The modified BQA 644 coating contains the same base formula of the BQA 644 however it only contains the cuprite pigment. This would have resulted in a higher concentration of cuprite at the coating surface and therefore a greater availability of copper ions in the electrolyte when compared to the BQA 644. Several booster biocidal pigments are also present in this coating which are released from the coating surface and may interact with each other and the chloride in the electrolyte. This suggest that while the different chloride containing electrolytes can initiate copper chloride patina formation in antifouling coatings, the coating formula or the availability of copper ions may influence its colour.

Table 24 – Table showing images of the modified BQA 644 coated samples when exposed to 0%, 1%, 3.5%, 10% and 30% NaCl electrolytes at 25°C and 45°C after 0, 24, 48, 72, 96, 168, 336, 504 and 672 hours under immersion conditions. The height of the images equals 45 mm.

NaCl	Modified BQA 644 – Evaporation – 25°C											Modified BQA 644 – Evaporation – 45°C									
%	0	0	24	48	72	96	168	336	504	672	Final	0	0	24	48	72	96	168	336	360	Final
0																					
1																					
3.5																					
10																					
30																				-	

[263]

7.1.2 XRD Analysis Of The Copper Patina

The following section reports the semi-quantitative XRD analysis of the 99.9% pure copper coupons (Figure 102), the cuprite powder (Figure 103), the BQA 644 antifouling coating (Figure 104), and the modified BQA 644 containing only the cuprite biocidal pigment (Figure 105), after they had been exposed to different electrolytes at 25°C and 45°C. The XRD analysis was performed weekly, up to 672 hours, for the samples under immersion conditions, showing how the concentration of detected phases changed with time. The samples undergoing evaporating conditions were measured either after 672 hours or once the electrolyte had evaporated, depending on which came first.

Following the testing, the electrolyte was filtered and the cell rinsed with deionised water to remove traces of sodium chloride, capturing the loose cuprite powder and any dislodged patina from the copper coupon or coatings. The evaporation test cells were also rehydrated with deionised water to dissolve the sodium chloride crystals that had formed, allowing the surface of the coatings and coupons to be examined. This electrolyte was also filtered to ensure no loose patina was lost.

7.1.2.1 *XRD Traces*

Figure 100 shows an example of the XRD data captured on each of the following: BQA 644 coating, modified BQA 644 coating, metallic copper coupon and cuprite powder after exposure to the neutral 3.5% electrolyte for 672 hours under immersion conditions at 25°C. Further examples of the XRD traces are shown in Appendix 8. Clinoatacamite was determined to be the major copper chloride phase present on each sample.
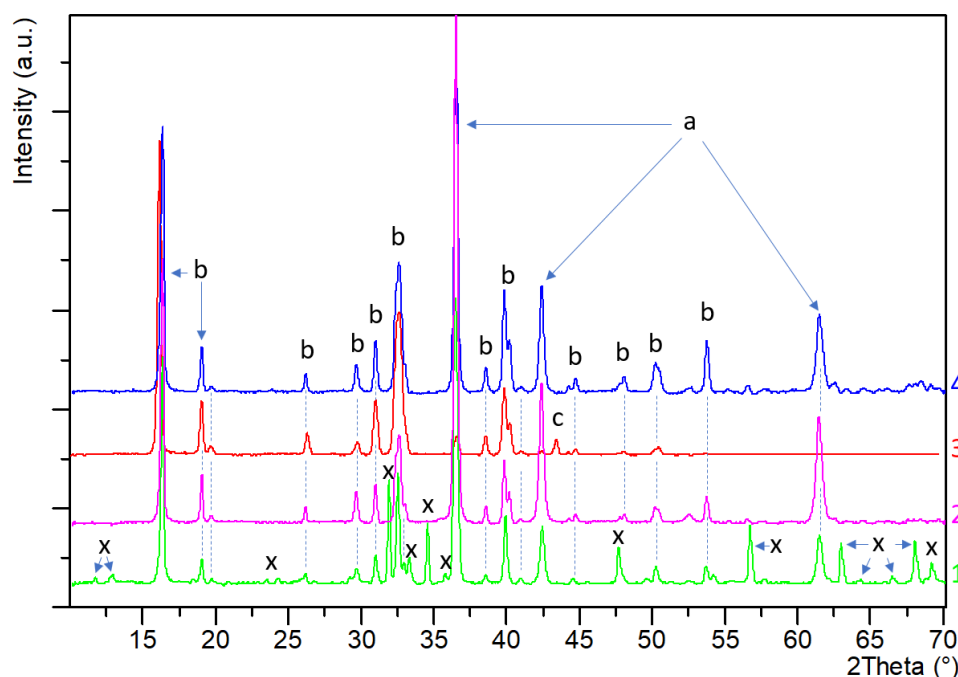
Figure 100 – Example XRD traces following the 672 hour immersion period at 25 ℃ in the 3.5% electrolyte for samples 1) BQA 644, 2) Modified BQA 644 coating, 3) copper coupon and 4) cuprite powder. The peak labels are identified as a = cuprite, b= clinoatacamite, c = copper and x = paint pigment.

Further detailed analysis of the major peaks associated with the clinoatacamite phase (Figure 101) formed on the BQA 644 and the modified BQA 644 coated samples found that the clinoatacamite phase had two different profiles. The shape of the XRD profiles remained consistent regardless of temperature or sodium chloride concentration suggesting that the clinoatacamite phases that had formed were independent of these variables. The only difference between the two coatings was the availability of cuprite pigment at the surface. In the BQA 644 coating the major pigment is cuprite, however it also contains high concentrations of other pigments such as zinc oxide, zineb and other bulking pigments including haematite. The presence of these other pigments can separate the cuprite pigment, lowering the overall concentration at the surface. While competing reactions may also be occurring such as the zinc ions from the zinc oxide pigment may compete with the copper ions to form a chloride compound. Whereas in the modified BQA 644 coating, only cuprite was present, resulting in higher concentrations of cuprite at the surface with only copper ions being released into the

[265]

electrolyte. This may result in the formation of greater concentrations of $CuCl_2^-$-, known to influence the $Cu_2Cl(OH)_3$ compounds that are formed (Pollard et al., 1989). Therefore, it can be surmised that the formation of the two clinoatacamite phases was due to the amount of cuprite available at the surface and hence the number copper ions present in the electrolyte. The high concentrations of copper ions released from the modified BQA 644 resulted in the formation of the broad and additional peaks between 32° and 33° (Figure 101) when compared to the BQA 644 samples. This may also be confirmed where the relatively high concentration of Cu^{2+} available when testing the copper coupon and cuprite powder also produced an XRD pattern which matched that of the modified BQA 644 samples.

The intensity of the clinoatacamite peaks tended to be highest in the 10% electrolytes followed by the 3.5%, 1% and 30% electrolytes for both coatings, suggesting that the sodium chloride concentration affected the amount of clinoatacamite that was formed, with the highest concentrations or density found in the 10% electrolytes.

The peaks observed on the modified BQA 644 coating were associated with the reference phase present in the PDF-2 database (reference I.D. 01-086-1391). Whereas the clinoatacamite peaks detected on the BQA 644 coating did not follow the pattern associated with the clinoatacamite phases present in the PDF-2 database. It was also missing the peak intensities of 100% at 15.5°, and 58% at 17.65°, associated with the presence of botallackite or atacamite, respectively, and therefore are unlikely to be these phases. However, it closely matched the clinoatacamite phase observed in the RRUFF database (reference I.D. R100198.9). Both clinoatacamite compounds were also observed on the paint flakes removed from in-service marine vessels, confirming the suitability of the laboratory testing to reproduce the natural patina compounds.

[266]
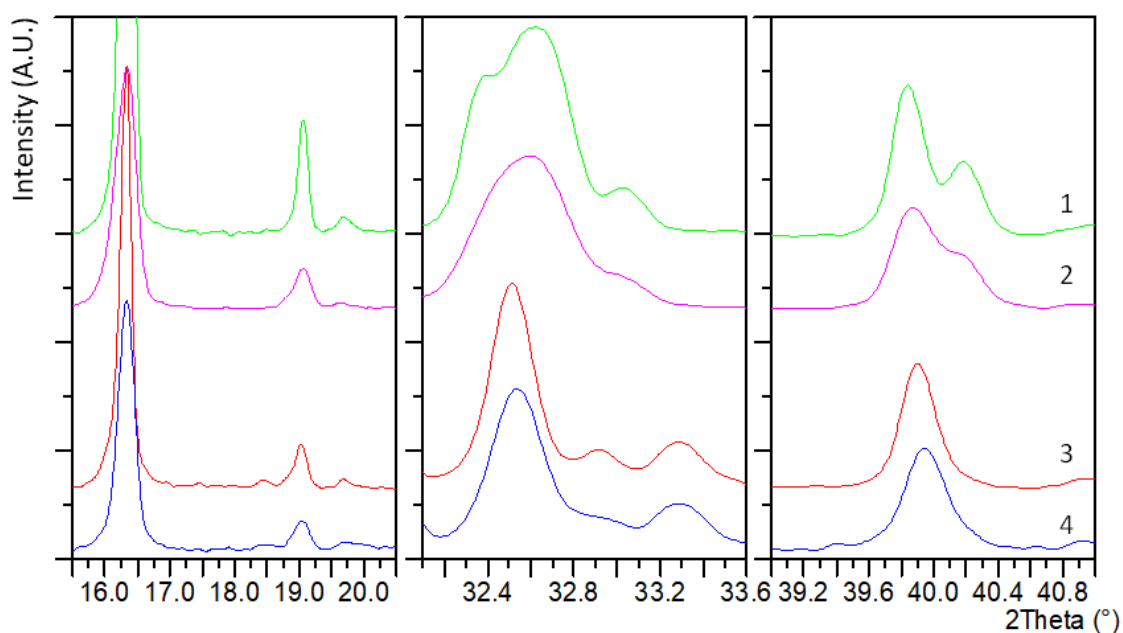
Figure 101 – Example XRD traces following 672-hour immersion in a 3.5% NaCl at 25 (1 and 3) and 45℃ (2 and 4) comparing the major peaks associated with the clinoatacamite phase detected on the modified BQA 644 coating containing only the cuprite pigment (1 and 2) and BQA 644 coating (3 and 4).

Table 25 shows the crystallographic parameters associated with the two clinoatacamite phases. Both phases were closely matched, however, the size and volume of the R100198.9 phase crystal unit cell was larger when compared to the 01-086-1391 phase. This larger lattice may allow the X-rays to penetrate deeper into the patina structure changing the position, intensity, and breadth of some of the refracted peaks.

Table 25 – Clinoatacamite crystallographic parameters retrieved from reference pattern 01-086-1391 from the PDF-2 database and R100198.9 from (RRUFF™, N/D)

Parameter	Clinoatacamite pattern	
	01-086-1391	R100198.9
Crystal system	Monoclinic	Monoclinic
a (Å)	6.1440	6.1452
b (Å)	6.8050	6.8372
c (Å)	9.1120	9.1593
α (°)	90	90
β (°)	99.55	99.56
γ (°)	90	90
Volume (Å³)	375.69	379.42

7.1.2.2 *Semi-Quantitative XRD*

Further interrogation of the XRD data produced from the cuprite powder, copper coupon, BQA 644 and the modified BQA 644 coatings was performed to produce a semi-quantitative analysis of the phases present following the testing. The immersion and evaporation cells used to hold the cuprite powder ensured that only particles smaller than the pores in the filter paper (<11μm) could be lost from further analysis, while powder XRD allowed most of the filtered sample to be positioned beneath the X-ray beam, allowing for an accurate semi-quantitative analysis to be performed. However, in the cells containing the copper coupon, the BQA 644 and the modified BQA 644, a loosely adhered porous copper patina formed on the surface of these samples, which could be easily washed away as the electrolyte was removed from the cell or during the rinsing procedure used to remove traces of sodium chloride. While both the electrolytes from the cells and the rinse water was filtered, the removal of the patina from the surface of the samples could lower the accuracy of the semi-quantitative analysis compared to the cuprite samples, however this data can be used within each sample set to observe changes at the surface. Therefore, greater emphasis should be on the phases present and not necessarily the concentration.

7.1.2.2.1 Copper Coupon

Due to the formation of a thin patina layer on the surface of the copper coupon, the XRD analysis was performed using a 5° glancing angle. This reduces the signal from the copper substrate while increasing the signal from any potential copper patina layers.

When exposing the oxide stripped copper coupons to the 0% electrolyte (deionised water) under immersion conditions, where the electrolyte volume was maintained at 25°C over the exposure time, the surface developed an orange hue suggesting the

[268]

formation of a thin oxide layer. XRD analysis of the coupons at 168 hours confirmed that a cuprite layer had formed on the surface, at 16 ± 0.8%, with similar levels being observed at 45°C of 17 ± 0.85% (Figure 102a). With increasing immersion time, the amount, and therefore thickness and/or coverage, of cuprite continued to grow at both temperatures, where at 25°C a relatively slow increase in cuprite was recorded reaching 35 ± 1.75% after 672 hours while at 45°C higher concentrations were detected at each inspection period reaching 54 ± 2.7% after 672. This suggests that cuprite formation was accelerated at higher temperatures on the copper coupon, which was also associated with more active OCP (Chapter 5.2.2.2), and higher corrosion rates (Chapter 6.1.2) observed at higher temperatures.

Liao et al. (2011) surmised that the corrosion of copper was controlled by the oxygen diffusion, which is the rate determining step, especially with short immersion times. EL-Mahdy (2005) also observed that the diffusion of oxygen through the electrolyte and its reduction on the copper surface was increased as the thickness of the electrolyte layer was reduced. A similar enhancement in the patination rate was observed between the two cells where an oxygen gradient may have formed in the immersion cell due to the stagnant conditions where the solution was not agitated or replenished, resulting in oxygen saturation at the electrolyte-atmosphere boundary layer. Small droplets of deionised water (<1mL) were added to the electrolyte, approximately every 48 hours, to maintain the electrolyte volume. This may slightly agitate the electrolyte and introduce a small amount of dissolved oxygen into the electrolyte, which was unlikely to affect the overall gradient.

However, under evaporating conditions, the path of oxygen diffusion through the electrolyte was reduced as the volume was reduced, enhancing oxygen reduction at

the coupon surface, and therefore accelerating the patination rate. Where the highest levels of cuprite were detected on the coupons exposed to the 0% electrolyte at 25°C of 90 ± 4.5%, approximately 2.6x greater than that found in the immersion cell. Furthermore at 45°C once the electrolyte had fully evaporated after 360 hours 40 ± 2% cuprite was detected, which was at a similar level to that found after 336 hours in the immersion cell of 43 ± 2.15%. This suggests that at 45°C the electrolyte was evaporated at a faster rate than the patination rate.

Clinoatacamite developed when sodium chloride was present, with higher concentrations tending to form at 25°C (Figure 102b-e). Semi-quantitative XRD analysis of the copper coupons under immersion conditions exposed to the 1% electrolyte determined that cuprite was the first compound to develop, with it being detected at 168 hours and remaining the sole compound at 336 hours at both temperatures. With increasing exposure time, the clinoatacamite compound was detected while the copper and cuprite levels reduced, suggesting a thickening of the clinoatacamite layer peaking after 672 hours with 96 ± 4.9% being detected and traces of copper and cuprite also being present. However, at 45°C clinoatacamite concentration had reduced from 55 ± 2.75% at 504 hours to 20 ± 1% at 672 hours, highlighting the probable loss of clinoatacamite from the coupon surface, possibly through the cleaning operations.

In high sodium chloride electrolytes, the amount and speed of copper patination also increases with similar levels of clinoatacamite of 79 ± 3.95% and 80 ± 4.0%, and a reduction in cuprite of 7 ± 0.35% and 1 ± 0.05% in the 3.5% and 10% electrolytes, respectively, after 168 hours. Peaks in the clinoatacamite concentration were detected after 336 hours, 504 hours and 672 hours in the 3.5% and 10%, respectively at 25°C.

[270]
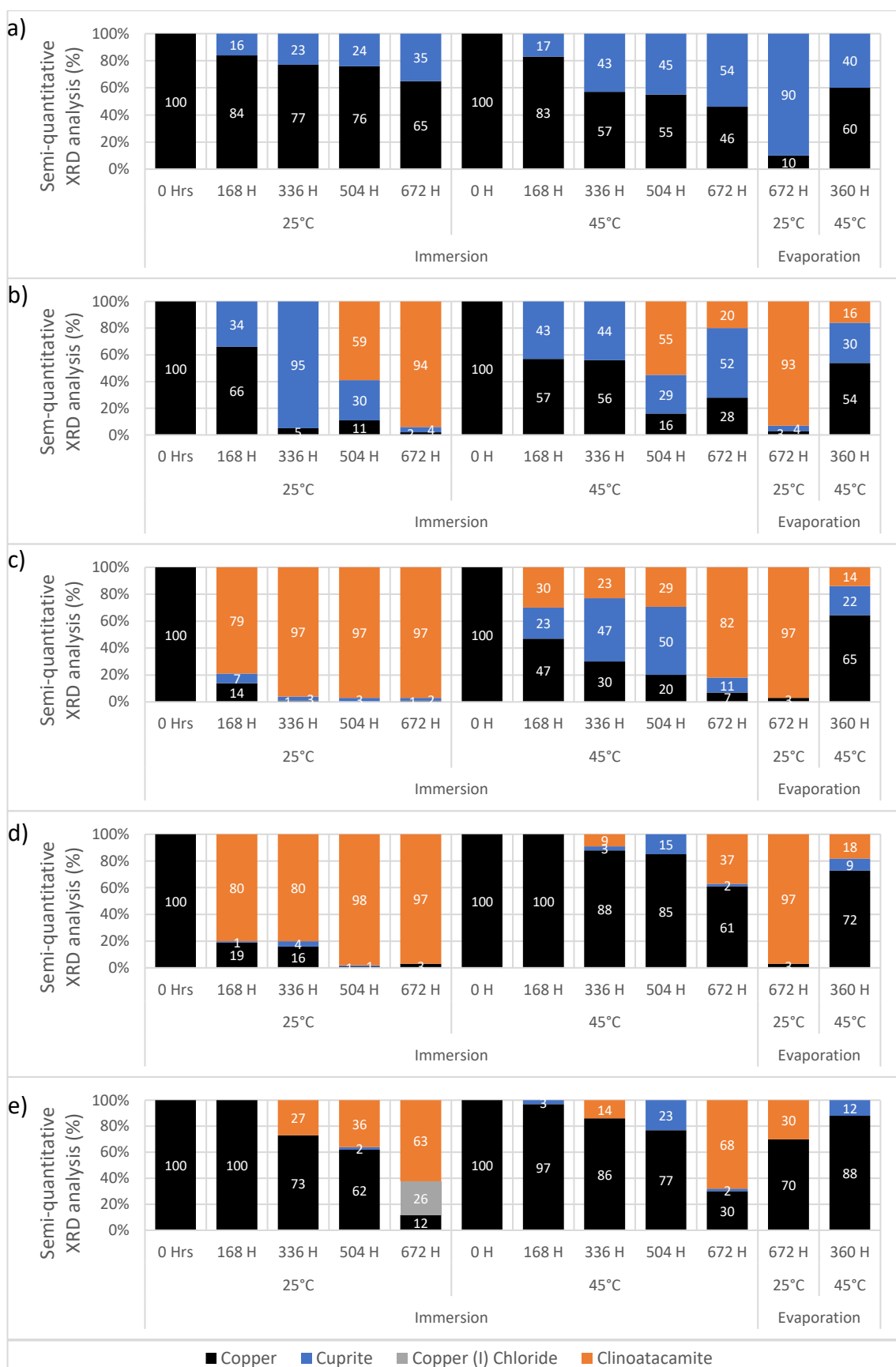
Figure 102 – Glancing angle semi-quantitative XRD analysis of copper coupon samples exposed to a) 0%, b) 1%, c) 3.5, d) 10% and e) 30% NaCl, at 25℃ and 45℃, after 0, 168, 336, 504 and 672 hours under immersion and evaporating conditions, showing only the detected copper, cuprite and the copper chloride patina products. Assuming a 95% confidence interval.

The lowest levels of clinoatacamite were measured in the 30% electrolyte which may be associated with the high surface dissolution rate observed in Chapter 5.4.2.4, which may have prevented the formation of an adherent patina and/or resulted in an increase in patina porosity. This reduced the adhesion to the coupon surface allowing it to be easily removed during cleaning operations. Copper (I) chloride, a precursor to clinoatacamite (Zhang et al., 2014), was also detected in the 30% electrolyte at 25°C after 672 hours, suggesting that the speed of clinoatacamite formation had reduced.

Under immersion conditions the electrolyte ion concentration remained comparatively constant throughout the testing, however a relative increase in ion concentration was observed in the evaporation cell, leading to saturation and the formation of salt crystals. This can enhance the corrosion and therefore the patination rate of copper (Lopesino et al., 2018), while the formation of salt crystals could disrupt the patina film allowing it to be easily removed during cleaning operations, resulting in the lower concentrations found after the semi-quantitative analysis.

7.1.2.2.2 Cuprite Powder

Figure 103 shows the semi-quantitative analysis of the cuprite powder as it was exposed to various concentrations of sodium chloride. In the 0% electrolyte (deionised water) under immersion conditions the cuprite powder remained relatively unaffected, with no additional compounds being detected at 25°C until 672 hours where a small amount of tenorite (5 ± 0.25%) was found (Figure 103a). The cuprite powder has been shown to react with water to form tenorite through Equation 50 or through the presence of dissolved oxygen through Equation 51.

$$Cu_2O + H_2O = 2CuO + 2H^+ + 2e^- \qquad \text{\textit{Equation 50}}$$
$$2Cu_2O + O_2 = 4CuO \qquad \text{\textit{Equation 51}}$$
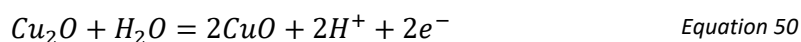
However, under immersion conditions at 45°C 8 ± 0.4% tenorite was detected after 168 hours, increasing to 61 ± 3.05% after 672 hours. This suggests that higher temperatures promote tenorite formation as observed previously (Adeloju & Hughes, 1986; Feng et al., 1996; Lytle & Nadagouda, 2010; Montes et al., 2014) where tenorite had formed on copper pipes at elevated temperatures. The pH of the 0% electrolyte remained relatively unaffected throughout the exposure with a pH of 6.8 ± 0.5 at 25°C and 45°C (Appendix 9a). This pH, according to the Pourbaix diagrams (Chapter 5.2.1), lies on the theoretical pH equilibrium line between stability domains of CuO and Cu^{2+} at 25°C and therefore a competition between the two compounds may occur, resulting in the small amount of tenorite detected after long exposures. Whereas at 45°C, the equilibrium line had shifted to more acidic values of 6.5 indicating that only tenorite could develop from the cuprite powder.

[273]
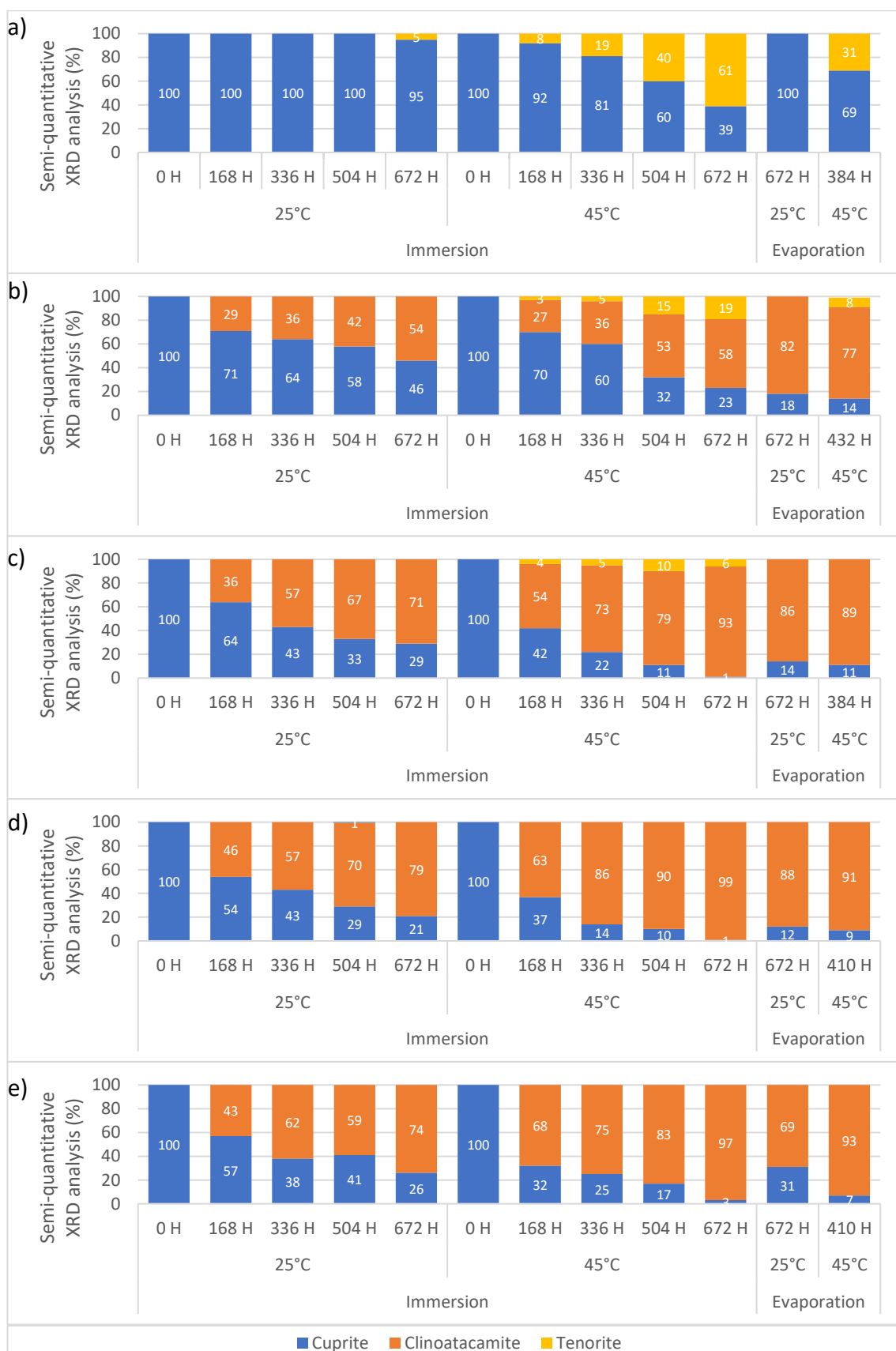
Figure 103 – Semi-quantitative XRD analysis of the Cuprite pigment samples exposed to a) 0%, b) 1%, c) 3.5, d) 10% and e) 30% NaCl, at 25℃ and 45℃, after 0, 168, 336, 504 and 672 hours under immersion and evaporating conditions, showing only the detected cuprite pigment and the copper chloride patina products. Assuming a 95% confidence interval.

[274]

Under evaporating conditions, no tenorite was present after 672 hours testing in the 0% electrolyte cell. While at 45°C, the electrolyte had evaporated after 384 hours, resulting in a relatively high concentration of tenorite being detected (31 ± 1.55%). This was approximately 1.6x greater than that found following similar exposure times in the immersion cell (Figure 103a). This indicates that there was an acceleration in tenorite formation in the evaporation cell which may be associated with the increase in the oxygen diffusion, known to be a rate determining step (Liao et al., 2011), as the electrolyte volume decreased (Equation 51).

Clinoatacamite had formed in the chloride containing electrolytes with tenorite also being detected at 45°C in the 1% and 3.5% electrolytes under immersion conditions, after 168 hours, raising to 19 ± 0.95% after 672 hours (Figure 103d) and 14 ± 0.7% after 504 hours (Figure 103e), respectively. The pH of the electrolytes was found to shift to alkaline values after 24 hours allowing tenorite to develop, stabilising at 9.4 ± 0.3% regardless of the chloride concentration at 25°C, with a similar trend also being observed at 45°C with a pH of 9.45 ± 0.45. This increasing alkalinity suggests that the formation $CuCl_2^-$, from cuprite, and its precipitation as clinoatacamite resulted in the formation of an acidic salt, consuming Cl^- and H^+ and releasing OH^- (Equations 52 (page 275) and 43 (page 223), or Equation 53 to 13 (page 36) to 43) to balance the reaction. Therefore, the production of $CuCl_2^-$ was the rate determining step.

$$Cu_2O + 2H^+ + 4Cl^- = 2CuCl_2^- + H_2O \qquad \text{\textit{Equation 52}}$$
$$Cu_2O + 2H^+ = Cu^{2+} + H_2O \qquad \text{\textit{Equation 53}}$$
$$Cu^{2+} + 2Cl^- = CuCl \qquad \text{\textit{Equation 54}}$$
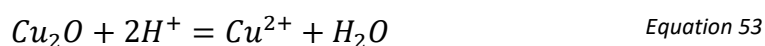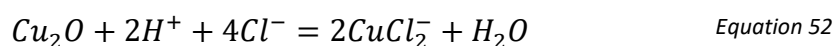
However, no tenorite was detected in the 10% and 30% electrolytes, suggesting that tenorite formation was limited to the electrolytes that contained less than 10% sodium

[275]

chloride. Ferry & Carritt (1946) determined that the solubility of cuprite was proportional to the H^+ concentration and a linear function of the square of chloride ion concentration. This suggests that higher levels of Cu^{2+} and $CuCl_2^-$ were formed at faster rates as the chloride concentration was increased, which may slow and/or prevent the formation of tenorite at a critical chloride concentration or allow for the rapid transformation of tenorite to clinoatacamite through Equation 55.

$$2CuO + H^+ + Cl^- + H_2O = Cu_2Cl(OH)_3 \qquad \textit{Equation 55}$$
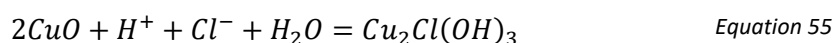
The evaporation cells experience a relative increase in chloride concentration as the electrolyte was evaporated, which may slow the formation of tenorite as the dissolution of the cuprite powder increased. For example, the 3.5% electrolyte reached the apparent 10% limit for tenorite formation more quickly lasting longer (168 hour) than the 1% solution (48 hours), before fully evaporating allowing the tenorite to convert to clinoatacamite. Whereas more time was needed to convert the tenorite formed in the 1% electrolyte.

Under immersion conditions a non-linear increase in clinoatacamite concentration was found with increasing chloride concentrations peaking at 10%, which was approximately equal to that found in the 3.5% and 30% electrolytes. This suggests that although the higher chloride concentration can increase the concentration of clinoatacamite, as it enhances the solubility of the cuprite powder, the complexation of Cu^{2+} to $CuCl_2^-$ and $Cu_2Cl(OH)_3$ becomes rate limiting, with no significant enhancement being observed at higher chloride concentrations. This may also have resulted in the linear increase in clinoatacamite being detected as the immersion time was increased from 168 hours in the respective electrolytes.

[276]

Under evaporating conditions similar levels of clinoatacamite tended to be found at both temperatures, which were greater than that detected after similar times under immersion conditions. This suggests the concentrating effect of the evaporation cell accelerated the complexation of cuprite to clinoatacamite with elevated temperatures also accelerating its formation.

7.1.2.2.3 BQA 644

While the BQA 644 coating contained several crystalline compounds, the semi-quantitative XRD analysis was measured using the relatively high amounts of cuprite and zinc oxide pigments in, and the copper patina compounds on, the coating. No additional copper compounds were found when analysing the coating exposed to the 0% electrolyte (deionised water) under both immersion and evaporating conditions at either 25°C or 45°C (Figure 104a), with only the phases associated with the coating being detected. However, tenorite was detected at 45°C in the cuprite containing cells under both testing conditions. This cell contained a significantly larger number of available cuprite particles when compared to the coating surface. Therefore, if tenorite was present on the coating it may be below the detection limit of the XRD.

Clinoatacamite was detected on the coatings after 168 hours exposure to the sodium chloride containing electrolytes, the concentration of which tended to increase with exposure time, suggesting the formation of a thicker, denser and/or more uniform layer. Visual inspection of the coatings exposed to the 1% electrolyte at 45°C found that it had become discoloured forming a blue-green hue at 168 and 336 hours indicating a copper patina was present. However, no additional phases were detected at 168 and 336 hours, while at 504 and 672 hours relatively small levels of clinoatacamite were detected of 17 ± 0.85% and 13 ± 0.65%, respectively (Figure

[277]

104b). This suggests that the patina layer was loosely adhered to the coating surface allowing it to be easily removed during the cleaning procedure. Similar levels of clinoatacamite were found when comparing that found in the evaporation and immersion cells at 25°C suggesting there was not an increase in patination rate due to the evaporation, such as that observed in the cuprite powder. However, at 45°C approximately 2.85x more clinoatacamite was detected after 432 hours in the evaporation cell when compared to the immersion cell after 672 hours suggesting more patina was present on the coating.

As observed on the cuprite samples, as the sodium chloride concentration was increased so did the amount of clinoatacamite following a non-uniform trend, where large increases were found in the 1% and 3.5% electrolytes, while the highest levels were detected in the 10% electrolyte (Figure 104a-d). However, in the 30% electrolyte the clinoatacamite concentration was significantly lower with an additional botallackite compound being detected at each measurement period at 25°C and at 168 hours at 45°C (Figure 104e). Botallackite was not found in the cuprite powder under similar conditions or on paint flakes removed from in-service marine vessels. Pollard et al. (1989) determined that low concentrations of aqueous $CuCl_2$ ($4.25 \times 10^{-3} \, mol. \, dm^{-3}$), was required for botallackite to precipitate, while at $0.2 \, mol. \, dm^{-3}$ botallackite recrystallised to atacamite and clinoatacamite. Therefore, it can be surmised that the relative abundance of Cu^{2+} and $CuCl_2^-$ ions released from the cuprite powder, when compared to the coating, was sufficiently high to prevent botallackite formation. While in the 30% electrolyte at 25°C the dissolution of the cuprite pigment was reduced resulting in low concentration of copper ions, which may be associated with an increase in viscosity (Fair & Ozbek, 1977). The Noyes-Whitney

[278]

dissolution model, determined that the thickness of the boundary layer around an object is increased in high viscosity electrolytes, reducing the dissolution rate when compared to the lower viscosity electrolytes (Banakar, 1991). Whereas, at 45°C the dissolution rate of the cuprite pigment was high enough to allow the recrystallization of botallackite to clinoatacamite.

Clinoatacamite was also the major $Cu_2Cl(OH)_3$ compound detected on the paint flakes removed from in-service vessels (Chapter 4.2.1). This shows that similar patina compounds can be produced under laboratory conditions to formed naturally on coatings. While under immersion conditions the patination was found to be accelerated in the 10% electrolyte, with high levels (45 ± 2.25%) of clinoatacamite being recorded after 168 hours at 25°C under immersion conditions, and a marginal increase being measured after 672 hours (58 ± 2.9%).
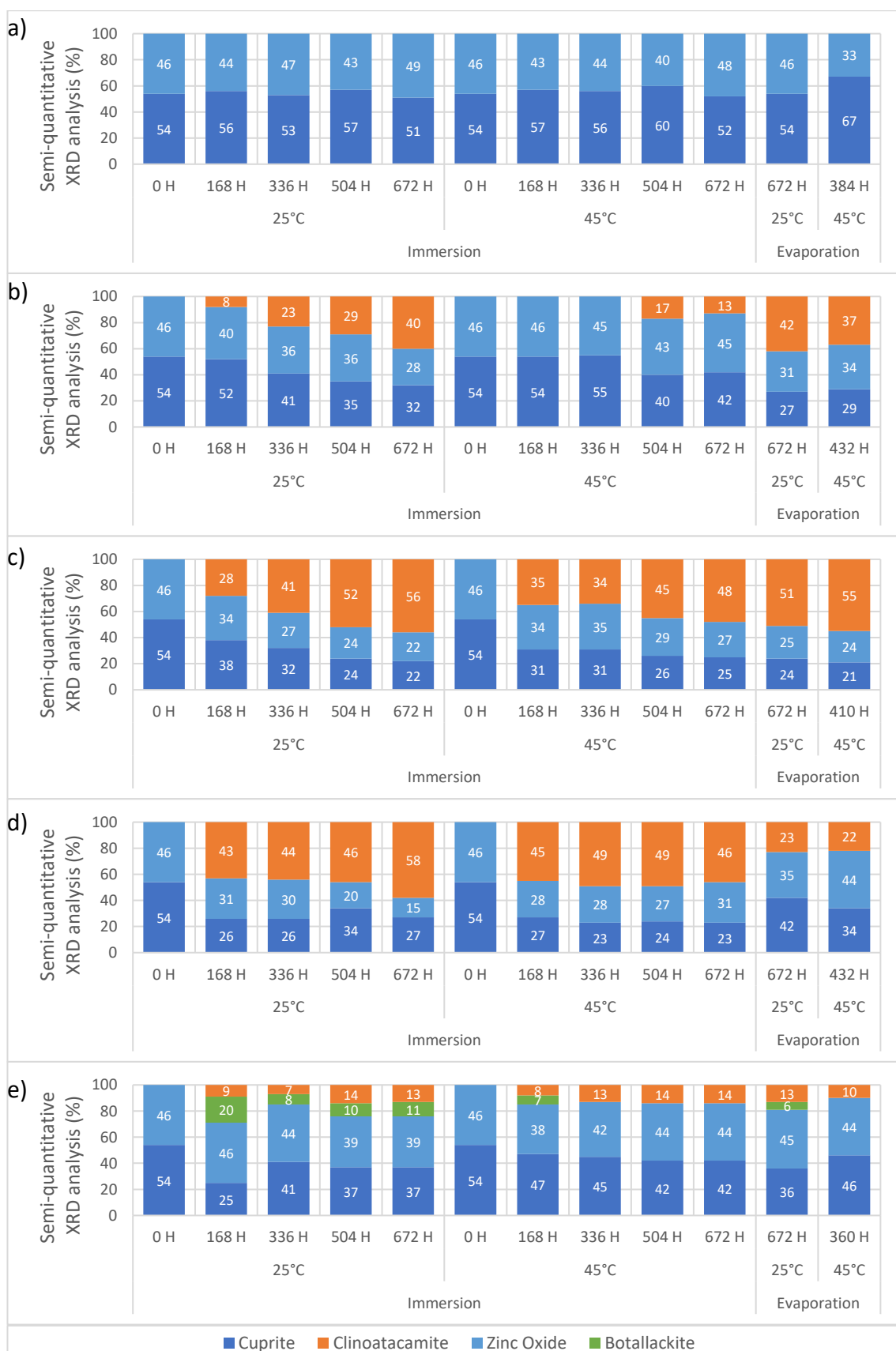
Figure 104 – Semi-quantitative XRD analysis of the BQA 644 coated samples exposed to a) 0%, b) 1%, c) 3.5, d) 10% and e) 30% NaCl, at 25℃ and 45℃, after 0, 168, 336, 504 and 672 hours under immersion and evaporating conditions, showing only the detected copper, cuprite, and the copper chloride patina products. Assuming a 95% confidence interval.

7.1.2.2.4   Modified BQA 644

Similarities between the compounds detected on the BQA 644 and the modified BQA 644 coating were observed when analysing the compounds formed on the surface of the sample following the immersion and evaporation experiments, at both temperatures.

As observed on the BQA 644 coating, when exposing the modified BQA 644 coating to the 0% electrolyte no additional copper compounds were detected (Figure 105a). While clinoatacamite was detected at each inspection period in the sodium chloride containing electrolytes (Figure 105b-e). This reinforces the ability of the immersion and evaporation testing to reproduce the same copper compounds, found on the coatings removed from in-service marine vessels, under laboratory conditions on different coatings.

Furthermore, under immersion conditions the modified BQA 644 coating also followed the trend towards a non-linear increase in clinoatacamite with chloride concentration, as discussed previously, where the lowest concentrations were detected in the 1% electrolyte and the highest in the 10% electrolytes. While increasing the immersion time and temperature from 25°C to 45°C also tended to increase the amount of clinoatacamite that had formed. This indicates that higher temperatures, chloride concentrations and immersion times produces more clinoatacamite. Similarly, under evaporating conditions the amount of clinoatacamite that had formed was approximately 1.07x − 1.32x greater, suggesting an acceleration in clinoatacamite formation, than that formed under immersion conditions after equivalent times.

The largest amounts of clinoatacamite were found in the 10% electrolyte of 50 ± 2.5% 25°C after 168 hours, continuing to increase to 68 ± 3.4% after 672 hours (Figure

105d), however it was more variable at 45°C. A reduction in concentration was observed between 336 hours (84 ± 4.2%) and 504 hours (67 ± 3.35%) before increasing again at 672 hours (80 ± 4%). Furthermore, unlike what has been observed in the lower chloride concentration electrolytes, the amount of clinoatacamite in the 25°C evaporation experiment was lower than that found following equivalent immersion time. It is possible that the variability in the results was due to the cleaning process used to remove traces, and dissolve crystals of sodium chloride, which may have dislodged loose patina products from the coating surface, reducing the amount that was detected.

Additional similarities between the BQA 644 and modified BQA 644 coatings were found when analysing the samples exposed to the 30% electrolyte where botallackite was detected in addition to clinoatacamite and cuprite. Botallackite was detected at each inspection period and under both immersion and evaporation conditions at 25°C, with the largest concentrations being found at 336 hours of 48 ± 2.4% (Figure 105e). However, as observed on the BQA 644 samples, at 45°C no botallackite was present, while the immersion and evaporation cells detected similar concentration of clinoatacamite at each inspection period. Furthermore, botallackite was not found on the paint flakes removed from in-service marine vessels and therefore testing of antifouling coating under laboratory conditions should not be carried out in the 30% electrolyte at 25°C. While the higher concentrations of clinoatacamite after shorter immersion times suggests that the accelerated patination testing of antifouling coatings should be performed in the 10% electrolyte.

[282]
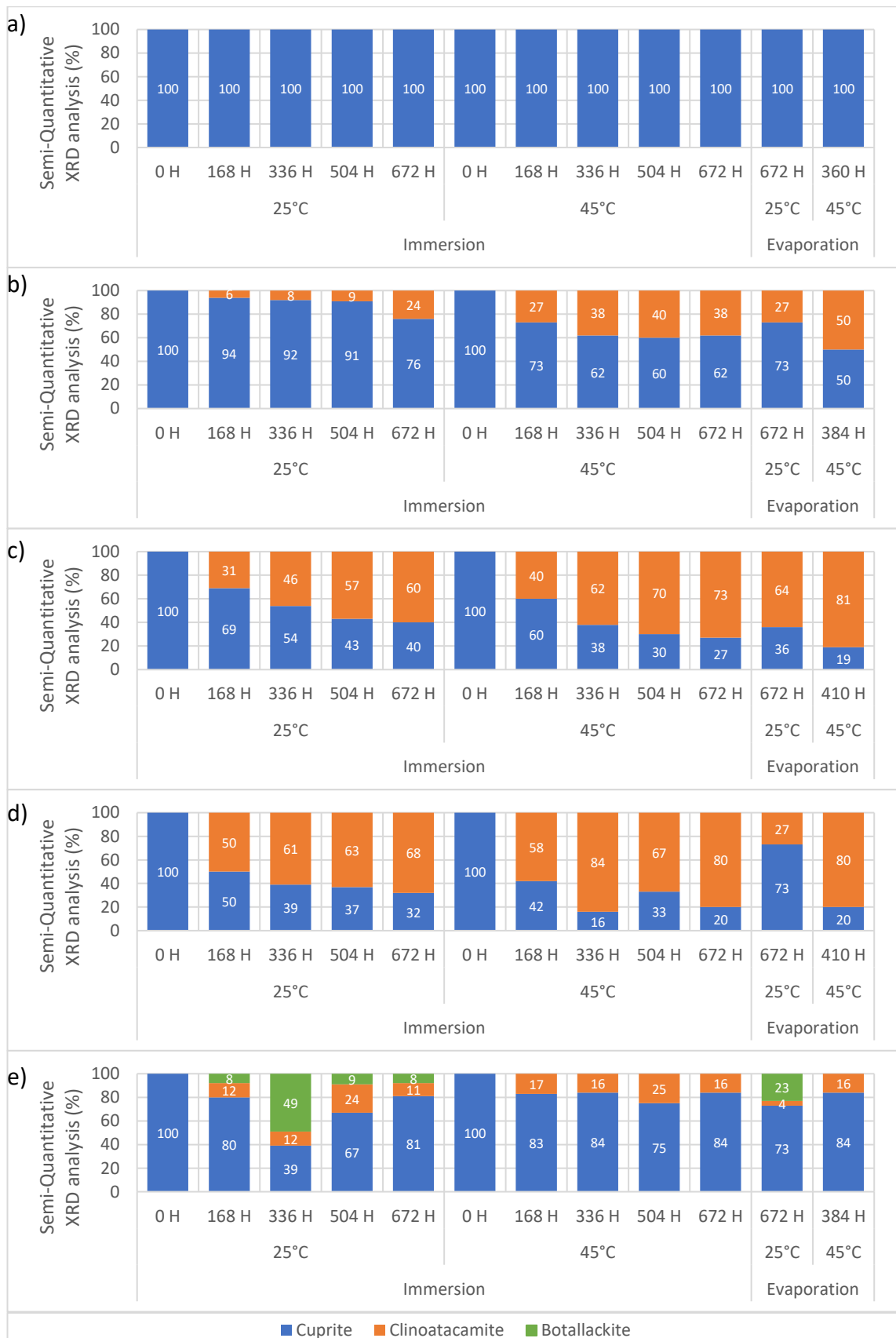
Figure 105 – Semi-quantitative XRD analysis of the modified BQA 644 coating samples exposed to a) 0%, b) 1%, c) 3.5, d) 10% and e) 30% NaCl, at 25°C and 45°C, after 0, 168, 336, 504 and 672 hours under immersion and evaporating conditions, showing only the detected copper, cuprite and the copper chloride patina products. Assuming a 95% confidence interval.

7.1.2.3 *In-Service Paint Flakes*

XRD analysis of the paint flakes removed from the hull of in-service marine vessels detected clinoatacamite on 13 of the 14 samples, along with the pigments from the coatings and other compounds (Chapter 4.2.1). Semi-quantitative XRD analysis of the phases present on the paint flakes (Figure 106) determined that the average concentration was 41% with the largest levels being detected on Paint Flake 3 of 85% with the smallest amount being detected on Paint Flake 14 of 17%.
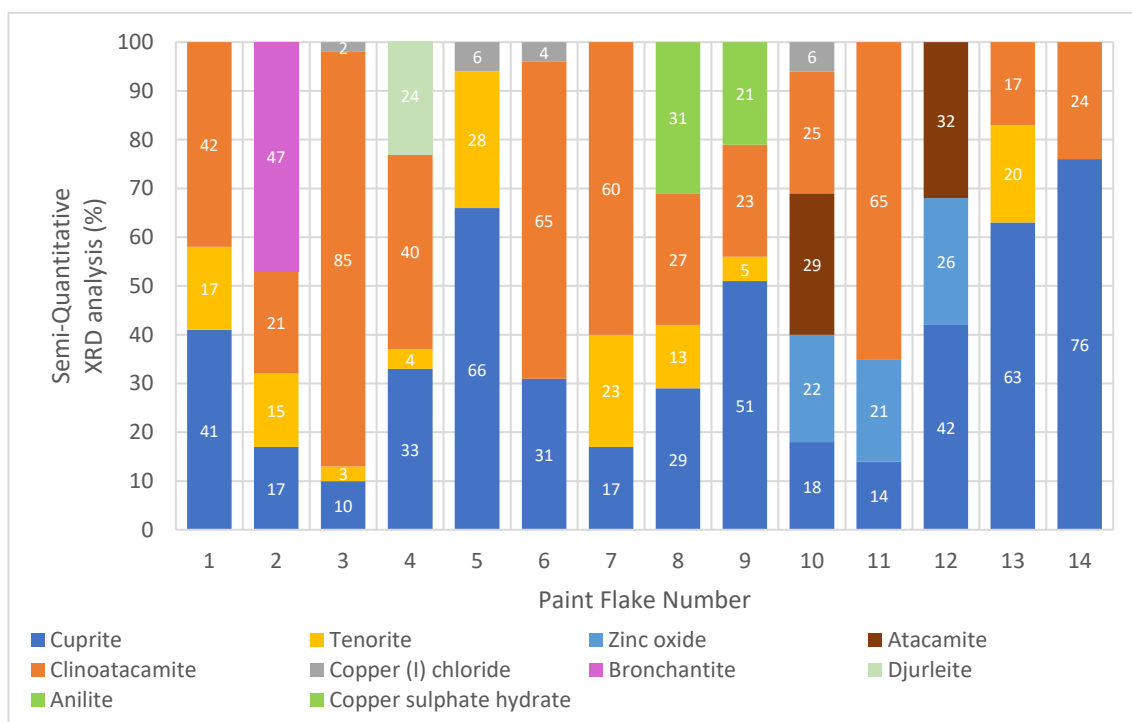
Figure 106 – Semi-quantitative XRD analysis of the copper patina compounds detected on the in-service paint flakes analysed in Chapter 4.2.1

Using the average concentration and the semi-quantitative analysis of the cuprite pigment, BQA 644 and modified BQA coatings it was possible to estimate the amount of time required to replicate the long-term immersion of the in-service paint flakes under the different laboratory conditions. It was determined that a 168 hour immersion test in a neutral 10% NaCl solution at 25°C would produce approximately equivalent concentrations of clinoatacamite to the average clinoatacamite concentration of the 13 paint flakes.

[284]

NaCl %	Cuprite				BQA 644				Modified BQA			
	Immersion		Evaporation		Immersion		Evaporation		Immersion		Evaporation	
	25℃	*45℃*	*25℃*	*45℃*	*25℃*	*45℃*	*25℃*	*45℃*	*25℃*	*45℃*	*25℃*	*45℃*
1	504	336	<672	<432	672	>672	672	432	>168	504	>672	384
3.5	168	<168	<672	<384	336	504	672	410	336	168	<672	<410
10	168	<168	<672	<410	168	168	>672	>432	<168	<168	>672	<410
30	168	<168	<672	<410	*	*	>672	>360	*	*	>672	>384

* Increasing the immersion period did not result in an increase in clinoatacamite detected on the paint and therefore testing beyond 672 hours appears to be of little benefit.

The relatively low concentration of and friable nature of the clinoatacamite present on the coatings in the 30% NaCl electrolytes, after each time period, suggests that this would not be a suitable environment in which to replicate in-service patination of antifouling coatings.

7.1.3 Scanning Electron Microscopy
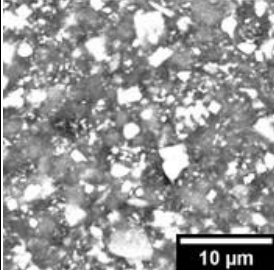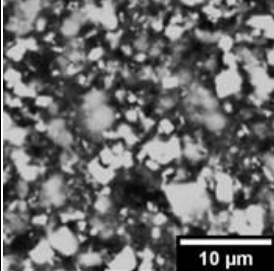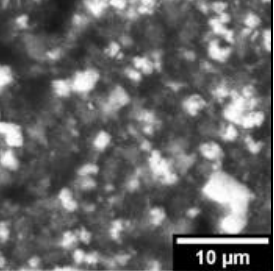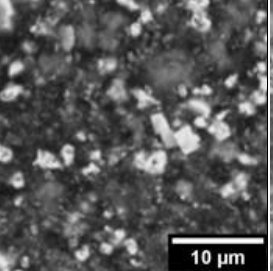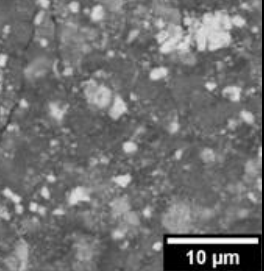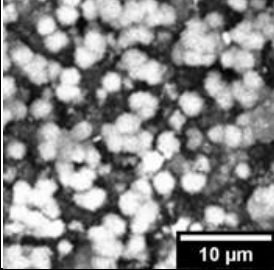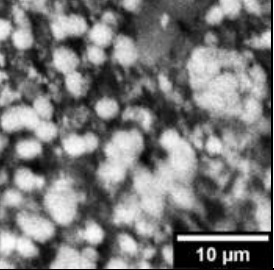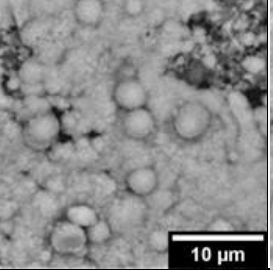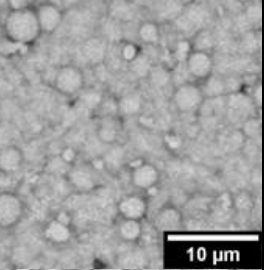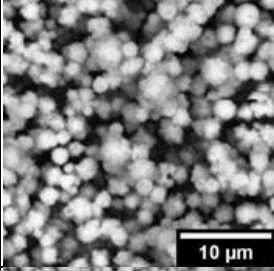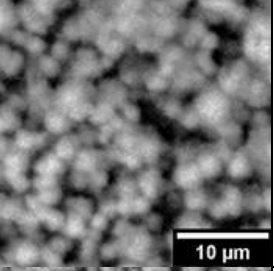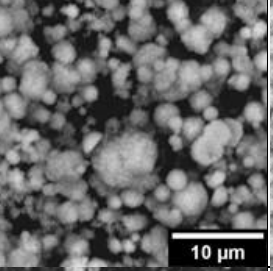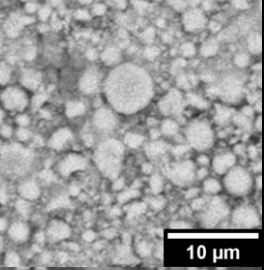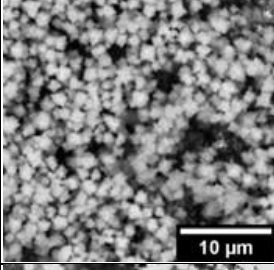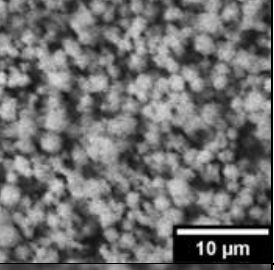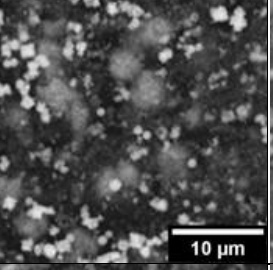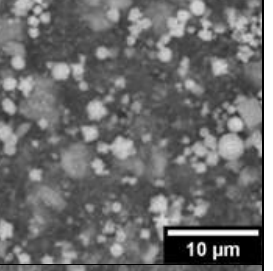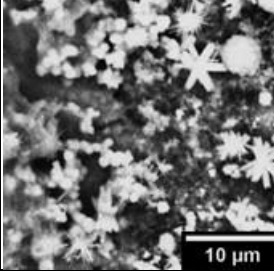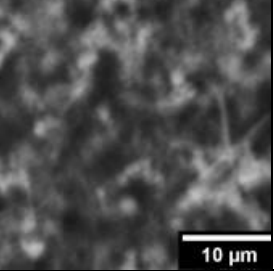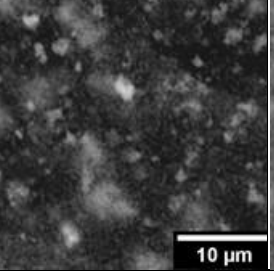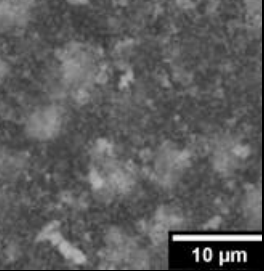
While the reference materials of copper and cuprite powder were exposed to the same conditions as the antifouling coatings, it was decided that SEM and EDX analysis would concentrate on the BQA 644 and modified BQA 644 coatings as they could be directly compared to the paint flakes removed from the in-service marine vessel. The surface and cross-sections through the coatings after exposure to the different environments were analysed to observed how they affected the patination, leaching of pigments, and the detachment of the antifouling coatings. Cross-sections were taken and mounted in a two-part epoxy resin, left to cure under vacuum, ground and polished to a 1 μm finish using standard metallographic techniques, and carbon coated for analysis in the SEM.

7.1.3.1 *Surface morphology*

7.1.3.1.1 BQA 644

Table 27 shows examples of the BQA 644 coating surface following exposure to the sodium chloride electrolytes at 25°C and 45°C when immersed for 672 hours, and for 672 hours, under evaporation conditions, or until the electrolyte had fully evaporated. Qualitative analysis of the surface of the BQA 644 samples after exposure to the 0% electrolyte found that it remained relatively unaffected throughout the duration of the test. Where the BSE micrographs show the bright contrast, low sphericity when qualitatively compared to the roundness and sphericity classification described by Powers (1953) and the chart in Appendix 10 Figure 170, angular cuprite particles, <5 µm diameter, dispersed within the coating matrix containing the other pigments (Table 27). In the sodium chloride electrolytes, spherical copper- and chlorine-rich compounds formed, which have been identified previously as clinoatacamite (Chapter 7.1.2.2). The temperature of the electrolyte did not appear to influence the morphology of the patina with similar shapes, sizes and distributions being found at both temperatures.

Table 27 – BSE micrographs showing examples of the surface morphology observed on the BQA 644 samples which had been exposed to immersion and evaporation conditions for 672 hours or until the electrolyte had fully evaporated at 25°C and 45°C. Full SEM analysis of the surface is shown in the Appendix 10a.

	Immersion		Evaporation	
	25°C	45°C	25°C	45°C
Unexposed		-	-	-
0%				
1%				
3.5%				
10%				
30%				

In the 1% electrolyte under immersion conditions, at both 25°C and 45°C, copper patina particles, which were rounded with a high sphericity (Powers, 1953) i.e., they had a smooth appearance with a near perfect spherical shape, were distributed across the coating surface, with parts of the substrate being visible in places, suggesting that the patina layer was highly porous. Similar patina morphology was observed by (Liao et al., 2011) and (Ochoa et al., 2015). However, under evaporating conditions the porosity appeared reduced, with the spherical particles being encapsulated in a uniform film covering the coating (Table 27 at 1% and 3.5%). This also suggests that, for a given sodium chloride concentration and temperature, a higher concentration of copper patina was observed under evaporating conditions. This was confirmed by the semi-quantitative XRD analysis (Chapter 7.1.2.2). This increase in patina density compared to the immersion conditions may be due to relative increase in chloride concentration as the electrolyte evaporated. This could increase both the release of copper ions from the coating matrix and the complexation to, and precipitation of, copper chloride compounds.

The patina formed on the coating exposed to the 3.5% electrolyte had a similar morphology to that found in the 1% electrolyte where the particles were qualitatively rounded with a medium sphericity i.e., they had a smooth appearance with a moderately spherical shape (Maroof et al., 2020; Rawle, N/D). However the 3.5% electrolyte, qualitatively, had a greater number of individual patina particles when comparing the two electrolytes under similar exposure conditions and temperatures, with the substrate no longer being visible. This may be due to the acceleration of the dissolution of the cuprite pigment as the chloride concentration was increased allowing greater concentrations of copper chloride compounds to form.

A further increase in the number of copper patina particles was observed in the 10% electrolyte under immersion conditions where the particles were more angular with a low sphericity morphology. However, under evaporating conditions the substrate was visible with fewer patina particles being present. It is possible that a more loosely adhered copper patina had become detached due to the cleaning procedures. While each sample underwent a similar cleaning procedure, as the chloride concentration increased so did the number of sodium chloride crystals that formed within the evaporation cell. The formation of these crystals may have disrupted the loosely adhered patina layer allowing it to fail more easily than that formed under immersion conditions. Furthermore, the presence of these crystals required the evaporation cell to be refilled with deionised water to allow them to dissolve which may have also affected the weakened the loosely adhered patina allowing it to be easily removed as the cell was subsequently refilled to remove traces of sodium chloride from the coating. The semi-quantitative XRD analysis (Chapter 7.4.2.3) determined that a lower concentration of clinoatacamite was detected on the surface of the coatings in the evaporation cell at 25°C and 45°C confirming that the thickness, density or number of particles was less than that found in the immersion cells.

Under immersion conditions at 25°C in the 30% electrolyte a mixture of star or branched star-like acicular particles and angular medium sphericity particles were observed, suggesting the presence of two different compounds. XRD analysis identified, in addition to the cuprite from the coating, clinoatacamite and botallackite. No literature sources were available describing the shape of naturally formed botallackite as it is known to be unstable compared to the other copper hydroxychloride polymorphs and is therefore rarely observed. However synthetically

[289]

formed botallackite was found to form "nanoflowers", from Au-Cu nanospheres in chloroauric acid (Siao & Yeh, 2005) and star shaped agglomerate from 0.1M $CuCl_2.2H_2$ at 50°C (Rangel et al., 2020). The formation of these particles may act as precursors to the growth of the larger crystals found in the 30% electrolyte.
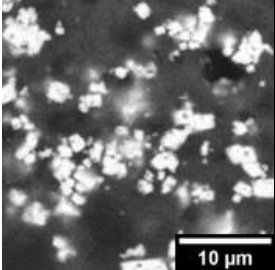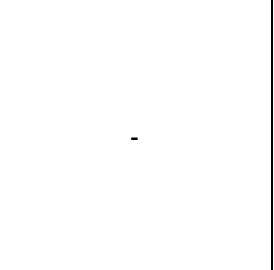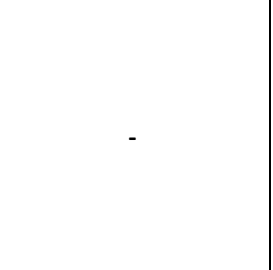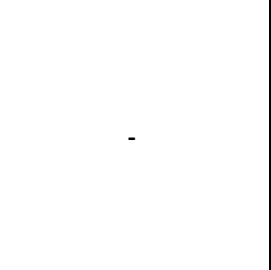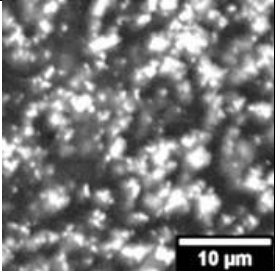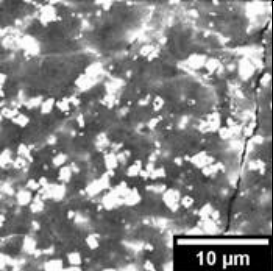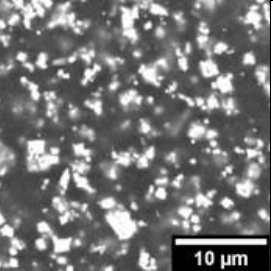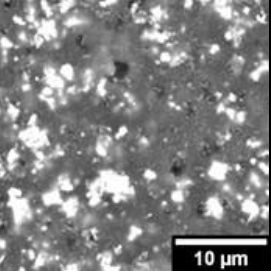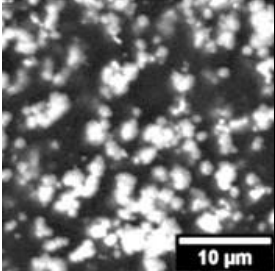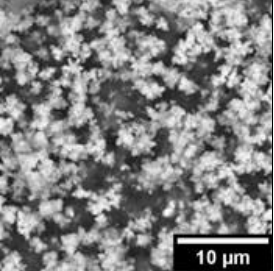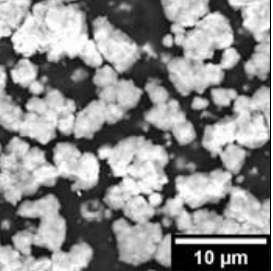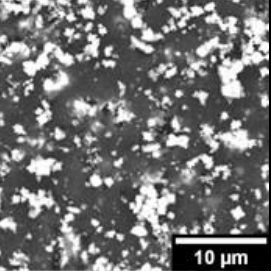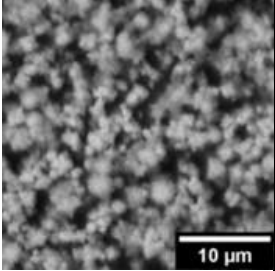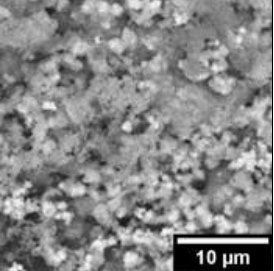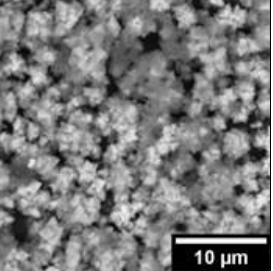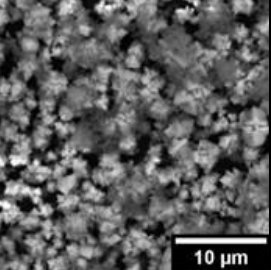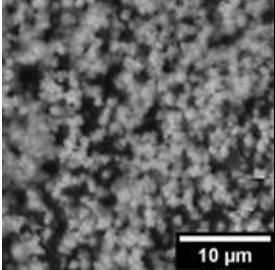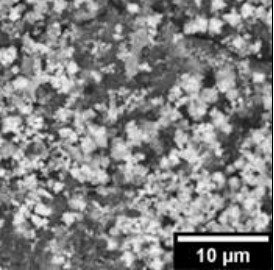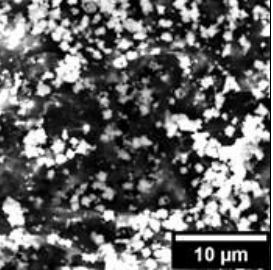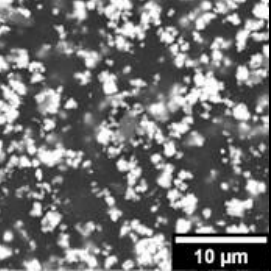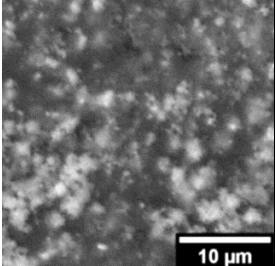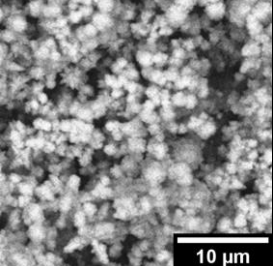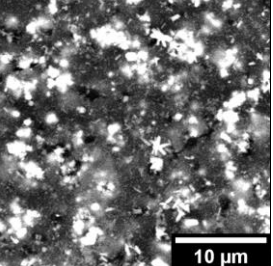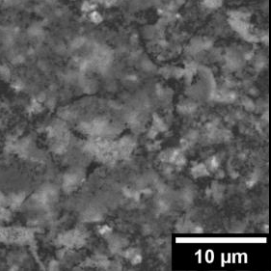
In the 30% electrolyte under immersion cell conditions at 45°C, fewer particles were observed on the sample surface with thinner branches to the star-like particles being observed. This may account for the lower concentration of clinoatacamite detected using XRD when compared to the 25°C sample, while any X-rays produced from the botallackite particles could have been lost in the background radiation. However, in the evaporation cell, at both temperatures, the surface appeared to be free of patina particles with the coating being visible and some surface deposit. As seen in the 10% electrolyte, salt crystals had formed in the evaporation cell containing the 30% electrolyte, becoming visible within the first 24-48 hours after initiating the testing. This resulted in the saturation of sodium chloride and increase in viscosity of the electrolyte which may have reduced the amount of copper ions that could be released from the coating into the electrolyte therefore limiting the amount of patina that could precipitate. Furthermore, the formation of salt crystals at the coating surface may have disrupted the weakly adhered patina as discussed earlier allowing it to be washed away as it was rehydrated. It is therefore suggested that a 30% electrolyte would not allow for the reproduction of the patination observed on the paints taken from in-service marine vessels under laboratory conditions.

7.1.3.1.2 Modified BQA 644

The modified BQA 644 samples were found to follow a similar trend to that observed on the BQA 644 samples; example micrographs of the surface are shown in Table 28. In the 0% electrolyte the surface of the coatings appeared to remain unaffected, with the cuprite particles being clearly visible in the coating. In the electrolytes containing chloride ions, copper and chlorine rich particles were formed. With increasing electrolyte chloride concentration up to 10% NaCl, the number of particles present on the coating surface also increased. The concentration of particles following exposure to evaporation conditions in the 10% electrolyte had reduced from the 3.5% electrolyte exposing the substrate in places, as observed on the BQA 644 samples

However, the patina morphology was different to that observed on the BQA 644 samples, where the particles tended to have a very angular, medium sphericity morphology. This change in patina morphology relates to the difference in the XRD traces measured from the two coatings (Chapter 7.1.2.1). The difference in the morphology may be attributed to the higher concentration of cuprite pigments at the coating surface and resulting in the release of more cupric ions into the environment, when compared to the BQA 644 coating. Consequently, this also increases the concentration of copper chloride, where Pollard et al. (1989) observed that this can influence the type of copper hydroxychloride produced, resulting in the difference in clinoatacamite compounds.

Table 28 – BSE micrographs showing examples of the surface morphology observed on the Modified BQA 644 samples which had been exposed to immersion and evaporation conditions for 672 hours or until the electrolyte had fully evaporated at 25°C and 45°C. Full SEM analysis of the surface is shown in the appendix 10a.

| | Immersion | | Evaporation | |
	25°C	45°C	25°C	45°C
Unexposed		-	-	-
0%				
1%				
3.5%				
10%				
30%				

[292]

7.1.3.2 *EDX analysis of the chlorine concentration*

Semi-quantitative EDX analysis was performed on the surface of the coatings following the weekly exposure period (Appendix 10) where the relative concentration of the copper patina was estimated based on the chloride concentration, which could only come from two sources: the electrolyte or the formation of a copper chloride patina, Furthermore, as the samples were washed to remove traces of sodium chloride using deionised water, prior to further analysis, and no sodium chloride phases were detected in the XRD traces, it can therefore be surmised that any chlorine detected on the surface of the coatings was associated with the copper chloride patina.

Figures 107 and 108 show the semi-quantitative EDX analysis of chlorine concentration detected on the surface of the coatings that were under immersion and evaporation conditions at 25°C and 45°C. Chlorine was found to be present when the coatings were exposed to chloride-containing electrolytes, which tended to increase with exposure time, as shown in the immersion cells data. This suggests that the patination of the coatings was continuous, leading to the increasing levels of chlorine on the coatings.

Furthermore, the amount of chlorine detected on the coatings was found to be related to the chloride concentration of the electrolytes, with the 1% electrolyte tending to have the lowest concentrations and the 30% electrolyte tending to have the highest levels. Within the first 168 hours the 3.5%, 10% and 30% electrolytes had a similar trend, with a rapid increase in chlorine concentration, which began to stabilise over the immersion period, suggesting that the coating rapidly patinates in the presence of chloride. Watanabe et al. (2007) also observed an increase in chlorine with time however this was measured monthly, in a suburban environment, on 99.9% pure copper, where higher concentration of copper ions and lower chloride levels may be

[293]

expected, resulting in a linear trend being found. The rapid patination of the coatings exposed to the 3.5%, 10% and 30% electrolytes was also observed in Chapter 7.1.1 where a blue-green layer had formed after 168 hours, which tended to remain constant for the remainder of the experiment. SEM analysis of the coatings also observed the formation of a uniform layer of patina particles after 168 hours (Appendix 10).

A continuous increase in chlorine concentration was found on the coatings immersed in the 1% electrolyte, tending to peak after 672 hours. The low chlorine concentration also presented fewer patina particles when analysed in the SEM (Appendix 10), with the substrate remaining visible and therefore leaving the coating colour relatively unaffected.

However, the evaporation cell did not follow the same trend, with the 30% electrolyte samples tending to have the lowest chlorine concentration at both temperatures on each coating. The highest chlorine concentrations were measured in the 1% and 10% electrolytes at 25°C for the BQA 644 and the Modified BQA 644 coatings, respectively, and in the 3.5% electrolyte at 45°C for both coatings. It is possible that the dissolution of the sodium chloride crystals and the rinsing of the evaporation cells to remove traces of sodium chloride may have affected the results from the EDX analysis as some of the weakly adhered patina may have become loose and was washed away, lowering the chlorine concentration.

Similar trends in the EDX (Figures 107 and 108) and XRD (Chapter 7.1.3.2.1) analyses were observed when comparing the two datasets, confirming a link between the chlorine concentration and the amount of copper chloride patina that is produced.
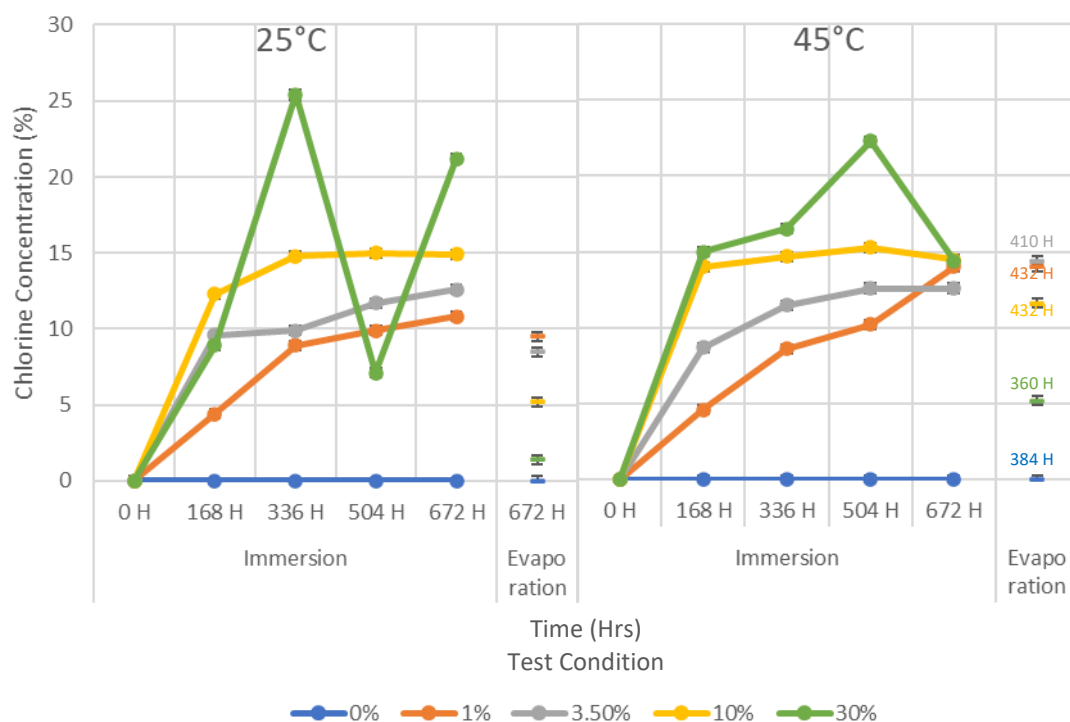
Figure 107 – Charts showing the semi-quantitative analysis EDX of the chlorine concentration detected on the surface of the BQA 644 samples following immersion and evaporation exposure conditions at 25°C and 45°C. The error bars are hidden by the marker and are based on ±1-hour in the x-direction and 3x sigma in the y-direction (Oxford Instruments Nanotechnology Tools Ltd, 2021).
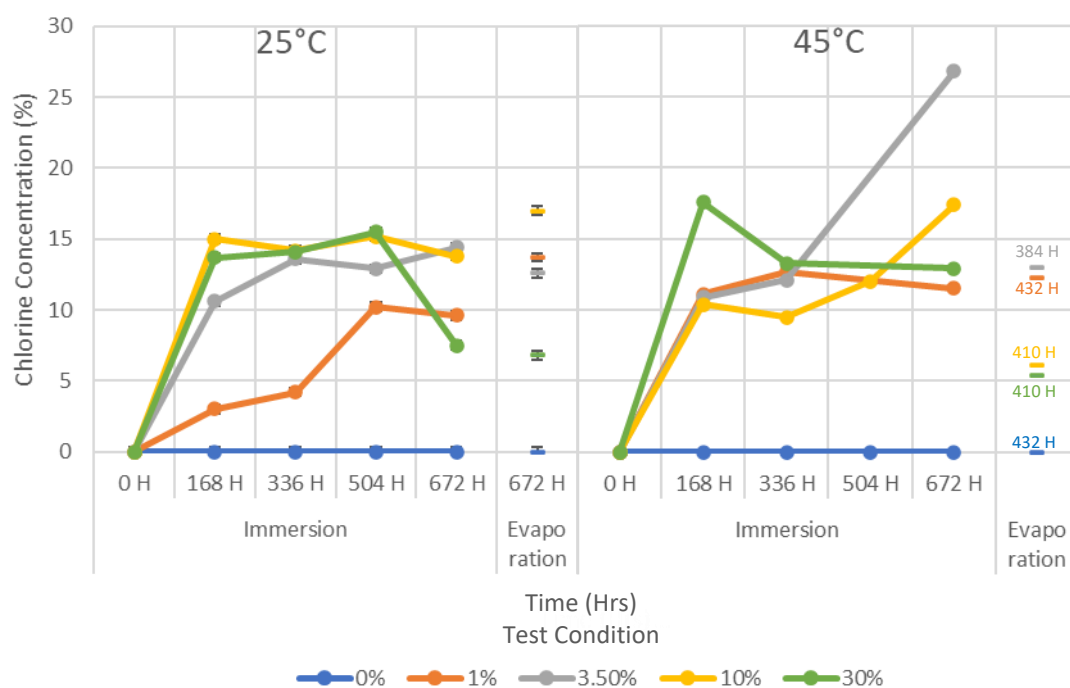
Figure 108– Charts showing the semi-quantitative EDX analysis of the chlorine concentration detected on the surface of the Modified BQA 644 samples following immersion and evaporation exposure conditions at 25°C and 45°C. The error bars are hidden by the marker and are based on ±1-hour in the x-direction and 3x sigma in the y-direction (Oxford Instruments Nanotechnology Tools Ltd, 2021).

[295]

7.1.3.3 *Patina Particle Size*

Figures 109 and 110 show the average diameter taken from 10 patina particles measured from the SEM images shown in the Appendix 10, examples of which are shown in Tables 27 and 28. Analysis of the data found similar trends occurring on both coating types.
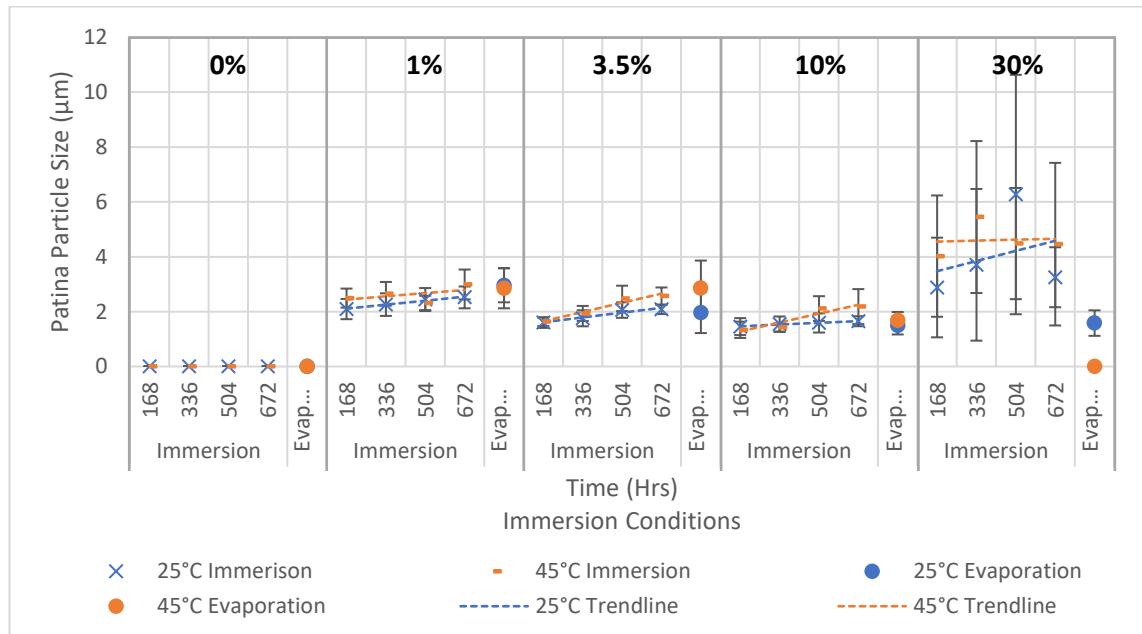
Figure 109 – Chart showing the average diameter of the patina particles observed on the BQA 644 sample after testing at 25°C and 45°C under immersion and evaporation conditions in the different electrolytes. Error bars are the standard deviation of the 10 particles measured.
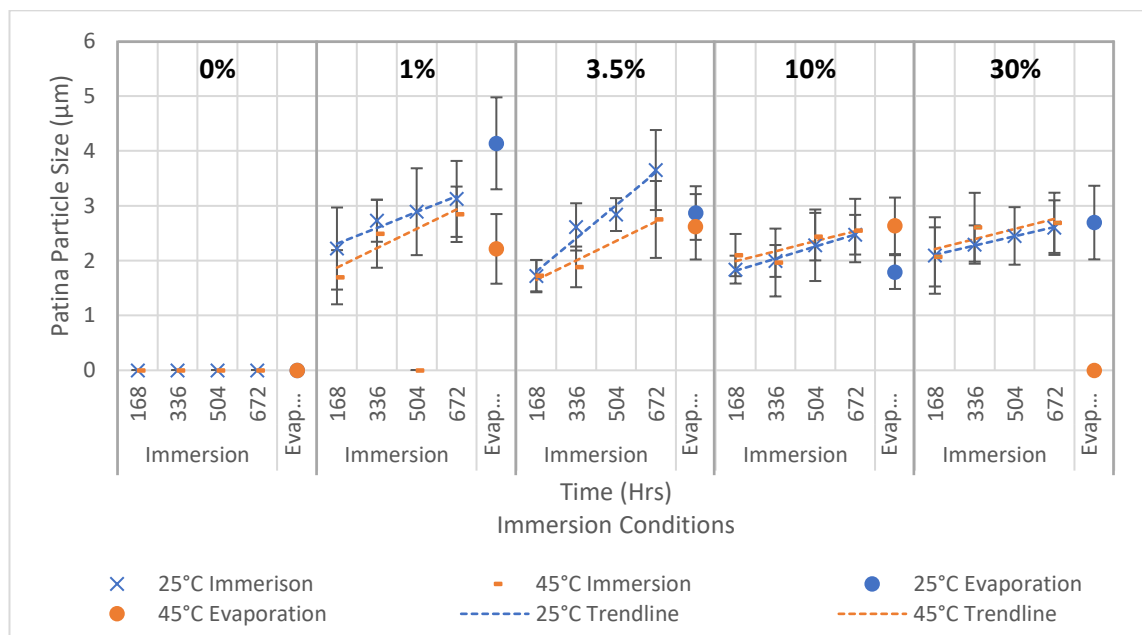
Figure 110 – Chart showing the average diameter of the patina particles observed on the Modified BQA 644 sample after testing at 25°C and 45°C under immersion and evaporation conditions in the different electrolytes. Error bars are the standard deviation of the 10 particles measured

[296]

A linear increase in the patina particle diameter was observed with increasing immersion time between 168 and 672 hours, regardless of temperature, sodium chloride concentration or coating type. This indicates that the particles continue to grow at a steady rate during this exposure period, a trend that would probably only be affected by the availability of copper ions in the environment.

Copper patina formation follows a parabolic growth where there is a rapid initial increase in thickness which then tends to slow after long exposure periods as access to copper ions becomes limited due to the patina growth (FitzGerald et al., 2006; Graedel, 1987b; Veleva & Farro, 2012). While the initial dissolution of the cuprite pigment may follow linear characteristics, as it is leached from the surface the release rate is slowed due to the increased path length. This may also reduce the patination rate over time. Hybrid and self-polishing antifouling coatings mitigate against this by removing the leach layer through hydrolysis of the coating matrix (Lejars et al., 2012) or mechanical action causing the brittle matrix to become detached as the hydrodynamic drag on the porous coating increases (Bressy et al., 2009). However, the patina found on the hybrid antifouling coating suggests that the leach layer had not become detached. While the linear increase in patina particle diameter suggests that it had not entered the parabolic phase of its development. Furthermore, this linear increase in patina was consistent with both coatings in all electrolytes and temperatures, except for the BQA 644 coating exposed to the 30% electrolyte at 25°C (Figures 109 and Figure 110). The patina found in this electrolyte had a mixture of star-shaped particles with a larger diameter compared to the angular medium sphericity particles. This resulted in the large variation in the average particle diameter at each inspection period, as well as the high standard deviation.

[297]

Further analysis determined that the average patina particle diameter generally decreased with increasing chlorine concentration (Figure 111). The formation of a copper chloride patina follows a precipitation reaction, where the nucleation and growth stages are observed. There are two type of nucleation, homogenous nucleation which occurs away from the surface of the system, and heterogenous, which is faster and occurs at the surface of the system and more commonly observed (Kelton & Greer, 2010). The nucleation of copper chloride patina on the antifouling coatings is likely to be heterogeneous where a new, distinct phase is formed. The growth of the precipitate occurs as the copper ions released from the coating diffuse on to the precipitate and become incorporated into the crystal structure. The diffusion of the copper ions becomes the rate determining step as they must travel over larger distances as the precipitate grows, resulting in the typical parabolic growth rate of copper patinas (Graedel, 1987a; Graedel, 1987b).
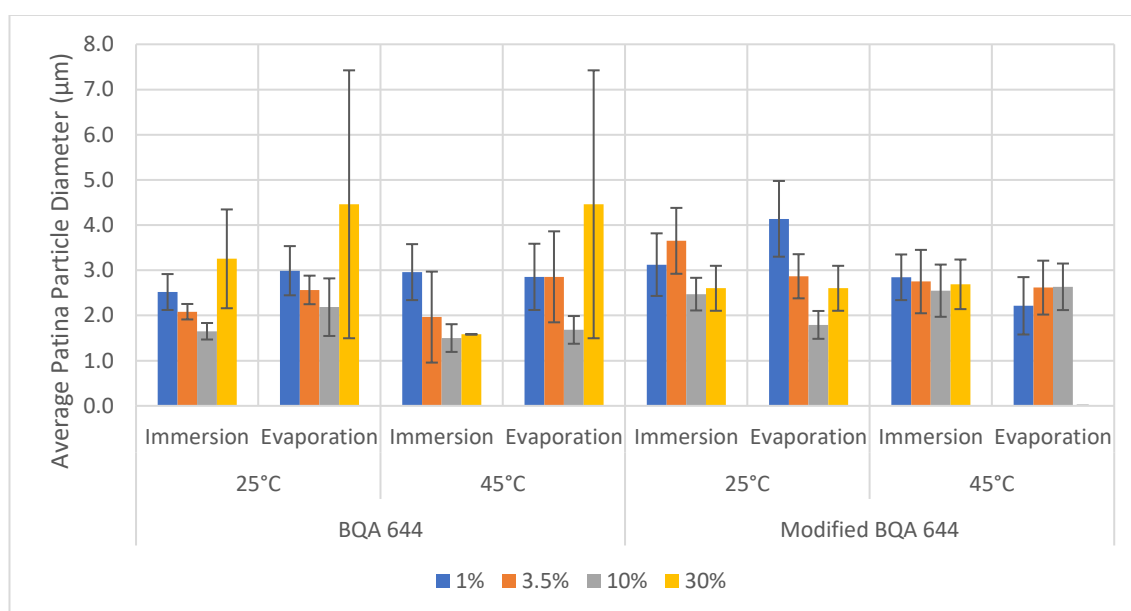
Figure 111 – Chart showing the effect of sodium chloride concentration on the average diameter of 10 patina particles after 678 hours exposure to the different environments. The error bars are the standard deviation of the 10 particles.

It has also been observed that larger precipitates tend to be formed when the growth rate exceeds the nucleation rate (Harvey, 2020). Therefore, the low levels of copper

and chloride ions available in the 1% electrolyte resulted in the growth of the precipitates being favoured over their nucleation, leading to fewer but larger precipitates being observed on the coatings in this environment. However, in the 10% electrolyte higher concentrations of copper and chloride ions are expected at the coating surface resulting in more nucleation events, and therefore smaller but greater number and density of patina particles compared to the other electrolytes. In the 30% solution the relative ratio of chloride ions to copper ions is greater than at 10% which may promote the growth of larger particles.

The patina particles formed in the evaporation cell were found to have an equivalent diameter to those produced in the immersion cell suggesting that it was the initial chloride concentration that influenced their size, with the continuous increase in chloride concentration having no effect. The analysis of the diameter of the patina particles may therefore be used to assess the age of the patina or the concentration of sodium chloride the substrate was exposed to.

The adhesion and subsequent removal of the precipitated particles is governed by three main forces: Van der Waals forces resulting in the physisorption of the newly formed precipitate on to the coating substrate, electrostatic forces acting between the particles and the electrolyte, and hydrodynamic flow within the electrolyte (Clark & Wagener, 2008). In the generally stagnant environment of the immersion and evaporation cells the hydrodynamic force would have minimal effect on the particles, only exerting an influence when the cells were topped up with fresh deionised water or when they were emptied and rinsed. This mechanism would however be more relevant for when the antifouling coatings were used in-service. The ease with which the particles can be removed from the coating could point to a method which could

prevent the precipitation of the patina. For example, if the coating and the patina particle had the same electrostatic charge in water then they would repel each other resulting in a coating free from patination.

Clark & Wagener (2008) observed that as the particle size decreases, the hydrodynamic removal forces decrease at a faster rate than the adhesive force making the removal of the particles more difficult. Therefore, it may be surmised that the patina formed in the 10% electrolyte would be more difficult to remove from the coatings than that formed in the 1% electrolyte.

7.1.3.4 Cross-sectional analysis

Table 29 shows examples of the cross-sections taken through the BQA 644 and the modified BQA 644 coatings which were in the immersion cell for 168, 336, 506 and 672 hours and the evaporation cell for 672 hours following exposure to the different neutral electrolytes at 25°C and 45°C. The images show the typical progression of hybrid coatings, with evidence of leach, detachment, and patina layers, similar to that observed when examining the cross-section through the paint flakes removed from in-service vessels (Figure 112).
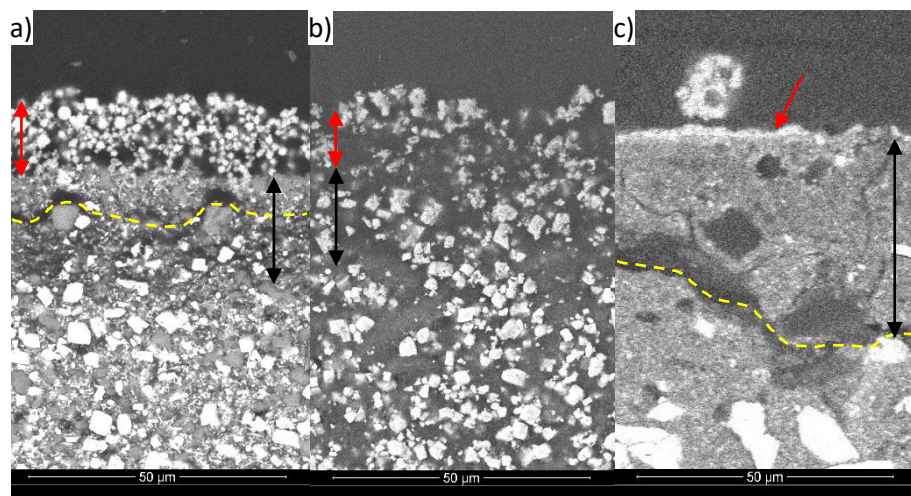
Figure 112 – BSE micrographs comparing the cross-section through a) BQA 644, b) modified BQA 644 following 504 hours immersion in 3.5% NaCl electrolyte and c) In-service paint flake showing the position of the patina (red arrows), leach (black arrows) and detachment layer (dashed yellow line).

[300]
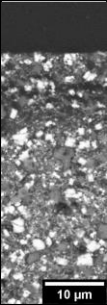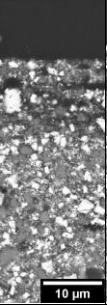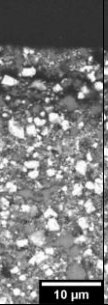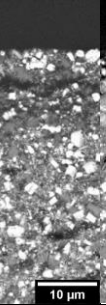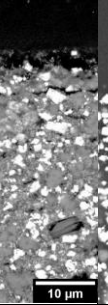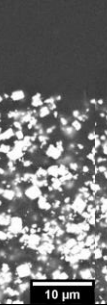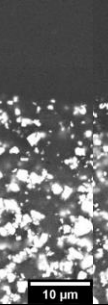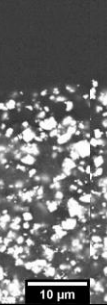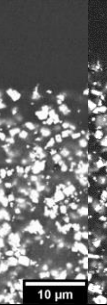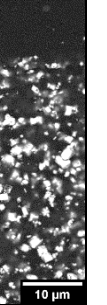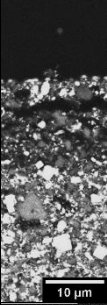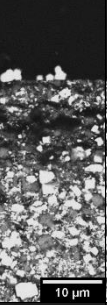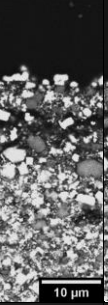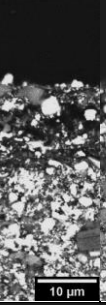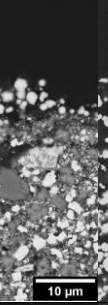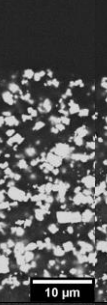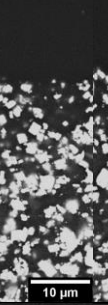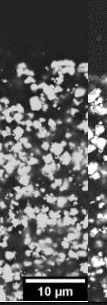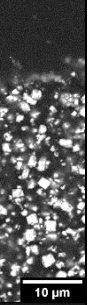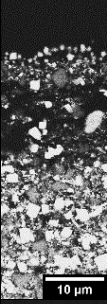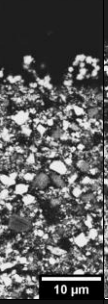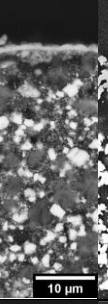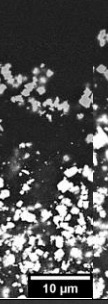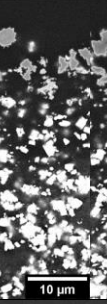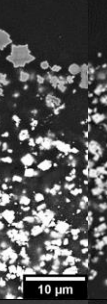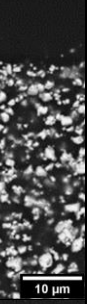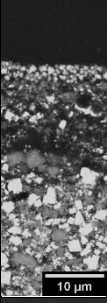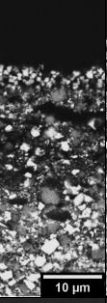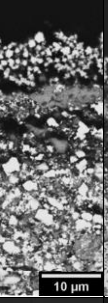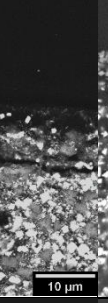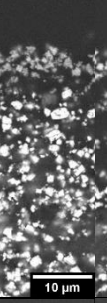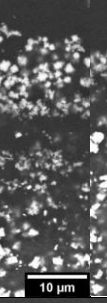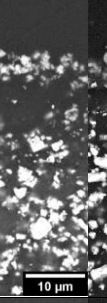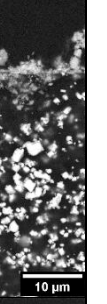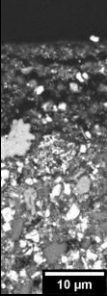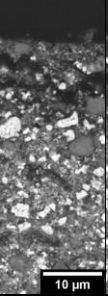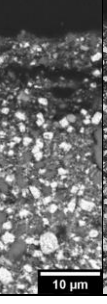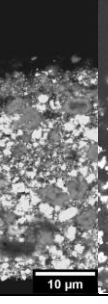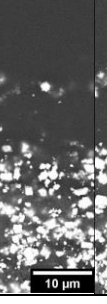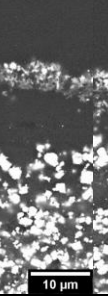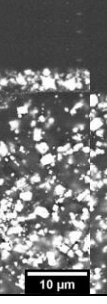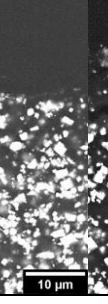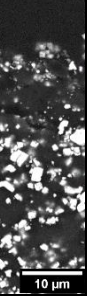
The BQA 644 coating formulation uses a seawater soluble rosin-based binder to hold the pigments (International, 2017), which prevents the electrolyte from entering the coating (Yebra et al., 2004). This allowed discoloured "leach" layer to form within the first

10-30μm from the surface. Leach layers are typically observed within the outer layer of the antifouling coatings exposed to the seawater environment where the biocidal pigments are dissolved, leaving a porous matrix (Caprari et al., 1986; Kojima et al., 2016), which may lead to the degradation of the matrix in hybrid coatings (Azemar et al., 2015).

A leach layer in the modified BQA 644 coating samples was less obvious. This coating contained fewer pigments while the coating matrix between each cuprite particle was more compact, preventing the electrolyte from penetrating deeply and reacting with the coating. To identify this layer, the amount of cuprite pigments visible in surface layer was compared to the bulk of the coating.

A linear crack was observed running parallel to the surface of the BQA 644 samples exposed to each electrolyte, identified as the "detachment layer" and highlighting the self-polishing nature of the coating, maintaining the antifouling properties of the coating. A detachment layer was however not visible in the modified BQA 644 samples, suggesting the removal of some of the pigments from the BQA 644 coating affected the self-polishing behaviour of the coating.

[301]

Table 29 – Table showing the cross-section through the BQA 644 and the Modified BQA 644 coatings following immersion and evaporation conditions at 25°C in the different electrolytes after the specified invervals. Additional SEM images and analysis of the coatings exposed at 45°C is availble in the appendix 10b.

The average thickness of the patina, detachment, and leach layers was measured from the SEM images and is shown in Table 30. The leach layer thickness was determined to increase with sodium chloride concentration, up to 10%, which was consistent for both coatings. Ytreberg et al. (2016) made similar observations where the dissolution of the cuprite pigment in antifouling coatings was accelerated as the chloride concentration was increased between fresh, brackish and seawater, resulting in an increase in the leach layer.

However, the leach layer thickness was reduced with increasing temperatures between 25°C to 45°C. Kiil et al. (2001) found a similar trend which was thought to be caused hydrolysis reaction having a higher activation energy at elevated temperatures when compared to pigment dissolution. This results in an increase in polishing rate with temperature and reduction in the leach layer thickness (Monfared & Sharif, 2008). Furthermore, in the 0% electrolyte at 45°C, no patina, leach, or detachment layers were observed in either coating.

Similarities were found when comparing the leach layer thickness of the BQA 644 and modified BQA 644 coatings tested under laboratory conditions to that observed from the paint flakes removed from in-service marine vessels (Figure 112), with average thicknesses of 15.97 ± 8.73 µm 15.27 ± 7.59 µm and 15.13 ± 1.74 µm, being measured respectively. This suggests that the ingress of the electrolyte and the leaching of pigments under laboratory conditions replicated real world conditions.

Table 30 - Table showing the cross-sectional analysis measuring the thickness of the patina, detachment and leach layers observed in the BQA 644 and Modified BQA 644 samples which had been under immersion and evaporation conditions at 25°C and 45°C in the different electrolytes following the exposure at the specified intervals.

[304]
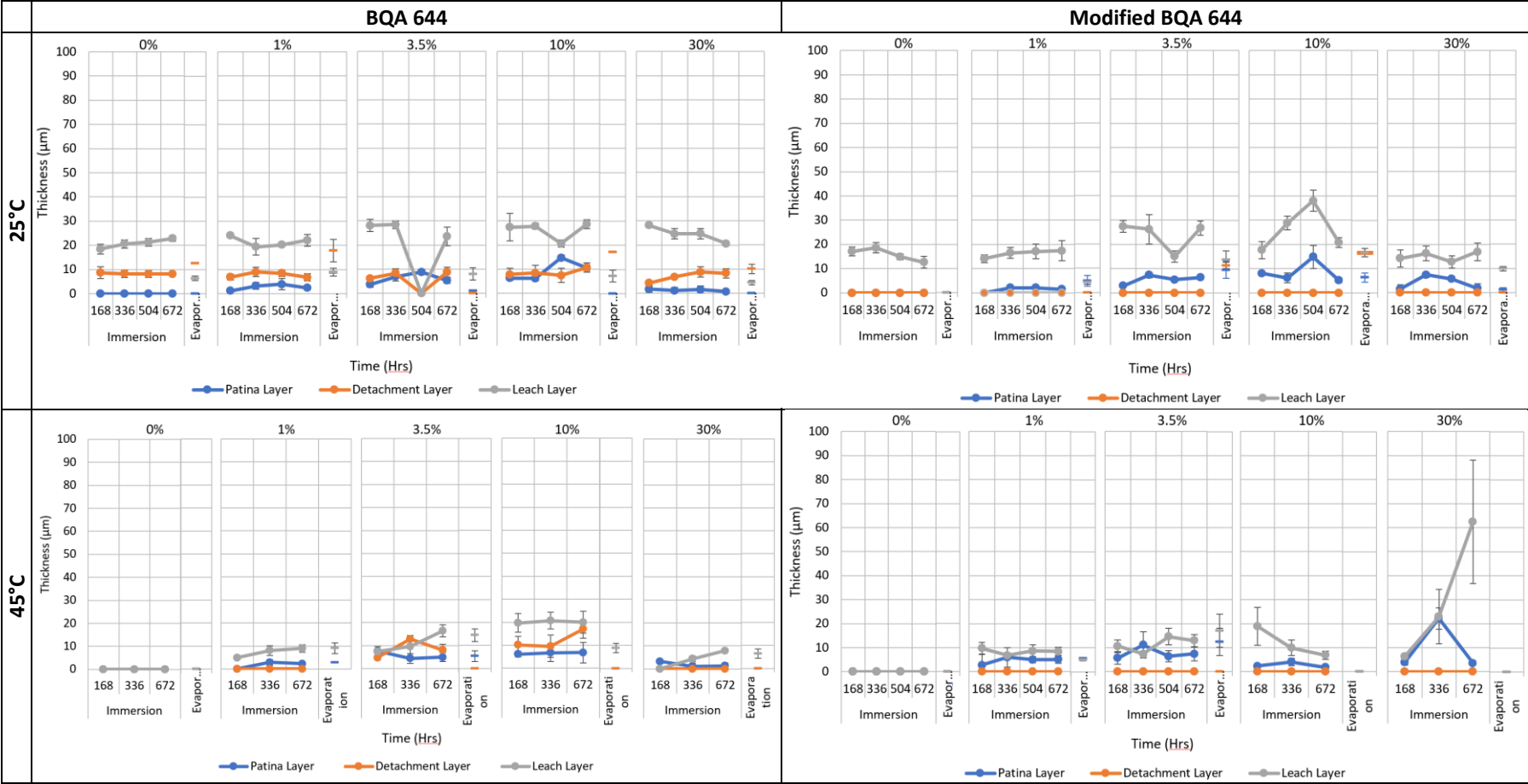
The thickness of the detachment layer found in the BQA 644 samples at 25°C remained stable at 7.9 ± 1.3 μm from the coating surface, regardless of the exposure time or electrolyte in the immersion cell. This suggests the hydrolysis of the coating initiates at a consistent depth once exposed to the electrolyte. However, the average detachment layer thickness in the evaporation cell was increased to 14.2 ± 4.1 μm, which may be associated with the increase in relative chloride concentration as the electrolyte was evaporated aiding in the dissolution of the cuprite pigment (Liao et al., 2011). At 45°C the detachment layer was only visible in the 3.5% and μ% electrolytes, which may indicate that the surface layers are affected by the hydrolysis at a faster rate preventing the formation of a detachment layer deep in coating. While in the modified BQA 644 sample a detachment layer was not found under any condition.

A patina layer was also evident on both coatings when exposed to the chloride containing electrolytes, which was found to increase in thickness with immersion time and sodium chloride concentration, up to 10% (Table 29). The thickening of the patina layer was associated with the leaching of the cuprite pigment, which had been shown to increase with chloride concentration, causing either patina growth, or the nucleation of further patina particles. In the 30% electrolyte, a general reduction in patina thickness compared to the 10% electrolyte was observed. It was noted that in this electrolyte the patina was loosely adhered to the substrate, becoming easily removed during the emptying of the test cell and cleaning procedures, resulting in a reduction in the observed thickness.

The patina layer formed under laboratory conditions on the BQA 644 and the modified BQA 644 was generally larger than that found on the in-service paint flakes, which may

have been exposed to the sea water environment for several months or years prior to removal, with average thicknesses of 5.33 ± 2.54 µm, 7.48 ± 3.93 µm and 0.88 ± 0.02 µm, respectively. This suggests that the immersion and evaporation testing was successful at accelerating the patination of the coatings. However, under laboratory conditions the horizontal orientation and enclosed nature of the test cell retained all patina compounds allowing them to settle on the coating surface. This was unlike what may be expected in-service where once released the infinite dilution of the ocean allows the cuprous ions to rapidly dissipate, rather than concentrate, decreasing their availability and therefore reducing the amount of patina that can form. The movement of the ship through water causes hydrodynamic drag and wave action against the hull which can dislodge loose patina from the surface which is thick enough to surpass the boundary layer and enter the free stream ad therefore ensure that a relatively thin patina layer is maintained. Finally, the orientation of the paint is another factor which may influence patina thickness. Generally, due to the shape of the hull, antifouling paints are applied at orientations greater than 90°, this may reduce the precipitation of patina products as they fall into the ocean rather than settle on to the paint itself.

7.1.3.5 *Patination Rate*

7.1.3.5.1   Visual Assessment

The photographs taken at 24-hour intervals (Tables 17-24) provide a snapshot of the samples as they were being tested, under the different conditions, allowing an estimated patination rate to be recorded. While the initiation of the patination may occur within the 24-hour time frame, it was thought that this period would represent a balance between providing detailed enough information to allow visible changes of the surface to be seen but not so far apart that subtle changes were missed. A subjective analysis of the images was performed to ascertain the onset of patination, which was determined to occur when the surface developed a blue-green coloration, typically associated the formation of copper chloride compounds, or, as in the case of the copper coupons, a red/brown colouration associated with the formation of copper oxides such as cuprite.

Tables 31 and 32 were produced following the visual assessment of the coatings where the patination rate was found to increase with sodium chloride concentration up to 10%. For example, while the cuprite powder was found to develop a blue colouration after 504 hours in the 1% electrolyte, this reduced to 72 hours in the 10% electrolyte under immersion conditions at 25°C. Similarly, the BQA 644 samples did not form a visible patina in the 1%, while in the 3.5% and 10% electrolytes a patina formed after 168 and 24 hours, respectively. However, in the 30% electrolytes the time taken for visible patination on the surface of the coatings to occur tended to increase.

A similar pattern was observed at 45°C, where an increase in sodium chloride concentration up to 10% tended to result in an acceleration in patination rate.

However, the elevated temperature also reduced the time it took for the samples to patinate. This was comparable to the results collected from the Tafel analysis (Chapter 6.1.2) the highest corrosion rate was found in the 10% electrolyte at elevated temperatures. Furthermore, a general acceleration in patination was found when comparing the evaporation cell to the immersion cell which may be due to the constantly increasing chloride concentration as the cell evaporates.

Table 31 – Table showing the typical time in hours for patina to initiate on the samples under immersion and evaporation conditions, at 25℃, in the various sodium chloride electrolytes. N/P indicates that no visible patination formed on the surface of the samples, however loose patina in the electrolyte maybe present. The colours represent the patination rate with green being the fastest and red being the slowest.

Sample	Immersion					Evaporation				
	0%	1%	3.5%	10%	30%	0%	1%	3.5%	10%	30%
Cuprite	N/P	504	96	72	48	N/P	336	168	24	24
Copper coupon (brown patina)	336	24	24	24	336	168	24	24	24	N/P
Copper coupon (blue patina)	N/P	338	168	168	336	N/P	96	336	336	N/P
BQA 644	N/P	N/P	168	24	72	N/P	336	48	48	24
Modified BQA 644	N/P	96	96	24	72	N/P	672	72	24	48

Table 32 – Table showing the typical time in hours for patinate to initiate on the samples under immersion and evaporation conditions, at 45°C, in the various sodium chloride electrolytes. N/P indicates that no visible patination formed on the surface of the samples, however loose patina in the electrolyte maybe present. The colours represent the patination rate with green being the fastest and red being the slowest.

Sample	Immersion					Evaporation				
	0%	1%	3.5%	10%	30%	0%	1%	3.5%	10%	30%
Cuprite	168	336	96	48	48	168	336	96	48	48
Copper coupon (brown patina)	24	24	24	24	336	24	48	24	N/P	N/P
Copper coupon (blue patina)	N/P	N/P	168	336	336	N/P	N/P	168	N/P	N/P
BQA 644	N/P	N/P	24	24	N/P	N/P	384	48	24	24
Modified BQA 644	N/P	48	24	24	24	N/P	24	24	24	24

7.1.3.5.2 Empirical Assessment

The early stage of copper patination has been shown to follow a parabolic growth law where the speed of patination is reduced over time as the cuprite patina layer thickens, slowing the cupric ion diffusion into the environment (Fuente et al., 2008). Under longer immersion times linear growth may be established where a porous patina compound, such as clinoatacamite, develops on the surface through which ions can diffuse through and maintain a constant patination rate.

When assessing the patination rate of the cuprite powder and coatings it may be possible to assume that they would experience linear patination rates as the coatings are designed to release cupric ions at a constant rate, while the ions are freely released from the powder. Once released into the electrolyte they can react with the chloride ions and precipitate out as a porous clinoatacamite layer on the coating (Chapter 7.1.2) or as clinoatacamite particles in the powder.

The mass of the cuprite powder samples was recorded using a 2 decimal place digital balance, following the immersion testing after it was rinsed with deionised water, filtered and dried in a 50°C oven for 4 hours. This allowed for the patination rate, in $mg.day^{-1}$, to be determined based on the semi-quantitative XRD analysis of tenorite, in the 0% electrolytes, and clinoatacamite in the chloride containing electrolytes, divided by the respective immersion time. The results were then averaged to give an average patination rate for each sodium chloride concentration, the results of which are shown in Figure 113.
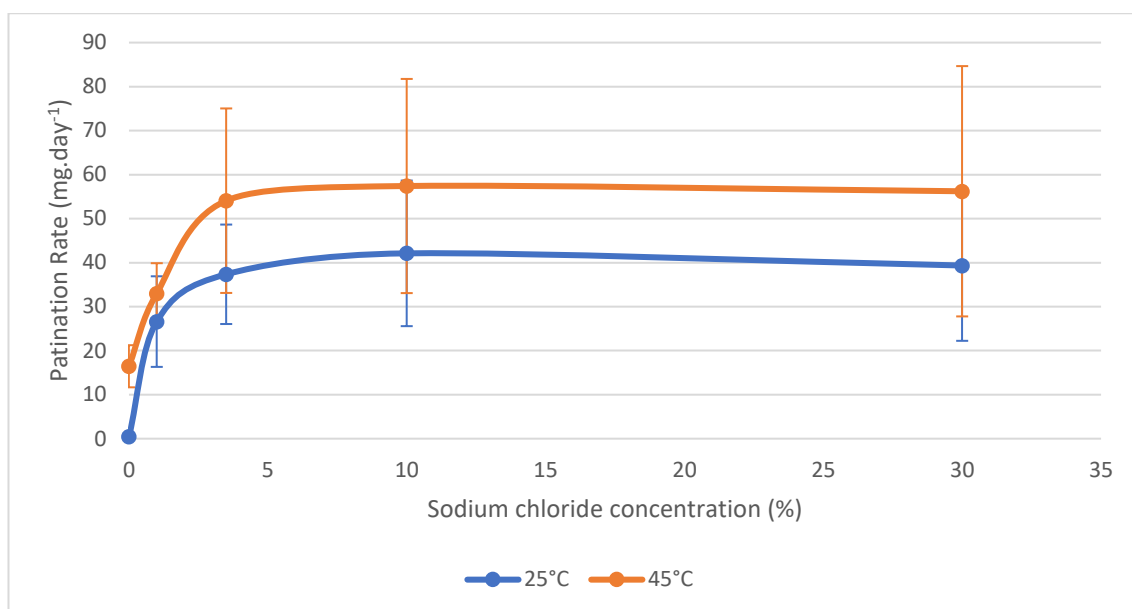
Figure 113 – Average patination rate of cuprite under immersion conditions at pH 7

The largest increase in patination rate was observed between 0 and 3.5%, with a slight increase of ~11% and ~5% at 25°C and 45°C, respectively, between 3.5% and 10% NaCl electrolytes. The patination rate remained unaffected as the sodium chloride concentration was increased to 30% suggesting that electrolytes above 10% NaCl do not accelerate the patination rate of the cuprite powder. Furthermore an increase in temperature also increased the patination rate by between 70% and 80% in each electrolyte. This was similar to the trend observed when measuring the corrosion rate of copper coupons (Chapter 6.2). It is therefore suggested that elevated temperatures and a sodium chloride concentration of no more that 10% would be required to rapidly evaluate the risk of patination on antifouling coatings.

Analysis of the patination rate of the BQA 644 coating (Figure 114) found that at both temperatures had approximately equivalent patination rates in each of the electrolytes. Furthermore the modified BQA 644 coating at 25°C (Figure 115) also had similar patination rates to the BQA 644, where the patination rate peaked in the 10% electrolyte, which was also observed with the cuprite powder. As both coatings were

[310]

of a similar composition it may be suggested that the cuprite pigment leach rate was the limiting factor controlling patination rate, which was minimally affected by elevated temperatures. Therefore lower temperatures may be used to examine the patination of antifouling coatings.

A reduction in the patination rate was observed in the 30% electrolyte which was not replicated in the powder sample. The patina formed in the 30% electrolyte was loosely adhered to the coating surface and was easily removed when emptying the cell, lowering the accuracy of this measurement. This can be seen in the modified BQA 644 coating where an increase in patination rate was measured in the 30% electrolyte at 45°C.
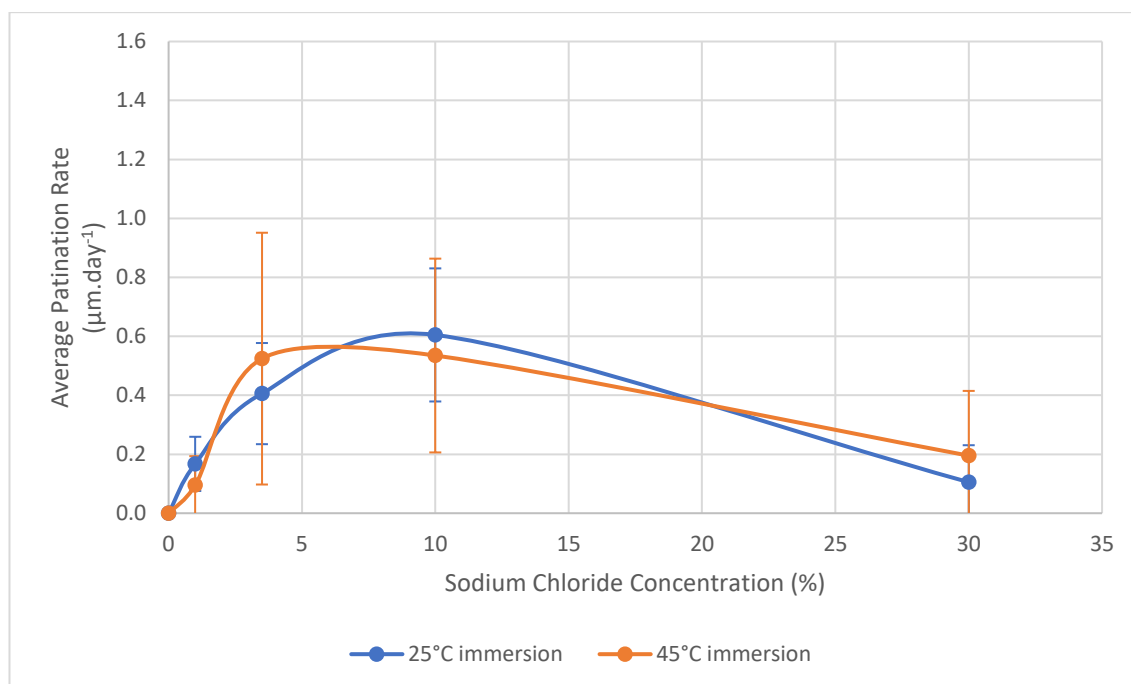
Figure 114 – Average patination rate of the BQA 644 coating in the different electrolytes based on the thickness of the patina layer measured using SEM analysis in the different electrolytes at the different immersion periods.
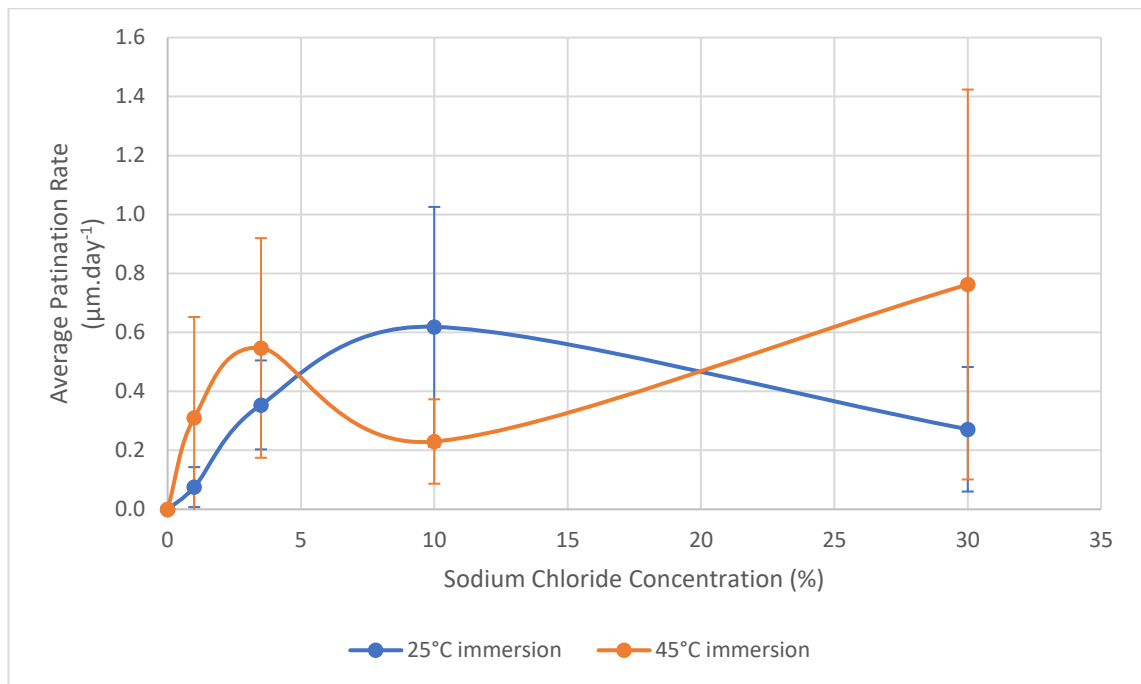
Figure 115 – Average patination rate of the modified BQA 644 coating in the different electrolytes based on the thickness of the patina layer measured using SEM analysis in the different electrolytes at the different immersion periods.

[312]

7.2 Salt Spray Testing of Antifouling Coatings

7.2.1 Introduction

In an open ocean environment, seawater spray develops caused by waves breaking, crashing against the hull or through high winds. Depending on the amount of cargo a ship is carrying it is possible that the boot top can be above the waterline, exposing the antifouling coating to the salt spray environment. This can result in saltwater droplets settling on the coating surface, which concentrates as it evaporates, leaving a salt deposit on the surface. Through subsequent settling of water droplets, the sodium chloride concentration may continue to climb until it reaches the saturation point.

To simulate this environment and to determine whether this technique could increase the patination rate of the antifouling coatings they were exposed to a neutral salt spray environment, under laboratory conditions to ASTM B117. The typical sodium chloride deposition rate in the natural environment was estimated to $4.1 \, \mu g.m^{-2}.day^{-1}$ (BS EN ISO 9223). However, the constantly refreshing saline fog under salt spray corrosion testing resulted in significantly higher deposition rates of $1.5 \times 10^8 - 3 \times 10^8 \, \mu g.m^{-2}.day^{-1}$, assuming a rate of $1 - 2 \, mL$ per hour over a $80 \, cm^2$ collection area (ASTM International, 2019). This may reduce the accuracy of the test when compared to the real-world conditions, as the surface was constantly wet, reducing the ability for the water droplets to evaporate, while the high chloride deposition may enhance the patination rate. However, salt spray tests are generally used to qualitatively assess different materials and coatings at an accelerated rate (Cecchel et al., 2019; Palm & Krieg, 2012) and therefore the high deposition rate would be preferred.

[313]

7.2.2 Effect Of Salt Spray Testing On The Coating Colour

Following a two-week exposure, the discolouration of the coatings was less pronounced than that observed under immersion conditions in the 3.5% NaCl electrolyte for the same time period (Chapters 7.1.1.3 and 7.1.1.4). Therefore, the testing was halted, as it was concluded that this technique did not accelerate the patination of the coatings to a similar or greater extent than immersion testing. It is possible that the orientation of the sample, angled at 30° from vertical, and the continuously refreshing saline fog allowed most of the copper ions released from the coating to be washed away leaving only a thin layer, causing a slight change in colour. Whereas in the immersion cells the coating was position horizontally with the released copper ions remaining in solution, which were able to precipitate out as complex compounds in a thick layer on the coating surface. Further testing of the coatings in the salt spray testing may involve positioning the coatings horizontally matching that of the immersion test. While the introduction of wet/dry cyclic salt spray testing to ASTM G85 annex A2 enabling the water droplets to settle and evaporate and therefore simulate real-world in-service conditions which may also enhance the patination of the coatings.

Tables 33 and 34 show the surface of the BQA 644 and the modified BQA 644 samples, respectively, once they had been removed from the salt spray cabinet, rinsed, and dried. Some discolouration of the BQA 644 coated samples was noted after 72 hours with a uniform surface layer being present after 336 hours. However, after 24 hours, discoloured patches had formed on the modified coating, which continued to develop, forming a less uniform layer than that observed on the BQA 644 samples.

[314]

Due to the deep red colour of the coating and the relatively thin film formed on the surface it is difficult to determine whether a blue-green patina found in the immersion cells and associated with the formation of clinoatacamite, was present. The BQA 644 samples appeared to have a green hue, while the modified BQA 644 samples were bluer. Further analysis of these samples was required to determine if a copper patina compound had formed or whether this is discolouration due to the presence of sodium chloride precipitate.

Table 33– Table showing the progression of patination of the BQA 644 coating when exposed to salt spray for a) 0 hours, b) 24 hours, c) 48 hours, d) 72 hours, e) 168 hours and f) 336 hours.
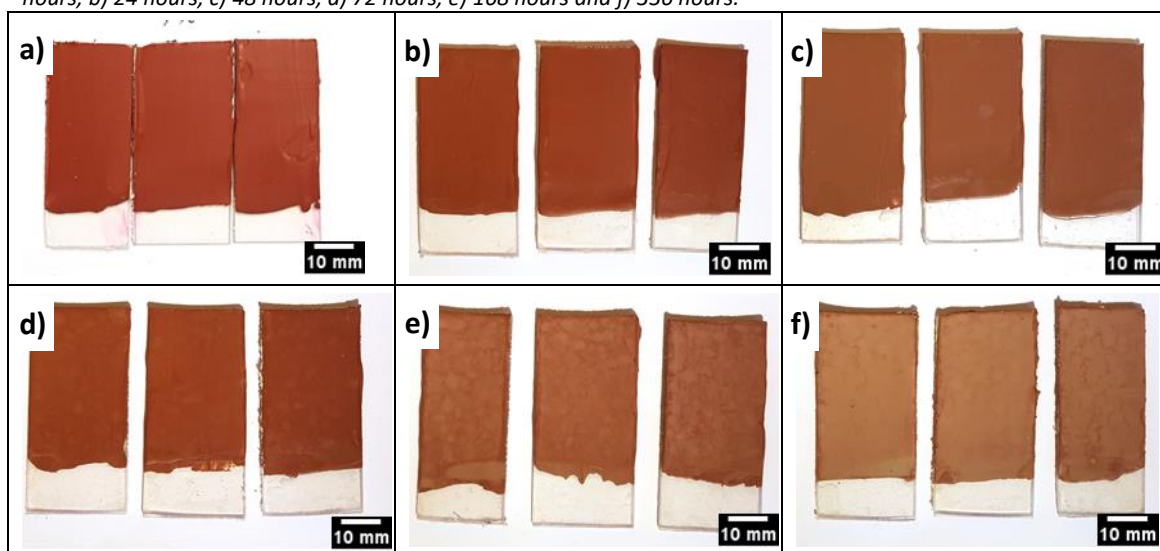
Table 34 – Table showing the progression of patination of the modified BQA 644 coating when exposed to salt spray for a) 0 hours, b) 24 hours, c) 48 hours, d) 72 hours, e) 168 hours and f) 336 hours.
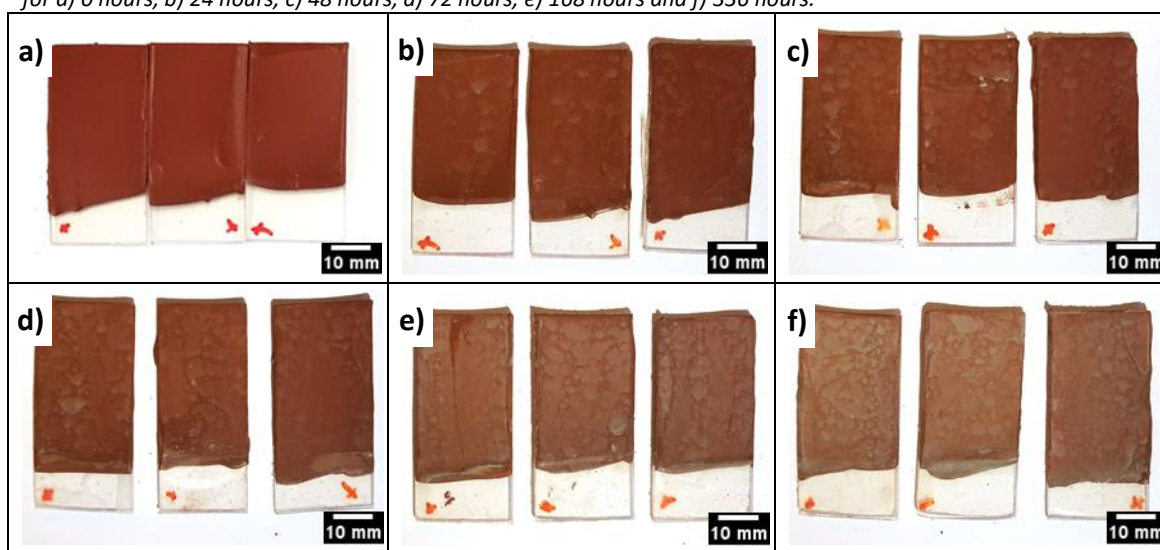
7.2.3 SEM Analysis Of The Coating

Of the three samples removed from the salt spray cabinet after each exposure period one representative sample was selected for further analysis. Each representative sample was sectioned into approximately µmm X 10 mm coupons, one coupon was used for analysis of the surface while the other coupon was mounted, in cross-section, in a 2-part epoxy and ground and polished to 1 µm finish, using standard metallographic practices, to allow the interface between the coating and the environment to be analysed and therefore determine the thickness of any cuprite-depleted surface region, the detachment of the outer layer of the coatings, or the thickness of any patina that may have formed.

Both the surface and cross-section samples were coated with a thin layer of carbon (<20 nm) was evaporated onto the surface, while silver paint was used to provide a conductive path, to ground the samples. The samples were analysed using the SE, BSE and EDX detectors.

7.2.3.1 *Surface Analysis*

Analysis of the surface of the BQA 644 and the modified BQA 644 coatings found evidence of small 'ring' features with a diameter of between 5 and 10 µm (Figure 116b and Figure 119b) consisting of nanocrystalline particulates (200-400 nm) after 72 and 48 hours, respectively. These rings are observed following the evaporation of water droplets containing particles, such as salt crystals or patina compounds that precipitate out as it evaporates, resulting in a "coffee ring" effect where the particles are deposited at the perimeter of the droplet (Shen et al., 2010; Zhang et al., 2018). EDX mapping of the surface found that these nanocrystalline particles were rich in chlorine

(Figure 116d and Figure 119d), however, no sodium enrichment was observed and therefore the particles were not sodium chloride crystals. A slight enrichment in the copper maps can be seen (Figure 116c and Figure 119c), suggesting the nanocrystalline particles were a copper chloride compound.
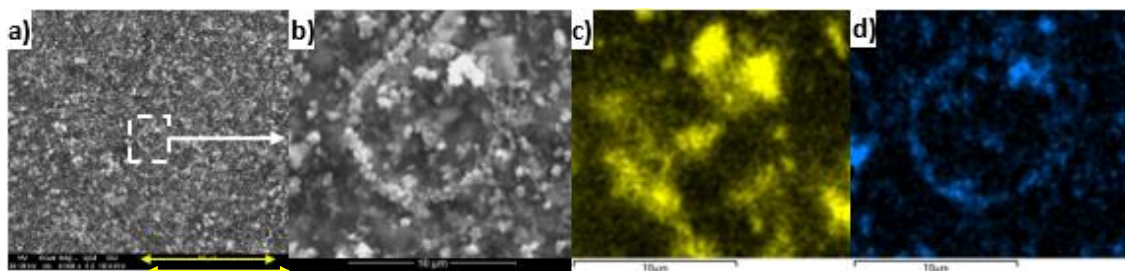
Figure 116 – SEM analysis of the surface of the BQA 644 samples after 72 hours showing a) SE image at 4000x magnification with the yellow scale bar of 50 µm, b) SE image at 16000x magnification with the yellow scale bar of 10 µm, c) Copper EDX map of the image shown in b) and d) chlorine EDX map of the image shown in b).
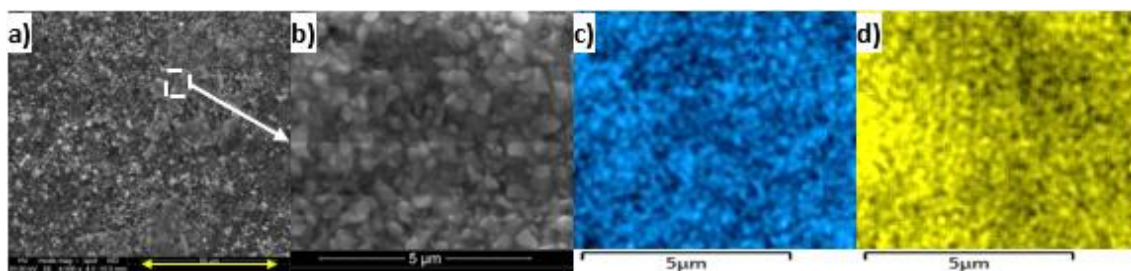
Figure 117 – SEM analysis of the surface of the BQA 644 samples after 168 hours showing a) BSE image at 4000x magnification with the yellow scale bar of 50 µm, b) High magnification SE image, c) Copper EDX map of the image shown in b) and d) chlorine EDX map of the image shown in b).
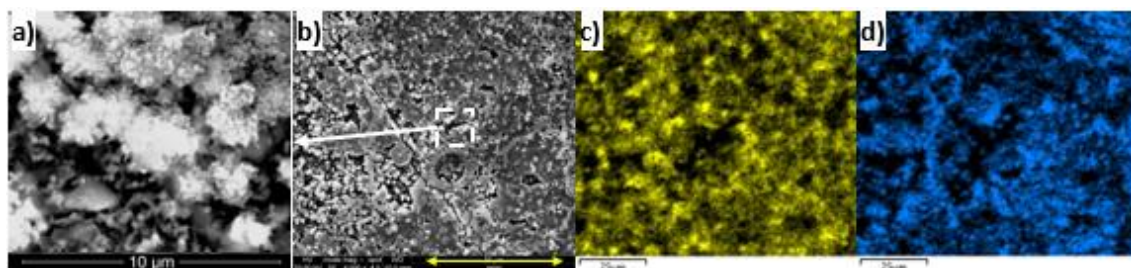
Figure 118 – SEM analysis of the surface of the BQA 644 samples after 336 hours showing a) High magnification SE image of the area shown in b), b) SE image at 4000x magnification with the yellow scale bar of 50 µm, b) Copper EDX map of the image shown in b) and d) Chlorine EDX map of the image shown in b).

With increasing exposure time, the nanocrystalline deposit continued to spread on the BQA 644 sample increasing the coverage of the copper/chlorine rich compounds after 168 hours (Figure 117). After 336 hours the copper and chlorine rich nanocrystalline deposit had spread to form a uniform porous layer while the substrate was visible in places (Figure 118).

[317]

The modified BQA 644 samples had a similar morphology with a copper and chlorine rich deposit forming in patches with features the "coffee ring" effect observed after 48 hours, while the rest of the surface remained clear (Figure 119b and d). Unlike the BQA 644 sample, the particulate on the modified sample formed a cubic structure which grew from approximately 300 nm at 48 hours (Figure 119b) to 500-800 nm after 168 hours (Figure 120b) and 1-2 µm after 336 hours (Figure 121b).
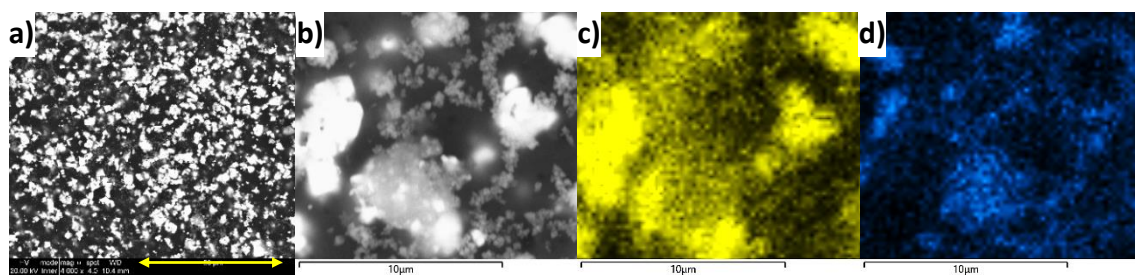
Figure 119 – SEM analysis of the surface of the Modified BQA 644 samples after 48 hours showing a) BSE image at 4000x magnification with the yellow scale bar of 50 µm, b) High magnification SE image, c) Copper EDX map of the image shown in b) and d) chlorine EDX map of the image shown in b).
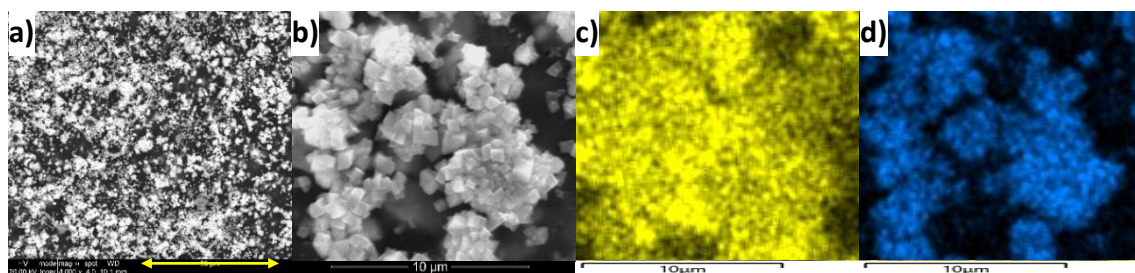
Figure 120 – SEM analysis of the surface of the Modified BQA 644 samples after 168 hours showing a) BSE image at 4000x magnification with the yellow scale bar of 50 µm, b) High magnification SE image, c) Copper EDX map of the image shown in b) and d) chlorine EDX map of the image shown in b).
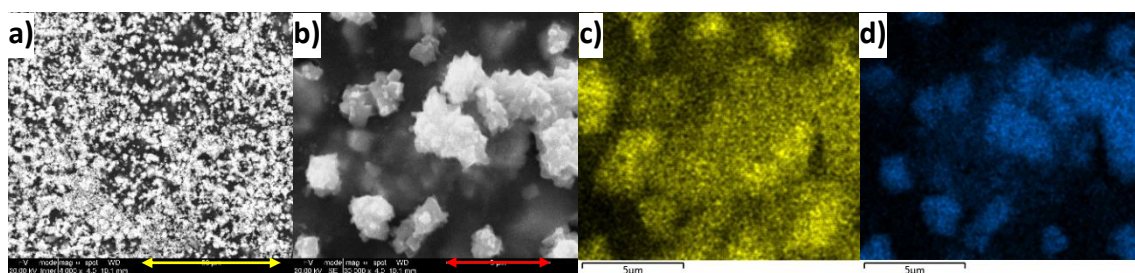
Figure 121 – SEM analysis of the surface of the Modified BQA 644 samples after 336 hours showing a) BSE image at 4000x magnification with the yellow scale bar of 50 µm, b) SE image at 30000x magnification with the red scale bar of 5 µm, c) Copper EDX map of the image shown in b) and d) chlorine EDX map of the image shown in b).

Semi-quantitative EDX analysis of the coatings determined that while carbon was detected in each spectrum it was excluded from the analysis due to the low quantitative accuracy. Furthermore, the samples were carbon coated which would

[318]

further lower the accuracy of the analysis. Therefore, the analysis concentrated on the pigments that were present as well as any external source elements such as chlorine from the salt spray environment.

Table 35 shows the semi-quantitative EDX analysis of the elements present in the two coatings, where the BQA 644 samples contained sulphur (4.4-7.8%), iron (4.3-5.8%) and zinc (25.2-32.2%) which were not detected in the Modified BQA 644 coating. This confirmed that these were removed from the Modified BQA 644 allowing an increase in cuprite loading (Figure 123), which was approximately double that of the BQA 644 coating.

Table 35 – Semi-quantitative EDX analysis of the BQA 644 and the modified BQA 644 samples at each time period.

Sample	BQA 644 (wt%)									Modified BQA 644 (wt%)					
	O	Al	Si	S	Cl	Ca	Fe	Cu	Zn	O	Al	Si	Cl	Ca	Cu
24 Hours	17.0	0.6	2.9	7.4	0.5	1.1	5.8	32.6	32.2	16.9	0.8	6.1	1.6	0.4	74.2
48 Hours	17.8	0.5	2.8	7.8	0.7	0.8	5.7	32.5	31.5	17.0	0.6	4.2	2.8	0.2	75.2
72 Hours	17.0	0.4	2.5	7.3	1.1	0.6	5.8	33.2	32.2	18.4	0.6	3.6	3.2	0.3	73.9
168 Hours	17.1	0.4	1.6	6.2	2.8	0.3	5.5	34.8	31.3	19.9	0.4	1.8	7.6	0.3	70.1
336 Hours	19.4	0.2	0.8	4.4	7.0	0.3	4.3	38.5	25.2	21.4	0.3	1.4	9.9	0.2	66.8

Chlorine was also detected on both coatings the concentrations of which continued to increase with exposure time in the salt spray environment (Table 35). However, sodium was not found suggesting that the increase in chlorine was associated with a reaction between the pigments in the coatings, probably cuprite to form an insoluble copper chloride compound, as suggested by the EDX maps (Figures 116 to 121) and not due to the formation of sodium chloride crystals from the saline fog.

Both samples were exposed to the same salt spray environment in similar location in the chamber, therefore deposition rate of the salt solution should have been

comparable, hence it would be expected that equivalent amounts of chloride would be present on each coating. However, Figure 122 shows that chlorine detected on the modified BQA 644 samples was higher at each time when compared to the BQA 644 samples. A large increase in chlorine concentration was observed within the first 48 hours, after which the increase in chlorine tended to slow, peaking at 9.9% after 336 hours. The opposite behaviour was observed on the BQA 644 sample, where the chlorine level had a slower increase in concentration peaking at 7% after 336 hours. While the trendlines in Figure 122 show a good agreement to the data provided additional data points at 125, 225, 275 and 400 hours would help to confirm this trend.
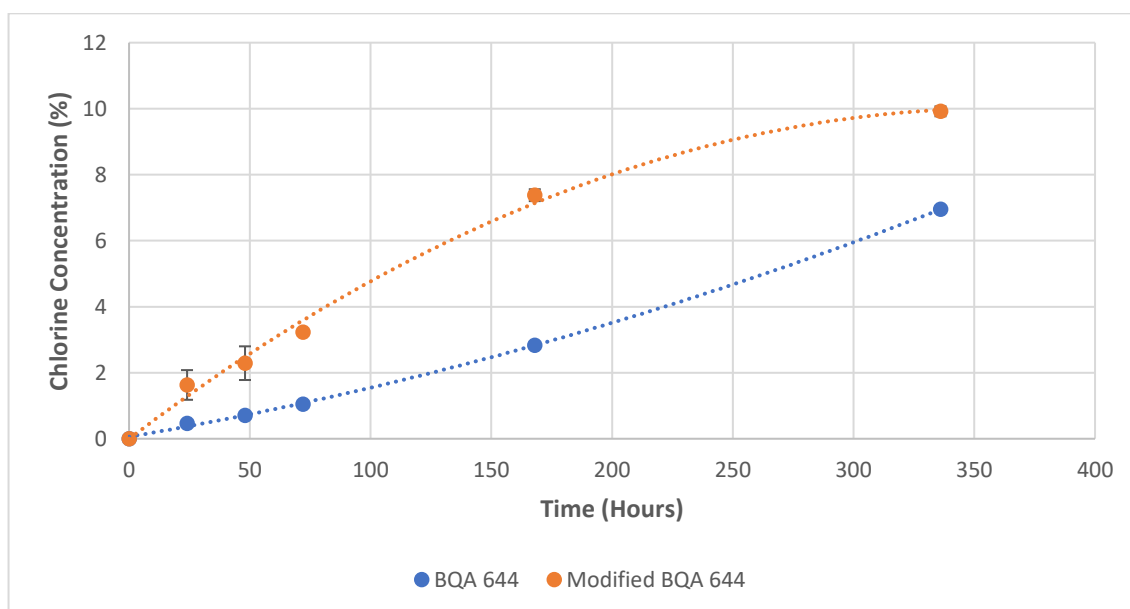
Figure 122 – Graph detailing the semi-quantitative EDX analysis of chlorine found on the BQA 644 and Modified BQA 644 samples as they were in the salt spray environment under increasing exposure time. The error bars are hidden by the marker and are based on ±1 hour in the x-direction and 3x sigma in the y-direction (Oxford Instruments Nanotechnology Tools Ltd, 2021).

The different chlorine concentrations found on the two coatings may be related to the pigment loading where the modified BQA 644 coatings had a higher amount of cuprite available at the coating surface when compared to the BQA 644 coatings as they did not contain any additional pigments (Figure 123). This resulted in the greater availability of copper ions which could react with the chlorine in the environment and

[320]

form higher amounts of insoluble copper chloride compounds more quickly than on the BQA 644 coatings.
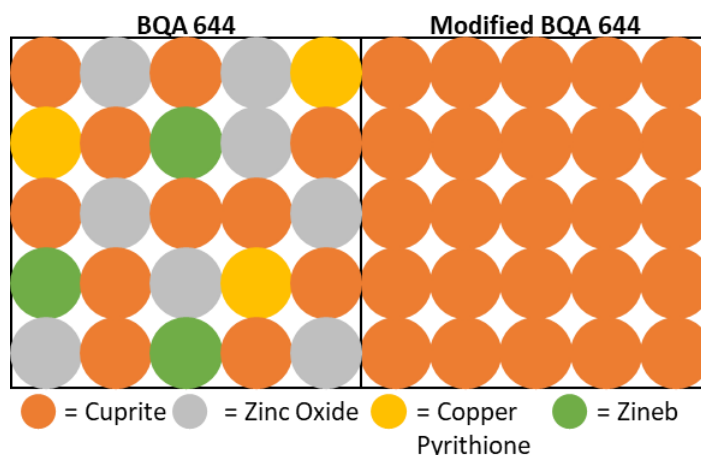
Figure 123 – Idealised schematic of the pigment loading in the BQA 644 and modified BQA 644 coatings

7.2.3.2 Cross-Sectional Analysis

Cross-sectional analysis of the coatings exposed to the salt spray environment did not show any evidence of coating patination, depletion, or detachment (Figures 124a, b and c [i] and 125 a, b and c [i]), observed on the in-service paint flakes (Chapter 4.2.2) or following the immersion and evaporation testing (Chapter 7.1.3.4). After performing EDX maps of the surface, a thin chlorine-rich lay could be seen after 336 hours on the BQA 644 sample (Figure 124c [ii]) and after 168 hours on the modified BQA 644 sample (Figure 125b [ii]). The chlorine-rich layer continued to develop after 336 hours becoming thicker and more uniform (Figure 125 c[ii]).
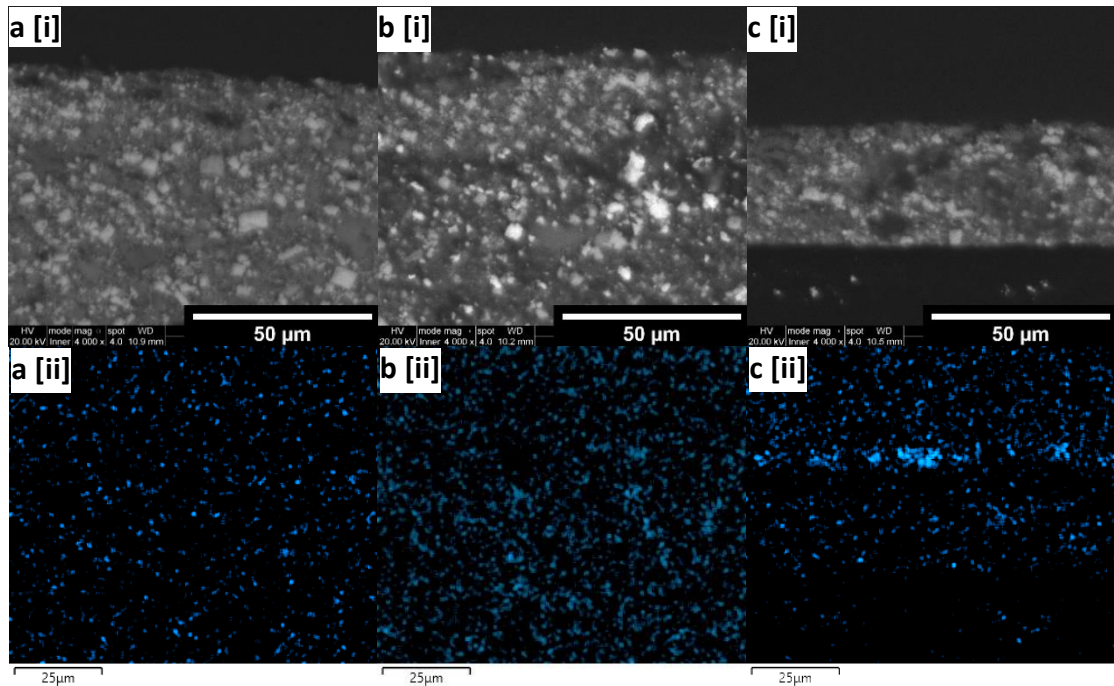
Figure 124 – Cross-sectional SEM analysis of the BQA 644 sample after salt spray testing for a) 72, b) 168 and c) 336 hours showing [i] the BSE image and [ii] the chlorine elemental map.

The distribution of the pigments in the two coatings was observed when analysing the cross-sections where the pigments in the BQA 644 samples were dispersed through the cross-section (Figure 124). However, in the modified BQA 644 the cuprite pigments are more tightly packed together (Figure 125).
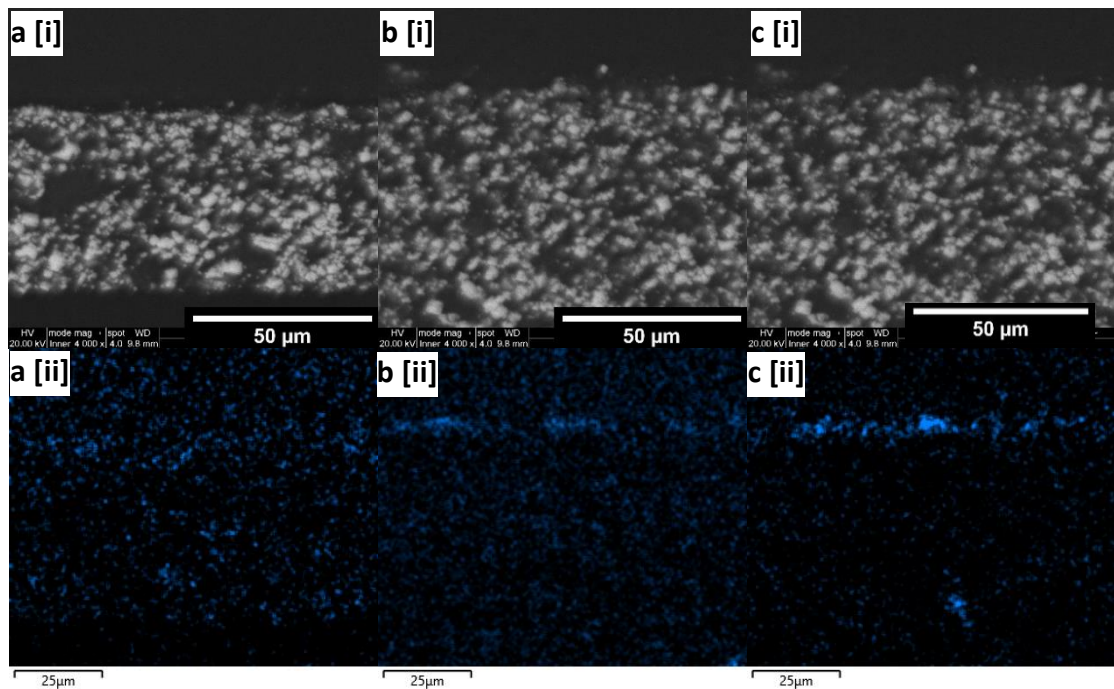
Figure 125 – Cross-sectional SEM analysis of the modified BQA 644 sample after salt spray testing for a) 72, b) 168 and c) 336 hours showing [i] the BSE image and [ii] the chlorine elemental map.

[322]

7.2.4 Determination Of The Compounds Formed On The Coating Surface

The crystalline pigments detected in the BQA 644 coating included haematite, zinc oxide, zineb, and copper pyrithione. While the presence of these pigments was notable the most important peaks relate to cuprite and any additional peaks that may form during the exposure. Therefore, these peaks were identified with an "a" and "b" respectively while the other peaks were identified with an "X" (Figure 126).

From Figure 126 a single peak was found at 18.3° after 72 hours, while after 168 hours two further peaks formed at 32.5° and 39.9°. These peaks were associated with the formation of clinoatacamite ($Cu_2Cl(OH)_3$) (indicated as 'b' in Figure 126). With increasing exposure time to 336 hours the intensity of these additional peaks increased, suggesting an increase in the concentration of this phase.
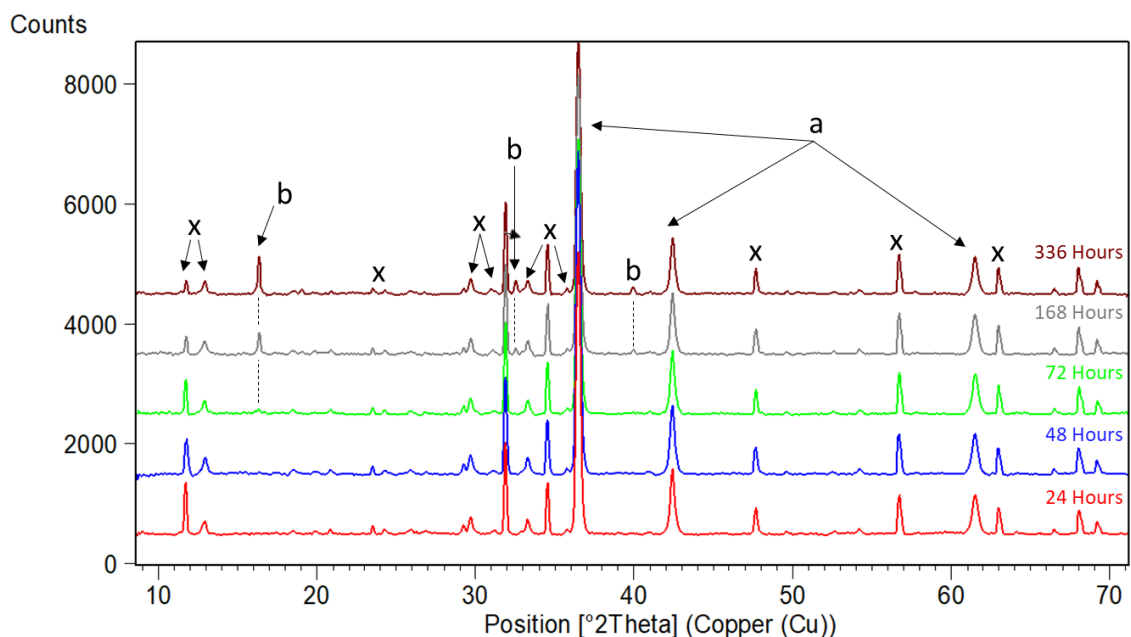
Figure 126 – XRD traces of the BQA 644 coated samples following 24 hrs, 48 hrs, 72 hrs, 168 hrs and 336 hrs salt spray testing. The peaks labelled as a= Cuprite, b= Clinoatacamite and x= paint pigment.

Figure 127 shows the XRD analysis of the modified BQA 644 sample after each exposure period where a small peak was identified after 24 hours at 16.3°. After 72 hours two additional peaks were identified at 30.9° and 32.5° with an additional peak

being observed after 168 hours at 39.9°. These peaks were also associated with the presence of clinoatacamite (b), the intensity and therefore concentration of which increase with exposure time up to 336 hours.
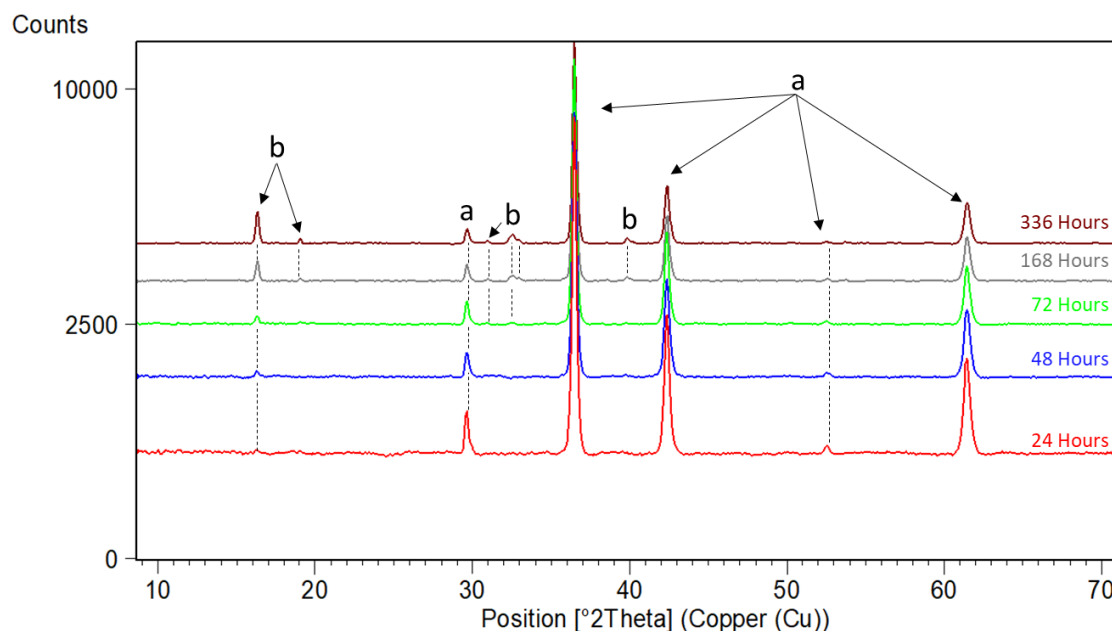
Figure 127 – XRD traces of the modified BQA 644 coating containing only the cuprite pigment following 24 hrs, 48 hrs, 72 hrs, 168 hrs and 336 hrs salt spray testing. The peaks labelled as a= Cuprite and b= Clinoatacamite.

Figure 128 shows a semi-quantitative analysis of the clinoatacamite phase relative to the major phases present in the two coatings, identified from the XRD analysis, namely cuprite and zinc oxide in the BQA 644 sample and cuprite in the modified BQA 644 sample. A linear increase in clinoatacamite concentration, relative to cuprite, was detected within the first 48 hours on the modified BQA 644 sample, after which the increase in clinoatacamite slowed. This followed a similar trend to the semi-quantitative EDX chlorine concentration analysis (Figure 122). However, the same trend was not observed on the BQA 644 coating where no detectable clinoatacamite was found within the first 48 hours while after 72 hours there was a near linear increase in clinoatacamite relative to the cuprite and zinc oxide compounds, similar to the increase in chlorine concentration between 72 and 336 hours. This suggests that

either the detection limit of clinoatacamite occurred when the chlorine concentration was above 1%, increasing the size of the peaks in the XRD pattern above the background radiation, or that clinoatacamite formed on the coating when the chlorine concentration was above 1%.
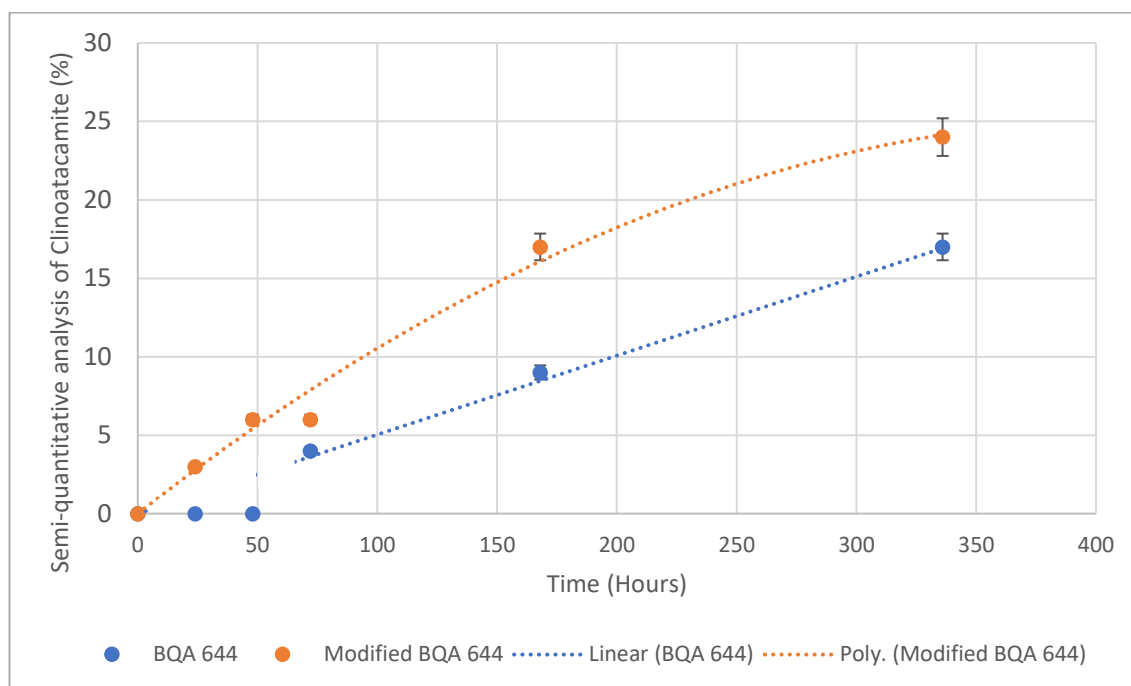
Figure 128 – Semi-quantitative XRD analysis of the clinoatacamite phase relative to the major phases in the coatings namely cuprite and zinc oxide in the BQA 644 sample and cuprite in the modified BQA 644 sample. The error bars are mostly hidden by the markers with a ±1-hour error in the x-direction and assuming a 95% confidence interval in the y-direction

7.2.5   Discussion

Visual inspection of the BQA 644 sample found that the surface of the coating remained unaffected by the salt spray environment for the first 48 hours with discolouration occurring after 72 hours. SEM analysis confirmed that while chlorine was detected in the first 48 hours it was in relatively low concentrations, with no visible crystalline material being found on the surface when examined at high magnification. The XRD analysis also confirmed that no other phases had formed on the coating surface with only those peaks attributable to the pigments in the coatings being visible. After 72 hours the discolouration of the coating was noted with higher

concentrations of chlorine being detected along with nanocrystalline material. XRD analysis confirmed the presence of a characteristic clinoatacamite ($Cu_2Cl(OH)_3$) peaks. The discolouration of the coating increased with increasing exposure time, increasing the amount of nanocrystalline particles, chlorine concentration and the intensity of the clinoatacamite peaks until a near uniform film had formed after 336 hours.

The modified BQA 644 coating also became discoloured, occurring after 24 hours. Further analysis of the coating found evidence of chlorine via EDX analysis and XRD analysis showed a low intensity peak identified as clinoatacamite. After 48 hours a nanocrystalline particulate was visible which grew into larger cubic structures after longer immersion times with an increase in the chlorine and clinoatacamite concentrations.

The main difference between the two coatings was the cuprite loading (Figure 123). The BQA 644 coating contained various pigments to enhance the fouling resistance of the cuprite containing coating, such as copper pyrithione and zinc oxide. While fillers such as calcium, silicon and haematite may also be used to bulk out the paint. These pigments may interact with the environment and each other. For example, an increase in the zinc dissolution may occur if they were in electrical contact with the cuprite pigment due to galvanic corrosion. Furthermore, the incorporation of zinc ions into the $Cu_2Cl(OH)_3$ structure may result in the formation of paratacamite (Grice et al., 1996; Jambor et al., 1996), however this was not detected on these coatings. Furthermore, zinc ions can form soluble compounds, while copper chloride compounds are insoluble.

The extra pigments in the BQA 644 coating also reduces the availability of cuprite particles at the surface, and therefore limits the amount of copper ions that can be released to react with chloride in the environment, compared to the tightly packed cuprite found in the modified BQA 644 coating (Figures 124 and 125). The lower level of copper ions therefore results in the small amount of clinoatacamite detected on the BQA 644 when compared to the modified BQA 644 coating.

7.3 Potentiostatic Polarisation To Accelerate The Patination Of Antifouling Coatings

7.3.1 Introduction

The immersion and evaporation testing was shown to produce the same clinoatacamite patina as that formed on antifouling coatings taking up to 672 hours to develop, depending on the chloride concentration. While this is generally quicker than what may be observed from in-service testing, it limits the number of different coatings that could be tested, where it may be preferred that evidence of patination would be determined within several hours. A significant acceleration in clinoatacamite formation was observed following the potentiostatic polarisation and therefore this technique was applied to determine if similar accelerations could be measured.

Typical antifouling coatings supplied by AkzoNobel contain between 40% and 65% volume solids of which 25-50% by weight is cuprite (AkzoNobel, N/D). Therefore, it would be expected that under short exposure times the different antifouling coatings i.e., controlled depletion, hybrid, or self-polishing co-polymer, would behave identically with the surface cuprite pigments being released at comparable rates. Therefore, due to its availability, using the Intersmooth 7460HS® SPC coating instead of the BQA 644 coating, used previously, would not be detrimental as they had similar volume solid of 55% to 60%, respectively, and cuprite concentrations of 25-50 wt%.

Using the potentiostatic polarisation results from the analysis of copper (Chapter 6.1.3) and the immersion testing on the BQA 644 coating (Chapter 7.1.1.3) it was determined that the potentiostatic polarisation of the antifouling coating would be performed in 20 mL of freshly mixed neutral 3.5% NaCl at 25°C, using a potential of 260 mV vs Ag/AgCl, for 48 hours. These conditions were selected as no obvious blue-

green patina was found until after 168 hours under immersion conditions where clinoatacamite was detected, while polarising at 260 mV vs Ag/AgCl resulted in the formation of mainly clinoatacamite after 5 hours. Three test cells were manufactured to the design shown in Chapter 3.3.5.2. Samples 1 and 2 were made into a three-electrode electrochemical cell, allowing the OCP to be measured and the coating to be polarised, by using the steel substrate as the working electrode and adding a Ag/AgCl reference electrode and platinum counter electrode into the electrolyte. Sample 3 was used as a reference and was not polarised.

7.3.2 Visual Examination

Figure 129 shows the visual analysis of the surface of the coatings during the testing where no obvious copper patination was found on the control sample after 48 hours exposition to the neutral 3.5% NaCl electrolyte. However, after 24 hours a small imperfection with a reddish appearance in the coating was observed (Figure 129b). This continued to grow into a relatively large blister after 48 hours (Figure 129c). The coatings were applied directly onto a mild steel substrate, without the primer, tie or anticorrosion coatings which protect the steel hull of a marine vessel from corrosion due to the adsorption of seawater or from galvanic corrosion forming between the cuprite steel couple. This therefore suggests that the electrolyte had penetrated through to the substrate causing it to corrode, forming a large volume of iron oxide corrosion product. Defects in the coating such as holidays and cracks allow direct access to the substrate and can occur during the application and curing stages. The application of multiple thinner layers can reduce the internal stresses in the coating layers as it dries, reducing the likelihood of these defects from occurring, as well as covering any defects that may have formed in the previous layer.

[329]

After 24 hours the potentiostatic polarisation caused the coating to degrade (Sample 1 Figure 129e) where copious amounts of a red/orange corrosion product was visible along with cracks in the coating, suggesting that corrosion of the substrate had been accelerated. Furthermore after 48 hours (Figure 129f) the coating was shown to peel away from the substrate in flakes. However, the steel substrate in Sample 2 was unaffected with no corrosion products being observed after 24 hours (Figure 129h), while after 48 hours a string like compound had formed (Figure 129i). This was not found on the control sample and may suggest an acceleration in the formation of a corrosion product or patina compound.
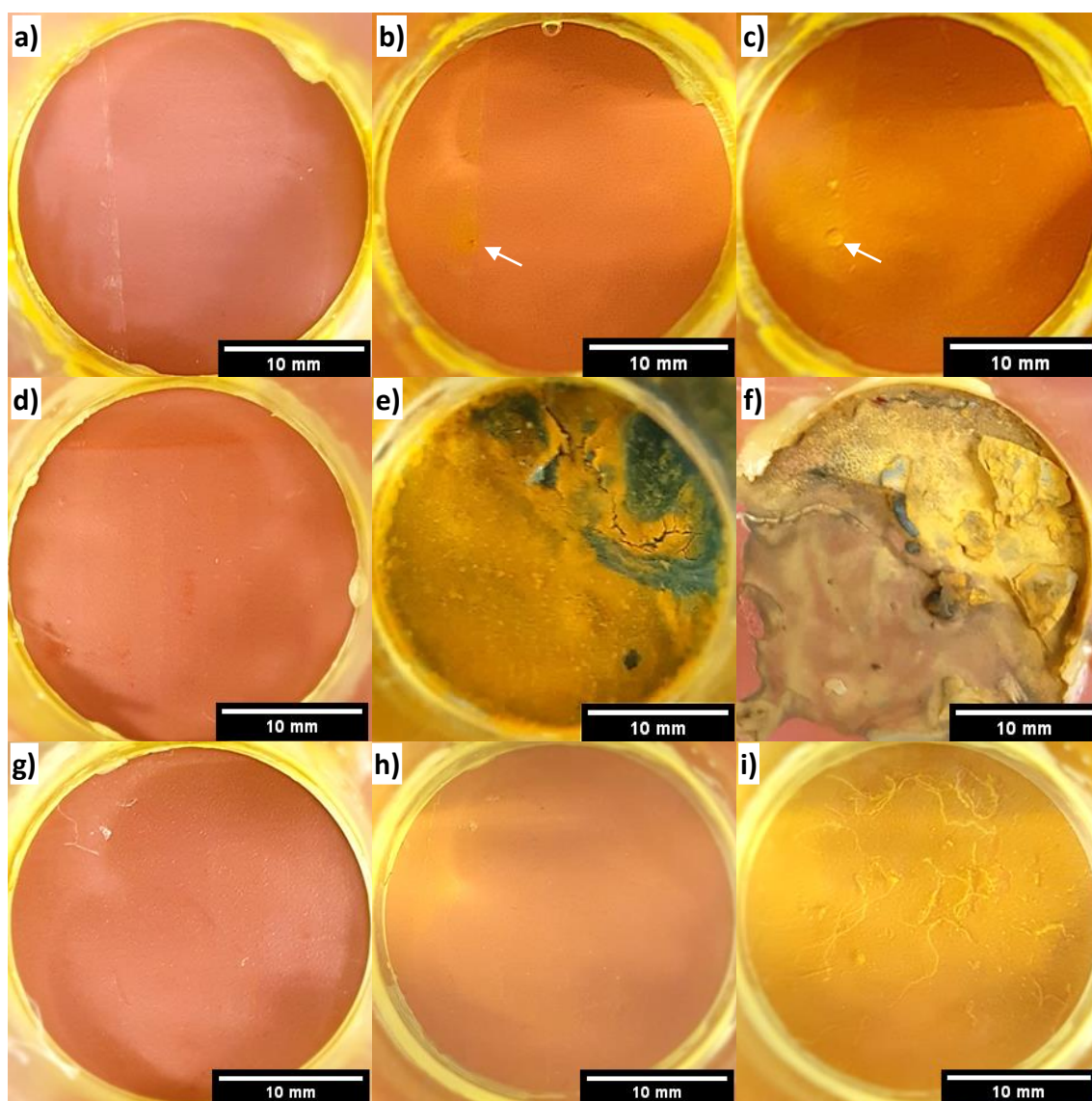
Figure 129 – Photographs of the surface of the antifouling coatings following different testing conditions. Top row shows the control immersion sample a) prior to testing, b) after 24 hours and c) after 48 hours. The middle and bottom rows show the Samples 1 and 2, respectively, before (d and g) and after 24 hours (e and h) and 48 hours (f and i) potentiostatic polarisation at 260 mV vs Ag/AgCl in a neutral 3.5% NaCl electrolyte.

[331]

7.3.3 Coating Potential

Using the OCP technique, measurements of the coating potential relative to the saturated potassium chloride Ag/AgCl reference electrode were performed to provide a means of determining whether any defects were present prior to potentiostatic polarisation. Murray (1997) showed that a newly exposed coating with excellent barrier properties and no defects have a potential of 0-300 mV vs Ag/AgCl, with approximately 0.001% of the substrate forming an anodic or corroding area (Figure 130). This feature was found on the OCP of Sample 2 where a stable potential of approximately 60 mV was recorded for the around 10 minutes. This was also found on Sample 1 however it had a more electronegative potential of approximately -440 mV suggesting, according to Figure 130, that the coating coverage was <90% or the size of the anodic or corroding area was >10% or >47.5 mm^2 of the total 475 mm^2 area. This may also account for the condition of Sample 1 following the potentiostatic polarisation testing shown previously.
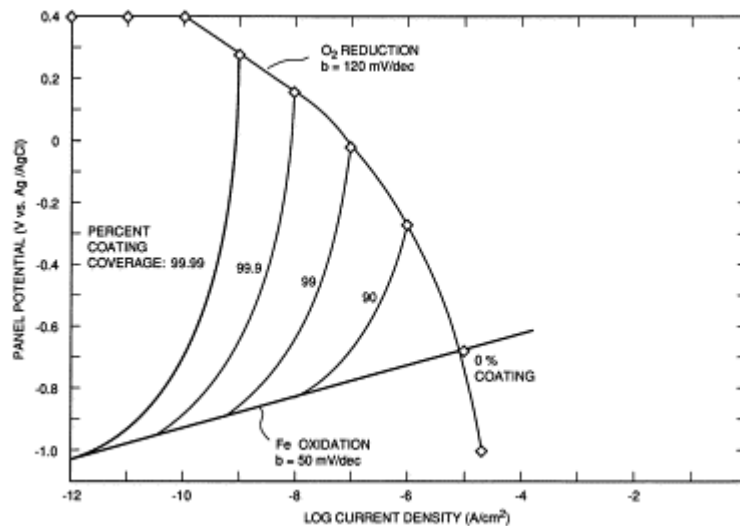
Figure 130 – Schematic Evans' diagram for coated steel taken from (Murray, 1997).

With increasing immersion times, the coating potential of both samples was shown to become more electronegative where the potential of Sample 1 drifted to match and stabilise around the potential of the steel control sample, while Sample 2 stabilised at

[332]

approximately -300 mV vs Ag/AgCl after 30 minutes. This change in potential was attributed to the adsorption of the electrolyte through the coating to the interface with the steel substrate allowing the potential to stabilise at more electronegative values, such as that observed previously (Deyá et al., 2002; Leidheiser, 1991; Murray, 1997; Nikravesh et al., 2011). Furthermore, the rate at which the potential stabilised at a more electronegative potential was slower in Sample 2 taking approximately 40 minutes compared to approximately 25 minutes shown in Sample 1. This also indicates that the Sample 2 offered a better barrier to the environment than Sample 1. The thickness of the coating may also influence the coating potentials however they were measured to be nominally the same with a dry film thickness of 147 ± 17.9 µm.
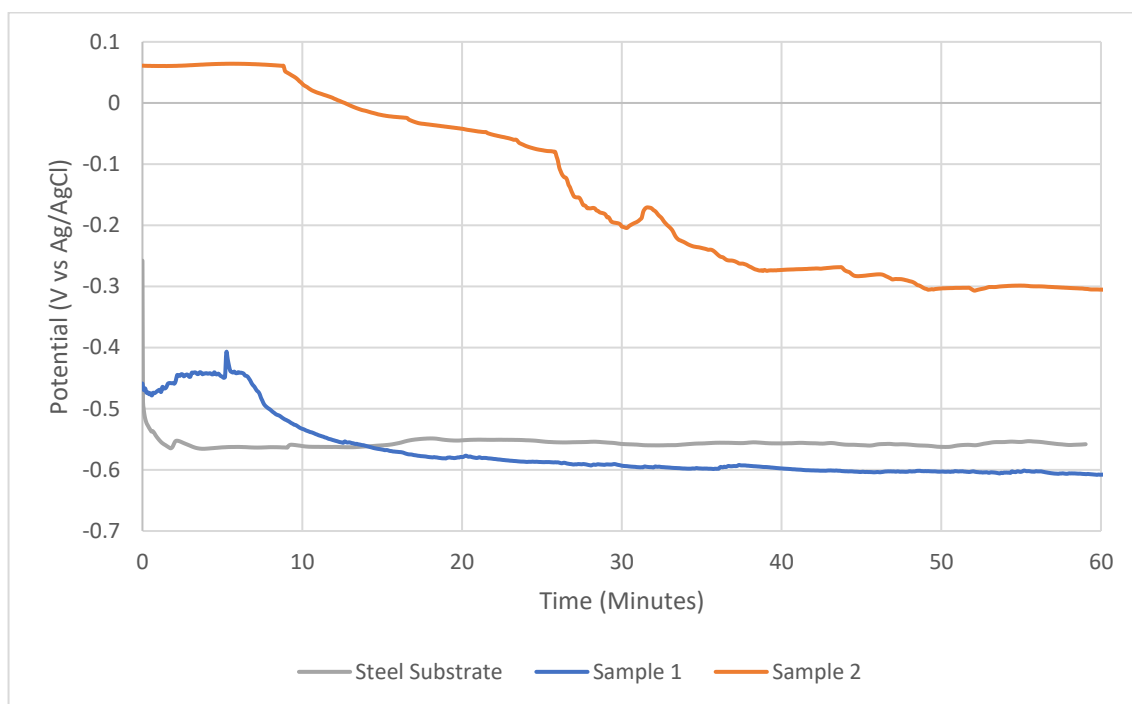
Figure 131 – OCP measurements of the Steel control and Samples 1 and 2 over a 24-hour period

[333]

7.3.4   Potentiostatic Polarisation Curves

Samples 1 and 2 were potentiostatically polarised at 260 mV vs Ag/AgCl for 48 hours following the stabilisation period where the OCP of the test cell was measured for 1 hour. Figure 132 shows the current density-time curves for the first and last 12 hours of the testing. The curves show that Sample 2 was effective at providing a barrier to the environment, under short immersion times, as the lowest current density was recorded throughout the immersion period and therefore would experience the lowest amount of corrosion. This was confirmed through the visual examination where the coating was shown to remain intact with the formation of string like compounds being found. However, Sample 1 had the highest current density where the corrosion of the substrate was unimpeded by the coating allowing a red rust corrosion product to form and the coating to be removed from the substrate.
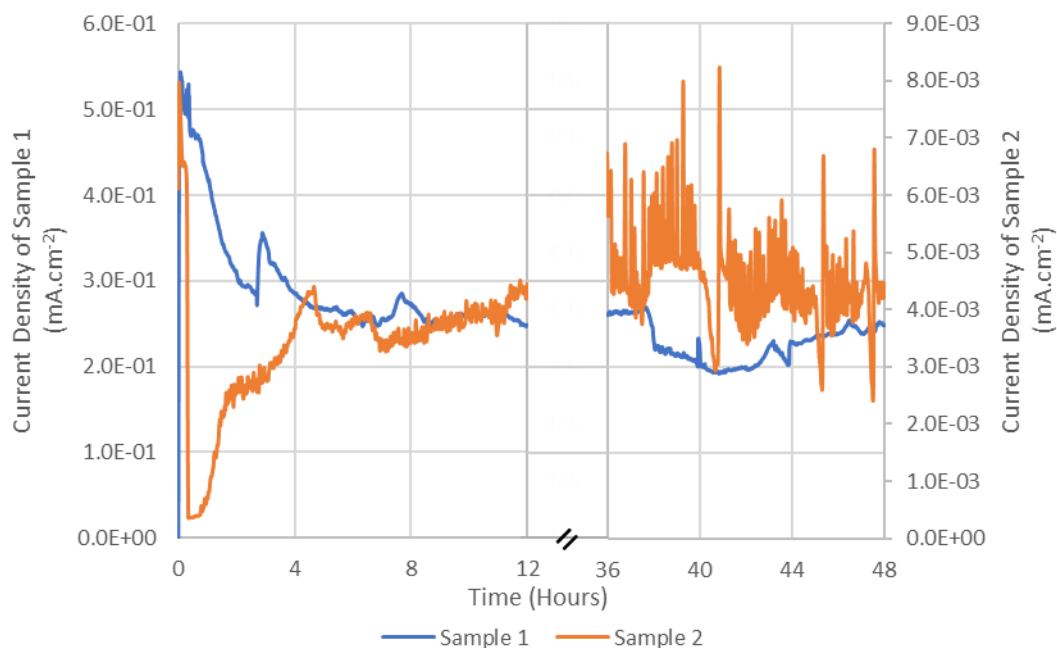
Figure 132 – Potentiostatic polarisation of the coated at 260 mV vs Ag/AgCl showing the current time trace over a 24-hour period.

[334]

7.3.5   Corrosion Product Identification

The gross contamination of the surface of Sample 1 following the potentiostatic polarisation testing due to the corrosion of the steel substrate prevented it from being analysed as the iron oxide corrosion products dominated the surface. Therefore, the testing focused on the control sample, which showed no evidence of patination, and Sample 2, which showed the formation of a string like compound. The electrolyte from these samples were filtered to capture any loose insoluble corrosion product that had formed which may be indicative of copper patination for XRD analysis.
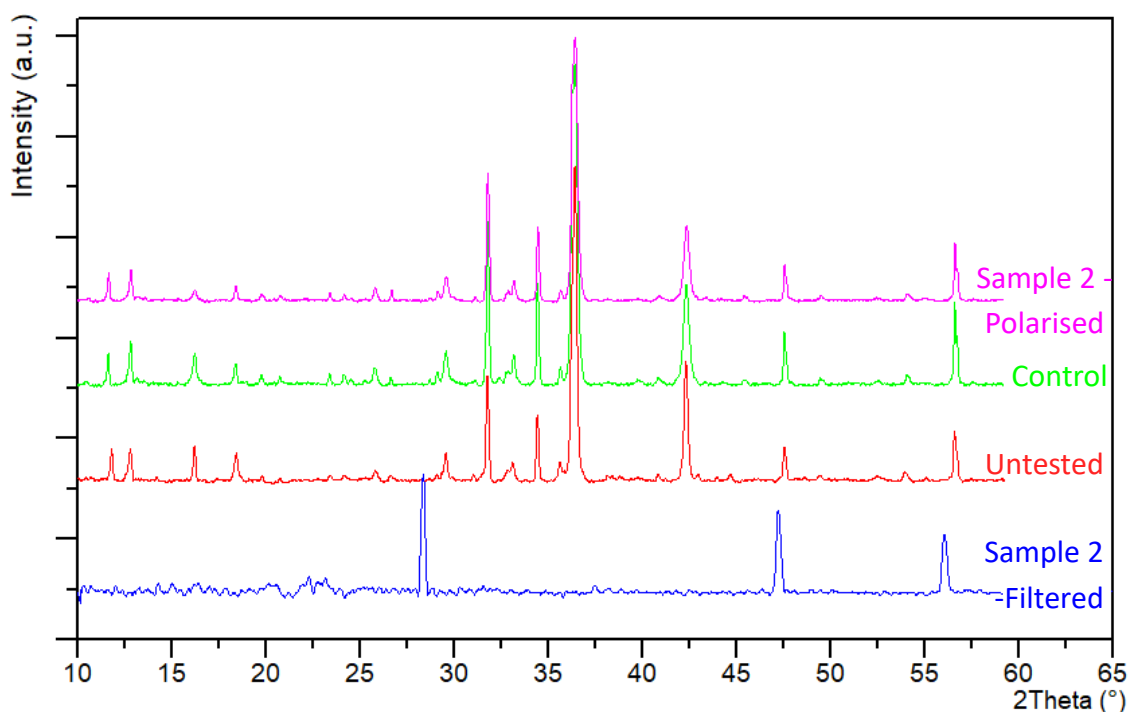
Figure 133 – XRD analysis of the coating surface in the untested condition, after immersion for 48 hours, after potentiostatic polarisation for 48 hours at 260 mV vs Ag/AgCl (Sample 2 – Polarised) and of the filtered particulate collected from the polarised coating (Sample 2 – Filtered).

No additional compounds were detected on the surface of the control sample or Sample 2 to that found on the untested coating (Figure 133), suggests that a patina layer had not formed or adhered to the surface during the 48-hour immersion or polarisation experiments. Furthermore, no particulate was found after filtering the electrolyte from the control cell however the string like compound found in Sample 2

[335]

was captured in the filter paper and was characterised as copper (I) chloride ($CuCl$), a precursor to the clinoatacamite ($Cu_2Cl(OH)_3$) compound detected on the paint flakes removed from in-service marine vessels. This may indicate that the polarisation of the paint increased the rate of patination.

7.4   Summary

7.4.1   Immersion And Evaporation Testing

Immersion and evaporation testing of the copper coupon, cuprite pigment and the BQA 644 and modified BQA 644 coatings resulted in the formation of a blue-green clinoatacamite patina compound similar to that which was detected on paint flakes removed from in-service marine vessels. The quickest and largest amount of the clinoatacamite compounds were found when exposing the samples to a 10% sodium chloride electrolyte at 45°C under immersion conditions. While the continuous increase in chloride concentration, associated with the evaporation cell, resulted in more clinoatacamite forming than that observed under similar immersion times.

7.4.1.1 *Copper Coupon*

A brown cuprite patina formed on the oxide stripped copper coupons when they were exposed to the neutral 0% electrolyte (deionised water) under both immersion and evaporation conditions. High temperatures promoted cuprite development with higher concentrations and quicker formation being observed under immersion conditions. When sodium chloride was present in the electrolyte a blue-green clinoatacamite patina developed on top of the cuprite layer highlighting the duplex patination of copper. In the 10% and 30% electrolytes only small traces of cuprite were detected while at 30% clinoatacamite was also reduced. This was thought to be due to

the active dissolution of the coupon surface preventing the patina layers from forming. Furthermore, the highest clinoatacamite concentrations tended to be found in the 25°C electrolytes under both immersion and evaporation conditions and may be due it being more strongly adhered to the surface allowing it to remain following the cleaning process.

7.4.1.2 Cuprite pigment

A tenorite compound developed in the cuprite powder once it was exposed to the 0% electrolyte at 45°C, resulting in the development of a black colouration. A blue-green clinoatacamite compound formed in the chloride containing electrolyte which followed a linear increase with exposure time, while a non-linear increase was observed with increasing chloride concentration. This suggested that the formation of $CuCl_2^-$ and $Cu_2Cl(OH)_3$ was rate limiting, where the highest concentration was found in the 10% electrolyte. The tenorite compound was also detected in the 1% and 3.5% electrolytes however in reducing amounts with chloride concentration, which may be associated with the increase in pH allowing it to form while the higher solubility of the cuprite may have reduced the amount of tenorite that could develop.

The concentrating effect of the evaporation cell accelerated the complexation of cuprite to clinoatacamite with higher levels being detected following equivalent immersion times.

7.4.1.3 Antifouling coatings

Both the BQA 644 and modified BQA 644 coatings were unaffected by the 0% electrolyte with no additional phases being detected. This suggests that tenorite was

either below the detection limit of the XRD, or it required higher concentrations of copper ions to form, such as that present in the cuprite cell.

When sodium chloride was present, blue-green compounds had developed, which were determined to be of two different clinoatacamite phases, following a non-linear trend like that observed in the cuprite cell. The modified BQA 644 matched the XRD pattern found in the PDF-2 database of (01-086-1391), while the clinoatacamite formed on the BQA 644 matched that found in the RRUFF database (R100198.9), which may be present in a more up-to-date version of the PDF database. The difference in the clinoatacamite phase may be associated with the availability of the cuprite pigment at the surface of the coating. The modified BQA 644 coating contained only the cuprite pigment and therefore potentially more Cu^{2+} ions could be released in the electrolytes when compared to the BQA 644 coating. This clinoatacamite compound was also found on the copper coupon and in the cuprite pigment where more Cu^{2+} ions would be available.

As observed on the copper coupons and in the cuprite powder at higher sodium chloride concentrations the speed at which the antifouling coatings became discoloured, indicating the initiation of patination, also increased. An adherent blue-green clinoatacamite compound was developed on the coatings surface in the chloride containing electrolytes, with this colouration developing after 24 hours in the 10% electrolyte. While in the 30% electrolyte a loose compound was found which consisted of clinoatacamite and botallackite.

SEM analysis of the surface of the coatings found that in the 0% electrolyte it remained relatively unaffected with the angular cuprite particles <5 µm diameter still being

[338]

visible in both coatings after the immersion and evaporation experiments. Medium sphericity chloride rich particles were found to develop in the chloride containing electrolytes. The size of the particles was unaffected by the temperature however they tended to decrease with increasing chloride concentration as the nucleation of the particles was preferred over their growth, associated with increasing amounts of Cu^{2+} ions released from the cuprite pigment. This increased the number and therefore density of particles in a given area, increasing the levels of clinoatacamite being detected at higher chloride concentrations. In the 30% electrolyte star or branched star like acicular particles were found and were thought to be botallackite crystals.

Cross-sectional analysis through the BQA 644 coating found the formation of a leach, detachment, and patina layer. The leach layer was present from the coating surface penetrating a short distance into the coating releasing the soluble pigments. The coating was designed to react with the electrolyte forming a brittle binder matrix, allowing it to be polished away through wave action. Yet this was not possible under the stagnant conditions of the cell allowing a detachment layer to be visible. This in turn allowed for the formation of a thick clinoatacamite patina layer which precipitated onto the surface in increasing amounts. The thickness of the leach, detachment and patina layers tended to increase with immersion time and chloride concentration, up to 10% regardless of temperature. The modified BQA 644 coating also followed similar trends, however, only the leach and patina layers were visible, suggesting that the removal of the other pigments affected its self-polishing ability.

7.4.2   Patination Rate

The patination rate was assessed both visually, using the photographs of the samples taken every 24 hours, and empirically, using the semi-quantitative XRD analysis of the cuprite powder and the cross-sectional thickness measurements of the patina layer on the two coatings. Under both methods of assessment the highest patination rate was found in the 10% electrolyte. While an increase in patination rate was also observed with elevated temperatures of 45°C within the cuprite powder, this was not found in the coatings. This suggests that the release of the cupric ions into the environment was a rate limiting step where the coatings are designed to control their release rate, which was unaffected by the temperature, while in the cuprite powder sample the ions are unimpeded and are released in higher concentrations. The results from the patination rate measurements suggest that electrolytes of 10% NaCl should be used to rapidly evaluate the risk of patination on copper containing antifouling coatings while the temperature is of less importance.

7.4.3   Salt Spray Corrosion Testing

Salt spray testing of the BQA 644 and the modified BQA 644 coatings resulted in the formation of nanocrystalline patina rich in copper and chlorine, which were identified as clinoatacamite, after 72 and 48 hours, respectively. A close relationship between the chlorine and clinoatacamite concentrations was noted on both coatings, with similar increases being observed with exposure time, once the chlorine concentration on the coating was above 1%. The red colouration of the coatings developed a blue, blue-green hue suggesting that only a thin clinoatacamite layer had formed. This was confirmed via cross-sectional analysis where the patina layer such as that observed from the paint flakes removed from in-service marine vessels (Chapter 4.2.2) and the

coatings exposed to immersion and evaporation conditions (Chapter 7.1.3.4) was not visible. However, cross-sectional EDX mapping found chlorine enrichment at the coating-electrolyte interface. Therefore this method of accelerated testing of copper containing antifouling coatings for patination would be unsuitable due to the relatively thin patina layer formed under neutral salt spray corrosion conditions when compared to the other methods.

7.4.4   Potentiostatic Polarisation

The potentiostatic polarisation of the antifouling coatings at 260 mV vs Ag/AgCl appeared to have accelerated the formation of copper (I) chloride. However due to coating defects, such as holidays and cracks, the electrolyte could reach the substrate. This resulted in the steel substrate corroding, forming large quantities of iron oxide, masking the patination of the cuprite pigments in the coating. Therefore, further development of the sample preparation, such as the application of a barrier layer used when applying the coatings to marine vessels hulls, would be required to minimise the formation of coating defects and ensure that only the cuprite pigment is polarised.

Chapter 8: Conclusions

Antifouling (fouling control) coatings are generally applied to marine vessels to prevent the settlement of marine organisms, such as barnacles, which can reduce the efficiency of the vessel. These coatings contain cuprite (Cu_2O) as the main biocidal pigment, which releases toxic Cu^{2+} as it dissolves in seawater. Three different antifouling coatings have been developed including controlled depletion (CPD), where the pigments are dissolved a constant rate leaving a porous network, self-polishing co-polymer (SPC) where the coating is polished through hydrodynamic drag and a hybrid of the two where the porous network is polished away to maintain a constant level of protection.

While cuprite provides a good protection against the settlement of marine organisms these coatings have been found to develop a blue/blue-green colour, indicating the formation of a copper patina compound. This may influence the aesthetics of the coating, while reducing the Cu^{2+} release rate by increasing the distance for which the ions must travel. Therefore, an accelerated test is required to allow for the rapid development of the antifouling coatings which can resist this patina formation.

8.1 Analysis Of Paint Flakes

Paint flakes from below the waterline were taken from 14 merchant vessels by AkzoNobel affiliates, which were deemed to have patinated and were analysed to determine the compounds that were present, which would therefore be compared to that formed under laboratory conditions. It was found that:

- A thin clinoatacamite layer ($Cu_2Cl(OH)_3$) was the most commonly detected copper compound found on the surface of the paint flakes with the polymorph

of atacamite ($Cu_2Cl(OH)_3$) and precursor copper (I) chloride ($CuCl$) compounds also being detected.

- Further copper sulphide phases were detected suggesting some paint flakes had been exposed to sulphate (SO_4^{2-}) polluted waters, such as that found in and around marine ports, increasing the complexity of the coating patination.

8.2   Copper Patination

99.9% pure copper electrodes were used as a substitute for cuprite to examine the effect of the different environments using DC electrochemical techniques, where it was found that:

- With increasing chloride concentrations and temperatures, the OCP of the copper electrode became more electronegative (active) forming a thin brown cuprite layer with a cubic morphology in the 0-3.5% electrolytes after 24 hours.
- In the 10% and 30% electrolytes, the surface of the electrodes showed evidence of dissolution with the formation of crystallographic etch pits, confirming the increase in activity.
- Potentiodynamic polarisation and Tafel analysis found that:
    - The E_{Corr} values continued to shift to more electronegative values following a linear trend in the chloride containing electrolytes.
    - The anodic and cathodic branches of the polarisation curves moved to higher current densities with increasing chloride concentration up to 10%, associated with an increase in the corrosion rate.
    - Increasing temperature also enhanced the E_{Corr} and corrosion rate, while the pH of the electrolyte had a minimal effect. Therefore the pH

[343]

of the electrolytes was maintained at near neutral values where the Pourbaix diagrams indicated that $Cu_2Cl(OH)_3$ would form.

- o The neutral 10% electrolyte at elevated temperature would enhance the copper patination rate which may therefore accelerate the patination of cuprite in the coatings to form clinoatacamite.

- Potentiostatic polarisation of copper within the $Cu_2Cl(OH)_3$ stability window, according to the Pourbaix diagrams, found:

  - o Large concentrations of clinoatacamite and traces of botallackite can be formed within 30 minutes in the chloride containing electrolytes with the mass loss peaking at 700 mV vs Ag/AgCl. A faradic efficiency of 1 ηF was recorded when polarising at 500 mV vs Ag/AgCl and would therefore be a favourable parameter to form clinoatacamite at an accelerated rate.

  - o A linear increase in mass loss was recorded with increasing sodium chloride concentrations up to 30%. Where the patina was dominated by clinoatacamite in the 1% and 3.5% electrolytes, and cuprite in the 10% and 30% electrolytes. This may suggest that the production of the Cu^{2+} ions and therefore the dissolution of the copper electrode was faster than the complexation to other copper chloride species. This indicates that the lower chloride containing solutions should be used to form clinoatacamite under potentiostatic polarisation.

  - o Botallackite formed in small and clinoatacamite formed in large volumes of 3.5% sodium chloride electrolyte. This suggests that the botallackite formation was affected by the ratio of copper to chloride ions where

[344]

1:<100 allows botallackite to be present in addition to clinoatacamite while 1:>100 produces only clinoatacamite. Botallackite was shown to recrystallise to clinoatacamite after 24 hours in the electrolyte.

8.3   Accelerated Patination Of Antifouling Coatings

The commercially available BQA 644 antifouling coating and a modified version, removing all but the cuprite pigment, were used to examine techniques designed to accelerate their patination. These coatings were exposed to neutral sodium chloride electrolytes (0% - 30%) at 25°C and 45°C, under long term immersion, evaporation, and salt spray environments to simulate the underwater, saltwater evaporation and splash/spray zones that may be experienced on marine vessels, while potentiostatic polarisation methods were used to accelerate coating patination. It was found that:

- An adherent blue-green clinoatacamite patina formed on the coating, under immersion and evaporating conditions, in the neutral electrolytes containing sodium chloride, occurring after 24 hours in the 10% electrolyte with relatively high levels of clinoatacamite detected after 168 hours.

- The patina particle size was reduced as the chloride concertation was increase up to 10%, which was also associated with an increase in patina thickness, along with amount of chloride and clinoatacamite detected.

- A loose patina developed in the 30% electrolyte on the coating surface consisting of both botallackite, which was not found on the in-service paint flakes, and clinoatacamite compounds.

- Higher clinoatacamite levels were associated with the evaporation cell however the formation of salt crystals may disrupt the patina layer formed on the

[345]

coating surface reducing the accuracy of the results, therefore immersion testing may be preferred.

- Under immersion conditions similar or lower levels of patina were detected at 45°C when compared to 25°C. While under evaporating conditions similar levels of clinoatacamite were detected at both temperatures, with the 45°C evaporating more quickly. Whereas higher levels of clinoatacamite were detected at elevated temperatures on the modified BQA 644 coating, indicating that the presence of the additional pigments in the BQA 644 coating influenced the patination of the coating.

- Similar levels of clinoatacamite were detected on the BQA 644 and modified BQA 644 coatings after 168 hours in neutral 10% NaCl electrolytes at 25°C when compared the long term exposure of paint flakes removed from in-service marine vessels. Furthermore the highest patination rate was found in the neutral 10% NaCl electrolytes for the cuprite powder and coating samples and may therefore be used to accelerate the clinoatacamite formation under these conditions.

- Under salt spray conditions, a thin clinoatacamite layer had formed on the surface of the coatings developing a blue, blue-green hue, at relatively low concentrations when compared to the immersion or evaporation cells, after similar exposure times and is therefore less suited to the accelerated patination of antifouling coatings

- The potentiostatic polarisation of antifouling coatings accelerated the formation of copper (I) chloride compound, a precursor to clinoatacamite. However, this acceleration was not a significant increase when compared to

[346]

the immersion testing at 10%, while imperfections in the coating may allow the substrate to corrode preferentially.

8.4 Testing Of Antifouling Coatings To Accelerate Patination

Accelerated testing of antifouling coatings containing the cuprite pigment should be performed in a neutral 10% NaCl electrolyte, at 25°C, under stagnant conditions, to determine the susceptibility of the coating formula to form the clinoatacamite patina compound. Using this accelerated testing method, the coating formulas which were either least likely to, or took the longest to patinate could then be developed for use.

Chapter 9: Future work

Clinoatacamite was the most commonly detected copper patina patinated paint in Chapter 4. However additional copper chloride and sulphide compounds were also detected on some of the paint flakes, while multiple antifouling coatings were also observed in cross-section. Therefore, a full history of the vessels the paint flakes had been removed from including where the vessels operated, the length of time the coatings had been applied, what previous antifouling coatings had been used and if they were removed prior to the application of new coatings, etc. This would allow for a better understanding into the conditions forming the different copper patinas under natural conditions. Further analysis of additional coatings should also be performed to allow the results to be statistically significant.

In Chapter 5.4 copper coupons were exposed to different electrolyte for 24 hours allowing for the formation of a patina layer. The analysis of these coupons focused on those at 45°C as they appeared to have the greatest change in colour when compared to the oxide stripped surface. However, analysis of the coupons exposed at different temperatures may also provide useful information such as whether the crystallographic etch pit found in the 10% and 30% electrolytes or the size of the patina crystals are influenced by temperature. In addition, a high standard deviation of the patina particle sizes was measured on the copper coupons and therefore a particle size distribution analysis should be performed to observe the effect of the different environments more accurately. Furthermore, the thickness of the patina layers was determined through XRD analysis however other techniques such as Focused Ion Beam SEM milling, where direct measurements could be made, would verify the XRD results.

The patina compound produced when potentiostatically polarising a copper electrode resulted in the formation of high concentrations of clinoatacamite and traces of botallackite within the potential window of 200-1000 mV vs Ag/AgCl. However, the blue-green colouration associated with these compounds was found to vary from being richer in green at 200 and 1000 mV vs Ag/AgCl to being richer in blue at 300, 500 and 700 mV vs Ag/AgCl. Similar differences in the colouration were noted on the electrode surface when polarising at fixed potentials in the electrolytes containing different concentrations of sodium chloride however analysis of the compounds present on the surface using XRD is required to confirm what had formed. Moreover, in Chapter 7 the copper coupons, cuprite powder, and antifouling coatings also seen to develop a blue-green patina of varying shades. Therefore, further analysis of these samples using a spectrocolorimeter to quantify the colour as well as Raman may improve the understanding into what is causing the change in colour and whether there are any specific variables which may be contributing to their colour.

In Chapter 6.2.1.3 the SEM and XRD analysis of the electrode surface polarised at 700 mV vs Ag/AgCl did not detect any copper chloride patina compounds on the electrode surface, such as that observed at 500 and 1000 mV vs Ag/AgCl. It may be that a relatively thin film had formed on the electrode producing small diffraction peaks which were hidden within the background radiation. However this anomaly would require further investigation.

Ferry & Carritt (1946) observed that there was a linear increase in cuprite dissolution from antifouling coatings with increasing chloride concentrations up to $1M$. However, coating technology has developed since this was published which may have led to

different dissolution characteristics, while higher chloride concentrations may also be of influence. For example, it was shown in Chapter 7 that there was a non-linear increase in the amount of clinoatacamite detected with increasing sodium chloride, peaking at 10%. This suggests that either the rate of cuprite dissolution was not linear at higher chloride concentrations or its complexation to clinoatacamite slows. Further evidence of a reduction in cuprite dissolution may be observed at 30% where botallackite, thought to form in low Cu^{2+} concentrations in chloride electrolytes (Pollard et al., 1989), was detected. Therefore, measurements of the dissolution of cuprite from the coatings and the copper ions present in solution is required to verify this. Measurements to determine the dissolved oxygen concentration in the different electrolytes during the immersion and evaporation experiments, purging oxygen from the electrolytes using nitrogen and enriching the electrolytes with oxygen may also be done to show oxygens' influence on the patination of antifouling coatings.

Further testing of different coatings and coating types, repeating the immersion and evaporation methodology, introducing a "waterline" test which would simulate the boundary between the full immersion and the splash/spray zones, as well as observing effects of orientation of the coating would verify the validity of the results.

Chapter 10:   References

Ab Rahman, N., Romli, N., Ghani, M. H., Phoa, C. W., & Lim, P. (2016). Design and development of air flow sensor and pressure sensor for air flow bench part 2. *2nd Integrated Design Project Conference (IDPC) 2015*, https://doi.org/10.13140/RG.2.1.4978.1846

Abarzua, S., & Jakubowski, S. (1995). Biotechnological investigation for the prevention of biofouling. I. biological and biochemical principles for the prevention of biofouling. *Marine Ecology Progress Series, 123*, 130. https://doi.org/10.3354/meps123301

Adeloju, S. B., & Hughes, H. C. (1986). The corrosion of copper pipes in high chloride-low carbonate mains water. *Corrosion Science, 26*(10), 851-870. https://doi.org/10.1016/0010-938X(86)90068-5

Adland, R., Cariou, P., Jia, H., & Wolff, F. (2018). The energy efficiency effects of periodic ship hull cleaning. *Journal of Cleaner Production, 178*, 1-13. https://doi.org/10.1016/j.jclepro.2017.12.247

AkzoNobel. (N/D). Antifoulings. Retrieved July 27, (2014) from https://www.international-marine.com/type/antifoulings

Al-Abdallah, M. M., Maayta, A. K., Al-Qudah, M. A., & Al-Rawashdeh, N. A. F. (2009). Corrosion behaviour of copper in chloride media. *The Open Corrosion Journal, 2*, 71-76. https://doi.org/10.13140/2.1.1556.4808

Alberto J Martín-Rodríguez, Jose, M. F. B., Lahoz, F., Marta Sansón, Víctor S Martín, Norte, M., & José J Fernández. (2015). From broad-spectrum biocides to quorum sensing disruptors and mussel repellents: Antifouling profile of alkyl triphenylphosphonium salts. *PLoS ONE, 10*(4), e0123652. https://doi.org/10.1371/journal.pone.0123652

Aljinović, L., Gudić, S., & Šmith, M. (2000). Inhibition of CuNi10Fe corrosion in seawater by sodium-diethyl-dithiocarbamate: An electrochemical and analytical study. *Journal of Applied Electrochemistry, 30*(8), 973-979. https://doi.org/10.1023/A:1004074405514

Almeida, E., Diamantino, T. C., & de Sousa, O. (2007). Marine paints: The particular case of antifouling paints. *Progress in Organic Coatings, 59*(1), 2-20. https://doi.org/10.1016/j.porgcoat.2007.01.017

Al-Mobarak, N., Khaled, K. F., Hamed, M. N. H., & Abdel-Azim, K. (2011). Employing electrochemical frequency modulation for studying corrosion and corrosion inhibition of copper in sodium chloride solutions. *Arabian Journal of Chemistry, 4*(2), 185-193. https://doi.org/10.1016/j.arabjc.2010.06.036

Al-Mobarak, N., Khaled, K. F., Hamed, M. N. H., Abdel-Azim, K., & Abdelshafi, N. S. (2010). Corrosion inhibition of copper in chloride media by 2-mercapto-4-(p-methoxyphenyl)-6-oxo-1,6-dihydropyrimidine-5-carbonitrile: Electrochemical and theoretical study. *Arabian Journal of Chemistry, 3*(4), 233-242. https://doi.org/10.1016/j.arabjc.2010.06.007

Alzieu, C. L., Sanjuan, J., Deltreil, J. P., & Borel, M. (1986). Tin contamination in arcachon bay: Effects on oyster shell anomalies. *Marine Pollution Bulletin, 17*(11), 494-498. https://doi.org/10.1016/0025-326X(86)90636-3

[351]

Alzieu, C. (1998). Tributyltin: Case study of a chronic contaminant in the coastal environment. *Ocean and Coastal Management, 40*(1), 23-36. https://doi.org/10.1016/S0964-5691(98)00036-2

Amatore, C., Bouret, Y., Maisonhaute, E., Abruña, H. D., & Goldsmith, J. I. (2003). Electrochemistry within molecules using ultrafast cyclic voltammetry. *Comptes Rendus Chimie, 6*(1), 99-115. https://doi.org/10.1016/S1631-0748(03)00019-5

Anderson, C., Atlar, M., Callow, M., Candries, M., Milne, A., & L. Townsin, R. (2003). The development of foul-release coatings for seagoing vessels. *Proceedings of the Institute of Marine Engineering, Science and Technology Part B: Journal of Marine Design and Operations, 4*, 11-23.

Angel, B. M., Apte, S. C., Batley, G. E., & Raven, M. (2021). Geochemical factors affecting the solubility of copper in seawater. *Environmental Chemistry, 18*(1), 1. https://doi.org/10.1071/EN20133

Anish. (2020a). Safety of life at sea (SOLAS) – the ultimate guide. Retrieved August 17, 2021 from https://www.marineinsight.com/guidelines/dry-dock-types-of-dry-docks-requirements-for-dry-dock/#:~:text=As%20per%20SOLAS%20requirements%2C%20all,not%20more%20than%2036%20months.&text=For%20a%20passenger%20vessel%2C%20the,is%20to%20be%20done%20annually

Anish. (2020b). Understanding sacrificial anodes on ships. Retrieved August 17, 2021 from https://www.marineinsight.com/tech/understanding-sacrificial-anodes-on-ships/

Annibaldi, V., Rooney, A. D., & Breslin, C. B. (2012). Corrosion protection of copper using polypyrrole electrosynthesised from a salicylate solution. *Corrosion Science, 59*, 179. https://doi.org/10.1016/j.corsci.2012.03.014

Anon. (2007). *Assessment of introduced marine pest risks associated with niche areas in commercial shipping.* Australian Shipowners Association. Retrieved January 22, 2016 from http://citeseerx.ist.psu.edu/viewdoc/download?doi=10.1.1.364.7706&rep=rep1&type=pdf

Anthony, J. W., Bideaux, R. A., Bladh, K. W., & Nichols, M. C. (2003). Botallackite. *Handbook of mineralogy*. Chantilly, VA 20151-1110, USA: Mineralogical Society of America. Retrieved December 9, 2016 from http://www.handbookofmineralogy.org/

Antonijevic, M. M., Alagic, S. C., Petrovic, M. B., Radovanovic, M. B., & Sramenkovic, A. T. (2009). The influence of pH on electrochemical behaviour of copper in presence of chloride ions. *International Journal of Electrochemical Science, 4*, 516-524.

Arjmand, F., & Adriaens, A. (2012). Influence of pH and chloride concentration on the corrosion behaviour of unalloyed copper in NaCl solutions: A comparative study between the micro and macro scales. *Materials, 5*, 2439-2464.

ASTM International. (2014). *Standard test method for Conducting potentiodynamic polarization resistance measurements.* (Standard No. ASTM G59 -97(2014)). US: ASTM International.

ASTM International. (2017). ASTM G1 - 03 standard practice for preparing, cleaning, and evaluating corrosion test specimens ASM International.

ASTM International. (2019). ASTM B117: Standard practice for operating salt spray (fog) apparatus.

Atlas, D., Coombs, J., & Zajicek, O. T. (1982). The corrosion of copper by chlorinated drinking waters. *Water Research, 16*(5), 693-698. https://doi.org/10.1016/0043-1354(82)90093-8

Azemar, F., Faÿ, F., Réhel, K., & Linossier, I. (2015). Development of hybrid antifouling paints. *Progress in Organic Coatings, 87*, 10-19. https://doi.org/10.1016/j.porgcoat.2015.04.007

Babić, R., Metikoš-Huković, M., & Jukić, A. (2001). A study of copper passivity by electrochemical impedance spectroscopy. *Journal of the Electrochemical Society, 148*(4), B146-B151. https://doi.org/10.1149/1.1354608

Bacarella, A. L., & Griess, J. C. (1973). The anodic dissolution of copper in flowing sodium chloride solutions between 25° and 175°C. *Journal of the Electrochemical Society, 120*(4), 459. https://doi.org/10.1149/1.2403477

Badawy, W., & Al-Kharafi, F. (1999). Corrosion behavior of brass alloys in aqueous solutions of different pH. *Corrosion, 55*(3), 268. https://doi.org/10.5006/1.3283987

Baier, R. E., Shafrin, E. G., & Zisman, W. A. (1968). Adhesion: Mechanisms that assist or impede it. Science (American Association for the Advancement of Science); *Science*, 162(3860), 1360-1368. https://doi.org/10.1126/science.162.3860.1360

Baier, R. E. (1972) Influence of the initial surface condition of materials on bioadhesion. Paper presented at the *Proceedings Third International Congress Marine Corrosion and Fouling,* 633-639.

Baier, R. E. (1980). Substrata influences on adhesion of microorganisms and their resultant new surface properties. *Adsorption of microorganisms to surfaces.* (pp. 59-104). New York: Wiley-Interscience.

Baier, R. E. (1981). Early events of micro-biofouling of all heat transfer equipment. *Fouling of heat transfer equipment* (pp. 293-304). Washington, DC: Hemisphere Publishing Company.

Bakker, D. P., Klijnstra, J. W., Busscher, H. J., & Van Der Mei, H.,C. (2003). The effect of dissolved organic carbon on bacterial adhesion to conditioning films adsorbed on glass from natural seawater collected during different seasons. *Biofouling, 19*(6), 391-397. https://doi.org/10.1080/0892701031000163498

Banakar, U. V. (1991). *Pharmaceutical dissolution testing* (1st ed.) CRC Press. https://doi.org/10.1201/b14198

Barrass, C. B., & Derrett, D. R. (2012). Chapter 35 - load lines and freeboard marks. In C. B. Barrass, & D. R. Derrett (Eds.), *Ship stability for masters and mates (seventh edition)* (pp. 299-312). Oxford: Butterworth-Heinemann. https://doi.org/10.1016/B978-0-08-097093-6.00035-9

[353]

Becerra, J. G., Salvarezza, R. C., & Arvia, A. J. (1988). The influence of slow cu(OH) 2 phase formation on the electrochemical behaviour of copper in alkaline solutions. *Electrochimica Acta, 33*(5), 613-621. https://doi.org/10.1016/0013-4686(88)80059-8

Bech-Nielsen, G., Jaskula, M., Chorkendorff, I., & Larsen, J. (2002). The initial behaviour of freshly etched copper in moderately acid, aerated chloride solutions. *Electrochimica Acta, 47*(27), 4279-4290. https://doi.org/10.1016/S0013-4686(02)00415-2

BENDEZU H, R. del P., GONCALVES, R. P., NEIVA, A. C., & MELO, H. G. d. (2007). EIS and microstructural characterization of artificial nitrate patina layers produced at room temperature on copper and bronze. *Journal of the Brazilian Chemical Society, 18*, 54-64. https://doi.org/10.1590/S0103-50532007000100006

Benson, B. B., & Krause Jr., D. (1984). The concentration and isotopic fractionation of oxygen dissolved in freshwater and seawater in equilibrium with the atmosphere. *Limnology and Oceanography, 29*(3), 620-632. https://doi.org/10.4319/lo.1984.29.3.0620

Benson, J. M., Ebert, J. W., & Beery, T. D. (1938). *Investigation in the NACA tank of the effect of immersion in salt water on the resistance of plates coated with different shipbottom paints.* (Experimental No. C&R C-S19-1(3)).NACA Memorandum Report.

Berglin, M., Lönn, N., & Gatenholm, P. (2003). Coating modulus and barnacle bioadhesion. *Biofouling, 19*, 63-69. https://doi.org/10.1080/0892701021000048774

Beverskog, B., & Puigdomenech, I. (1998). *Pourbaix diagrams for the system copper-chlorine at 5–100 °C.* Nykoping: Swedish Nuclear Powder Inspectorate.

Bianchi, G., & Longhi, P. (1973). Copper in sea-water, potential-pH diagrams. *Corrosion Science, 13*, 853-864. https://doi.org/10.1016/S0010-938X(73)80067-8

Boden, P. J. (1971). Corrosion of cu and cu-base alloys under conditions of boiling heat transfer—I. corrosion of cu. *Corrosion Science, 11*(6), 353-362. https://doi.org/10.1016/S0010-938X(71)80118-X

Bohlander, G. (1991) Biofilm effects on drag: Measurements on ships. Paper presented at the *Transactions Institute Marine Engineering,* 135.

Böhni, H. (1987). Breakdown of passivity and localized corrosion processes. *Langmuir, 3*(6), 924-930. https://doi.org/10.1021/la00078a010

Boulay, N., & Edwards, M. (2001). Role of temperature, chlorine and organic matter in copper corrosion by-product release in soft water. *Water Research, 35*(3), 683-690. https://doi.org/10.1016/S0043-1354(00)00320-1

Braithwaite, R., Mereiter, K., Paar, W., & Clark, A. (2004). Herbertsmithite, $Cu_3Zn(OH)_6Cl_2$, a new species, and the definition of paratacamite. *Mineralogical Magazine, 68*, 527. https://doi.org/10.1180/0026461046830204

Braun, M. (1979). Electrodissolution kinetics of copper in acidic chloride solutions. *Journal of the Electrochemical Society, 126*(10), 1666. https://doi.org/10.1149/1.2128773

Bressy, C., Margaillan, A., Faÿ, F., Linossier, I., & Réhel, K. (2009). *Tin-free self-polishing marine antifouling coatings-18* https://doi.org/10.1533/9781845696313.3.445

Brossard, L. (1983). Anodic dissolution of copper in concentrated LiCl solution at pH between 3 and 7. *Journal of the Electrochemical Society, 130*(2), 403. https://doi.org/10.1149/1.2119719

Brusic, V., Frisch, M., Eldridge, B., Novak, F., Kaufman, F., Rush, B., . . . Brusic, V. (1991). Copper corrosion with and without inhibitors. *Journal of the Electrochemical Society, 138*(8), 2253-2259. https://doi.org/10.1149/1.2085957

Bryan, G. W., Gibbs, P. E., Hummerstone, L. G., & Burt, G. R. (1986). The decline of the gastropod nucella lapillus around south-west england: Evidence for the effect of tributyltin from antifouling paints. *Journal of the Marine Biological Association of the United Kingdom; J.Mar.Biol.Ass., 66*(3), 611-640. https://doi.org/10.1017/S0025315400042247

Cabot, P. L., Centellas, F. A., Garrido, J. A., Pérez, E., & Vidal, H. (1991). Electrochemical study of aluminium corrosion in acid chloride solutions. *Electrochimica Acta, 36*(1), 179-187. https://doi.org/https://doi.org/10.1016/0013-4686(91)85199-H

Cáceres, L., Vargas, T., & Herrera, L. (2007). Determination of electrochemical parameters and corrosion rate for carbon steel in un-buffered sodium chloride solutions using a superposition model. *Corrosion Science, 49*(8), 3168-3184. https://doi.org/10.1016/j.corsci.2007.03.003

Callow, J. A., & Callow, M. E. (2006). Biofilms. *Progress in Molecular and Subcellular Biology, 42*, 141-169. https://doi.org/10.1007/3-5403-0016-3_6

Callow, M., & Callow, J. (2002). Marine biofouling: A sticky problem. *Biologist (London, England), 49*, 10-14. PMID: 11852279.

Candries, M., Anderson, C., Atlar, M., & Candries, M. (2001). Foul release systems and drag: Observations on how the coatings work. *Journal of Protective Coatings & Linings (USA), 18*(4), 38-43.

Cao, S., Wang, J., Chen, H., & Chen, D. (2011). Progress of marine biofouling and antifouling technologies. *Chinese Science Bulletin, 56*(7), 598-612. https://doi.org/10.1007/s11434-010-4158-4

Caprari, J. J., Slutzky, O., Pessi, P. L., & Rascio, V. (1986). A study of the leaching of cuprous oxide from vinyl antifouling paints. *Progress in Organic Coatings, 13*(6), 431-444. https://doi.org/10.1016/0033-0655(86)85004-X

Caron, D. A., & Sieburth, J. M. (1981). Disruption of the primary fouling sequence on fiber glass-reinforced plastic submerged in the marine environment. *Applied and Environmental Microbiology, 41*(1), 268. https://doi.org/10.1128/aem.41.1.268-273.1981

Catao, E. C. P., Gallois, N., Fay, F., Misson, B., & Briand, J. (2021). Metal resistance genes enrichment in marine biofilm communities selected by biocide-containing surfaces in temperate and tropical coastal environments. *Environmental Pollution, 268*, 115835. https://doi.org/https://doi.org/10.1016/j.envpol.2020.115835

[355]

Cecchel, S., Cornacchia, G., & Gelfi, M. (2019). A study of a non-conventional evaluation of results from salt spray test of aluminum high pressure die casting alloys for automotive components. *Materials and Corrosion, 70*(1), 70-78. https://doi.org/10.1002/maco.201810307

Chambers, L. D., Stokes, K. R., Walsh, F. C., & Wood, R. J. K. (2006). Modern approaches to marine antifouling coatings. *Surface & Coatings Technology, 201*(6), 3642-3652. https://doi.org/10.1016/j.surfcoat.2006.08.129

Chan, H. Y. H., Takoudis, C. G., & Weaver, M. J. (1999). *Oxide film formation and oxygen adsorption on copper in aqueous media as probed by surface-enhanced Raman spectroscopy* https://doi.org/10.1021/jp983787c

Chen, J., Lin, Z., Chen, S., Nie, L., & Yao, S. (1998). An XPS and BAW sensor study of the structure and real-time growth behaviour of a complex surface film on copper in sodium chloride solutions (pH = 9), containing a low concentration of benzotriazole. *Electrochimica Acta, 43*(3), 265-274. https://doi.org/10.1016/S0013-4686(97)00090-X

Cheng, Y., Feng, G., & Moraru, C. I. (2019). Micro- and nanotopography sensitive bacterial attachment mechanisms: A review. *Frontiers in Microbiology, 10* https://doi.org/10.3389/fmicb.2019.00191

Chernysheva, Y., Berin, I., & Presnyakov, A. (1976). Effect of rolling temperature on the properties of copper wire rod. *Metal Science and Heat Treatment, 18*(9), 823-825. https://doi.org/10.1007/BF00704136

Chialvo, G. D., Zerbino, J., Marchiano, S., & Arvia, A. (1986). Correlation of electrochemical and ellipsometric data in relation to the kinetics and mechanism of cu 2 O electroformation in alkaline solutions. *Journal of Applied Electrochemistry, 16*(4), 517-526. https://doi.org/10.1007/BF01006847

Chialvo, M., Marchiano, S., & Arvía, A. (1984). The mechanism of oxidation of copper in alkaline solutions. *Journal of Applied Electrochemistry, 14*(2), 165-175. https://doi.org/10.1007/BF00618735

Chico, B., Fuente, D. d. l., Simancas, J., & Morcillo, M. (2005). *Corrosión atmosférica de metales. efecto de parámetros meteorológicos y de contaminación.* Madrid: Institutional Repository of the Spanish National Research Council.

Chu, S., Müller, P., Nocera, D. G., & Lee, Y. S. (2011). Hydrothermal growth of single crystals of the quantum magnets: Clinoatacamite, paratacamite, and herbertsmithite. *Applied Physics Letters, 98*(9), 092508. https://doi.org/10.1063/1.3562010

Chunyan, X. U., Yan, Q., & Ying, M. A. (2012). Microorganisms colonizing surface in coastal marine water as revealed by 16S rRNA gene clone library analysis. *Afr.J.Microbiol.Res., 6*, 7271-7277. https://doi.org/10.5897/AJMR12.1401

Cid, A., Herrero, C., Torres, E., & Abalde, J. (1995). Copper toxicity on the marine microalga phaeodactylum tricornutum: Effects on photosynthesis and related parameters. *Aquatic Toxicology, 31*(2), 165-174. https://doi.org/10.1016/0166-445X(94)00071-W

Clarelli, F., De Filippo, B., & Natalini, R. (2012). Mathematical model of copper corrosion. *Applied Mathematical Modelling, Volume 38, Issues 19–20, Pages 4804-4816, https://doi.org/10.1016/j.apm.2014.03.040*.

Clark, P. G., & Wagener, T. J. (2008). Chapter 12 - removal of particles by chemical cleaning. In R. Kohli, & K. L. Mittal (Eds.), *Developments in surface contamination and cleaning (second edition)* (pp. 579-593). Oxford: William Andrew Publishing. https://doi.org/10.1016/B978-0-323-29960-2.00012-5

Colwell, R. R. (1983). Biotechnology in the marine sciences. *Science (New York), 222*(4619), 19. https://doi.org/10.1126/science.222.4619.19

Comber, S. D. W., Franklin, G., Gardner, M. J., Watts, C. D., Boxall, A. B. A., & Howcroft, J. (2002). Partitioning of marine antifoulants in the marine environment. *Science of the Total Environment, 286*(1-3), 61-71. https://doi.org/10.1016/S0048-9697(01)00963-9

Compère, C., Bellon-Fontaine, M., Bertrand, P., Costa, D., Marcus, P., Poleunis, C., Walls, M. G. (2001). Kinetics of conditioning layer formation on stainless steel immersed in seawater. *Biofouling, 17*(2), 129-145. https://doi.org/10.1080/08927010109378472

Connan, J., Carter, R., Crawford, H., Tobey, M., Charrié-Duhaut, A., Jarvie, D., . . . Norman, K. (2005). A comparative geochemical study of bituminous boat remains from H3, As-Sabiyah (kuwait), and RJ-2, ra's al-Jinz (oman. *Arabian Archaeology and Epigraphy, 16*(1), 21-66. https://doi.org/10.1111/j.1600-0471.2005.00041.x

Cooksey, K. E., & Wigglesworth-Cooksey, B. (1995). Adhesion of bacteria and diatoms to surfaces in the sea: A review. *Aquatic Microbial Ecology, 9*(1), 87-96. https://doi.org/10.3354/ame009087

Cooper, R. S., & Bartlett, J. H. (1958). Convection and film instability copper anodes in hydrochloric acid. *Journal of the Electrochemical Society, 105*(3), 109. https://doi.org/10.1149/1.2428773

Copper Development Association Inc. (2013). *Building & architecture news*

Copper Development Association Inc. (2018). Copper facts. Retrieved April 6, 2013 from https://www.copper.org/education/c-facts/

Costerton, J. W. (1999). Introduction to biofilm. *International Journal of Antimicrobial Agents, 11*(3), 217. https://doi.org/10.1016/S0924-8579(99)00018-7

Cuba, T. R., & Blake, N. J. (1983). The initial development of a marine fouling assemblage on a natural substrate in a subtropical estuary. *Botanica Marina – BOT MAR, 26*, 259-264. https://doi.org/10.1515/botm.1983.26.6.259

Cui, Y., Qin, Y., Dilimulati, D., & Wang, Y. (2019). The effect of chlorine ion on metal corrosion behavior under the scratch defect of coating. *International Journal of Corrosion, 2019*, 7982893. https://doi.org/10.1155/2019/7982893

Cullity, B. D. (2014). *Elements of X-ray diffraction*. Harlow: Pearson Education.

[357]

Dafforn, K. A., Lewis, J. A., & Johnston, E. L. (2011). Antifouling strategies: History and regulation, ecological impacts and mitigation. *Marine Pollution Bulletin, 62*(3), 453-465. https://doi.org/10.1016/j.marpolbul.2011.01.012

Davis, J. R., & Committee, A. S. M. I. H. (2001). *Copper and copper alloys* ASM International. Retrieved April 21, 2013from https://books.google.co.uk/books?id=sxkPJzmkhnUC

de Carvalho, Carla C. C. R. (2018). Marine biofilms: A successful microbial strategy with economic implications. *Frontiers in Marine Science, 5*, 126. https://doi.org/10.3389/fmars.2018.00126

de Chialvo, M. R. G., Salvarezza, R. C., Vasquez Moll, D., & Arvia, A. J. (1985). Kinetics of passivation and pitting corrosion of polycrystalline copper in borate buffer solutions containing sodium chloride. *Electrochimica Acta, 30*(11), 1501-1511. https://doi.org/10.1016/0013-4686(85)80012-8

Denny, M. E. (1951). B.S.R.A. resistance experiments on the "lucy ashton": Part I full - scale measurements. *Transactions of the Institution of Naval Architects, 93*, 40-57.

Deslouis, C., Tribollet, B., Mengoli, G., & Musiani, M. M. (1988). Electrochemical behaviour of copper in neutral aerated chloride solution. I. steady-state investigation. *Journal of Applied Electrochemistry, 18*(3), 374-383. https://doi.org/10.1007/BF01093751

Despić, A., & Parkhutik, V. P. (1989). Electrochemistry of aluminum in aqueous solutions and physics of its anodic oxide. In J. O. Bockris, R. E. White & B. E. Conway (Eds.), *Modern aspects of electrochemistry no. 20* (pp. 401-503). Boston, MA: Springer US. https://doi.org/10.1007/978-1-4684-8762-6_6

Deyá, M. C., Blustein, G., Romagnoli, R., & del Amo, B. (2002). The influence of the anion type on the anticorrosive behaviour of inorganic phosphates. *Surface and Coatings Technology, 150*(2), 133-142. https://doi.org/10.1016/S0257-8972(01)01522-5

Di Quarto, F., Piazza, S., & Sunseri, C. (1985). Photoelectrochemical study of the corrosion product layers on copper in weakly acidic solutions. *Electrochimica Acta, 30*(3), 315-324. https://doi.org/10.1016/0013-4686(85)80190-0

Diop, E. H. A., Niang, M. F., Gassama, D., Dione, N. P., & Fall, M. (2017). Comparative study of the copper electrical earthing corrosion in three mediums in senegal. *American Journal of Chemistry, 7*(1), 16-20. https://doi.org/10.5923/j.chemistry.20170701.03

Dortwegt, R., & Maughan, E. V. (2001). (2001). The chemistry of copper in water and related studies planned at the advanced photon source. Paper presented at the Particle Accelerator Conference, 2 1456-1458 vol.2. https://doi.org/10.1109/PAC.2001.986712

Egerton, R. F. (2005). *Physical principles of electron microscopy an introduction to TEM, SEM, and AEM /*. New York, NY: Springer.

Eklund, G. (1974). Initiation of pitting at sulfide inclusions in stainless steel. *Journal of the Electrochemical Society, 121*(4), 467. https://doi.org/10.1149/1.2401840

[358]

El Warraky, A., El Shayeb, H. A., & Sherif, E. M. (2004). Pitting corrosion of copper in chloride solutions. *Anti-Corrosion Methods and Materials, 51*(1), 52-61. https://doi.org/10.1108/00035590410512735

Elhousni, L., Galai, M., ElKamraoui, F. Z., Dkhireche, N., Touir, R., & Ebn Touhami, M. (2017). Corrosion and scale studies of copper used in moroccan industrial cooling water systems. *Euro-Mediterranean Journal for Environmental Integration, 2*(1), 12. https://doi.org/10.1007/s41207-017-0024-y

EL-Mahdy, G. (2005). Atmospheric corrosion of copper under wet/dry cyclic conditions. *Corrosion Science, 47*, 1370-1383. https://doi.org/10.1016/j.corsci.2004.07.034

Elsner, C. I., Salvarezza, R. C., & Arvia, A. J. (1988). The influence of halide ions at submonolayer levels on the formation of oxide layer and electrodissolution of copper in neutral solutions. *Electrochimica Acta, 33*(12), 1735-1741. https://doi.org/10.1016/0013-4686(88)85008-4

El-Tantawy, Y., Al-Kharafi, F., & Katrib, A. (1981). Nature and mechanism of anodic film formation on cu in alkaline phosphate media. *Journal of Electroanalytical Chemistry, 125*(2), 321-331. https://doi.org/10.1016/S0022-0728(81)80351-8

EMITECH. (2008). *K950X turbo evaporator instruction manual*

Evans, U. R. (1960). *The corrosion and oxidation of metals: Scientific principles and practical applications.* Edward Arnold.

Evans, U. R. (1971). Inhibition, passivity and resistance: A review of acceptable mechanisms. *Electrochimica Acta, 16*(11), 1825-1840. https://doi.org/10.1016/0013-4686(71)85141-1

Fair, J. A., & Ozbek, H. (1977). Viscosity and density tables of sodium chloride solutions. https://doi.org/10.2172/6765156

Faita, G., Fiori, G., & Salvadore, D. (1975). Copper behaviour in acid and alkaline brines—I kinetics of anodic dissolution in 0.5M NaCl and free-corrosion rates in the presence of oxygen. *Corrosion Science, 15*(6), 383-392. https://doi.org/10.1016/0010-938X(75)90005-0

Farro, N. W., Veleva, L., & Aguilar, P. (2009). Copper marine corrosion: I. corrosion rates in atmospheric and seawater environments of Peruvian port. *The Open Corrosion Journal, 2*, 130-138. https://doi.org/10.2174/1876503300902010130

Feng, Y., Siow, K., Teo, W., Tan, K., & Hsieh, A. (1997). Corrosion mechanisms and products of copper in aqueous solutions at various pH values. *Corrosion, 53*(5), 389. https://doi.org/10.5006/1.3280482

Feng, Y., Teo, W. -., Siow, K. -., Tan, K. -., & Hsieh,]. -. (1996). The corrosion behaviour of copper in neutral tap water. part I: Corrosion mechanisms. *Corrosion Science, 38*(3), 369-385. https://doi.org/10.1016/0010-938X(96)00110-2

Ferreira, J., Rodrigues, J., & Fonseca, I. (2004). Copper corrosion in buffered and non-buffered synthetic seawater: A comparative study. *Journal of Solid State Electrochemistry; Current Research and Development in Science and Technology, 8*(4), 260-271. https://doi.org/10.1007/s10008-003-0445-1

[359]

Ferry D., J., & Ketchum H., B. (1946). Action of antifouling paints: Maintenance of the leaching rate of antifouling paints formulated with insoluble, impermeable matrices. *Industrial and Engineering Chemistry*, 806-810.

Ferry, J. D., & Carritt, D. E. (1946). Action of antifouling paints. *Industrial & Engineering Chemistry, 38*(6), 612-617. https://doi.org/10.1021/ie50438a021

Figueroa, M. G., Salvarezza, R. C., & Arvia, A. J. (1986). The influence of temperature on the pitting corrosion of copper. *Electrochimica Acta, 31*(6), 665-669. https://doi.org/10.1016/0013-4686(86)87033-5

Finnie, A. (2015). *Discussion on the patination of antifouling paints*

Finnie, A., & Williams, D. (2010). Paint and coatings technology for the control of marine fouling. (pp. 185) https://doi.org/10.1002/9781444315462.ch13

Fitzgerald P., K., Nairn, J., & Atrens, A. (1998). The chemistry of copper patination. *Corrosion Science, 40*(12), 2029-2050. https://doi.org/10.1016/S0010-938X(98)00093-6

FitzGerald, K. P., Nairn, J., Skennerton, G., & Atrens, A. (2006). Atmospheric corrosion of copper and the colour, structure and composition of natural patinas on copper. *Corrosion Science, 48*, 2480-2509. https://doi.org/10.1016/j.corsci.2005.09.011

Fleet, M. E. (1975). The crystal structure of paratacamite, Cu2(OH)3Cl. *Acta Crystallographica Section B; Acta Cryst.B, 31*(1), 183-187. https://doi.org/10.1107/S0567740875002324

Fletcher, M., & Loeb, G. I. (1979). Influence of substratum characteristics on the attachment of a marine pseudomonad to solid surfaces. *Applied and Environmental Microbiology, 37*(1), 67. https://doi.org/10.1128/aem.37.1.67-72.1979

Fletcher, R., Baier, R., & Fornalik, M. (1984). The influence of surface energy on spore development in some common marine fouling algae. *Proc.6th Int.Congr.Mar.Corr.and Foul.* 129-144. https://doi.org/10.1098/rsif.2005.0041

Floerl, O., Wilkens, S., & Woods, C. (2010). *Temporal development of biofouling assemblages.* (Review No. CHC2012-103). New Zealand: National Institute of Water & Atmospheric Research Ltd. https://doi.org/10.3354/meps08074

Franey, J. P., & Davis, M. E. (1987). Metallographic study of copper patina formed in the atmosphere. *Corrosion Science, 27*(7), 659-668. https://doi.org/10.1016/0010-938X(87)90048-5

Frankel, G. S. (2016). Fundamentals of corrosion kinetics. In A. Hughes, J. Mol, M. Zheludkevich & R. Buchheit (Eds.), *Active protective coatings* (Springer Series in Materials Science, vol 233 ed., pp. 17-32) Springer, Dordrecht. https://doi.org/10.1007/978-94-017-7540-3_2

Fredj, N., & Burleigh, T. D. (2011). Transpassive dissolution of copper and rapid formation of brilliant colored copper oxide films. *Journal of the Electrochemical Society, 158*(4), C104. https://doi.org/10.1149/1.3551525

Frost, R. L. (2003). Raman spectroscopy of selected copper minerals of significance in corrosion. *Spectrochemica Acta Part A, 59*, 1195-1204. https://doi.org/10.1016/S1386-1425(02)00315-3

Frost, R. L., Martens, W., Kloprogge, J. T., & Williams, P. A. (2002). Raman spectroscopy of the basic copper chloride minerals atacamite and paratacamite: Implications for the study of copper brass and bronze objects of archaeological significance. *Journal of Raman Spectroscopy, 33*, 801-806. https://doi.org/10.1002/jrs.921

Fuente, D. d. l., Simancas, J., & Morcillo, M. (2008). Morphological study of 16-year patinas formed on copper in a wide range of atmospheric exposures. *Corrosion Science, 50*, 268-285. https://doi.org/10.1016/j.corsci.2007.05.030

Galvele, J. R. (1978). Effect of molybdenum on the pitting potential of high purity 18% Cr ferritic stainless steels. *Journal of the Electrochemical Society, 125*(8), 1204. https://doi.org/10.1149/1.2131650

Galvele, J. R. (1976). Transport processes and the mechanism of pitting of metals. *Journal of the Electrochemical Society, 123*(4), 464. https://doi.org/10.1149/1.2132857

Gao, J., Hu, A., Li, M., & Mao, D. (2009). Influence of crystal orientation on copper oxidation failure. *Applied Surface Science; Applied Surface Science, 255*(11), 5943-5947. https://doi.org/10.1016/j.apsusc.2009.01.040

Garg, A., Jain, A., & Bhosle, N. B. (2009). Chemical characterization of a marine conditioning film. *International Biodeterioration & Biodegradation, 63*(1), 7-11. https://doi.org/10.1016/j.ibiod.2008.05.004

gCaptain. (2014). New satellite data reveals major uptick in global maritime traffic. Retrieved June 6, 2019 from https://gcaptain.com/new-satellite-data-reveals-major-uptick-in-global-maritime-traffic/

Geng, M., & Duan, Z. (2010). Prediction of oxygen solubility in pure water and brines up to high temperatures and pressures. *Geochimica Et Cosmochimica Acta, 74*(19), 5631-5640. https://doi.org/10.1016/j.gca.2010.06.034

Georgopoulos, P. G., Roy, A., Yonone-Lioy, M. J., Opiekun, R. E., & Lioy, P. J. (2001). Environmental copper: Its dynamics and human exposure issues. *Journal of Toxicology and Environmental Health, Part B, 4*(4), 341-394. https://doi.org/10.1080/109374001753146207

Gibbs, P., & Bryan, G. (1987). *TBT paints and the demise of the dog-whelk, nucella lapillus (gastropoda)* https://doi.org/10.1109/OCEANS.1987.1160635

Goulding, G. (2016). The ultimate antifouling group test. Retrieved September 18, 2018 from https://www.mby.com/maintenance/tried-tested-antifoul-81351

Graedel, T. E. (1987a). Copper patinas formed in the atmopshere - II. A qualitative assessment of mechanisms. *Corrosion Science, 27*(7), 721-740. https://doi.org/10.1016/0010-938X(87)90053-9

Graedel, T. E. (1987b). Copper patinas formed in the atmosphere—III. A semi-quantitative assessment of rates and constraints in the greater New York metropolitan area. *Corrosion Science, 27*(7), 741-769. https://doi.org/10.1016/0010-938X(87)90054-0

Graedel, T. E., Nassau, K., & Franey, J. P. (1987). Copper patinas formed in the atmosphere - I introduction. *Corrosion Science, 27*(7), 639-657. https://doi.org/10.1016/0010-938X(87)90047-3

Grice, J. D., Szymanski, J. T., & Jambor, J. L. (1996). The crystal structure of clinoatacamite. a new polymorph of $Cu_2(OH)_3Cl$. *The Canadian Mineralogist, 34*, 73-78.

Grosell, M. (2011). 2 - copper. In C. M. Wood, A. P. Farrell & C. J. Brauner (Eds.), *Fish physiology: Homeostasis and toxicology of essential metals* (Volume 31, Part A ed., pp. 237-295) Elsevier Science.

Gu, Z. H., Xia, S. J., & Fahidy, T. Z. (1996). Comparison of dynamic behaviour of the anodic dissolution of copper in aqueous chloride and bromide solutions. *Electrochimica Acta; Electrochimica Acta, 41*(13), 2045-2054. https://doi.org/10.1016/0013-4686(96)00010-2

Gucinski, H., & Baier, R. E. (1983). Surface properties of porpoise and killer whale skin invivo. Utica, N.Y. : American Society of Zoologists.

Hålenius, U., Hatert, F., Pasero, M., & Mills, S. J. (2015). New minerals and nomenclature modifications approved in 2015. *Mineralogical Magazine, 79*(4), 941-947. https://doi.org/10.1180/minmag.2015.079.4.05

Hall, A. (1980). Heavy metal co-tolerance in a copper-tolerant population of the marine fouling alga, ectocarpus siliculosus (dillw.) lyngbye. *New Phytologist, 85*(1), 73-78. https://doi.org/10.1111/j.1469-8137.1980.tb04449.x

Harper, D. (2015). *Online etymology dictionary*

Harris, Z. L., & Gitlin, J. (1996). Genetic and molecular basis for copper toxicity.(copper nutrition in humans: Essentiality and toxicity). *American Journal of Clinical Nutrition, 63*(5), 836S. https://doi.org/10.1093/ajcn/63.5.836

Harvey, D. (2020). *Precipitation gravimetry*

Hawthorne, F. (1985). Refinement of the crystal structure of botallackite. *Mineralogical Magazine - MINER MAG, 49*, 87-89. https://doi.org/10.1180/minmag.1985.049.350.12

Haynes, W. M. (2012). *CRC handbook of chemistry and physics, 93rd edition* Taylor \& Francis. Retrieved July 3, 2020 from https://books.google.co.uk/books?id=-BzP7Rkl7WkC

Hernández, R. D. P., Aoki, I. V., Tribollet, B., & de Melo, H. G. (2011). Electrochemical impedance spectroscopy investigation of the electrochemical behaviour of copper coated with artificial patina layers and submitted to wet and dry cycles. *Electrochimica Acta; Electrochimica Acta, 56*(7), 2801-2814. https://doi.org/10.1016/j.electacta.2010.12.059

Heusler, K. E., & Fischer, L. (1976a). Kinetics of pit initiation at passive iron. *Materials and Corrosion, 27*(8), 551-556. https://doi.org/10.1002/maco.19760270802

[362]

Heusler, K. E., & Fischer, L. (1976b). Kinetics of pit initiation at the alloy Fe5Cr. *Materials and Corrosion, 27*(11), 788-791. https://doi.org/10.1002/maco.19760271105

Hinsa, S. M., Espinosa-Urgel, M., Ramos, J. L., & O' Toole, G. A. (2003). Transition from reversible to irreversible attachment during biofilm formation by pseudomonas fluorescens WCS365 requires an ABC transporter and a large secreted protein. *Molecular Microbiology, 49*(4), 905-918. https://doi.org/10.1046/j.1365-2958.2003.03615.x

Hoar, T. P. (1967). The production and breakdown of the passivity of metals. *Corrosion Science, 7*, 341-355. https://doi.org/10.1016/0010-938X(90)90086-K

Hoar, T. P., Mears, D. C., & Rothwell, G. P. (1965). The relationships between anodic passivity, brightening and pitting. *Corrosion Science, 5*(4), 279-289. https://doi.org/10.1016/S0010-938X(65)90614-1

Holm, R., & Matterson, E. (1982). Atmospheric corrosion tests of copper and copper alloys in sweden - 16 year results. *Atmospheric corrosion of metals* (pp. 85-105). Philadelphia: ASTM Special Technical Publication 767.

Hosford, W. F. (2005). Alloys: Copper. In F. Bassani, G. L. Liedl & P. Wyder (Eds.), *Encyclopedia of condensed matter physics* (pp. 24-45). Oxford: Elsevier. https://doi.org/10.1016/B0-12-369401-9/00533-7 Retrieved March 2, 2015 from https://www.sciencedirect.com/science/article/pii/B0123694019005337

Howell, D., & Behrends, B. (2006). A methodology for evaluating biocide release rate, surface roughness and leach layer formation in a TBT-free, self-polishing antifouling coating. *Biofouling, 22*(5), 303-315. https://doi.org/10.1080/08927010600924304

Hua, Q., Shang, D., Zhang, W., Chen, K., Chang, S., Ma, Y., . . . Huang, W. (2011). Morphological evolution of Cu2O nanocrystals in an acid solution: Stability of different crystal planes. *Langmuir; Langmuir, 27*(2), 665-671. https://doi.org/10.1021/la104475s

Hung, O., Thiyagarajan, V., Wu, R., & Qian, P. (2005). Effect of ultraviolet radiation on biofilms and subsequent larval settlement of hydroides elegans. *Marine Ecology Progress Series, 304*, 155-166. https://doi.org/10.3354/meps304155

Hutchison, M. J., & Scully, J. R. (2018). Solute capture and doping of al in Cu2O: Corrosion, tarnish resistance, and cation release of high-purity cu-al alloys in artificial perspiration. *Journal of the Electrochemical Society; J.Electrochem.Soc, 165*(10), C689-C702. https://doi.org/10.1149/2.1301810jes

Hwang, G., Kang, S., El-Din, M. G., & Liu, Y. (2012). Impact of conditioning films on the initial adhesion of burkholderia cepacia. *Colloids and Surfaces B: Biointerfaces, 91*, 181-188. https://doi.org/10.1016/j.colsurfb.2011.10.059

Ijsseling, F. P., Drolenga, L. J. P., & Kolstert, B. H. (1982). Influence of temperature on corrosion product film formation on CuNi10Fe in the low temperature range: I. corrosion rate as a function of temperature in well aerated sea water. *British Corrosion Journal, 17*(4), 162-167. https://doi.org/10.1179/000705982798274282

Imai, M., Yamashita, Y., Futatsuki, T., Shiohara, M., Kondo, S., & Saito, S. (2009). Effect of dissolved oxygen on cu corrosion in single wafer cleaning process. *Japanese Journal of Applied Physics, 48*(4), 04023. https://doi.org/10.1143/jjap.48.04c023

International. (2017). *Interspeed® 6400/6400NA controlled depletion polymer antifouling*. Brochure:

International. (N/D). Why does my antifouling sometimes go green, especially at the waterline? Retrieved from https://www.international-yachtpaint.com/en/gb/support/boat-paint-expert-advice/green-copper-patina

International Maritime Organization. (2009). *Second IMO GHG study 2009*. London: International Maritime Organization. Retrieved September 14 2014 from http://www.imo.org/en/OurWork/Environment/PollutionPrevention/AirPollution/Documents/

International Paint Ltd. (2008). *Safety data sheet: BEA469 intersmooth 460 SPC dark red*

International Paint Ltd. (2010). Intersmooth®360/365 SP TBT free self-polishing copolymer antifouling.

International Paint Ltd. (2016). *Interspeed 640 TBT free polishing antifouling*

IPCC (Intergovernmental Panel on Climate Change). (2019). Special report on the ocean and cryosphere in a changing climate. Retrieved October 22, 2020 from https://www.ipcc.ch/srocc/

Jain, A., & Bhosle, N. B. (2009). Biochemical composition of the marine conditioning film: Implications for bacterial adhesion. *Biofouling, 25*(1), 13-19. https://doi.org/10.1080/08927010802411969

Jambor, J. L., Dutrizac, J. E., Roberts, A. C., Grice, J. D., & Szymanski, J. T. (1996). Clinocatacamite a new polymorph of Cu2(OH)3, and its relationship to paratacamite and "anarakite". *The Canadian Mineralogist, 34*, 61-72.

Janik-Czachor, M., & Janik-Czachor, M. (1981). An assessment of the processes leading to pit nucleation on iron. *Journal of the Electrochemical Society, 128*(12), 513C-519C. https://doi.org/10.1149/1.2127344

Jenkins, H. D. B., & Thakur, K. P. (1979). Reappraisal of thermochemical radii for complex ions. *Journal of Chemical Education, 56*(9), 576-577.

Jenkins, L. H. (1960). Dissolution of single crystals of copper in aqueous ethylenediamine. *Journal of the Electrochemical Society, 107*(5), 371. https://doi.org/10.1149/1.2427702

JEOL. (2019). *JEOL EDS periodic table*

Jmol. (2021). Jmol: An open-source java viewer for chemical structures in 3D [computer software]

Johansson, L. E. (1985). The local effect of hull roughness on skin friction. calculations based on floating element data and three-dimensional boundary layer theory. *Naval Architect,* 187-201.

Josefowicz, J. Y., Xie, L., & C. Farrington, G. (1993). Observation of intermediate CuCl species during the anodic dissolution of cu using atomic force microscopy. *The Journal of Physical Chemistry, 97*, 11995-11998. https://doi.org/10.1021/j100148a025

Judge, W. D., Bishop, D. P., & Kipouros, G. J. (2017). Effect of sizing on the corrosion behaviour of alumix 123 P/M alloy in 3.5 wt-% NaCl solution. *Corrosion Engineering, Science and Technology, 52*(1), 29-37. https://doi.org/10.1080/1478422X.2016.1179845

Kakaei, K., Esrafili, M. D., & Ehsani, A. (2019). *Chapter 8 - graphene and anticorrosive properties* https://doi.org/10.1016/B978-0-12-814523-4.00008-3

Kear, G., Barker, B. D., & Walsh, F. C. (2004). Electrochemical corrosion of unalloyed copper in chloride media - a critical review. *Corrsion Science, 46*, 109-135. https://doi.org/10.1016/S0010-938X(02)00257-3

Keil, P., Lützenkirchen-Hecht, D., & Frahm, R. (2007). *Investigation of room temperature oxidation of cu in air by Yoneda-XAFS* American Institute of Physics. https://doi.org/10.1063/1.2644569

Kelton, K. F., & Greer, A. L. (2010). Chapter 6 - heterogeneous nucleation. *Pergamon Materials Series, 15*, 165-226. https://doi.org/10.1016/S1470-1804(09)01506-5

Kempf, G. F. (1937) On the effect of roughness on the resistance of ships. Paper presented at the *Trans. Institution of Naval Architects, 79* 109-119.

Ketchum, B. H., Ferry, J. D., Redfield, A. C., & Burns, A. E. (1945). Evaluation of AntiFouling paints by leaching rate determinations. *Industrial & Engineering Chemistry, 37*(5), 456-460. https://doi.org/10.1021/ie50425a021

Khaled, K. F. (2011). Studies of the corrosion inhibition of copper in sodium chloride solutions using chemical and electrochemical measurements. *Materials Chemistry and Physics, 125*(3), 427-433. https://doi.org/10.1016/j.matchemphys.2010.10.037

Kiil, S., Weinell, C. E., Pedersen, M. S., & Dam-Johansen, K. (2001). Analysis of self-polishing antifouling paints using rotary experiments and mathematical modelling. *Industrial & Engineering Chemistry Research, 40*(18), 3906-3920. https://doi.org/10.1021/ie010242n

Kim, S. J., Jung, H. G., Park, G. T., & Kim, K. Y. (2014). Effect of Cu and Ni on sulfide film formation and corrosion behavior of pressure vessel steel in acid sour environment. *Applied Surface Science, 313*, 396-404. https://doi.org/10.1016/j.apsusc.2014.06.003

King, F. (2002). *Corrosion of copper in alkaline chloride environments.* (No. TR-02-25). Retrieved September 15 (2013) from https://inis.iaea.org/collection/NCLCollectionStore/_Public /33/064/33064747.pdf

King, F., Litke, C. D., Quinn, M. J., & LeNeveu, D. M. (1995). The measurement and prediction of the corrosion potential of copper in chloride solutions as a function of oxygen

concentration and mass-transfer coefficient. *Corrosion Science, 37*(5), 833-851. https://doi.org/10.1016/0010-938X(95)80013-1

King, F., Quinn, M. J., & Litke, C. D. (1995). Oxygen reduction on copper in neutral NaCl solution. *Journal of Electroanalytical Chemistry, 385*(1), 45-55. https://doi.org/10.1016/0022-0728(94)03705-8

King, F., Lilja, C., Pedersen, K., Vähänen, M., & Pitkänen, P. (2012). *An update of the state-of-the-art report on the corrosion of copper under expected conditions in a deep geologic repository*

Kojima, R., Shibata, T., & Ueda, K. (2016). Leaching phenomena of antifouling agents from ships' hull paints. *Journal of Shipping and Ocean Engineering, 6* https://doi.org/10.17265/2159-5879/2016.05.002

Kokuhennadige, H., Asanthi, H., & Kumara, P. B. T. (2013). An assessment of water quality and pollution in Puranawella fishery harbour, Dewinuwara, Sri Lanka.1 https://doi.org/10.4038/jur.v1i1.6157

Kong, D., Dong, C., Wei, X., Man, C., Lei, X., Mao, F., & Li, X. (2018). Size matching effect between anion vacancies and halide ions in passive film breakdown on copper. *Electrochimica Acta, 292*, 817-827. https://doi.org/10.1016/j.electacta.2018.10.004

Kong, D., Dong, C., Xiao, K., & LI, X. (2017). Effect of temperature on copper corrosion in high-level nuclear waste environment. *Transactions of Nonferrous Metals Society of China; Transactions of Nonferrous Metals Society of China, 27*(6), 1431-1438. https://doi.org/10.1016/S1003-6326(17)60165-1

Kristiansen, H. (1977). Corrosion of copper by water of various temperatures and carbon dioxide contents. *Materials and Corrosion, 28*(11), 743-748. https://doi.org/10.1002/maco.19770281102

Kruger, J. (1959). The oxide films formed on copper single crystal surfaces in pure water: I. nature of the films formed at room temperature. *Journal of the Electrochemical Society, 106*(10), 854-860. https://doi.org/10.1149/1.2427162

Kruger, J. (2003). Vol 13A; corrosion: Fundamentals, testing and protection. *ASM handbook* (pp. 61-67) ASM International.

Kunze, J., Maurice, V., Klein, L. H., Strehblow, H., & Marcus, P. (2001). *In situ scanning tunnelling microscopy study of the anodic oxidation of cu(111) in 0.1 M NaOH* https://doi.org/10.1021/jp004012i

Kunze, J., Maurice, V., Klein, L. H., Strehblow, H., & Marcus, P. (2004). In situ STM study of the duplex passive films formed on cu(1 1 1) and cu(0 0 1) in 0.1 M NaOH. *Corrosion Science, 46*(1), 245-264. https://doi.org/10.1016/S0010-938X(03)00140-9

Lackenby, H. (1962). The thirty-fourth Thomas Lowe Gray lecture: Resistance of ships, with special reference to skin friction and hull surface condition. *Proceedings of the Institution of Mechanical Engineers, 176*(1), 981-1014. https://doi.org/10.1243/PIME_PROC_1962_176_077_02

Laferrere, A., Parson, N., Zhou, X., & Thompson, G. (2013). Effect of microstructure on the corrosion behaviour of extruded heat exchanger aluminium alloys. *Surface and Interface Analysis, 45*(10), 1597-1603. https://doi.org/10.1002/sia.5282

Lagerström, M., Lindgren, J. F., Holmqvist, A., Dahlström, M., & Ytreberg, E. (2018). In situ release rates of Cu and Zn from commercial antifouling paints at different salinities. *Marine Pollution Bulletin*, 289-296. https://doi.org/10.1016/j.marpolbul.2017.12.027

Lapeire, L., Martinez Lombardia, E., De Graeve, I., Terryn, H., & Verbeken, K. (2017). Influence of grain size on the electrochemical behavior of pure copper. *Journal of Materials Science, 52*(3), 1501-1510. https://doi.org/10.1007/s10853-016-0445-z

Lau, S. C. K., Harder, T., & Qian, P. (2003). Induction of larval settlement in the serpulid polychaete hydroides elegans (haswell): Role of bacterial extracellular polymers. *Biofouling, 19*(3), 197-204. https://doi.org/10.1080/08927014.2003.10382982

Lee, H., & Nobe, K. (1986). Kinetics and mechanisms of copper electrodissolution in chloride media. *J.Electrochem.Soc, 133*(10), 2035-2043. https://doi.org/10.1149/1.2108335

Leggat, R. (2018). Delamination of a coating from a ship's hull. Retrieved September 16, (2020) from https://kta.com/kta-university/delamination-of-a-coating-from-a-ships-hull/

Leidheiser, H. J. (1991). Electrochemical methods for appraising corrosion protective coatings. *JCT, Journal of Coatings Technology, 63*(802), 21-31. Retrieved August 5, (2014) from http://pascal-francis.inist.fr/vibad/index.php?action=getRecordDetail&idt=5071026

Lejars, M., Margaillan, A., & Bressy, C. (2012). Fouling release coatings: A nontoxic alternative to biocidal antifouling coatings. *Chemical Reviews, 112*(8), 4347. https://doi.org/10.1021/cr200350v

Lewis, M. A., Masin, J. G., & O'Hare, P. A. (2009). Evaluation of alternative thermochemical cycles, part I: The methodology. *International Journal of Hydrogen Energy, 34*(9), 4115-4124. https://doi.org/10.1016/j.ijhydene.2008.06.045

Lewkowicz, A. K., & Das, D. K. (1986). Turbulent boundary layers on rough surfaces with and without a pliable overlayer: A simulation of marine fouling. *International Shipbuilding Progress, 33*(386), 1774-186. https://doi.org/10.3233/ISP-1986-3338601

Lewthwaite, J. C., Molland, A., & Thomas, K. W. (1985) An investigation into the variation of ship skin frictional resistance with fouling. Paper presented at the *Transactions of the Royal Institution of Naval Architects,*

Leygraf, C., Chang, T., Herting, G., & Odnevall Wallinder, I. (2019). The origin and evolution of copper patina colour. *Corrosion Science, 157*, 337-346. https://doi.org/10.1016/j.corsci.2019.05.025

Li, J. (2016). Internal stress formation and changes in oxide films on a lead alloy anode surface. *International Journal of Electrochemical Science, 11*(12), 10659-10674. https://doi.org/10.20964/2016.12.07

Li, W., & Li, D. Y. (2005). Variations of work function and corrosion behaviors of deformed copper surfaces. *Applied Surface Science, 240*(1-4), 388-395. https://doi.org/10.1016/j.apsusc.2004.07.017

Liao, X., Cao, F., Zheng, L., Liu, W., Chen, A., Zhang, J., & Cao, C. (2011). Corrosion behaviour of copper under chloride-containing thin electrolyte layer. *Corrosion Science, 53*(10) https://doi.org/10.1016/j.corsci.2011.06.004

Ligrani, P. M. (1989). Structure of turbulent boundary layers. In N. P. Cheremisinoff (Ed.), *Encyclopedia of fluid mechanics* (pp. 112-189) Gulf Publishing.

Lim, C., Yoo, Y., Sidharthan, M., Ma, C., Bang, I., Kim, J., Lim, C. Y. (2006). Effects of copper (I) oxide on growth and biochemical compositions of two marine microalgae. *Journal of Environmental Biology, 27*(3), 461-466. PMID: 17402234

Lin, H., Chen, W., & Huang, C. (2019). Chapter 15 - graphene in electrochemical biosensors. In M. Nurunnabi, & J. R. McCarthy (Eds.), Biomedical applications of graphene and 2D nanomaterials (pp. 321-336) Elsevier. https://doi.org/10.1016/B978-0-12-815889-0.00015-5.

Lindgren, J. F., Ytreberg, E., Holmqvist, A., Dahlström, M., Dahl, P., Berglin, M., . . . Dahlström, M. (2018). Copper release rate needed to inhibit fouling on the west coast of sweden and control of copper release using zinc oxide. *Biofouling, 34*(4), 453-463. https://doi.org/10.1080/08927014.2018.1463523

Lindholdt, A., Dam-Johansen, K., Olsen, S., Yebra, D., & Kiil, S. (2015). Effects of biofouling development on drag forces of hull coatings for ocean-going ships: A review. *Journal of Coatings Technology and Research, 12*(3), 415-444. https://doi.org/10.1007/s11998-014-9651-2

Lindner, E. (1988). Failure mechanism of copper antifouling coatings. *International Biodeterioration, 24*(4-5), 247-253. https://doi.org/10.1016/0265-3036(88)90008-5

Little, B. J. (1984). Succession in microfouling. In J. D. Costlow (Ed.), *Marine biodeterioration an interdisciplinary study* (1st ed., pp. 63-67) Springer US.

Little, B. J., & Zsolnay, A. (1985). Chemical fingerprinting of adsorbed organic materials on metal surfaces. *Journal of Colloid and Interface Science, 104*(1), 79-86. https://doi.org/10.1016/0021-9797(85)90011-6

Liu, J., Huang, X., Li, Y., Sulieman, K. M., He, X., & Sun, F. (2006a). Hierarchical nanostructures of cupric oxide on a copper substrate: Controllable morphology and wettability. *Journal of Materials Chemistry, 16*(45), 4427-4434. https://doi.org/10.1039/B611691D

Liu, J., Huang, X., Li, Y., Sulieman, K. M., He, X., & Sun, F. (2006b). Self-assembled CuO monocrystalline nanoarchitectures with controlled dimensionality and morphology. *Crystal Growth & Design, 6*(7), 1690-1696. https://doi.org/10.1021/cg060198k

Locarnini, R. A., Mishonov, A. V., Antonov, J. I., Boyer, T. P., Garcia, H. E., Baranova, O. K., . . . Seidov, D. (2013). Volume 1: Temperature. *World ocean atlas 2013* (73rd ed., pp. 40) NOAA Atlas NESDIS.

Loeb, G. I., Laster, D., & Gracik, T. (1984). The influence of microbial fouling films on hydrodynamic drag of rotating discs. In J. D. Costlow, & R. Tipper (Eds.), *Marine biodeterioration: An interdisciplinary study.* (pp. 88-94). Annapolis MD: Naval Institute Press.

Lohrengel, M. M., Schultze, J. W., Speckmann, H. D., & Strehblow, H. (1987). Growth, corrosion and capacity of copper oxide films investigated by pulse techniques. *Electrochimica Acta, 32*(5), 733-742. https://doi.org/10.1016/0013-4686(87)85103-4

Lopesino, P., Alcántara, J., de la Fuente, D., Chico, B., Jiménez, J., & Morcillo, M. (2018). Corrosion of copper in unpolluted chloride-rich atmospheres. *Metals (Basel), 8*(11), 866. https://doi.org/10.3390/met8110866

Lyman, J., & Abel, R. B. (1958). Chemical aspects of physical oceanography. *Journal of Chemical Education, 35*(3), 119. https://doi.org/10.1021/ED035P113

Lytle, D. A., & Nadagouda, M. N. (2010). A comprehensive investigation of copper pitting corrosion in a drinking water distribution system. *Corrosion Science, 52*(6), 1927-1938. https://doi.org/10.1016/j.corsci.2010.02.013

Macdonald, D. D., & Lei, X. (2016). Theoretical interpretation of anion size effects in passivity breakdown. *Journal of the Electrochemical Society, 163*(13), C738-C744. https://doi.org/10.1149/2.0571613jes

Maki, J. S., Little, B. J., Wagner, P., & Mitchell, R. (1990). Biofilm formation on metal surfaces in antarctic waters. *Biofouling, 2*(1), 27-38. https://doi.org/10.1080/08927019009378127

Marine Corrosion Sub-Committee. (1944). *Fouling of ships' bottoms: Identification of marine growths* Creative Media Partners, LLC. Retrieved April 18, 2013 from https://books.google.co.uk/books?id=N162vQEACAAJ

Marine Superstore. (N/D). The complete guide to antifouling paint. Retrieved January 7, 2016 from https://www.marinesuperstore.com/antifouling-paint-guide#:~:text=Copper%20oxide%20based%20antifouling%20can%20turn%20green%20when,can%20even%20be%20scrubbed%20or%20cleaned%20off%20mid-season

Maroof, M. A., Mahboubi, A., Noorzad, A., & Safi, Y. (2020). A new approach to particle shape classification of granular materials. *Transportation Geotechnics, 22*, 100296. https://doi.org/10.1016/j.trgeo.2019.100296

Marshall, K. C., Stout, R., & Mitchell, R. (1971). Mechanism of the initial events in the sorption of marine bacteria to surfaces. *Journal of General Microbiology, 68*(3), 337-348. https://doi.org/10.1099/00221287-68-3-337

Marszalek, D. S., Gerchakov, S. M., & Udey, L. R. (1979). Influence of substrate composition on marine microfouling. *Applied and Environmental Microbiology, 38*(5), 987. https//doi.org/10.1128/aem.38.5.987-995.1979

Martinez-Lombardia, E., Gonzalez-Garcia, Y., Lapeire, L., De Graeve, I., Verbeken, K., Kestens, L., Terryn, H. (2014). Scanning electrochemical microscopy to study the effect of

crystallographic orientation on the electrochemical activity of pure copper. *Electrochimica Acta, 116*, 89-96. https://doi.org/10.1016/j.electacta.2013.11.048

Masudome, H., & Abe, H. (2011). Chemical depth profiling of copper oxide film by ToF-SIMS using Bi3. *Surface and Interface Analysis, 43*, 664-668. https://doi.org/10.1002/sia.3504

Maurice, V., Strehblow, H., & Marcus, P. (2000). In situ STM study of the initial stages of oxidation of cu(111) in aqueous solution. *Surface Science, 458*(1), 185-194. https://doi.org/10.1016/S0039-6028(00)00442-8

Maurice, V., Strehblow, H., Marcus, P., & Maurice, V. (1999). In situ scanning tunnelling microscope study of the passivation of cu(111). *Journal of the Electrochemical Society (USA), 146*(2), 524-530. https://doi.org/10.1149/1.1391638

Mayanna, S., & Setty, T. (1974). Role of chloride ions in relation to copper corrosion and inhibition. *Proceedings of the Indian Academy of Sciences - Section A, 80*(4), 184-193. https://doi.org/10.1007/BF03046676

Mccafferty, E. (2005). Validation of corrosion rates measured by the Tafel extrapolation method. *Corrosion Science, 47*(12), 3202-3215. https://doi.org/10.1016/j.corsci.2005.05.046

Melchers, R. E., & Jeffrey, R. (2012). Corrosion of long vertical steel strips in the marine tidal zone and implications for ALWC. Corrosion Science, 65, 26-36. https://doi.org/10.1016/j.corsci.2012.07.025

Melchers, R. E. (2015). Effect of water nutrient pollution on long-term corrosion of 90:10 copper nickel alloy. *Materials (Basel, Switzerland), 8*(12), 8047-8058. https://doi.org/10.3390/ma8125443

The merchant shipping (load line) regulations, (1998). Retrieved February 13, (2015) from https://www.legislation.gov.uk/cy/uksi/1998/2241/made

Metikoš-Huković, M., Babić, R., & Paić, I. (2000). Copper corrosion at various pH values with and without the inhibitor. *Journal of Applied Electrochemistry, 30*(5), 617-624. https://doi.org/10.1023/A:1003956102631

Michelis, A., & Gougoulidis, G. (2015) Current and future trends in marine antifouling coatings and the study of energy efficiency benefits for a naval fleet. Paper presented at the Environment & Energy in Ships EEinS 2015, ASHRAEAt: Athens, Greece

Milić, S. M., & Antonijević, M. M. (2009). Some aspects of copper corrosion in presence of benzotriazole and chloride ions. *Corrosion Science, 51*(1), 28-34. https://doi.org/10.1016/j.corsci.2008.10.007

Milić, S. M., Antonijević, M. M., Šerbula, S. M., & Bogdanović, G. D. (2008). Influence of benzotriazole on corrosion behaviour of CuAlNiSi alloy in alkaline medium. *Corrosion Engineering, Science and Technology, 43*(1), 30-37. https://doi.org/10.1179/174327808X286329

[370]

Millet, B., Fiaud, C., Hinnen, C., & Sutter, E. M. M. (1995). A correlation between electrochemical behaviour, composition and semiconducting properties of naturally grown oxide films on copper. *Corrosion Science, 37*(12), 1903-1918. https://doi.org/10.1016/0010-938X(95)00072-R

Milne, A. (1990). Roughness and drag from the marine paint chemist's viewpoint. Marine Roughness and Drag Workshop, London.

Milošev, I., Mikić, T. K., & Gaberšček, M. (2006). The effect of cu-rich sub-layer on the increased corrosion resistance of cu– xZn alloys in chloride containing borate buffer. *Electrochimica Acta, 52*(2), 415-426. https://doi.org/10.1016/j.electacta.2006.05.024

Min-Dian Siao, & Chen-Sheng Yeh. (2005). *Fabrication of copper chloride hydroxide nanoflowers from au cu hollow nanospheres using a solution phase methodology* IEEE. https://doi.org/10.1109/NANO.2005.1500834

Modestov, A. D., Zhou, G., Ge, H., & Loo, B. H. (1995). A study by voltammetry and the photocurrent response method of copper electrode behavior in acidic and alkaline solutions containing chloride ions. *Journal of Electroanalytical Chemistry, 380*(1), 63-68. https://doi.org/10.1016/0022-0728(94)03577-P

Mohammed Ali Al-Sammarraie, A., & Hasan Raheema, M. (2017). Electrodeposited reduced graphene oxide films on stainless steel, copper, and aluminum for corrosion protection enhancement. *International Journal of Corrosion, 2017* https://doi.org/10.1155/2017/6939354

Monfared, H., & Sharif, F. (2008). Design guidelines for development of tin-free antifouling self-polishing coatings using simulation. *Progress in Organic Coatings, 63*(1), 79-86. https://doi.org/10.1016/j.porgcoat.2008.04.010

Montes, J. C., Hamdani, F., Creus, J., Touzain, S., & Correc, O. (2014). Impact of chlorinated disinfection on copper corrosion in hot water systems. *Applied Surface Science, 314*, 686-696. https://doi.org/10.1016/j.apsusc.2014.07.069

Monty, J. P., Dogan, E., Hanson, R., Scardino, A. J., Ganapathisubramani, B., & Hutchins, N. (2016). An assessment of the ship drag penalty arising from light calcareous tubeworm fouling. *Biofouling, 32*(4), 451-464. https://doi.org/10.1080/08927014.2016.1148140

Murray, J. N. (1997). Electrochemical test methods for evaluating organic coatings on metals: An update. part II: Single test parameter measurements. *Progress in Organic Coatings, 31*(3), 255-264. **Error! Hyperlink reference not valid.**https://doi.org/10.1016/S0300-9440(97)00084-2

Muthukrishnan, T., Abedd, R. M. M., Dobretsov, S., Kidd, B., & Finnie, A. A. (2014). Long-term microfouling on commercial biocidal fouling control coatings. *Biofouling, ,* 1155-1164. https://doi.org/10.1080/08927014.2014.972951

Nairn, J. D., Skennerton, S. G., & Atrens, A. (2003). Comparative atmospheric corrosion of primary and cold rolled copper in Australia. *Journal of Materials Science, 38*, 995-1005. https://doi.org/10.1023/A:1022337511592

Nassau, K., Miller, A. E., & Graedel, T. E. (1987). The reaction of simulated rain with copper, copper patina, and some copper compounds. *Corrosion Science*, 703-719. https://doi.org/10.1016/0010-938X(87)90052-7

Natural Resources Research Institute. (2015). DO %Saturation calculator. Retrieved May 2, (2018) from https://www.waterontheweb.org/under/waterquality/dosatcalc.html

Navarro, M., May, P. M., Hefter, G., & Königsberger, E. (2014). Solubility of CuO(s) in highly alkaline solutions. *Hydrometallurgy, 147-148*, 68-72. https://doi.org/10.1016/j.hydromet.2014.04.018

Nessim, R. B., Tadros, H. R. Z., Abou Taleb, Amaal E. A, & Moawad, M. N. (2015). Chemistry of the Egyptian Mediterranean coastal waters. *The Egyptian Journal of Aquatic Research, 41*(1), 1-10. https://doi.org/10.1016/j.ejar.2015.01.004

Nikolov, T., & Girginov, A. (1983). Potentiostatic formation of high resistance anodic films on bismuth in phosphate esters. *Surface Technology, 18*(3), 243-248. https://doi.org/10.1016/0376-4583(83)90054-7

Nikravesh, B., Ramezanzadeh, B., Sarabi, A. A., & Kasiriha, S. M. (2011). Evaluation of the corrosion resistance of an epoxy-polyamide coating containing different ratios of micaceous iron oxide/al pigments. *Corrosion Science, 53*(4), 1592-1603. https://doi.org/https://doi.org/10.1016/j.corsci.2011.01.045

North, R. F., & Pryor, M. J. (1970). *The influence of corrosion product structure on the corrosion rate of cu-ni alloys*. Oxford] : Pergamon Press. https://doi.org/10.1016/S0010-938X(70)80022-1

NSTM. (2006). Chapter 081 - WATERBORNE UNDERWATER HULL CLEANING OF NAVY SHIPS. *Naval ships' technical manual* (5th ed., pp. 81-2)

Nunez, N., Reguera, E., Corvo, F., & Gonzalez, E. (2005). Corrosion of copper in seawater and its aerosols in a tropical island. *Corrosion Science, 47*, 461-484. https://doi.org/10.1016/j.corsci.2004.05.015

Ochoa, M., Rodríguez, M. A., & Farina, S. B. (2015). Corrosion of high purity copper in solutions containing NaCl, Na2SO4 and NaHCO3 at different temperatures. *Procedia Materials Science, 9*, 460-468. https://doi.org/10.1016/j.mspro.2015.05.017

Ogata, S., Kobayashi, N., Kitagawa, T., Shima, S., Fukunaga, A., Takatoh, C., & Fukuma, T. (2016). Nanoscale corrosion behavior of polycrystalline copper fine wires in dilute NaCl solution investigated by in-situ atomic force microscopy. *Corrosion Science, 105*, 177-182. https://doi.org/10.1016/j.corsci.2016.01.015

Oliveira, D., Larsson, A. I., & Granhag, L. (2018). Effect of ship hull form on the resistance penalty from biofouling. *Biofouling, 34*(3), 262-272. https://doi.org/10.1080/08927014.2018.1434157

O'Neill, T. B., & Wilcox, G. L. (1971). The formation of a "primary film" on materials submerged in the sea at port hueneme, California. *Pacific Science, 25*

[372]

Opila, R. L. (1987). Copper patinas: An investigation by auger electron spectroscopy. *Corrosion Science, 27*(7), 685-694. https://doi.org/10.1016/0010-938X(87)90050-3

Örnek, C. (2019). Stress corrosion cracking and hydrogen embrittlement of type 316L austenitic stainless steel beneath $MgCl_2$ and $MgCl_2$: $FeCl_3$ droplets. *Corrosion, 75*(6), 657-667. https://doi.org/10.5006/3090

Oswald, H. R., & Feitknecht, W. (1964). Über die hydroxidhalogenide Me2(OH)3Cl, -br, -J zweiwertiger metalle (me = Mg, Ni, Co, Cu, Fe, Mn). *Helvetica Chimica Acta, 47*(1), 272-289. https://doi.org/10.1002/hlca.19640470136

Otmačić, H., & Stupnišek-Lisac, E. (2003). Copper corrosion inhibitors in near neutral media. *Electrochimica Acta, 48*(8), 985-991. https://doi.org/10.1016/S0013-4686(02)00811-3

Outotec. (2019). *HSC chemistry references.* Outokumpu Research Oy. Retrieved July 27, 2020 from https://www.outotec.com/globalassets/products/digital-solutions/hsc/hsc-chemistry-literature-references.pdf

Oxford Instruments Nanotechnology Tools Ltd. (2021). Errors associated with the analysis [computer software]

Palm, M., & Krieg, R. (2012). Neutral salt spray tests on Fe–Al and Fe–Al–X. *Corrosion Science, 64*, 74-81. https://doi.org/ https://doi-org.hallam.idm.oclc.org/10.1016/j.corsci.2012.07.013

Palmer, D. (2011). Solubility measurements of crystalline cu 2 O in aqueous solution as a function of temperature and pH. *Journal of Solution Chemistry, 40*(6), 1067-1093. https://doi.org/10.1007/s10953-011-9699-x

PANalytical. (2006). HighScore plus: MAC calculator [computer software]. Almelo: Panalytical.

Parise, J. B., & Hyde, B. G. (1986). The structure of atacamite and its relationship to spinel. *Acta Crystallographica Section C, 42*(10), 1277-1280. https://doi.org/10.1107/S0108270186092570

Peres, R. S., Baldissera, A. F., Armelin, E., Alemán, C., & Ferreira, C. A. (2014). Marine-friendly antifouling coating based on the use of a fatty acid derivative as a pigment. *Materials Research, 17*(3), 720-727. https://doi.org/10.1590/S1516-14392014005000032

Perez, N., & Springerlink. (2004). *Electrochemistry and corrosion science*. Boston, MA: Springer US. https://doi.org/10.1007/978-3-319-24847-9

Picologlou, B., Characklis, W., Zelver, N., & Picologlou, B. (1980). Biofilm growth and hydraulic performance. *Journal of Hydraulic Engineering, 106*(5), 733-746. https://doi.org/10.1061/JYCEAJ.0005421

Pidgeon, J. D. (1993). *Marine antifouling coating — critical review of current and future marine antifouling coatings.* (Technical No. report 93/TIPEE/478719). Propulsion and Environmental Engineering Department.

[373]

Pistorius, P. C., & Burstein, G. T. (1992). Growth of corrosion pits on stainless steel in chloride solution containing dilute sulphate. *Corrosion Science, 33*(12), 1885-1897. https://doi.org/10.1016/0010-938X(92)90191-5

Pistorius, P., Burstein, G., & Pistorius, P. (1994). Aspects of the effects of electrolyte composition on the occurrence of metastable pitting on stainless steel. *Corros.Sci, 36*(3), 525-538. https://doi.org/10.1016/0010-938X(94)90041-8

Plutarch. (2018). BOOK II. - question VII: About a fish called remora or echeneis. *Essays and miscellanies*. B&R Samizdat Express.

Pollard, A. M., Thomas, R. G., & Williams, P. A. (1989). Synthesis and stabilities of the basic copper(II) chlorides atacamite, paratacamite and bollackite. *Mineralogical Magazine, 53*(373), 557-563. https://doi.org/10.1180/minmag.1989.053.373.06

Pourbaix, M. (1966). *Atlas of electrochemical equilibria in aqueous solutions* Pergamon.

Powell, C., & Michels, H. (N/D). *Review of splash zone corrosion and biofouling of C70600 sheathed steel over 20 years exposure*. Copper Development Association Inc. Retrieved from July 6, 2022 https://www.copper.org/applications/marine/cuni/pdf/splash_zone_michels_powell.pdf

Powers, M. C. (1953). A new roundness scale for sedimentary particles. *Journal of Sedimentary Research, 23* https://doi.org/10.1306/D4269567-2B26-11D7-8648000102C1865D

Prajatelistia, E., Nurrochman, A., & Cho, K. (2019). Effect of temperature on corrosion behavior of copper silver phosphorus brazing alloys in chloride containing solution. *IOP Conference Series: Materials Science and Engineering, 547*, 012044. https://doi.org/10.1088/1757-899X/547/1/012044

Presuel-Moreno, F., Jakab, M. A., Tailleart, N., Goldman, M., & Scully, J. R. (2008). Corrosion-resistant metallic coatings. *Materials Today, 11*(10), 14-23. https://doi.org/10.1016/S1369-7021(08)70203-7

Princeton Applied Research. (N/D). Application note CORR-4 subject: Electrochemistry and corrosion: Overview and techniques. Retrieved October 10 2016, from https://www.ameteksi.com/-/media/ameteksi/download_links/documentations/library/princetonappliedresearch/application_note_corr-4.pdf?dmc=1&revision=eabdb6b9-130e-4d45-85d2-ec3d8e6fdec6

Puigdomenech, I. (2015). Kth/che/medusa [computer software]. https://www.kth.se/che/medusa/: KTH Royal Institute of Technology

Ramesh, U. S., Mukherjee, A., Misra, S. C., & Joshi, M. Failure analysis of antifouling paints on ships hull. Paper presented at the *Management of Ballast Water & Biofouling Conference ,* Chennai. Retrieved September 16 2019, from http://www.imuv.edu.in/Publications/35.%20Failure%20Analysis%20of%20Antifouling%20Paints%20on%20Ships%20Hull.pdf

[374]

Rangel, W. M., Boca Santa, Rozineide A. Antunes, & Riella, H. G. (2020). A facile method for synthesis of nanostructured copper (II) oxide by coprecipitation. *Journal of Materials Research and Technology, 9*(1), 994-1004. https://doi.org/10.1016/j.jmrt.2019.11.039

Raship, A., Sahdan, M. Z., Adriyanto, F., Fauzee, N. M., & Bakri, A. S. (2016). The effects of pH value on the preparation of copper oxide thin films by dip coating technique. *ARPN Journal of Engineering and Applied Sciences, 11*(14), 8829-8833.

Rawle, A. (N/D). *Basic principles of particle size analysis*. Malvern Instruments Limited.

Rehmatulla, N., & Smith, T. (2015). Barriers to energy efficient and low carbon shipping. *Ocean Engineering, 110*, 102-112. https://doi.org/10.1016/j.oceaneng.2015.09.030

Reiber, S. H. (1989). Copper plumbing surfaces: An electrochemical study. *Journal - American Water Works Association, 81*(7), 114-122. https://doi.org/10.1002/j.1551-8833.1989.tb03246.x

Rice, D. W., Peterson, P., Rigby, E. B., Phipps, P. B. P., Cappell, R. J., & Tremoureux, R. (1981). Atmospheric corrosion of copper and silver. *Journal of the Electrochemical Society, 128*, 25-284. https://doi.org/10.1149/1.2127403

Robin, A. (2005). Effect of temperature and concentration on electrochemical corrosion behaviour of nb-20Ta alloy in sodium hydroxide solutions. *Corrosion Engineering, Science and Technology, 40*(1), 51-56. https://doi.org/10.1179/174327805X29831

Robin, A., Martinez, G. A. S., & Suzuki, P. A. (2012). Effect of cold-working process on corrosion behavior of copper. *Materials and Design, 34*, 319-324. https://doi.org/10.1016/j.matdes.2011.08.018

Roine, A. (2006). HSC chemistry® version 6.0 [computer software]. www.outotec.com/HSC: Outokumpu Research Oy.

RRUFF™. (N/D). Clinoatacamite R100198. Retrieved December 5, (2014) from https://rruff.info/clinoatacamite/display=default/R100198

S M Abd, El Haleem. (2006). Electrochemical behavior of copper in alkaline-sulfide solutions. *Corrosion, 62*(2), 121-128. https://doi.org/10.5006/1.3278257

Salta, M., Chambers, L., Wharton, J., Wood, R., Briand, J., Blache, Y., & Stokes, K. Marine fouling organisms and their use in antifouling bioassays. Paper presented at the *EuroCorr,* Southampton.

Samie, F., Tidblad, J., Kucera, V., & Leygraf, C. (2007). Atmospheric corrosion effects of HNO3- : Influence of temperature and relative humidity on laboratory-exposed copper. *Atmospheric Environment (1994), 41*(7), 1374-1382. https://doi.org/10.1016/j.atmosenv.2006.10.018

Santhakumaran, L. (1988). Biodeterioration of wooden boats - a major problem facing marine fisheries. *Journal of the Indian Fisheries Association. Bombay, 18*, 275-282.

Sato, N. (1971). A theory for breakdown of anodic oxide films on metals. *Electrochimica Acta, 16*(10), 1683-1692. https://doi.org/10.1016/0013-4686(71)85079-X

Sato, N. (1982). Anodic breakdown of passive films on metals. *Journal of the Electrochemical Society, 129*(2), 255. https://doi.org/10.1149/1.2123808

Sawant, S. S., Venkat, K., & Wagh, A. B. (1993). Corrosion of metals and alloys in the coastal and deep waters of the Arabian sea and the Bay of Bengal. Indian Journal of Technology, 31(12), 862-866.

Schatzberg, P. (1996). 19. measurement and significance of the release rate for tributyltin 19.5 role of the biofilm. In M. A. Champ, & P. F. Seligman (Eds.), *Organotin: Environmental fate and effects* (First Edition ed., pp. 397-398). London: Chapman & Hall.

Schleich, W. Typical failures of CuNi 90/10 seawater tubing systems and how to avoid them. Paper presented at the *Eurocorr,* Nice. Retrieved February 19, (2016) from https://www.copper.org/applications/marine/cuni/pdf/124_schleich.pdf

scholar.google.com. (2020). Search for MEDUSA and Pourbaix. Retrieved February 18, (2020) from https://scholar.google.com/scholar?hl=en&as_sdt=0%2C5&q=medusa+pourbaix&btnG=

Schultz, M. P. (2004). Frictional resistance of antifouling coating systems. *Journal of Fluids Engineering (Transactions of the ASME), 126*(6), 1039-1047. https://doi.org/10.1115/1.1845552

Schultz, M. P. (2007). Effects of coating roughness and biofouling on ship resistance and powering. *Biofouling, 23*(5), 331-341. https://doi.org/10.1080/08927010701461974

Schultz, M. P., Bendick, J. A., Holm, E. R., & Hertel, W. M. (2011). Economic impact of biofouling on a naval surface ship. *Biofouling, 27*(1), 87-98. https://doi.org/10.1080/08927014.2010.542809

Schultz, M. P., & Swain, G. W. (2000). The influence of biofilms on skin friction drag. *Biofouling, 15*(1-3), 129-139. https://doi.org/10.1080/08927010009386304

Schultz, M. P. (2000). Turbulent boundary layers on surfaces covered with filamentous algae. *Journal of Fluids Engineering, 122*(2), 357. https://doi.org/10.1115/1.483265

Schumacher, M. (Ed.). (1979). *Seawater corrosion handbook*. New Jersey: Noyes Data Corporation.

Scott, D. A. (2000). A review of copper chlorides and related salts in bronze corrosion and as painting pigments. *Studies in Conservation, 45*(1), 39-53. https://doi.org/10.2307/1506682

Sharkey, J. B., & Lewin, S. Z. (1971). Conditions governing the formation of atacamite and paratacamite. *The American Mineralogist, 56*, 179-192.

Shen, X., Ho, C. M., & Wong, T. S. (2010). Minimal size of coffee ring structure. *The Journal of Physical Chemistry.B, 114*(16), 5269-5274. https://doi.org/10.1021/jp912190v

[376]

Shifler, D. A. (2005). Understanding material interactions in marine environments to promote extended structural life. *Corrosion Science, 47*, 2335-2352. https://doi.org/10.1016/j.corsci.2004.09.027

Shreir, L. L., Jarman, R. A., & Burstein, G. T. (1994a). *Corrosion / vol.1, metal/environment reactions* (3rd ed.) Butterworth-Heinemann.

Shreir, L. L., Jarman, R. A., & Burstein, G. T. (1994b). Corrosion / vol.2, corrosion control (3rd ed.) Butterworth-Heinemann.

Sieradzke, K., & Kim, J. S. (1992). Etch pitting and stress-corrosion cracking of copper. *Acta Metallurgica Et Materialia, 40*(4), 625-635. https://doi.org/10.1016/0956-7151(92)90003-W

Smallman, R. E., & Ngan, A. H. W. (2014). In Smallman R. E., Ngan A. H. W.(Eds.), *Chapter 5 - characterization and analysis*. Oxford: Butterworth-Heinemann. https://doi.org/10.1016/B978-0-08-098204-5.00005-5

Smith, H., G.F. (1906). Paratacamite, a new oxychloride of copper. *Mineralogical Magazine and Journal of the Mineralogical Society, 14*(65), 170-177. https://doi.org/10.1180/minmag.1906.014.65.09

Soltis, J. (2015). Passivity breakdown, pit initiation and propagation of pits in metallic materials – review. *Corrosion Science, 90*, 5-22. https://doi.org/10.1016/j.corsci.2014.10.006

Solve, C., & Anders, L. S. (1956). In Bolidens Gruvaktiebolag (Ed.), *Annealing properties of copper* (US2897107A ed.). United States: C22F1/08.

Speckmann, H. -, Lohrengel, M. M., Schultze, J. W., & Strehblow, H. -. (1985). The growth and reduction of duplex oxide films on copper. *Berichte Der Bunsengesellschaft Für Physikalische Chemie, 89*(4), 392-402. https://doi.org/10.1002/bbpc.19850890408

Starosvetsky, D., Khaselev, O., Auinat, M., & Ein-Eli, Y. (2006). Initiation of copper dissolution in sodium chloride electrolytes. *Electrochimica Acta, 51*(26), 5660-5668. https://doi.org/10.1016/j.electacta.2006.01.058

Stoch, A., Stoch, J., Gurbiel, J., Cichocinska, M., Mikolajaczyk, M., & Timler, M. (2001). FTIR study of copper patinas in the urban atmosphere. *Journal of Molecular Structure, ,* 201-206. https://doi.org/10.1016/S0022-2860(01)00718-9

Stull, D. R., & Prophet, H. (1971). *JANAF thermochemical tables* (2nd ed.) NSRDS.

Strandberg, H. (1998a). Reactions of copper patina compounds - II. influence of sodium chloride in the presence of some air pollutants. *Atmospheric Environment, 32*(20), 3521-3526. https://doi.org/10.1016/S1352-2310(98)00058-2

Strandberg, H. (1998b). Reactions of copper patina compounds—I. influence of some air pollutants. *Atmospheric Environment, 32*(20), 3511-3520. https://doi.org/10.1016/S1352-2310(98)00057-0

Strandberg, H., & Johansson, L. G. (1998). Some aspects of the atmospheric corrosion of copper in the presence of sodium chloride. *Journal of Electrochemical Society, 145*(4), 1093-1100. https://doi.org/10.1149/1.1838422

Strehblow, H., & Titze, B. (1980). The investigation of the passive behaviour of copper in weakly acid and alkaline solutions and the examination of the passive film by esca and ISS. *Electrochimica Acta, 25*(6), 839-850. https://doi.org/10.1016/0013-4686(80)90036-5

Strehblow, H., Maurice, V., & Marcus, P. (2001). Initial and later stages of anodic oxide formation on cu, chemical aspects, structure and electronic properties. *Electrochimica Acta, 46*, 3755-3766. https://doi.org/10.1016/S0013-4686(01)00657-0

Strehblow, H. (2016). Passivity of metals studied by surface analytical methods, a review. *Electrochimica Acta, 212*, 630-648. https://doi.org/10.1016/j.electacta.2016.06.170

Streicher, M. A. (1956). Pitting corrosion of 18Cr-8Ni stainless steel. *Journal of the Electrochemical Society, 103*(7), 375. https://doi.org/10.1149/1.2430359

Suwas, S., & Gurao, N. P. (2014). In Hashmi S., Batalha G. F., Van Tyne C. J., and Yilbas B.(Eds.), *3.05 - development of microstructures and textures by cross rolling*. Oxford: Elsevier. https://doi.org/10.1016/B978-0-08-096532-1.00308-3

Swain, G., Farrar, R., & Hutton, S. (1982). The use of controlled copper dissolution as an anti-fouling system. *Journal of Materials Science, 17*(4), 1079-1094. https://doi.org/10.1007/BF00543527

Szklarska-Smialowska, Z., & Janik-Czachor, M. (1967). *Pitting corrosion of 13Cr-fe alloy in Na2SO4 solutions containing chloride ions*. Oxford] : Pergamon Press. https://doi.org/10.1016/S0010-938X(67)80103-3

Taylan, M. (2010) An overview: Effect of roughness and coatings on ship resistance. Paper presented at the *International Conference on Ship Drag Reduction, SMOOTH-SHIPS,* Istanbul.

Taylor, C. D., Li, S., & Samin, A. J. (2018). *Oxidation versus salt-film formation: Competitive adsorption on a series of metals from first-principles* Elsevier Ltd. https://doi.org/10.1016/j.electacta.2018.02.150

Taylor, G. T., Zheng, D., Lee, M., Troy, P. J., Gyananath, G., & Sharma, S. K. (1997). Influence of surface properties on accumulation of conditioning films and marine bacteria on substrata exposed to oligotrophic waters. *Biofouling, 11*(1), 31-57. https://doi.org/10.1080/08927019709378319

The British Standards Institution. (2012). BS EN ISO 9223:2012: Corrosion of metals and alloys. corrosivity of atmospheres. classification, determination and estimation.

The Editors of Encyclopaedia Britannica. (2016). Bragg law. Retrieved June 9, (2017) from https://www.britannica.com/science/Bragg-law

The International Union of Crystallography. (2004). In Prince. E. (Ed.), *International tables for crystallography, vol. C, mathematical, physical and chemical tables* (Third ed.). Dordrecht/Boston/London: Kluwer Academic Publishers.

Thomas, J. G. N., & Tiller, A. K. (1972). Formation and breakdown of surface films on copper in sodium hydrogen carbonate and sodium chloride solutions: II. effects of temperature and pH. *British Corrosion Journal, 7*(6), 263-267. https://doi.org/10.1179/000705972798322702

Thomas, J., Tiller, A., & Thomas, J. (1972). Formation and breakdown of surface films on cu in NaHCO3 and NaCl solutions. pt. 1. effects of anion concentrations. *Brit. Corrosion J, 7*(6), 256-262. https://doi.org/10.1179/000705972798322784

Thome, I., Pettitt, M. E., Callow, M. E., Callow, J. A., Grunze, M., & Rosenhahn, A. (2012). Conditioning of surfaces by macromolecules and its implication for the settlement of zoospores of the green alga ulva linza. *Biofouling, 28*(5), 501-510. https://doi.org/10.1080/08927014.2012.689288

Thompson, N. G., & Payer, J. H. (1998). *DC electrochemical test methods*. Houston, Tex: NACE International.

Titus, D., James Jebaseelan Samuel, E., & Roopan, S. M. (2019). Chapter 12 - nanoparticle characterization techniques. In A. K. Shukla, & S. Iravani (Eds.), *Green synthesis, characterization and applications of nanoparticles* (pp. 303-319) Elsevier. https://doi.org/ https://doi.org/10.1016/B978-0-08-102579-6.00012-5 Retrieved March 20, 2020 from https://www.sciencedirect.com/science/article/pii/B9780081025796000125

Toshev, Y., Mandova, V., Boshkov, N., Stoychev, D., Petrov, P., Tsvetkova, N., Kostadinov, K. (2006). *Protective coating of zinc and zinc alloys for industrial applications* Elsevier Ltd. https://doi.org/10.1016/B978-008045263-0/50073-8

Townsin, R. (2003). The ship hull fouling penalty. *Biofouling, 19*, 9-15.

Townsin, R. L., & Anderson, C. D. (2009). *Fouling control coatings using low surface energy, foul release technology-26* https://doi.org/10.1533/9781845696313.4.693

Tromans, D., & Silva, J. (1997). Anodic behavior of copper in chloride/tolytriazole and chloride/benzotriazole solutions. *Corrosion, 53*(1), 16. https://doi.org/10.5006/1.3280429

Tupper, E. C. (2013). Chapter 7 - resistance. In Eric C. Tupper (Ed.), *Introduction to naval architecture (fifth edition)* (Fifth Edition ed., pp. 131). Oxford: Butterworth-Heinemann. https://doi.org/10.1016/B978-0-08-098237-3.00007-2

U.S. Geological Survey. (2018). Dotables. Retrieved April 16, (2019) from https://water.usgs.gov/cgi-bin/dotables

Ulusoy, U. (2019). Quantifying of particle shape differences of differently milled barite using a novel technique: Dynamic image analysis. Materialia, 8, 100434. https://doi.org/10.1016/j.mtla.2019.100434

Van Mulylder, J., de Zoubov, N., & Pourbaix, M. (1962). *Diagrammes d'équilibres tension-pH des systèmes cu-H2O et cu-cl-H2O à 25°C [diagrammes d'équilibres, cu, cu et cl].* (Technical No. 101). Centre Belge D'etude de la Corrosion: CEBELCOR. Retrieved August 2, (2014) from https://drive.google.com/file/d/1XoezLMX6ZAtI2tdIyHjyNC4uTlLqLsyN/view

Van Santen, R. A. (1984). The ostwald step rule. *The Journal of Physical Chemistry, 88*(24), 5768-5769. https://doi.org/10.1021/j150668a002

Veleva, L., & Farro, W. (2012). Influence of seawater and its aerosols on copper patina composition. *Applied Surface Science, 258*(24), 10072-10076. https://doi.org/10.1016/j.apsusc.2012.06.077

Veleva, L., Quintana, P., Pomes, R., & Maldonado, L. (1996). Mechanism of copper patina formation in marine environments. *Electrochemica Acta, 41*(10), 1641-1646. https://doi.org/10.1016/0013-4686(95)00417-3

Venkatraman, M. S., Cole, I. S., & Emmanuel, B. (2011). Model for corrosion of metals covered with thin electrolyte layers: Pseudo-steady state diffusion of oxygen. *Electrochimica Acta, 56*(20), 7171-7179. https://doi.org/10.1016/j.electacta.2011.05.009

Verhoeven, J. D. (1986). Scanning electron microscopy. In R. E. Whan (Ed.), *Materials characterization* (pp. 0) ASM International. https://doi.org/10.31399/asm.hb.v10.a0001767

Videm, K., & Institutt, F. A. (1974). The electrochemistry of uniform corrosion and pitting of aluminum. *Kjeller, Norway: Institutt for Atomenergi.*

Von Oertzen, J. A., Scharf, E. M., Arndt, E. A., Sandrock, S., Dettmann, L., Holzapfel, H., Gunther, R. (1989). Spezialstudie 'alternative antifouling systeme'. *Fachbereich Biologie, Universitat Rostock.*

Vrsalović, L., Gudić, S., Gracić, D., Smoljko, I., Ivanić, I., Kliškić, M., & Oguzie, E. E. (2018). Corrosion protection of copper in sodium chloride solution using propolis. *International Journal of Electrochemical Science, 13*, 2011-2117. https://doi.org/10.20964/2018.02.71

Vrsalović, L., Gudić‡, S., Kliškić, M., Oguzie, E., & Carev, L. (2016). *Inhibition of copper corrosion in NaCl solution by caffeic acid.* Int. J. Electrochem. Sci. 11. 459-474.

Vrsalović, L., Ivanić, I., Čudina, D., Lokas, L., kožuh, S., & Gojić, M. (2017). The influence of chloride ion concentration on the corrosion behavior of the CuAlNi alloy. *Tehnički Glasnik – Technical Journal, 11*, 67-72.

Wahl, M. (1989). Marine epibiosis. I. fouling and antifouling: Some basic aspects. *Marine Ecology Progress Series, 58*, 175-189. https://doi.org/10.3354/meps058175

Walmsley, S. (2006). *Tributyltin pollution on a global scale. An overview of relevant and recent research: Impacts and issues.* (Review No. FND053998). Godalming: World Wildlife Fund. Retrieved December 8, (2016) from http://assets.wwf.no/downloads/tbt_global_review_wwf_uk_oct_2006.pdf

Walt, D. R., Smulow, J. B., Turesky, S. S., & Hill, R. G. (1985). The effect of gravity on initial microbial adhesion. *Journal of Colloid and Interface Science, 107*(2), 334-336. https://doi.org/10.1016/0021-9797(85)90185-7

Walter-Levy, L., & Goreaud, M. (1969). Sur la formation des chlorures basiques cuivriques en solution aqueuse de 25 a 200°C. *Bulletin De La Société Chimique De France, 8*, 2623-2634.

Wan, Y., Wang, X., Sun, H., Li, Y., Zhang, K., & Wu, Y. (2012). Corrosion behavior of copper at elevated temperature. *International Journal of Electrochemical Science, 7*(9), 7902-7914.

Wang, D., Xiang, B., Liang, Y., Song, S., & Liu, C. (2014). Corrosion control of copper in 3.5wt.% NaCl solution by domperidone: Experimental and theoretical study. *Corrosion Science, 85*, 77-86. https://doi.org/10.1016/j.corsci.2014.04.002

Wang, W., Varghese, O. K., Ruan, C., Paulose, M., & Grimes, C. A. (2003). Synthesis of CuO and Cu2O crystalline nanowires using cu(OH)2 nanowire templates. *Journal of Materials Research, 18*(12), 2756-2759. https://doi.org/10.1557/JMR.2003.0384

Wang, X., Olsen, S., Andres Martinez, E., Olsen, K., & Kiil, S. (2018). Drag resistance of ship hulls: Effects of surface roughness of newly applied fouling control coatings, coating water absorption, and welding seams. *Journal of Coatings Technology and Research, 15*(4), 657-669. https://doi.org/10.1007/s11998-018-0054-7

Watanabe, M., Toyoda, E., Handa, T., Ichino, T., Kuwaki, N., Higashi, Y., & Tanaka, T. (2007). Evolution of patinas on copper exposed in a suburban area. *Corrosion Science, 49*(2), 766-780. https://doi.org/10.1016/j.corsci.2006.05.044

Watanabe, S., Nagamatsu, N., Yokoo, K., & Kawakami, Y. (1969). Augmentation in frictional resistance due to slime. *J. Kansai Society of Naval Architects, 131*, 45-51.

Webmineral. (2012a). Cuprite mineral data. Retrieved June 9, (2019) from http://webmineral.com/data/Cuprite.shtml

Webmineral. (2012b). Tenorite mineral data. Retrieved June 9, (2019) from http://webmineral.com/data/Tenorite.shtml

Webster, D. C., & Chisholm, B. J. (2010). New directions in antifouling technology. In S. Durr, & T. C. Thomason (Eds.), *Biofouling* (1st ed., pp. 366-387) Blackwell Publishing.

Wen, X., Xie, Y., Choi, C. L., Wan, K. C., Li, X., & Yang, S. (2005). Copper-based nanowire materials: Templated syntheses, characterizations, and applications. *Langmuir, 21*(10), 4729-4737. https://doi.org/10.1021/la050038v

Widodo, C. S., Sela, H., & Santosa, D. R. (2018). The effect of NaCl concentration on the ionic NaCl solutions electrical impedance value using electrochemical impedance spectroscopy methods. *AIP Conference Proceedings, 2021*(1), 050003. https://doi.org/10.1063/1.5062753

Wiener, M. S., Salas, B. V., Quintero- Nuñez, M., & Zlatev, R. (2010). Effect of H2S on corrosion in polluted waters. *Advanced Materials Research, 95*, 33-36. https://doi.org/10.4028/www.scientific.net/AMR.95.33

[381]

Williams D.B., Carter C. B. (1996). Electron sources. *Transmission electron microscopy* (pp. 67-83). Boston, MA: Springer, Boston, MA. https://doi.org/ https://doi.org/10.1007/978-1-4757-2519-3_5

Woods Hole Oceanographic Institute. (1952a). Chapter 11: The history of the prevention of fouling. *Marine fouling and its prevention* (pp. 211-223). Annapolis: George Banta Publishing.

Woods Hole Oceanographic Institute. (1952b). Chapter 12: The invention of protective devices. *Marine fouling and its prevention* (pp. 224-229). Annapolis: George Banta Publishing.

Woods Hole Oceanographic Institute. (1952c). CHAPTER 2: Ship resistance. *Marine fouling and its prevention* (pp. 21-34). Annapolis: George Banta Publishing.

Woody, C. A., & O'Neal, S. L. (2012). *Effects of copper on fish and aquatic resources.* (Review). Alaska: The Nature Conservancy. Retrieved July 27, 2017 from https://www.conservationgateway.org/ConservationByGeography/NorthAmerica/UnitedStates/alaska/sw/cpa/Documents/W2013ECopperF062012.pdf

Wu, G., & Singh, P. (2019). Effect of plastic deformation on pitting mechanism of SS304. *Metallurgical and Materials Transactions A, 50*(10), 4750-4757. https://doi.org/10.1007/s11661-019-05394-8

Xiong, L., Huang, S., Yang, X., Qiu, M., Chen, Z., & Yu, Y. (2011). *P-type and n-type Cu2O semiconductor thin films: Controllable preparation by simple solvothermal method and photoelectrochemical properties* https://doi.org/10.1016/j.electacta.2010.12.054

Xu, Y. (1993). On electric field induced breakdown of passive films and the mechanism of pitting corrosion. *Journal of the Electrochemical Society, 140*(12), 3448. https://doi.org/10.1149/1.2221108

Yamashita, M., Omura, K., & Hirayama, D. (1980). Passivating behavior of copper anodes and its illumination effects in alkaline solutions. *Surface Science, 96*(1), 443-460. https://doi.org/10.1016/0039-6028(80)90319-2

Yan, C., Yuan, B., Li, Z., Li, L., & Wang, C. (2020). Digital holographic study of pH effects on anodic dissolution of copper in aqueous chloride electrolytes. *Metals (Basel), 10*(4), 487. https://doi.org/10.3390/met10040487

Yan, X., & Sun, J. (2017). Effect of water hardness and pH value on the corrosion behaviour of copper in an emulsion. *International Journal of Electrochemical Science, 12*, 11580-11593. https://doi.org/10.20964/2017.12.43

Yebra, D. M., Kiil, S., & Dam-Johansen, K. (2004). Antifouling technology—past, present and future steps towards efficient and environmentally friendly antifouling coatings. *Progress in Organic Coatings*, 75-104. https://doi.org/10.1016/j.porgcoat.2003.06.001

Yeginbayeva, I. A., & Atlar, M. (2018). An experimental investigation into the surface and hydrodynamic characteristics of marine coatings with mimicked hull roughness ranges. *Biofouling, 34*(9), 1001-1019. https://doi.org/10.1080/08927014.2018.1529760

Yin, S., & Li, D. Y. (2005). Effects of prior cold work on corrosion and corrosive wear of copper in HNO 3 and NaCl solutions. *Materials Science & Engineering A, 394*(1), 266-276. https://doi.org/10.1016/j.msea.2004.11.054

Yoder, C. H., Schaeffer, R. W., McWilliams, P., Rowand, A., Liu, X., & Shambeda, J. (2011). The synthesis of copper/zinc solid solutions of hydroxyl carbonates, sulphates, nitrates, chlorides and bromides. *Mineralogical Magazine, 75*(5), 2573-2582. https://doi.org/10.1180/minmag.2011.075.5.2573

Ytreberg, E., Bighiu, M. A., Lundgren, L., & Eklund, B. (2016). XRF measurements of tin, copper and zinc in antifouling paints coated on leisure boats. *Environmental Pollution (1987); Environ Pollut, 213*, 594-599. https://doi.org/10.1016/j.envpol.2016.03.029

Zhang, D., Zhang, H., LIN, G. U. O., Zheng, K., Han, X., & Zhang, Z. (2009). Delicate control of crystallographic facet-oriented Cu_2O nanocrystals and the correlated adsorption ability. *Journal of Materials Chemistry, 19*(29), 5220-5225. https://doi.org/10.1039/b816349a

Zhang, R., Cao, S. A., & Pan, H. (2018). Evaluation of hollow copper strands corrosion behavior in stator cooling water using response surface methodology. *Materials and Corrosion, 69*(6), 804-813. https://doi.org/10.1002/maco.201709770

Zhang, X. L., Jiang, Z. H., Yao, Z. P., Song, Y., & Wu, Z. D. (2009). Effects of scan rate on the potentiodynamic polarization curve obtained to determine the Tafel slopes and corrosion current density. *Corrosion Science, 51*(3), 581-587. https://doi.org/10.1016/j.corsci.2008.12.005

Zhang, X., Odnevall Wallinder, I., & Leygraf, C. (2014a). Mechanistic studies of corrosion product flaking on copper and copper-based alloys in marine environments. *Corrosion Science, 85*, 15-25. https://doi.org/10.1016/j.corsci.2014.03.028

Zhang, X., Odnevall Wallinder, I., & Leygraf, C. (2014b). Mechanistic studies of corrosion product flaking on copper and copper-based alloys in marine environments. *Corrosion Science, 85*, 15-25. https://doi.org/10.1016/j.corsci.2014.03.028

Zhang, X., Zhou, X., Hashimoto, T., & Liu, B. (2017). Localized corrosion in AA2024-T351 aluminium alloy: Transition from intergranular corrosion to crystallographic pitting. *Materials Characterization, 130*, 230-236. https://doi.org/10.1016/j.matchar.2017.06.022

Zhang, Y., Chen, X., Liu, F., Li, L., Dai, J., & Liu, T. (2018). Enhanced coffee-ring effect via substrate roughness in evaporation of colloidal droplets. *Advances in Condensed Matter Physics, 2018*, 9795654. https://doi.org/10.1155/2018/9795654

Zhao, H., Chang, J., Boika, A., & Bard, A. J. (2013). Electrochemistry of high concentration copper chloride complexes. *Analytical Chemistry, 85*(16), 7696. https://doi.org/10.1021/ac4016769

Zhao, L., Xia, Z., & Wang, F. (2014). Zebrafish in the sea of mineral (iron, zinc and copper) metabolism. *Frontiers in Pharmacology, 5* https://doi.org/10.3389/fphar.2014.00033

Zhou, G., & Yang, J. C. (2004). Temperature effects on the growth of oxide islands on cu(110). *Applied Surface Science, 222*(1), 357-364. https://doi.org/10.1016/j.apsusc.2003.09.008

[383]

Zhou, G., Shao, H., & Loo, B. H. (1997). A study of the copper electrode behavior in borax buffer solutions containing chloride ions and benzotriazole-type inhibitors by voltammetry and the photocurrent response method. *Journal of Electroanalytical Chemistry, 421*(1), 129-135. https://https://doi.org/10.1016/S0022-0728(96)04838-3

Zittlau, A. H., Shi, Q., Boerio-Goates, J., Woodfield, B. F., & Majzlan, J. (2013). Thermodynamics of the basic copper sulfates antlerite, posnjakite, and brochantite. *Geochemistry, 73*(1), 39-50. https://doi.org/10.1016/j.chemer.2012.12.002

Zweng, M. M., Reagan, J. R., Antonov, J. I., Locarnini, R. A., Mishonov, A. V., Boyer, T. P., Biddle, M. M. (2013). Volume 2: Salinity. *World ocean atlas 2013* (74th ed., pp. 39) NOAA Atlas NESDIS.

Appendix 1 – Paint Flake Analysis
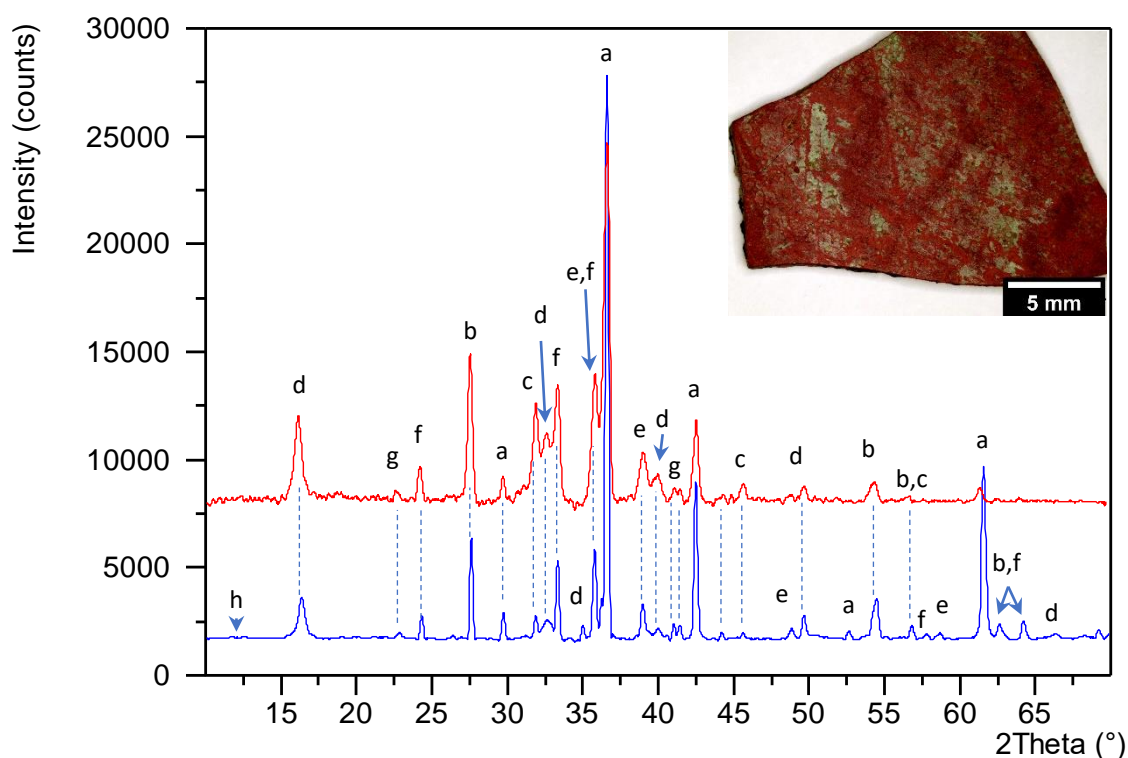
Figure 134 – XRD analysis of the Paint Flake 2, shown above, removed from YK Sovereign. The blue and red lines represent the glancing angle and gonio XRD techniques. Peaks labelled a = cuprite, b = rutile, c = Sodium chloride, d = clinoatacamite, e = Tenorite, f = hematite and g = brochantite.
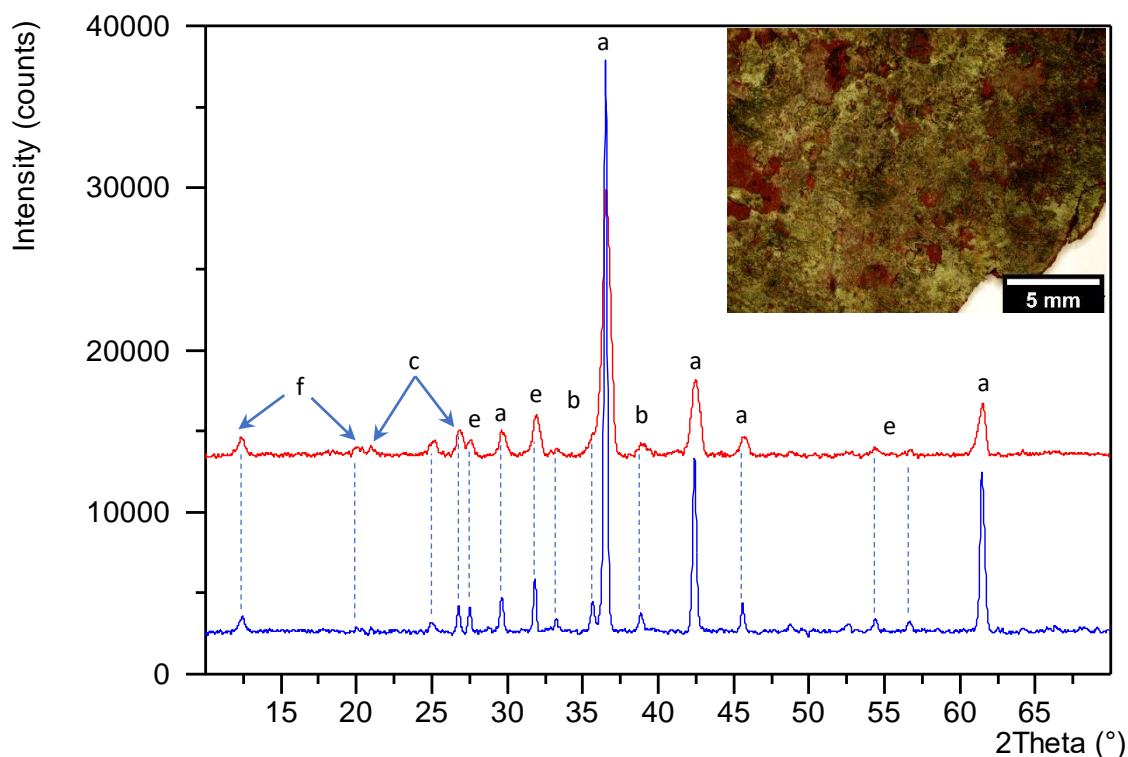
Figure 135 – XRD analysis of the Paint Flake 3, shown above, removed from Leonis. The blue and red lines represent the glancing angle and gonio XRD techniques, respectively. Peaks labelled a = cuprite, b = tenorite, c = silicon dioxide, d = nantokite, e = sodium chloride and f = copper pyrithione.
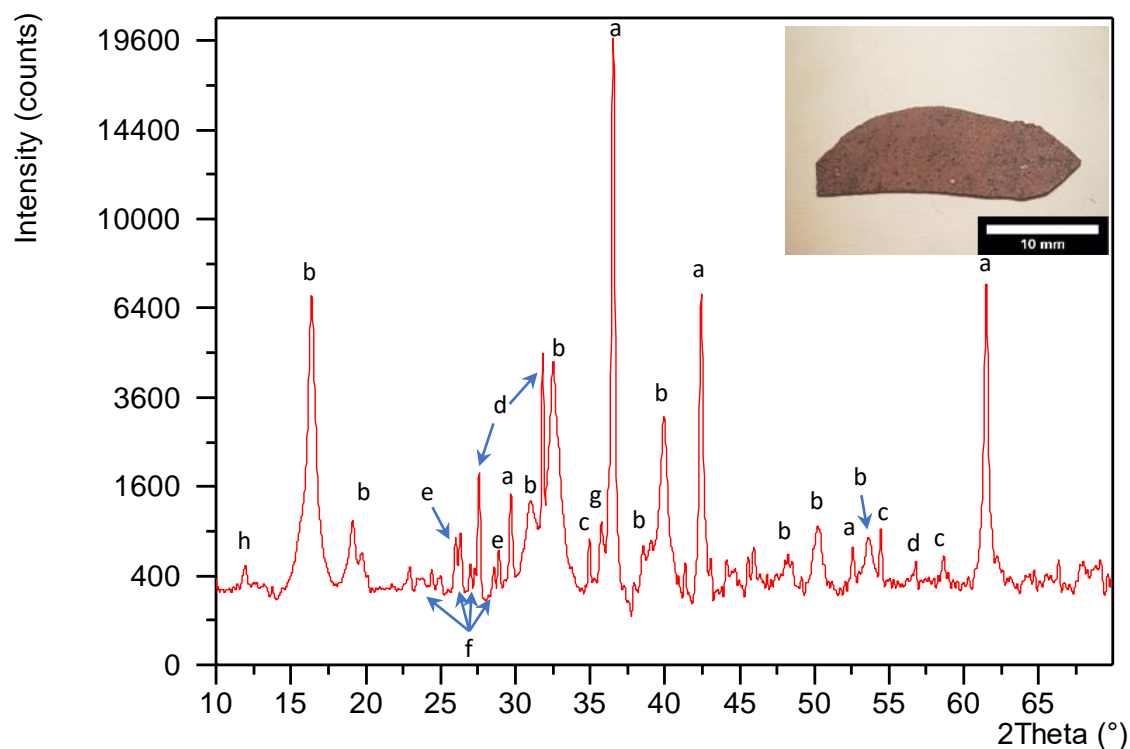
Figure 136 – Gonio XRD analysis of the Paint Flake 4, shown above, removed from MSC Tasmania. Peaks labelled a = cuprite, b = clinoatacamite, c = copper (I) chloride, d = sodium chloride, e = silicon dioxide, f = copper sulphide, g = tenorite and h = zinc pyrithione.
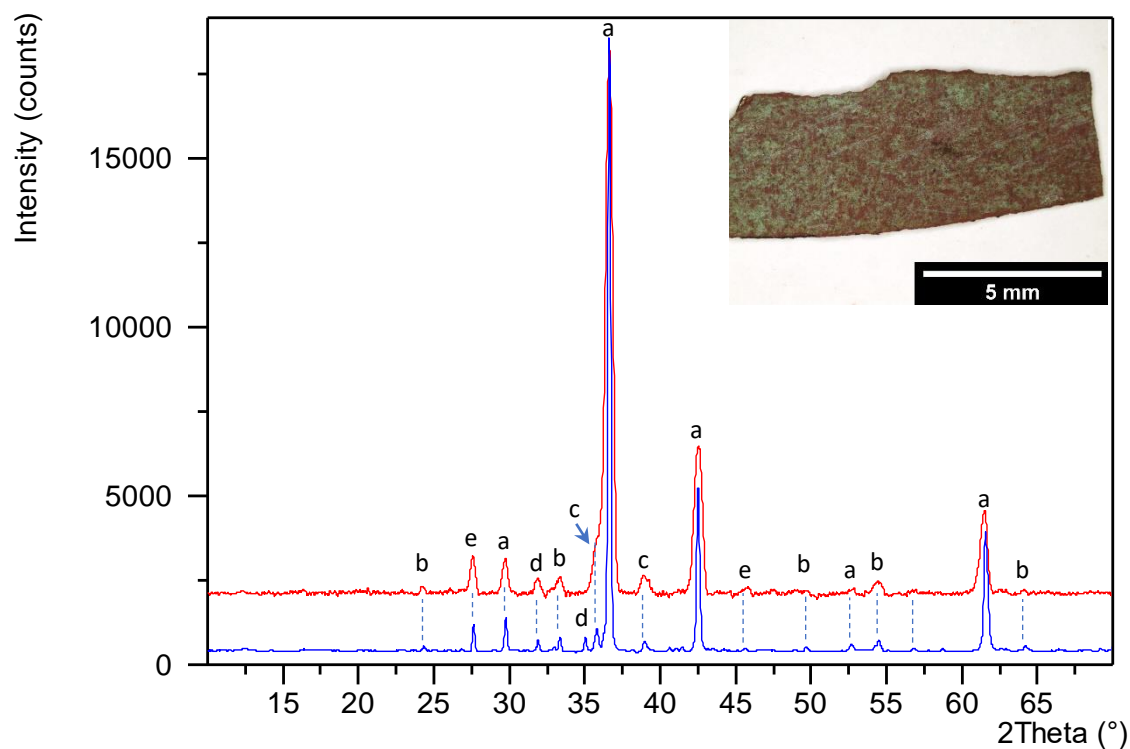
Figure 137 – XRD analysis of the Paint Flake 5, shown above, removed from Champion Pride. The blue and red lines represent the glancing angle and gonio XRD techniques, respectively. Peaks labelled a = cuprite, b = hematite, c = tenorite, d = copper chloride and e = sodium chloride.

[386]
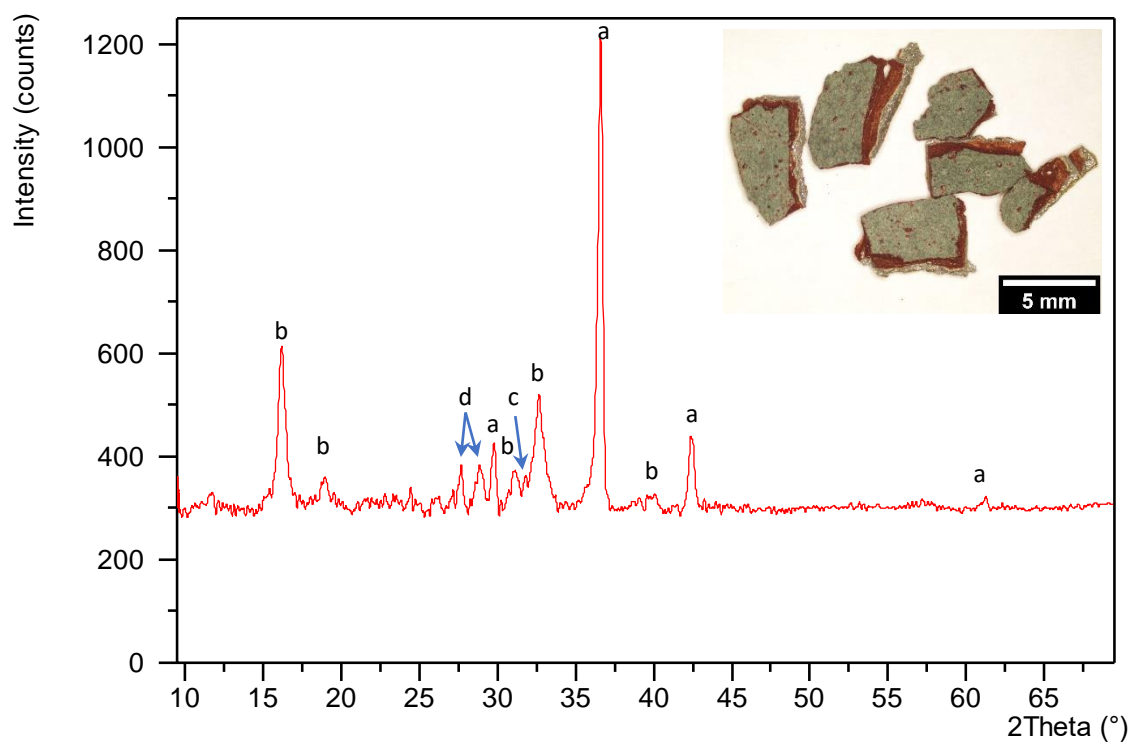
Figure 138 – Glancing angle XRD analysis of the Paint Flake 6, shown above, removed from BR Cormorant. Peaks labelled a = cuprite, b = clinoatacamite, c = copper chloride and d = copper sulphide.
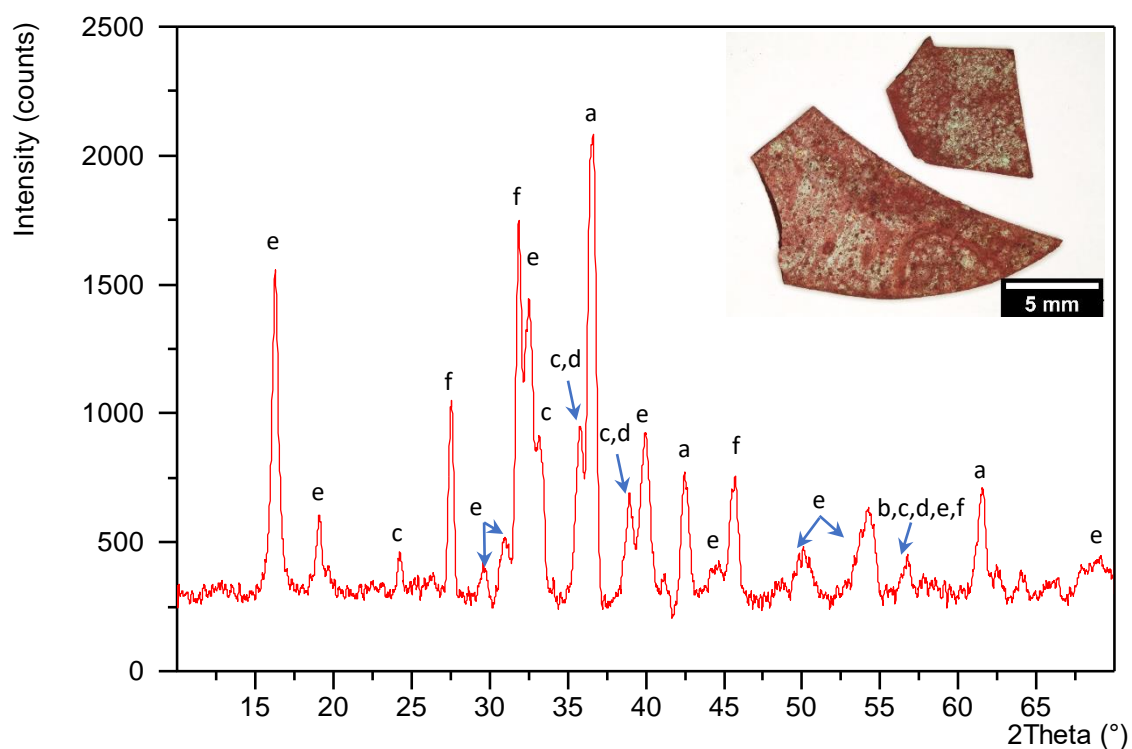
Figure 139 – Glancing angle XRD analysis of the Paint Flake 7, shown above, removed from British Integrity. Peaks labelled a = cuprite, b = titanium dioxide, c = haematite, d = tenorite, e = clinoatacamite and f = sodium chloride.

[387]
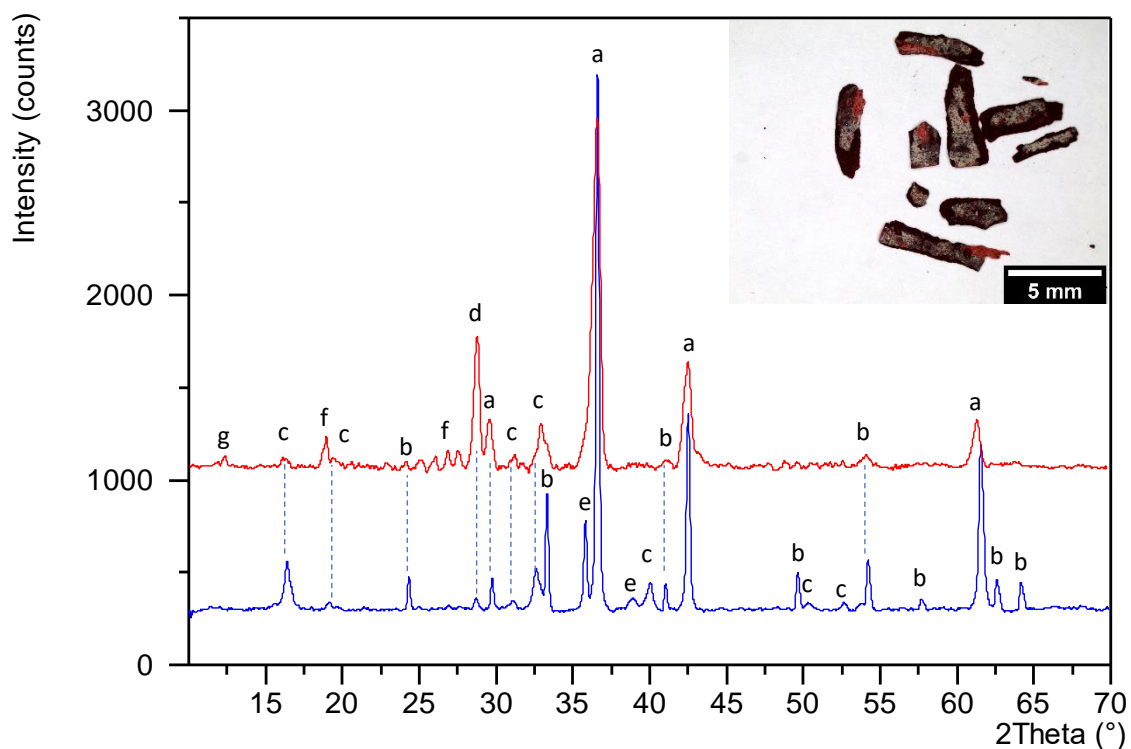
Figure 140 – XRD analysis of the Paint Flake 8, shown above, removed from Sonagol. The blue and red lines represent the glancing angle and gonio XRD techniques, respectively. Peaks labelled a = cuprite, b = hematite, c = clinoatacamite, d = silicon dioxide, e = tenorite, f = copper sulphate hydrate and g = copper pyrithione.
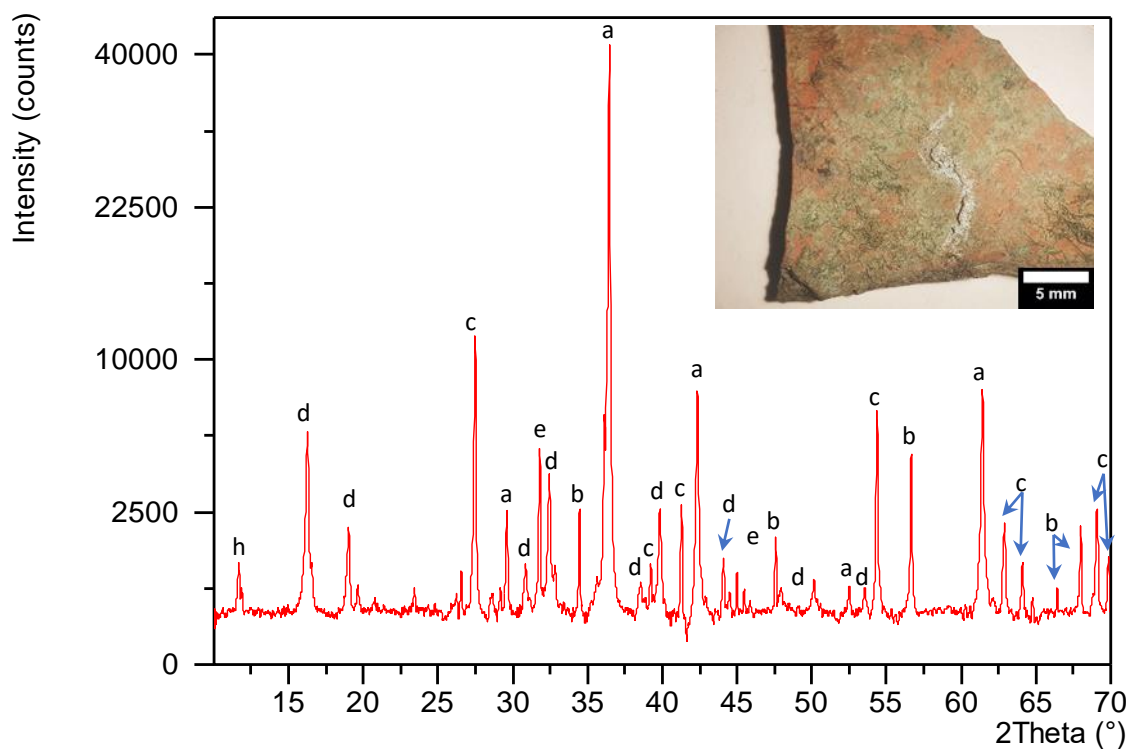
Figure 141 – Gonio XRD analysis of the Paint Flake 9, shown above, removed from Old patinated panel. Peaks labelled a = cuprite, b = zinc oxide, c = titanium dioxide, d = clinoatacamite, e = sodium chloride, f = silicon dioxide and g = copper pyrithione.
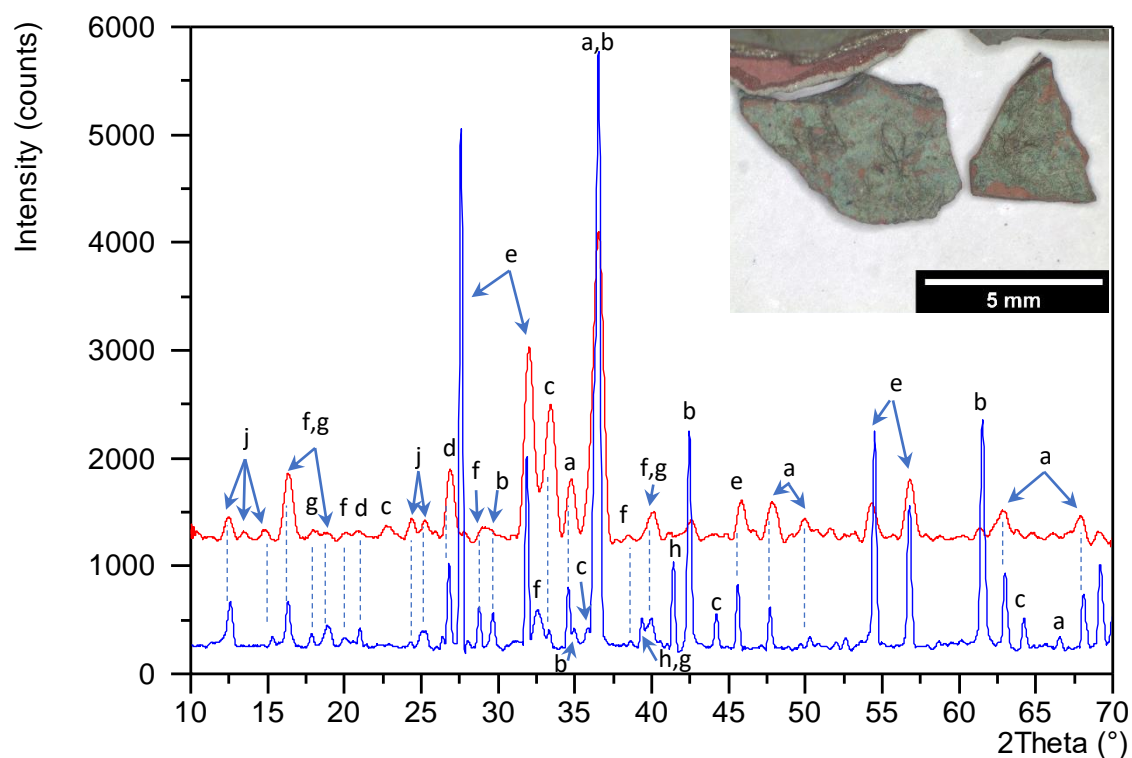
Figure 142 – XRD analysis of the Paint Flake 10, shown above, removed from Orpheus Orchid. The blue and red lines represent the glancing angle and gonio XRD techniques, respectively. Peaks labelled a = cuprite, b = zinc oxide, c = haematite, d = quartz, e = sodium chloride, f = clinoatacamite, g = atacamite h =titanium dioxide, i= copper pyrithione and j zinc pyrithione.
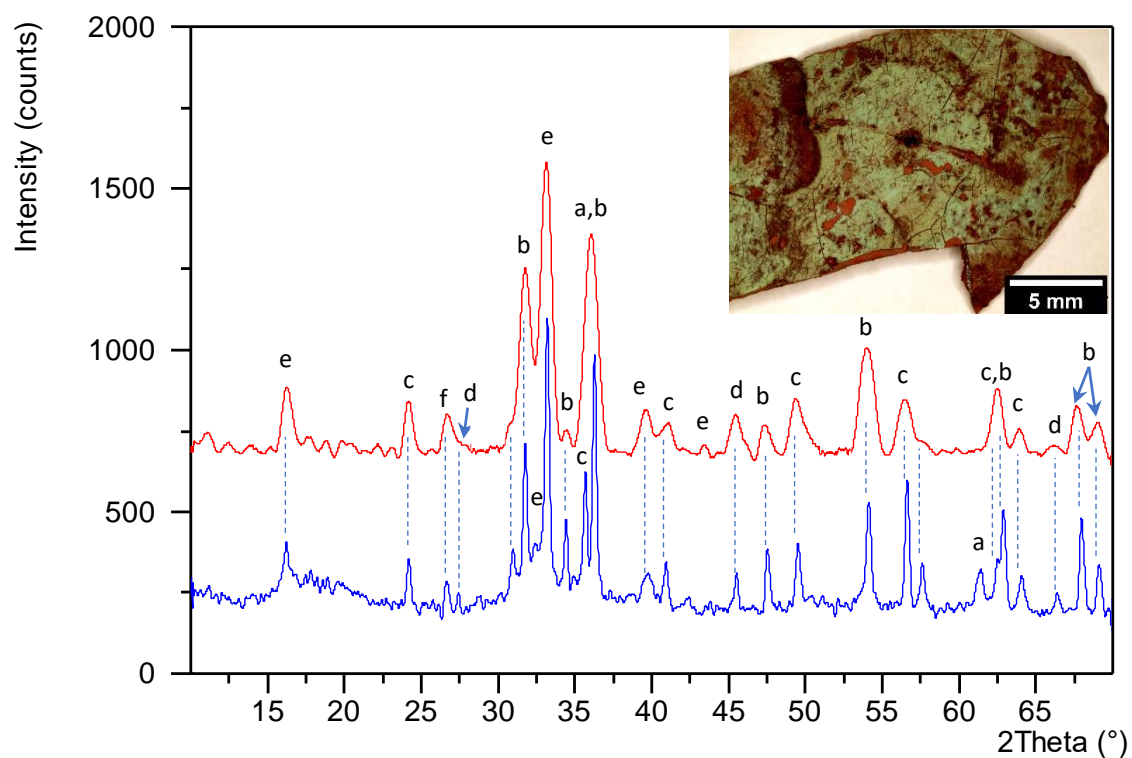
Figure 143 – XRD analysis of the Paint Flake 11, shown above, removed from Sitamarie. The blue and red lines represent the glancing angle and gonio XRD techniques, respectively. Peaks labelled a = cuprite, b = zinc oxide, c = hematite, d = sodium chloride, e = clinoatacamite and f = silicon dioxide.

[389]
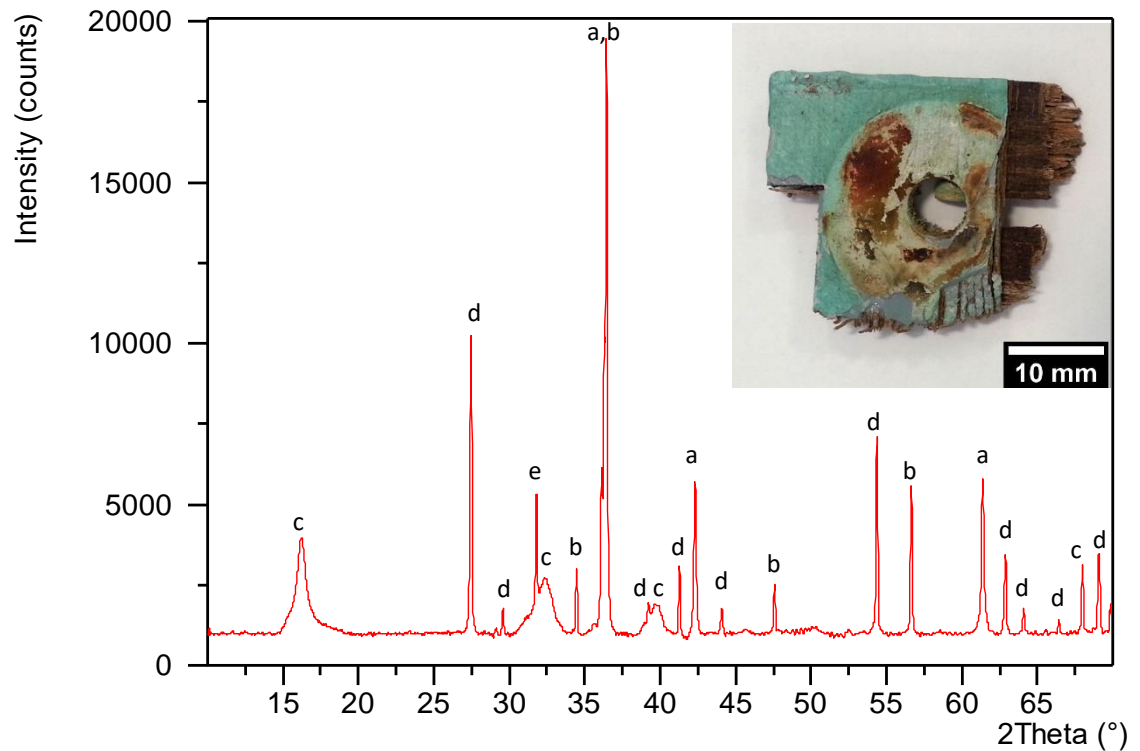
Figure 144 – Gonio XRD analysis of the Paint Flake 12, shown above, removed from "wooden panel". Peaks labelled a = cuprite, b = zinc oxide, c = atacamite, d = titanium dioxide and e = sodium chloride.
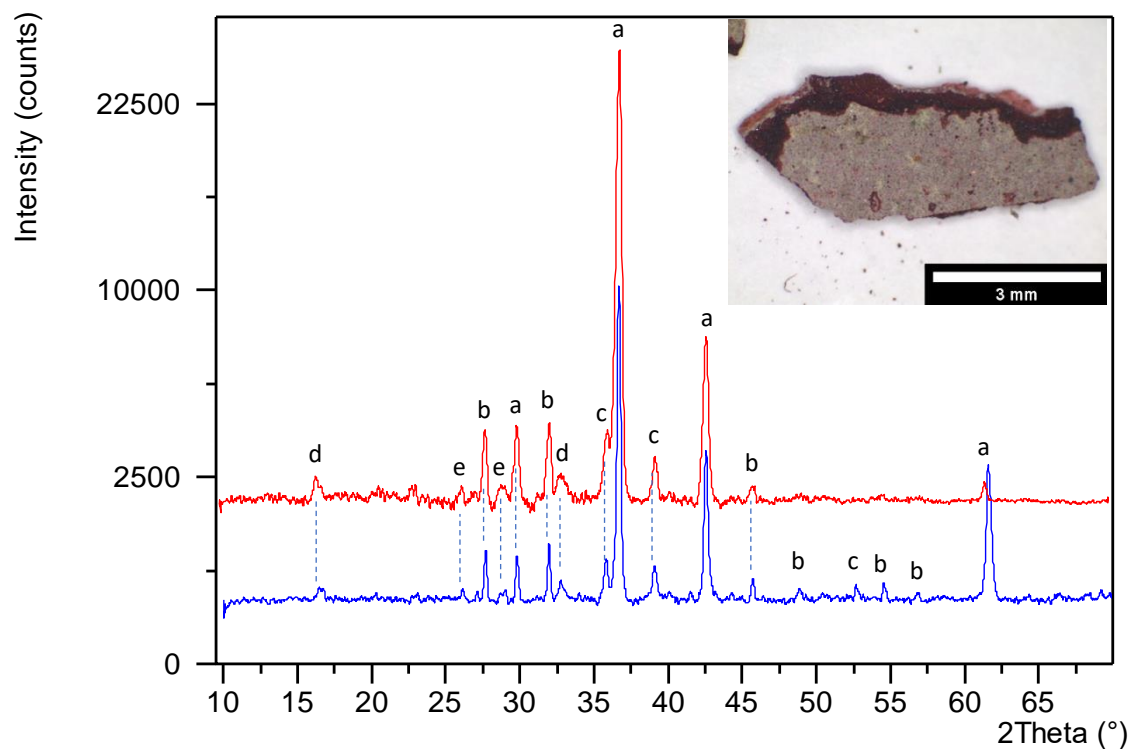
Figure 145 – XRD analysis of the Paint Flake 13, shown above, removed from Overseas Mindoro. The blue and red lines represent the glancing angle and gonio XRD techniques, respectively. Peaks labelled a = cuprite, b = Sodium chloride, c = Tenorite, d = clinoatacamite and e = silicon dioxide.
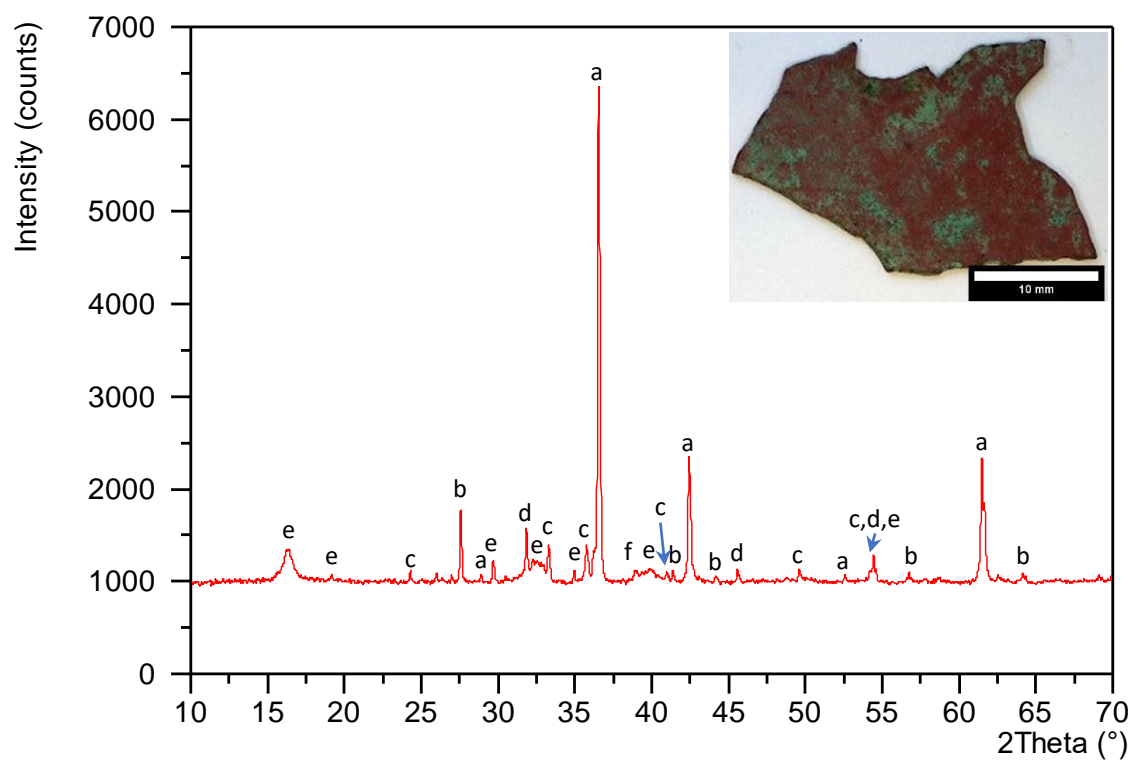
Figure 146 – Gonio XRD analysis of the Paint Flake 14, shown above, removed from "large". Peaks labelled a = cuprite, b = titanium dioxide, c = haematite, d = sodium chloride and e = clinoatacamite

Appendix 2 – XRD Analysis Of Coating Pigments

a)

b)

c)

d)

e)

f)
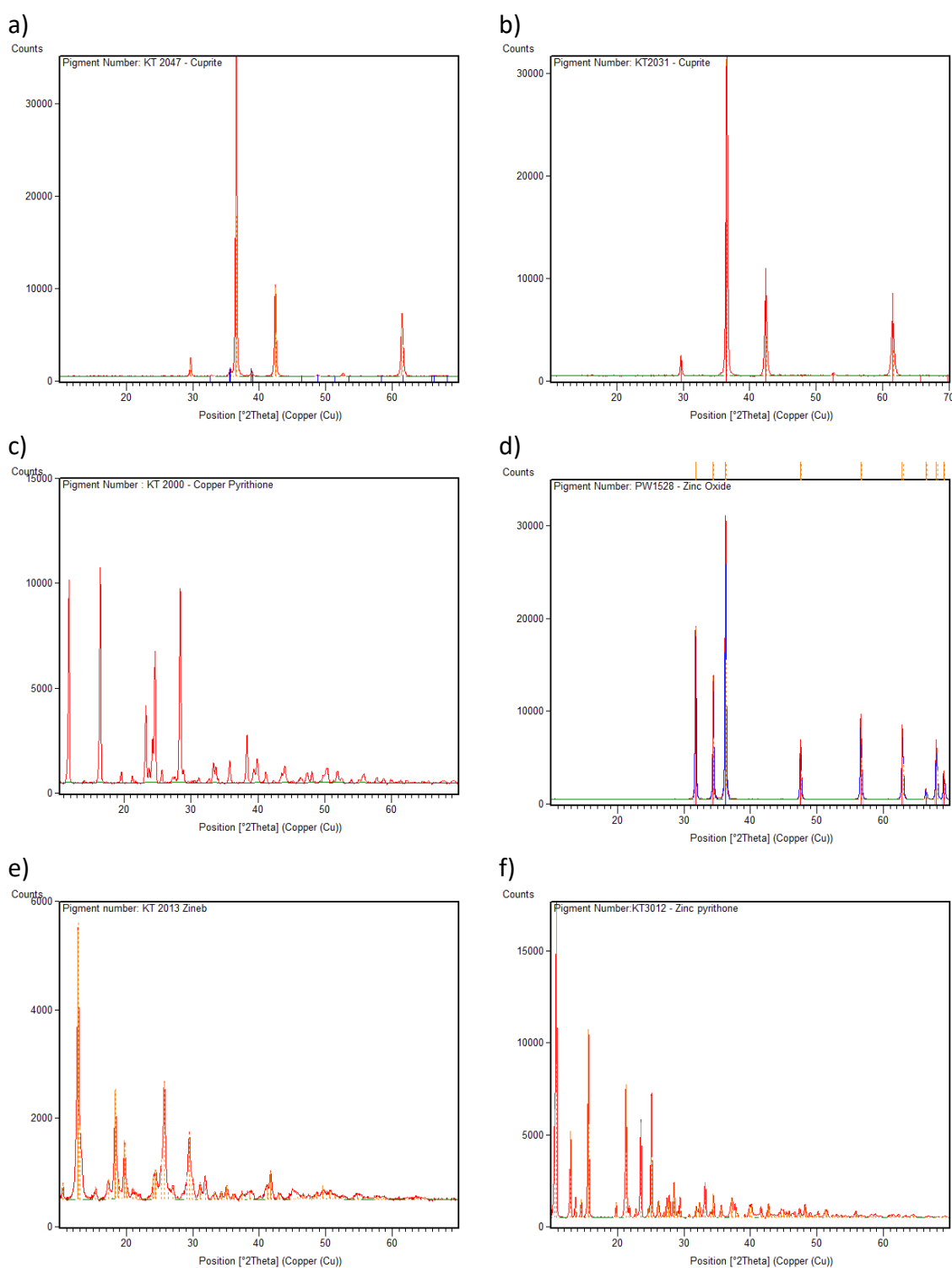
Figure 147 – XRD analysis of the pigments used in antifouling coatings showing the XRD trace of a) cuprite (KT2047), b) cuprite (KT2031), c) copper pyrithione, d) zinc oxide, e) zineb and f) zinc pyrithione

a)

b)

c)
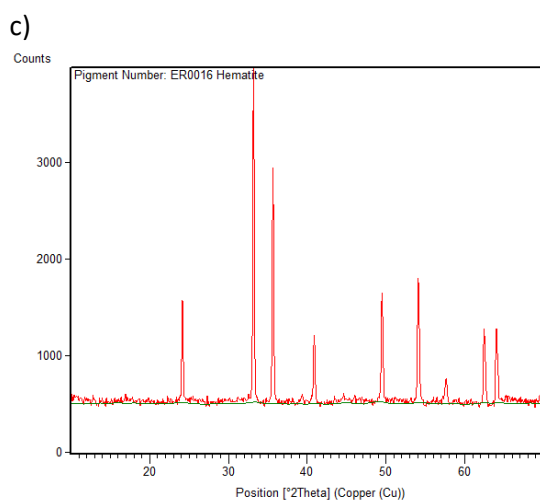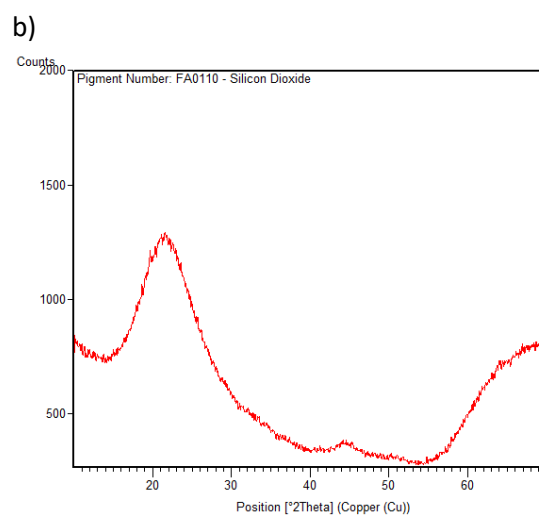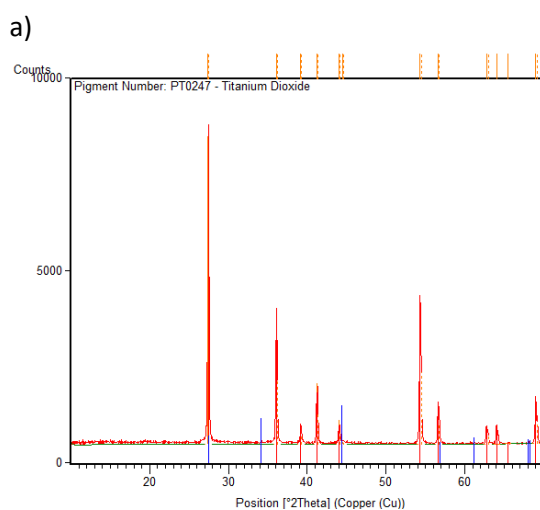
Figure 148 – XRD analysis of further pigments used in antifouling coatings showing the XRD trace of a) titanium dioxide, b) silicon dioxide and c) haematite

[393]

Appendix 3 – Copper OCP Analysis

a) Effect Of Temperature On The OCP Of Copper
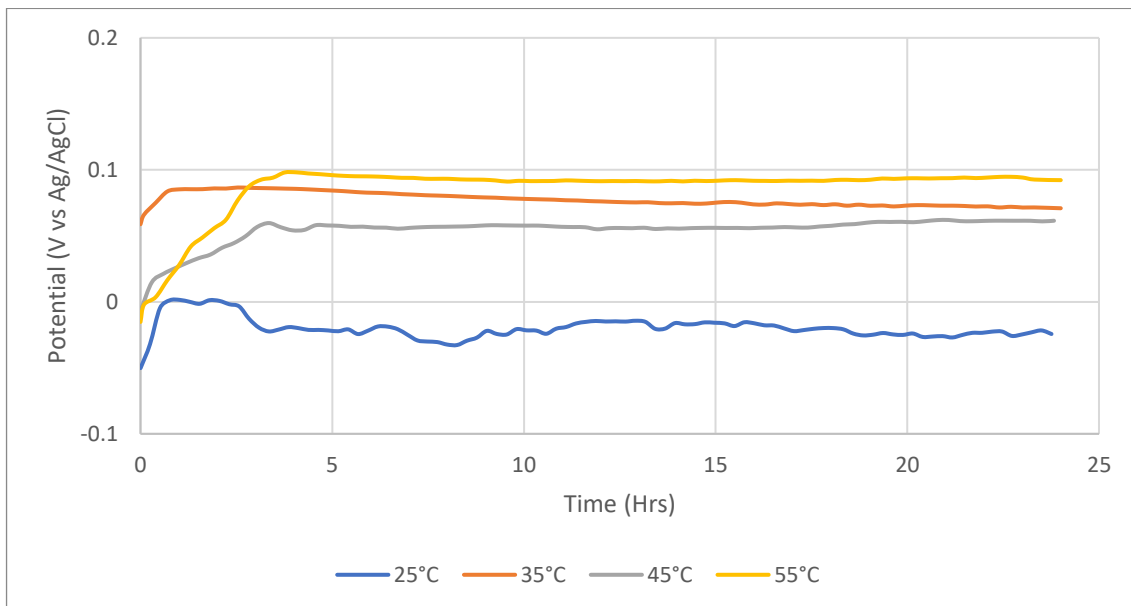
Figure 149 – Chart showing the effect of temperature on the OCP of copper in a 0% NaCl electrolyte at pH 7.
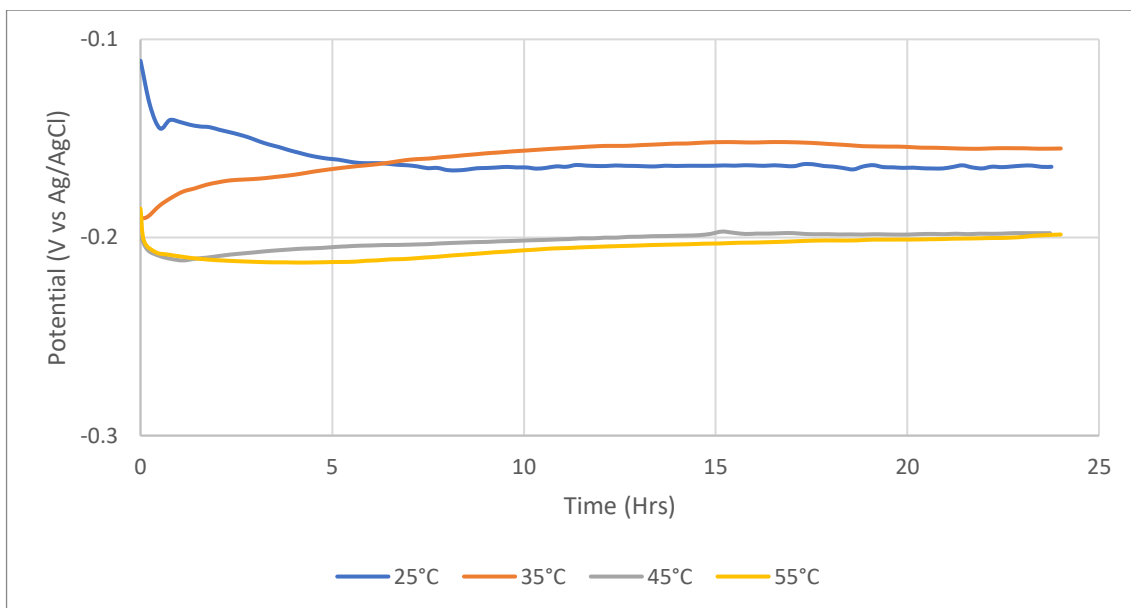
Figure 150 – Chart showing the effect of temperature on the OCP of copper in a 1% NaCl electrolyte at pH 7.
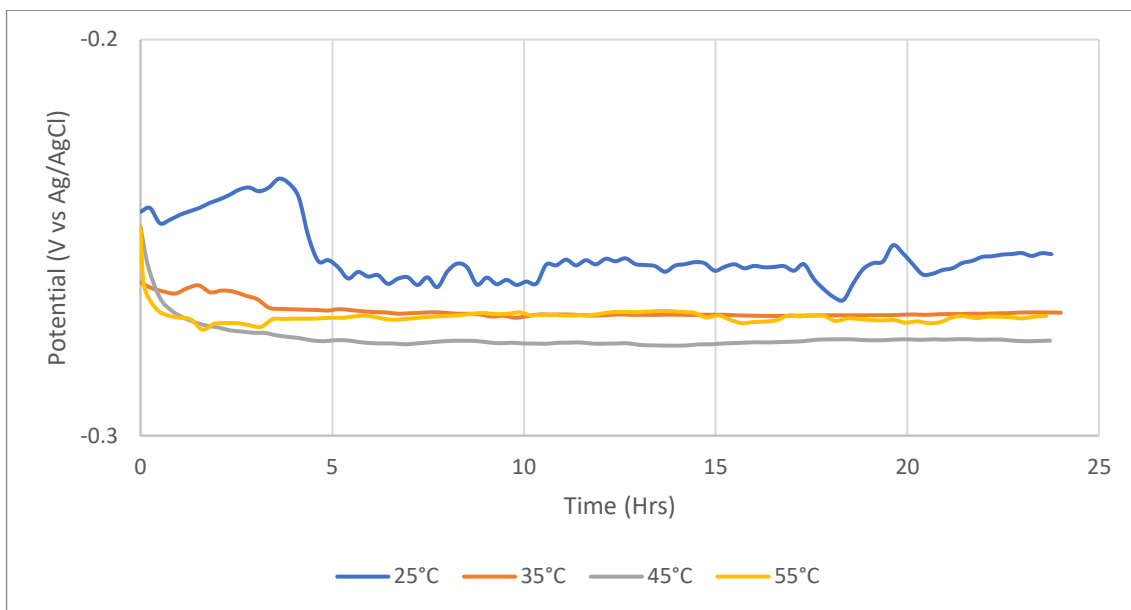
Figure 151 – Chart showing the effect of temperature on the OCP of copper in a 10% NaCl electrolyte at pH 7.
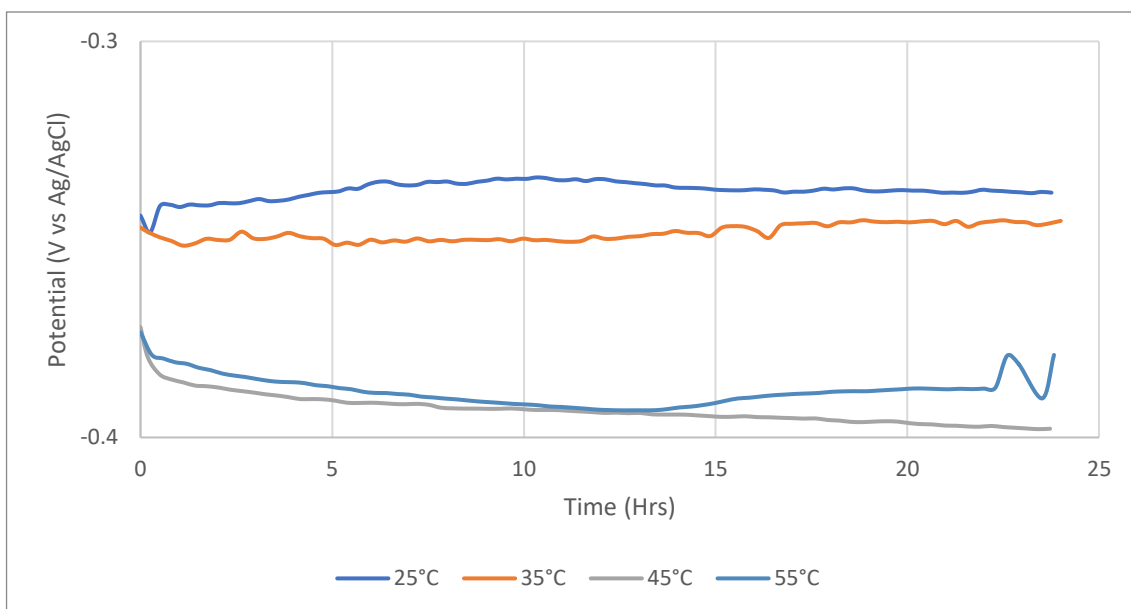
Figure 152 – Chart showing the effect of temperature on the OCP of copper in a 30% NaCl electrolyte at pH 7.

[395]

b) Effect Of pH On The OCP Of Copper
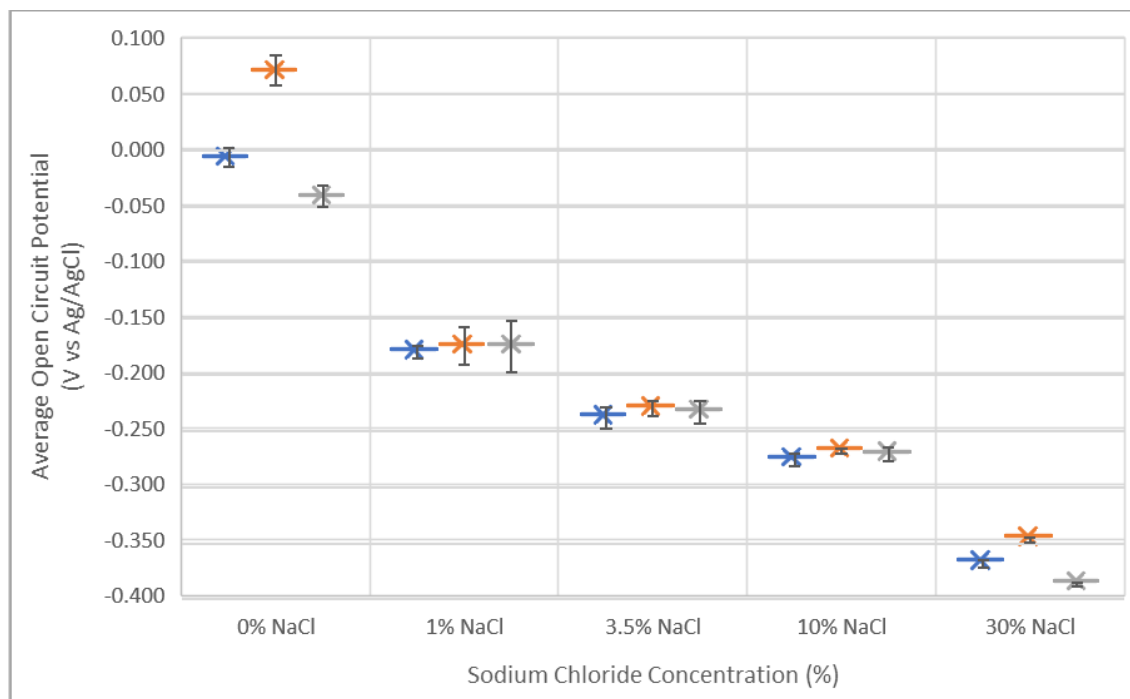
Figure 153 – Chart showing the effect of pH on the OCP at 35°C in the different NaCl concentration electrolytes
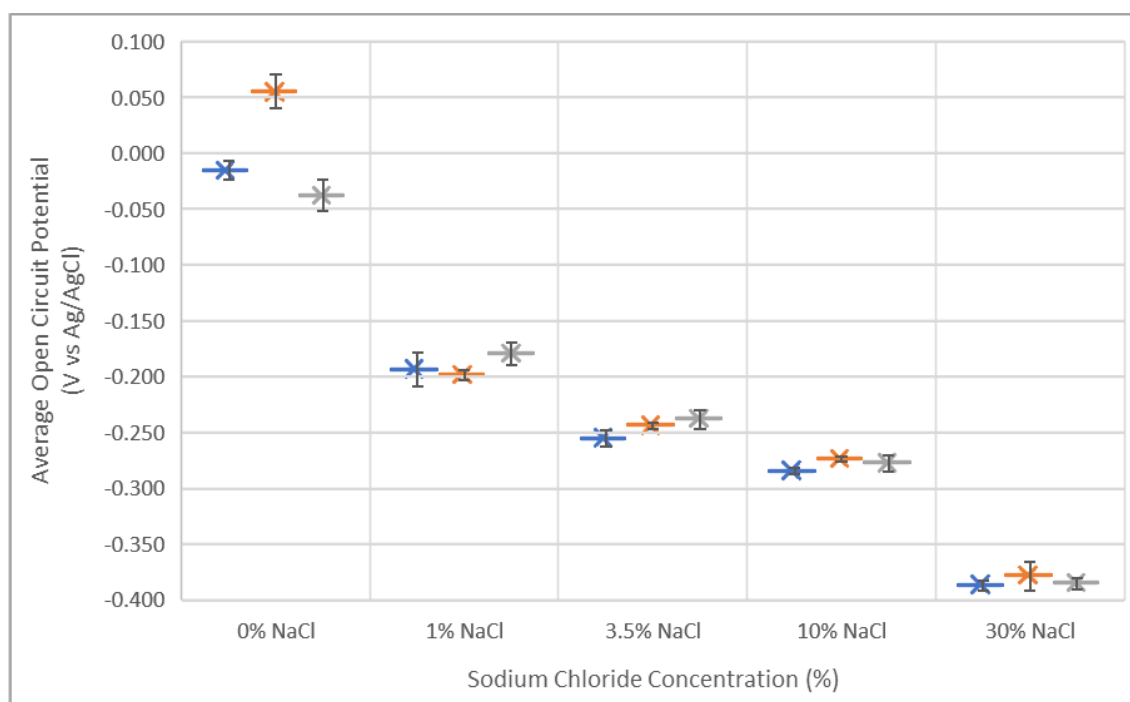
Figure 154 – Chart showing the effect of pH on the OCP at 45°C in the different NaCl concentration electrolytes

[396]
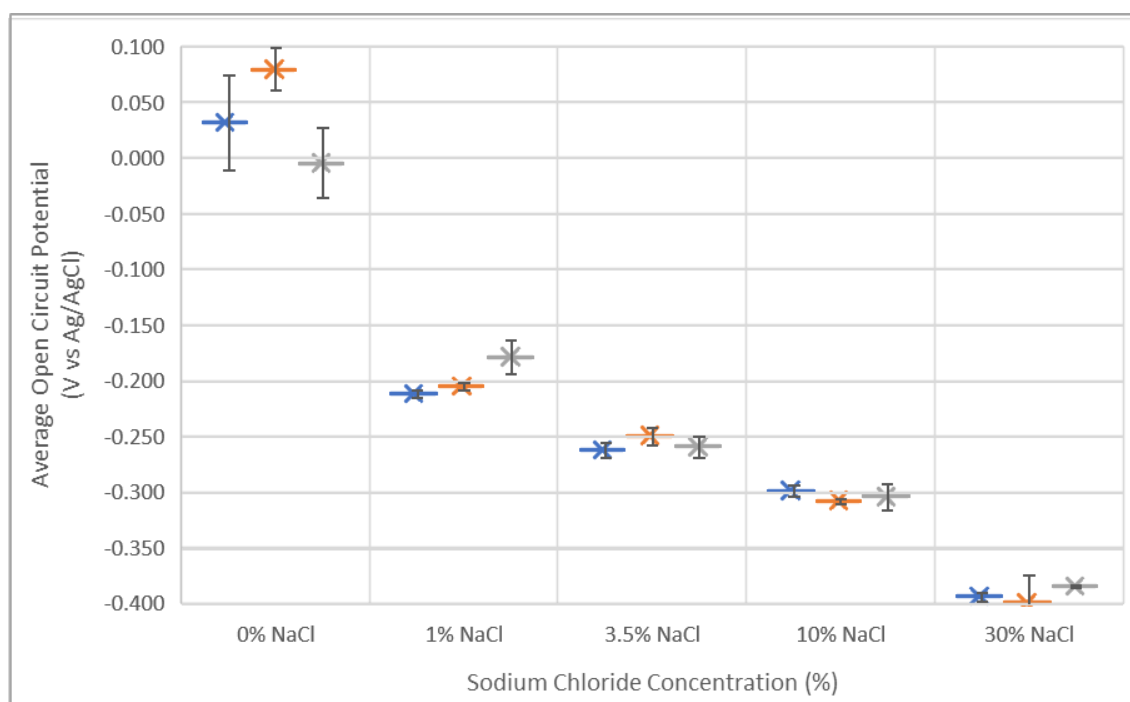
Figure 155 – Chart showing the effect of pH on the OCP at 55°C in the different NaCl concentration electrolytes

Appendix 4 - Effect Of pH On The E_{corr} Of Copper
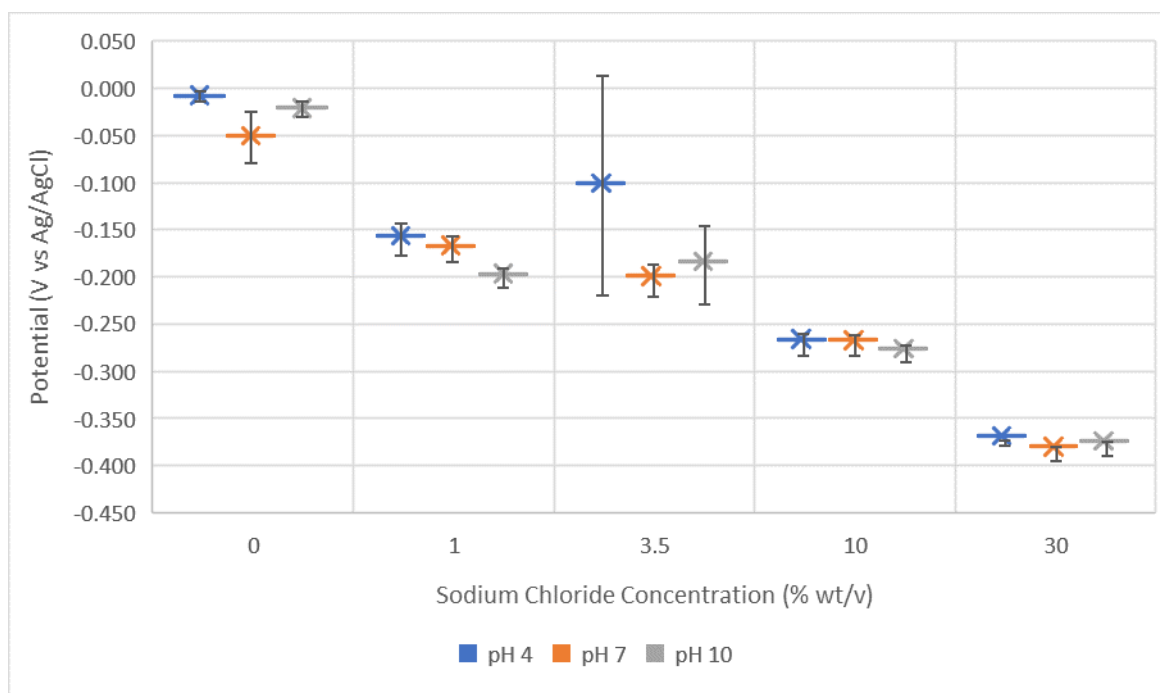
Figure 156 – The effect of pH on the average E_{corr} for the different NaCl concentration electrolytes at 25℃. The pH was modified to ± 0.1 the target value. The y-axis error bars represent the standard deviation measured between the E_{corr} values recorded from multiple potentiodynamic polarisation curves
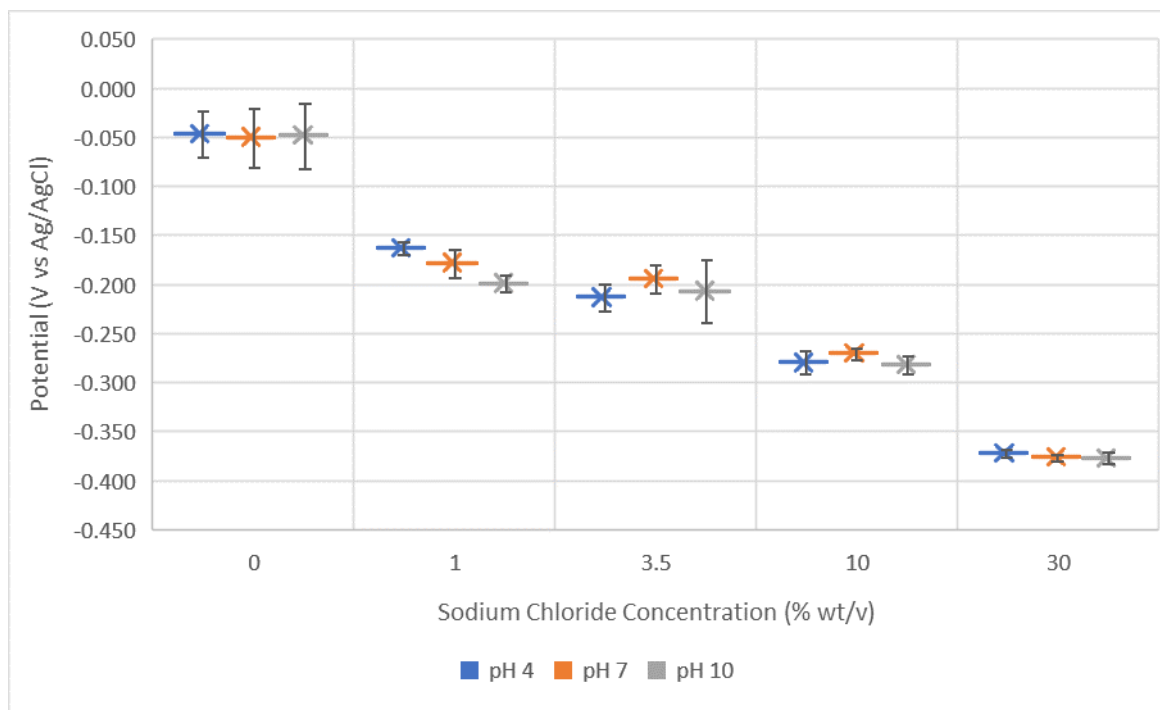
Figure 157 – The effect of pH on the average E_{corr} for the different NaCl concentration electrolytes at 35℃. The pH was modified to ± 0.1 the target value. The y-axis error bars represent the standard deviation measured between the E_{corr} values recorded from multiple potentiodynamic polarisation curves
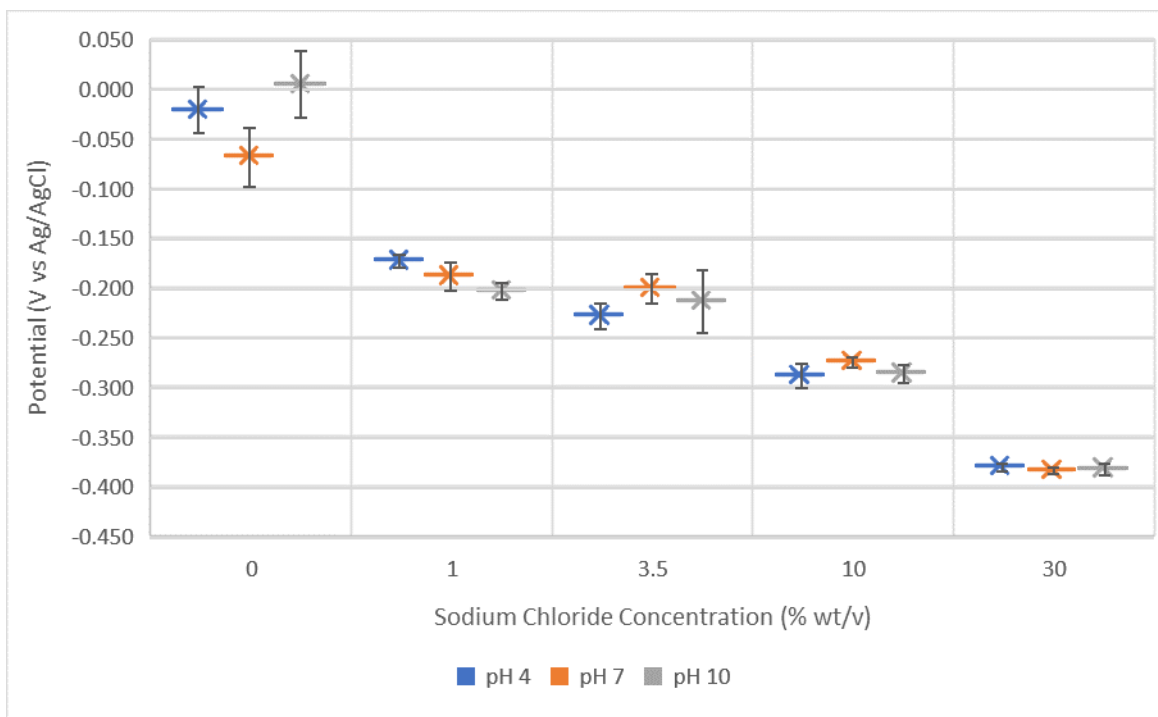
Figure 158 – The effect of pH on the average E_{corr} for the different NaCl concentration electrolytes at 45℃. The pH was modified to ± 0.1 the target value. The y-axis error bars represent the standard deviation of the E_{corr} values recorded from multiple potentiodynamic polarisation curves
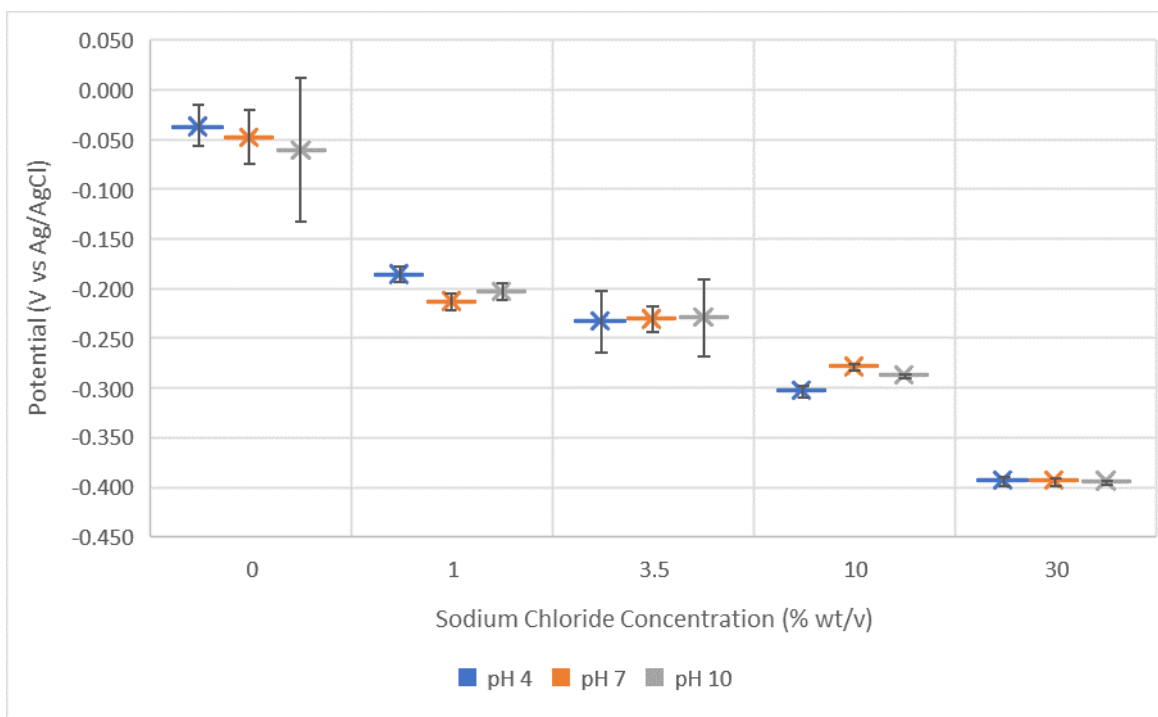
Figure 159 – The effect of pH on the average E_{corr} for the different NaCl concentration electrolytes at 55℃. The pH was modified to ± 0.1 the target value. The y-axis error bars represent the standard deviation of the E_{corr} values recorded from multiple potentiodynamic polarisation curves

[399]

Appendix 5 – Polarisation Curve Analysis

a) Copper Tafel Curves

Table 36 – Example Tafel analysis of copper in the pH 4, 0% electrolyte at different temperatures
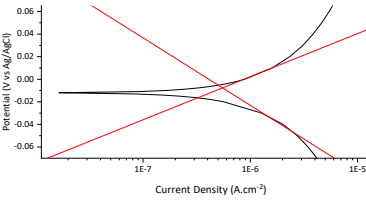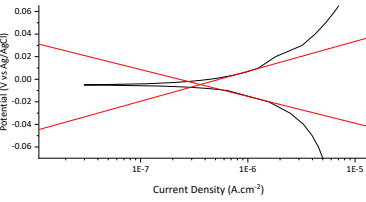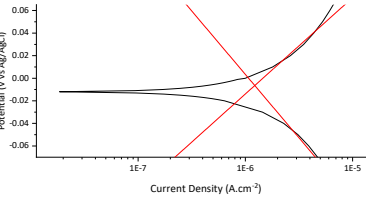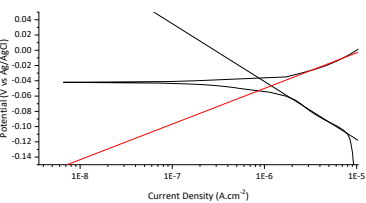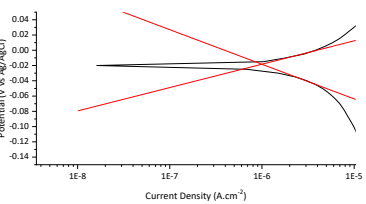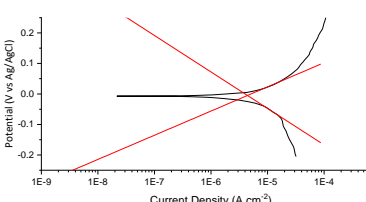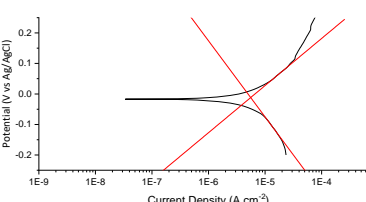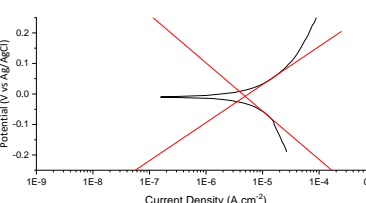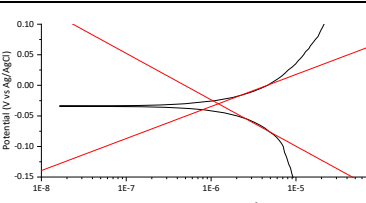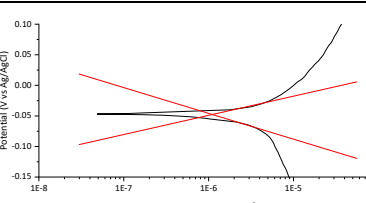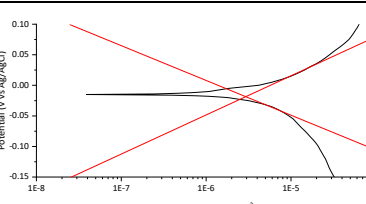
25°C		
$Ecorr = -7.84\ mV$ $Icorr = 0.55 \times 10^{-6} A.\,cm^{-2}$	$Ecorr = -4.65\ mV$ $Icorr = 0.36 \times 10^{-6} A.\,cm^{-2}$	$Ecorr = -6.41\ mV$ $Icorr = 1.22 \times 10^{-6} A.\,cm^{-2}$

35°C		
$Ecorr = -19.7\ mV$ $Icorr = 1.02 \times 10^{-6} A.\,cm^{-2}$	$Ecorr = -46.3\ mV$ $Icorr = 1.18 \times 10^{-6} A.\,cm^{-2}$	$Ecorr = -18.2\ mV$ $Icorr = 1.00 \times 10^{-6} A.\,cm^{-2}$

45°C		
$Ecorr = -5.18\ mV$ $Icorr = 4.41 \times 10^{-6} A.\,cm^{-2}$	$Ecorr = -11.8\ mV$ $Icorr = 5.60 \times 10^{-6} A.\,cm^{-2}$	$Ecorr = -7.37\ mV$ $Icorr = 4.91 \times 10^{-6} A.\,cm^{-2}$

55°C		
$Ecorr = -30.5\ mV$ $Icorr = 1.22 \times 10^{-6} A.\,cm^{-2}$	$Ecorr = -47.70\ mV$ $Icorr = 1.10 \times 10^{-6} A.\,cm^{-2}$	$Ecorr = -18.50\ mV$ $Icorr = 2.93 \times 10^{-6} A.\,cm^{-2}$

[400]

Table 37 – Example Tafel analysis of copper in the pH 4, 1% electrolyte at different temperatures

25°C		
$Ecorr = -171.8 \ mV$ $Icorr = 1.30 \times 10^{-6} A.cm^{-2}$	$Ecorr = -162.3 \ mV$ $Icorr = 0.91 \times 10^{-6} A.cm^{-2}$	$Ecorr = -161.1 \ mV$ $Icorr = 0.92 \times 10^{-6} A.cm^{-2}$

35°C		
$Ecorr = -171.3 \ mV$ $Icorr = 5.60 \times 10^{-6} A.cm^{-2}$	$Ecorr = -160.1 \ mV$ $Icorr = 4.37 \times 10^{-6} A.cm^{-2}$	$Ecorr = -168.1 \ mV$ $Icorr = 3.18 \times 10^{-6} A.cm^{-2}$

45°C		
$Ecorr = -168.7 \ mV$ $Icorr = 7.51 \times 10^{-6} A.cm^{-2}$	$Ecorr = -166.0 \ mV$ $Icorr = 8.16 \times 10^{-6} A.cm^{-2}$	$Ecorr = -175.7 \ mV$ $Icorr = 7.45 \times 10^{-6} A.cm^{-2}$

55°C		
$Ecorr = -175.4 mV$ $Icorr = 9.30 \times 10^{-6} A.cm^{-2}$	$Ecorr = -196.7 \ mV$ $Icorr = 7.01 \times 10^{-6} A.cm^{-2}$	$Ecorr = -190.6 \ mV$ $Icorr = 9.29 \times 10^{-6} A.cm^{-2}$

[401]

Table 38 – Example Tafel analysis of copper in the pH 4, 3.5% electrolyte at different temperatures

25°C		

$$Ecorr = -222.2\ mV$$
$$Icorr = 4.13 \times 10^{-6} A.cm^{-2}$$

$$Ecorr = -223.0\ mV$$
$$Icorr = 3.34 \times 10^{-6} A.cm^{-2}$$

$$Ecorr = -191.6\ mV$$
$$Icorr = 6.03 \times 10^{-6} A.cm^{-2}$$

35°C		

$$Ecorr = -193.6\ mV$$
$$Icorr = 7.53 \times 10^{-6} A.cm^{-2}$$

$$Ecorr = -206.5\ mV$$
$$Icorr = 2.40 \times 10^{-6} A.cm^{-2}$$

$$Ecorr = -207.0\ mV$$
$$Icorr = 1.48 \times 10^{-6} A.cm^{-2}$$

45°C		

$$Ecorr = -232.9\ mV$$
$$Icorr = 7.91 \times 10^{-6} A.cm^{-2}$$

$$Ecorr = -217.0\ mV$$
$$Icorr = 7.68 \times 10^{-6} A.cm^{-2}$$

$$Ecorr = -229.2\ mV$$
$$Icorr = 8.44 \times 10^{-6} A.cm^{-2}$$

55°C		

$$Ecorr = -229.3\ mV$$
$$Icorr = 19.2 \times 10^{-6} A.cm^{-2}$$

$$Ecorr = -222.9\ mV$$
$$Icorr = 13.8 \times 10^{-6} A.cm^{-2}$$

$$Ecorr = -223.9\ mV$$
$$Icorr = 13.2 \times 10^{-6} A.cm^{-2}$$

[402]

Table 39 – Example Tafel analysis of copper in the pH 4, 10% electrolyte at different temperatures

25°C		
$Ecorr = -261.2\ mV$ $Icorr = 5.79 \times 10^{-6} A.cm^{-2}$	$Ecorr = -273.7\ mV$ $Icorr = 5.72 \times 10^{-6} A.cm^{-2}$	$Ecorr = -259.0\ mV$ $Icorr = 5.40 \times 10^{-6} A.cm^{-2}$

35°C		
$Ecorr = -267.7\ mV$ $Icorr = 6.11 \times 10^{-6} A.cm^{-2}$	$Ecorr = -277.8\ mV$ $Icorr = 6.50 \times 10^{-6} A.cm^{-2}$	$Ecorr = -274.7\ mV$ $Icorr = 7.65 \times 10^{-6} A.cm^{-2}$

45°C		
$Ecorr = -289.9\ mV$ $Icorr = 10.2 \times 10^{-6} A.cm^{-2}$	$Ecorr = -275.5\ mV$ $Icorr = 11.8 \times 10^{-6} A.cm^{-2}$	$Ecorr = -297.2\ mV$ $Icorr = 17.5 \times 10^{-6} A.cm^{-2}$

55°C		
$Ecorr = -302.0\ mV$ $Icorr = 11.4 \times 10^{-6} A.cm^{-2}$	$Ecorr = -302.8\ mV$ $Icorr = 10.4 \times 10^{-6} A.cm^{-2}$	$Ecorr = -300.0\ mV$ $Icorr = 10.8 \times 10^{-6} A.cm^{-2}$

[403]

Table 40 – Example Tafel analysis of copper in the pH 4, 30% electrolyte at different temperatures

25°C		
$Ecorr = -371.6\ mV$ $Icorr = 3.68 \times 10^{-6} A.cm^{-2}$	$Ecorr = -371.6\ mV$ $Icorr = 4.26 \times 10^{-6} A.cm^{-2}$	$Ecorr = -369.8\ mV$ $Icorr = 4.04 \times 10^{-6} A.cm^{-2}$

35°C		
$Ecorr = -378.4\ mV$ $Icorr = 3.13 \times 10^{-6} A.cm^{-2}$	$Ecorr = -376.6\ mV$ $Icorr = 4.8 \times 10^{-6} A1.cm^{-2}$	$Ecorr = -380.0\ mV$ $Icorr = 5.38 \times 10^{-6} A.cm^{-2}$

45°C		
$Ecorr = -379.7\ mV$ $Icorr = 7.50 \times 10^{-6} A.cm^{-2}$	$Ecorr = -330.1\ mV$ $Icorr = 8.61 \times 10^{-6} A.cm^{-2}$	$Ecorr = -381.0\ mV$ $Icorr = 7.41 \times 10^{-6} A.cm^{-2}$

55°C		
$Ecorr = -387.5\ mV$ $Icorr = 9.97 \times 10^{-6} A.cm^{-2}$	$Ecorr = -386.0\ mV$ $Icorr = 9.56 \times 10^{-6} A.cm^{-2}$	$Ecorr = -399.8\ mV$ $Icorr = 9.25 \times 10^{-6} A.cm^{-2}$

[404]

Table 41 – Example Tafel analysis of copper in the pH 7, 0% electrolyte at different temperatures

25°C		
$Ecorr = -45.5\ mV$ $Icorr = 0.34 \times 10^{-6} A.cm^{-2}$	$Ecorr = -74.0\ mV$ $Icorr = 0.42 \times 10^{-6} A.cm^{-2}$	$Ecorr = -16.5\ mV$ $Icorr = 0.25 \times 10^{-6} A.cm^{-2}$
35°C		
$Ecorr = -33.5\ mV$ $Icorr = 0.29 \times 10^{-6} A.cm^{-2}$	$Ecorr = -15.5\ mV$ $Icorr = 0.79 \times 10^{-6} A.cm^{-2}$	$Ecorr = -65.1\ mV$ $Icorr = 0.34 \times 10^{-6} A.cm^{-2}$
45°C		
$Ecorr = -54.0\ mV$ $Icorr = 0.68 \times 10^{-6} A.cm^{-2}$	$Ecorr = -76.7\ mV$ $Icorr = 1.19 \times 10^{-6} A.cm^{-2}$	$Ecorr = -50.7\ mV$ $Icorr = 0.64 \times 10^{-6} A.cm^{-2}$
55°C		
$Ecorr = -61.8\ mV$ $Icorr = 1.93 \times 10^{-6} A.cm^{-2}$	$Ecorr = -17.6\ mV$ $Icorr = 0.87 \times 10^{-6} A.cm^{-2}$	$Ecorr = -67.0\ mV$ $Icorr = 1.62 \times 10^{-6} A.cm^{-2}$
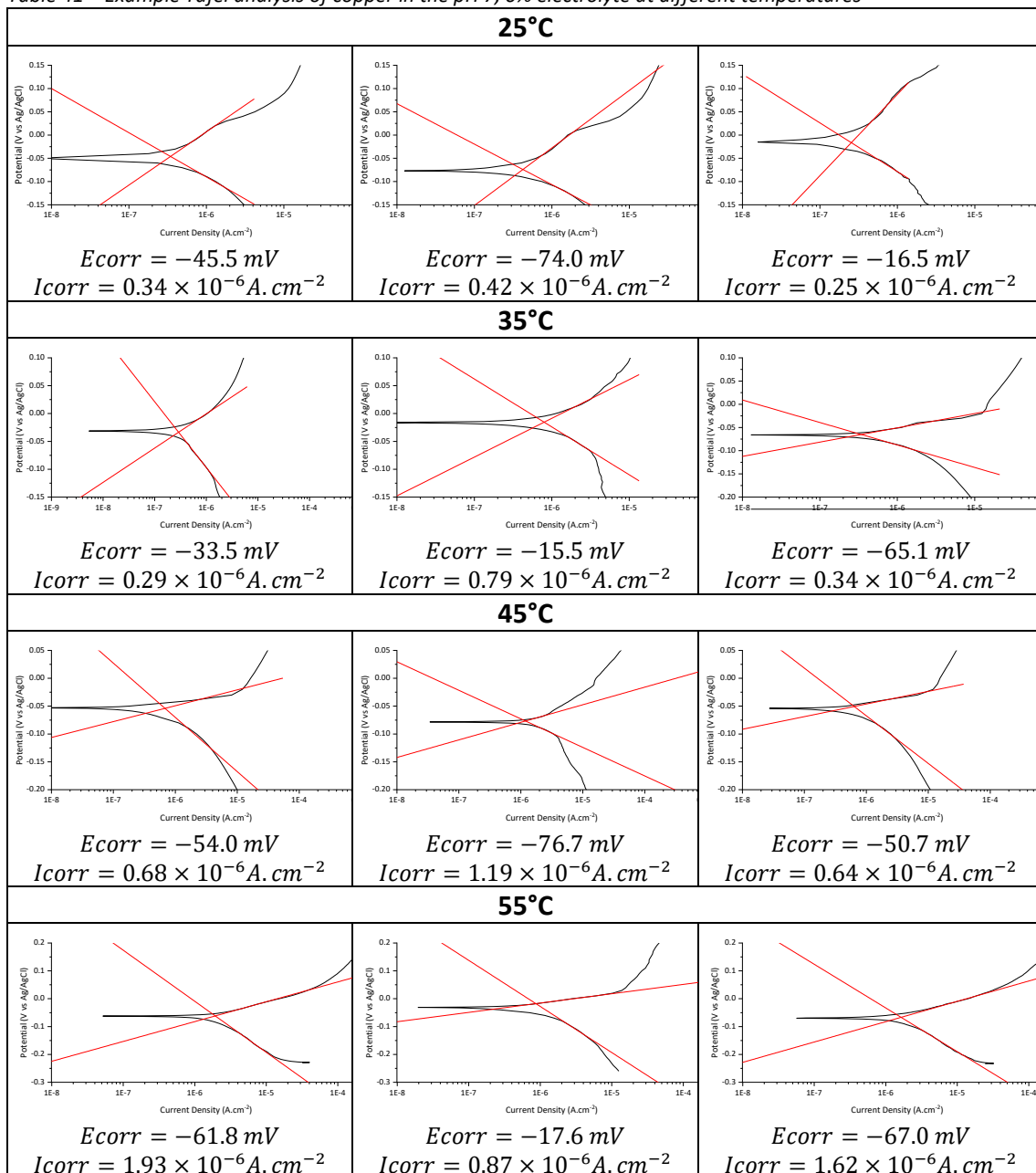
Table 42 – Example Tafel analysis of copper in the pH 7, 1% electrolyte at different temperatures

25°C		
$Ecorr = -210.8\ mV$ $Icorr = 0.93 \times 10^{-6} A.cm^{-2}$	$Ecorr = -195.4\ mV$ $Icorr = 0.93 \times 10^{-6} A.cm^{-2}$	$Ecorr = -227.3\ mV$ $Icorr = 1.23 \times 10^{-6} A.cm^{-2}$

35°C		
$Ecorr = -170.2\ mV$ $Icorr = 5.94 \times 10^{-6} A.cm^{-2}$	$Ecorr = -188.4\ mV$ $Icorr = 6.01 \times 10^{-6} A.cm^{-2}$	$Ecorr = -173.0\ mV$ $Icorr = 2.50 \times 10^{-6} A.cm^{-2}$

45°C		
$Ecorr = -177.8\ mV$ $Icorr = 5.84 \times 10^{-6} A.cm^{-2}$	$Ecorr = -162.8\ mV$ $Icorr = 10.9 \times 10^{-6} A.cm^{-2}$	$Ecorr = -193.5\ mV$ $Icorr = 8.14 \times 10^{-6} A.cm^{-2}$

55°C		
$Ecorr = -192.6\ mV$ $Icorr = 11.3 \times 10^{-6} A.cm^{-2}$	$Ecorr = -181.0\ mV$ $Icorr = 12.7 \times 10^{-6} A.cm^{-2}$	$Ecorr = -187.0\ mV$ $Icorr = 13.3 \times 10^{-6} A.cm^{-2}$

[406]

Table 43 – Example Tafel analysis of copper in the pH 7, 3.5% electrolyte at different temperatures

25°C		
$Ecorr = -169.7\ mV$ $Icorr = 1.65 \times 10^{-6} A.cm^{-2}$	$Ecorr = -208.7\ mV$ $Icorr = 1.92 \times 10^{-6} A.cm^{-2}$	$Ecorr = -205.6\ mV$ $Icorr = 1.30 \times 10^{-6} A.cm^{-2}$

35°C		
$Ecorr = -198.6\ mV$ $Icorr = 2.40 \times 10^{-6} A.cm^{-2}$	$Ecorr = -219.2\ mV$ $Icorr = 4.52 \times 10^{-6} A.cm^{-2}$	$Ecorr = -217.9\ mV$ $Icorr = 5.91 \times 10^{-6} A.cm^{-2}$

45°C		
$Ecorr = -216.2\ mV$ $Icorr = 7.77 \times 10^{-6} A.cm^{-2}$	$Ecorr = -217.9\ mV$ $Icorr = 10.4 \times 10^{-6} A.cm^{-2}$	$Ecorr = -214.9\ mV$ $Icorr = 6.73 \times 10^{-6} A.cm^{-2}$

55°C		
$Ecorr = -245.6\ mV$ $Icorr = 19.0 \times 10^{-6} A.cm^{-2}$	$Ecorr = -239.4\ mV$ $Icorr = 10.9 \times 10^{-6} A.cm^{-2}$	$Ecorr = -219.1\ mV$ $Icorr = 9.50 \times 10^{-6} A.cm^{-2}$

[407]

Table 44 – Example Tafel analysis of copper in the pH 7, 10% electrolyte at different temperatures

25°C

$Ecorr = -258.7 \, mV$
$Icorr = 6.77 \times 10^{-6} A.cm^{-2}$

$Ecorr = -249.0 \, mV$
$Icorr = 6.34 \times 10^{-6} A.cm^{-2}$

$Ecorr = -266.8 \, mV$
$Icorr = 4.50 \times 10^{-6} A.cm^{-2}$

35°C

$Ecorr = -268.1 \, mV$
$Icorr = 5.26 \times 10^{-6} A.cm^{-2}$

$Ecorr = -279.8 \, mV$
$Icorr = 6.17 \times 10^{-6} A.cm^{-2}$

$Ecorr = -270.5 \, mV$
$Icorr = 6.85 \times 10^{-6} A.cm^{-2}$

45°C

$Ecorr = -271.1 \, mV$
$Icorr = 15.7 \times 10^{-6} A.cm^{-2}$

$Ecorr = -282.8 \, mV$
$Icorr = 17.6 \times 10^{-6} A.cm^{-2}$

$Ecorr = -292.8 \, mV$
$Icorr = 15.3 \times 10^{-6} A.cm^{-2}$

55°C

$Ecorr = -309.0 \, mV$
$Icorr = 12.6 \times 10^{-6} A.cm^{-2}$

$Ecorr = -293.4 \, mV$
$Icorr = 24.6 \times 10^{-6} A.cm^{-2}$

$Ecorr = -300.0 \, mV$
$Icorr = 22.8 \times 10^{-6} A.cm^{-2}$

[408]

Table 45 – Example Tafel analysis of copper in the pH 7, 30% electrolyte at different temperatures

25°C		
$Ecorr = -387.0\ mV$ $Icorr = 3.21 \times 10^{-6} A.cm^{-2}$	$Ecorr = -384.6\ mV$ $Icorr = 2.57 \times 10^{-6} A.cm^{-2}$	$Ecorr = -375.8\ mV$ $Icorr = 3.88 \times 10^{-6} A.cm^{-2}$

35°C		
$Ecorr = -380.1\ mV$ $Icorr = 3.90 \times 10^{-6} A.cm^{-2}$	$Ecorr = -379.1\ mV$ $Icorr = 5.42 \times 10^{-6} A.cm^{-2}$	$Ecorr = -379.1\ mV$ $Icorr = 4.59 \times 10^{-6} A.cm^{-2}$

45°C		
$Ecorr = -384.9\ mV$ $Icorr = 4.43 \times 10^{-6} A.cm^{-2}$	$Ecorr = -384.8\ mV$ $Icorr = 5.05 \times 10^{-6} A.cm^{-2}$	$Ecorr = -386.5\ mV$ $Icorr = 4.51 \times 10^{-6} A.cm^{-2}$

55°C		
$Ecorr = -389.6\ mV$ $Icorr = 4.84 \times 10^{-6} A.cm^{-2}$	$Ecorr = -392.2 mV$ $Icorr = 5.91 \times 10^{-6} A.cm^{-2}$	$Ecorr = -395.5\ mV$ $Icorr = 7.27 \times 10^{-6} A.cm^{-2}$

[409]

Table 46 – Example Tafel analysis of copper in the pH 10, 0% electrolyte at different temperatures

25°C		
$Ecorr = -1.05 \; mV$ $Icorr = 1.09 \times 10^{-6} A.cm^{-2}$	$Ecorr = -13.4 \; mV$ $Icorr = 0.57 \times 10^{-6} A.cm^{-2}$	$Ecorr = -25.2 \; mV$ $Icorr = 0.31 \times 10^{-6} A.cm^{-2}$
35°C		
$Ecorr = -99.5 \; mV$ $Icorr = 1.31 \times 10^{-6} A.cm^{-2}$	$Ecorr = -7.30 \; mV$ $Icorr = 1.07 \times 10^{-6} A.cm^{-2}$	$Ecorr = -106.8 \; mV$ $Icorr = 1.35 \times 10^{-6} A.cm^{-2}$
45°C		
$Ecorr = -8.85 \; mV$ $Icorr = 1.15 \times 10^{-6} A.cm^{-2}$	$Ecorr = -12.4 \; mV$ $Icorr = 0.90 \times 10^{-6} A.cm^{-2}$	
55°C		
$Ecorr = -67.7 \; mV$ $Icorr = 0.38 \times 10^{-6} A.cm^{-2}$	$Ecorr = -8.60 \; mV$ $Icorr = 0.25 \times 10^{-6} A.cm^{-2}$	$Ecorr = -45.7 \; mV$ $Icorr = 0.43 \times 10^{-6} A.cm^{-2}$

[410]

Table 47 – Example Tafel analysis of copper in the pH 10, 1% electrolyte at different temperatures

25°C		
$Ecorr = -204.9\ mV$ $Icorr = 1.04 \times 10^{-6} A.cm^{-2}$	$Ecorr = -182.6\ mV$ $Icorr = 1.02 \times 10^{-6} A.cm^{-2}$	$Ecorr = -188.1\ mV$ $Icorr = 1.12 \times 10^{-6} A.cm^{-2}$

35°C		
$Ecorr = -193.8\ mV$ $Icorr = 1.69 \times 10^{-6} A.cm^{-2}$	$Ecorr = -219.3\ mV$ $Icorr = 2.93 \times 10^{-6} A.cm^{-2}$	$Ecorr = -189.2\ mV$ $Icorr = 3.30 \times 10^{-6} A.cm^{-2}$

45°C		
$Ecorr = -204.1\ mV$ $Icorr = 3.24 \times 10^{-6} A.cm^{-2}$	$Ecorr = -208.8\ mV$ $Icorr = 4.85 \times 10^{-6} A.cm^{-2}$	$Ecorr = -192.0\ mV$ $Icorr = 4.88 \times 10^{-6} A.cm^{-2}$

55°C		
$Ecorr = -195.0\ mV$ $Icorr = 14.9 \times 10^{-6} A.cm^{-2}$	$Ecorr = -198.7\ mV$ $Icorr = 5.39 \times 10^{-6} A.cm^{-2}$	$Ecorr = -202.5\ mV$ $Icorr = 16.4 \times 10^{-6} A.cm^{-2}$

[411]

Table 48 – Example Tafel analysis of copper in the pH 10, 3.5% electrolyte at different temperatures

25°C		
$Ecorr = -225.9\ mV$ $Icorr = 1.96 \times 10^{-6} A.cm^{-2}$	$Ecorr = -207.4\ mV$ $Icorr = 3.25 \times 10^{-6} A.cm^{-2}$	$Ecorr = -227.1\ mV$ $Icorr = 2.00 \times 10^{-6} A.cm^{-2}$
35°C		
$Ecorr = -247.4\ mV$ $Icorr = 5.73 \times 10^{-6} A.cm^{-2}$	$Ecorr = -201.4\ mV$ $Icorr = 3.36 \times 10^{-6} A.cm^{-2}$	$Ecorr = -215.2\ mV$ $Icorr = 4.47 \times 10^{-6} A.cm^{-2}$
45°C		
$Ecorr = -252.6\ mV$ $Icorr = 5.1 \times 10^{-6} A.cm^{-2}$	$Ecorr = -233.3\ mV$ $Icorr = 8.67 \times 10^{-6} A.cm^{-2}$	$Ecorr = -215.4\ mV$ $Icorr = 10.4 \times 10^{-6} A.cm^{-2}$
55°C		
$Ecorr = -292.6\ mV$ $Icorr = 9.67 \times 10^{-6} A.cm^{-2}$	$Ecorr = -289.7\ mV$ $Icorr = 14.6 \times 10^{-6} A.cm^{-2}$	$Ecorr = -263.3\ mV$ $Icorr = 8.82 \times 10^{-6} A.cm^{-2}$

[412]

Table 49 – Example Tafel analysis of copper in the pH 10, 10% electrolyte at different temperatures

25°C		
$Ecorr = -268.2\ mV$ $Icorr = 4.15 \times 10^{-6} A.cm^{-2}$	$Ecorr = -268.8\ mV$ $Icorr = 3.28 \times 10^{-6} A.cm^{-2}$	$Ecorr = -290.3\ mV$ $Icorr = 4.63 \times 10^{-6} A.cm^{-2}$

35°C		
$Ecorr = -286.3\ mV$ $Icorr = 7.52 \times 10^{-6} A.cm^{-2}$	$Ecorr = -281.2\ mV$ $Icorr = 8.63 \times 10^{-6} A.cm^{-2}$	$Ecorr = -297.1\ mV$ $Icorr = 8.97 \times 10^{-6} A.cm^{-2}$

45°C		
$Ecorr = -283.5\ mV$ $Icorr = 6.63.\times 10^{-6} A.cm^{-2}$	$Ecorr = -291.4\ mV$ $Icorr = 9.71 \times 10^{-6} A.cm^{-2}$	$Ecorr = -291.7\ mV$ $Icorr = 16.0 \times 10^{-6} A.cm^{-2}$

55°C		
$Ecorr = -299.1\ mV$ $Icorr = 20.5 \times 10^{-6} A.cm^{-2}$	$Ecorr = -286.9\ mV$ $Icorr = 24.1 \times 10^{-6} A.cm^{-2}$	$Ecorr = -291.1\ mV$ $Icorr = 24.3 \times 10^{-6} A.cm^{-2}$

[413]

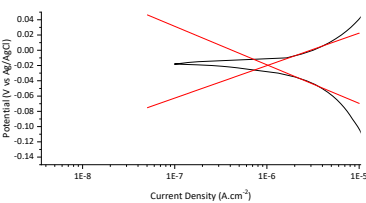*Table 50 – Example Tafel analysis of copper in the pH 10, 30% electrolyte at different temperatures*

25°C		
$Ecorr = -378.6\ mV$ $Icorr = 4.15 \times 10^{-6} A.cm^{-2}$	$Ecorr = -377.3\ mV$ $Icorr = 4.93 \times 10^{-6} A.cm^{-2}$	$Ecorr = -374.8\ mV$ $Icorr = 3.45 \times 10^{-6} A.cm^{-2}$

35°C		
$Ecorr = -380.5\ mV$ $Icorr = 4.87 \times 10^{-6} A.cm^{-2}$	$Ecorr = -384.5\ mV$ $Icorr = 3.37 \times 10^{-6} A.cm^{-2}$	$Ecorr = -394.5\ mV$ $Icorr = 5.30 \times 10^{-6} A.cm^{-2}$

45°C		
$Ecorr = -378.9\ mV$ $Icorr = 4.61 \times 10^{-6} A.cm^{-2}$	$Ecorr = -377.7\ mV$ $Icorr = 5.22 \times 10^{-6} A.cm^{-2}$	$Ecorr = -382.4\ mV$ $Icorr = 4.91 \times 10^{-6} A.cm^{-2}$

55°C		
$Ecorr = -394.3\ mV$ $Icorr = 4.53 \times 10^{-6} A.cm^{-2}$	$Ecorr = -398.5\ mV$ $Icorr = 4.25 \times 10^{-6} A.cm^{-2}$	$Ecorr = -394.3\ mV$ $Icorr = 4.50 \times 10^{-6} A.cm^{-2}$

[414]

b) Tafel Parameters

NaCl %	pH	Temperature (°C)	Ba Average	Ba SD	Bc Average	Bc SD	i_{corr} ($\mu A.cm^{-2}$) Average	SD	Rp (Ω) Average	SD	Tafel constant Average	SD	a Average	SD	E_{corr} (V vs Ag/AgCl) Average	SD	Corrosion Rate ($mm.yr^{-1}$) Average	SD
0	4	25	52.52	25.92	66.96	36.53	0.73	0.37	17200.49	1504.31	12.71	6.62	0.78	0.46	-0.005	0.003	0.017	0.009
		35	35.71	10.92	65.02	21.89	1.07	0.09	8910.10	1354.37	9.54	2.03	1.06	0.21	-0.025	0.015	0.025	0.002
		45	97.16	42.20	186.76	55.65	3.72	1.87	9114.48	5616.58	26.62	9.56	0.48	0.15	-0.017	0.022	0.086	0.043
		55	103.34	24.45	148.63	45.11	1.11	1.53	19048.58	11728.45	60.61	15.57	0.24	0.05	-0.040	0.020	0.041	0.024
	7	25	132.06	28.84	95.53	7.27	0.33	0.07	75471.42	25655.60	23.96	3.01	0.33	0.04	-0.048	0.024	0.008	0.002
		35	47.76	20.81	91.12	31.67	0.50	0.23	23412.33	22834.13	13.12	4.71	0.83	0.31	-0.045	0.025	0.012	0.005
		45	30.01	6.11	88.74	29.00	0.90	0.28	11153.66	2920.68	9.55	2.02	1.27	0.24	-0.059	0.012	0.021	0.006
		55	55.01	20.08	182.42	28.50	1.42	0.46	12382.17	963.62	41.17	11.39	0.36	0.11	-0.038	0.030	0.033	0.011
	10	25	82.51	26.59	107.14	47.06	0.71	0.34	30143.34	7754.87	19.61	6.68	0.44	0.17	-0.012	0.011	0.016	0.008
		35	174.61	26.71	174.16	33.82	1.24	0.12	37748.17	8645.63	37.37	3.79	0.26	0.03	-0.081	0.049	0.029	0.003
		45	136.88	11.16	138.77	12.93	1.02	0.18	33544.18	6050.60	29.81	0.16	0.39	0.00	0.011	0.002	0.024	0.004
		55	69.38	28.50	78.47	47.83	0.36	0.09	50055.41	17523.28	36.38	18.24	0.44	0.18	-0.004	0.058	0.008	0.002
1	4	25	36.4	9.0	76.1	18.2	1.20	0.30	8915.92	1861.35	10.31	0.93	0.76	0.07	-0.164	0.005	0.028	0.007
		35	41.5	5.8	97.7	15.5	4.38	1.20	2964.95	450.31	12.65	1.83	0.78	0.11	-0.167	0.006	0.102	0.028
		45	49.2	5.4	108.3	10.3	7.71	0.40	1900.98	130.65	14.65	1.22	0.48	0.15	-0.170	0.005	0.179	0.009
		55	55.8	8.2	102.0	48.5	11.18	5.58	1496.32	400.96	35.42	8.95	0.41	0.09	-0.183	0.013	0.260	0.130
	7	25	52.1	16.3	41.0	10.1	1.03	0.17	9555.93	1173.97	9.95	2.75	0.82	0.21	-0.174	0.011	0.022	0.000
		35	54.2	11.6	93.2	20.3	4.20	2.04	4882.54	1286.60	14.37	3.16	0.71	0.18	-0.181	0.014	0.098	0.047
		45	61.1	11.5	104.9	34.5	8.79	2.29	1909.69	158.55	16.53	3.26	0.74	0.16	-0.187	0.005	0.204	0.053
		55	64.1	5.6	94.7	6.6	12.01	1.23	1389.05	150.36	16.58	1.07	0.83	0.06	-0.211	0.016	0.279	0.028
	10	25	49.2	3.7	38.9	6.8	1.22	0.32	7950.27	1528.38	9.36	0.99	0.84	0.10	-0.199	0.016	0.028	0.007
		35	106.9	38.4	49.4	16.0	2.28	1.00	7164.01	3819.35	14.15	3.58	0.73	0.21	-0.202	0.013	0.053	0.023
		45	97.2	27.4	55.4	9.8	4.42	0.79	3896.62	404.16	15.13	2.85	0.80	0.16	-0.201	0.007	0.103	0.018
		55	69.7	4.3	114.9	51.2	11.76	4.97	1917.04	516.04	41.96	9.80	0.34	0.09	-0.202	0.007	0.273	0.115

[415]

NaCl %	pH	Temperature (°C)	Ba		Bc		i_{corr} ($\mu A.cm^{-2}$)		Rp (Ω)		Tafel constant		a		E_{corr} (V vs Ag/AgCl)		Corrosion Rate ($mm.yr^{-1}$)	
			Average	*SD*	*Average*	*SD*	*Average*	*SD*	*Average*	*SD*	*Average*	*SD*	*Average*	*SD*	*Average*	*SD*	*Average*	*SD*
3.5	4	25	36.5	10.3	98.1	19.7	3.74	1.89	3085.12	1555.16	11.42	2.71	0.71	0.18	-0.211	0.015	0.087	0.044
		35	30.9	6.7	64.3	9.4	4.39	2.75	2447.21	951.98	8.99	1.36	1.10	0.17	-0.206	0.012	0.102	0.064
		45	43.1	13.4	135.9	74.2	8.68	1.37	1673.48	695.76	14.03	5.08	0.93	0.35	-0.225	0.008	0.201	0.032
		55	48.2	21.3	79.5	37.2	14.32	3.50	791.67	85.81	26.22	7.83	0.55	0.14	-0.243	0.035	0.332	0.081
	7	25	42.4	8.1	60.4	35.3	1.69	0.25	5932.00	770.44	25.98	7.34	0.35	0.05	-0.195	0.022	0.039	0.006
		35	56.3	30.6	69.4	25.0	3.93	1.60	3741.57	718.71	8.21	1.39	0.85	0.35	-0.213	0.010	0.091	0.037
		45	59.7	39.1	83.7	32.4	10.44	4.56	1256.48	147.90	20.66	1.62	1.00	0.29	-0.221	0.009	0.242	0.106
		55	52.5	10.1	79.0	15.9	13.17	5.17	1102.29	292.40	20.17	3.47	1.03	0.22	-0.235	0.014	0.306	0.120
	10	25	79.6	42.8	45.7	6.3	2.40	0.73	5156.82	317.84	10.41	3.45	0.66	0.16	-0.220	0.011	0.056	0.017
		35	46.7	15.9	75.2	42.7	4.52	1.18	2625.42	528.59	8.74	0.36	0.92	0.43	-0.221	0.024	0.105	0.027
		45	139.8	53.9	77.2	26.5	8.18	2.46	2937.03	217.92	9.76	1.11	0.60	0.20	-0.234	0.019	0.190	0.057
		55	89.4	19.2	54.7	26.7	13.92	6.31	1186.80	283.64	50.26	2.57	0.47	0.18	-0.285	0.015	0.323	0.146
10	4	25	51.3	8.3	90.2	102.2	5.56	0.23	2183.06	1035.84	12.02	5.27	0.72	0.22	-0.269	0.010	0.129	0.005
		35	40.2	9.9	32.1	11.0	6.75	0.81	1085.07	135.91	7.30	0.95	1.36	0.19	-0.273	0.005	0.157	0.019
		45	59.5	5.8	217.5	31.7	13.40	3.17	1549.36	248.26	20.19	1.48	0.58	0.04	-0.288	0.009	0.311	0.073
		55	64.6	3.0	185.7	24.2	15.78	5.71	1458.92	536.05	47.74	1.86	0.29	0.01	-0.304	0.003	0.366	0.132
	7	25	59.9	17.6	67.8	40.6	5.50	1.00	2444.19	1055.84	25.98	7.34	0.32	0.09	-0.268	0.014	0.131	0.025
		35	37.4	7.8	38.4	5.4	6.11	0.65	1345.80	203.20	8.21	1.39	1.22	0.22	-0.270	0.007	0.142	0.015
		45	57.5	4.1	285.9	74.9	15.78	1.32	1310.93	69.77	20.66	1.62	0.57	0.04	-0.280	0.010	0.288	0.165
		55	60.3	5.3	215.7	83.9	20.01	6.45	1050.89	201.45	20.17	3.47	0.70	0.13	-0.301	0.008	0.464	0.150
	10	25	84.6	73.3	37.7	2.9	4.02	0.69	2740.85	1420.70	10.41	3.45	0.80	0.23	-0.276	0.013	0.093	0.016
		35	62.4	3.2	25.0	9.0	8.29	0.64	1047.26	59.41	8.74	0.36	1.12	0.05	-0.285	0.010	0.194	0.018
		45	49.2	0.8	42.0	8.8	10.80	4.81	1157.88	502.88	9.76	1.11	1.22	0.14	-0.287	0.007	0.251	0.112
		55	60.7	2.2	299.1	60.3	22.98	2.12	1081.23	69.69	50.26	2.57	0.27	0.01	-0.292	0.006	0.533	0.049

[416]

NaCl %	pH	Temperature (°C)	Ba		Bc		i_corr (μA.cm^{-2})		Rp (Ω)		Tafel constant		a		E_corr (V vs Ag/AgCl)		Corrosion Rate (mm.yr^{-1})	
			Average	*SD*	*Average*	*SD*	*Average*	*SD*	*Average*	*SD*	*Average*	*SD*	*Average*	*SD*	*Average*	*SD*	*Average*	*SD*
30	4	*25*	47.5	1.8	142.8	52.8	3.97	0.41	3634.27	380.32	15.31	1.93	0.51	0.06	-0.372	0.000	0.092	0.009
		35	51.4	1.3	87.5	4.4	5.10	0.41	3204.12	768.76	14.06	0.49	0.70	0.02	-0.378	0.002	0.118	0.009
		45	57.7	1.8	285.6	129.5	8.16	0.85	2512.75	317.69	20.38	2.04	0.58	0.06	-0.379	0.002	0.189	0.020
		55	118.4	17.7	197.6	138.2	8.81	1.04	2776.67	1485.96	63.97	28.09	0.25	0.14	-0.393	0.007	0.205	0.024
	7	*25*	54.3	3.3	303.5	120.6	2.97	1.05	6953.25	1922.99	45.50	5.33	0.17	0.02	-0.386	0.010	0.069	0.024
		35	52.1	7.8	178.8	87.9	5.00	0.59	3427.38	290.39	17.33	4.06	0.58	0.14	-0.379	0.000	0.116	0.014
		45	50.0	8.3	146.8	81.7	6.23	2.60	2692.22	297.93	15.89	4.27	0.77	0.19	-0.385	0.000	0.145	0.060
		55	46.5	9.7	131.5	69.4	6.15	1.03	2341.20	149.92	13.16	2.39	1.07	0.20	-0.396	0.007	0.134	0.020
	10	*25*	52.1	9.4	136.6	27.6	4.19	0.72	3879.16	408.23	16.06	1.37	0.49	0.04	-0.377	0.003	0.097	0.017
		35	60.5	10.6	161.0	99.9	4.42	0.84	4166.40	1052.61	18.20	4.97	0.57	0.16	-0.381	0.012	0.102	0.020
		45	45.2	3.3	88.7	92.0	5.03	0.34	2532.22	729.18	11.30	3.69	1.11	0.30	-0.382	0.006	0.117	0.008
		55	42.9	11.2	59.3	13.3	5.15	1.30	2371.58	379.52	24.10	2.92	0.58	0.07	-0.398	0.005	0.120	0.030

Appendix 6 – XRD Analysis Of The Patina In Different Volumes Of Sodium Chloride
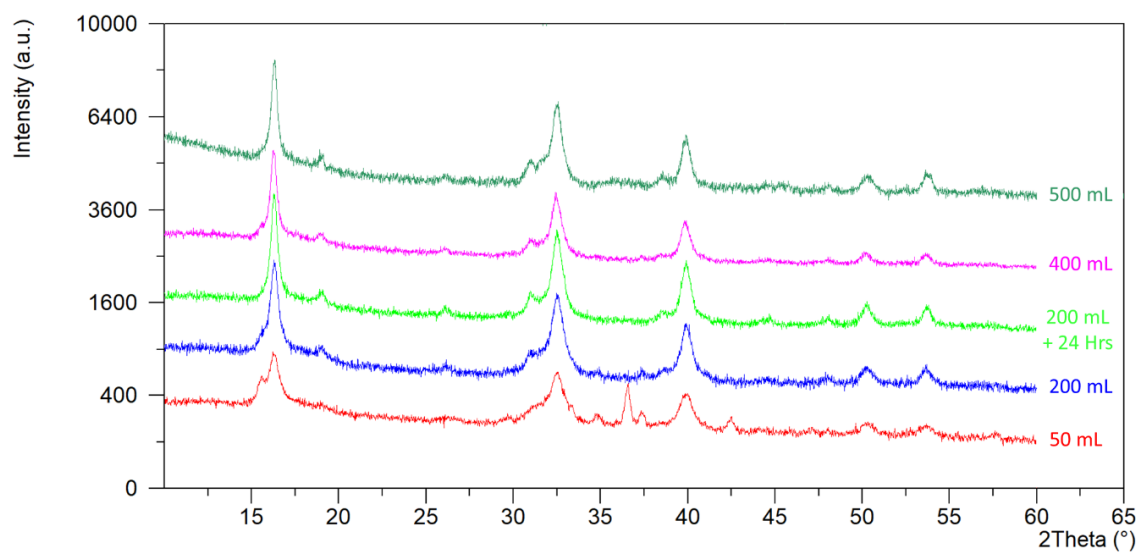
Figure 160 – XRD analysis showing the effect of electrolyte volume on copper when polarised at 500 mV vs Ag/AgCl.

Appendix 7 – XRD analysis of the Patina produced when polarising in different NaCl electrolytes
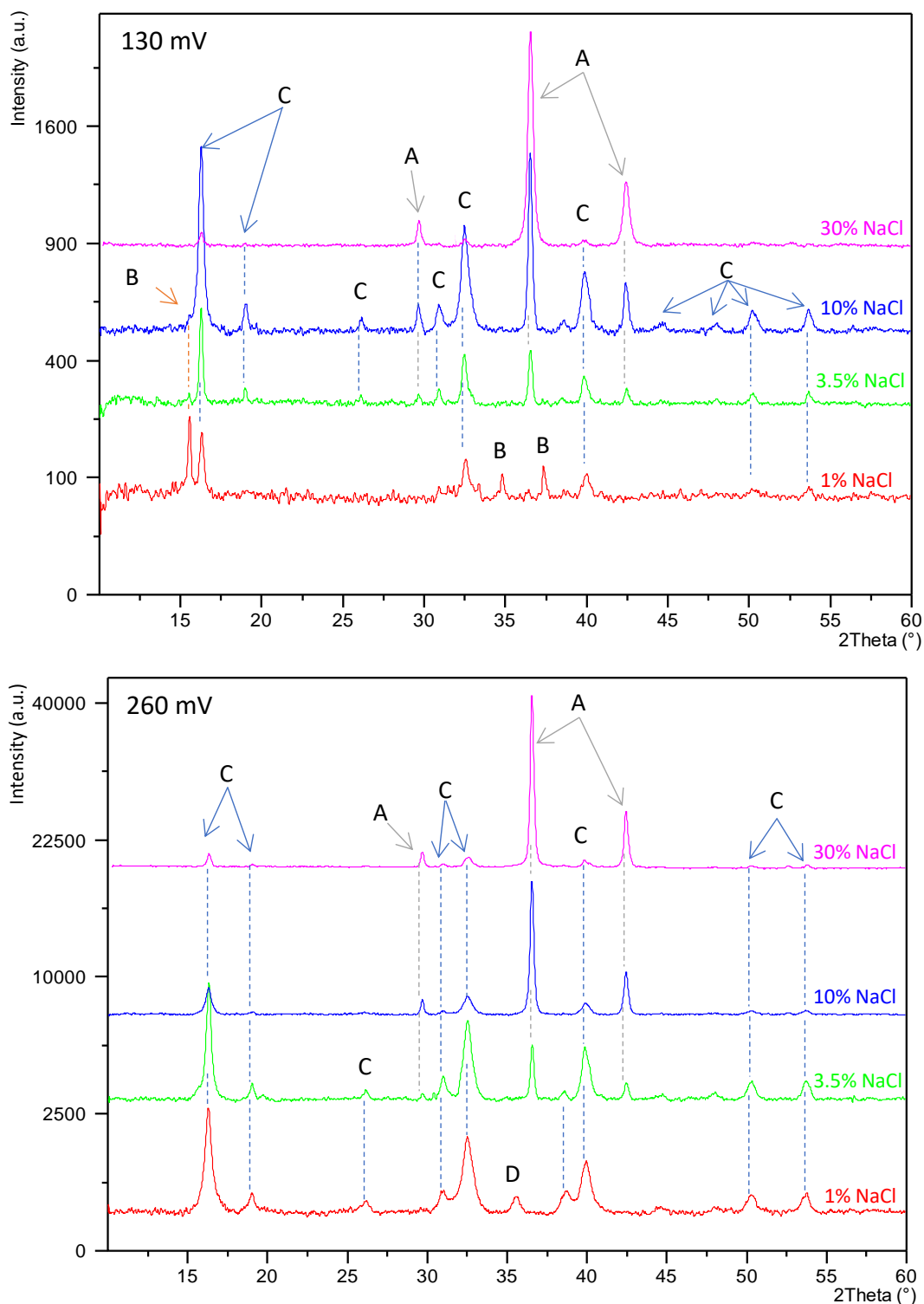
Figure 161 – Comparative XRD analysis of the compounds formed when polarising the copper electrode at 130 and 260 mV vs Ag/AgCl in a pH 7 electrolyte containing various concentrations of sodium chloride at 25 ℃. Peaks labelled A = Cuprite, B = Botallackite, C = Clinoatacamite and D=Tenorite.

Appendix 8 - XRD Patterns Following Immersion And Evaporation Testing

a) Cuprite
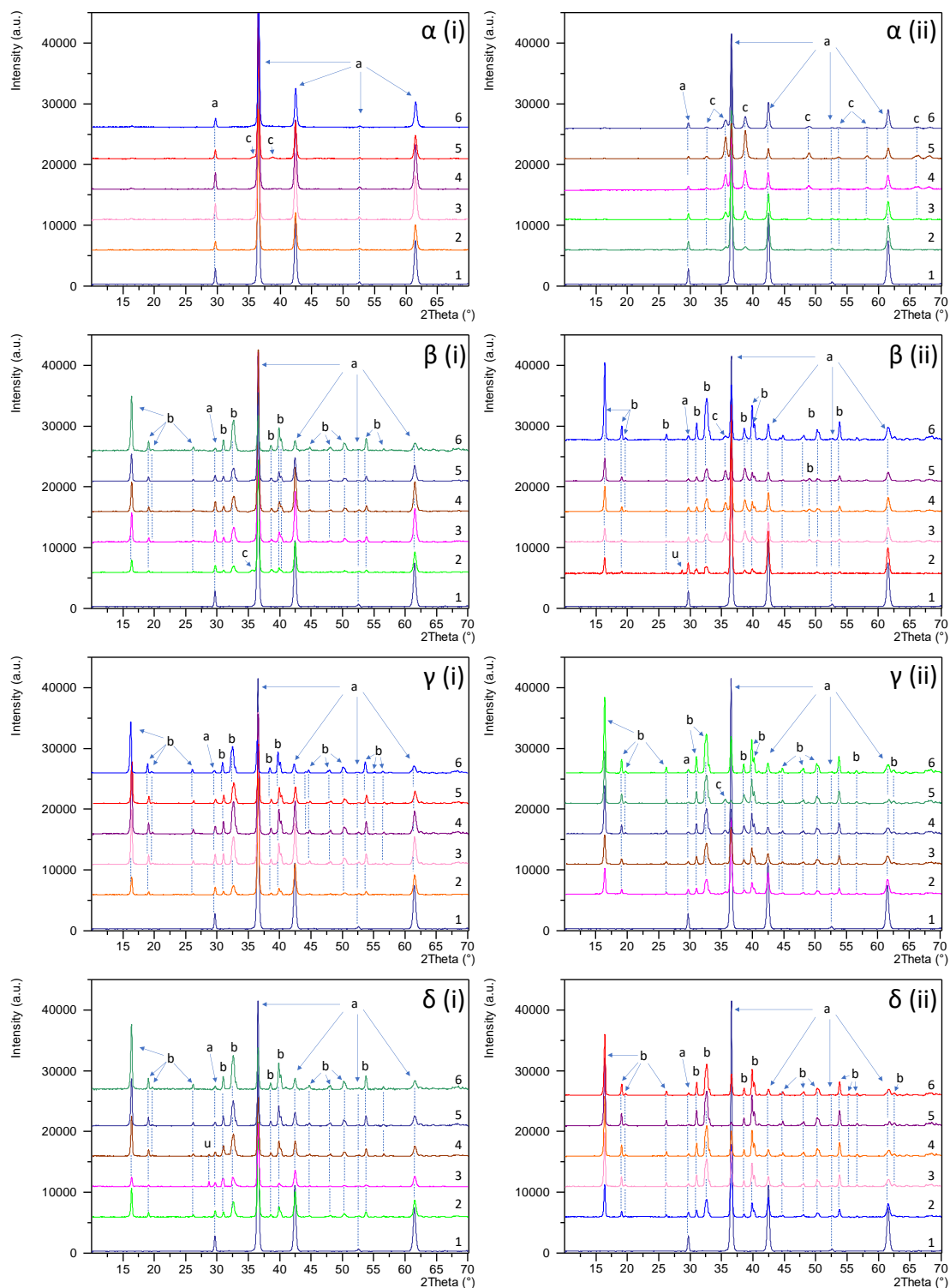
Figure 162 – XRD traces of Cu₂O following immersion periods of 1 = 0 hrs, 2 = 168hrs, 3 = 336 hrs, 4 = 504hrs, 5 = 672hrs and 6 = 672 hours while being exposed to α = 0%, β = 1%, γ = 3.5%, δ = 10% and ε = 30% NaCl at 25℃ (i) and 45℃ (ii) respectively. The peak labels are identified as a= Cuprite, b = Clinoatacamite, c = Tenorite and u = unidentified peak

b) Copper Coupon – 2-Theta XRD

Figure 163 – Glancing angle XRD traces of copper sheet samples following immersion periods of 1 = 0 hrs, 2 = 168hrs, 3 = 336 hrs, 4 = 504hrs, 5 = 672hrs and 6 = 672 hours while being exposed to α = 0%, β = 1%, γ = 3.5%, δ = 10% and ε = 30% NaCl at 25℃ (i) and 45℃ (ii), respectively. The peak labels are identified as a = Copper, b = Cuprite, c = Clinoatacamite, d = Sodium chloride and s = Copper Kβ peak

c) Copper Coupon – Gonio XRD
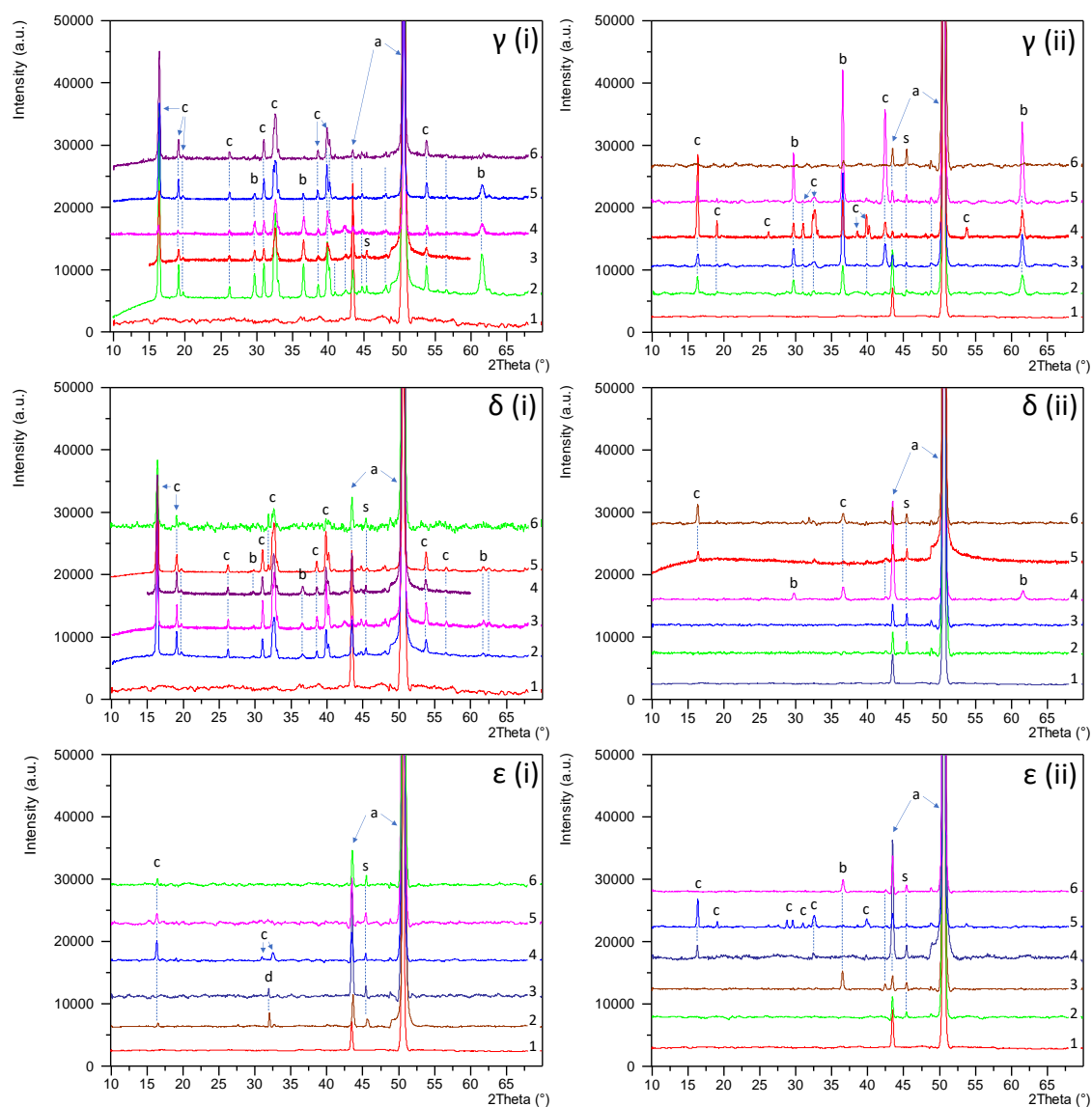
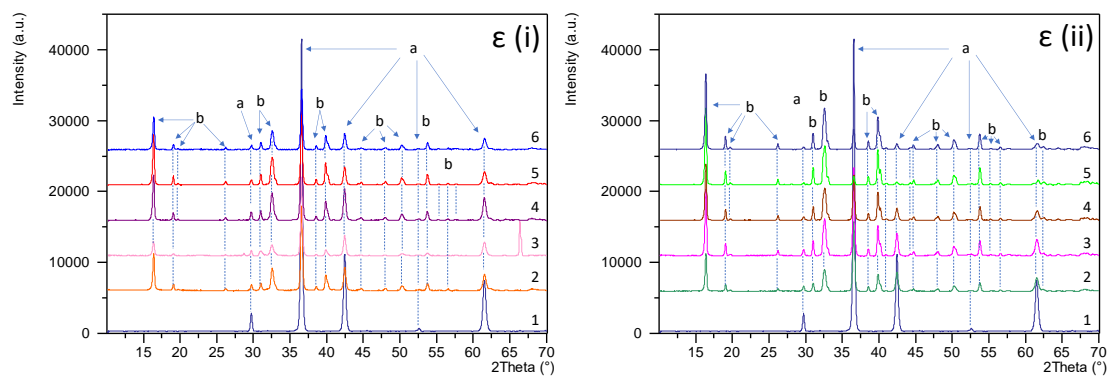*Figure 164 – Gonio XRD traces of copper sheet samples following immersion periods of 1 = 0 hrs, 2 = 168hrs, 3 = 336 hrs, 4 = 504hrs, 5 = 672hrs and 6 = 672 hours while being exposed to a = 0%, b = 1%, c = 3.5%, d = 10% and e = 30% NaCl at 25℃ (i) and 45℃ (ii) respectively. The peak labels are identified as a = Copper, b = Cuprite, c = Clinoatacamite, d = Sodium chloride and s = Copper Kβ peak*
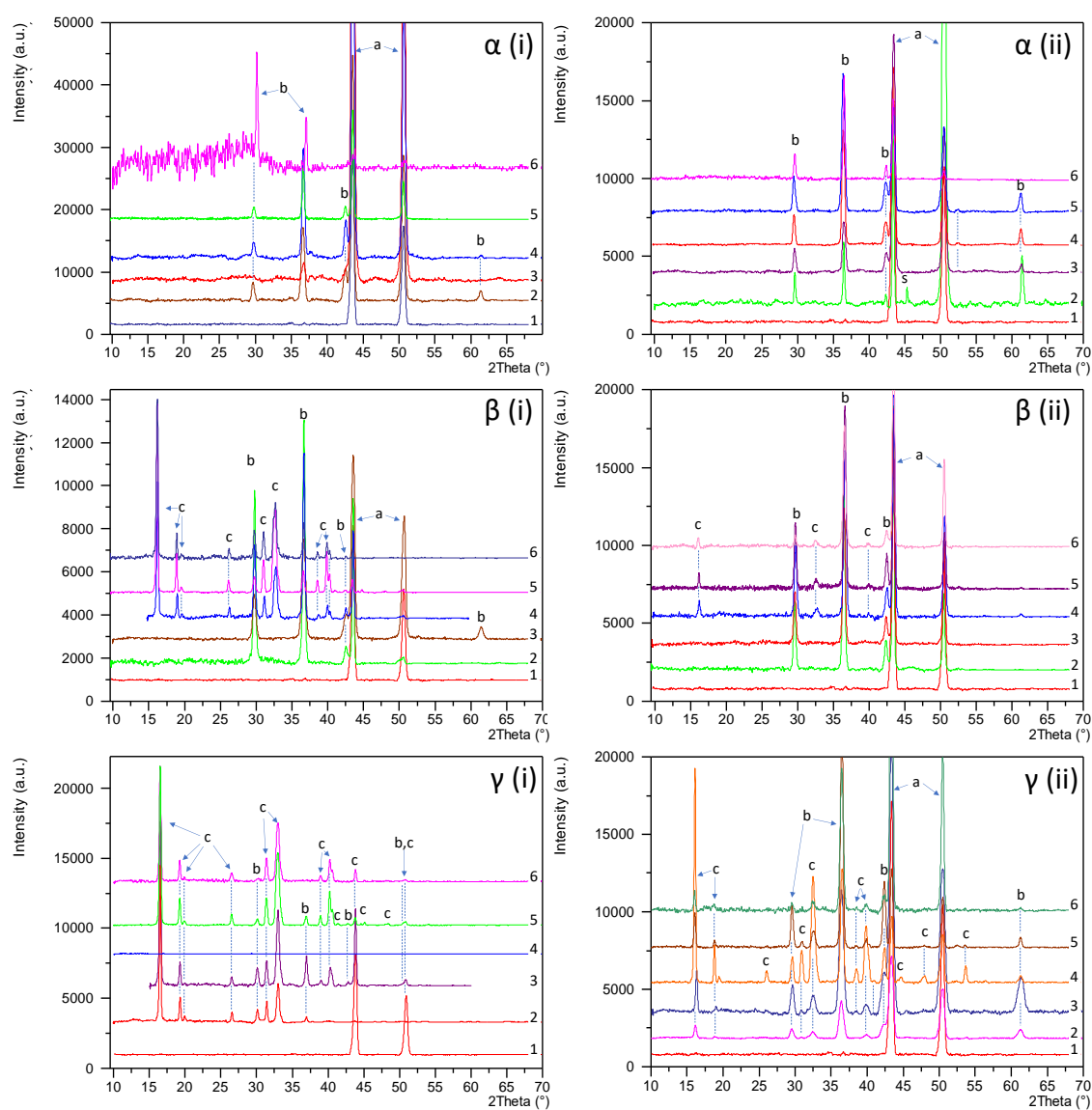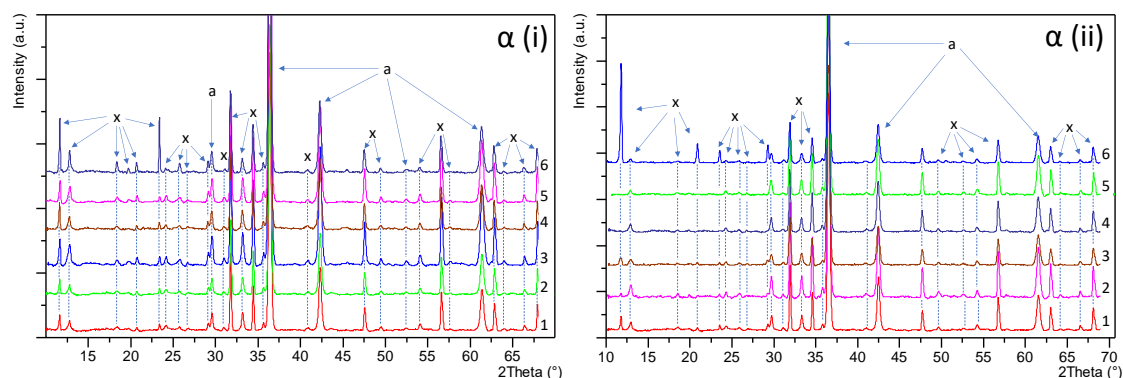
d) BQA 644

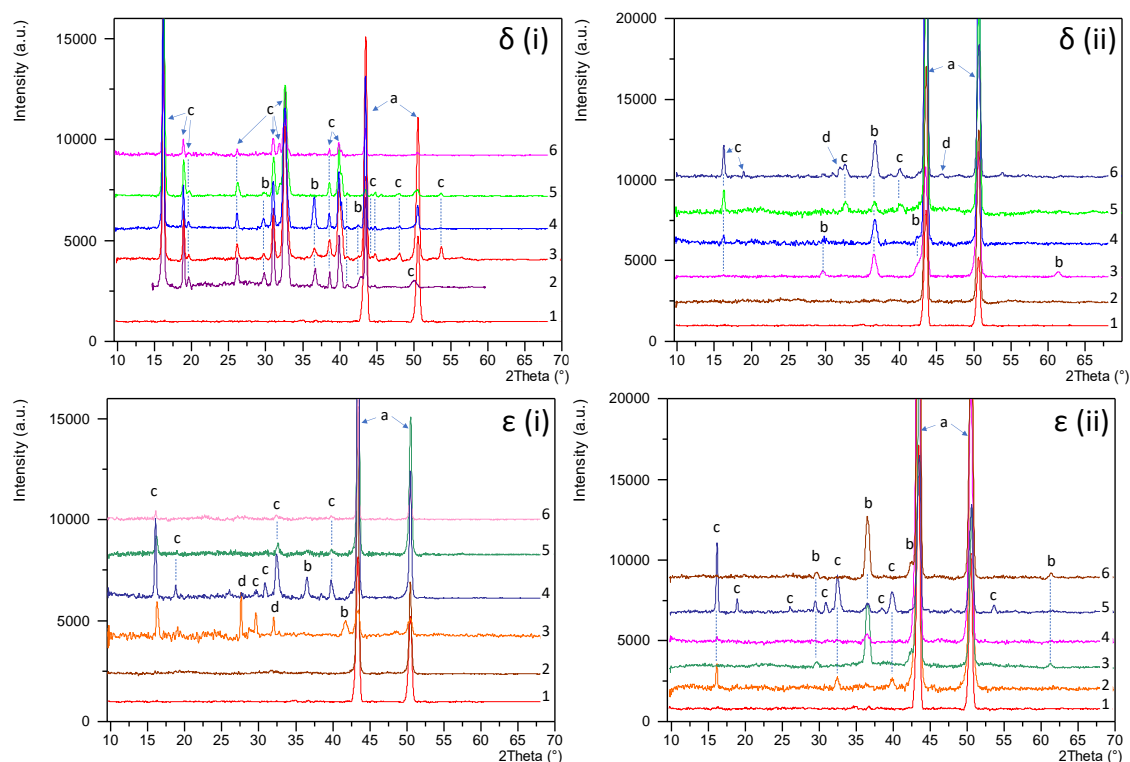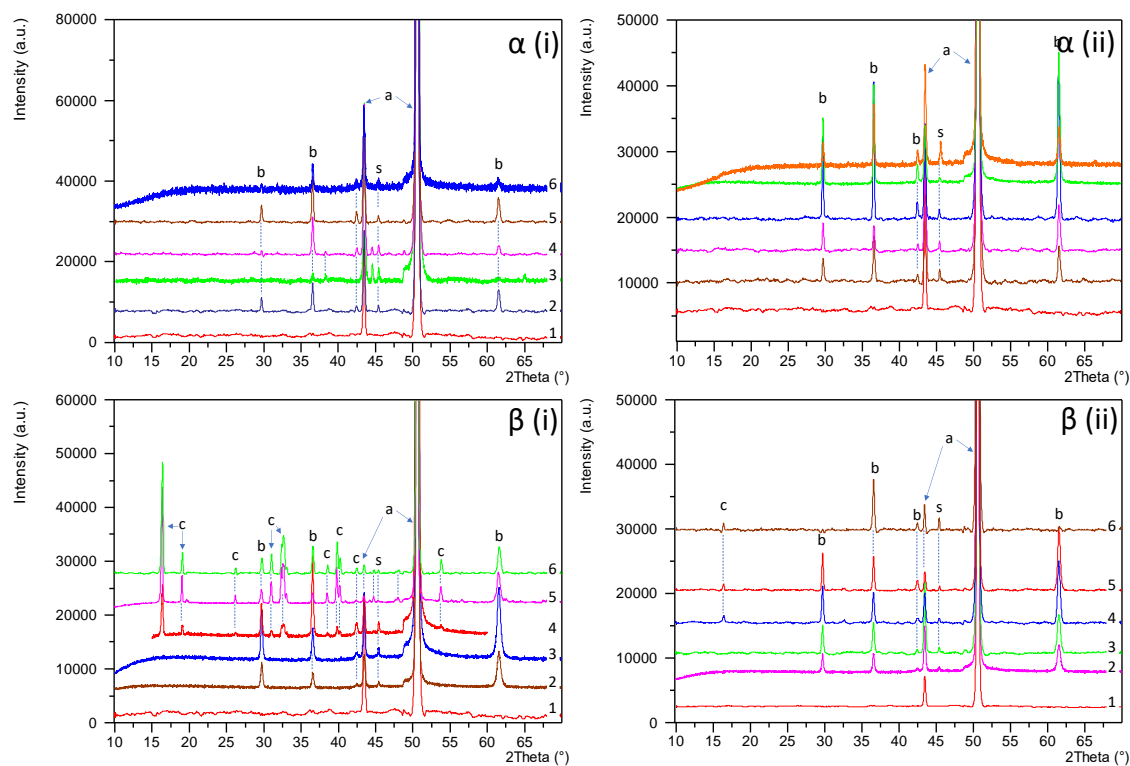Figure 165 – XRD traces of BQA 644 coated sample following immersion periods of 1 = 0 hrs, 2 = 168hrs, 3 = 336 hrs, 4 = 504hrs, 5 = 672hrs and 6 = 672 hours while being exposed to α = 0%, β = 1%, γ = 3.5%, δ = 10% and ε = 30% NaCl at 25℃ (i) and 45℃ (ii) respectively. The peak labels are identified as a= Cuprite, b = Clinoatacamite, c = Botallackite and x = paint pigment

[424]

e) Modified BQA 644

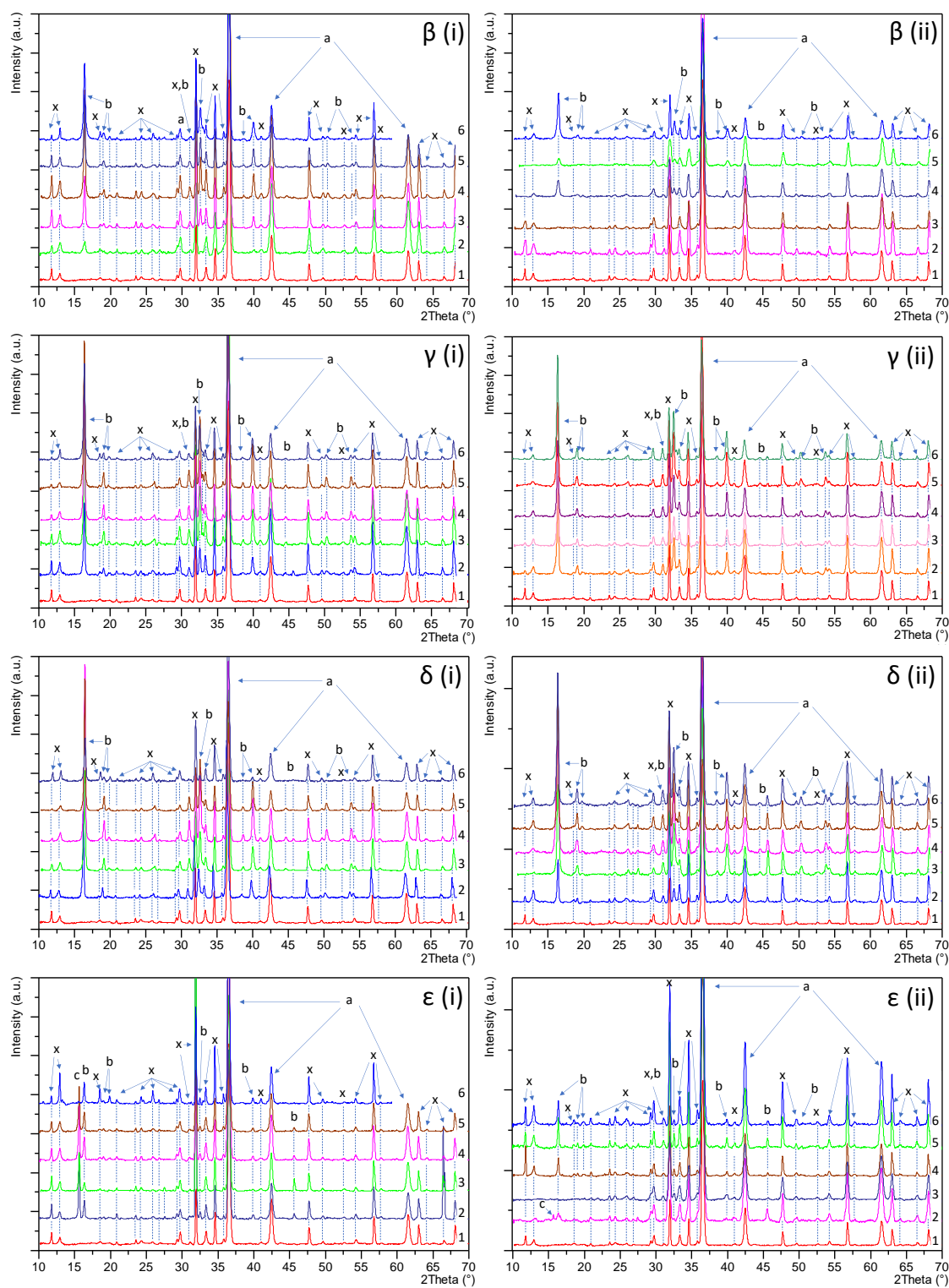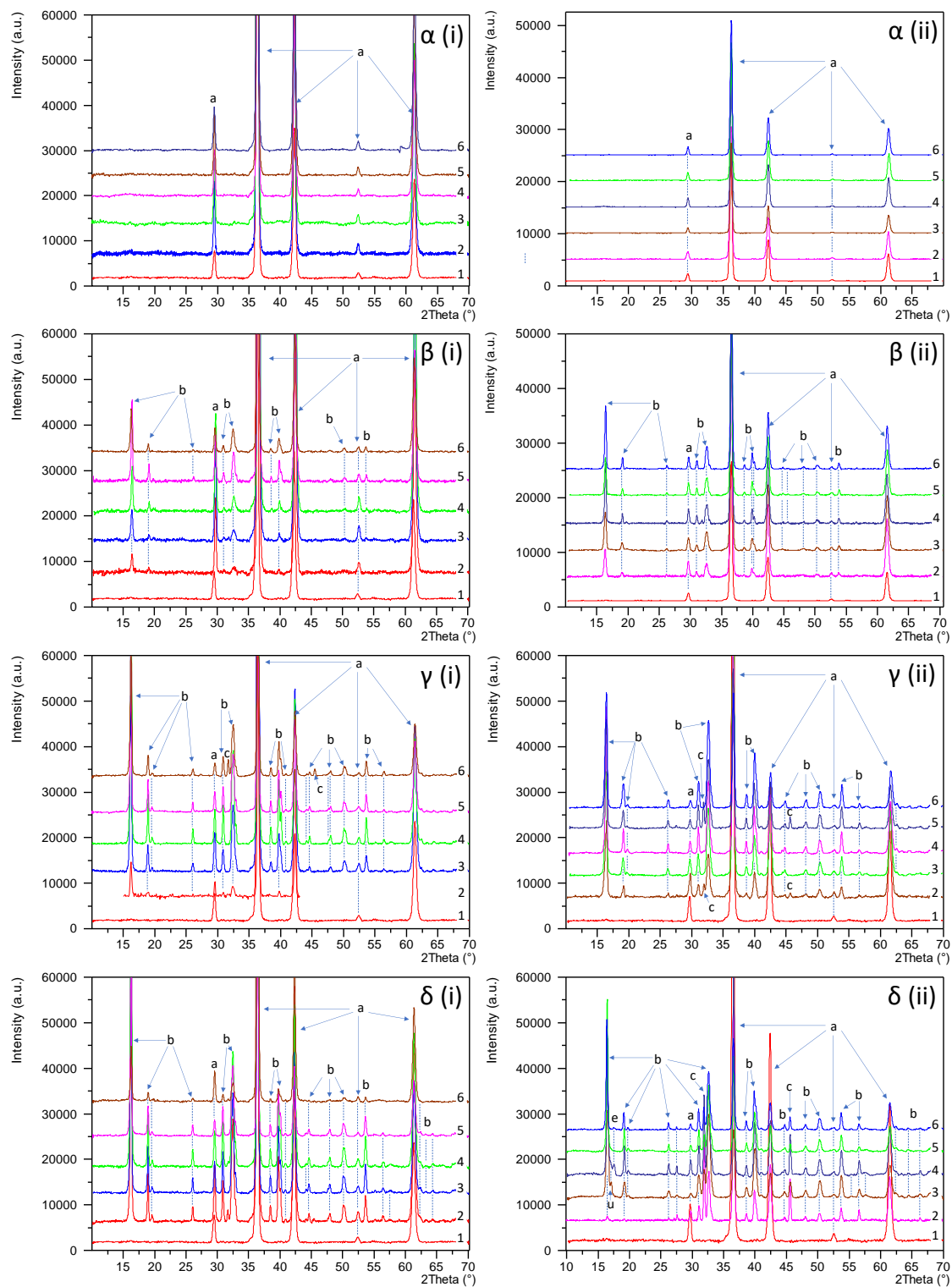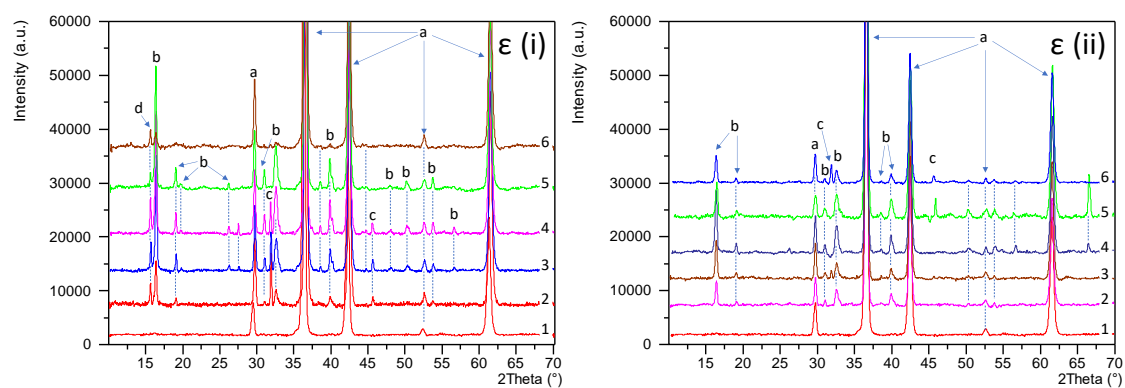*Figure 166 – XRD traces of the modified BQA 644 coating following immersion periods of 1 = 0 hrs, 2 = 168hrs, 3 = 336 hrs, 4 = 504hrs, 5 = 672hrs and 6 = 672 hours while being exposed to α = 0%, β = 1%, γ = 3.5%, δ = 10% and ε = 30% NaCl at 25℃ (i) and 45℃ (ii) respectively. The peak labels are identified as a = Cuprite, b = Clinoatacamite, c = Sodium Chloride, d = Botallackite, e = Atacamite and u = Unidentified*

Appendix 9 – Patination Cell Measurements

a) Rate Of Evaporation

The rate of evaporation of each test cells was recorded by measuring the daily mass loss of the water in the cell. As the electrolyte evaporated the amount of sodium chloride remained constant while the volume of water reduced. This increased the relative concentration of the electrolytes until it reached a saturation point, which at 25°C was 36% and at 45°C was 36.5% (Standnes, 2020). At the saturation point sodium chloride can no longer be dissolved into the electrolyte resulting in the formation of salt crystals which continue to form and grow until either the water evaporated or 672 hours, which ever came first. Each of the sodium chloride containing electrolyte reached the saturation point prior to the end of the experiment however it was achieved much more quickly at 45°C when compared to 25°C. Figure 167 a [i] and [ii] shows the change in sodium chloride concentration in the electrolyte as it was evaporated at 25°C and 45°C respectively. At both temperatures, the electrolytes followed a similar trend with the 1% electrolyte taking the longest to reach the saturation point followed by the 3.5%, 10% and 30% electrolytes. This pattern was to be expected due to the relative initial concentration of the electrolytes where approximately 12 mL of water needed to be evaporated for the 30% electrolyte to reach the saturation point, whereas approximately 77 mL was needed to be evaporated in the 1% electrolyte.

A high initial mass loss was recorded in each of the electrolytes within approximately the first 170 hours of immersion at 25°C (Figure 167 c[i]) and the first 100 hours in the electrolytes at 45°C (Figure 167 c[ii], after which the mass loss tended to stabilised at lower values. Furthermore, at both temperatures the electrolytes followed a similar trend with the highest mass loss being recorded in the 0% electrolyte followed by 1%, 3.5%, 10% and 30%. However, the mass loss at 45°C was higher and less stable than that found at 25°C.
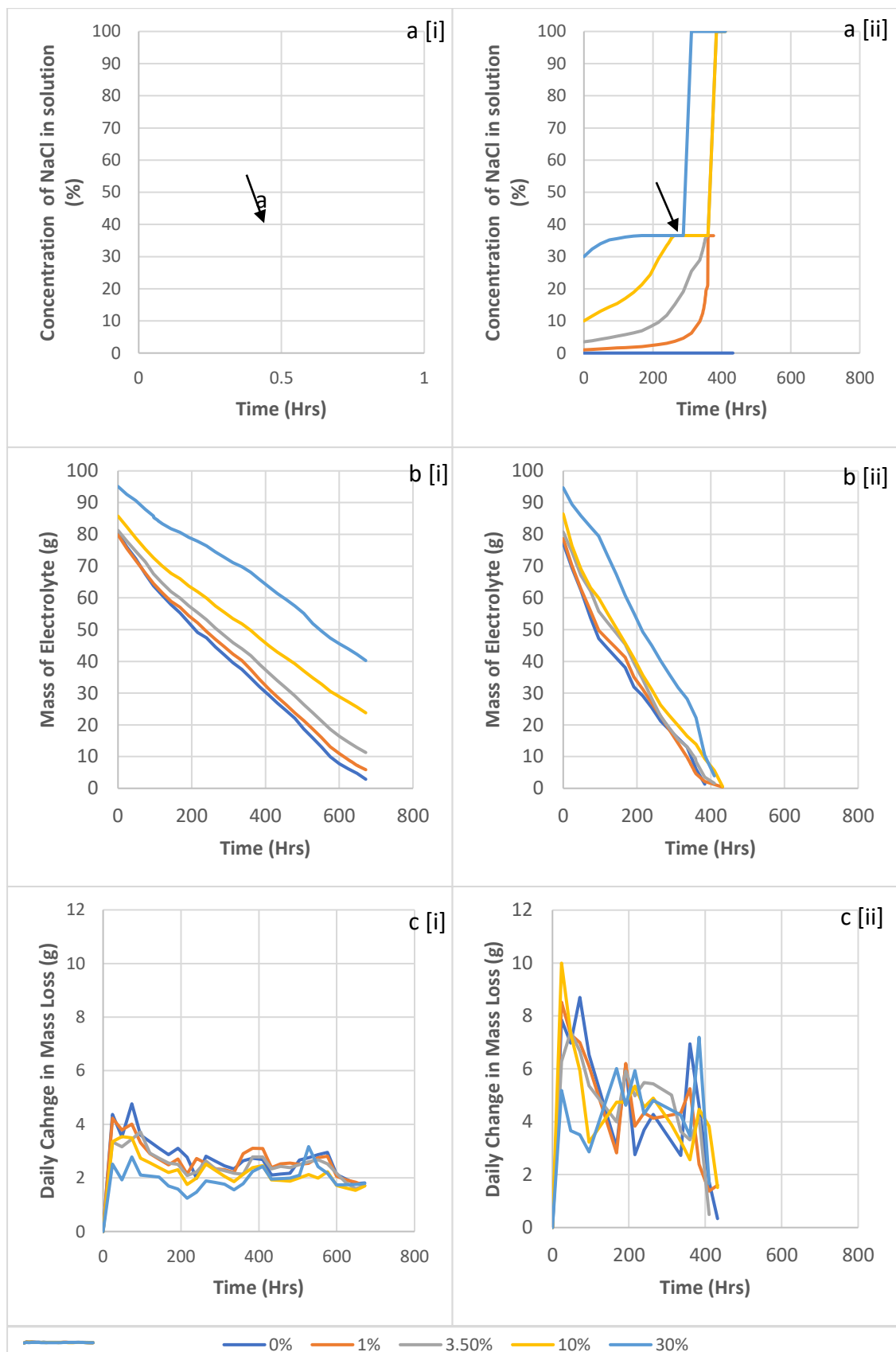
[427]

Figure - Average data recorded from the evaporating corrosion test cells shown a) the increase in NaCl concentration as it evaporates, b) the mass of the evaporation test cell following evaporation and c) the daily mass loss at 25°C (i) and 45°C (ii). The black arrow indicates the saturation point of sodium chloride at the respective temperatures.

[428]

b) pH Measurement

i) Immersion Test Cell

To maintain a constant pH 7 throughout the immersion testing it was regularly monitored and modified using the Hanna Edge pH meter and dilute sodium hydroxide and hydrochloric acid solutions. At each measurement period and temperature, it was found that the presence of sodium chloride in the electrolyte resulted in the increase in its alkalinity. The largest increase was recorded in the test cells containing the cuprite powder followed by the modified BQA 644, the BQA 644 coating and the copper coupon (Figure 168a and b).

When measuring the immersion cell containing the cuprite powder at 25°C the pH reached a similar level regardless of sodium chloride concentration of between 9.34 ± 0.09 and 9.47 ± 0.13. However, at 45°C the pH of the electrolytes was less consistent with a peak in alkalinity being recorded in the 3.5% electrolyte at 9.71 ± 0.35. At higher sodium chloride concentrations, the increase in alkalinity was to a lesser extent of 9.61 ± 0.36 and 9.35 ± 0.57 for the 10% and 30% electrolytes, respectively.

An increase in alkalinity was also observed for the BQA 644 and the modified BQA 644 coatings, peaking in the 10% electrolyte at 25°C 7.87 ± 0.08 and 8.43 ± 0.33, respectively. At 30% the increase in alkalinity was to a lesser extent of 7.66 ± 0.25 and 7.62 ± 0.54, respectively. This trend was also observed for the BQA 644 antifouling coating containing only the cuprite biocidal pigment at 45°C with the highest pH being recorded in the 10% electrolyte at 8.18 ± 0.72. However, for the BQA 644 antifouling coating at 45°C and copper coupons at 25°C and 45°C the electrolyte became more alkaline with increasing sodium chloride concentrations up to 30%
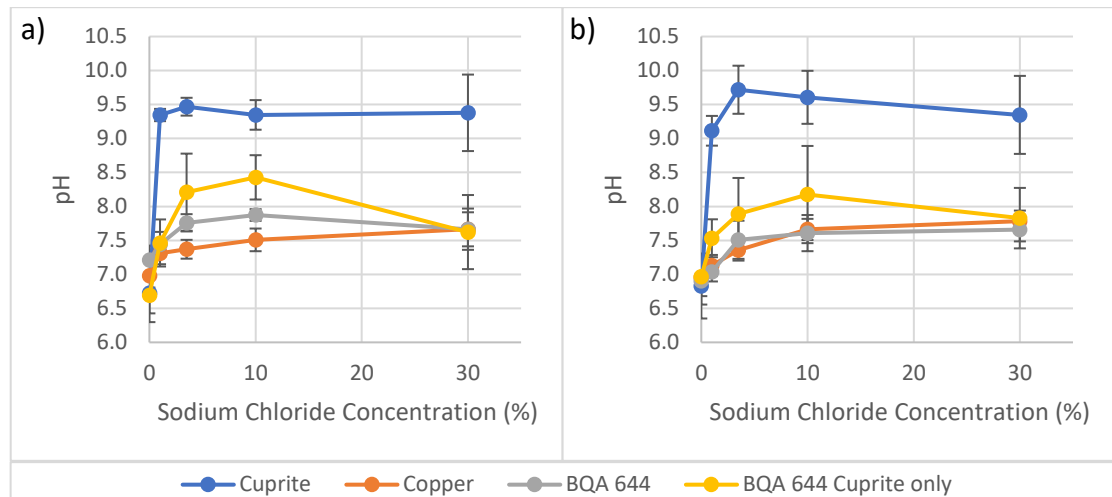
Figure 168 – Chart plotting the average change in pH when exposing cuprite powder, copper coupon, antifouling coatings BQA 644 and Modified BQA 644 to a neutral electrolyte containing 0%, 1%, 3.5%, 10% and 30% NaCl at a) 25℃ and b) 45℃

ii)   pH In The Evaporation Test Cell

The pH of the evaporation test cells was measured at regular periods throughout the experimental period until the volume of the electrolyte was too low for the pH electrode to measure to observe how the pH changes with time (Figure 169). The pH of the test cells that containing the 0% electrolyte remained neutral throughout the evaporation period, being unaffected by the sample they contained. When the electrolytes contained sodium chloride their pH tended to shift towards progressively higher alkaline values over time.

In the test cells containing the cuprite powder the highest increase in alkaline was recorded of between 9.4 and 9.64 at 25°C (Figure 169 a[i]) and between 9.32 and 10.43 at 45 (Figure 169 a[ii]) within the first 24 hours. Small changes in the alkalinity were measured where after 264 hours the pH of the electrolyte drifted closer together with the pH at 25°C of 9.41-9.48 and at 45°C pH values of 9.01 and 9.84 were recorded.

The pH of the 10% electrolyte was either the most alkaline (Figure 169 b [i], b[ii]), c[i], c[ii] and d[i]) or second most alkaline (Figure 169 a[i] and a[ii]) followed by the 3.5% and/or 30% electrolytes with the 1% electrolyte generally resulting in the lowest increase in alkalinity over time.

[430]
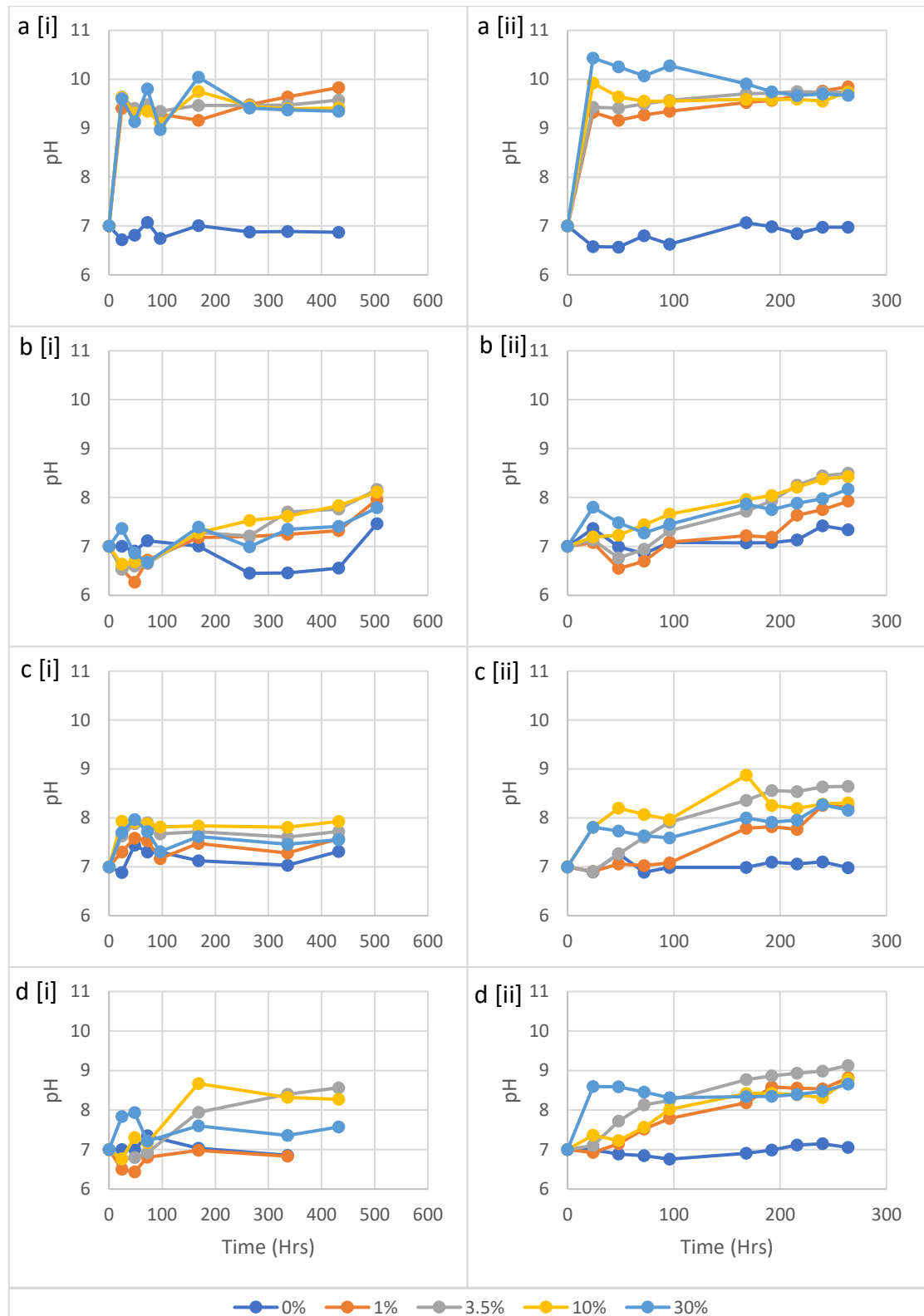
Figure 169 – Charts showing the change in pH during the evaporation of the 0%, 1%, 3.5%, 10% and 30% NaCl electrolytes containing a) cuprite powder, b) copper coupon, c) BQA 644 coating and d) modified BQA 644 coating at [i] 25℃ and [ii] 45℃.

Appendix 10 – Coating SEM Analysis

a) Surface

Particle Roundness and Sphericity

Figure 170 – Particle roundness and sphericity classification following microscopic evaluation, retrieved from (Ulusoy, 2019)

i) BQA 644 – Immersion – 25°C

   a. *0% Electrolyte*
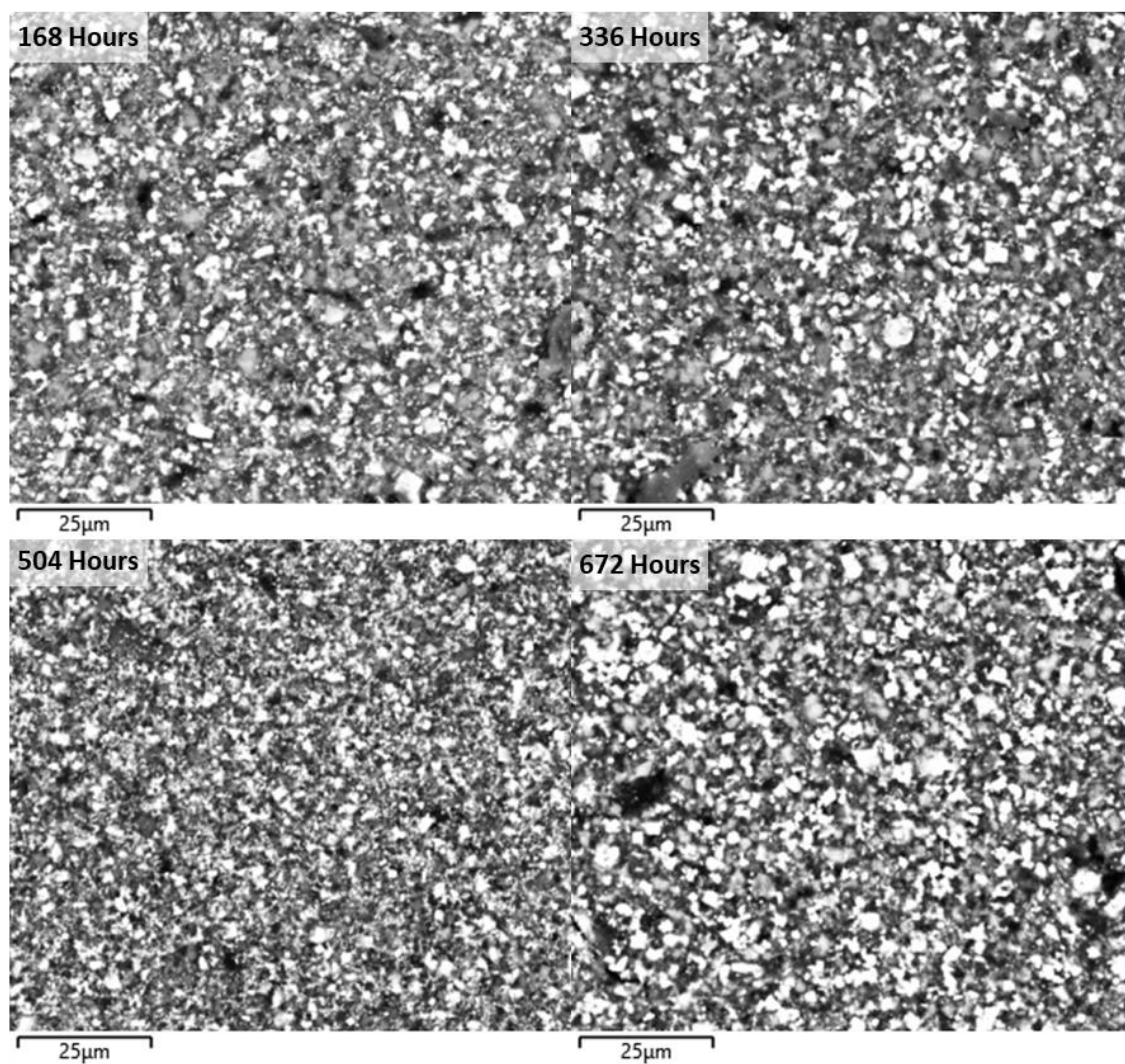
Spectrum	Element (wt%)							
Label	O	Al	Si	S	Ca	Fe	Cu	Zn
168 Hours	19.38	0.41	3.45	8.10	0.26	6.45	34.25	27.71
336 Hours	17.72	0.57	3.64	8.73	0.44	6.80	37.71	24.39
504 Hours	18.83	0.57	3.14	7.65	1.27	5.63	31.18	31.74
672 Hours	19.82	0.73	3.27	9.61	0.54	6.63	36.35	23.04

Figure 171 – BSE micrographs and semi-quantitative EDX analysis of the surface of the BQA 644 coating exposed to the neutral 0% electrolyte at 25°C under different immersion times.
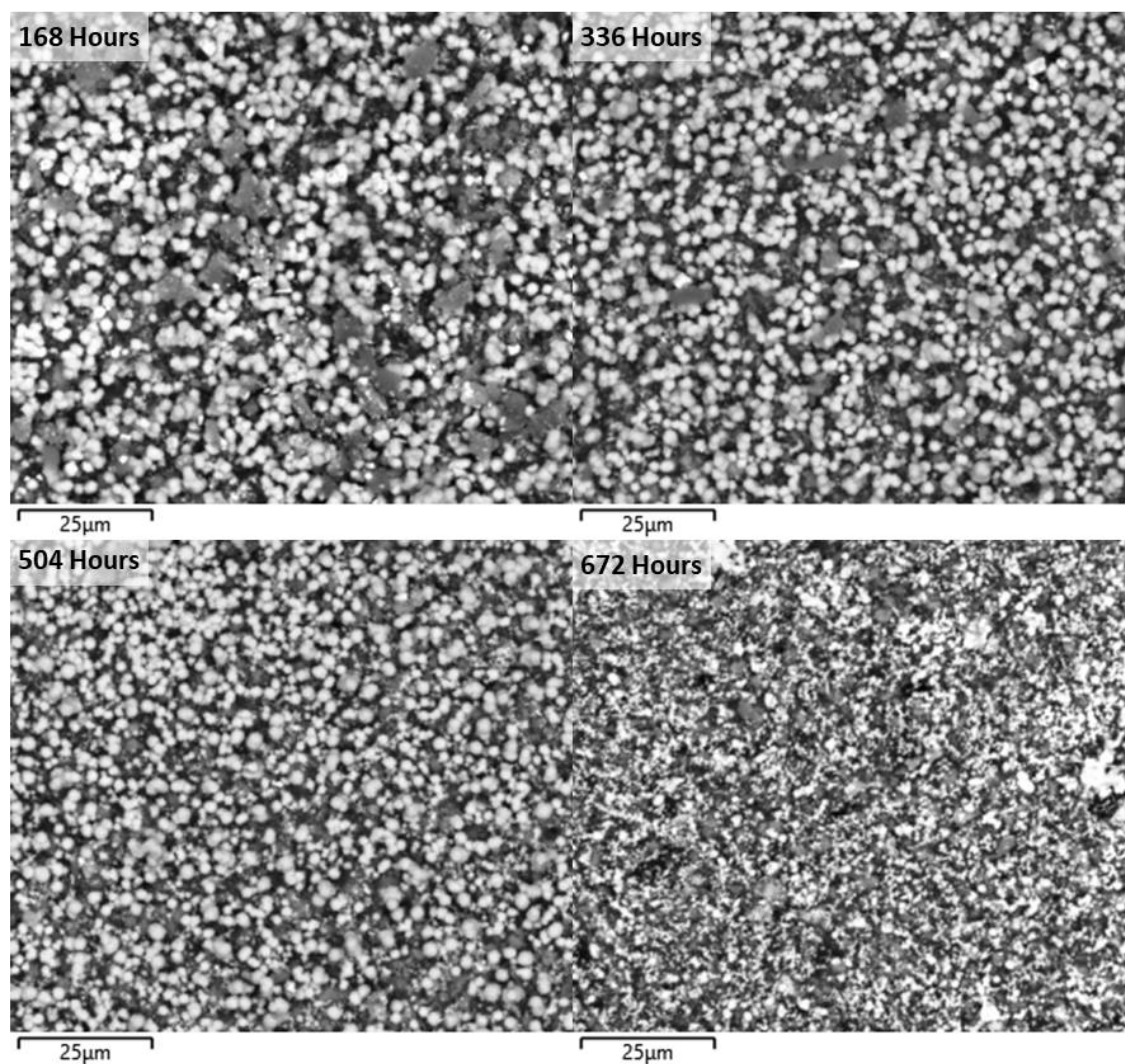
Spectrum	Element (wt%)								
Label	O	Al	Si	S	Cl	Ca	Fe	Cu	Zn
168 Hours	36.30	0.46	2.45	4.57	6.23	1.40	4.26	30.71	13.62
336 Hours	22.36	0.19	1.03	3.89	9.85	0.11	4.28	38.41	19.89
504 Hours	23.82	0.15	1.58	4.58	8.87	0.20	4.30	35.78	20.72
672 Hours	26.32	0.61	2.81	7.97	4.44	0.17	5.79	29.74	22.15

Figure 172 – BSE micrographs and semi-quantitative EDX analysis of the surface of the BQA 644 coating exposed to the neutral 1% electrolyte at 25°C under different immersion times.

Spectrum Label	Element (wt%)								
	O	Al	Si	S	Cl	Ca	Fe	Cu	Zn
168 Hours	22.80	0.23	1.20	4.13	9.55	0.13	4.36	35.09	22.50
336 Hours	20.52	0.06	0.67	4.52	9.88	0.04	4.10	37.92	22.30
504 Hours	20.77	0.11	0.57	2.46	11.74	0.18	3.70	42.42	18.06
672 Hours	18.83	0.09	0.27	1.30	12.58	0.02	2.74	48.47	15.70

Figure 173 – BSE micrographs and semi-quantitative EDX analysis of the surface of the BQA 644 coating exposed to the neutral 3.5% electrolyte at 25°C under different immersion times.

Spectrum Label	Element (wt%)								
	O	Al	Si	S	Cl	Ca	Fe	Cu	Zn
168 Hours	23.30	0.22	0.64	4.21	12.29	0.07	4.58	38.54	16.15
336 Hours	20.41	0.08	0.17	0.59	14.77	0.00	1.51	52.95	9.52
504 Hours	22.72	0.09	0.07	0.35	14.98	0.16	1.13	52.21	8.29
672 Hours	21.35	0.08	0.40	1.57	14.94	0.28	2.22	46.38	12.79

Figure 174 – BSE micrographs and semi-quantitative EDX analysis of the surface of the BQA 644 coating exposed to the neutral 10% electrolyte at 25°C under different immersion times.

e. 30% Electrolyte

Spectrum Label	Element (wt%)									
	O	Na	Al	Si	S	Cl	Ca	Fe	Cu	Zn
168 Hours	22.99	8.25	0.68	2.63	7.85	8.94	0.42	6.24	21.05	20.95
336 Hours	15.37	19.25	0.18	1.02	3.53	25.41	0.23	3.28	19.97	11.76
504 Hours	19.46	5.32	0.54	2.61	7.55	7.08	0.38	7.52	27.52	22.01
672 Hours	19.65	16.39	0.20	1.25	4.21	21.24	0.57	3.62	21.22	11.65

Figure 175 – BSE micrographs and semi-quantitative EDX analysis of the surface of the BQA 644 coating exposed to the neutral 30% electrolyte at 25°C under different immersion times.

ii) BQA 644 – Immersion – 45°C

    a. *0% Electrolyte*
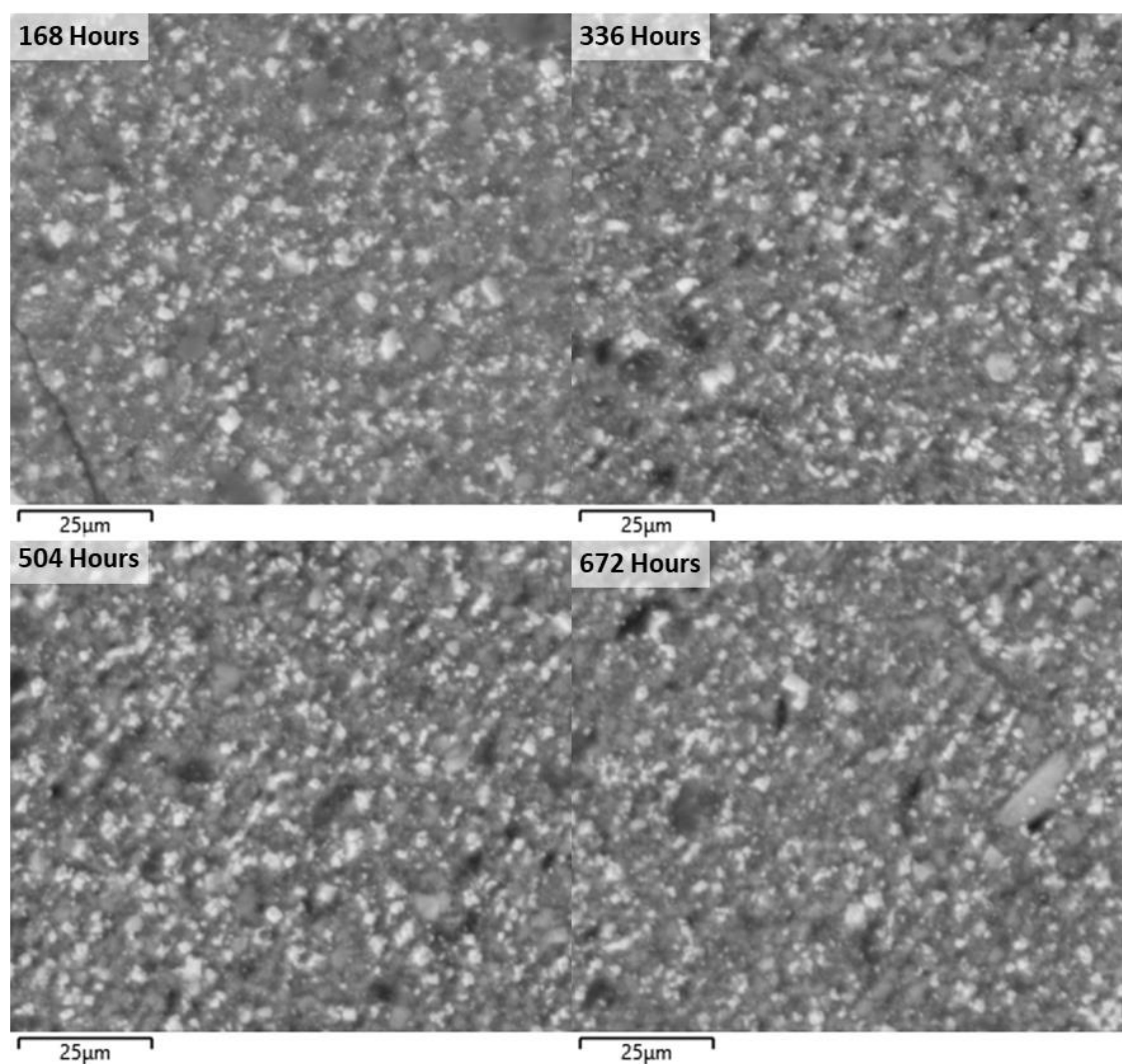
Spectrum	Element (wt%)							
Label	O	Al	Si	S	Ca	Fe	Cu	Zn
168 Hours	19.69	0.66	3.28	8.04	0.63	5.97	35.63	26.09
336 Hours	18.60	0.91	3.86	8.28	0.43	6.84	36.19	24.88
504 Hours	16.09	0.63	3.35	9.07	0.48	6.93	38.74	24.72
672 Hours	21.88	0.59	3.72	9.76	0.34	7.48	34.66	21.57

Figure 176 – BSE micrographs and semi-quantitative EDX analysis of the surface of the BQA 644 coating exposed to the neutral 0% electrolyte at 45°C under different immersion times.

b.   1% Electrolyte
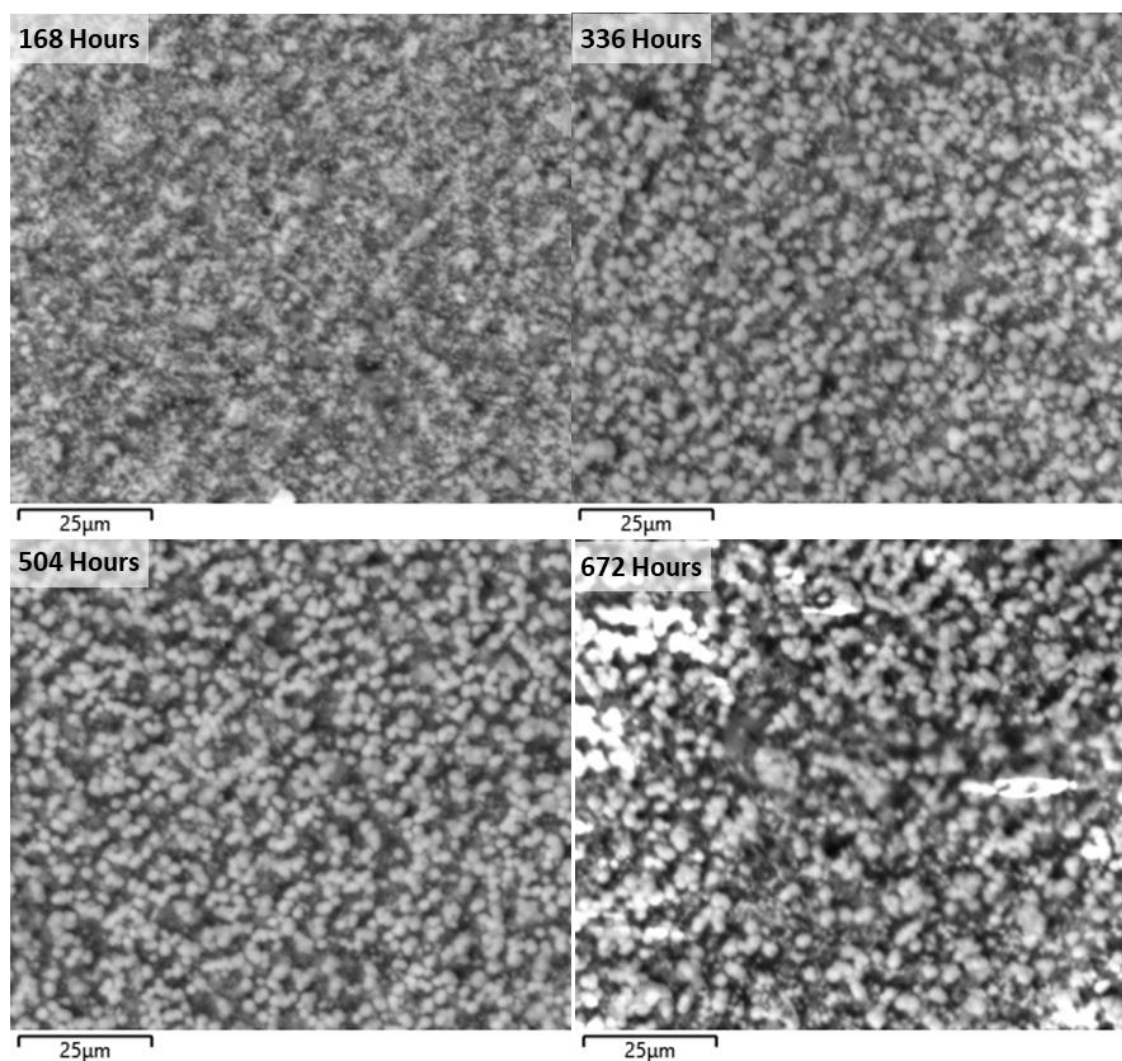
Spectrum	Element (wt%)								
Label	O	Al	Si	S	Cl	Ca	Fe	Cu	Zn
168 Hours	22.95	0.40	2.45	6.61	4.64	0.27	6.37	33.18	23.12
336 Hours	24.56	0.30	1.56	5.36	8.64	0.26	5.01	33.69	20.62
504 Hours	22.63	0.16	1.10	4.14	10.22	0.14	4.28	37.82	19.51
672 Hours	25.29	0.19	1.04	4.41	13.99	0.20	4.16	35.44	15.28

Figure 177 – BSE micrographs and semi-quantitative EDX analysis of the surface of the BQA 644 coating exposed to the neutral1% electrolyte at 45°C under different immersion times.

c.   3.5% Electrolyte
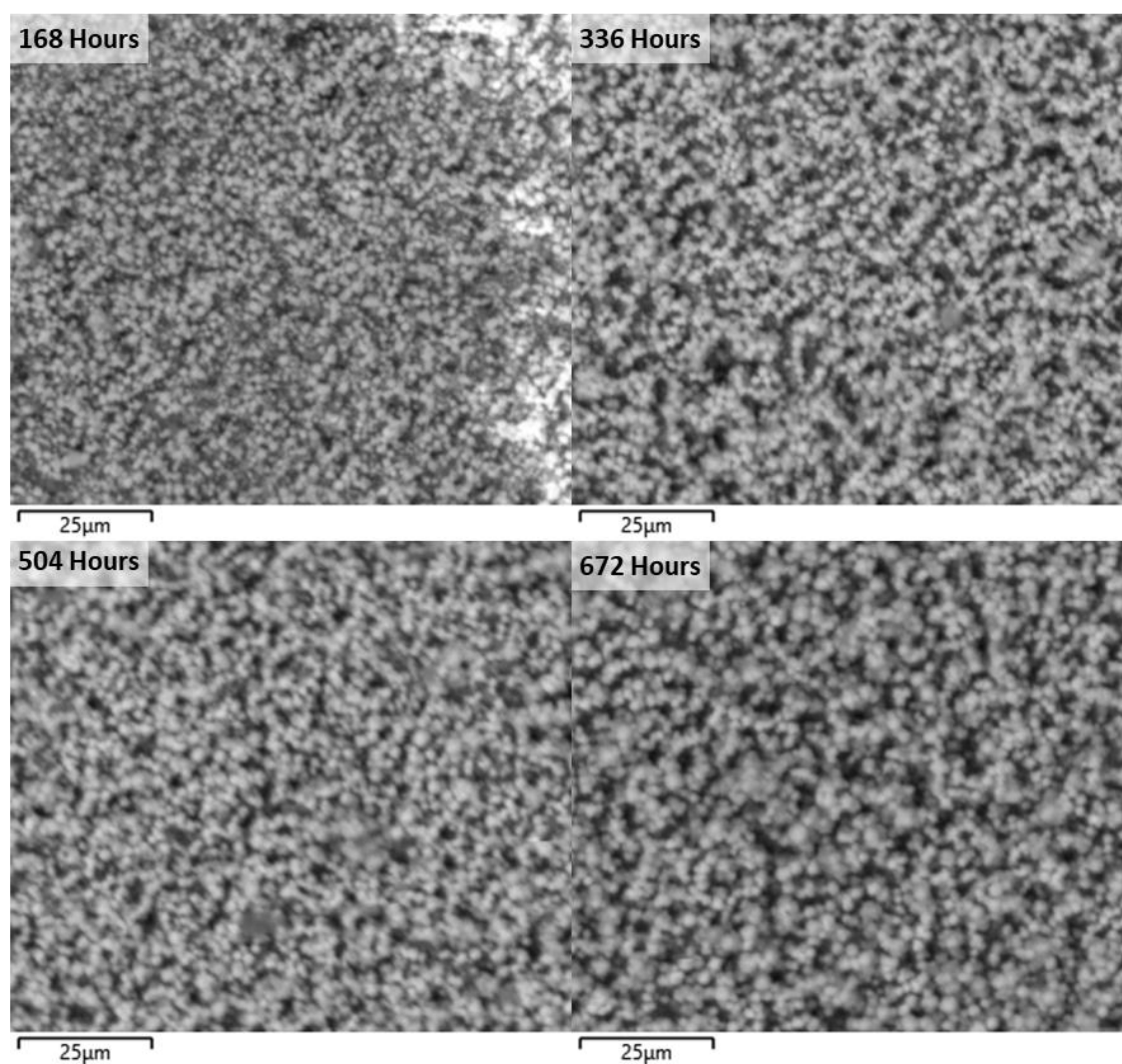
Spectrum	Element (wt%)								
Label	O	Al	Si	S	Cl	Ca	Fe	Cu	Zn
168 Hours	25.44	0.36	1.50	4.85	8.69	0.11	4.90	31.65	22.51
336 Hours	21.04	0.11	0.49	2.39	11.48	0.14	3.56	42.85	17.93
504 Hours	20.60	0.08	0.40	2.00	12.55	0.04	3.00	45.82	15.51
672 Hours	18.88	0.09	0.20	1.27	12.61	0.03	2.68	49.00	15.25

Figure 178 – BSE micrographs and semi-quantitative EDX analysis of the surface of the BQA 644 coating exposed to the neutral3.5% electrolyte at 45°C under different immersion times.
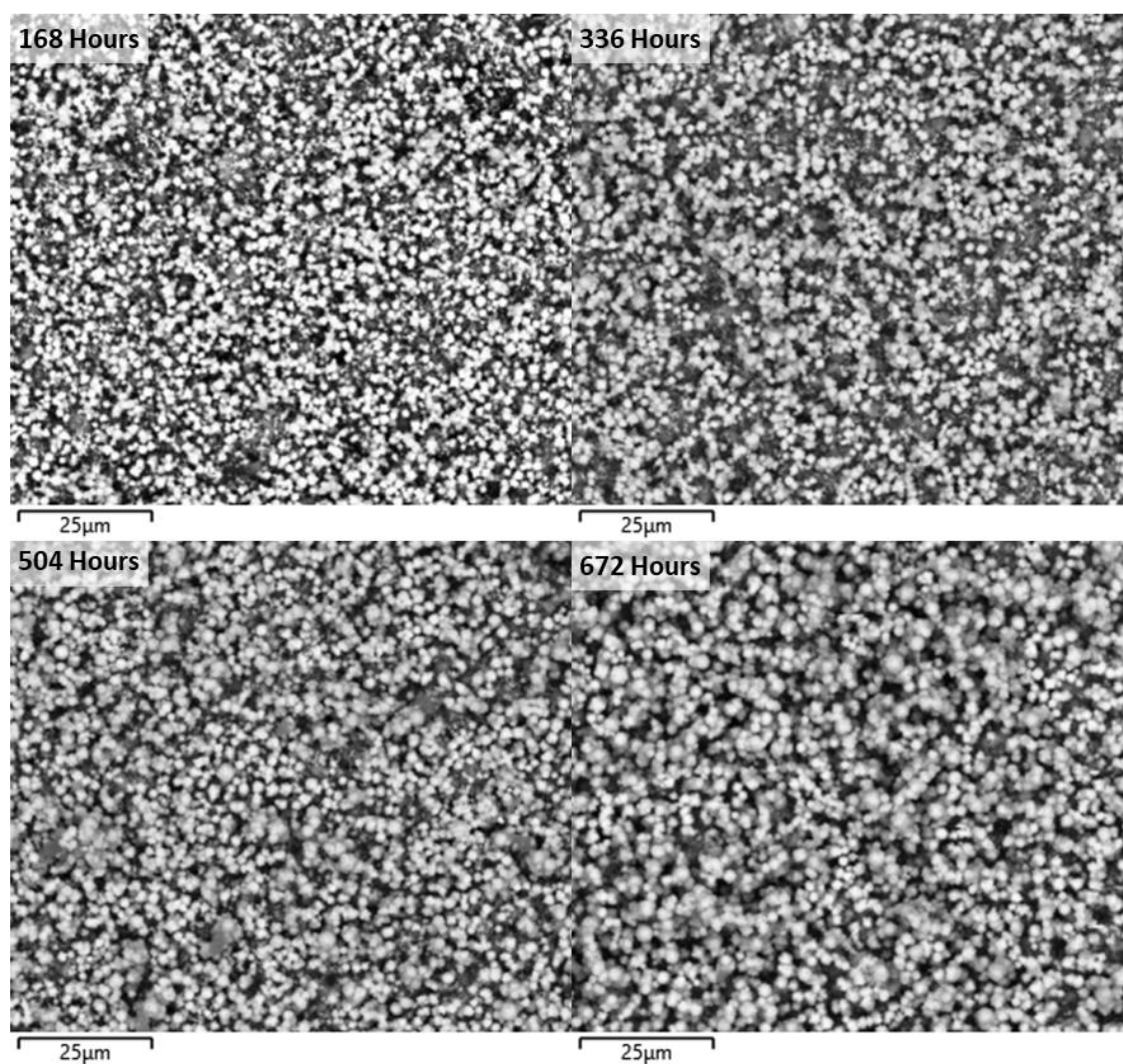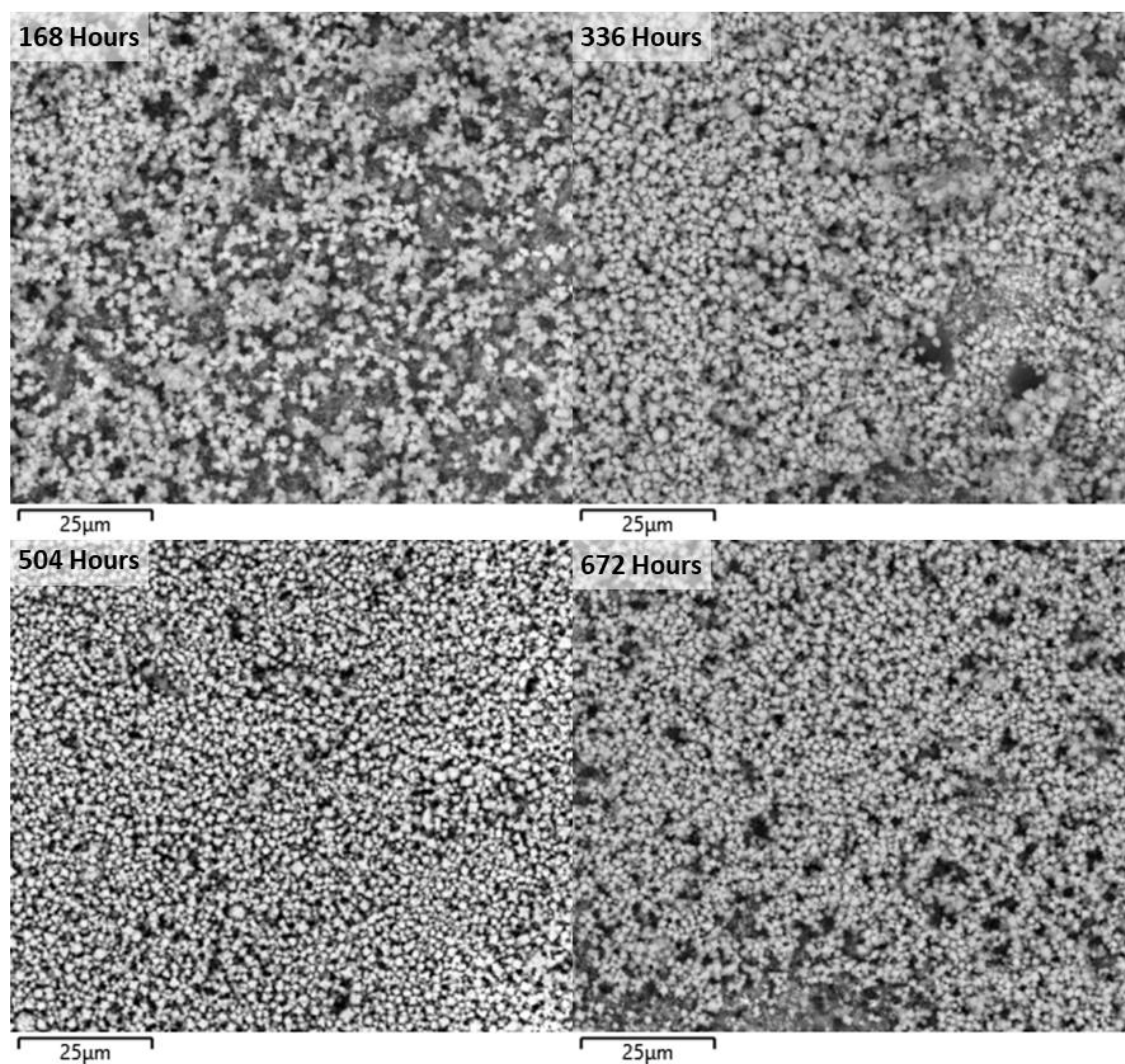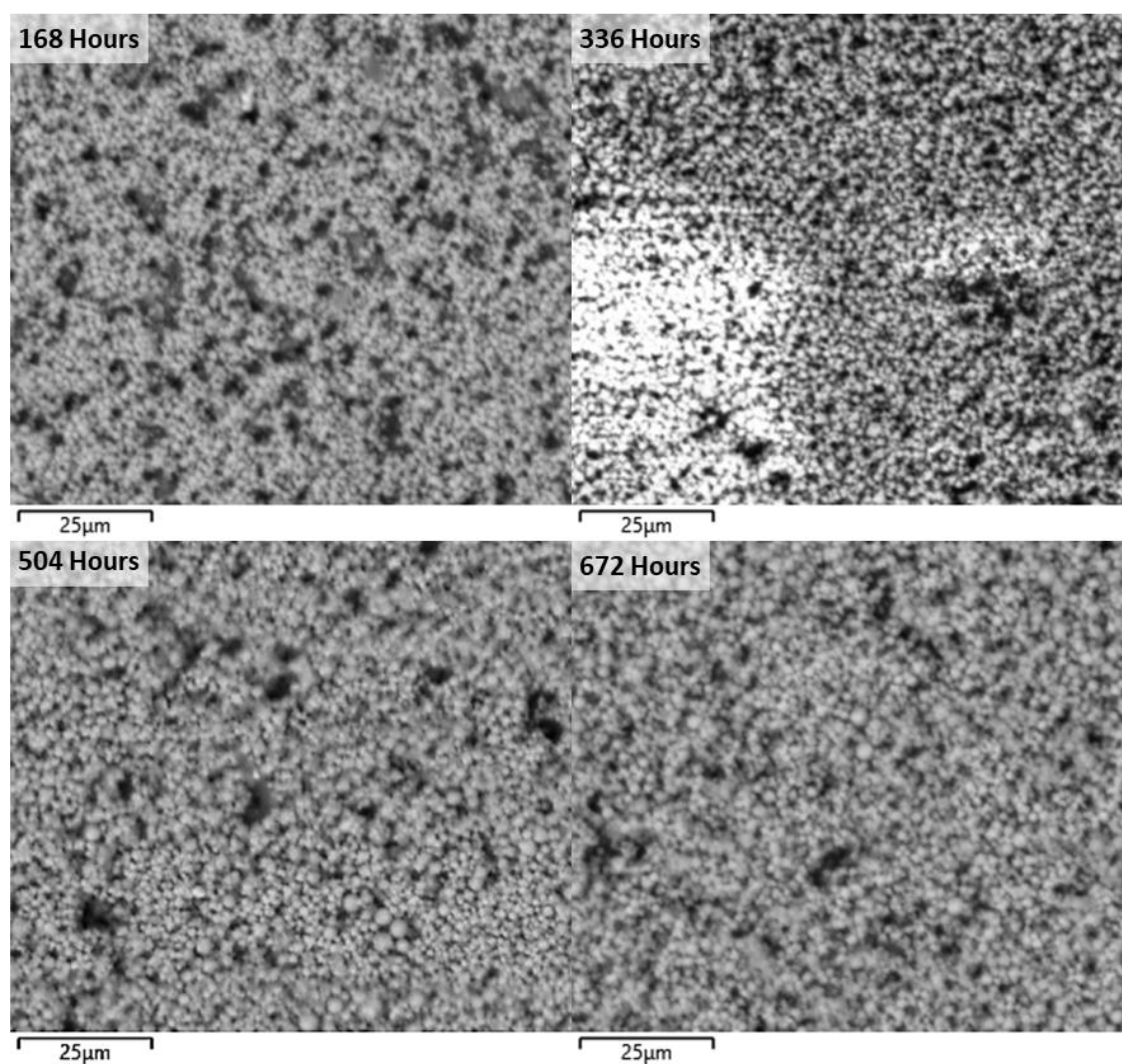
Spectrum	Element (wt%)								
Label	O	Al	Si	S	Cl	Ca	Fe	Cu	Zn
168 Hours	21.91	0.11	0.38	1.74	14.01	0.12	2.43	45.44	13.85
336 Hours	20.64	0.04	0.12	0.44	14.66	0.09	1.33	53.48	9.21
504 Hours	19.95	0.04	0.06	0.13	15.25	0.00	0.85	55.35	8.36
672 Hours	20.07	0.00	0.06	0.21	14.51	0.09	1.02	55.64	8.38

Figure 179 – BSE micrographs and semi-quantitative EDX analysis of the surface of the BQA 644 coating exposed to the neutral 10% electrolyte at 45°C under different immersion times.
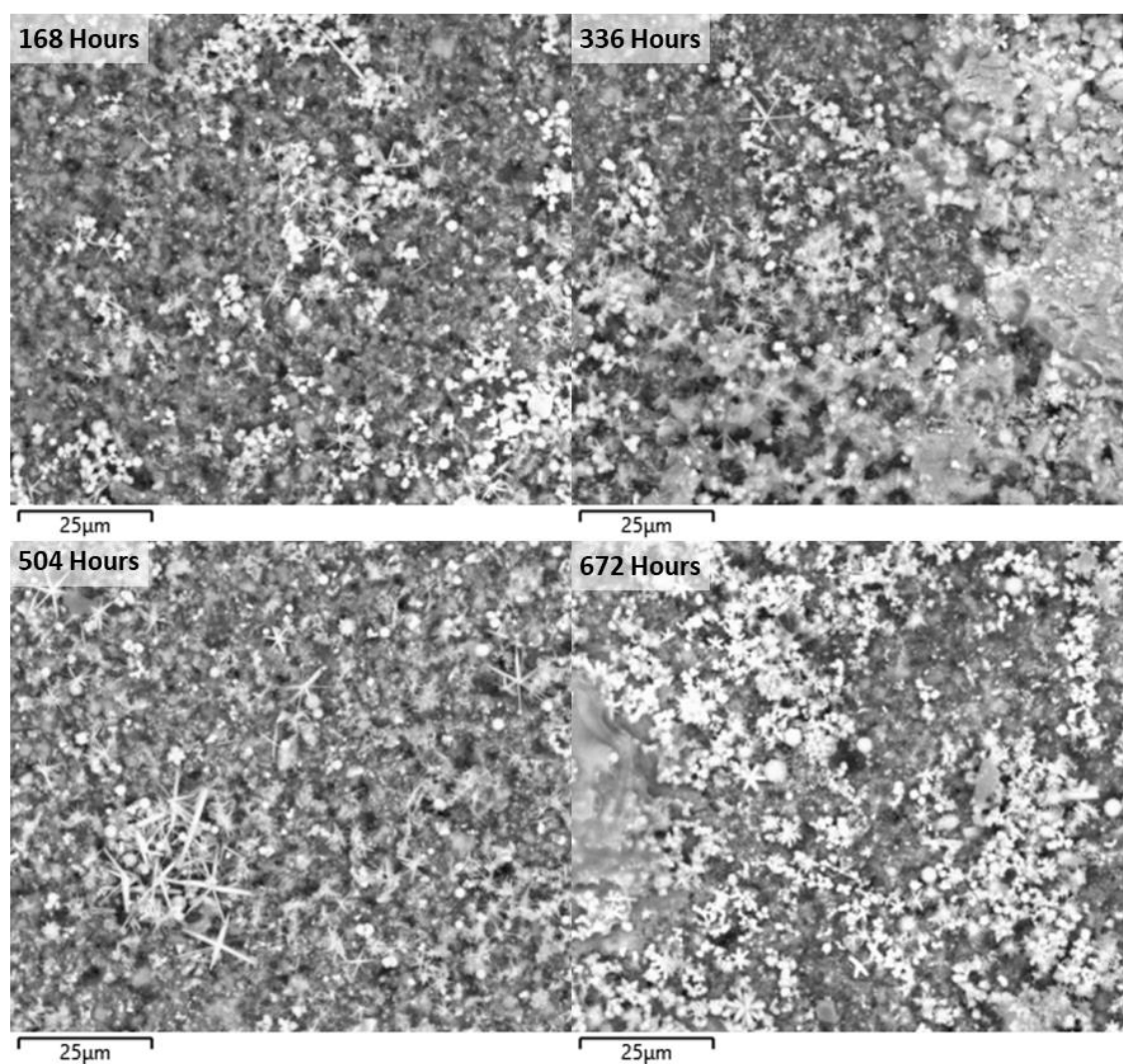
Spectrum	Element (wt%)								
Label	O	Al	Si	S	Cl	Ca	Fe	Cu	Zn
168 Hours	25.48	0.45	2.12	6.65	15.00	0.51	6.19	26.94	16.65
336 Hours	23.29	0.36	1.88	7.10	16.48	0.44	6.54	25.08	18.83
504 Hours	23.32	0.23	1.47	5.49	22.33	0.51	4.54	26.41	15.69
672 Hours	23.77	0.52	2.30	8.09	14.39	0.48	7.10	23.30	20.03

Figure 180 – BSE micrographs and semi-quantitative EDX analysis of the surface of the BQA 644 coating exposed to the neutral 30% electrolyte at 45°C under different immersion times.

iii) BQA 644 – Evaporation cell – 25°C
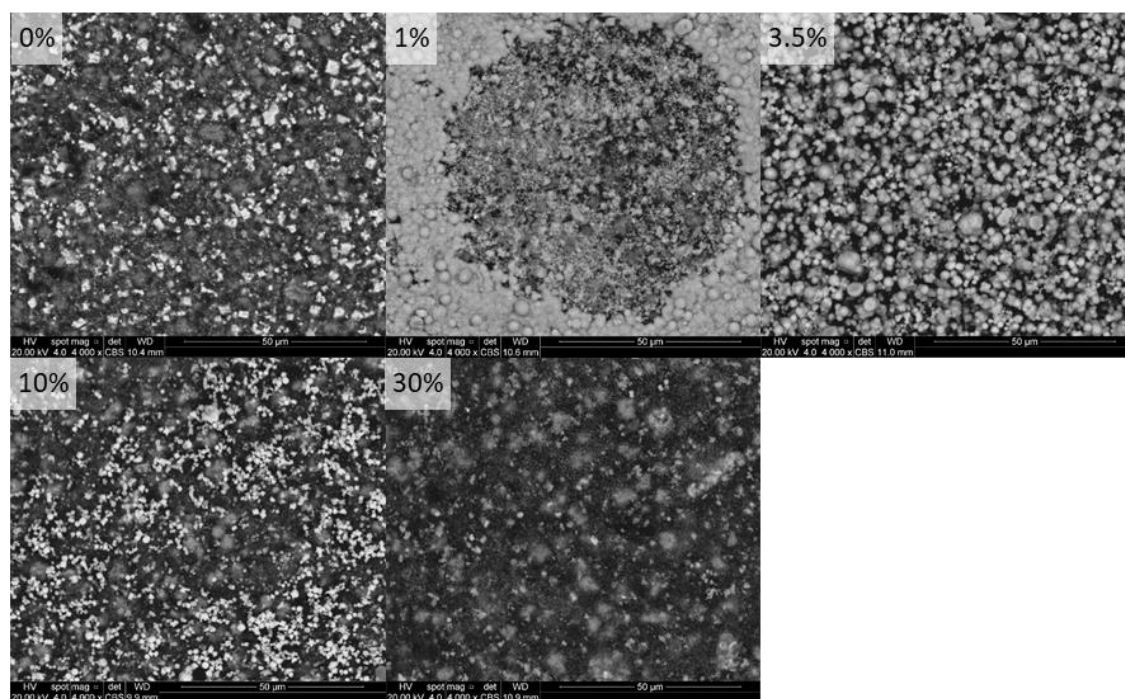
Spectrum	Element (wt%)									
Label	Cu	Zn	O	S	Fe	Na	Si	Ca	Al	Cl
0%	32.61	27.39	17.81	9.82	4.32	3.76	3.37	0.71	0.21	0.00
1%	53.80	8.73	26.61	0.50	0.52	0.00	0.00	0.31	0.00	9.53
3.5%	47.21	14.14	27.53	1.33	1.04	0.00	0.28	0.00	0.00	8.48
10%	36.90	30.97	14.86	6.52	4.50	0.00	1.04	0.00	0.00	5.19
30%	20.07	19.18	37.64	10.02	5.43	2.03	1.83	0.00	0.40	3.39

Figure 181 – BSE micrographs and semi-quantitative EDX analysis of the surface of the BQA 644 coating exposed to the neutral electrolytes containing different NaCl concentrations at 25°C under evaporating conditions after 672 hours.

[443]

iv) BQA 644 – Evaporation – 45°C

Spectrum	Element (wt%)								
Label	O	Al	Si	S	Cl	Ca	Fe	Cu	Zn
0%	25.27	0.35	2.26	8.73	0.00	3.37	2.24	33.39	24.39
1%	23.35	0.09	0.41	0.44	14.10	0.65	1.00	50.53	9.43
3.5%	25.47	0.18	0.84	0.77	14.51	0.85	1.67	45.96	9.76
10%	25.99	0.52	3.09	11.22	11.64	0.48	5.12	19.79	22.16
30%	30.01	0.85	4.11	12.67	5.22	0.28	6.25	17.64	22.97

*Figure 182 – BSE micrographs and semi-quantitative EDX analysis of the surface of the BQA 644 coating exposed to the neutral electrolytes containing different NaCl concentrations at 45°C once the electrolyte had fully evaporated after ≤408 hours.*

[444]

v) Modified BQA 644 – Immersion Cell – 25°C

a. *0% Electrolyte*
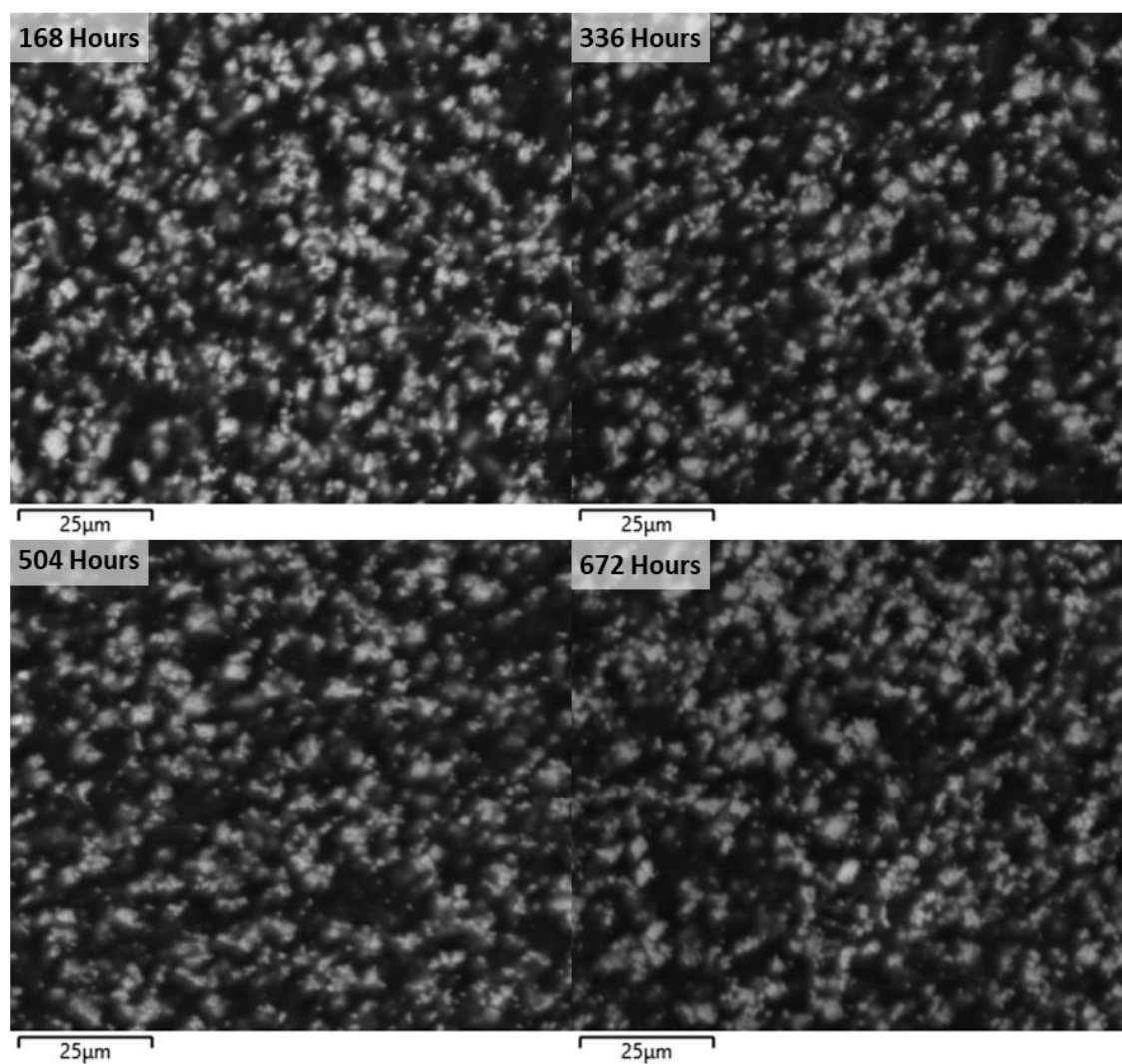
Spectrum Label	Element (wt%)				
	O	Al	Si	S	Cu
168 Hours	17.07	0.67	5.97	0.18	76.12
336 Hours	19.91	0.74	6.60	0.18	72.58
504 Hours	20.15	0.73	6.92	0.16	72.03
672 Hours	20.26	0.76	7.05	0.15	71.78

Figure 183 – BSE micrographs and semi-quantitative EDX analysis of the surface of the modified BQA 644 coating exposed to the neutral 0% electrolyte at 25°C under different immersion times.
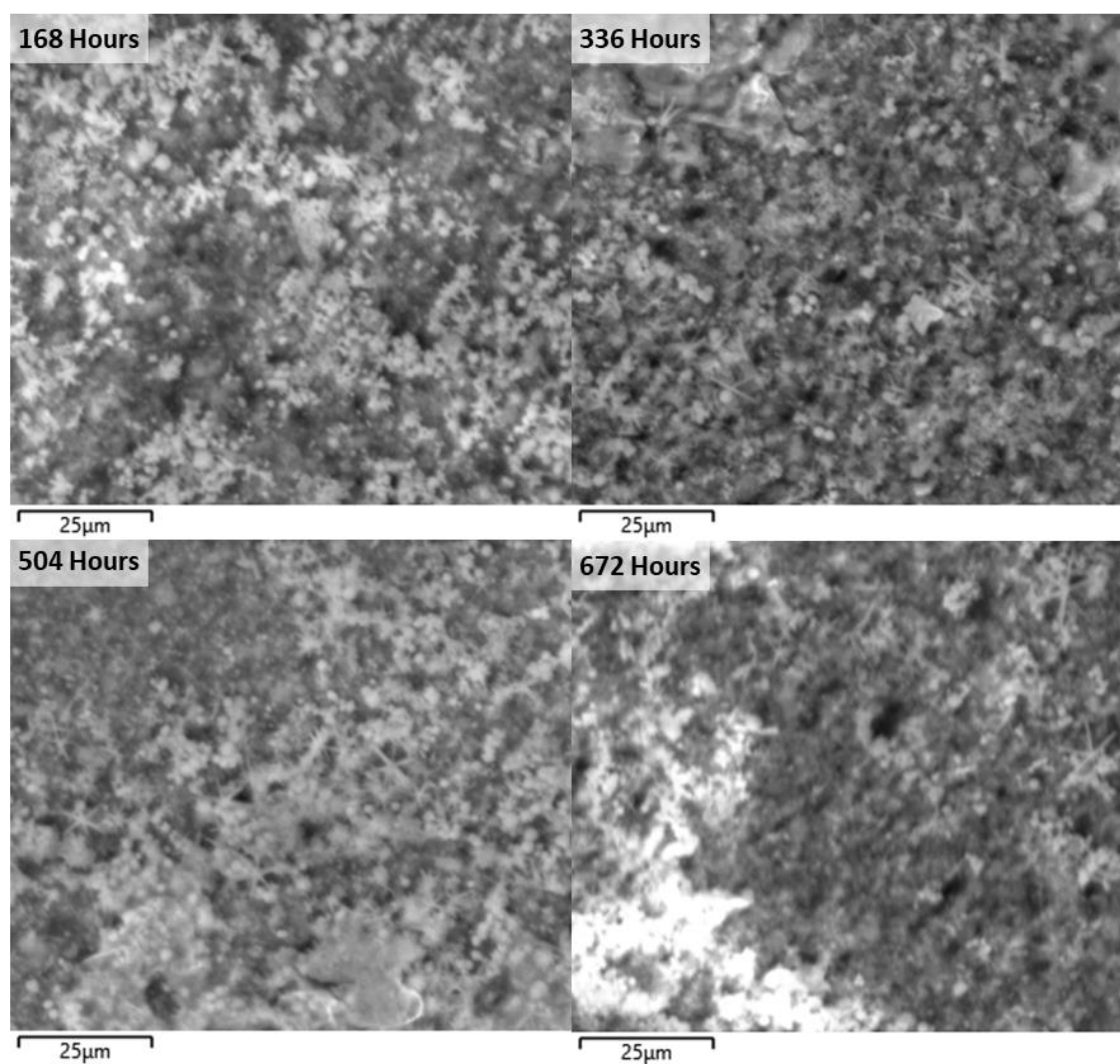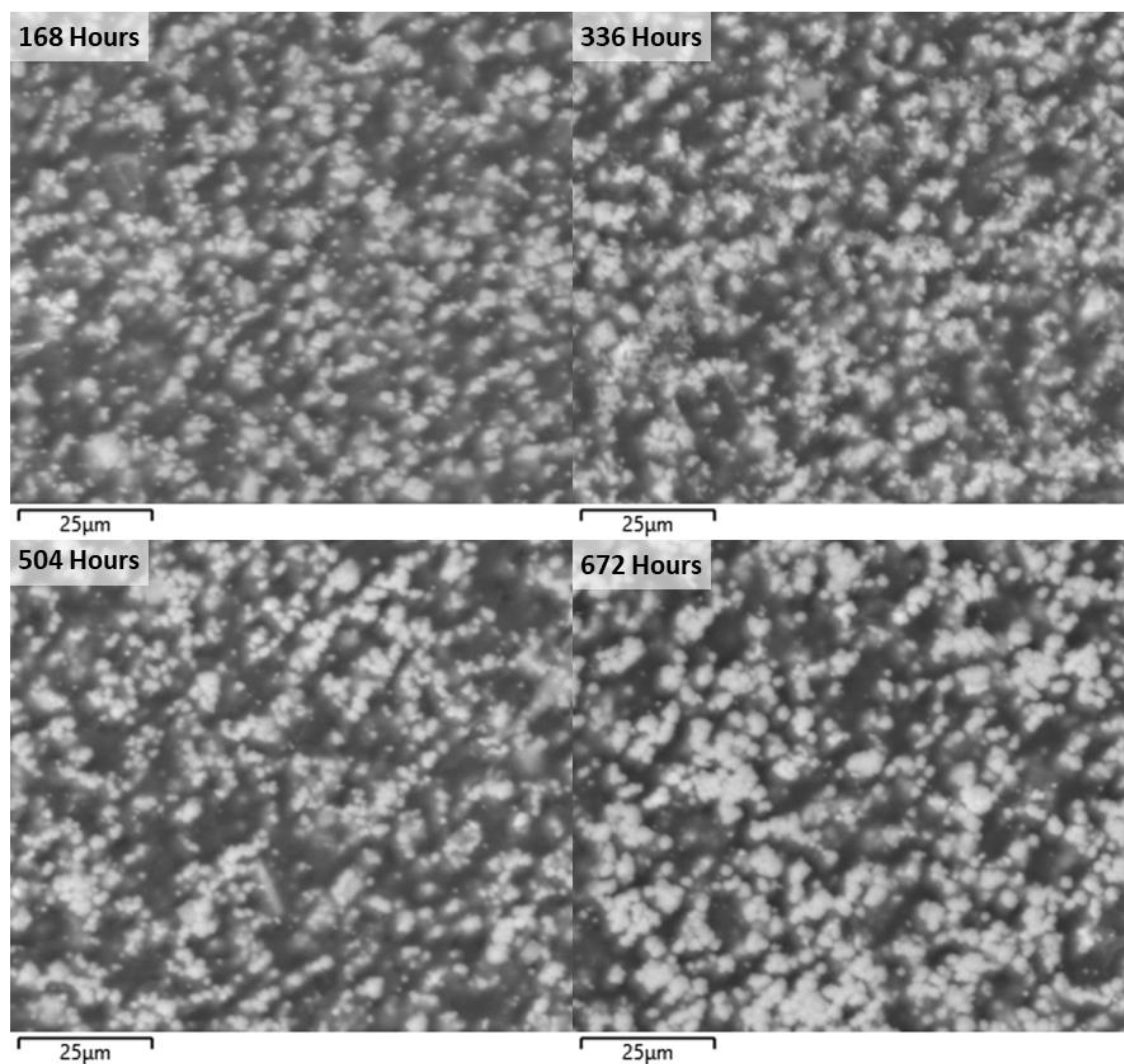
Spectrum	Element (wt%)				
Label	O	Al	Si	Cl	Cu
168 Hours	20.73	0.78	5.41	3.00	70.09
336 Hours	20.74	0.72	4.30	4.17	70.08
504 Hours	20.27	0.51	3.06	10.18	65.97
672 Hours	23.24	0.40	1.41	9.60	65.34

Figure 184 – BSE micrographs and semi-quantitative EDX analysis of the surface of the modified BQA 644 coating exposed to the neutral 1% electrolyte at 25°C under different immersion times.

[446]
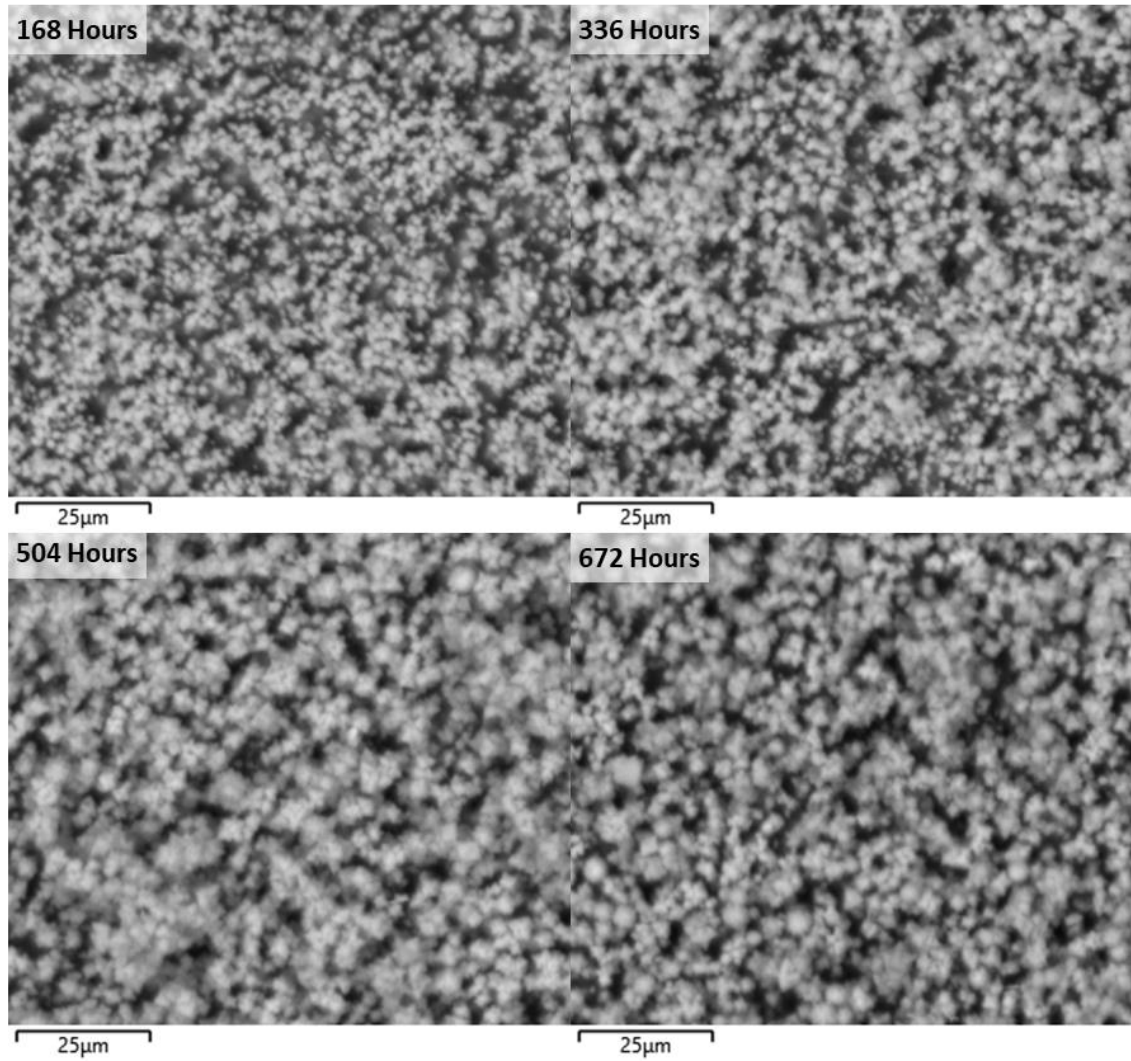
Spectrum	Element (wt%)				
Label	O	Al	Si	Cl	Cu
168 Hours	22.95	0.27	1.05	10.56	65.17
336 Hours	21.60	0.08	0.41	13.57	64.34
504 Hours	16.82	0.02	0.15	12.90	70.11
672 Hours	18.39	0.00	0.10	14.35	67.16

Figure 185 – BSE micrographs and semi-quantitative EDX analysis of the surface of the modified BQA 644 coating exposed to the neutral 3.5% electrolyte at 25°C under different immersion times.
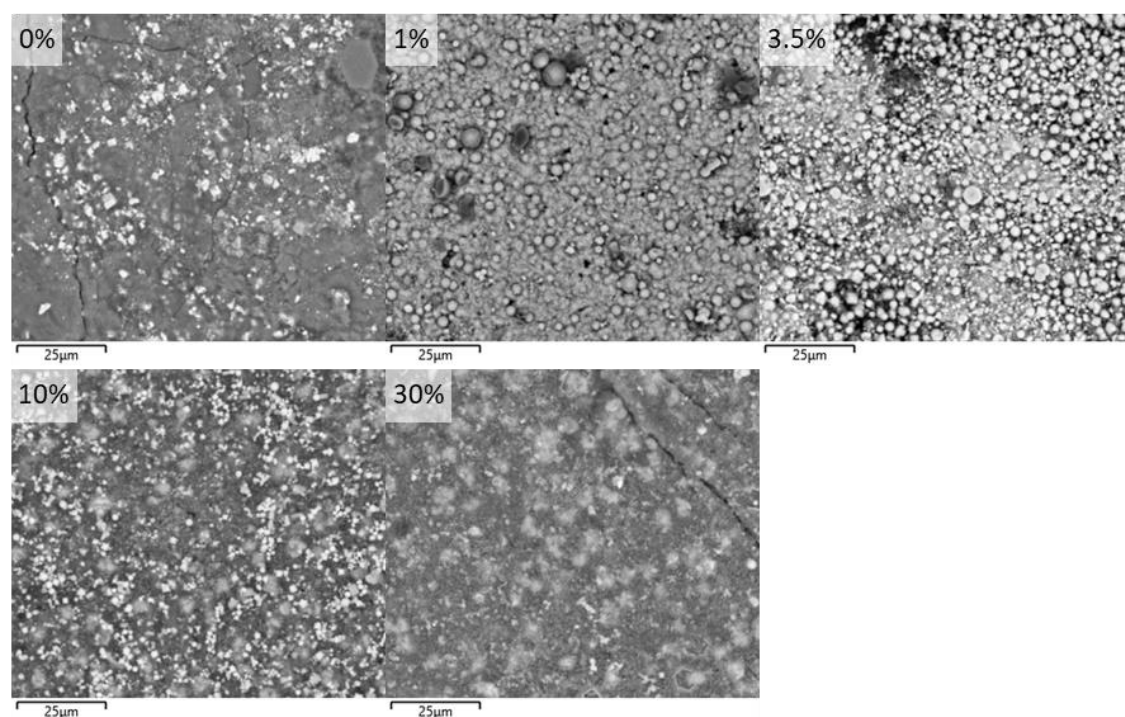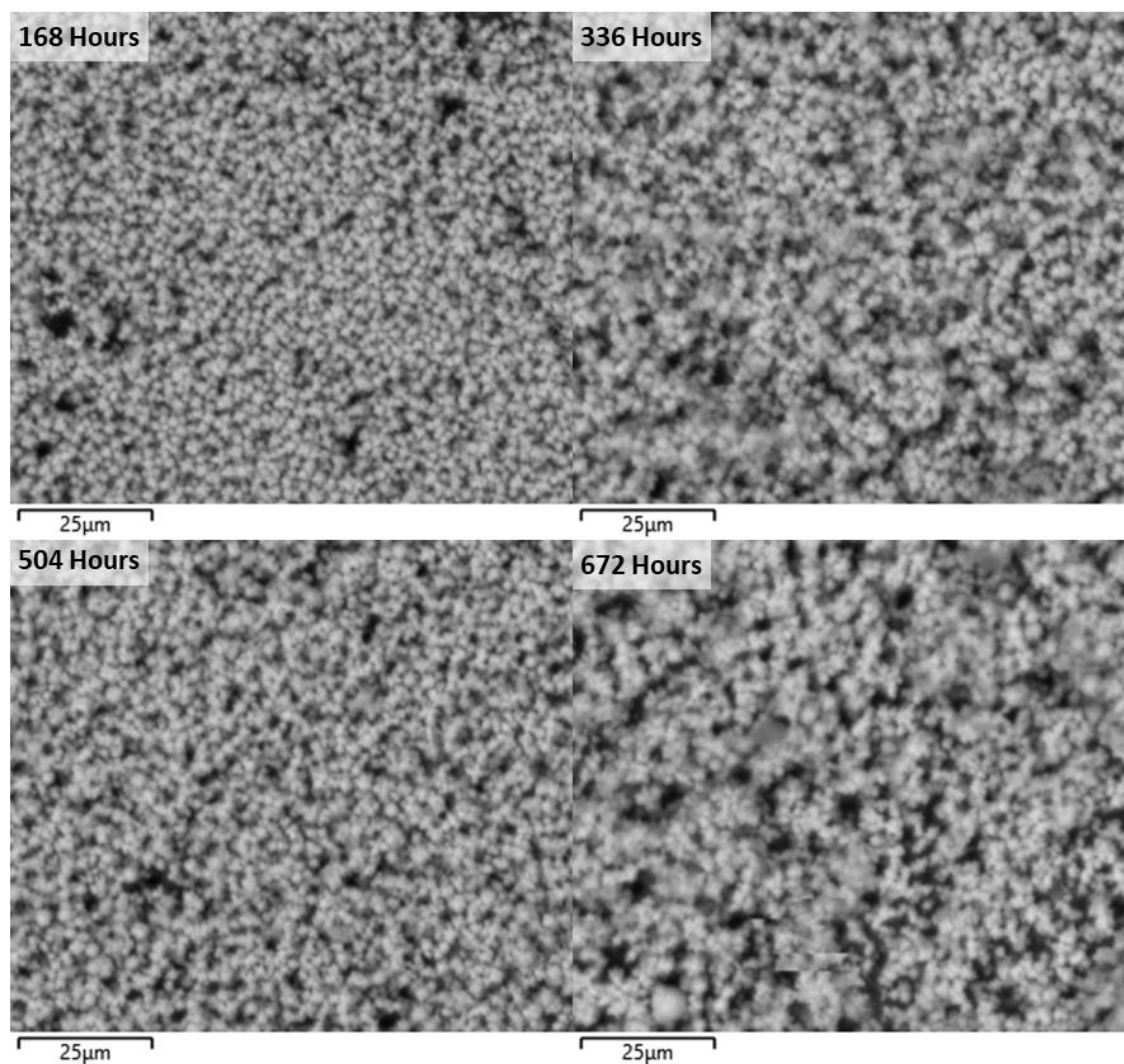
Spectrum	Element (wt%)				
Label	**O**	**Al**	**Si**	**Cl**	**Cu**
168 Hours	21.19	0.06	0.14	14.99	63.63
336 Hours	18.99	0.03	0.07	14.21	66.70
504 Hours	20.47	0.08	0.12	15.19	64.13
672 Hours	17.28	0.04	0.14	13.78	68.77

Figure 186 – BSE micrographs and semi-quantitative EDX analysis of the surface of the modified BQA 644 coating exposed to the neutral 10% electrolyte at 25°C under different immersion times.

e. *30% Electrolyte*
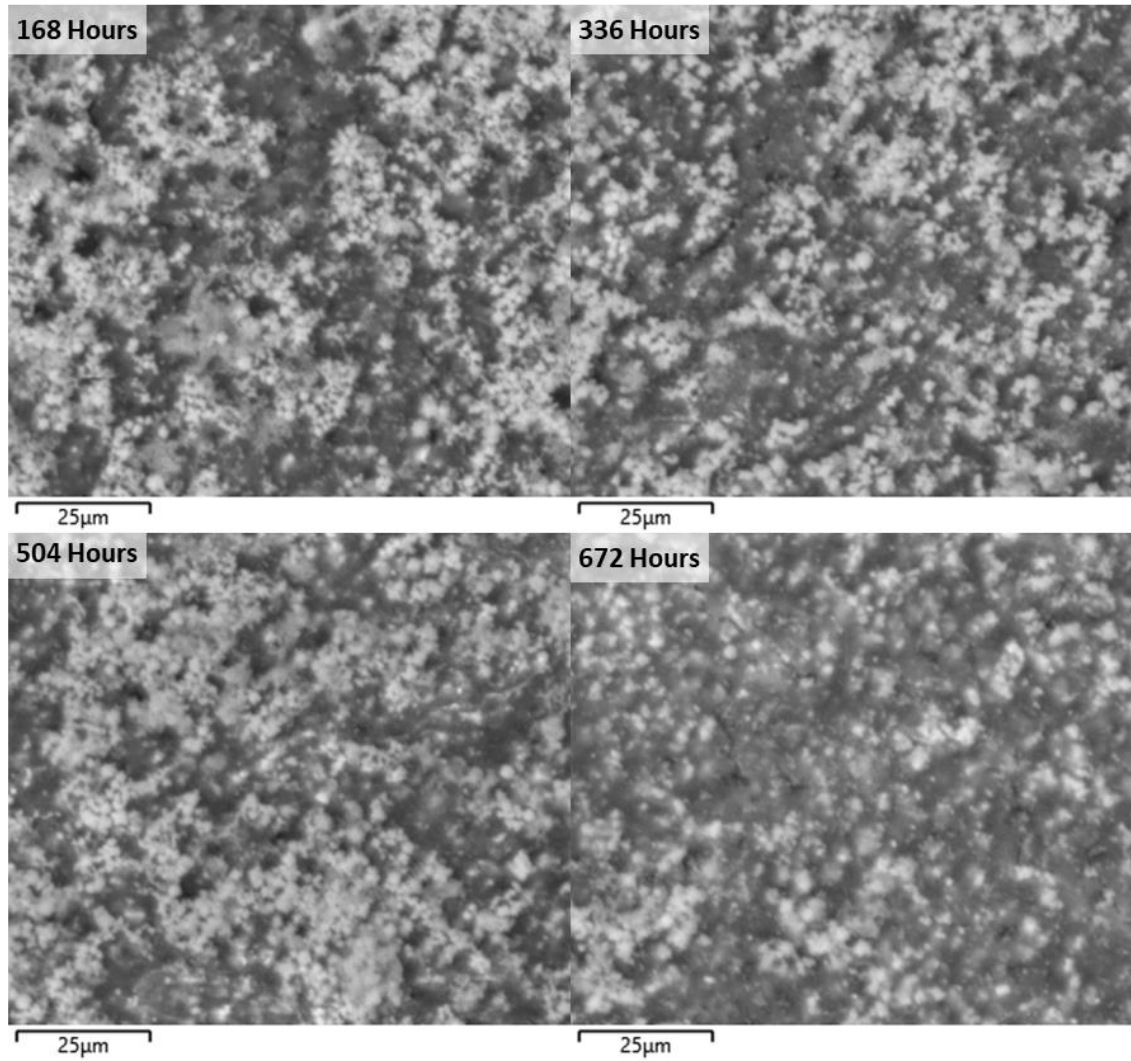
Spectrum	Element (wt%)				
Label	O	Al	Si	Cl	Cu
168 Hours	27.30	0.34	2.23	13.72	56.41
336 Hours	27.80	0.49	2.58	14.11	55.01
504 Hours	27.20	0.32	1.84	15.54	55.11
672 Hours	25.48	0.83	4.55	7.48	61.66

Figure 187 – BSE micrographs and semi-quantitative EDX analysis of the surface of the modified BQA 644 coating exposed to the neutral 30% electrolyte at 25°C under different immersion times.

a. *0% Electrolyte*
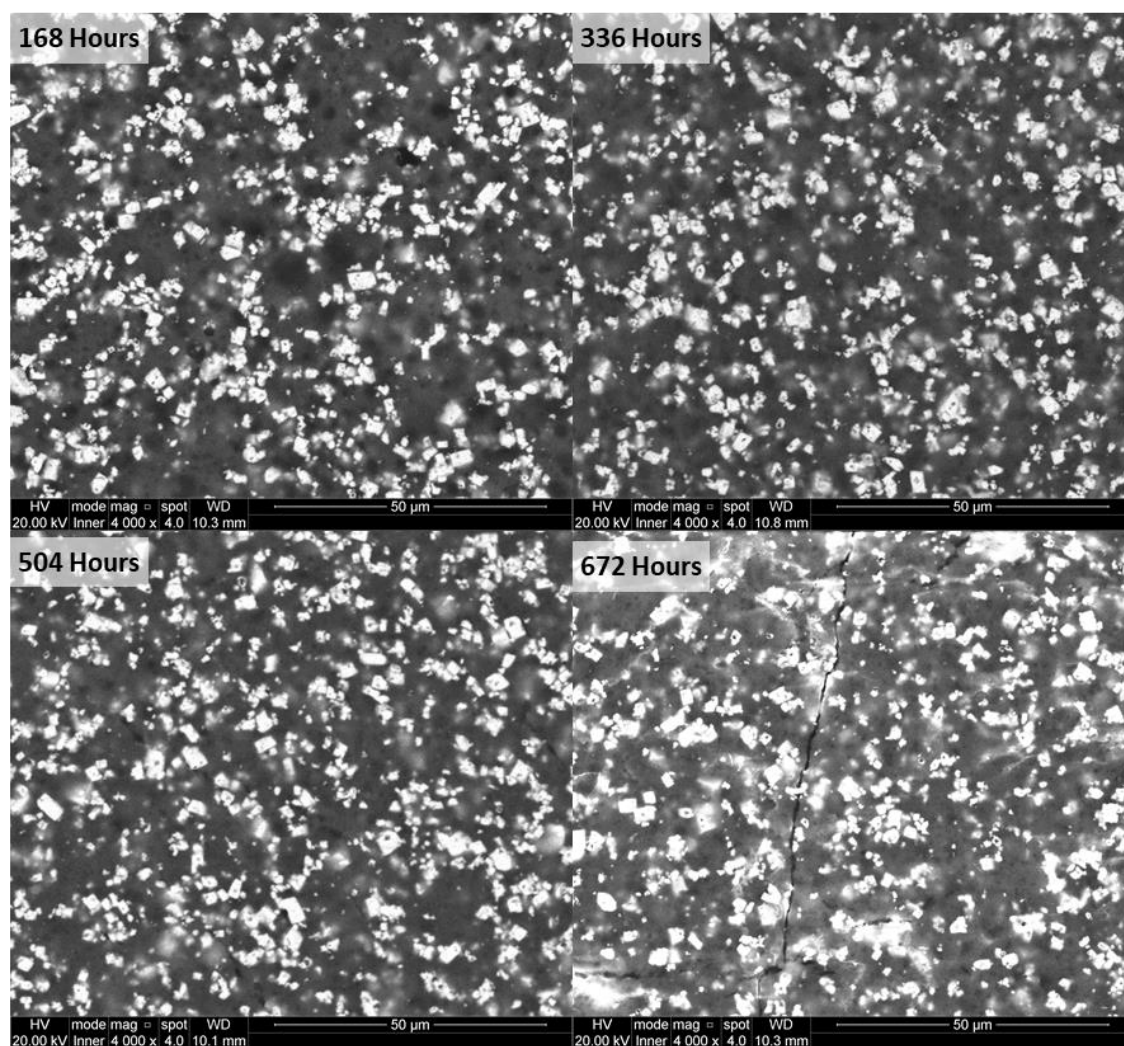
Spectrum Label	Element (wt%)				
	O	**Al**	**Si**	**Ca**	**Cu**
168 Hours	16.96	0.87	5.43	0.00	76.75
336 Hours	17.20	0.48	5.59	0.09	76.64
504 Hours	18.79	0.49	5.45	0.00	75.27
672 Hours	27.06	1.05	7.76	0.22	63.91

Figure 188 – BSE micrographs and semi-quantitative EDX analysis of the surface of the modified BQA 644 coating exposed to the neutral 0% electrolyte at 45°C under different immersion times.
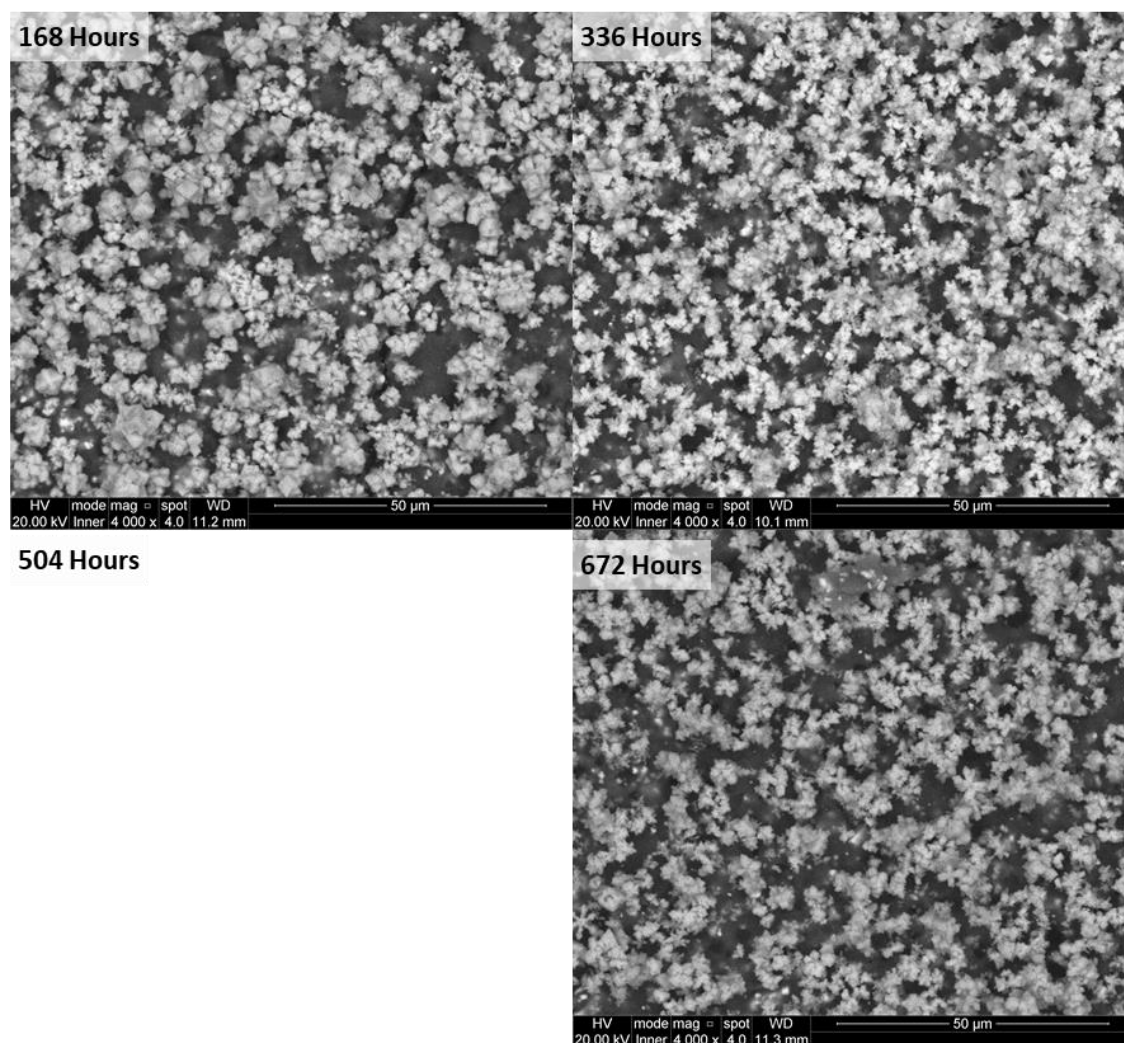
Spectrum	Element (wt%)					
Label	O	Al	Si	Cl	Ca	Cu
168 Hours	21.80	0.07	1.91	11.05	0.07	65.10
336 Hours	22.02	0.20	1.15	12.71	0.01	63.90
672 Hours	19.15	0.09	1.11	11.48	0.00	68.17

Figure 189 – BSE micrographs and semi-quantitative EDX analysis of the surface of the modified BQA 644 coating exposed to the neutral 0% electrolyte at 45°C under different immersion times.

[451]

c. *3.5% Electrolyte*
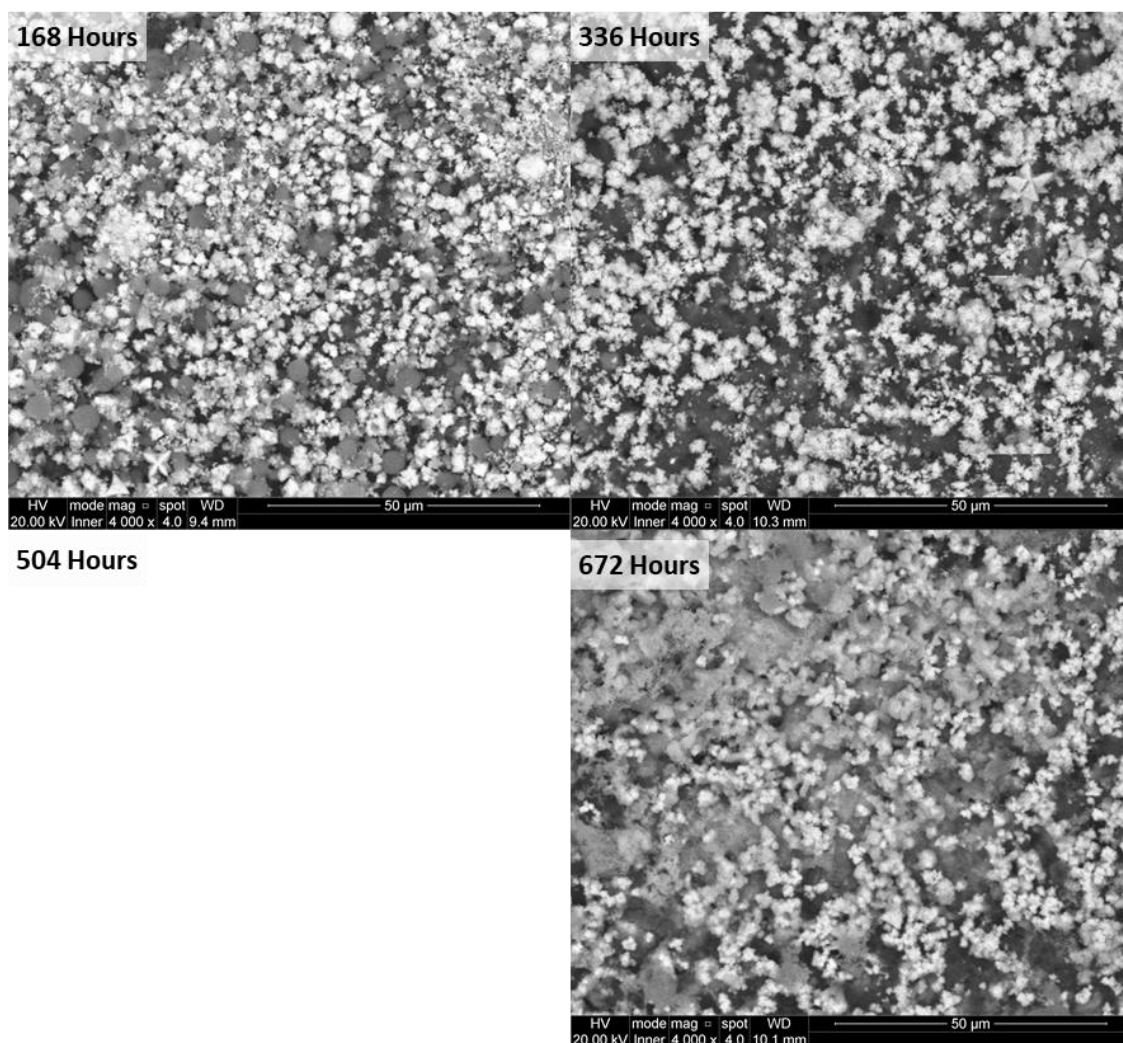
Spectrum	Element (wt%)						
Label	O	Na	Al	Si	Cl	Ca	Cu
168 Hours	24.79	-	0.05	4.55	10.91	0.10	59.60
336 Hours	24.65	-	0.57	2.27	12.14	0.07	60.30
672 Hours	15.82	20.36	0.12	1.19	26.84	0.14	35.52

Figure 190 – BSE micrographs and semi-quantitative EDX analysis of the surface of the modified BQA 644 coating exposed to the neutral 3.5% electrolyte at 45°C under different immersion times.

d. 10% Electrolyte
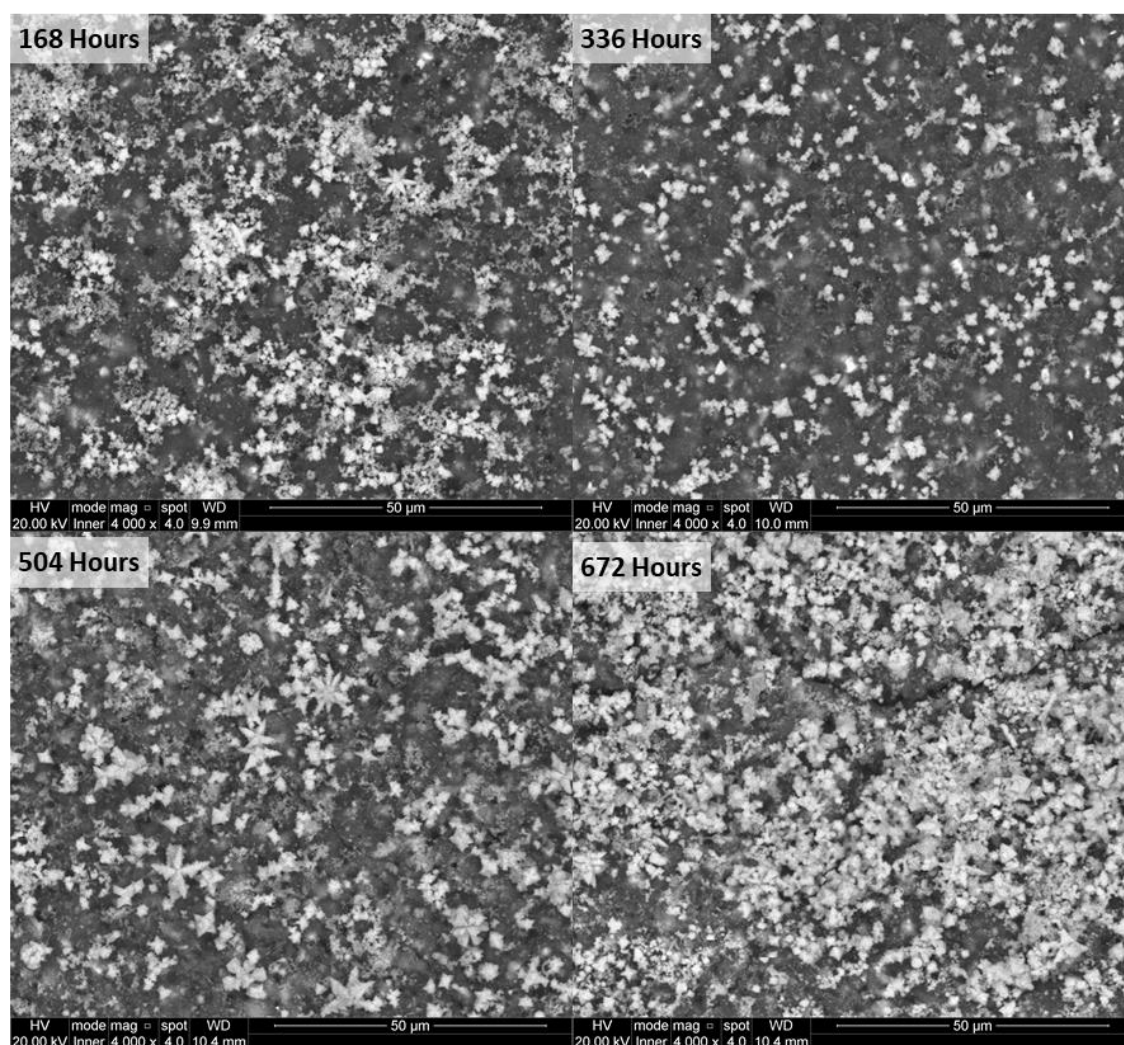
Spectrum	Element (wt%)					
Label	O	Al	Si	Cl	Ca	Cu
168 Hours	28.37	0.83	5.09	9.53	0.18	56.00
336 Hours	30.68	1.05	7.88	10.99	0.20	49.19
504 Hours	25.61	0.59	4.43	11.96	0.16	57.25
672 Hours	27.48	0.43	2.44	17.38	0.06	52.21

Figure 191 – BSE micrographs and semi-quantitative EDX analysis of the surface of the modified BQA 644 coating exposed to the neutral 10% electrolyte at 45°C under different immersion times.

[453]

e. 30% Electrolyte
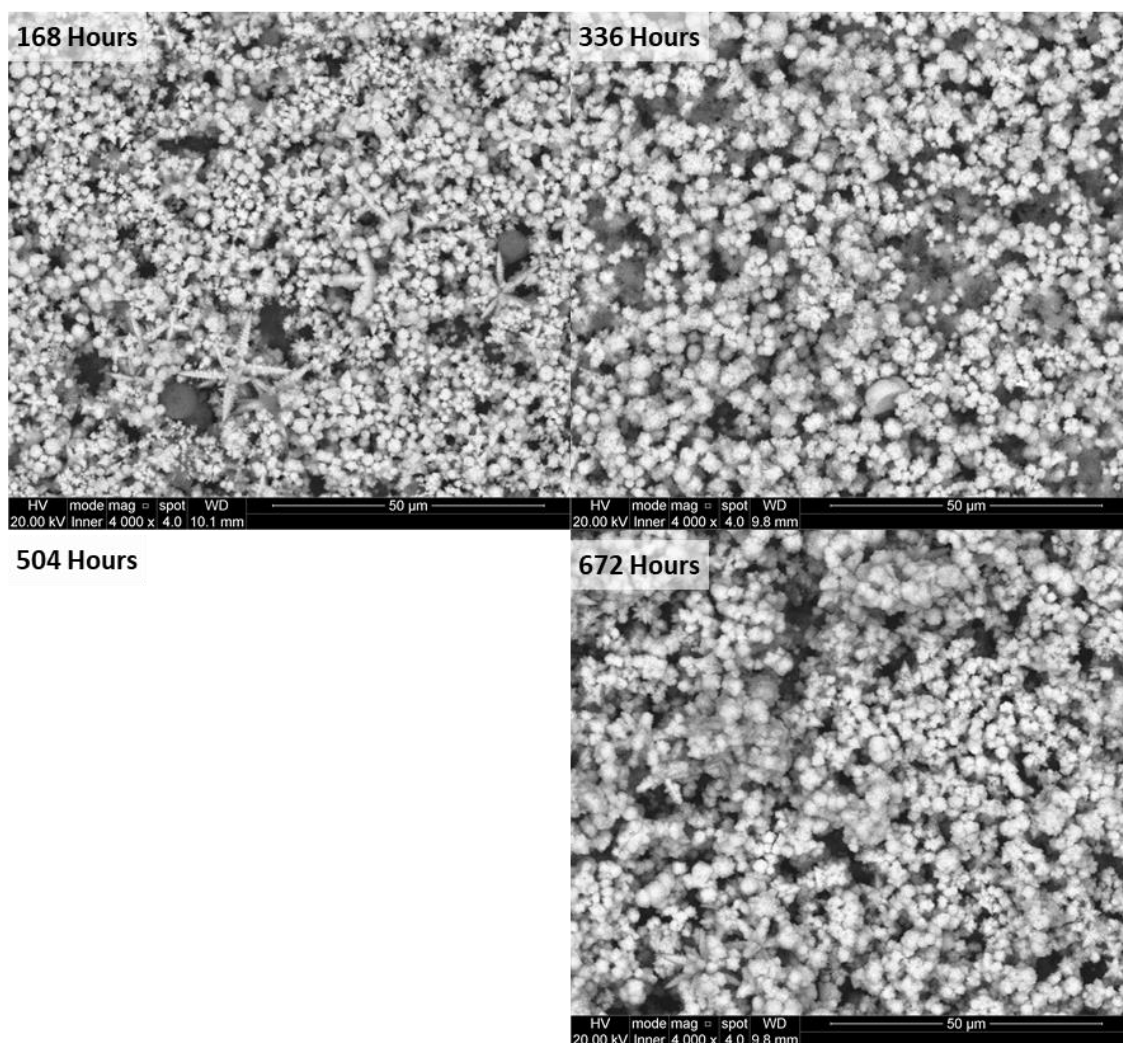
Spectrum Label	Element (wt%)					
	O	Al	Si	Cl	Ca	Cu
168 Hours	23.19	0.02	1.15	17.61	0.00	58.03
336 Hours	20.02	0.00	1.31	13.27	0.00	65.40
672 Hours	19.91	0.00	0.40	12.90	0.01	66.78

Figure 192 – BSE micrographs and semi-quantitative EDX analysis of the surface of the modified BQA 644 coating exposed to the neutral 0% electrolyte at 45°C under different immersion times.

vii) Modified BQA 644 – Evaporation Cell – 25°C
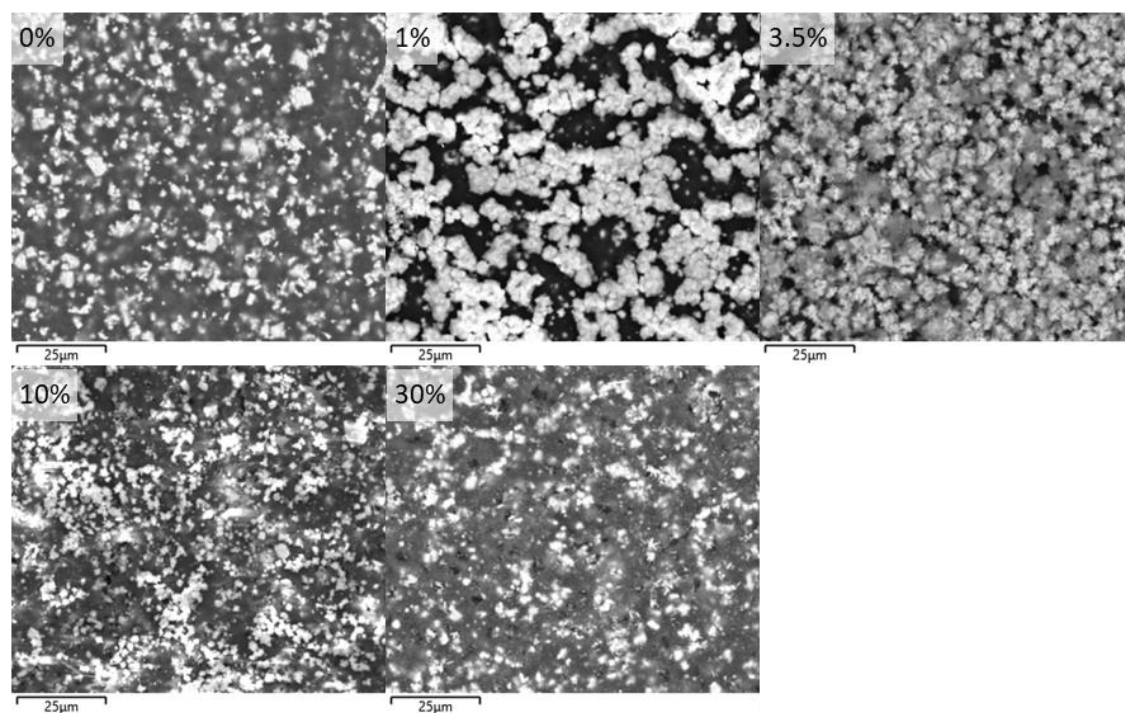
Spectrum	Element (wt%)				
Label	O	Al	Si	Cl	Cu
0%	19.90	0.71	6.56	0.00	72.83
1%	26.30	0.10	1.08	13.89	58.63
3.5%	20.98	0.03	2.26	12.70	64.04
10%	32.34	0.64	2.65	18.21	46.16
30%	24.80	1.01	5.56	6.84	61.79

Figure 193 – BSE micrographs and semi-quantitative EDX analysis of the surface of the modified BQA 644 coating exposed to the neutral electrolytes at 25°C under evaporating conditions after 672 hours.

viii) Modified BQA 644 – Evaporation Cell – 45°C
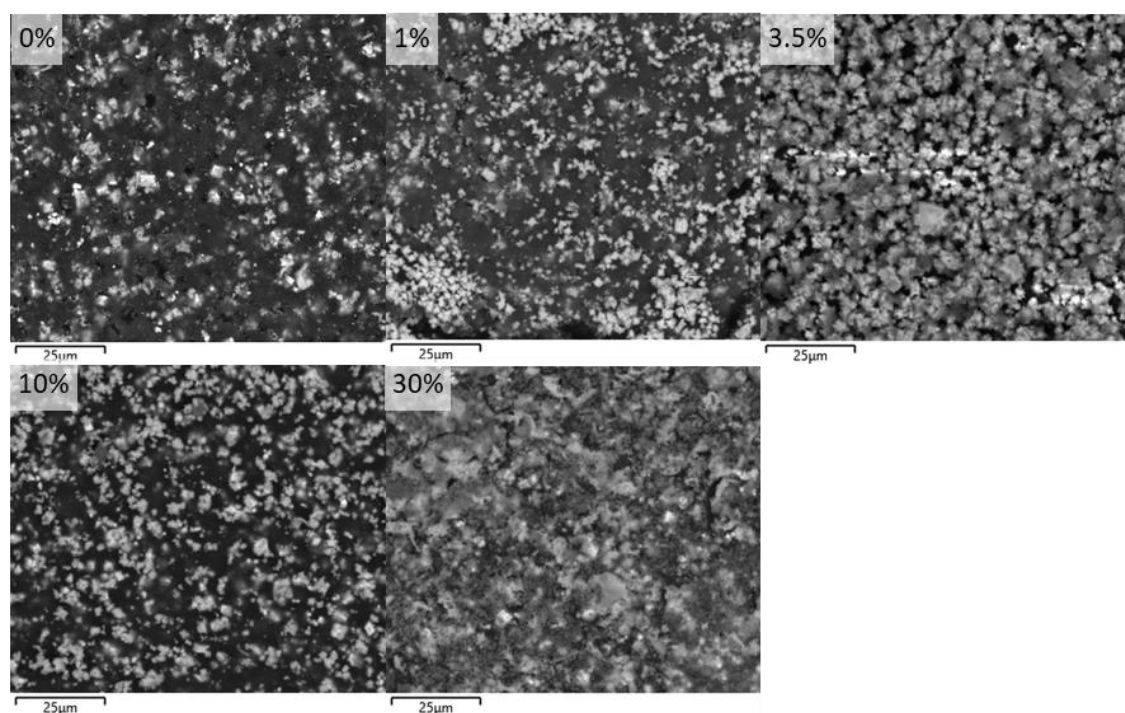
Spectrum	Element (wt%)				
Label	O	Al	Si	Cl	Cu
0%	21.20	0.91	6.04	0.00	71.85
1%	28.08	0.59	2.88	12.33	56.11
3.5%	23.93	0.08	2.20	13.15	60.64
10%	22.17	0.71	2.34	6.21	68.57
30%	25.61	0.43	3.37	5.49	65.11

Figure 194 – BSE micrographs and semi-quantitative EDX analysis of the surface of the BQA 644 coating exposed to the neutral electrolytes containing different sodium chloride concentrations at 45°C under evaporating conditions after the electrolyte had fully evaporated up to 360 hours.

[456]

b) Cross-section

i) BQA 644 – Immersion Cell – 25°C

a. *0% Electrolyte*
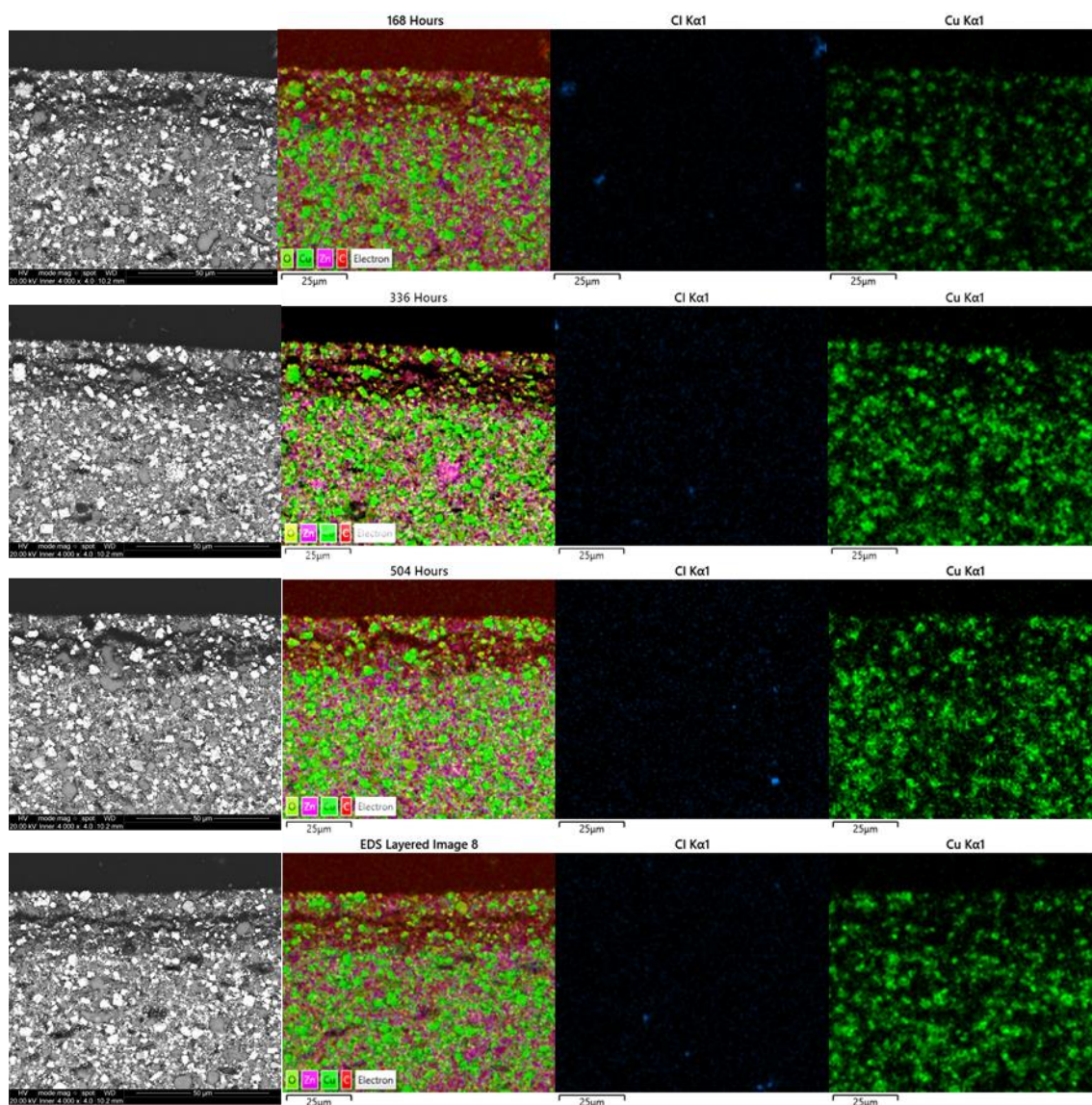
Spectrum	Element (wt%)								
Label	O	Al	Si	S	Cl	Ca	Fe	Cu	Zn
168 Hours	18.49	0.53	2.32	8.88	0.75	0.78	5.05	34.86	28.34
336 Hours	17.93	0.48	2.24	6.49	0.61	0.49	4.77	38.26	28.74
504 Hours	18.12	0.32	2.35	7.80	0.60	0.57	5.07	37.20	27.97
678 Hours	18.18	0.56	2.28	7.62	0.69	0.49	5.14	37.22	27.82

Figure 195 – BSE micrographs of the cross-section through the BQA 644 coating including an elemental composite image, chlorine and copper maps and the semi-quantitative EDX analysis of the mapped area after being exposed to the neutral 0% electrolyte at 25°C under different immersion times.

[457]

*b. 1% Electrolyte*
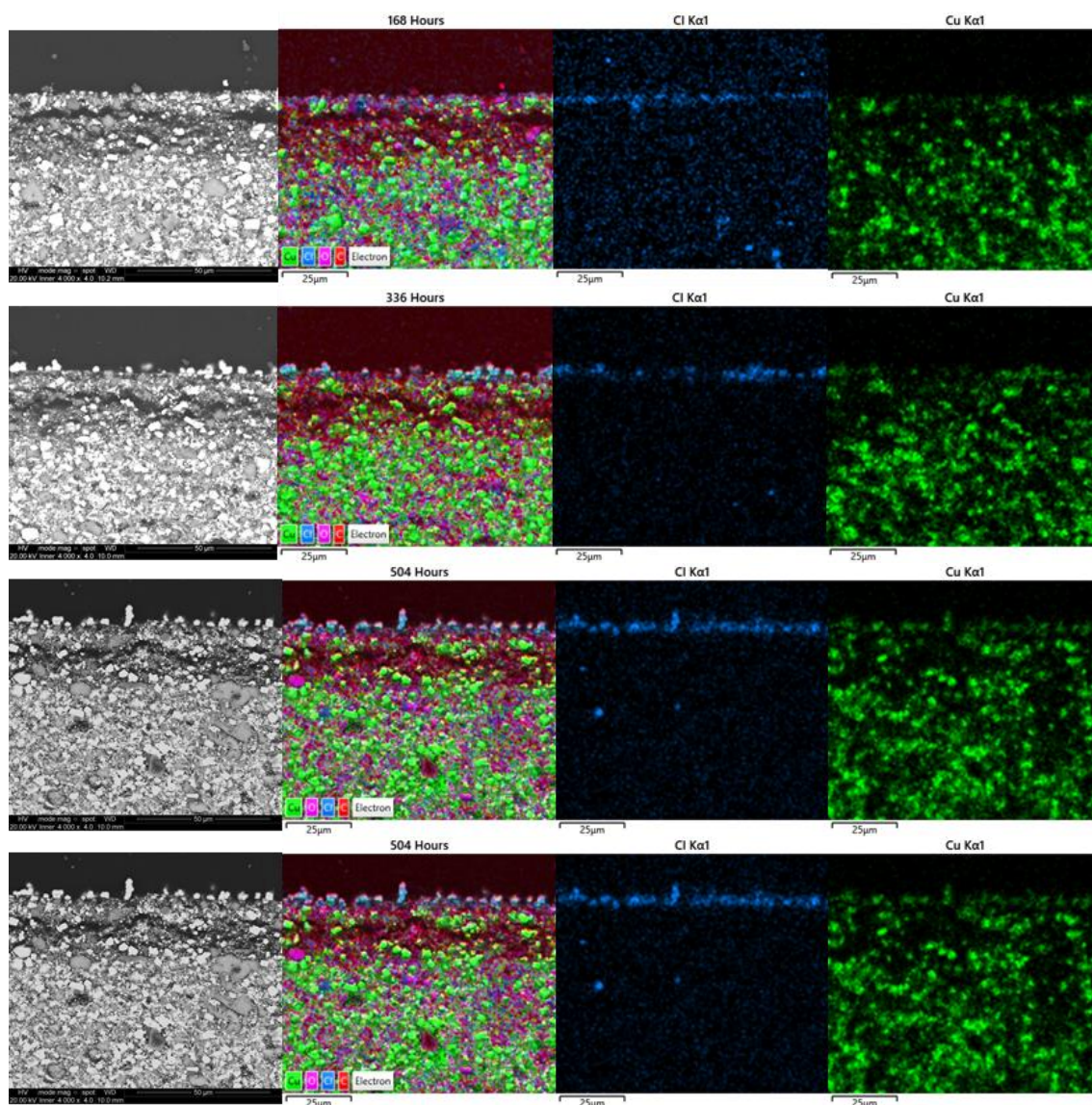
Spectrum	Element (wt%)								
Label	O	Al	Si	S	Cl	Ca	Fe	Cu	Zn
168 Hours	21.51	0.58	2.59	7.38	1.12	0.87	5.65	33.32	26.96
336 Hours	20.98	0.47	2.44	6.84	1.52	0.99	4.66	35.75	26.34
504 Hours	19.14	0.61	2.35	8.82	1.36	0.64	4.77	34.37	27.94
672 Hours	20.32	0.79	3.07	7.21	1.50	1.38	4.89	34.96	25.88

Figure 196 – BSE micrographs of the cross-section through the BQA 644 coating including an elemental composite image, chlorine and copper maps and the semi-quantitative EDX analysis of the mapped area after being exposed to the neutral 1% electrolyte at 25°C under different immersion times.

c.   3.5% Electrolyte
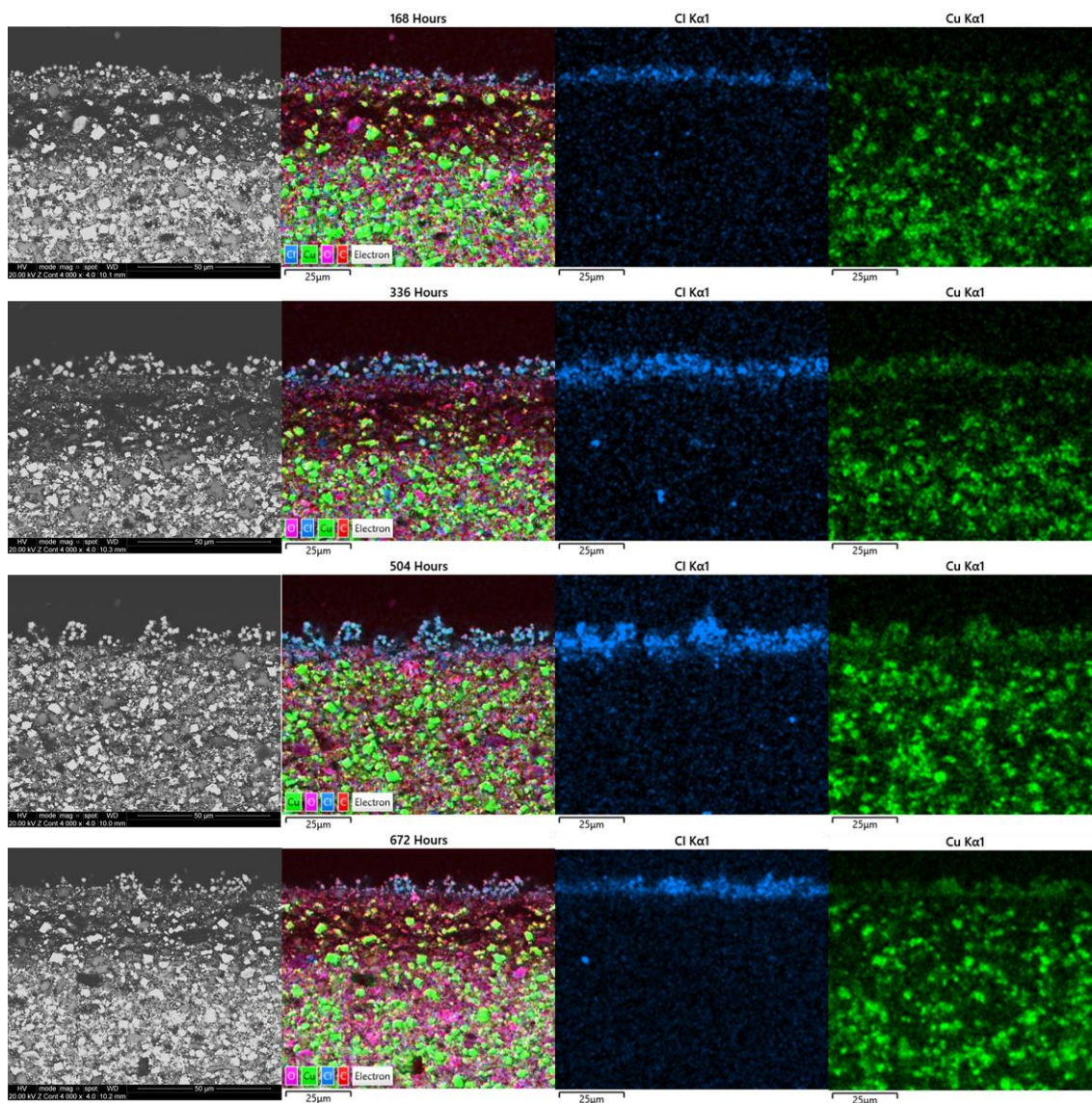
Spectrum	Element (wt%)								
Label	O	Al	Si	S	Cl	Ca	Fe	Cu	Zn
168 Hours	21.26	0.44	2.21	8.04	1.51	0.47	4.71	34.48	26.88
336 Hours	23.32	0.50	2.15	7.69	2.54	0.69	4.23	33.22	25.67
504 Hours	22.18	0.62	2.45	7.23	2.02	0.64	4.75	32.19	27.93
672 Hours	20.57	0.47	2.49	7.10	1.29	0.90	5.11	32.64	29.42

Figure 197 – BSE micrographs of the cross-section through the BQA 644 coating including an elemental composite image, chlorine and copper maps and the semi-quantitative EDX analysis of the mapped area after being exposed to the neutral 3.5% electrolyte at 25°C under different immersion times.

[459]

d. 10% Electrolyte
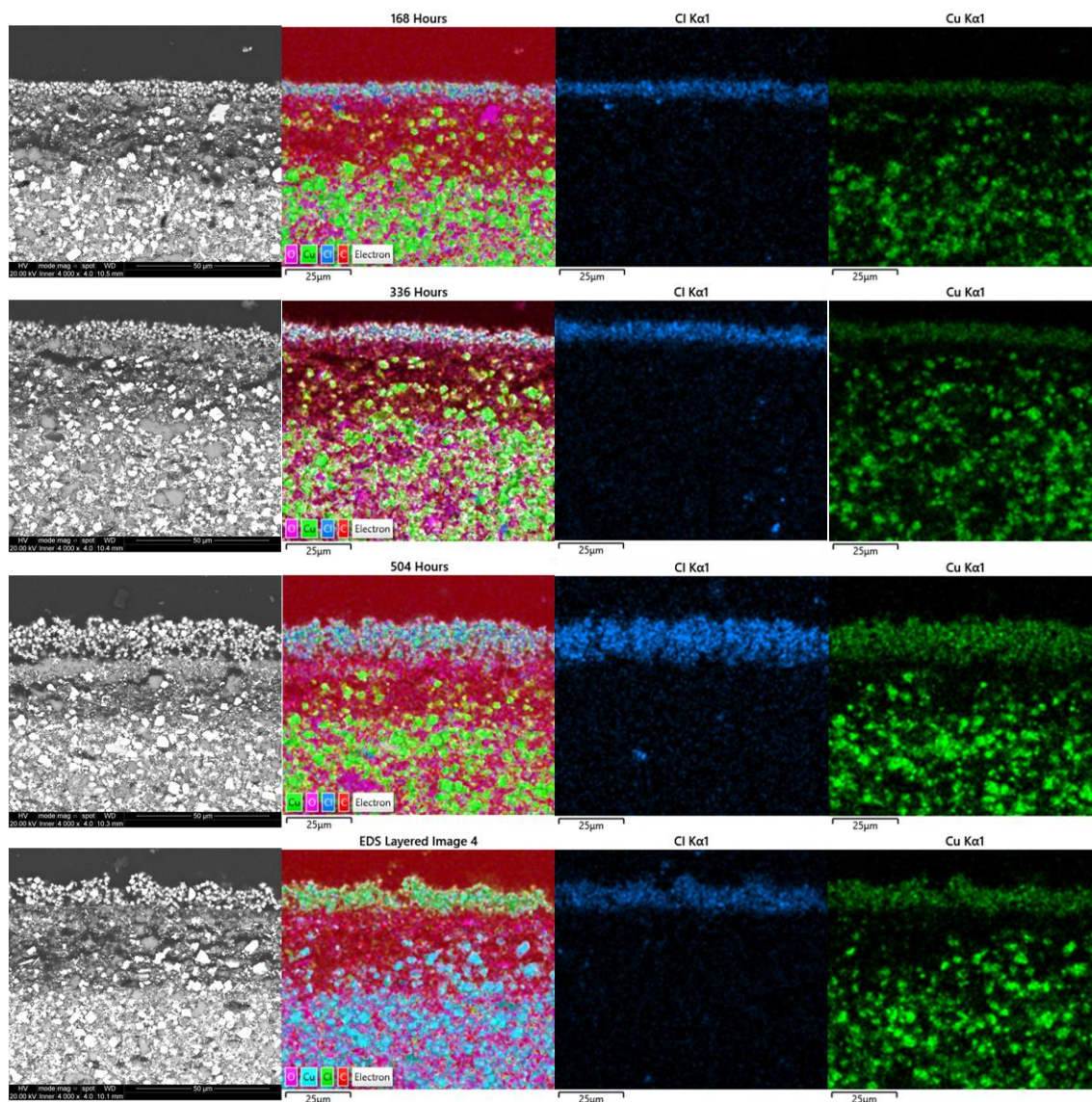
Spectrum	Element (wt%)								
Label	O	Al	Si	S	Cl	Ca	Fe	Cu	Zn
168 Hours	21.06	0.55	2.43	7.69	2.31	0.51	5.04	36.70	23.71
336 Hours	19.76	0.52	2.31	7.88	1.89	0.90	4.87	35.32	26.55
504 Hours	20.84	0.33	1.95	7.07	3.76	0.83	4.47	36.55	24.20
678 Hours	19.36	0.39	2.20	7.92	2.69	0.49	5.25	34.92	26.77

Figure 198 – BSE micrographs of the cross-section through the BQA 644 coating including an elemental composite image, chlorine and copper maps and the semi-quantitative EDX analysis of the mapped area after being exposed to the neutral 10% electrolyte at 25°C under different immersion times.

e. *30% Electrolyte*
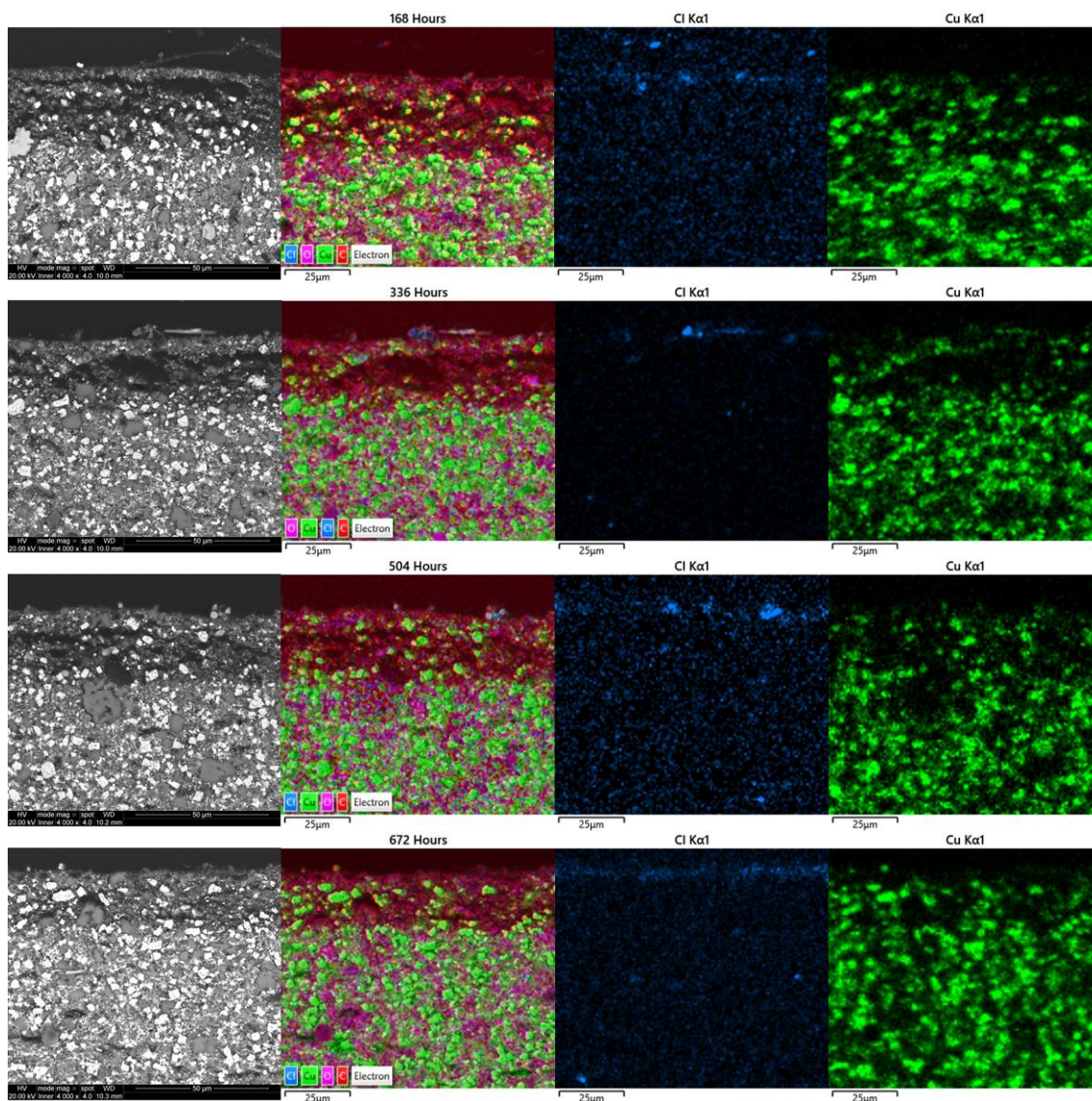
Spectrum Label	O	Al	Si	S	Cl	Ca	Fe	Cu	Zn
168 Hours	18.06	0.43	2.26	7.95	0.79	0.74	4.61	37.27	27.89
336 Hours	17.59	0.45	2.35	9.01	0.95	0.62	5.25	34.51	29.27
504 Hours	17.51	0.38	2.34	9.36	0.75	0.76	4.86	35.72	28.31
672 Hours	16.55	0.39	2.45	8.26	0.60	0.90	5.24	36.14	29.48

Figure 199 – BSE micrographs of the cross-section through the BQA 644 coating including an elemental composite image, chlorine and copper maps and the semi-quantitative EDX analysis of the mapped area after being exposed to the neutral 30% electrolyte at 25°C under different immersion times.

ii) BQA 644 – Immersion Cell – 45°C

a. 0% Electrolyte

Spectrum	Element (wt%)				
Label	O	Al	Si	Cl	Cu
168 Hours	20.01	0.47	4.94	1.18	73.39
336 Hours	18.18	0.91	6.74	0.96	73.21
504 Hours	18.22	0.71	5.29	1.04	74.74
672 Hours	18.61	0.64	6.06	0.94	73.75

Figure 200 – BSE micrographs of the cross-section through the BQA 644 coating including an elemental composite image, chlorine and copper maps and the semi-quantitative EDX analysis of the mapped area after being exposed to the neutral 0% electrolyte at 45°C under different immersion times.

[462]
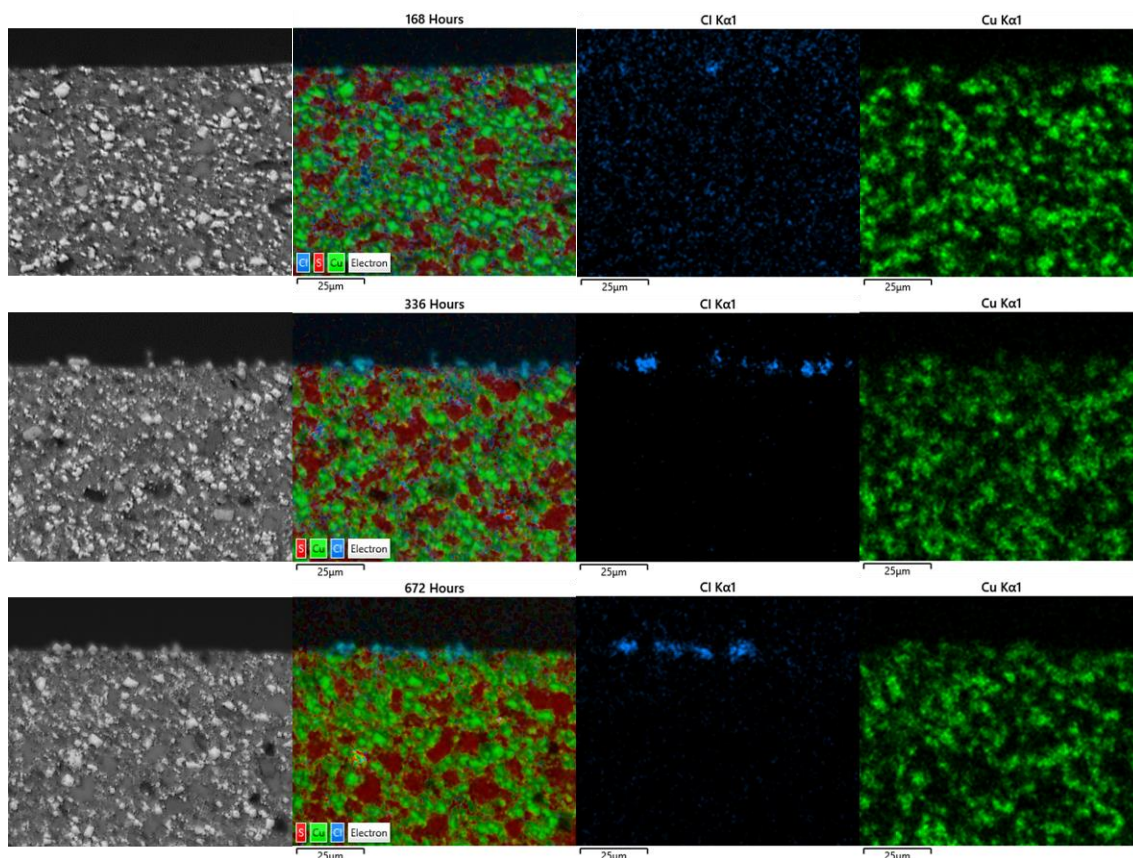
Spectrum Label	Element (wt%)								
	O	Al	Si	S	Cl	Ca	Fe	Cu	Zn
168 Hours	16.93	0.64	2.52	8.54	0.47	1.19	4.95	37.57	27.19
336 Hours	17.48	0.68	2.23	7.50	0.91	1.01	5.57	37.03	27.59
672 Hours	17.86	0.64	2.45	8.51	0.94	0.92	4.95	35.40	28.33

Figure 201 – BSE micrographs of the cross-section through the BQA 644 coating including an elemental composite image, chlorine and copper maps and the semi-quantitative EDX analysis of the mapped area after being exposed to the neutral 1% electrolyte at 45°C under different immersion times.
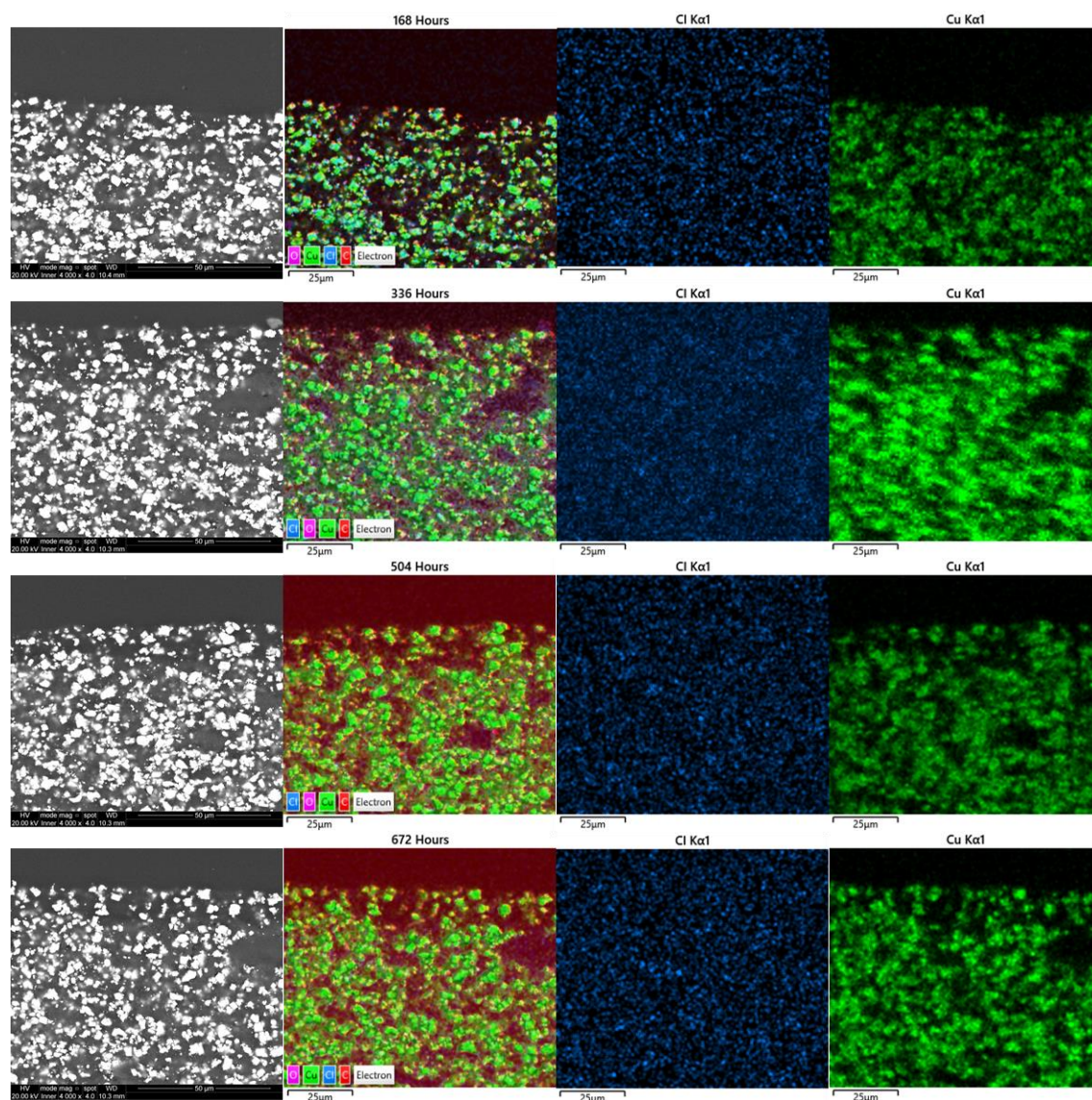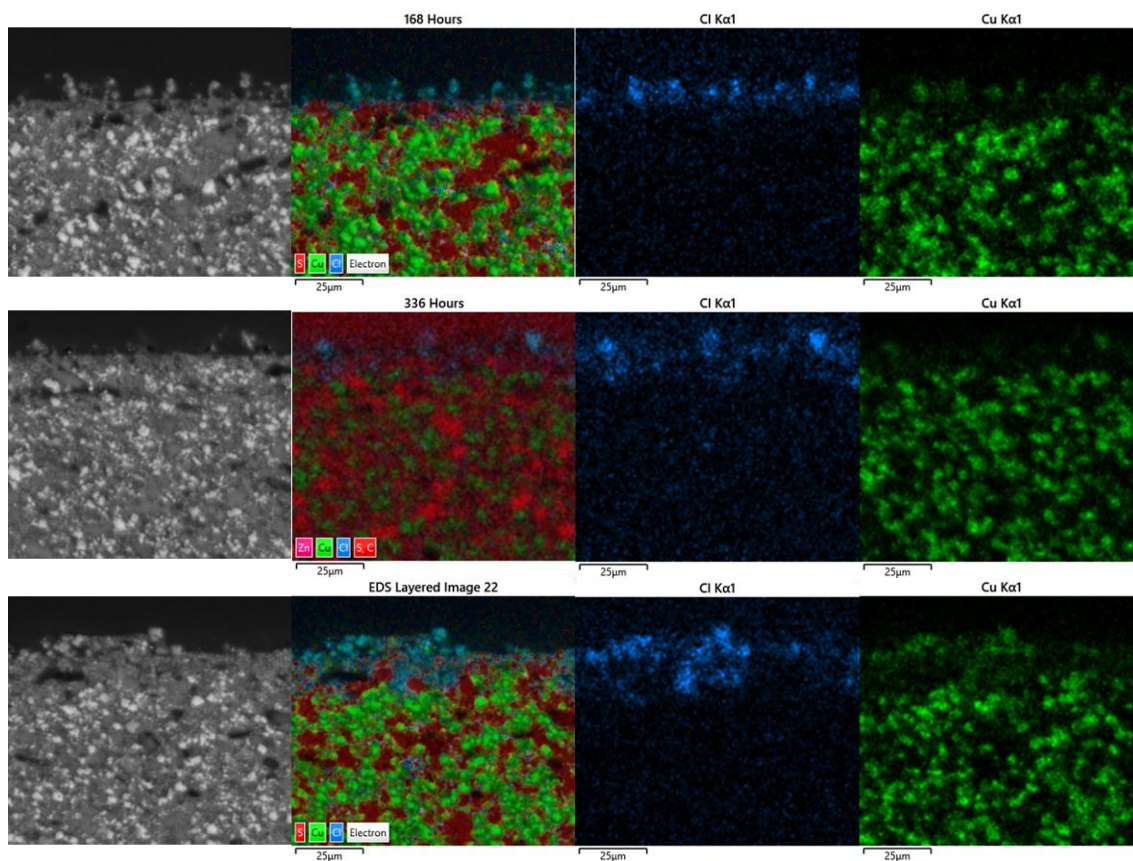
Spectrum	Element (wt%)								
Label	O	Al	Si	S	Cl	Ca	Fe	Cu	Zn
168 Hours	17.01	0.66	2.41	9.34	1.43	0.86	4.68	35.75	27.87
336 Hours	16.01	0.71	2.66	10.06	1.04	0.90	4.49	35.68	28.45
672 Hours	17.97	0.63	2.08	8.96	2.04	1.34	5.51	34.43	27.02

Figure 202 – BSE micrographs of the cross-section through the BQA 644 coating including an elemental composite image, chlorine and copper maps and the semi-quantitative EDX analysis of the mapped area after being exposed to the neutral 3.5% electrolyte at 45°C under different immersion times.

d.   10% Electrolyte
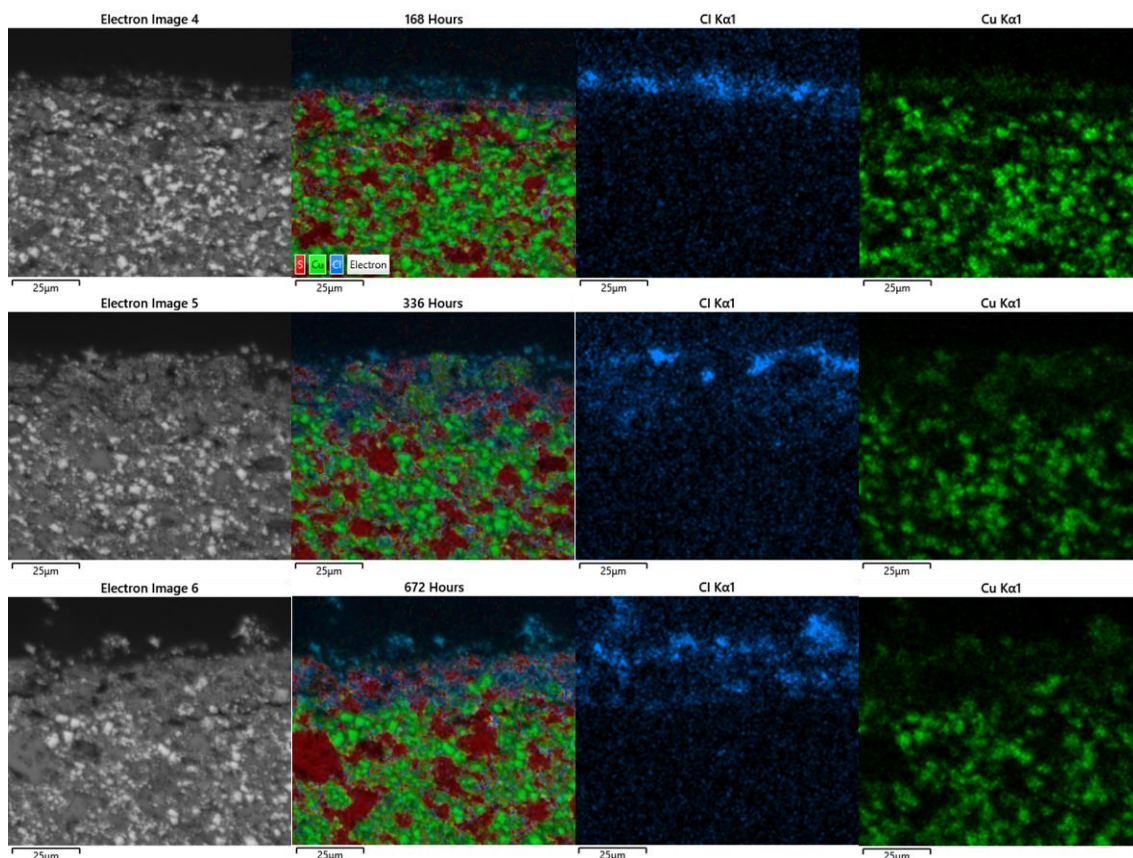
Spectrum	Element (wt%)								
Label	O	Al	Si	S	Cl	Ca	Fe	Cu	Zn
168 Hours	18.24	0.93	2.33	8.00	1.55	1.35	5.15	36.22	26.24
336 Hours	18.82	1.05	2.67	10.03	1.48	1.24	4.74	32.61	27.36
672 Hours	18.61	0.79	2.21	10.41	1.95	0.95	5.20	33.03	26.85

Figure 203 – BSE micrographs of the cross-section through the BQA 644 coating including an elemental composite image, chlorine and copper maps and the semi-quantitative EDX analysis of the mapped area after being exposed to the neutral 10% electrolyte at 45°C under different immersion times.

e. *30% Electrolyte*
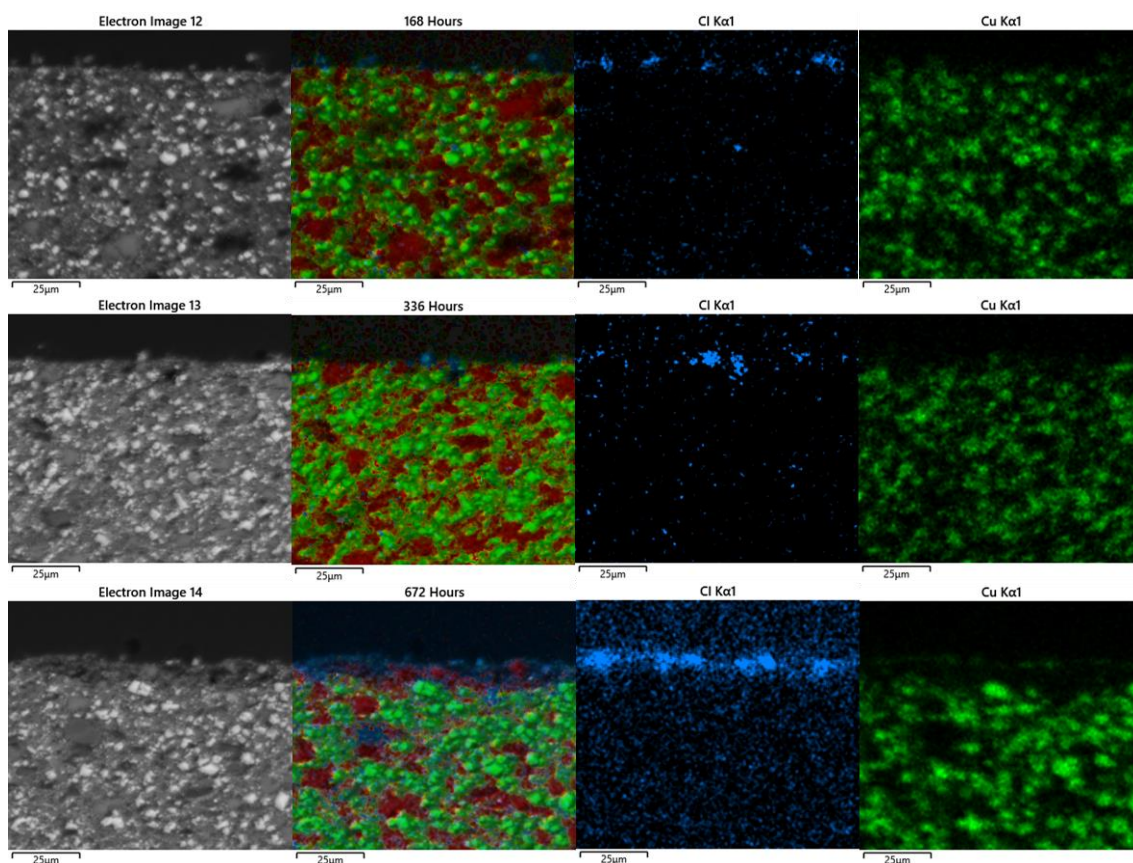
Spectrum	Element (wt%)								
Label	O	Al	Si	S	Cl	Ca	Fe	Cu	Zn
168 Hours	11.89	0.91	2.79	10.59	0.99	1.04	4.99	39.16	27.64
336 Hours	16.81	0.61	3.13	8.13	0.75	1.37	4.71	37.75	26.75
678 Hours	18.35	0.58	2.23	8.28	0.96	2.19	5.01	35.81	26.59

Figure 204 – BSE micrographs of the cross-section through the BQA 644 coating including an elemental composite image, chlorine and copper maps and the semi-quantitative EDX analysis of the mapped area after being exposed to the neutral 30% electrolyte at 45°C under different immersion times.

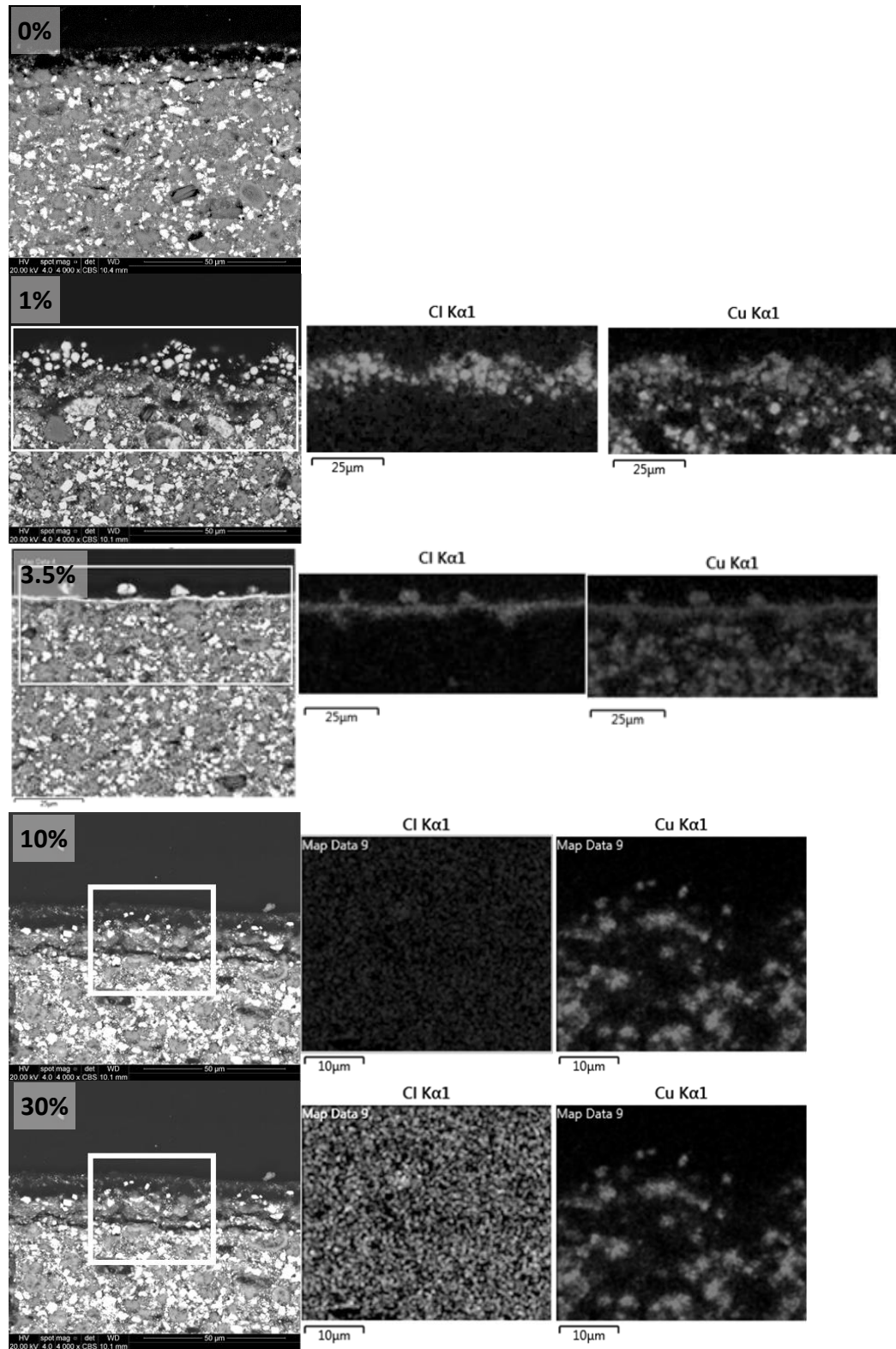iii) BQA 644 – Evaporation Cell – 25°C

Figure 205 – BSE micrographs of the cross-section through the BQA 644 coating after exposure to the different neutral electrolytes containing different concentrations of sodium chloride including the chlorine and copper elemental maps of the highlighted areas

[467]

iv) BQA 644 – Evaporation Cell – 45°C
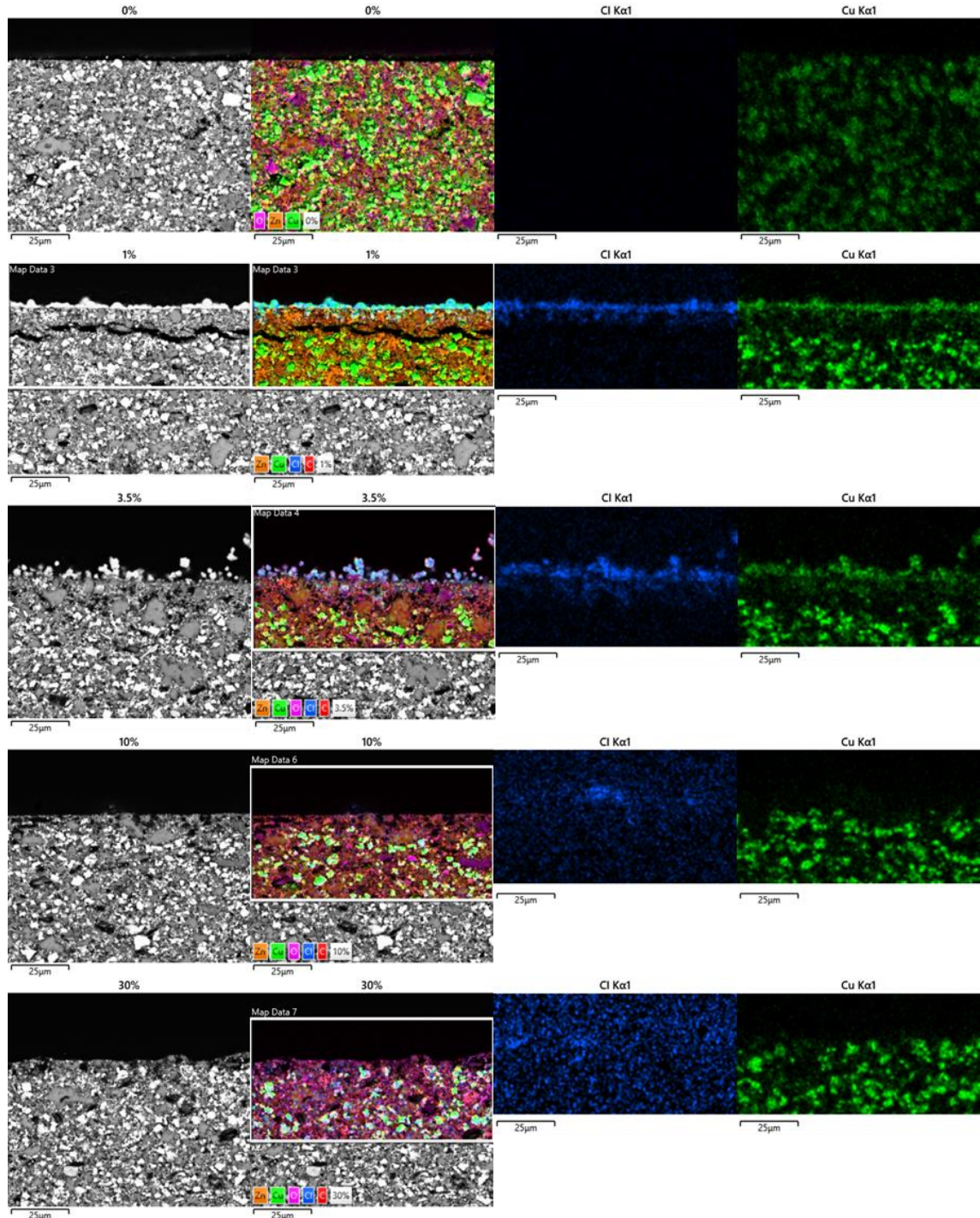
Spectrum	Element (wt%)								
Label	O	Al	Si	S	Cl	Ca	Fe	Cu	Zn
0%	19.63	0.65	2.60	8.44	0.46	0.55	5.31	35.08	27.28
1%	23.69	0.50	2.20	6.40	3.05	0.68	4.38	31.26	27.84
3.5%	26.38	0.40	1.78	11.41	4.53	1.21	4.40	25.65	24.23
10%	23.63	0.97	2.88	11.13	1.58	1.01	5.23	27.40	26.17
30%	22.62	0.54	2.28	9.92	1.30	0.84	4.52	30.43	27.54

Figure 206 – BSE micrographs and semi-quantitative EDX analysis of the surface of the BQA 644 coating exposed to the neutral electrolytes containing different sodium chloride concentrations at 45°C under evaporating conditions after the electrolyte had fully evaporated up to 408 hours.

[468]

a. *0% Electrolyte*
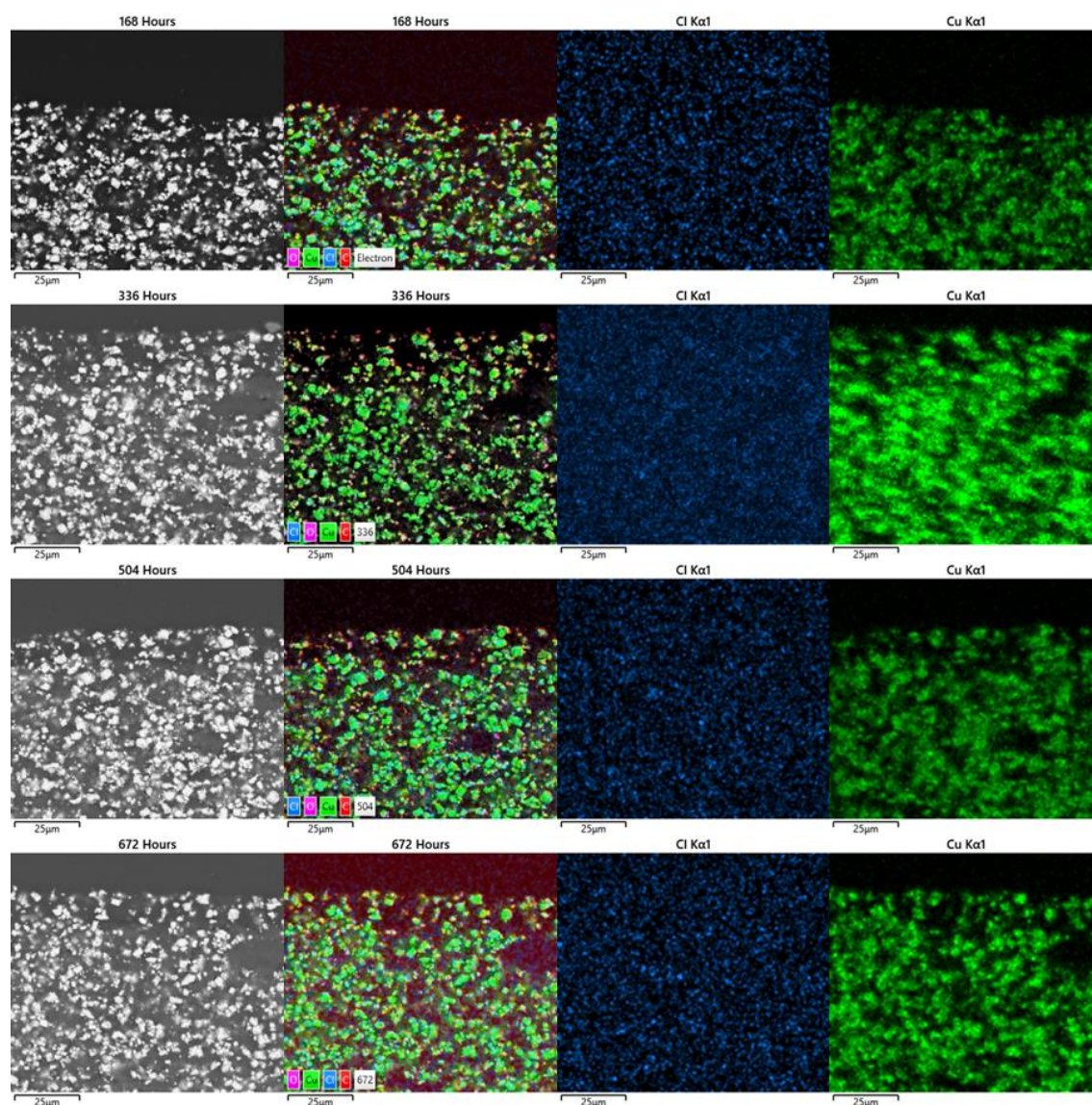
Spectrum	Element (wt%)				
Label	**O**	**Al**	**Si**	**Cl**	**Cu**
168 Hours	20.01	0.47	4.94	1.18	73.39
336 Hours	18.18	0.91	6.74	0.96	73.21
504 Hours	18.22	0.71	5.29	1.04	74.74
672 Hours	18.61	0.64	6.06	0.94	73.75

Figure 207 – BSE micrographs of the cross-section through the modified BQA 644 coating including an elemental composite image, chlorine and copper maps and the semi-quantitative EDX analysis of the mapped area after being exposed to the neutral 0% electrolyte at 25°C under different immersion times.

[469]

b.   1% Electrolyte
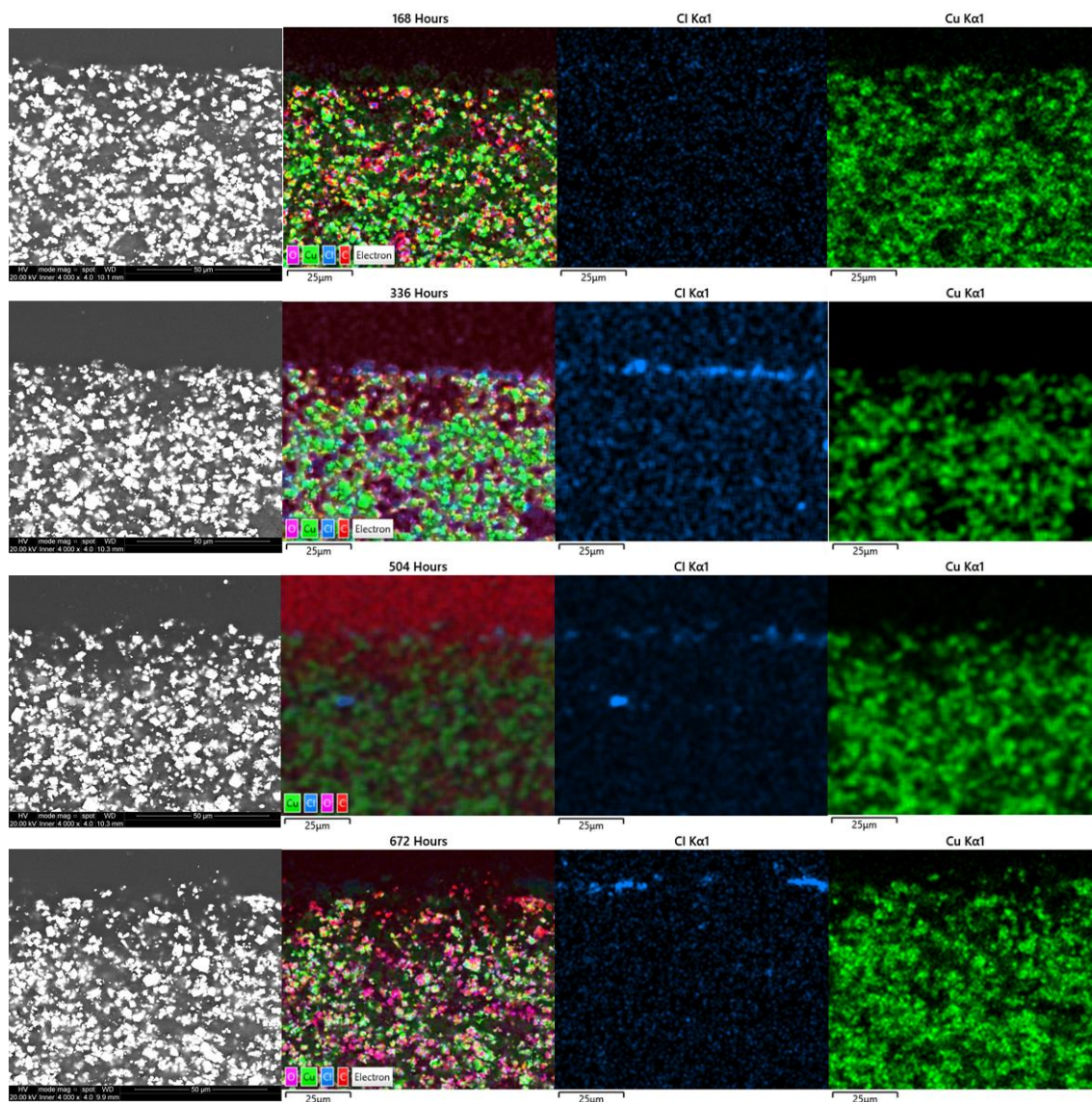
Spectrum	Element (wt%)				
Label	O	Al	Si	Cl	Cu
168 Hours	18.49	1.02	5.38	0.86	74.25
336 Hours	19.55	0.64	4.70	1.25	73.87
504 Hours	19.23	0.51	5.01	1.40	73.85
672 Hours	17.50	0.63	5.60	1.13	75.14

Figure 208 – BSE micrographs of the cross-section through the modified BQA 644 coating including an elemental composite image, chlorine and copper maps and the semi-quantitative EDX analysis of the mapped area after being exposed to the neutral 0% electrolyte at 25°C under different immersion times.
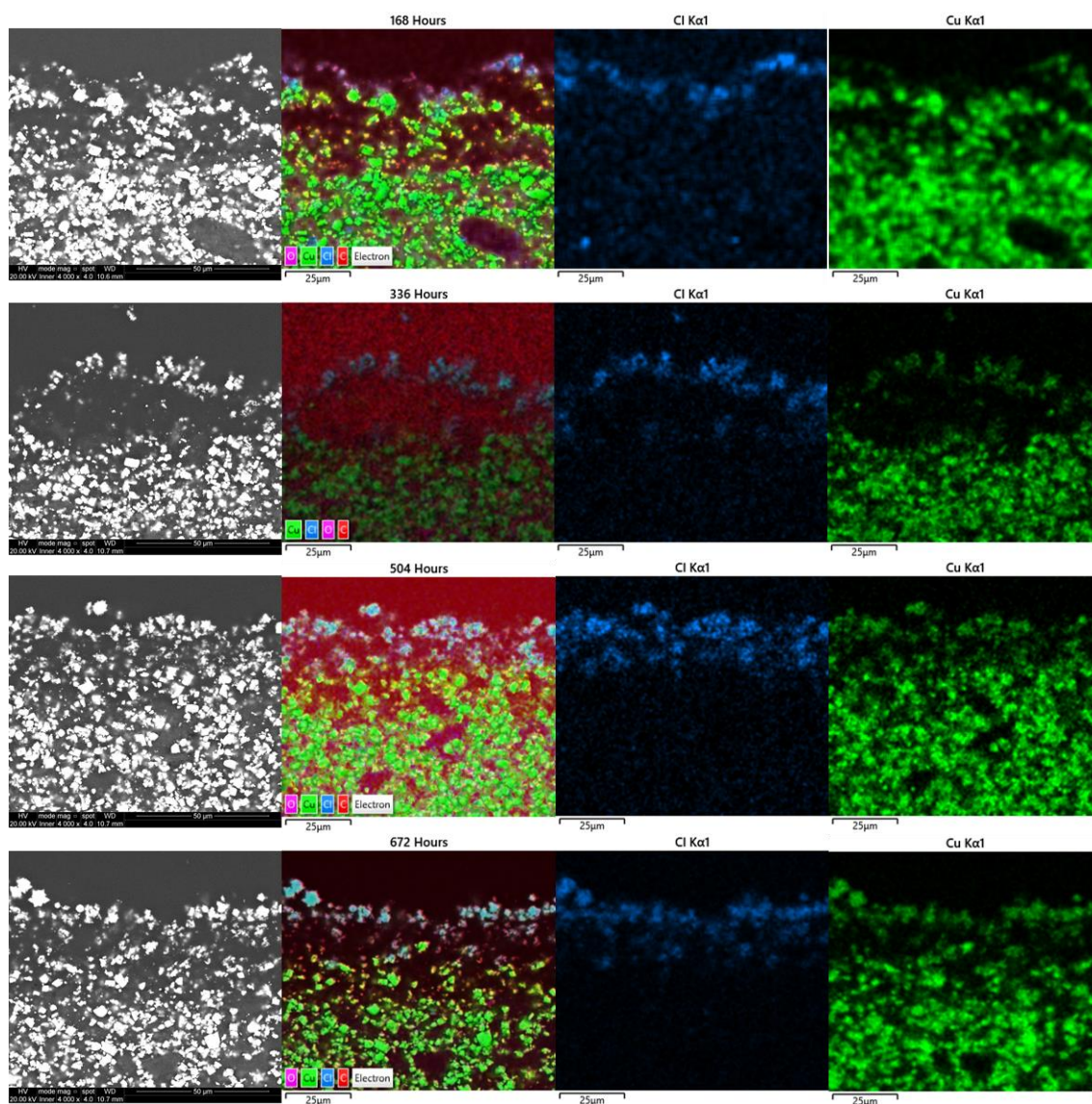
Spectrum Label	Element (wt%)					
	O	Al	Si	Cl	Ca	Cu
168 Hours	21.56	0.95	5.30	1.85	0.17	70.17
336 Hours	25.68	0.68	3.85	3.43	0.22	66.12
504 Hours	21.04	0.61	4.16	3.44	0.08	70.67
672 Hours	22.93	0.61	4.20	4.28	0.05	67.93

Figure 209 – BSE micrographs of the cross-section through the modified BQA 644 coating including an elemental composite image, chlorine and copper maps and the semi-quantitative EDX analysis of the mapped area after being exposed to the neutral 1% electrolyte at 25°C under different immersion times.

[471]
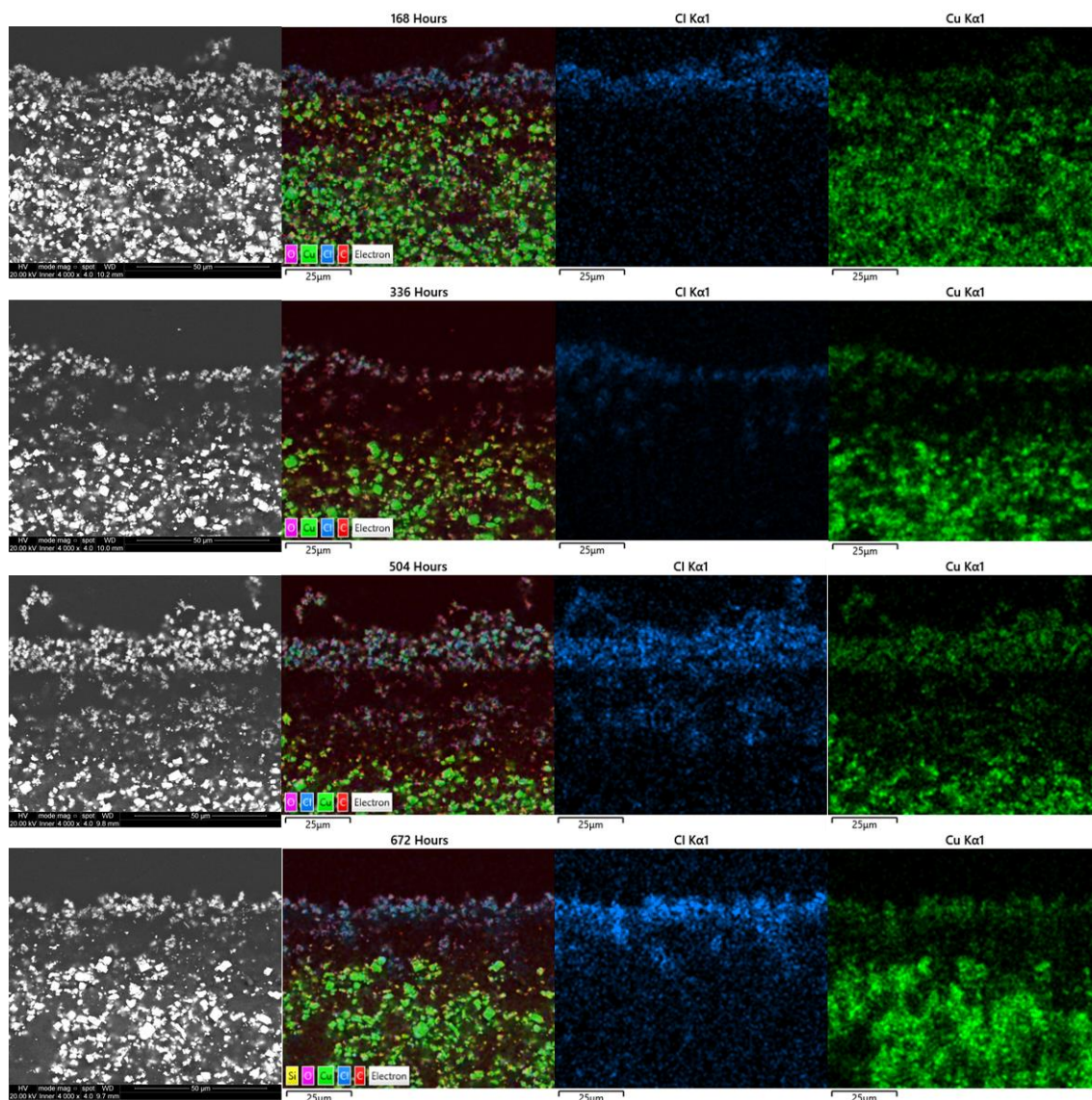
Spectrum	Element (wt%)				
Label	**O**	**Al**	**Si**	**Cl**	**Cu**
168 Hours	19.98	0.69	5.57	2.75	71.01
336 Hours	24.73	0.78	5.03	3.95	65.51
504 Hours	26.73	0.46	3.33	8.98	60.50
672 Hours	23.62	0.74	5.57	4.06	66.02

Figure 210 – BSE micrographs of the cross-section through the modified BQA 644 coating including an elemental composite image, chlorine and copper maps and the semi-quantitative EDX analysis of the mapped area after being exposed to the neutral 10% electrolyte at 25°C under different immersion times.

e.   30% Electrolyte
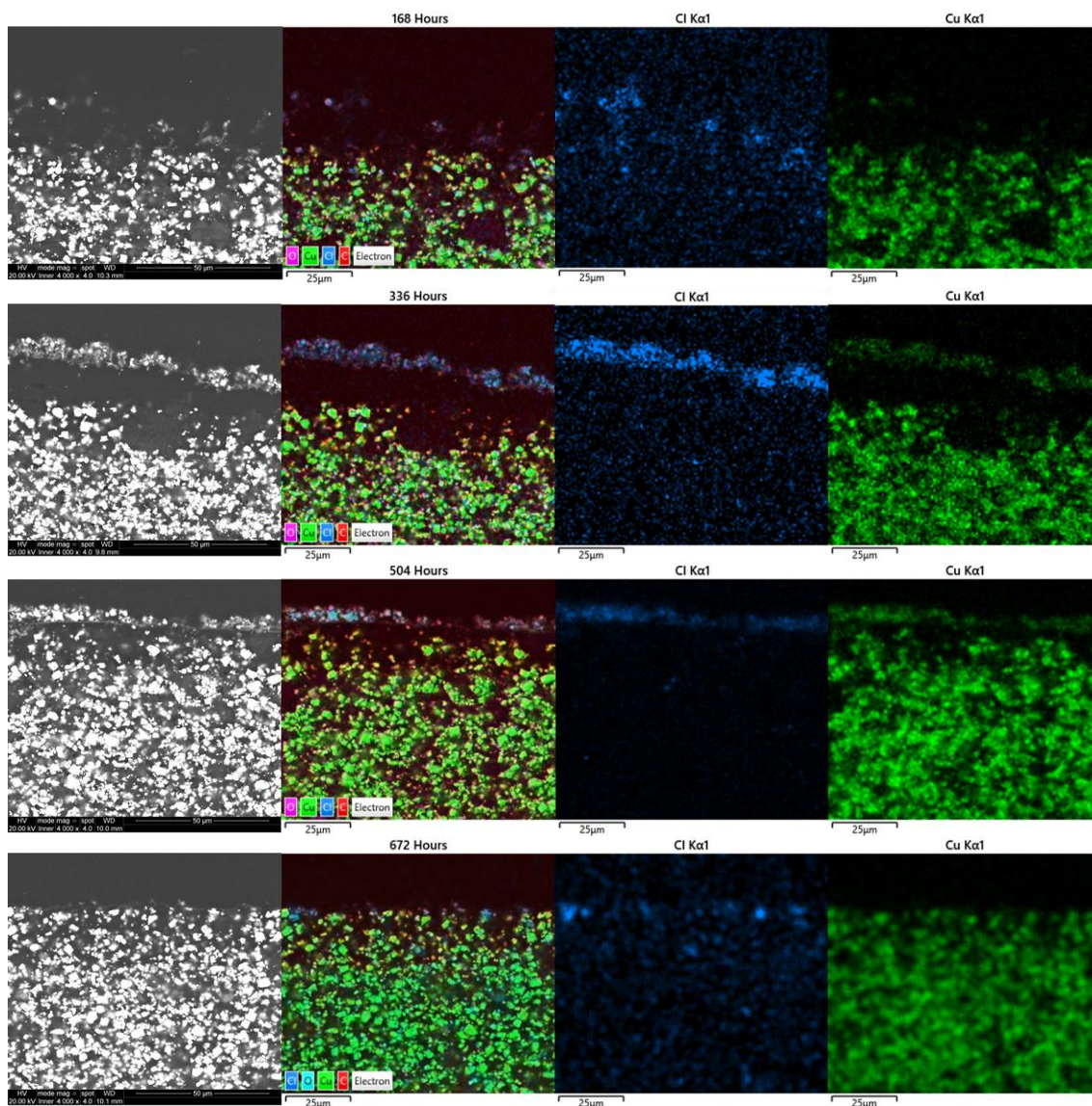
Spectrum Label	Element (wt%)					
	O	Al	Si	Cl	Ca	Cu
168 Hours	27.61	1.02	5.82	2.22	0.20	63.13
336 Hours	23.93	0.83	5.47	2.62	0.24	66.90
504 Hours	20.56	0.73	5.73	1.99	0.21	70.78
672 Hours	21.54	0.69	5.38	1.19	0.34	70.86

Figure 211 – BSE micrographs of the cross-section through the modified BQA 644 coating including an elemental composite image, chlorine and copper maps and the semi-quantitative EDX analysis of the mapped area after being exposed to the neutral 30% electrolyte at 25°C under different immersion times.

vi) Modified BQA 644 – Immersion Cell – 45°C
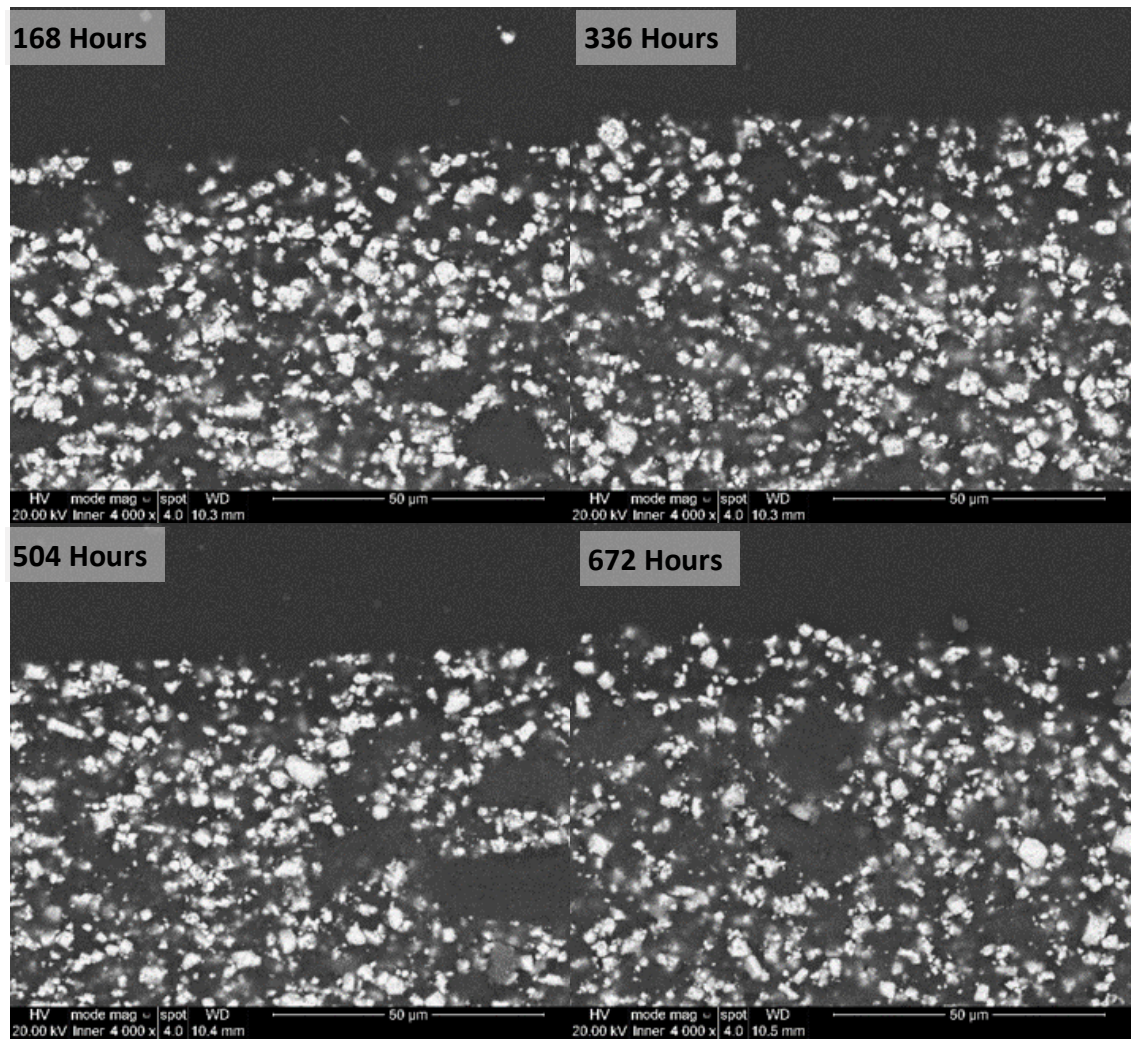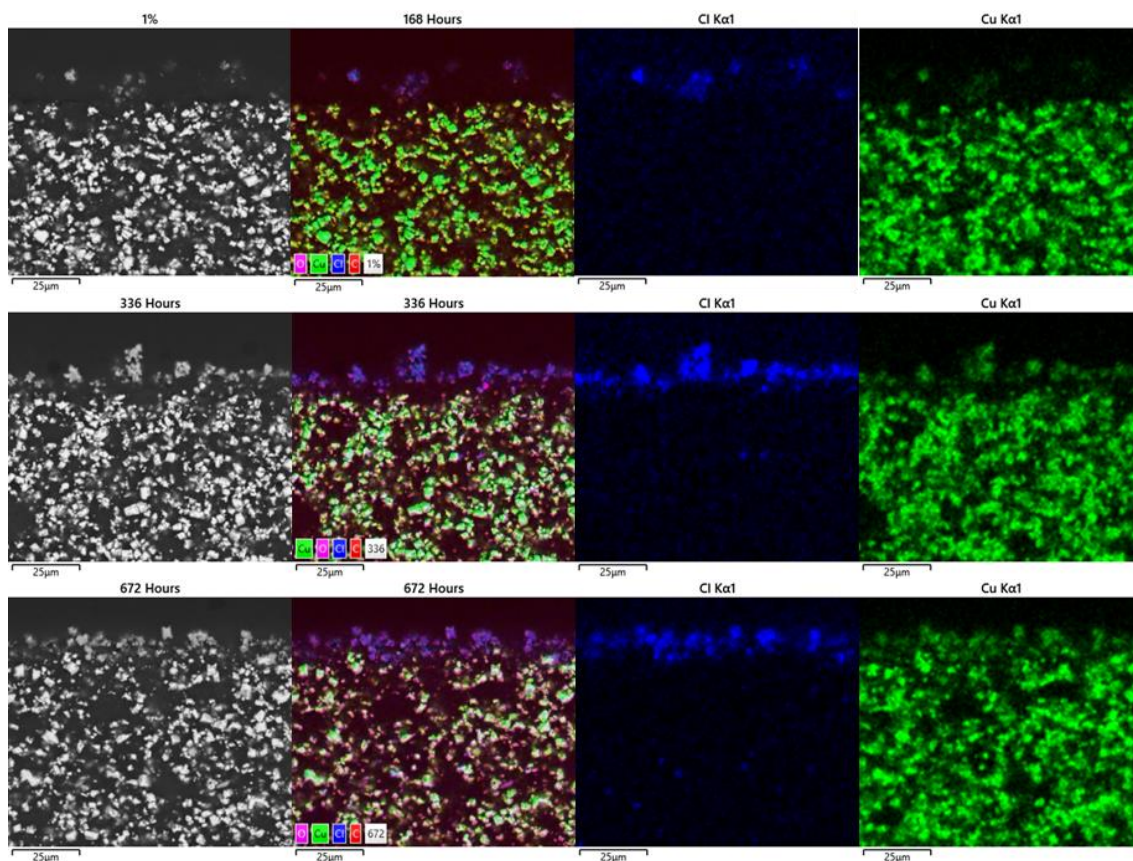
a. *0% Electrolyte*

Figure 212 – BSE micrographs of the cross-section through the modified BQA 644 coating after being exposed to the neutral 0% electrolyte at 25°C under different immersion times.

b. *1% Electrolyte*

Spectrum Label	Element (wt%)						
	O	Al	Si	P	S	Cl	Cu
168 Hours	19.06	0.59	4.70	0.22	0.28	1.53	73.63
336 Hours	18.92	0.50	4.36	0.21	0.27	2.41	73.33
672 Hours	19.37	0.70	4.93	0.11	0.93	2.63	71.33

Figure 213 – BSE micrographs of the cross-section through the modified BQA 644 coating including an elemental composite image, chlorine and copper maps and the semi-quantitative EDX analysis of the mapped area after being exposed to the neutral 1% electrolyte at 45°C under different immersion times.

[475]

c.   3.5% Electrolyte
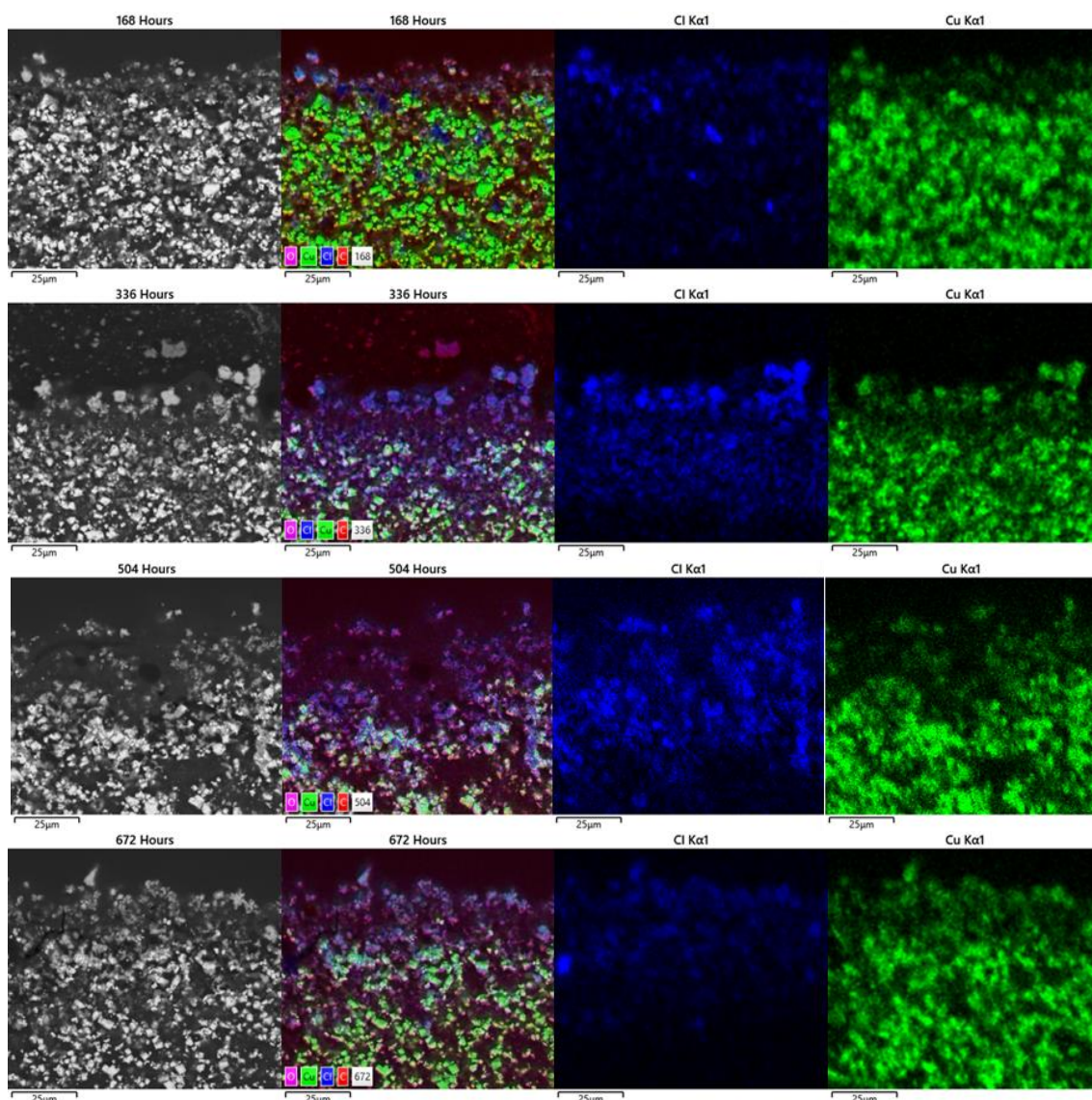
Spectrum	Element (wt%)					
Label	O	Al	Si	S	Cl	Cu
168 Hours	17.83	0.41	3.26	0.81	4.43	73.26
336 Hours	21.02	0.47	3.61	0.62	7.10	67.19
504 Hours	21.84	0.52	2.73	0.74	7.63	66.54
672 Hours	20.71	0.49	3.22	0.76	7.21	67.60

Figure 214 – BSE micrographs of the cross-section through the modified BQA 644 coating including an elemental composite image, chlorine and copper maps and the semi-quantitative EDX analysis of the mapped area after being exposed to the neutral 3.5% electrolyte at 45°C under different immersion times.

[476]

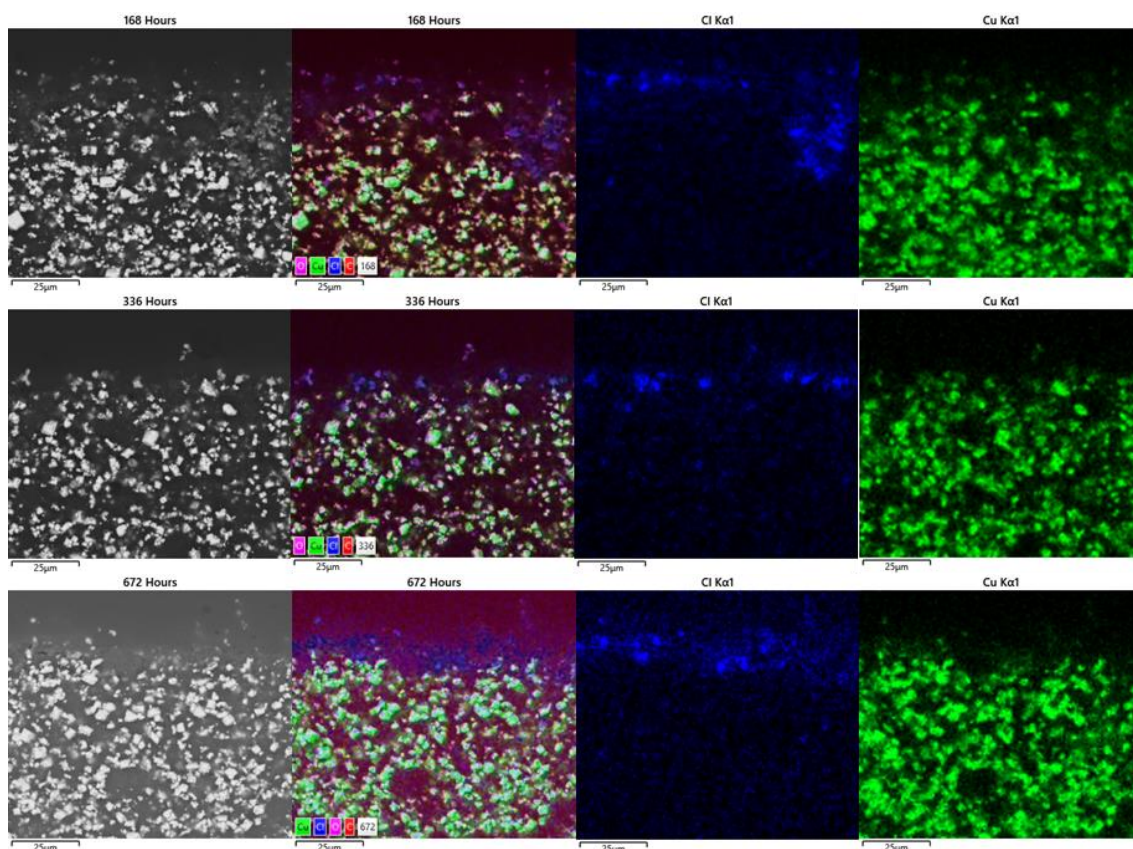| Spectrum	Element (wt%)					
Label	O	Al	Si	S	Cl	Cu
168 Hours	18.70	0.77	5.47	0.23	2.85	71.98
336 Hours	20.21	0.76	4.78	0.36	3.44	70.45
62 Hours	17.13	0.69	5.15	0.21	2.06	74.78

Figure 215 – BSE micrographs of the cross-section through the modified BQA 644 coating including an elemental composite image, chlorine and copper maps and the semi-quantitative EDX analysis of the mapped area after being exposed to the neutral 10% electrolyte at 45°C under different immersion times.
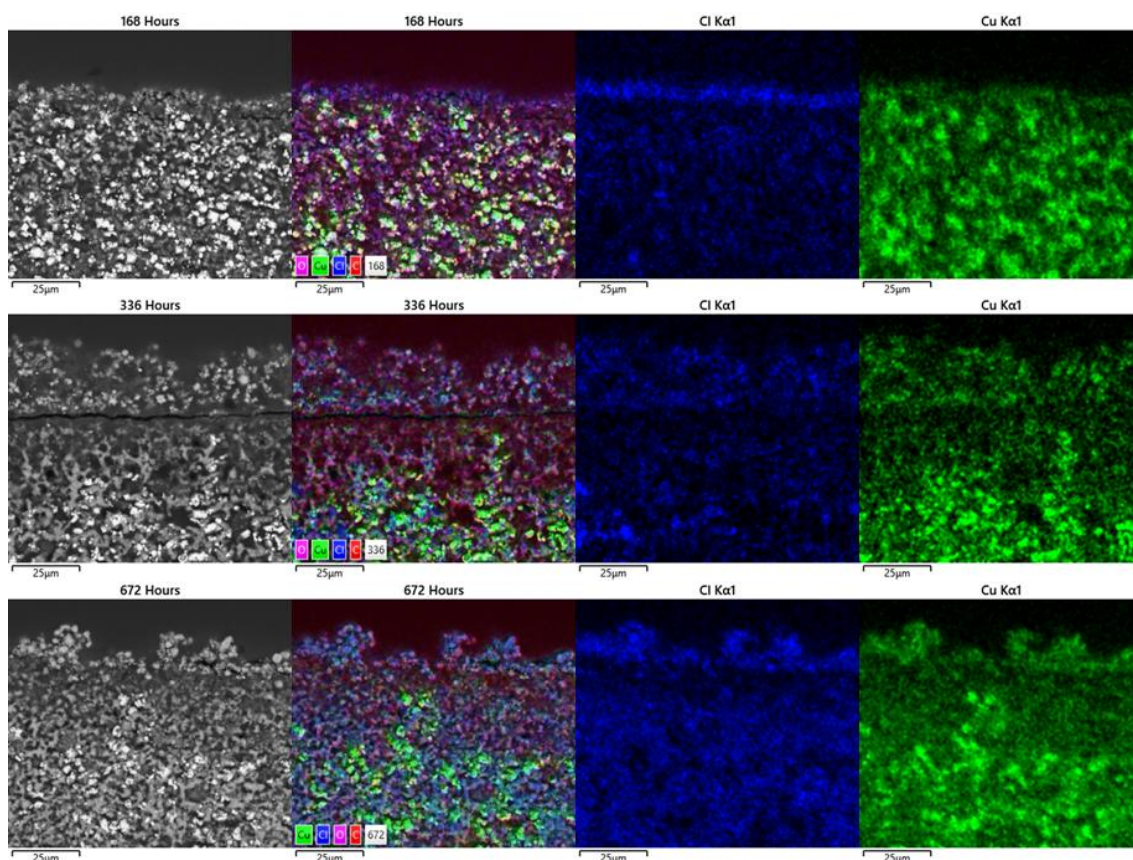
e. *30% Electrolyte*

Spectrum Label	Element (wt%)					
	O	**Al**	**Si**	**S**	**Cl**	**Cu**
168 Hours	21.05	0.55	4.96	0.18	4.86	68.40
336 Hours	26.31	0.52	4.97	0.37	10.62	57.22
672 Hours	23.75	0.41	3.63	0.38	10.88	60.94

Figure 216 – BSE micrographs of the cross-section through the modified BQA 644 coating including an elemental composite image, chlorine and copper maps and the semi-quantitative EDX analysis of the mapped area after being exposed to the neutral 30% electrolyte at 45°C under different immersion times.
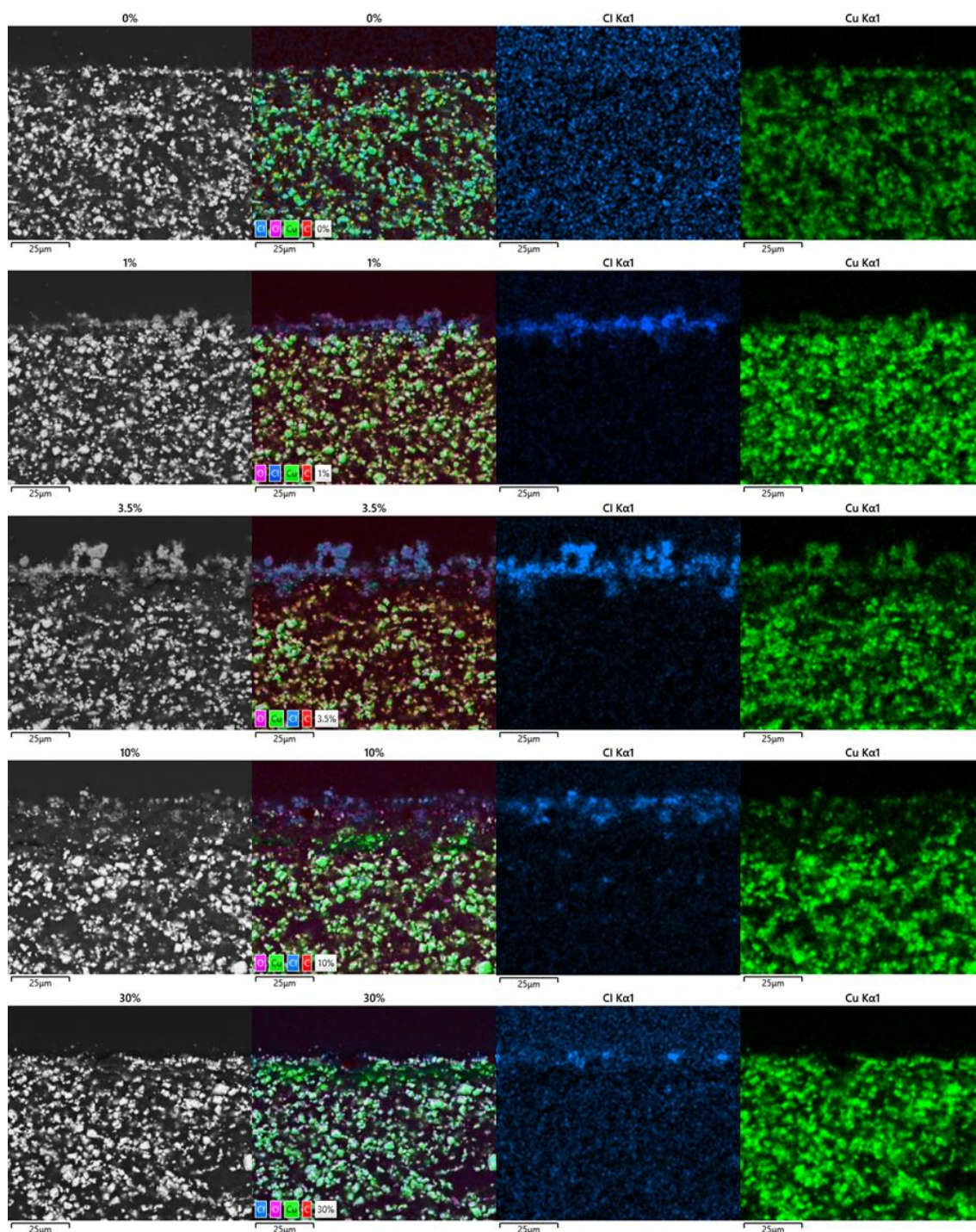
vii) Modified BQA 644 – Evaporation Cell – 25°C

Spectrum	Element (wt%)					
Label	O	Al	Si	S	Cl	Cu
0%	16.72	0.66	5.67	0.22	0.88	75.85
1%	17.06	0.53	4.18	0.20	2.12	75.90
3.5%	18.20	0.65	4.27	0.24	3.80	72.84
10%	17.32	0.67	4.96	0.21	2.47	74.37
30%	15.50	0.68	4.96	0.24	1.18	77.45

Figure 217 – BSE micrographs and semi-quantitative EDX analysis of the surface of the BQA 644 coating exposed to the neutral electrolytes containing different sodium chloride concentrations at 45°C under evaporating conditions after the electrolyte had fully evaporated up to 672 hours.

[479]

viii) Modified BQA 644 – Evaporation Cell – 45°C
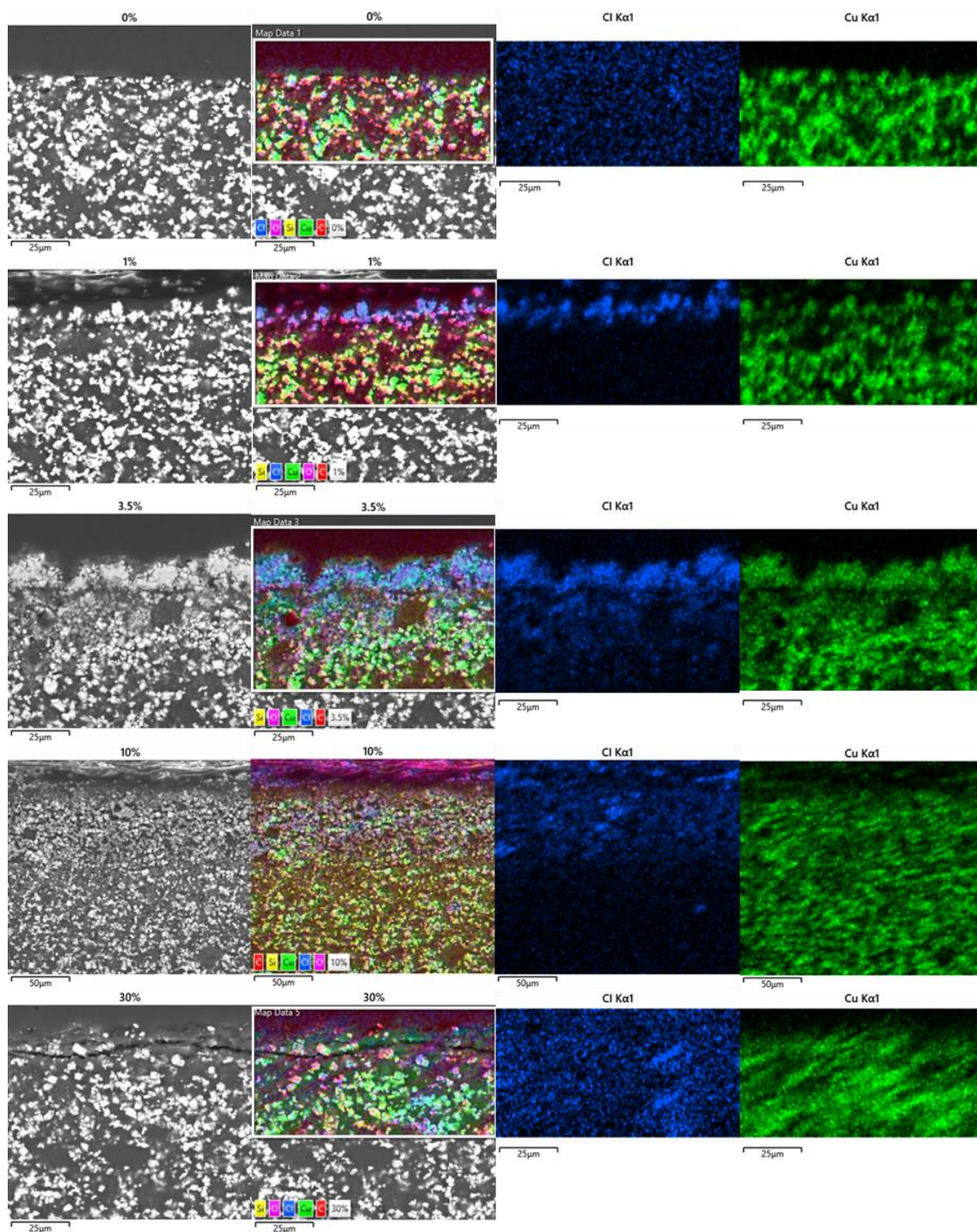
Spectrum Label	Element (wt%)					
	O	Al	Si	S	Cl	Cu
0%	18.23	0.54	5.31	0.20	1.30	74.41
1%	23.42	0.70	4.88	0.15	4.07	66.78
3.5%	23.20	0.57	3.64	0.26	8.68	63.65
10%	23.57	0.67	6.12	0.23	3.69	65.72
30%	19.52	0.70	5.25	0.46	2.66	71.41

Figure 218 – BSE micrographs and semi-quantitative EDX analysis of the surface of the BQA 644 coating exposed to the neutral electrolytes containing different sodium chloride concentrations at 45°C under evaporating conditions after the electrolyte had fully evaporated up to 408 hours.

[480]

Appendix 11 – SEM Analysis Of Salt Spray Tested Coatings

a) BQA 644 – Salt spray testing
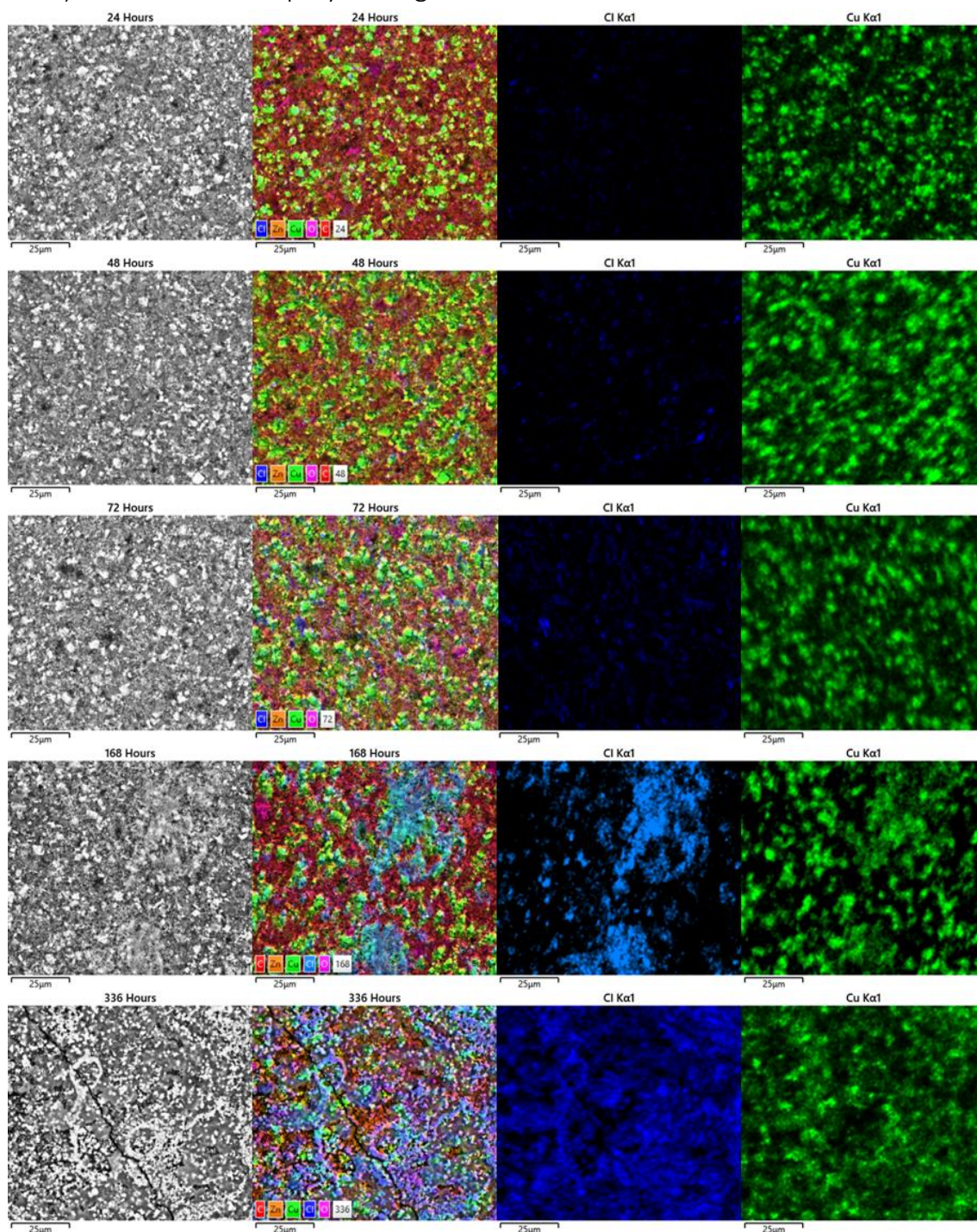
Spectrum	Element (wt%)								
Label	O	Al	Si	S	Cl	Ca	Fe	Cu	Zn
24 hours	16.98	0.58	2.86	7.36	0.47	1.06	5.82	32.62	32.24
48 Hours	17.79	0.51	2.75	7.83	0.71	0.75	5.68	32.53	31.45
72 Hours	17.01	0.41	2.51	7.26	1.05	0.56	5.77	33.22	32.22
168 Hours	17.09	0.40	1.62	6.22	2.83	0.30	5.45	34.77	31.32
336 Hours	19.42	0.24	0.84	4.36	6.95	0.26	4.27	38.48	25.18

Figure 219 – BSE micrographs and semi-quantitative EDX analysis of the surface of the BQA 644 coating exposed to the neutral salt spray environment after different immersion times.

[481]

b) Modified BQA 644 – Salt Spray Testing
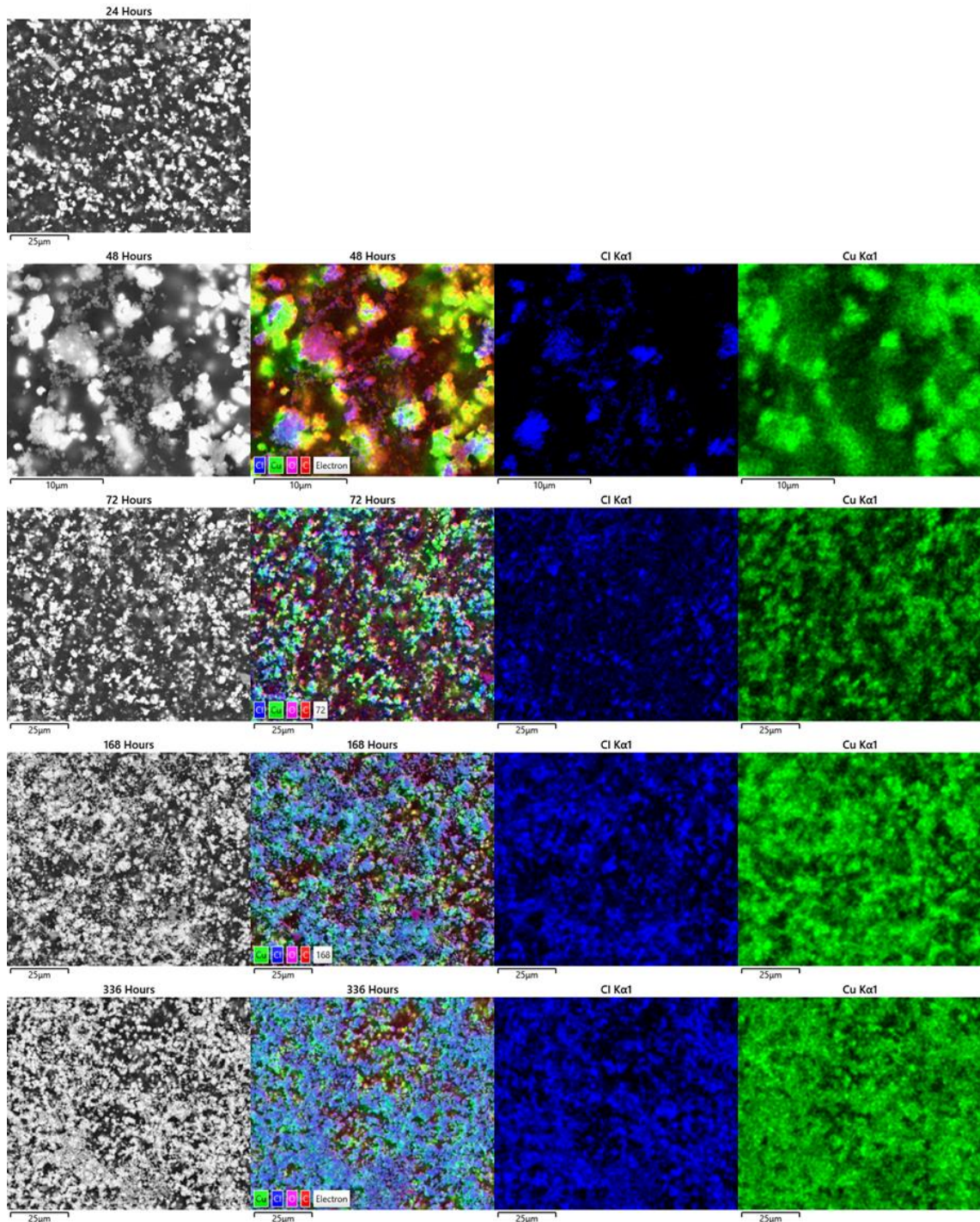
Spectrum	Element (wt%)						
Label	O	Al	Si	S	Cl	Ca	Cu
24 Hours	16.72	0.99	5.86	0.09	1.65	0.12	74.57
48 Hours	16.99	0.62	4.15	0.06	2.84	0.17	75.17
72 Hours	17.67	0.61	3.71	0.12	3.33	0.25	74.30
168 Hours	19.91	0.40	1.75	0.06	7.58	0.27	70.02
336 Hours	21.39	0.30	1.37	0.08	9.91	0.19	66.75

Figure 220 – BSE micrographs and semi-quantitative EDX analysis of the surface of the modified BQA 644 coating exposed to the neutral salt spray environment after different immersion times.
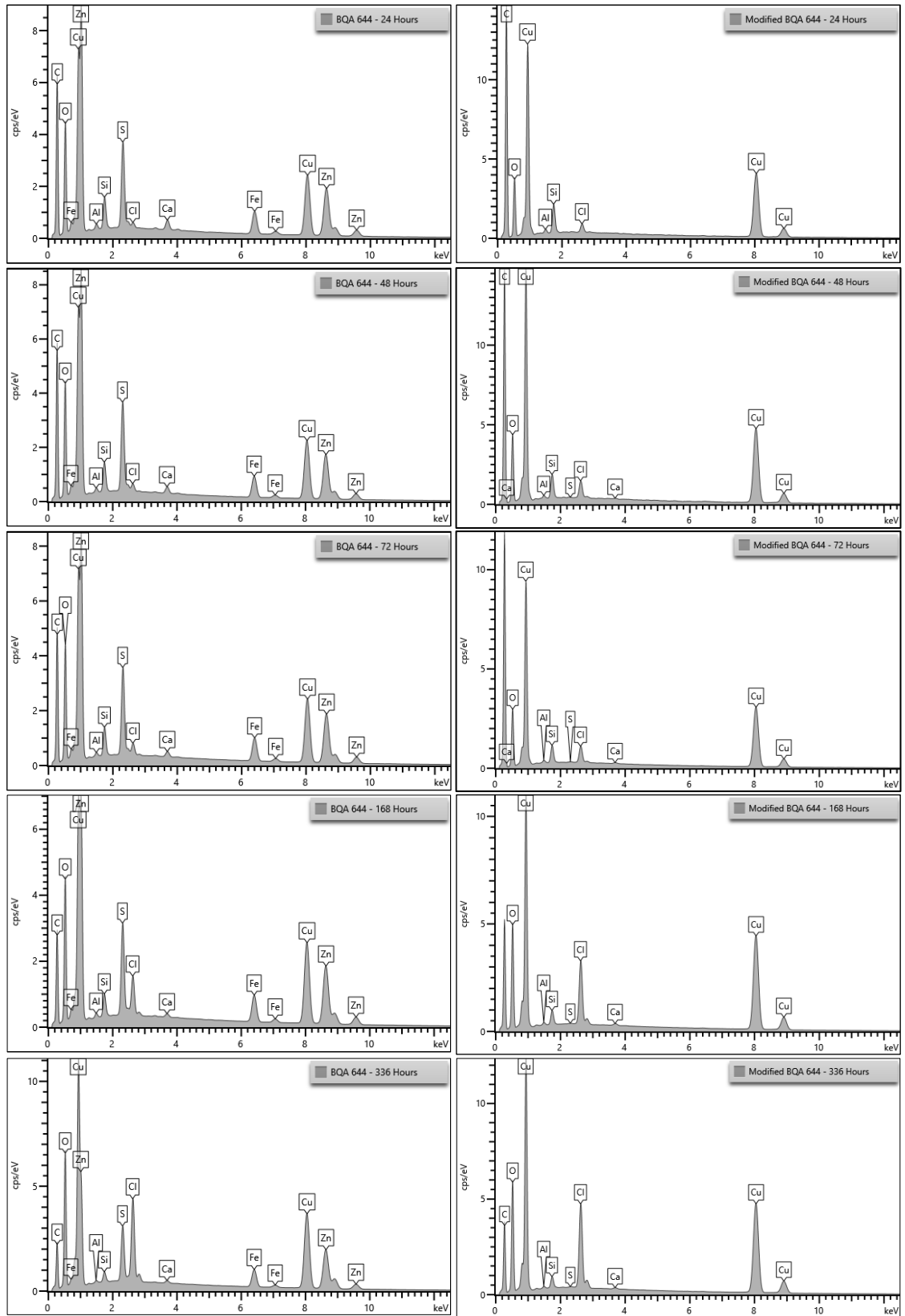
[482]

c) Salt Spray Test EDX Spectra

Figure 221 – EDX spectra of the surface of the BQA 644 and modified BQA 644 coatings following the salt spray testing after different exposure times.

[483]

Appendix 12 – Pourbaix Diagram Software

Two pieces of software were identified to aid in construction of the Pourbaix diagrams for the Copper—Cl—H_2O system MEDUSA (Make Equilibrium Diagrams Using Sophisticated Algorithms) with the associated database HYDRA (Hydrochemical Equilibrium Constant Database) (Puigdomenech, 2015) and HSC Chemistry® version 6.0 (Roine, 2006). Both software packages have been widely referenced in a range of peer review articles listed in (Outotec, 2019) for the HSC software and in (scholar.google.com, 2020) for the MEDUSA software. While both packages produced similar Pourbaix diagrams the HSC software offered greater flexibility in terms of the temperature ranges and was therefore selected to generate the Pourbaix diagrams.